Grupo FQM103

Espectroscopía y Estructura Molecular

2019

TESIS DOCTORAL

Daniel Aranda Ruiz

Tesis Doctoral

ESPECTROSCOPÍA COMPUTACIONAL DE SISTEMAS COMPLEJOS: SUPERFICIES METAL-MOLÉCULA Y MOLÉCULAS SEMIRRÍGIDAS

Daniel Aranda Ruiz

Directores:

Isabel López-Tocón

Francisco José Ávila Ferrer

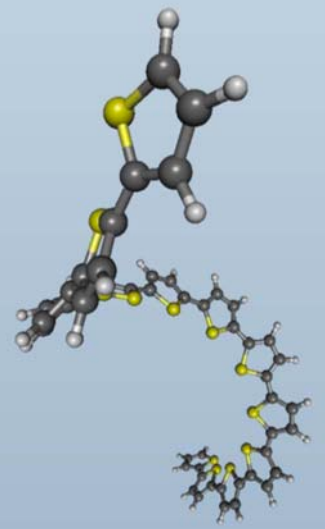

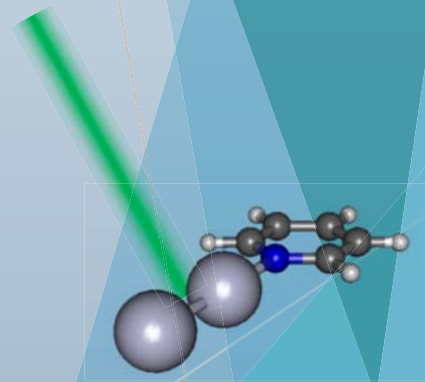

Universidad de Málaga

Facultad de Ciencias

Programa de Doctorado

"Química y Tecnologías Químicas. Materiales y Nanotecnología"

2019

AUTOR: Daniel Aranda Ruiz

http://orcid.org/0000-0003-0747-6266

EDITA: Publicaciones y Divulgación Científica. Universidad de Málaga

UNIVERSIDAD DE MÁLAGA

DEPARTAMENTO DE QUÍMICA FÍSICA,
FACULTAD DE CIENCIAS, CAMPUS DE
TEATINOS, 29071 MÁLAGA, ESPAÑA.

Telf: +34 952 13 1865- FAX: +34 952- 132000

DON JUAN CARLOS OTERO FERNÁNDEZ DE MOLINA, CATEDRÁTICO DE UNIVERSIDAD Y DIRECTOR DEL DEPARTAMENTO DE QUÍMICA FÍSICA DE LA UNIVERSIDAD DE MÁLAGA.

CERTIFICA: que la Tesis Doctoral titulada "ESPECTROSCOPÍA COMPUTACIONAL DE SISTEMAS COMPLEJOS: SUPERFICIES METAL-MOLÉCULA Y MOLÉCULAS SEMIRRÍGIDAS" que presenta D. Daniel Aranda Ruiz para optar al título de Doctor en Ciencias Químicas, ha sido realizada en este Departamento bajo la dirección de los Drs. Dª Isabel López Tocón y D. Francisco José Ávila Ferrer, profesores del área de Química Física.

Y para que así conste a los efectos oportunos, firma el presente certificado en Málaga a 16 de Enero de 2019.

Fdo: Juan C. Otero Fernández de Molina

UNIVERSIDAD DE MÁLAGA

DEPARTAMENTO DE QUÍMICA FÍSICA,
FACULTAD DE CIENCIAS, CAMPUS DE
TEATINOS, 29071 MÁLAGA, ESPAÑA.

Telf: +34 952 13 1865- FAX: +34 952- 132000

DOÑA ISABEL LÓPEZ TOCÓN Y DON FRANCISCO JOSÉ ÁVILA FERRER, PROFESORES DEL DEPARTAMENTO DE QUÍMICA FÍSICA DE LA UNIVERSIDAD DE MÁLAGA.

CERTIFICAN: que la Tesis Doctoral titulada "ESPECTROSCOPÍA COMPUTACIONAL DE SISTEMAS COMPLEJOS: SUPERFICIES METAL-MOLÉCULA Y MOLÉCULAS SEMIRRÍGIDAS" que presenta D. Daniel Aranda Ruiz para optar al título de Doctor en Ciencias Químicas, ha sido realizada en el Departamento de Química Física de la Universidad de Málaga bajo su dirección.

Y para que así conste a los efectos oportunos, firma el presente certificado en Málaga a 16 de Enero de 2019.

Fdo: Isabel López Tocón

Fdo: Francisco José Ávila Ferrer

Espectroscopía computacional de sistemas complejos: superficies metal-molécula y moléculas semirrígidas.

Computational spectroscopy of complex systems: metal-molecule surfaces and semirigid molecules.

TESIS DOCTORAL

Daniel Aranda Ruiz

Dirigido por:

Francisco José Ávila Ferrer

Isabel López Tocón

UNIVERSIDAD DE MÁLAGA

Veritatis simplex

oratio est.

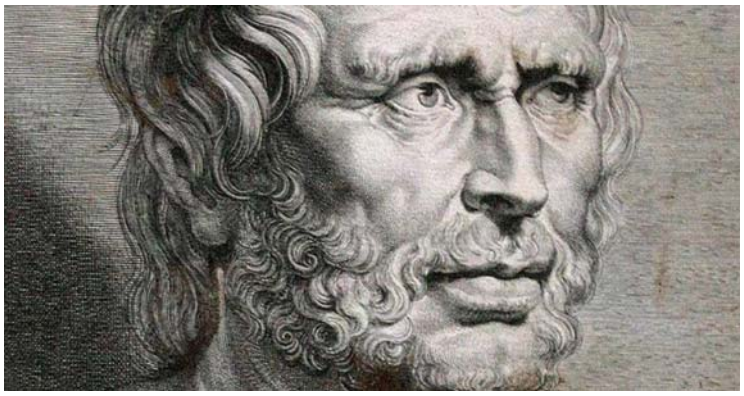

Homines dum docent,

discunt.

Agradecimientos

La presente tesis doctoral no habría sido posible sin la ayuda y el apoyo de muchas personas, a las cual quiero mostrar mi agradecimiento en las siguientes líneas.

Al Dr. Francisco José Ávila Ferrer, director de esta tesis doctoral, por el enorme esfuerzo realizado durante este periodo, por todo lo enseñado, por su amabilidad, por todos los buenos momentos durante estos años y por estar siempre que lo he necesitado.

A la Prof. Dra. Isabel López Tocón, directora y tutora de esta tesis doctoral, por todo lo enseñado, por su gran esfuerzo y dedicación durante estos años.

Al Catedrático de Química Física Juan Carlos Otero Fernández de Molina, por darme la oportunidad de realizar el doctorado en el grupo de investigación, por las innumerables y enriquecedoras discusiones tanto científicas como informales, por todo lo enseñado, por su dedicación, esfuerzo y gran calidad humana.

Al Catedrático de Química Física Juan Soto Martín, por todo el apoyo recibido, por todo lo enseñado, por su paciencia en las numerosas explicaciones, por su gran calidad científica y por ser una magnífica persona.

Al Catedrático Numerario Emérito de Química Física Juan Francisco Arenas Rosado, por ser un gran ejemplo de cómo debe ser un magnífico docente universitario.

A Samuel Valdivia Mantas, por los buenos momentos en el día a día y por estar siempre dispuesto a ayudar en todo lo posible.

A la Prof. María Rosa López Ramírez, por su amabilidad, su positividad y la ayuda prestada.

A la Dra. Cristina Ruano Frías y a la Dra. Jéssica Román Pérez, por la buena acogida en el grupo de investigación.

Al Primo Ricercatore Dr. Fabrizio Santoro per aver accettato di dirigere la permanenza predoctorale, per tutto ciò che mi ha insegnato, per la sua gentilezza e la sua infinita pazienza.

Al Ricercatore Dr. Giacomo Prampolini per la sua gentilezza, per le conversazioni divertenti e per tutto ciò che ha insegnato sulla scienza e sulla bella cultura italiana.

Al Professore Gennaro Pescitelli del Dipartimento di Chimica e Chimica Industriale dell'Università di Pisa per la sua gentilezza e il prezioso contributo alla collaborazione svolta.

A tutto il personale dell'unità ICCOM del centro CNR a Pisa per la loro gentilezza è ospitalità.

Al Prof. De la Universidad Autónoma de Madrid Javier Cerezo Bastida por todo lo enseñado, por su amabilidad y buena disposición a ayudar siempre.

Al Catedrático de Química Física Juan Casado Cordón, por su calidad científica, por su amabilidad y por las interesantes conversaciones.

Al Catedrático de Química Física Juan Teodomiro López Navarrete, por animarme a realizar el doctorado.

Al resto de compañeros del Departamento de Química Física, tanto profesores como alumnos, por su amabilidad y buenos ratos que hemos pasado juntos.

Al (próximamente) Dr. Juan Pedro Mora Fuentes, por su amistad, su amabilidad, su inagotable buen humor y por animarme a adentrarme en el mundo de la investigación en el Departamento de Química Física.

Al (próximamente) Dr. Jesús David Zea García, por su amistad y todos los buenos momentos durante estos casi 10 años.

A Mª Virginia Camarena Navas, por su cariño, apoyo y todos los buenos momentos durante este periodo.

A mi hermano José Francisco por ser un ejemplo de continua superación y esforzarse siempre al máximo, cualidades que realmente admiro.

A mi hermana Paula Remedios, por su cariño, por ser divertida y por toda su ayuda y apoyo.

Al pequeño Leo por traer tanta alegría a nuestras vidas.

A mis padres José Antonio y Remedios, para los cuales no tengo suficientes palabras de agradecimiento para el reconocer todo lo que merecen. Por haber trabajado incansablemente toda la vida, por su cariño y por su apoyo, sin los cuales no habría llegado hasta aquí.

Financiación y recursos

La realización de esta tesis doctoral ha sido financiada con los fondos asignados a los proyectos "Espectroscopía SERS" (CTQ2012-31846) y "Procesos Energéticos en Híbridos Cargados Metal-Molécula" (CTQ2015-65816-R), concedidos por el Ministerio de Economía y Competitividad (MINECO). El doctorando candidato agradece encarecidamente a los contribuyentes de España por el esfuerzo realizado.

La estancia predoctoral realizada ha sido parcialmente financiada por el Vicerrectorado de Estudios de Postgrado de la Universidad de Málaga.

La asistencia a congresos científicos ha sido financiada por el Vicerrectorado de Investigación y Transferencia de la Universidad de Málaga.

El doctorando candidato agradece al Servicio de Supercomputación y Bioinformática (SCBI) de la Universidad de Málaga por el uso de los recursos computacionales instalados en el superordenador Picasso y a Rafael Larrosa por soporte técnico.

El doctorando candidato agradece al Servicio de Apoyo a la Investigación (SCAI) de la Universidad de Málaga por la ayuda económica para adquirir la licencia actualizada del programa MOLCAS 8.2.

Resumen de la tesis.

Las interacciones entre la radiación electromagnética y la materia se pueden clasificar como fenómenos de absorción, emisión o dispersión. Esta interacción queda reflejada en los espectros que, para ser debidamente analizados, hay que explicar en base a la realidad atómico-molecular. Para ello, es muchas veces necesario recurrir a cálculos de estructura electrónica. Por tanto, la Espectroscopía Molecular y la Espectroscopía Computacional son técnicas complementarias la una a la otra y permiten obtener una información detallada sobre el sistema en estudio, en particular, de parámetros estructurales y energéticos.

Algunas de las técnicas espectroscópicas más utilizadas en investigación básica o en caracterización de materiales son las espectroscopías de absorción Ultravioleta-Visible (UV-VIS), Infrarroja (IR) y de dispersión Raman. Complementarias a éstas son las técnicas de Dicroísmo Circular Electrónico (ECD) y SERS (Surface-Enhanced Raman Scattering) ya que proporcionan información adicional, como la existencia de quiralidad molecular o supramolecular, en el caso de ECD, o cambios en la estructura electrónica del adsorbato cuando interacciona con superficies neutras o cargadas, como ocurre en las experiencias SERS.

Debido a la naturaleza atómico-molecular de los fenómenos bajo consideración, es necesario realizar su estudio apoyándose en los resultados obtenidos utilizando métodos mecanocuánticos. Pero en muchas ocasiones la propia naturaleza del sistema o su tamaño dificulta su tratamiento teórico, por lo que es necesario recurrir a simplificaciones, tanto en el nivel de teoría con el que abordarlo como en el uso de modelos aproximados del sistema, que permitan su tratamiento. La correcta aplicación de estas aproximaciones es la que avala los resultados obtenidos y su fiabilidad. Por ello, las metodologías pueden y deben ser revisadas y mejoradas de forma que el modelo propuesto sea adecuado para describir satisfactoriamente las propiedades del sistema que se pretenden discutir.

Este es justo el marco de trabajo en donde se sitúa la presente tesis doctoral. Las metodologías teóricas relevantes para las técnicas espectroscópicas más usuales para el caso de moléculas simples y rígidas están bien establecidas en la bibliografía. Incluso están implementadas en gran variedad de paquetes de programas de cálculo teórico de estructura electrónica, cuyo uso en la comunidad científica está ampliamente extendido.

Por el contrario, los métodos para sistemas que presenten un elevado grado de complejidad están aún por determinar y validar. En esta tesis se han seleccionado dos ejemplos de problemas complejos que plantean dificultades a la hora de ser tratados con las herramientas más convencionales.

La técnica SERS presenta numerosas dificultades para ser afrontada desde el punto de visto teórico. Una de las principales complicaciones es el modelo para representar al metal, que debe ser de un tamaño adecuado para poder ser tratado con los métodos mecanocuánticos y es necesario recurrir a simplificaciones para que la metodología teórica pueda ser utilizada con cierta facilidad. Por otro lado, los distintos mecanismos de intensificación – electromagnético (EM) o de transferencia de carga (CT) – pueden actuar simultáneamente en una determinada experiencia y no es posible determinar de forma sencilla en qué medida contribuye cada uno de ellos. Además, el uso de un sustrato metálico como electrodo plantea el reto adicional de simular el efecto del potencial eléctrico aplicado. Además, pueden ocurrir fenómenos de reactividad sobre la superficie, lo cual complica el análisis de los resultados. Todas estas características dificultan la discusión de los resultados SERS y justifican la necesidad de disponer de metodologías útiles, sencillas y fiables, para comprender mejor el origen del fenómeno y poder dar cuenta del comportamiento que muestran este tipo de espectros.

Otro ejemplo de sistemas complejos son los cromóforos flexibles, ya que para ciertas coordenadas internas la superficie de energía potencial no se siempre se puede tratar de forma adecuada mediante la aproximación armónica. Obtener la superficie de energía potencial anarmónica a nivel mecanocuántico tiene generalmente un alto coste computacional, por lo que solamente es posible para sistemas pequeños y con pocos átomos. Una alternativa muy utilizada en bibliografía es fijar la coordenada interna flexible a distintos valores y obtener el espectro global como una suma de los espectros individuales ponderados por las respectivas poblaciones de Boltzmann. Este método permite únicamente explorar conformaciones cercanas a la posición de equilibrio. Para estructuras más distorsionadas, aparecen frecuencias imaginarias que afectan a la fiabilidad del espectro calculado, por lo que es necesario el desarrollo de nuevas metodologías que permitan tratar este tipo de sistemas.

Por lo anteriormente expuesto, la presente tesis doctoral se ha centrado en el desarrollo de modelos y metodologías que permitan una correcta interpretación de distintos tipos de espectroscopías a partir de los datos obtenidos con cálculos de estructura electrónica.

Para obtener estas predicciones teóricas, se ha recurrido al modelo teórico más apropiado manteniendo un compromiso entre coste computacional y calidad de los resultados. Por ello, en aquellos casos en los que la reactividad molecular tiene relevancia, o fuera el objeto concreto de estudio, se han utilizado métodos multiconfiguracionales del Espacio Activo Completo en combinación con la Teoría de Perturbaciones de segundo orden (CASPT2). En sistemas que en los que el tamaño del sistema imposibilitara su uso, se ha recurrido a la Teoría del Funcional de la Densidad (DFT) seleccionando un nivel de teoría apropiado para estimar las propiedades de interés.

En los sistemas que implican una estructura metálica cargada, se ha recurrido a dos aproximaciones diferentes para simular el potencial de electrodo. Por un lado, se han utilizado sistemas híbridos metal-molécula constituidos por pequeños clústeres metálicos de forma lineal con diferente tamaño y carga, de modo que se module la densidad efectiva de carga por átomo (q_{eff}), simulando el exceso superficial de carga impuesto por el potencial de electrodo. Como alternativa, se ha utilizado un campo eléctrico externo aplicado al complejo metal-molécula modificando su módulo y su sentido.

El cálculo de intensidades Raman relativas se ha realizado bajo la condición de prerresonancia, considerando únicamente el término A, o de Franck-Condon, y utilizando la aproximación IMDHO (Independent Mode Displaced Harmonic Oscillator), de modo que los desplazamientos entre las geometrías de los estados resonantes se asumen proporcionales al gradiente de la superficie de energía potencial del estado excitado calculado en el punto de Franck-Condon. Bajo esta aproximación, la intensidad Raman de una banda es proporcional al cuadrado del parámetro adimensional de desplazamiento.

El cálculo de intensidades de absorción y de ECD se ha realizado utilizando la teoría vibrónica y teniendo en cuenta el acoplamiento de Duschinsky entre modos normales de los estados excitados implicados en cada caso. Se han considerado tanto los términos de Franck-Condon y como los Franck-Condon/Herzberg-Teller, tal como está implementado en el programa FCclasses y descrito en la bibliografía.

En esta tesis se ha aplicado un novedoso método desarrollado e implementado por el grupo del Dr. Fabrizio Santoro que permite retirar la contribución de coordenadas

internas seleccionadas y obtener espectros de estructuras parcialmente restringidas que no se corresponden con mínimos de la superficie de energía potencial. Esta metodología posibilita separar los modos vibracionales moleculares en rígidos y flexibles, y aplicar posteriormente un tratamiento diferenciado a cada uno de estos grupos. De este modo, se pueden calcular los espectros de estructuras que no sean mínimo de la superficie de energía potencial.

Esta tesis doctoral se presenta como compendio de artículos, de modo que los resultados que la avalan son aquellos ya publicados. Se incluyen seis artículos, y cada apartado del Capítulo III de Resultados se corresponde con una versión adaptada de cada uno de ellos. Los resultados obtenidos se clasifican en dos áreas temáticas: espectroscopía SERS y algunas cuestiones relacionadas, por un lado, y el estudio de cromóforos semirrígidos por otro.

En la primera parte de la discusión, el Apartado I muestra los resultados del estudio de los espectros SERS dependientes del potencial de electrodo y de la concentración de la molécula de *p*-aminotiofenol, considerando la existencia de distintas especies químicas y geometrías de adsorción, discutiéndose la posible contribución al espectro de su derivado nitreno.

Para conocer más acerca la formación de nitrenos, en el Apartado II se ha estudiado la fotodescomposición de la molécula *p*-metoxifenilazida, ya que hay disponibles resultados experimentales sobre esta reacción. Los resultados calculados apuntan a que en fase gas se forma el correspondiente nitreno en estado triplete fundamental y N_2, reacción que transcurre a través de un cruce entre sistemas y una posterior intersección cónica.

En el Apartado III, se revisan diferentes aproximaciones para calcular espectros SERS incluyendo el efecto del potencial de electrodo y su repercusión sobre las intensidades relativas. Sobre los resultados publicados recientemente por otros autores se han discutido las condiciones necesarias para que los resultados teóricos puedan ser directamente comparados con los experimentales.

El Apartado IV se dedica a demostrar la utilidad de la misma metodología desarrollada para analizar los espectros SERS en el área de la electrónica molecular, en sistemas del tipo *molecular junctions*. Los resultados proporcionan un nuevo punto de vista para entender los requisitos energéticos para que ocurran procesos relacionados con la

transferencia de carga en estas uniones moleculares, tanto en condiciones de resonancia como en aquellos casos en los que ese canal no esté permitido. También se discute cómo el potencial de electrodo modula las condiciones necesarias para que se den fenómenos de electroluminiscencia o la generación de fotocorrientes.

En la segunda parte de la tesis doctoral, se presentan los resultados obtenidos durante la estancia predoctoral del doctorando bajo dirección del Dr. Fabrizio Santoro en la sede en Pisa del instituto de investigación italiano Consiglio Nazionale delle Ricerche (CNR). Durante este periodo, se estudiaron los espectros electrónicos de cromóforos flexibles utilizando una metodología desarrollada e implementada por el grupo del Dr. Santoro. Esta metodología permite separar coordenadas internas en distintos espacios mediante un proceso iterativo de proyección, que hace posible obtener espectros de estructuras distorsionadas que no se corresponden con mínimos de la superficie de energía potencial.

Con este mismo método, en el apartado V se han calculado los espectros de absorción y de ECD de oligómeros de tiofeno de diferente tamaño y ángulo de torsión entre anillos. Se ha investigado la contribución espectral de especies monocatenarias y se ha comparado con los resultados experimentales en los que el polímero interacciona con distintos entornos. Los resultados permiten establecer de forma cualitativa si el espectro observado procede de especies monocatenarias en conformación de cintas *trans* distorsionadas o hélices *cis*.

Finalmente, en el apartado VI se estudia el caso del (S)-2,2,2-trifuoroantriletanol, un sistema con múltiples modos normales flexibles. Para ello se utiliza una aproximación cuántica/clásica mixta que generaliza el método estándar de cálculo espectros ECD en sistemas con varios confórmeros estables. Para ello se muestrea todo el espacio conformacional accesible. El método propuesto consigue reproducir efectos como la dependencia no lineal de la fuerza rotatoria o acoplamientos anarmónicos entre los modos flexibles.

En resumen, el trabajo que se ha llevado a cabo pone de manifiesto la utilidad de los cálculos de estructura electrónica en modelos simplificados para el estudio de los resultados espectroscópicos de sistemas complejos, tales como los que involucran a estructuras metálicas cargadas como a cromóforos flexibles.

Thesis abstract

Light-matter interactions can be classified in absorption, emission and scattering phenomena. These interactions are observed in the experimental spectra which, to be correctly analysed, must be explained attending to the atomic-molecular reality. To this aim, the studies must be reinforced by electronic structure theoretical calculations. Therefore, Molecular Spectroscopy and Computational Spectroscopy are techniques that complement each other and permit to obtain information about the studied system. In particular, structural parameters at the atomic and molecular level.

Some of the most used spectroscopic techniques in basic research or materials characterization are Ultraviolet-Visible (UV), Infrared (IR) and Raman scattering spectroscopies. There also exist others related techniques such as Electronic Circular Dichroism (ECD) or Surface-Enhanced Raman Scattering (SERS) that allow to obtain additional information. The first one is sensitive to molecular or supramolecular chiral arrangements, whereas the second permits to detect changes on the adsorbate electronic structure when interacts with neutral or charged surfaces.

Due to the atomic-molecular nature of the considered phenomena, they must be studied using quantum mechanical methods because they are appropriate to correctly describe those phenomena. However, it often happens that the systems under study or its size complicates its theoretical study and it is necessary to use simplifications both to the level of theory and to the structural model proposed, which permit to apply quantum mechanics calculations. The quality of the obtained results depends on an accurate application of these approximations, therefore, these methodologies and approximations must be revised and improved to verify that the proposed model is complete enough to properly describe the system at the desired level.

This is the framework of this doctoral thesis. The methodologies to describe simple and rigid molecules using the main spectroscopic techniques are well-established in the literature. They are also implemented in a large number of theoretical calculation program packages to calculate electronic structures and are widely used by the scientific community. On the contrary, the methodologies to face systems with a large complexity level are still to be determined and be validated. In this thesis, two type

of complex systems have been selected because of the problematic to apply standard methods on them.

SERS spectroscopy possesses numerous difficulties to be studied theoretically. One of the main problems is the model to reproduce the metal structure because it must have an appropriate size to be treated with quantum mechanical methods. Therefore, it is necessary to use simplifications, so these methods can be used. On the other hand, the different enhancement mechanism – electromagnetic (EM) and charge transfer (CT) – can operate simultaneously in a particular SERS experience and it is not possible to determine their individual contributions easily. In addition, using the metallic substrate as an electrode poses the additional challenge of reproducing the electrode potential. Finally, surface reactivity phenomena can occur, complicating the analysis of results. Therefore, all the features exposed manifest the complexity of discussing SERS results and justify the necessity of providing useful, simple and reliable methodologies to understand better the phenomenon causes and explaining the spectral behaviour of this type of spectroscopy.

Flexible chromophores are another example of high complexity system. Because of their own nature, some internal coordinates are not properly described by the harmonic approximation. Usually, obtaining the anharmonic potential energy surface at the quantum mechanical level has a large computational cost and it is only affordable for small systems. An alternative to be resorted to is using different structures where the value of the flexible coordinate is fixed to a set of values and then obtain the spectral contribution of each structure, weighted by the Boltzmann population. However, the values of the flexible coordinate are limited to the proximities of the minima of the potential energy surface, otherwise, imaginary frequencies rise and the spectrum cannot be reliably computed in many cases.

Because of the reasons previously exposed, this doctoral thesis focuses on the development of models and methodologies to correctly interpret different type of spectroscopies parting from the data obtained with electronic structure calculations.

For these theoretical predictions, the most suitable theoretical model was selected considering computational cost and quality of the results. Therefore, in those cases where the molecular reactivity could be relevant, or it was the main objective of the study, multiconfigurational methods were used in combination with the Complete

Active Space and second-order Perturbation Theory (CASPT2). For the systems whose size made impossible to use that model, Density Functional Theory (DFT) was used instead selecting the most appropriated level of theory to estimate the properties under study.

For systems involving a charged metallic structure, two different approximations were used to reproduce the electrode potential. On the one hand, hybrid metal-molecule systems where the metal structure was lineal and had variable size and charge were used. This way, the effective density of charge per atom (q_{eff}) parameter simulates the surface excess of charge imposed by the electrode potential. On the other hand, an external electric field model applied along a metal-molecule complex was also was utilized. The magnitude and the direction of the vector approximates to the electrode potential.

Relative Raman intensities were computed under resonance conditions considering the Frank-Condon term (A) and the Independent Mode Displaced Harmonic Oscillator approach (IMDHO). Therefore, the ground state geometry displacements are proportional to the gradient in the excited state potential energy surface. In this approach, the Raman intensity of a vibrational band is proportional to the square of the dimensionless shift parameter.

Absorption and ECD spectra were calculated in the framework of vibronic theory and including Duschinsky coupling between ground and excited states, in addition to temperature effects. Frank-Condon and Frank-Condon/Herzberg-Teller contributions were also considered. The methodology is described in the literature and implemented in the FCclasses program.

A novel method to remove internal coordinates developed and implemented by Dr. Fabrizio Santoro's group was also used in this thesis. The removal is done by projecting out the internal coordinates in different spaces and it is applied iteratively for more than one coordinate. For instance, they could be separated in stiff and flexible coordinates, and different theoretical models or approaches could be applied to each space. With this protocol it is possible to obtain spectra of distorted structures that are not minima of the potential energy surfaces.

This doctoral thesis is presented as compendium of articles and the results supporting it are the articles published in scientific journals. Six articles are included and each part of

the Results Chapter (Chapter III) is an adapted version of them. The results are classified in two topics: (i) SERS spectroscopy and related phenomena, and (ii) methodologies to compute spectra of semirigid chromophores.

In Part I, the potential-dependent SERS spectra at different concentrations of *p*-aminothiophenol was explained considering different surface species. The spectral contribution of the nitrene derivative is proposed.

The interest of the nitrene derivative on the previous results motivated to study the photodecomposition of p-methoxyphenylazide in Part II, because for this reaction there are experimental results available. The calculated results propose that in gas phase, the photodecomposition produce the corresponding nitrene in its triplet state plus N_2. This reaction goes through an intersystem crossing and a subsequent conical intersection.

In Part III, different approaches to compute SERS spectra are revised, including the electrode potential effect and its consequences on the relative intensities. The conditions to directly compare theoretical and experimental results are highlighted. The discussion is conducted on results obtained by other authors on a recent article.

The model applied to study SERS spectra is extended to molecular junction devices in Part IV. These results provide a new perspective to understand the energy requirements to make charge transfer or resonant charge transfer processes occur. The effect of the electrode potential and how it tunes the required conditions to cause electroluminescence or to generate photocurrents is also discussed.

In the second section of the Results chapter contains the results obtained during the candidate predoctoral stay under direction of Dr. Fabrizio Santoro in the Isitituto di Chimica dei Composti Organometallici (ICCOM) which is part of the Pisa unit of the Consiglio Nazionalle delle Ricerche (CNR) Italian research centre. In that period, the spectra of flexible chromophores were studied using the methodology developed and implemented by Dr. Santoro's group, which is able to separate internal coordinates in different spaces through an iterative projection process and it permits to calculate spectra of distorted structures that are not minima of the potential energy surface.

This method was used in Part V, and the absorption and ECD spectra of thiophene oligomers with different length and inter-ring torsion were computed.

The spectral contribution of single-chain oligomers was studied and compared with experimental results where polythiophenes were interacting with several environments that induced chirality upon them. These results qualitatively stablish if the observed spectra proceed from single-chain species or not, and if the conformation of the single-chain is a transoid twisted ribbon or a cisoid helix.

Finally, in Part VI, a system with several flexible modes and stable conformers with different chiral response ((S)-2,2,2-trifluoroanthylethanol) was studied. A quantum/classical approach was used to generalize the standard protocol to compute ECD intensities when several conformers contribute to it. This is done sampling the complete conformational accessible space. The proposed method achieves to capture effects like the nonlinearity of the rotatory strength or anharmonic coupling among flexible modes.

The results obtained manifest the great usefulness of both electronic structure calculations and the use of simple models to study spectroscopic results from complex systems such as those involving metallic structure or flexible chromophores.

Índice.

Capítulo I – Introducción.

1.1. Cálculos de estructura electrónica y espectroscopía computacional.

La compleja interacción entre la radiación electromagnética y la materia es la responsable de los distintos tipos de espectroscopías. En último término, el detalle de estos resultados experimentales plasmados en forma de espectros está determinado por la estructura electrónica del sistema en estudio, siendo ésta la causa última de todas las propiedades químicas de cualquier sistema y, muy especialmente, de aquellas que se evalúan desde la escala microscópica.

El análisis de los resultados espectroscópicos requiere fundamentarse en la realidad atómico-molecular sopesando, en su caso, el efecto de las interacciones entre los distintos componentes y su repercusión sobre los comportamientos observados. Por tanto, dejando aparte las aplicaciones espectroscópicas más triviales, la utilidad de un espectro radica en poder extraer una información detalladísima sobre la forma en que núcleos y electrones se organizan a diferentes escalas de complejidad. Por lo tanto, para comprender los resultados espectroscópicos es necesario tener el mínimo conocimiento necesario de la causa responsable de sus características, que es la propia estructura electrónica del sistema en estudio.

La Espectroscopía Molecular es, por tanto, una de las técnicas por excelencia para obtener información de la estructura electrónica de moléculas, tanto aisladas como en diferentes entornos, proporcionando información sobre los estados de los sistemas estudiados en las condiciones de medida en que han sido registrados los espectros. Las técnicas espectroscópicas se fundamentan en distintos procesos de interacción entre la radiación electromagnética y los sistemas materiales: absorción, emisión y dispersión, entre otras. Atendiendo al tipo de interacción, o al rango de energías de la radiación electromagnética, las técnicas espectroscópicas más comunes son las de absorción de un fotón en el Ultravioleta-Visible (UV) o en el Infrarrojo (IR) o de dispersión Raman, proceso que implica dos fotones. Derivadas de éstas, han aparecido técnicas relacionadas como el SERS (Surface-Enhanced Raman Scattering) o el Dicroísmo Circular Electrónico (ECD), que proporcionan información específica sobre el entorno del sistema en estudio (SERS, moléculas en interfaces metálicas) en un caso, o de la respuesta con características singulares de sistemas ópticamente activos (ECD, quiralidad molecular o supramolecular).

Si los resultados obtenidos mediante técnicas espectroscópicas estándar requieren ser analizados y discutidos con la ayuda de la información proporcionada por herramientas de cálculo teórico, unas predicciones teóricas suficientemente fiables son requisito imprescindible en los dos casos mencionados anteriormente. La complejidad de este tipo de espectros hace imprescindible apoyarse en estimaciones del espectro obtenidas a partir de cálculos de estructura electrónica.

Partiendo de la información proporcionada por cálculos mecanocuánticos (tales como geometrías de equilibrio, frecuencias vibracionales, energías de excitación electrónica, etc.) es posible predecir espectros teóricos de distinta naturaleza (absorción y emisión UV, IR, Raman…) pero para ello es necesario asumir simplificaciones y aproximaciones y limitar el tamaño del sistema a estudiar mediante modelos estructurales que sean suficientemente precisos y manejables. La fiabilidad de estos resultados en cada caso concreto estará condicionada por la robustez y correcta aplicación de las metodologías, que dependerá a su vez del nivel del detalle espectroscópico que se quiera analizar. Estas metodologías son siempre susceptibles de ser mejoradas, tanto en relación con el nivel de teoría como con la selección del modelo del sistema a estudiar. Planteado el objetivo del trabajo, se establecerá una estrategia para seleccionar uno y otro de manera que se presuma como suficiente para realizar el análisis de los espectros. Si esto no ocurre, habrá que plantearse si otra metodología alternativa o un modelo más completo proporcionaría una mejora de la calidad de los resultados.

Los protocolos convencionales para el cálculo de espectros de sistemas pequeños y/o rígidos están bien establecidos y se conoce su mayor o menor fiabilidad a la hora de predecir, de forma teórica, las características generales observadas en los espectros. Uno de los problemas se encuentra en sistemas que, por su propia naturaleza, tengan una elevada complejidad, lo que dificulta, y en ciertos casos incluso imposibilita, el análisis fundamentado de los correspondientes espectros, dándose frecuentemente interpretaciones más bien especulativas que dificultan el desarrollo y las aplicaciones de las técnicas que presentan estas características.

En esta tesis se han seleccionado dos buenos ejemplos de esta problemática en los que se va a evaluar la utilidad de las estimaciones teóricas de propiedades espectroscópicas mediante metodologías más o menos sencillas basadas en cálculos de estructura electrónica. El primero de estos ejemplos es el fenómeno SERS que consiste esencialmente en la enorme intensificación de la señal Raman de una molécula en las

proximidades de nanoestructuras de determinados metales.[1] Se da la circunstancia que a día de hoy no se conoce suficientemente el mecanismo responsable del fenómeno debido, esencialmente, a la complejidad del sistema y de los comportamientos experimentales observados.[2,3] Uno de los inconvenientes es que las dimensiones del sustrato metálico hacen imposible que pueda ser representado explícitamente en los cálculos mecanocuánticos, por lo que hay que recurrir a simplificar el sistema en estudio manteniendo su utilidad, es decir, manteniendo su capacidad para analizar convenientemente el complejo comportamiento observado. En este sentido, el grupo de investigación de "Espectroscopía y Estructura Molecular" del Departamento de Química Física de la Universidad de Málaga ha venido centrando su actividad investigadora. Se han estudiado los espectros SERS de moléculas derivadas del benceno tanto experimentalmente, utilizando nanopartículas y electrodos rugosos, como a nivel teórico. Para ello se han registrado series de espectros de moléculas de diferente naturaleza, para deducir patrones de comportamiento generales. Paralelamente, se han desarrollado metodologías teóricas para simular el efecto del metal sobre la estructura electrónica del complejo superficial y de su repercusión sobre las intensidades Raman, prestando especial interés en el estudio de la dependencia de los espectros con la diferencia de potencial eléctrico de la interfase.[4-16] Estos estudios han permitido clarificar algunas de las cuestiones fundamentales que vienen siendo objeto de controversia desde el descubrimiento del SERS en 1974[1] y en esta tesis se presentan algunos de los resultados obtenidos en este campo.

Otro ejemplo de sistemas de alta complejidad son los cromóforos flexibles. Estos sistemas presentan el problema del tratamiento de aquellos modos normales vibracionales que no se describen adecuadamente bajo la aproximación armónica, por lo que el estudio de las propiedades de este tipo de sistemas necesita del uso y desarrollo de metodologías específicas. Como paso previo, se está realizando un gran esfuerzo en la investigación de los sistemas semirrígidos que se componen de una parte rígida, que en general son sistemas π-conjugados, y una parte flexible, la que requiere un tratamiento diferente al resto.[17-20] Unas de las líneas de investigación del Dr. Fabrizio Santoro del "Istituto di Chimica dei Composti OrganoMetallici" (ICCOM, Consiglio Nazionalle delle Ricerche, Pisa) está dedicada a establecer protocolos fiables para el estudio computacional de los espectros electrónicos CD de este tipo de sistemas.[21-23] El Dr. Santoro ha desarrollado metodologías para el cálculo de espectros de absorción, absorción de dos fotones, emisión, dicroísmo circular electrónico y

resonancia Raman.[24-41] Recientemente, y en colaboración con uno de los directores de esta tesis, el Dr. Francisco Ávila, se han puesto a punto métodos para tratar sistemas con cierta flexibilidad, como es el caso de la molécula de ditiofeno y otros oligómeros relacionados.[42,43] En la estancia de investigación realizada por el doctorando en el grupo del Prof. Santoro se ha continuado en esta línea de trabajo estudiando sistemas de alta complejidad debido a su tamaño y/o flexibilidad. Esta investigación es otro buen ejemplo de la utilidad de la espectroscopía computacional en el análisis de resultados experimentales complejos y constituyen la otra parte de esta tesis.

En las siguientes secciones se describen las características más destacadas de la problemática del cálculo de estructuras electrónicas de espectros SERS y de espectros de moléculas flexibles.

1.1.1 Espectroscopía SERS.

El fenómeno SERS se caracteriza por la enorme intensificación de la señal Raman de una molécula cuando se encuentra en las proximidades de la superficie de ciertos metales con una morfología adecuada. Dicha superficie debe presentar necesariamente estructuras locales de tamaño nanométrico, ya que la mayor contribución de este fenómeno es debida a moléculas localizadas en irregularidades a escala sub-microscópica (de dimensiones entre 10 y 100 nm) o atómica (escalones, vértices, defectos, etc.), dependiendo del sistema. La mayoría de las experiencias SERS se realizan sobre coloides y en electrodos sometidos a varios ciclos de oxidación-reducción que permiten obtener morfologías rugosas más o menos nanoestructuradas.

Hoy en día, está aceptado que la intensificación observada en el fenómeno SERS se debe a la contribución conjunta de dos mecanismos que son el llamado mecanismo electromagnético o plasmónico (EM) y el mecanismo químico o de transferencia de carga (CT). El mecanismo EM se caracteriza porque el campo electromagnético efectivo sobre una molécula es mucho mayor en las proximidades de una superficie activa en SERS que en ausencia de ella. Además, el campo dispersado por las partículas metálicas resulta enormemente intensificado si la frecuencia de la radiación incidente se hace coincidir con la frecuencia de resonancia de los plasmones superficiales del metal, también llamados polaritones-plasmones, es decir, de las oscilaciones de los electrones de conducción del mismo. El metal actúa como una antena que amplifica tanto el campo de la radiación excitatriz incidente como la propia radiación Raman

dispersada por la molécula, siendo mayor la intensificación en unas posiciones privilegiadas en la superficie nanoestructurada del metal, denominadas "hot spots."

Según diversos estudios,[44-47] se ha llegado a la conclusión que la mayor intensificación de la radiación se produce en sitios especiales, vértices o recodos, de la superficie metálica. Este mecanismo EM es el que más contribuye a la intensificación SERS global y está presente en cualquier experiencia SERS. Permite también justificar la dependencia de los espectros con la naturaleza y morfología del metal, pero no proporciona explicación sobre la intensificación selectiva de bandas al utilizar distintos metales o al cambiar el potencial de electrodo. Para dar respuesta a estas cuestiones, hay que recurrir a otras contribuciones como el mecanismo de transferencia de carga CT.

Este mecanismo considera moléculas adsorbidas sobre la superficie metálica, dando lugar a un complejo superficial metal-adsorbato.[48,49] Este complejo posee estados electrónicos que no tienen correspondencia con estados del metal o de la molécula aislada, si no que aparecen como consecuencia de la unión de ambas entidades. La transferencia de carga fotoinducida se produce al promocionar un electrón de un orbital ocupado de una de las entidades (metal o molécula) a la otra, resultando en una transferencia de carga. Por tanto, la estructura electrónica de este nuevo sistema M-A determina la respuesta espectroscópica obtenida en resonancia con esos nuevos estados CT.

La principal dificultad para afrontar de forma teórica este tipo de sistemas es, como se ha adelantado en la sección anterior, que las dimensiones del metal son muy superiores a las de la molécula. Por tanto, no es posible tratar de forma explícita la compleja estructura metálica en los cálculos mecanocuánticos.

Es entonces necesario recurrir a estructuras simplificadas que mantengan las propiedades más relevantes de la estructura electrónica para intentar reproducir el fenómeno en estudio. El modelo más extendido consiste en utilizar clústeres de mayor o menor tamaño unidos o no a una red metálica cristalina, asumiendo que solo los átomos metálicos próximos al punto de unión son relevantes.[50-55]

Para el estudio de interfases electrificadas se introduce un campo eléctrico o se añade carga eléctrica al modelo metálico de los sistemas anteriores. Esto plantea una nueva problemática ya que la estructura electrónica de cada agrupación metálica particular

depende tanto del número de átomos considerados como de la carga eléctrica, por lo que las distintas estructuras seleccionadas pueden interaccionar de forma diferente con la molécula y en varias posiciones no equivalentes, complicando el proceso de extraer conclusiones generales.[56-58]

Para solucionar este problema, el grupo de Espectroscopía y Estructura Molecular de la UMA ha propuesto un modelo basado en clústeres lineales cargados, de forma que solo un átomo metálico interacciona con la molécula, y el proceso de carga del modelo de electrodo se modula variando la longitud la longitud del clúster. Los detalles se este modelo se describen en el Capítulo II. De esta forma, se garantiza que la interacción metal-adsorbato es siempre equivalente y no hay que hacer elecciones arbitrarias sobre la estructura del complejo superficial o sobre el sitio de unión.

Esta simple metodología ha permitido describir de forma cualitativa las principales características de los espectros SERS dependientes del potencial de moléculas derivadas del benceno analizando la estructura electrónica de los sistemas y los estados relevantes en cada caso.[4-16]

Los cálculos teóricos son claves en SERS ya que pueden permitir detectar la presencia de un determinado mecanismo de intensificación en cada espectro en particular. Aparte del interés fundamental en entender mejor los mecanismos que originan el SERS, la principal consecuencia de estos resultados es comprobar que espectros y estructura electrónica están estrechamente relacionados, que hay herramientas sencillas de cálculo teórico que permiten analizar los complejos resultados. Si se comprueba que existe esta relación, el SERS puede llegar a ser una de las técnicas más útiles para obtener información a nivel molecular sobre las interacciones metal-molécula que están implicadas en los fenómenos electroquímicos, de adsorción o catálisis sobre metales o en los procesos de transporte eléctrico en uniones moleculares, base de la electrónica molecular.

1.1.2. Sistemas flexibles.

Los cromóforos flexibles son de gran interés desde el punto de vista tecnológico y científico, ya que tienen aplicaciones en el área de los materiales y en las ciencias de la vida. Son especialmente interesantes por su capacidad de modulación ante diferentes estímulos del entorno, que alteran la estructura del sistema y por tanto su respuesta espectroscópica.

Para analizar estos cambios, es necesario justificar los resultados experimentales con cálculos teóricos que proporcionen una explicación de los fenómenos observados partiendo desde la estructura electrónica del sistema. Pero el cálculo de espectros de cromóforos flexibles tiene la problemática de que la aproximación armónica no es suficiente para describir la superficie de energía potencial de determinados modos normales. Esto limita las conformaciones a estudiar, restringiendo el problema a los mínimos de la superficie de energía potencial y a estructuras levemente distorsionadas respecto a la posición de equilibrio.

En estructuras más distorsionadas aparecen frecuencias imaginarias a lo largo de ciertos modos, lo que requiere metodologías específicas que permitan tratar este problema y tengan un coste computacional asumible.

Los métodos de dinámica molecular (MD) proporcionan una buena descripción de las posibles conformaciones que puede adquirir el sistema flexible, así como de sus energías, motivo por el cual se han utilizado extensamente con este fin.[59-64] Pero para reproducir los espectros es necesaria la estimación de las propiedades relevantes utilizando métodos mecanocuánticos por lo que se han desarrollado distintas metodologías relacionadas con la presencia de estos modos flexibles. Por ejemplo, se pueden utilizar coordenadas internas y diagonalizar por bloques la matriz de Duschinsky, separando los fundamentales más armónicos de los muy anarmónicos.[42] El espectro global se puede obtener como una convolución de las contribuciones de los distintos bloques a la forma de línea espectral. Desafortunadamente, este método está limitado a un número reducido de modos normales, por lo que es necesario seguir trabajando en el desarrollo de herramientas que permitan extender protocolos de este tipo a un número mayor de vibraciones.

Tras superar el obstáculo de los modos normales fuera de equilibrio, es posible calcular los espectros y compararlos con los datos experimentales. Las técnicas en las que más se ha trabajado son absorción molecular y ECD. Esta última es particularmente útil debido a su sensibilidad a distintas conformaciones (moleculares o supramoleculares), permitiendo determinar qué conformaciones son representativas y hay que considerar en un experimento en particular y estudiar su efecto sobre diferentes propiedades de interés, como la conductividad electrónica, utilizando las técnicas adecuadas para ello.

Otra aplicación interesante del ECD es el estudio de fenómenos de transferencia de quiralidad, que ocurren al interaccionar física o químicamente estructuras quirales con sistemas aquirales. En el primer caso, esta interacción induce un empaquetamiento quiral y ordenado en el sistema aquiral, que puede ser detectado por ECD. Las propiedades de este empaquetamiento ordenado pueden diferir de las de la estructura desordenada, lo cual tiene aplicaciones tecnológicas relevantes.

El interés intrínseco y las grandes posibilidades tecnológicas de los sistemas flexibles motivan justifican su estudio y el desarrollo de métodos que permitan caracterizarlos.

1.2. Estructura de la tesis.

En esta tesis se recogen dos ejemplos de la utilidad de los cálculos de espectroscopía computacional en el estudio de los complejos espectros SERS y de espectros ECD de moléculas semirrígidas.

Para ello, es necesario proponer y analizar la validez de una serie de aproximaciones y simplificaciones que permitan calcular los espectros. Las utilizadas en esta tesis doctoral se detallan en el Capítulo II, donde se describen los distintos modelos utilizados para reproducir el efecto de la adsorción de moléculas sobre superficies electrificadas y las distintas aproximaciones utilizadas en esta tesis para poder obtener espectros de Resonancia Raman, absorción y ECD.

En el Capítulo III se presentan y discuten los resultados obtenidos en esta tesis separados en apartados, donde cada uno de ellos se corresponde con la versión adaptada de las publicaciones que han surgido del trabajo realizado.

En el Apartado I se estudia el espectro SERS dependiente del potencial de electrodo de la molécula p-aminotiofenol (pATP) a distintas concentraciones. Esta molécula ha sido ampliamente estudiada, siendo quizás la que generado el mayor número de publicaciones en SERS al usarse habitualmente para contrastar cada nuevo sustrato propuesto. Sin embargo, ha sido objeto de una gran polémica centrada en el origen de sus bandas más características para lo que se ha propuesto un mecanismo de Resonancia Raman o la dimerización del producto para dar la correspondiente azida. Los resultados aquí presentados muestran que el espectro completo obtenido podría ser explicado considerando tres especies químicas superficiales distintas: pATP unido a la superficie por el átomo de azufre, una especie pATP bidentada unida mediante el azufre y el grupo amino, y su nitreno triplete correspondiente.

Debido al interés de la especie nitreno y del azocompuesto derivado del pATP en SERS, en el Apartado II del Capítulo IV se ha estudiado la generación de un nitreno triplete para una molécula muy relacionada en la que este proceso ha sido estudiado experimentalmente, la p-metoxifenilazida. Los cálculos de estructura electrónica indican que los pasos clave son un cruce intersistémico entre estados de la azida, y el posterior decaimiento a través de una intersección cónica a un estado repulsivo, que da como productos nitrógeno molecular y el nitreno triplete.

Continuando la sección de espectroscopía SERS y aprovechando la publicación de un artículo en el PCCP, en el Apartado III se ponen en evidencia los habituales errores que aparecen en trabajos sobre SERS en los que utilizan cálculos teóricos como soporte en la discusión. En esta parte, se discuten las distintas metodologías para el cálculo de espectros en condiciones de prerresonancia o en resonancia con el estado de transferencia de carga, así como el cálculo de espectros de espectros en resonancia mono- o multiestados, además de las condiciones para que puedan ser comparados directamente con los resultados experimentales. La discusión se realiza en base a los resultados teóricos obtenidos por otros autores y por nuestro grupo sobre la base de los espectros experimentales registrados previamente por nosotros.

Para finalizar la primera sección de resultados relacionados con los sistemas híbridos metal-molécula, se extendió el estudio a sistemas de interés en electrónica molecular del tipo $M-A-M$ (metal-molécula-metal), conocidos como *molecular junctions*. En el Apartado IV del Capítulo III, se estudia el efecto de distintos parámetros a las propiedades del dispositivo, mediante cálculos de estructura electrónica. Los parámetros seleccionados fueron la distancia intermetálica, el tamaño del clúster metálico y la densidad de carga del metal en estados excitados con separación de carga $M^{q}-A-M^{-q}$, comprobándose que ajustando dichos parámetros se puede modificar la *molecular junction* de manera que actúe como rectificador de corriente o como dispositivo electroluminiscente.

En la otra parte de la tesis referente al cálculo de estructuras electrónicas de sistemas semirrígidos realizada en colaboración con el grupo del Dr. Santoro, se ha utilizado un método desarrollado e implementado por ellos para proyectar las coordenadas flexibles fuera del espacio vibracional y así poder obtener espectros de sistemas alejados del mínimo de la superficie de energía potencial. La justificación para trabajar con estructuras que no corresponden al mínimo de energía es que se pretende que su

estructura electrónica sea más similar al sistema real, obteniendo predicciones más útiles que las que proporcionarían las estructuras totalmente optimizadas. En el Apartado V del Capítulo III se estudian de forma sistemática los espectros de absorción y ECD de oligotiofenos de distinta longitud, y con un ángulo de torsión entre anillos fijado, con el propósito de estudiar los espectros de polímeros basados en el tiofeno interaccionando con otros sistemas a los que transfiere quiralidad. Los resultados obtenidos permiten justificar de forma cualitativa si el espectro observado se debe o no a especies monocatenarias con estructura todo-*trans* o *todo*-cis.

Por último, en el Apartado III se ha estudiado una molécula semirrígida con confórmeros que proporcionan distintas señales de ECD, el (*S*)-2,2,2-trifluoroantriletanol. Se propone un método para computar el espectro ECD total a partir de la suma ponderada de la contribución de los espectros de distintos confórmeros, teniendo en cuenta los tres posibles modos normales flexibles. El protocolo desarrollado es más robusto y fiable que el método estándar, en el que sólo se consideran los confórmeros que son mínimos de la superficie de energía potencial.

En el Capítulo IV se ha realizado un resumen conjunto y global de los resultados, reseñándose lo resultados más destacados, y en el Capítulo V se recogen las conclusiones más importantes derivadas del trabajo que se ha llevado a cabo en esta tesis doctoral.

1.3. Objetivos de la tesis.

El objetivo general de la tesis es contrastar la utilidad de los cálculos de estructura electrónica en el análisis de resultados espectroscópicos relacionados con dos campos específicos y complejos, como son los espectros de sistemas en donde una molécula está enlazada a un agregado metálico cargado y aquellos en donde en una molécula se combinan quiralidad y flexibilidad estructural.

1.4. Publicaciones.

Esta tesis doctoral se presenta en formato de compendio de artículos. Por ello, en el Anexo I se detallan las tareas realizadas por el candidato en cada publicación, mostrando su contribución específica a cada uno de los trabajos que componen la tesis doctoral. En el Anexo II se reproducen los artículos que constituyen esta tesis presentada como compendio de publicaciones en el formato original en el han aparecido, y que son los siguientes:

1. **Analysis of the Potential Dependent Surface-Enhanced Raman Scattering of p-Aminothiophenol on the Basis of MS-CASPT2 Calculations**
   María R. López-Ramírez, Daniel Aranda, Francisco J. Avila, Silvia P. Centeno, Juan F. Arenas, Juan C. Otero,* and Juan Soto.*

   J. Phys. Chem. C, **2016**, 120, 19322.

2. **An MS-CASPT2 Study of the Photodecomposition of 4-Methoxyphenyl Azide: Role of Internal Conversion and Intersystem Crossing.**
   Daniel Aranda, Francisco J. Avila, Isabel López-Tocón, Juan F. Arenas, Juan C. Otero*, and Juan Soto*.

   Phys. Chem. Chem. Phys., **2018**, 20, 7764.

3. **Comment on "Elucidation of the charge-transfer SERS selection rules by considering the excited state properties and the role of electrode potential" by M. Mohammadpour, M. H. Khodabandeh, L. Visscher and Z. Jamshidi, *Phys. Chem. Chem. Phys*. 2017, 19, 7833.**
   D. Aranda, J. Román-Pérez, I. López-Tocón, J. Soto, F. Avila* and J. C. Otero.

   Phys. Chem. Chem. Phys., **2017**, 19, 27888.

4. **An approach to the electronic structure of molecular junctions with metal clusters of atomic thickness.**

   Daniel Aranda, Isabel López-Tocón, Juan Soto, Juan C. Otero* and Francisco Avila*.

   Phys. Chem. Chem. Phys., **2016**, 18, 27179.

5. **A Computational Study of the Vibrationally-Resolved Electronic Circular Dichroism Spectra of Single-Chain Transoid and Cisoid Oligothiophenes in Chiral Conformation.**

   Daniel Aranda, Javier Cerezo, Gennaro Pescitelli, Francisco J. Avila Ferrer, Juan Soto, Fabrizio Santoro.*

   Phys. Chem. Chem. Phys., **2018**, 20, 21864.

6. **Toward a General Mixed Quantum/Classical Method for the Calculation of the Vibronic ECD of a Flexible Dye Molecule with Different Stable Conformers: Revisiting the Case of 2,2,2-trifluoro-AnthrylEthanol.**

   Javier Cerezo, Daniel Aranda, Francisco J. Avila Ferrer, Giacomo Prampolini, Giuseppe Mazzeo, Giovanna Longhi, Sergio Abbate, Fabrizio Santoro.*

   Chirality, **2018**, 30, 730.

1.5. Referencias.

1. M. Fleischmann, P. J. Hendra, A. J. McQuillan. *Chem. Phys. Lett*., **1974**, 26, 163.
2. K. Kneipp, M. Moskovits, H. Kneipp. *Surface-Enhanced Raman Scattering - Physics and Applications*. Springer, **2006**.
3. N. Valley, N. Greeneltch, R. P. Van Duyne, G. C. Schatz. *J. Phys. Chem. Lett*., **2013**, 4, 2599.
4. J. F. Arenas, J. Soto, I. López-Tocón, D. J. Fernández, J. C. Otero, J. I. Marcos. *J. Chem. Phys*., **2002**, 116, 7207.
5. J. F. Arenas, I. López-Tocón, J. C. Otero, J. I. Marcos. *J. Phys. Chem*., **1996**, 100, 9254.
6. J. F. Arenas, M. S. Woolley, I. López-Tocón, J. C. Otero, Juan I. Marcos. *J. Chem. Phys*., **2000**, 112, 7669.
7. J. F. Arenas, I. López-Tocón, M. S. Woolley, J. C. Otero, J. I. Marcos. *J. Raman Spectrosc*., **1999**, 29, 673.
8. W. Grochala, A. Kudelski, J. Bukowska. *J. Raman Spectrosc*., **1999**, 29, 681.
9. R17. F. Avila, C. Ruano, Isabel López-Tocón, J. F. Arenas, J. Soto, Juan C. Otero., *Chem. Commun*., **2011**,4 7, 4213.
10. F. Avila, D. J. Fernández, J. F. Arenas, J. C. Otero, J. Soto., *Chem. Commun*., **2011**, 47, 4210.
11. M. Sardo, C. Ruano, J. L. Castro, I. López-Tocón, J. Soto, P. Ribeiro-Claro, J. C. Otero. *Phys. Chem. Chem. Phys*., **2009**, 11, 7437.
12. J. Román-Pérez, I. López-Tocón, J. L. Castro, J. F. Arenas, J. Soto, J. C. Otero. *Phys. Chem. Chem. Phys*., **2015**, 17, 2326.
13. F. Avila, J. Soto, J. F. Arenas, J. A. Rodríguez, D. Peláez, J. C. Otero. *J. Phys. Chem. C*, **2009**, 113, 105.
14. J. F. Arenas, I. López-Tocón, J. L. Castro, S. P. Centeno, M. R. López-Ramírez, J. C. Otero. *J. Raman Spectrosc*., **2005**, 36, 515.
15. J. L. Castro, M. R. López-Ramírez, J. F. Arenas, J. Soto, J. C. Otero. *Langmuir*, **2012**, 28, 8926.

16. J. Román-Pérez, S. P. Centeno, M. R. López-Ramírez, J. F. Arenas, J. Soto, I. López-Tocón, J. C. Otero. *Phys. Chem. Chem. Phys*., **2014**, 16, 22958.

17. T. J. Zuehlsdorff, J. A. Napoli, J. M. Milanese, T. E. Markland, C. M. Isborn. *J. Chem. Phys*., **2018**, 149, 024107.

18. D. Loco. L. Cupellini. *Int. J. Quantum Chem*., **2018**. Early view e25726.

19. C. Muñoz-Caro, A. Niño, D. C. Mouleb. *Chem. Phys*., **1994**, 186, 221.

20. L. Zanetti-Polzi, S. Del Galdo, I. Daidone, M. D'Abramo, V. Barone, M. Aschi, A. Amadei. *Phys. Chem. Chem. Phys*., **2018**, 20, 24369.

21. J. Cerezo, G. Mazzeo, G. Longhi, S. Abbate, F. Santoro. *J. Phys. Chem. Lett*., **2016**, 7, 4891.

22. D. Padula, F. Santoro, G. Pescitelli. *RSC Adv*., **2016**, 6, 37938.

23. D. Padula, D. Picconi, A.Lami, G.Pescitelli, F. Santoro. *J. Phys. Chem. A*, **2013**, 117, 3355.

24. Roberto Improta, Vincenzo Barone, Fabrizio Santoro. *J. Phys. Chem. B*, **2007**, 111, 14080.

25. F. Santoro, R. Improta, A. Lami, J. Bloino, V.Barone. *J. Chem. Phys*., **2008**, 128, 224311.

26. N. Lin, Y. Luo, F. Santoro, X. Zhao, A. Rizzo, *Chem. Phys. Lett*., **2008**, 464, 144.

27. N. Lin, F. Santoro, X. Zhao, A. Rizzo, V. Barone. *J. Phys. Chem. A*, **2008**, 112, 12401.

28. F. Santoro, V. Barone. *Int. J. Quantum. Chem*., **2009**, 110, 476.

29. A. Lami, F. Santoro. *Time-Dependent Approaches to Calculation of Steady-State Vibronic Spectra: From Fully Quantum to Classical Approaches*. In "Computational Strategies for Spectroscopy: From Small molecules to Nano Systems." John Wiley & Sons, **2011**.

30. N. Lin, Yi, Luo, K. Ruud, X. Zhao, F. Santoro, A. Rizzo. *ChemPhysChem*., **2011**, 12, 3392.

31. F. Avila, F. Santoro. *Phys. Chem. Chem. Phys*., **2012**,14, 13549.

32. F. J. Avila Ferrer, J. Cerezo, E. Stendardo, R. Improta, F. Santoro. *J. Chem. Theory Comput*., **2013**, 9, 2072.

33. F. J. Avila Ferrer, V. Barone, C. Cappelli, F. Santoro. *J. Chem. Theory Comput.*, **2013**, 9, 3597.

34. R. Improta, F. Avila, E. Stendardo, F. Santoro. *ChemPhysChem.*, **2014**, 15, 3320.

35. J. Cerezo, F. J. Avila, G. Prampolini, F. Santoro. *J. Chem. Theory Comput.*, **2015**, 11, 5810.

36. J. Cerezo, F. Avila, F. Santoro. *Phys. Chem. Chem. Phys.*, **2015**, 17, 11401.

37. A. Petrone, J. Cerezo, F. Avila, G. Donati, R. Improta, N. Rega, F. Santoro. *J. Phys. Chem. A*, **2015**, 119, 5426.

38. J. Cerezo, F. Santoro, G. Prampolini. *Theor. Chem. Acc.*, **2016**, 135, 143.

39. F. Santoro, D. Jacquemin. *WIREs Comput. Mol. Sci.*, **2016**, 6, 460.

40. J. Cerezo, F. Santoro. *J. Chem. Theory Comput.*, **2016**, 12, 4970.

41. Y. Liu, J. Cerezo, N. Lin, X. Zhao, R. Improta, F. Santoro. *Theor. Chem. Acc.*, **2018**, 137, 40.

42. E. Stendardo, F. Avila Ferrer, F. Santoro, R. Improta. *J. Chem. Theory Comput.*, **2012**, 8, 4483.

43. R. Improta, F. J. Avila Ferrer, E. Stendardo, F. Santoro. *ChemPhysChem*, **2014**, 15, 3320.

44. E. C. Le Ru, M. Meyer, E. Blackie, P. G. Etchegoin. *J. Raman Spectrosc.*, **2008**, 39, 1127.

45. C. Tao, Q. An, W. Zhu, H. Yang, W. Li, C. Lin, D. Xu, G. Li. *Chem. Commun.*, **2011**,47, 9867.

46. K. D. Alexander, M. J. Hampton, S. Zhang, A. Dhawan, H. Xu, R.Lopez. *J. Raman Spectrosc.*, **2009**, 40, 2171.

47. H. Chen, M. Lin, C. Wang, Y. Chan, S. Gwo. *J. Am. Chem. Soc.*, **2015**, 137, 1369.

48. P. Kambhampati, C. M. Child, M. C. Foster, A. Campion. *J. Chem. Phys.*, **1998**, 108, 5013.

49. J. R. Lombardi, R. L. Birke, T. Lu, J. Xu. *J. Chem. Phys.*, **1986**, 84, 4174**.**

50. A. Otto, J. Billmann, J. Eicksmans, U. Ertürk, C. Pettenkofer. *Surf. Sci.*, **1984**, 138, 319.

51. A. Vivoni, R. L. Birke, R. Foucault, J. R. Lombardi. *J. Phys. Chem. B*, **2003**, 107, 5547.

52. B. Gu, D. L. Akins. *Chem. Phys. Lett*., **1985**, 113, 558.
53. W. E. Doering, S. Nie. *J. Phys. Chem. B*, **2002**, 106, 311.
54. M.-E. Yu, B.-S. Cheong, H.-G. Cho. *Bull. Korean Chem. Soc*., **2017**, 38, 928.
55. D.-Y. Wu, B. R., Y.-X. Jiang, X. Xu, Z.-Q. Tian. *J. Phys. Chem. A*, **2002**, 106, 9042.
56. Y. Wang, X. G. Gong. *Eur. Phys. J. D*., **2005**, 34, 19.
57. M. N. Huda, A. K. Ray. *Eur. Phys. J. D*., **2003**, 22, 217.
58. M. N. Huda, A. K. Ray. *Phys. Rev*. A, **2003**, 67, 013201.
59. M. D'Alessandro, M. Aschi, C. Mazzuca, A. Palleschi, A. Amadei. *J. Chem. Phys*., **2013**, 139, 114102.
60. M. D'Abramo, M. Aschi, A. Amadei. *J. Chem. Phys*., **2014**, 140, 164104.
61. G. R. Medders, F. Paesani. *J. Chem. Theory Comput*., **2015**, 11, 1145.
62. M. Macchiagodena, G. Del Frate, G. Brancato, B. Chandramouli, G. Mancini, V. Barone. *Phys. Chem. Chem. Phys*., **2017**, 19, 30590.
63. U. N. Morzan, D. J. Alonso de Armiño, N. O. Foglia, F. Ramírez, M. C. González Lebrero, D. A. Scherlis, D. A. Estrin. *Chem. Rev*., **2018**, 118, 4071.
64. V. C. Nibali, M. Havenith. *J. Am. Chem. Soc*., **2014**, 136, 12800.

Capítulo II – Metodología.

En este capítulo se describe el tratamiento teórico y computacional que se ha utilizado en el desarrollo de esta tesis doctoral, y se ha dividido en tres apartados. En el primer apartado se describen, brevemente, los distintos métodos computacionales utilizados. En el segundo apartado, se describen los diferentes modelos teóricos utilizados para reproducir el potencial eléctrico aplicado a una superficie metálica presente en las experiencias SERS electroquímicas. En el siguiente apartado, se describe y se desarrolla en detalle el formalismo matemático de las distintas metodologías y aproximaciones utilizadas en el cálculo de los diferentes tipos de espectros que se han analizado en esta tesis como son, los espectros vibracionales Raman en condiciones de resonancia y los espectros de absorción y de dicroísmo circular electrónico. Finalmente, se proporciona la metodología para proyectar coordenadas internas, permitiendo su separación en varios espacios y el tratamiento de sistemas en conformaciones que no sean mínimos de la superficie de energía potencial.

2.1. Métodos computacionales para el cálculo de la densidad electrónica.

La elección del método va a resultar fundamental para calcular resultados teóricos que puedan predecir los obtenidos experimentalmente. En esta tesis, se ha seleccionado el nivel de cálculo teórico más apropiado para el análisis de los espectros provenientes de las técnicas espectroscópicas SERS y ECD.

Se han utilizado dos métodos distintos: la Teoría del Funcional de la Densidad (DFT) y métodos multiconfiguracionales de campo autoconsistente a nivel del Espacio Activo Completo (CASSCF) y su corrección de segundo orden utilizando la Teoría de Perturbaciones (CASPT2). El método DFT proporciona resultados en concordancia con los resultados experimentales para una gran variedad de sistemas, tal como demuestra el elevado número de estudios realizados con este método en campos muy diversos.[1-8] Otra de sus principales ventajas es el relativamente bajo coste computacional, que permite estudiar sistemas de muy variados tamaños moleculares que van desde decenas a cientos de átomos,[9-13] lo cual ha permitido que se use de forma generalizada.

Por otro lado, los métodos multiconfiguracionales son los únicos capaces de proporcionar resultados fiables cuando tratamos sistemas en los que los electrones tienen que reorganizarse, por ejemplo, excitaciones electrónicas o ruptura y formación de enlaces, ya que al menos, predicen correctamente de modo cualitativo la topología de

la superficie de energía potencial. Esto conlleva un coste computacional mucho más elevado que el caso de los métodos DFT y, por tanto, el uso del método CASPT2 está limitado en la actualidad a sistemas moleculares constituidos por unos pocos átomos.

2.1.1. – Teoría del Funcional de la Densidad (DFT).

El método DFT tiene la ventaja de ofrecer resultados razonables en las situaciones en las que tiene validez a un bajo coste computacional. En cambio, su principal limitación es la dependencia de los resultados con el funcional utilizado, por lo que se debe seleccionar cuidadosamente cuál es el apropiado para la propiedad molecular que se estudia.[8,14-16]

En esta tesis se han utilizado varios funcionales. Los funcionales M06-HF[17] y BP86,[18,19] son adecuados para el tratamiento del fenómeno SERS y del transporte de carga en uniones moleculares ya que, estiman en una buena aproximación las energías de los estados de transferencia de carga y las intensidades Raman en condiciones de resonancia, respectivamente. También se ha utilizado el funcional B3LYP,[20,21] que es muy utilizado en la determinación de parámetros moleculares para un sistema cuyos espectros de dicroísmo circular electrónico es muy dependiente de la estructura molecular. Por último, su extensión CAM-B3LYP[22] se ha usado en sistemas que requieren de unos valores fiables de las energías de los estados de transferencia de carga.

Para fijar el nivel de cálculo mecano cuántico se tiene que indicar, además del funcional, la base electrónica. Los resultados DFT son en general menos dependientes de la base electrónica que del funcional,[23,24] siempre y cuando la base sea lo bastante completa como para describir el comportamiento electrónico del sistema molecular en estudio. En el caso de átomos pesados que contienen un elevado número de electrones, el efecto de la base electrónica en los cálculos DFT se traduce en un importante coste computacional, que se puede atenuar en cierta forma, utilizando pseudopotenciales. Se trata de un tipo de base electrónica donde los electrones internos son tratados de forma implícita en una función matemática de potencial y los electrones de valencia, cuyo efecto en las propiedades bajo estudio se espera sea mayor, se tratan de forma explícita.

La descripción detallada del método y las aproximaciones en las que se basa se puede consultar en numerosos libros.[25-29]

2.1.2. Métodos multiconfiguracionales basados en la teoría del Espacio Activo Completo (CAS).

Los métodos multiconfiguracionales de campo autoconsistente (MCSCF) permiten describir de una forma más adecuada la correlación electrónica, la cual es el mayor inconveniente en el método Hartree-Fock. Uno de los métodos multiconfiguracionales más destacados es el método del Campo Autoconsistente del Espacio Activo Completo (CASSCF) en cual, al igual que en otros métodos CAS, los orbitales se separan en tres grupos: orbitales virtuales, orbitales inactivos y orbitales activos.

Los orbitales virtuales son aquellos que se encuentran desocupados, es decir su ocupación es cero en todas las configuraciones. No contribuyen a la función de onda, aunque sí son tenidos en cuenta en el proceso de optimización de ésta. Los orbitales inactivos son aquellos que se encuentran doblemente ocupados en todas las configuraciones y por tanto su contribución al proceso en estudio es de esperar que sea muy reducida. Finalmente, los orbitales activos son aquellos en los que la ocupación toma valores entre 0 y 2, ya que su valor cambia entre las distintas configuraciones. La función de onda CAS contendría todas las configuraciones resultantes al distribuir los electrones del espacio activo de todas las formas posibles entre los orbitales activos. Una vez especificado el espacio activo, se optimiza la función de onda CASSCF.

El método CASSCF al igual que otros métodos MCSCF, tiene en cuenta la correlación electrónica estática pero no la dinámica. Por ello, es necesario mejorar los resultados obtenidos con otros métodos. Uno de los más adecuados es el de Interacción de Configuraciones Completas (FCI) pero el coste computacional es muy elevado. Por tanto, se recurre a otras alternativas como aquellas basadas en la teoría de perturbaciones, por ejemplo, el método CASPT2. Este método utiliza como función de referencia la obtenida mediante métodos CASSCF y se aplica una corrección de segundo orden a la energía.

La descripción formal de estos métodos está establecida en la bibliografía y en diversos libros.[30-35]

2.2. Simulación de un sistema molecular unido a un metal que está sometido a un potencial eléctrico.

En los trabajos sobre SERS, la molécula a estudiar se encuentra adsorbida sobre un metal en una interfase sólido-líquido que está inevitablemente electrificada. Se trata, por tanto, de un sistema complejo, con multitud de componentes de distintas escalas de tamaño (molécula, metal macroscópico o nanopartículas, disolvente electrolito, etc.) y sometido al inevitable campo eléctrico de la interfase sólido-líquido. Todo ello dificulta la selección del modelo de supermolécula sobre el que realizar los cálculos de las propiedades relevantes en espectroscopía Raman/SERS. Especialmente interesante es estudiar el efecto del potencial de electrodo sobre los resultados SERS electroquímicos, por lo que habrá que llegar a una situación de compromiso para que la simplificación del modelo del sistema sea suficientemente manejable, pero, por el contrario, proporcione unos resultados de utilidad para analizar el comportamiento experimental. El potencial de electrodo es una magnitud macroscópica con efectos físicos y químicos que sintoniza el exceso de carga del metal, modifica las propiedades del complejo superficial metal-adsorbato e induce un campo eléctrico que afecta igualmente a la estructura electrónica global. La toma en consideración del potencial de electrodo en los cálculos teóricos es difícil de materializar, y en esta tesis se han empleado dos aproximaciones diferentes para representar el potencial de electrodo, que serán descritos brevemente a continuación.

2.2.1. *Clústeres* metálicos cargados.

La primera aproximación propuesta se basa en definir *clústeres* metálicos (M) de forma lineal con diferente número de átomos n y carga q, M_n^q, siendo n = 2, 3, 5, 7 y q = ±1 para n impar y q = 0 para n par. De esta forma, se puede definir el parámetro de carga efectiva (q_{eff}) como la relación:

$$q_{eff} = \frac{q}{n} \qquad (1)$$

Este parámetro q_{eff} representa la carga promedio por átomo metálico, y es el análogo microscópico del exceso superficial de carga. Cambiando el tamaño del *clúster* se puede modular la carga efectiva q_{eff}, la cual tendría un papel análogo al potencial de electrodo (Figura 1), ya que la densidad de carga del metal afecta a la estructura electrónica de las moléculas adsorbidas. Este sencillo modelo ha permitido explicar, satisfactoriamente, la

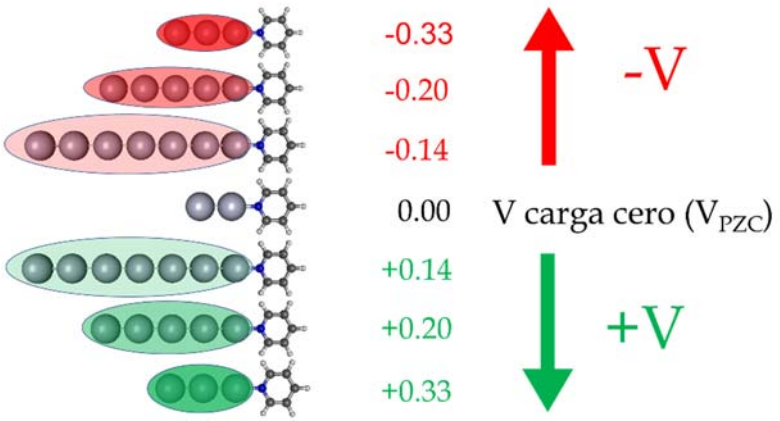

Figura 1. Modelo de los clústeres metálicos cargados para reproducir el potencial de electrodo. PZC hace referencia a las siglas en inglés del potencial de electrodo en el punto de carga cero (electrode potential at the point of zero charge).

intensificación selectiva de determinadas bandas registradas en los SERS de moléculas aromáticas[36-38] cuando el potencial de electrodo se va haciendo más negativo, en base a un mecanismo de intensificación químico o de transferencia de carga.

2.2.2. Campo eléctrico externo.

Una molécula adsorbida sobre una superficie metálica cargada se encuentra sometida a un campo eléctrico ($\vec{E}$) que es perpendicular a dicha superficie, ya que la componente del campo eléctrico paralela a la superficie es prácticamente nula al existir cancelaciones por parte del resto de cargas distribuidas de forma simétrica. De esta forma, en las distintas espectroscopías de superficie, como son la EELS (Electron Energy Loss Spectroscopy) y la IR en superficie, se establece como regla de selección aquella en la que se verán intensificadas las bandas pertenecientes a modos normales que presenten desplazamientos de los átomos en la misma dirección del campo eléctrico. En el caso de la espectroscopía SERS se puede considerar esta regla de selección como aproximada, conocida con el apelativo de *propensity rules* y ha sido muy utilizada en el análisis de las experiencias SERS, ya que ha permitido explicar la intensificación selectiva de ciertas bandas en función de la orientación molecular respecto a la superficie metálica. Experimentalmente, se ha observado que en la mayoría de los SERS de moléculas aromáticas se produce una intensificación selectiva de las bandas pertenecientes a la representación irreducible totalmente simétrica, lo que indicaría una orientación molecular perpendicular a la superficie.

Por tanto, es buena aproximación considerar un modelo teórico en donde el campo eléctrico aplicado a un sistema metal-molécula sea perpendicular a la superficie. Si

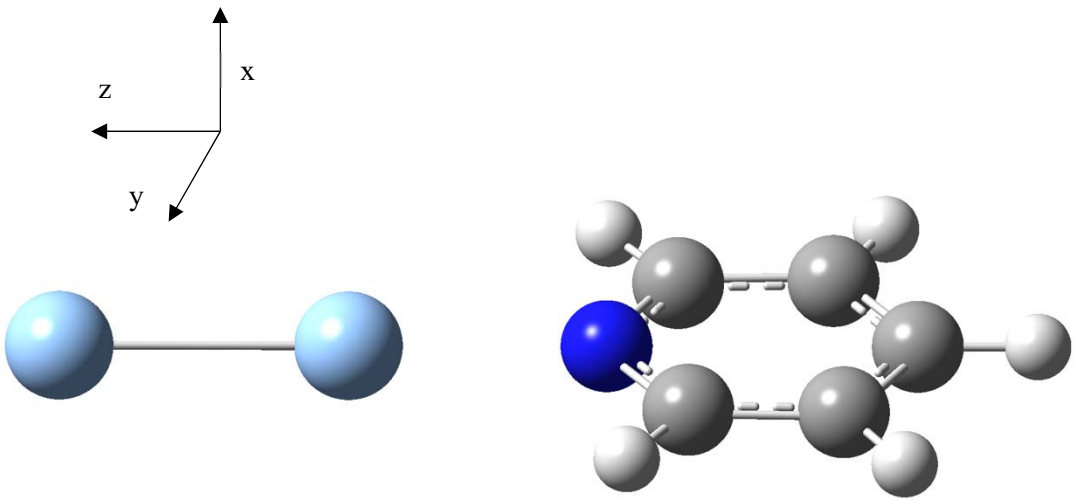

Figura 2. Ejemplo de orientación conveniente de los ejes cartesianos en un *clúster* Ag_2Py bajo el efecto de un campo eléctrico a lo largo de la dirección Z.

además este campo eléctrico es variable, se puede modular el efecto del potencial eléctrico en la estructura electrónica del sistema metal-molécula, al igual que en el modelo anterior, pero con la diferencia de que el clúster metálico utilizado es el mismo en todos los casos.

Este tipo de modelo para el potencial eléctrico (V) al que se encuentra sometido una molécula aplicando un campo eléctrico externo variable ($\vec{E}$), se ha utilizado tal cual se encuentra implementada en el programa Gaussian09.[39] Dado el carácter vectorial del campo eléctrico, es necesario especificar claramente el sistema de coordenadas cartesianas utilizadas. Es conveniente, por ejemplo, coincidir la dirección del campo eléctrico con la del eje Z, que a su vez contiene el eje de rotación de mayor simetría molecular y, además, con sentido positivo hacia el metal. De esta forma se consigue que, al aplicar campos eléctricos positivos, el efecto observado en las propiedades del sistema sea análogo a aplicar un potencial de electrodo positivo, lo cual simplifica el análisis de resultados. La Figura 2 muestra un ejemplo de esta orientación de los ejes cartesianos.

2.3. Tratamiento teórico para el cálculo de intensidades espectrales.

En este apartado se describe en detalle el tratamiento teórico y las distintas aproximaciones adoptadas para el cálculo de las intensidades Raman en condiciones de resonancia y de los espectros de absorción y de dicroísmo circular electrónico.

2.3.1. Intensidades para un proceso de dispersión Raman resonante.

El cálculo de las intensidades Raman para cualquier sistema molecular requiere un largo proceso en varias etapas. En primer lugar, se describe el marco teórico para obtener el tensor de polarizabilidad en condiciones de acoplamiento vibrónico, siguiendo la teoría descrita por Long.[40] Posteriormente, se considera el caso sencillo donde se obtiene la intensidad Raman a través de los factores de Frank-Condon en un sistema con un único modo normal vibracional perteneciente a la representación irreducible totalmente simétrica, y luego se extiende para el caso de múltiples modos normales. En ambos casos se considera un único estado electrónico, por tanto, daría como resultado el espectro teórico Raman correspondiente a una sola transición electrónica resonante. Finalmente, se puede considerar la contribución ponderada de varios estados electrónicos excitados a la intensidad Raman para una radiación incidente determinada. En el caso particular de una transición resonante entre estados electrónicos que presenta pequeños desplazamientos entre los mínimos de la superficie de energía potencial se puede hacer simplificaciones adicionales en el cálculo de las intensidades, y éstas han sido descritas en el último apartado.

2.3.1.1 – Expresión mecano-cuántica del tensor de polarizabilidad bajo condiciones de resonancia.

En el marco de la aproximación de Born-Oppenheimer,[41] la función de onda molecular puede ser factorizada en las funciones de ondas puramente electrónica (e), vibracional (v) y rotacional (r). Consecuentemente, su contribución a la energía también puede ser separada en estos mismos términos.

$$\Psi^{evr} = \Psi^{e}\Psi^{v}\Psi^{r} \qquad (2)$$

La parte rotacional tiene generalmente una contribución menor, y se puede ignorar en el tratamiento de la dispersión Raman.

Considérense estados vibraciones inicial *i* y final *f*, en el estado electrónico fundamental g, y un estado vibracional r en un estado excitado virtual e. En la notación de Dirac, dichos estados se pueden expresar como:

$$|i\rangle = |gm\rangle = |g\rangle|m\rangle \tag{3}$$

$$|f\rangle = |gn\rangle = |g\rangle|n\rangle \tag{4}$$

$$|r\rangle = |ev\rangle = |e\rangle|v\rangle \tag{5}$$

Donde $|e\rangle$ y $|g\rangle$ son funciones de onda electrónicas puras, y $|m\rangle$, $|n\rangle$ y $|v\rangle$ son funciones de onda vibracionales puras de los estados inicial, final y virtual, respectivamente.

Una transición Raman $|f\rangle \longleftarrow |i\rangle$ puede ser expresada como:

$$|f\rangle \longleftarrow |i\rangle = \langle n|\mu_{ge}|v\rangle\langle v|\mu_{eg}|m\rangle \tag{6}$$

Donde μ es el momento dipolar de la transición entre los estados electrónicos indicados como subíndices.

Los componentes de la polarizabilidad de una transición vibracional desde el estado *m* al estado *n* en el estado electrónico fundamental *g*, son:

$$[\alpha_{\rho\sigma}] = \frac{1}{hc}\sum_{ev}\left[\frac{\langle n|[\mu_\rho]_{ge}|v\rangle\langle v|[\mu_\sigma]_{eg}|m\rangle}{\bar{\upsilon}_{ev,gm} - \bar{\upsilon}_0 + i\Gamma_{ev}} + \frac{\langle n|[\mu_\sigma]_{ge}|v\rangle\langle v|[\mu_\rho]_{eg}|m\rangle}{\bar{\upsilon}_{ev,gn} + \bar{\upsilon}_0 + i\Gamma_{ev}}\right] \tag{7}$$

ρ y σ indican la componente del tensor de polarizabilidad, *h* es la constante de Planck, *c* es la velocidad de la luz, $\bar{\upsilon}_{ev,gm}$ es el número de onda de la transición vibrónica del estado vibracional inicial *m* en el estado electrónico fundamental *g* al estado vibracional *v* del estado electrónico virtual *e*, $\bar{\upsilon}_{ev,gn}$ es el número de onda de la transición vibrónica del estado vibracional *v* al en el estado electrónico virtual *e* al estado vibracional *n* del estado electrónico fundamental *g*, $\bar{\upsilon}_0$ es el número de onda de la radiación incidente y Γ_{ev} la semianchura de banda, magnitud relacionada con el tiempo de vida del estado. Las componentes de los momentos dipolares de la transición se pueden desarrollar en las siguientes expresiones:

$$[\mu_\rho]_{ge} = \langle g|\hat{\mu}_\rho|e\rangle \tag{8}$$

$$[\mu_\sigma]_{eg} = \langle e|\hat{\mu}_\sigma|g\rangle \tag{9}$$

Si se introduce el acoplamiento vibracional, la dependencia del Hamiltoniano electrónico con las coordinadas normales Q_k en las proximidades de la posición de equilibrio Q_0 se puede desarrollar como polinomio de Taylor:

$$\hat{H}_e(Q) = \left(\hat{H}_e\right)_0 + \sum_k \left(\frac{\partial \hat{H}_e}{\partial Q_k}\right)_0 Q_k + \cdots \tag{10}$$

La serie puede ser truncada en el segundo término cuando los desplazamientos son pequeños, situación que generalmente se da cuando $n = m + 1$. El acoplamiento entre estados se puede tratar mediante la teoría de perturbaciones. Un estado perturbado r' se acopla con otro estado s a través del modo vibracional k tal como describe la siguiente ecuación:

$$|r'(Q_0)\rangle = |r(Q_0)\rangle + \frac{1}{hc}\sum_k \frac{h_{rs}^k}{\Delta\bar{v}_{rs}} Q_k \, |s(Q_0)\rangle \tag{11}$$

Donde h_{rs}^k es:

$$h_{rs}^k = \left\langle g \left| \frac{\delta H_e}{\delta Q_k} \right| s \right\rangle_{Q_k=0} \tag{12}$$

El término $\frac{h_{rs}^k}{\Delta\bar{v}_{rs}}$ mide como de fuertemente están acoplados r y s a lo largo del modo Q_k. Esta expresión es solo válida si $\frac{h_{rs}^k}{\Delta\bar{v}_{rs}} \ll \bar{v}_k$ ya que de otro modo estaría fuera del marco de aplicabilidad de la aproximación de Born-Oppenheimer.

Para funciones reales, se cumple que $|r'(Q_0)\rangle = \langle r'(Q_0)|$, lo cual implica:

$$\langle r'(Q_0)| = \langle r(Q_0)| + \frac{1}{hc}\sum_k \langle s(Q_0)| \frac{h_{sr}^k}{\Delta\bar{v}_{sr}} Q_k \tag{13}$$

En este caso $h_{rs}^k = h_{sr}^k$. De aquí en adelante, se omitirá la etiqueta Q_0.

Considerando ahora un estado excitado s accesible por las reglas de selección de dipolo eléctrico, y un estado excitado t diferente que no es accesible por las reglas de selección de dipolo eléctrico, se obtiene la siguiente expresión al transferir las ecuaciones anteriores a μ_σ:

$$\langle e'|\mu_\sigma|g'\rangle = \left(\langle e| + \frac{1}{hc}\sum_k \langle s| \frac{h_{es}^k}{\Delta\bar{v}_{es}} Q_k\right) |\hat{\mu}_\sigma| \left(|g\rangle + \frac{1}{hc}\sum_k \frac{h_{tg}^k}{\Delta\bar{v}_{tg}} Q_k \, |t\rangle\right) \tag{14}$$

Desarrollando el producto, se obtiene:

$$\langle e'|\mu_\sigma|g'\rangle = \langle e|\mu_\sigma|g\rangle + \frac{1}{hc}\sum_k \frac{h_{es}^k}{\Delta\bar{\upsilon}_{es}} Q_k \langle s|\mu_\sigma|g\rangle + \frac{1}{hc}\sum_k \frac{h_{tg}^k}{\Delta\bar{\upsilon}_{tg}} Q_k \langle e|\mu_\sigma|t\rangle + \frac{1}{h^2c^2}\sum_k \frac{h_{es}^k}{\Delta\bar{\upsilon}_{es}} Q_k \sum_k \frac{h_{tg}^k}{\Delta\bar{\upsilon}_{tg}} Q_k \langle s|\mu_\sigma|t\rangle \quad (15)$$

Análogamente, para μ_ρ:

$$\langle g'|\mu_\rho|e'\rangle = \left(\langle g| + \frac{1}{hc}\sum_k \langle t| \frac{h_{gt}^k}{\Delta\bar{\upsilon}_{gt}} Q_k\right) |\hat{\mu}_\rho| \left(|e\rangle + \frac{1}{hc}\sum_k \frac{h_{se}^k}{\Delta\bar{\upsilon}_{se}} Q_k |s\rangle\right) \quad (16)$$

$$\langle g'|\mu_\rho|e'\rangle = \langle g|\mu_\rho|e\rangle + \frac{1}{hc}\sum_k \frac{h_{gt}^k}{\Delta\bar{\upsilon}_{gt}} Q_k \langle t|\mu_\rho|e\rangle + \frac{1}{hc}\sum_k \frac{h_{se}^k}{\Delta\bar{\upsilon}_{se}} Q_k \langle g|\mu_\rho|s\rangle + \frac{1}{h^2c^2}\sum_k \frac{h_{gt}^k}{\Delta\bar{\upsilon}_{gt}} Q_k \sum_k \frac{h_{se}^k}{\Delta\bar{\upsilon}_{se}} Q_k \langle t|\mu_\rho|s\rangle \quad (17)$$

El término de segundo orden en las ecuaciones 15 y 17 se puede despreciar, ya que asumimos que Q_k debe ser pequeño y además aparece elevado al cuadrado. Volviendo a la nomenclatura empleada en las ecuaciones 8 y 9, tras considerar el acoplamiento vibrónico propuesto por Herzberg y Teller,[42] y reemplazando las componentes del momento dipolar de la transición por $[\mu_\rho]_{ge}^0 = \langle g|\hat{\mu}_\rho|e\rangle$ y $[\mu_\sigma]_{eg}^0 = \langle e|\hat{\mu}_\sigma|g\rangle$ se obtiene:

$$[\mu_\rho]_{ge} = [\mu_\rho]_{ge}^0 + \frac{1}{hc}\sum_k \frac{h_{gt}^k}{\Delta\bar{\upsilon}_{gt}} Q_k [\mu_\rho]_{te}^0 + \frac{1}{hc}\sum_k \frac{h_{se}^k}{\Delta\bar{\upsilon}_{se}} Q_k [\mu_\rho]_{gs}^0 \quad (18)$$

$$[\mu_\sigma]_{eg} = [\mu_\sigma]_{eg}^0 + \frac{1}{hc}\sum_k \frac{h_{es}^k}{\Delta\bar{\upsilon}_{es}} Q_k [\mu_\sigma]_{sg}^0 + \frac{1}{hc}\sum_k \frac{h_{tg}^k}{\Delta\bar{\upsilon}_{tg}} Q_k [\mu_\sigma]_{et}^0 \quad (19)$$

Las ecuaciones resultantes se pueden introducir en la ecuación 7, pero antes se tendrá en consideración la siguiente simplificación. En Resonancia Raman, la energía de la radiación incidente $\bar{\upsilon}_0$ es próxima a la energía necesaria para alcanzar el estado excitado en resonancia, de modo que $\bar{\upsilon}_{ev,gm} \cong \bar{\upsilon}_0 \cong \bar{\upsilon}_{ev,gn}$ y por tanto, el segundo término de la ecuación 7 se puede despreciar, ya que su denominador es mucho mayor que el primer término. La expresión resultante es:

$$[\alpha_{\rho\sigma}] = \frac{1}{hc}\sum_{ev}\left[\frac{\langle n|[\mu_\rho]_{ge}|v\rangle\langle v|[\mu_\sigma]_{eg}|m\rangle}{\bar{\upsilon}_{ev.gm} - \bar{\upsilon}_0 + i\Gamma_{ev}}\right] \quad (20)$$

Reemplezando $[\mu_\rho]_{ge}$ y $[\mu_\sigma]_{eg}$ por las expresiones de las ecuaciones 17, 18 y 19, y expandiendo la suma, el tensor de la polarizabilidad se pueden expresar como suma de cuatro términos:

$$[\alpha_{\rho\sigma}] = A + B + C + D \tag{21}$$

Cada término viene dado por las siguientes expresiones:

$$A = \frac{1}{hc}[\mu_\rho]^0_{ge}[\mu_\sigma]^0_{eg}\sum_{e\neq g}\frac{\langle n|v\rangle\langle v|m\rangle}{\bar{\upsilon}_{ev,gm} - \bar{\upsilon}_0 + i\Gamma_{ev}} \tag{22}$$

$$B = \frac{1}{h^2c^2}[\mu_\rho]^0_{gs}[\mu_\sigma]^0_{eg}\sum_{e\neq g}\sum_k \frac{h^k_{se}}{\Delta\bar{\upsilon}_{se}}\frac{\langle n|Q_k|v\rangle\langle v|m\rangle}{\bar{\upsilon}_{ev,gm} - \bar{\upsilon}_0 + i\Gamma_{ev}} +$$

$$\frac{1}{h^2c^2}[\mu_\rho]^0_{ge}[\mu_\sigma]^0_{sg}\sum_{e\neq g}\sum_k \frac{h^k_{es}}{\Delta\bar{\upsilon}_{es}}\frac{\langle n|v\rangle\langle v|Q_k|m\rangle}{\bar{\upsilon}_{ev,gm} - \bar{\upsilon}_0 + i\Gamma_{ev}} \tag{23}$$

$$C = \frac{1}{h^2c^2}[\mu_\rho]^0_{te}[\mu_\sigma]^0_{eg}\sum_{e\neq g}\sum_k \frac{h^k_{gt}}{\Delta\bar{\upsilon}_{gt}}\frac{\langle n|Q_k|v\rangle\langle v|m\rangle}{\bar{\upsilon}_{ev,gm} - \bar{\upsilon}_0 + i\Gamma_{ev}} +$$

$$\frac{1}{h^2c^2}[\mu_\rho]^0_{ge}[\mu_\sigma]^0_{et}\sum_{e\neq g}\sum_k \frac{h^k_{tg}}{\Delta\bar{\upsilon}_{tg}}\frac{\langle n|v\rangle\langle v|Q_k|m\rangle}{\bar{\upsilon}_{ev,gm} - \bar{\upsilon}_0 + i\Gamma_{ev}} \tag{24}$$

$$D = \frac{1}{h^3c^3}[\mu_\rho]^0_{te}[\mu_\sigma]^0_{sg}\sum_{k,k'}\frac{h^k_{gt}}{\Delta\bar{\upsilon}_{gt}}\frac{h^{k'}_{es}}{\Delta\bar{\upsilon}_{es}}\frac{\langle n|Q_k|v\rangle\langle v|Q_k|m\rangle}{\bar{\upsilon}_{ev,gm} - \bar{\upsilon}_0 + i\Gamma_{ev}} +$$

$$\frac{1}{h^3c^3}[\mu_\rho]^0_{te}[\mu_\sigma]^0_{et}\sum_{k,k'}\frac{h^k_{gt}}{\Delta\bar{\upsilon}_{gt}}\frac{h^{k'}_{tg}}{\Delta\bar{\upsilon}_{tg}}\frac{\langle n|Q_k|v\rangle\langle v|Q_k|m\rangle}{\bar{\upsilon}_{ev,gm} - \bar{\upsilon}_0 + i\Gamma_{ev}} +$$

$$\frac{1}{h^3c^3}[\mu_\rho]^0_{gs}[\mu_\sigma]^0_{sg}\sum_{k,k'}\frac{h^k_{se}}{\Delta\bar{\upsilon}_{se}}\frac{h^{k'}_{es}}{\Delta\bar{\upsilon}_{es}}\frac{\langle n|Q_k|v\rangle\langle v|Q_k|m\rangle}{\bar{\upsilon}_{ev,gm} - \bar{\upsilon}_0 + i\Gamma_{ev}} +$$

$$\frac{1}{h^3c^3}[\mu_\rho]^0_{gs}[\mu_\sigma]^0_{et}\sum_{k,k'}\frac{h^k_{se}}{\Delta\bar{\upsilon}_{se}}\frac{h^{k'}_{tg}}{\Delta\bar{\upsilon}_{tg}}\frac{\langle n|Q_k|v\rangle\langle v|Q_k|m\rangle}{\bar{\upsilon}_{ev,gm} - \bar{\upsilon}_0 + i\Gamma_{ev}} \tag{25}$$

De los cuatro sumandos que presenta el término *D*, es de esperar que el tercero sea el más relevante y el que más peso tiene de todos ellos, ya que los términos, $\Delta\bar{v}_{se}, \Delta\bar{v}_{es}$, presentes en el denominador, involucran acoplamiento entre estados electrónicos excitados, que en general, suelen estar más próximos en energía entre ellos, que en el caso de un acoplamiento entre el estado electrónico fundamental *g* y otros estados excitados diferentes al resonante, como ocurre en los dos primeros y último sumandos, $\Delta\bar{v}_{gt}$ y $\Delta\bar{v}_{tg}$, respectivamente, del término D. Por tanto, el término *D* se puede simplificar a:

$$D = \frac{1}{h^3 c^3}\left[\mu_\rho\right]_{gs}^{0}\left[\mu_\sigma\right]_{sg}^{0}\sum_{k.k'}\frac{h_{se}^{k}}{\Delta\bar{v}_{se}}\frac{h_{es}^{k'}}{\Delta\bar{v}_{es}}\frac{\langle n|Q_k|v\rangle\langle v|Q_k|m\rangle}{\bar{v}_{ev.gm}-\bar{v}_0+i\Gamma_{ev}} \qquad (26)$$

Los diferentes términos de la polarizabilidad se agrupan atendiendo a razones de acoplamiento entre estados electrónicos. El término *A* no contiene acoplamiento de estados electrónicos, y es distinto de cero si se cumplen dos condiciones: (i) que las transiciones electrónicas resonantes están permitidas por las reglas de selección del mecanismo de dipolo eléctrico, y (ii) que además las integrales de solapamiento vibracional $\langle n|v\rangle\langle v|m\rangle$, también llamadas de Franck-Condon, sean distintas de cero para al menos algunos valores de v. Es por ello que la intensificación de una banda Raman a través del término A se encuentra asociada a los factores de Franck-Condon.

Los factores de Franck-Condon, son distintas de cero si se cumple al menos una de las dos condiciones siguientes:

1) Si $n = m = v$.

2) Si las funciones de onda vibracionales de n y v son no ortogonales. Esta condición se cumple en dos situaciones: (a) si existe una separación entre los mínimos de las superficies de energía potencial de los dos estados electrónicos implicados en el proceso resonante a lo largo de una coordena normal de vibración, esto es, $\Delta Q_k \neq 0$, o bien (b) si existe una variación en la curvatura de estas superficies resonantes a lo largo del modo Q_k, lo que significa un cambio en el número de onda de la vibración al pasar de un estado electrónico a otro, es decir, $\Delta v_k \neq 0$. En el primer caso (a) daría lugar a la intensificación de vibraciones totalmente simétricas, mientras que el segundo caso (b) permitiría activar modos no totalmente simétricos. En la Figura 3 se recogen los prosibles casos donde el término A es distinto de cero.

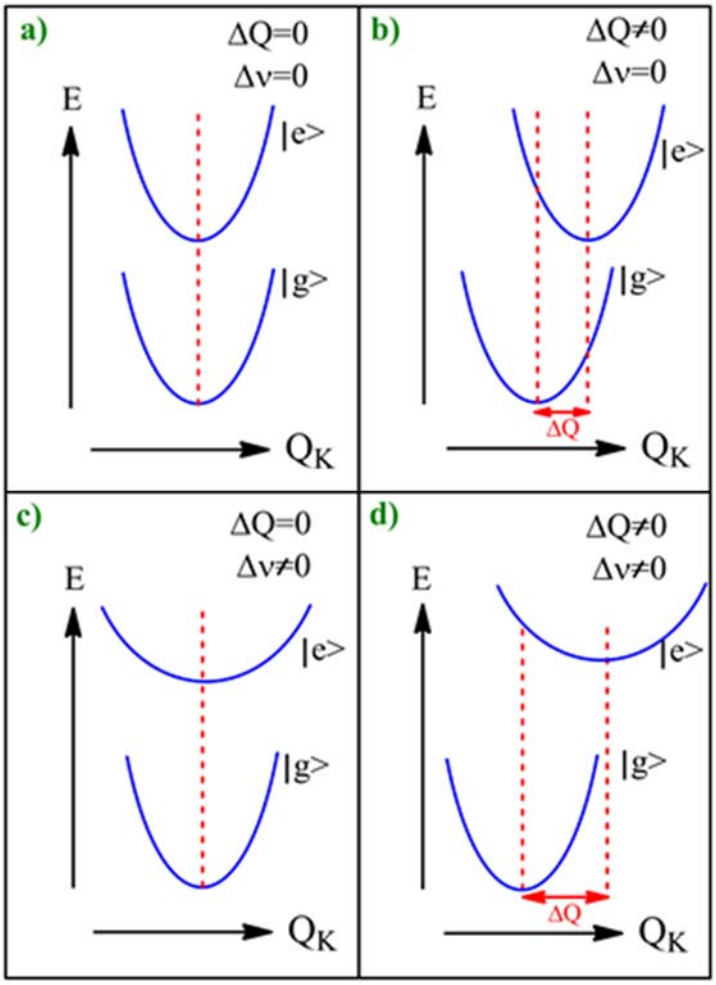

Figura 3. Tipos de transición desde un estado electónico fundamental $|g\rangle$ a otro excitado $|e\rangle$donde las integrales de solapamiento (Factores de Franck-Condon, Término A en resonancia Raman) son a) cero ($\Delta Q = 0, \Delta\bar{\nu} = 0$) y distinta de cero b) $\Delta Q \neq 0$, $\Delta\bar{\nu} = 0$, c) $\Delta Q = 0, \Delta\bar{\nu} \neq 0$)y d) $\Delta Q \neq 0, \Delta\bar{\nu} \neq 0$).

El término B, se caracteriza por el acoplamiento entre el estado electrónico excitado resonante y otro estado excitado próximo en energía. Este acoplamiento será tanto más efectivo cuanto más próximos en energía se encuentren dichos estados excitados, ya que el término $\Delta\bar{\nu}_{se}$ se encuentra en el denominador. Este no se anula cuando están permitidas las transiciones electrónicas a ambos estados excitados según las reglas de selección del mecanismo de dipolo eléctrico, y cuando las integrales mixtas de Frank-Condon y Herzberg-Teller, $\langle n|Q_k|v\rangle\langle v|m\rangle$ y $\langle n|v\rangle\langle v|Q_k|m\rangle$, sean distintas de cero, como es el caso cuando la simetría de los modos normales que acopla dichos estados está contenida en el producto directo de las representaciones irreducibles de los dos estados acoplados.

El término C involucra acoplamientos entre el estado fundamental y estados excitados, y no exige la condición de que la transición sea permitida por el mecanismo de dipolo

eléctrico. Su contribución es generalmente muy pequeña debido a que la separación energética entre estado fundamental y estados excitados.

El término *D*, involucra acoplamiento de los dos estados electrónicos que participan en el proceso de dispersión con otros estados. Su contribución es generalmente muy pequeña, y sería responsable de la aparición de sobretodos y bandas de combinación binarias.

Generalmente, los términos A y B de la polarizabilidad son los que más contribuyen a la intensidad Raman en condiciones de resonancia. Sin embargo, en una primera aproximación sólo se considerará el término A en el cálculo de las intensidades Raman, ya que en la mayoría de los experimentos SERS de moléculas aromáticas se intensifican las bandas pertenecientes a modos totalmente simétricos.

2.3.1.2. Intensidades de resonancia Raman a través del término A para modos normales totalmente simétricos.

Inicialmente se describirá el caso más sencillo correspondiente a una transición resonante considerando un único estado excitado en especies moleculares que poseen un único modo normal totalmente simétrico, como es el caso de moléculas diatómicas, tetraédricas o plano cuadrada tipo MX_4, y octaédricas tipo MX_6. En este caso se puede hacer las siguientes simplificaciones:

1) Se asume que un único estado excitado resonante *e* presenta una contribución significativa en el tensor de polarizabilidad.

2) Se considera que todas las moléculas se encuentran inicialmente en su estado vibracional más bajo, por tanto $m = 0$, y la población de Boltzmann del estado vibracional fundamental, N_0, es igual a 1.

3) Se asume únicamente la contribución del término *A* de la polarizabilidad al ser mucho mayor su contribución a la intensidad Raman que el resto de los términos.

En la situación propuesta, solo los componentes de la polarizabilidad de la diagonal principal tendrán una contribución no nula, esto es $\rho = \sigma$. Bajo estas suposiciones, la polarizabilidad se expresa como:

$$[\alpha_{\rho\rho}]_{gn.g0} = \frac{1}{hc}\left([\mu_\rho]_{eg}^0\right)^2 \sum_k \frac{\langle n|v\rangle\langle v|0\rangle}{\bar{\upsilon}_{ev.g0} - \bar{\upsilon}_0 + i\Gamma_{ev}} \qquad (27)$$

Considerando $\mu_{eg} = \mu_{ge}$. Las integrales de solapamiento son monodimensionales en este caso, y se pueden resolver utilizando las fórmulas de recurrencia de Manneback.[43]

$$\langle 0_k^a | 0_k^b \rangle = \left(\frac{2(\bar{v}_k^b \bar{v}_k^a)^{1/2}}{\bar{v}_k^b + \bar{v}_k^a} \right)^{1/2} e^{-\left(\frac{\Delta_k^2}{2}\right)} \tag{28}$$

$$\langle v_k^a | v_k^b + 1 \rangle = -\left(\frac{v_k^b}{v_k^b + 1} \right)^{1/2} \left(\frac{\bar{v}_k^a - \bar{v}_k^b}{\bar{v}_k^a + \bar{v}_k^b} \right) \langle v_k^a | v_k^b - 1 \rangle + \left(\frac{v_k^a}{v_k^b + 1} \right)^{1/2} \frac{2(\bar{v}_k^a \bar{v}_k^b)^{1/2}}{(\bar{v}_k^a + \bar{v}_k^b)} \langle v_k^a - 1 | v_k^b \rangle$$
$$- \left(\frac{1}{v_k^b + 1} \right)^{1/2} \Delta_k \left(\frac{2\bar{v}_k^a}{\bar{v}_k^a + \bar{v}_k^b} \right)^{1/2} \langle v_k^a | v_k^b \rangle \tag{29}$$

$$\langle v_k^a + 1 | v_k^b \rangle = -\left(\frac{v_k^a}{v_k^a + 1} \right)^{1/2} \left(\frac{\bar{v}_k^a - \bar{v}_k^b}{\bar{v}_k^a + \bar{v}_k^b} \right) \langle v_k^a - 1 | v_k^b \rangle + \left(\frac{v_k^b}{v_k^a + 1} \right)^{1/2} \frac{2(\bar{v}_k^a \bar{v}_k^b)^{1/2}}{(\bar{v}_k^a + \bar{v}_k^b)} \langle v_k^a | v_k^b - 1 \rangle$$
$$- \left(\frac{1}{v_k^a + 1} \right)^{1/2} \Delta_k \left(\frac{2\bar{v}_k^a}{\bar{v}_k^a + \bar{v}_k^b} \right)^{1/2} \langle v_k^a | v_k^b \rangle \tag{30}$$

$\bar{v}_k^a$ y $\bar{v}_k^b$ son los números de onda de las vibraciones clásicas, mientras que v_k^a and v_k^b son los números cuánticos vibracionales para el modo k. Δ_k se define como el desplazamiento adimensional, que está directamente relacionado con la separación entre los mínimos de energía de los dos estados electrónicos involucrados en el proceso resonante a lo largo del modo normal Q_k:

$$\Delta_k = \left(\frac{4\pi^2 c}{h} \right)^{1/2} \left(\frac{\bar{v}_k^a \bar{v}_k^b}{\bar{v}_k^a + \bar{v}_k^b} \right)^{1/2} \Delta Q_k \tag{31}$$

Con estas ecuaciones se puede calcular la polarizabilidad para una transición resonante.

Para conocer la intensidad asociada a dicha transición, hay que tener en cuenta, además, la relación matemática entre la intensidad Raman dispersada a 90 grados con respecto a la excitatriz, y la polarizabilidad de una transición Stokes $|f\rangle \longleftarrow |i\rangle$:

$$I_{fi}\left(\frac{\pi}{2}\right) = \left(\frac{\pi}{\varepsilon_0}\right)^2 (\bar{v}_0 - \bar{v}_{fi})^4 J_0 \sum_{\rho\sigma} [\alpha_{\rho\sigma}]_{fi} [\alpha_{\rho\sigma}]_{fi}^* \tag{32}$$

Siendo ε_0 la permitividad del vacío, $\bar{v}_0$ y $\bar{v}_{fi}$ los números de onda de los fotones incidente y dispersado, y J_0 la irradiancia de la radiación incidente.

Reemplazando en la anterior expresión la polarizabilidad para el caso particular de un único modo vibracional totalmente simétrico proporcionado por la ecuación 27, resulta:

$$[\alpha_{\rho\rho}]_{gn.g0}[\alpha_{\rho\rho}]^*_{gn.g0} = \frac{1}{h^2c^2}\left([\mu_\rho]^0_{eg}\right)^4 \sum_v \frac{\langle n|v\rangle\langle v|0\rangle}{\bar{\upsilon}_{ev.g0} - \bar{\upsilon}_0 + i\Gamma_v} \sum_{v'} \frac{\langle n|v\rangle\langle v|0\rangle}{\bar{\upsilon}_{ev'.g0} - \bar{\upsilon}_0 - i\Gamma_{v'}} \quad (33)$$

$$I_{gn.g0}\left(\frac{\pi}{2}\right) = KN_0(\bar{\upsilon}_0 - \bar{\upsilon}_{fi})^4 \left([\mu_\rho]^0_{eg}\right)^4 \sum_v \frac{\langle n|v\rangle\langle v|0\rangle}{\bar{\upsilon}_{ev.g0} - \bar{\upsilon}_0 + i\Gamma_v} \sum_{v'} \frac{\langle n|v\rangle\langle v|0\rangle}{\bar{\upsilon}_{ev'.g0} - \bar{\upsilon}_0 - i\Gamma_{v'}} \quad (34)$$

$$K = \left(\frac{\pi}{\varepsilon_0 hc}\right)^2 J_0 \quad (35)$$

Donde K es una constante para una irradiancia J_0 dada y N_0 es la población de Bolztmann del estado vibracional más bajo en energía en el estado electrónico fundamental g, a la que previamente se le asignó un valor de 1.

Por tanto, la ecuación 34 corresponde a la expresión matemática que proporciona la intensidad Raman teórica para especies con un único modo normal vibracional una vez que las integrales sean resueltas con las fórmulas de recurrencia de Manneback.

Este resultado se puede extender a especies moleculares con N modos vibracionales totalmente simétricos, si asumimos que las coordenadas normales del estado excitado son las mismas que en el estado fundamental. Esto ocurre si no hay acoplamiento entre los modos vibracionales, y por tanto la matriz de Duschinsky J, que indica la rotación o transformación entre modos normales, es igual a 1. Si se cumple esta condición, los factores de Frank-Condon multidimensionales se pueden expresan como un producto de factores monodimensionales.

$$\langle n|v\rangle = \langle n_1 n_2 n_3 \dots n_N | v_1 v_2 v_3 \dots v_N\rangle = \prod_{i=1}^{N} \langle n_i|v_i\rangle \quad (36)$$

$$\langle v|m\rangle = \langle v_1 v_2 v_3 \dots v_N | m_1 m_2 m_3 \dots m_N\rangle = \prod_{i=1}^{N} \langle v_i|m_i\rangle \quad (37)$$

Estas integrales pueden ser resueltas con las fórmulas de recurrencia de Manneback y es posible calcular la polarizabilidad y, en consecuencia, la intensidad Raman al igual que se ha realizado en el caso anterior.

En el caso de que haya varios estados excitados en resonancia, su contribución debe ser considerada. Al tensor de polarizabilidad descrito anteriormente en la ecuación 27 debe de incluir ahora todos los estados excitados relevantes e_i:

$$[\alpha_{\rho\rho}]_{gn.g0} = \frac{1}{hc} \sum_{e_i} \left([\mu_\rho]^0_{e_i g}\right)^2 \sum_k \frac{\langle n|v\rangle\langle v|0\rangle}{\bar{\upsilon}_{e_i v.g0} - \bar{\upsilon}_0 + i\Gamma_{e_i v}} \quad (38)$$

El procedimiento para calcular los factores de Frank-Condon $\langle n|v\rangle\langle v|0\rangle$ sigue siendo el mismo que se ha descrito anteriormente mediante el empleo de las fórmulas de recurrencia de Manneback. Bajo esta situación se obtiene el espectro resonante con una contribución ponderada de varios estados electrónicos excitados donde se tiene que seleccionar la energía del fotón inocente y la anchura de línea homogénea.

2.3.1.3. Intensidades Raman resonante a través del Término A en la aproximación de pequeños desplazamientos Δ_k.

En el caso particular en que cada uno de los desplazamientos, Δ_k son pequeños, pero no nulo, es decir, cuando los mínimos de energía de los estados involucrados en el proceso de resonancia a lo largo de cada coordenada normal Q_k estén próximos, se pueden aplicar las siguientes aproximaciones adicionales a los factores de Frank-Condon:

$$\left\langle 1_k^b | 1_k^a \right\rangle = \left\langle 0_k^b | 0_k^a \right\rangle = 1 \tag{39}$$

$$\left\langle 1_k^a | 0_k^b \right\rangle = -\left\langle 0_k^a | 1_k^b \right\rangle = \Delta_k \tag{40}$$

Cualquier transición involucrando un cambio de dos cuantos o más, contendría potencias de Δ_k y dada la suposición de que $\Delta_k \ll 1$, cualquier potencia de Δ_k resultaría en cantidades con muy poco peso en la suma de estados, por lo que pueden ser despreciados. El sumatorio extendido a todos los niveles v está restringida a contribuciones de v=0 y v=1 y los factores de Franck-Condon serán no cero solo para n=0 (Dispersión Rayleigh) y n=1 (Dispersión Raman). Por tanto, en esta aproximación de pequeños desplazamientos los sobretonos están prohibidos.

Incluyendo las anteriores aproximaciones en la ecuación 27, se obtiene:

$$\left[\alpha_{\rho\rho}\right]_{gn.g0} = \frac{1}{hc}\left(\left[\mu_\rho\right]_{eg}^0\right)^2 \Delta_k \left(\frac{-1}{\bar{\nu}_{e0,g0} - \bar{\nu}_0 - i\Gamma_{e0}} + \frac{1}{\bar{\nu}_{e1,g0} - \bar{\nu}_0 - i\Gamma_{e0}}\right) \tag{41}$$

Reagrupando los denominadores, e introduciendo el resultado en la intensidad:

$$I_k = KN_0(\bar{\nu}_0 - \bar{\nu}_{fi})^4 \left(\left[\mu_\rho\right]_{eg}^0\right)^4 \Delta_k^2 \left\{\frac{\Omega_0^2 + \Omega_1^2 - 2\Omega_0^2\Omega_1^2}{(\Omega_0^2 + \Gamma_{e0}^2)(\Omega_1^2 + \Gamma_{e0}^2)}\right\} \tag{42}$$

Donde $\Omega_0^2 = \left(\bar{\nu}_{e0,g0} - \bar{\nu}_0\right)^2$ y $\Omega_1^2 = \left(\bar{\nu}_{e1,g0} - \bar{\nu}_0\right)^2$. Al estar considerando osciladores armónicos, se puede utilizar el resultado:

$$\Omega_1 - \Omega_0 = \nu_k \tag{43}$$

Rescribiendo el numerador en la ecuación 42 y usando la ecuación 43, se obtiene finalmente:

$$I_k = KN_0(\bar{\upsilon}_0 - \bar{\upsilon}_{fi})^4 \left(\left[\mu_\rho \right]_{eg}^0 \right)^4 \Delta_k^2 \left\{ \frac{(\Omega_1 - \Omega_0)^2}{(\Omega_0^2 + \Gamma_{e0}^2)(\Omega_1^2 + \Gamma_{e0}^2)} \right\} \tag{44}$$

$$I_k = KN_0(\bar{\upsilon}_0 - \bar{\upsilon}_{fi})^4 \left(\left[\mu_\rho \right]_{eg}^0 \right)^4 \Delta_k^2 \left\{ \frac{\upsilon_k^2}{(\Omega_0^2 + \Gamma_{e0}^2)(\Omega_1^2 + \Gamma_{e0}^2)} \right\} \tag{45}$$

La ecuación 45 se puede extender a múltiples estados excitados, cuya fórmula para la intensidad se expresaría como:

$$I_k = KN_0\left(\bar{\upsilon}_0 - \bar{\upsilon}_{fi}\right)^4 \upsilon_k^2 \sum_e \left(G_{\Gamma_{e,k}}^e \Delta_{k,e} \right)^2 \tag{46}$$

Donde $G_{\Gamma_{e,k}}^e$es:

$$G_{\Gamma_{r.k}}^e = \frac{|\mu_e^0|^2}{\left(\bar{\upsilon}_{e0,g0} - \bar{\upsilon}_0 + \Gamma_{e,k}^2\right)^{1/2} \left(\bar{\upsilon}_{e0,g0} + \bar{\upsilon}_k - \bar{\upsilon}_0 + \Gamma_{e,k}^2\right)^{1/2}} \tag{47}$$

La ecuación 46 es análoga a la ecuación derivada por Jarzecki,[44] también para el cálculo de intensidades de resonancia Raman para múltiples estados. $G_{\Gamma_{r,k}}^e$ sería equivalente al factor de ponderación obtenido por Jarzecki, aunque $G_{\Gamma_{r,k}}^e$ no está normalizado en la ecuación 47.

Las intensidades Raman en condiciones de resonancia que se han calculado en esta tesis se ha realizado a partir de la ecuación 45, utilizando un valor estándar de $\Gamma_{e,k}^2 = 0.2\bar{\upsilon}_k$ y los desplazamientos adimensionales $\Delta_{k,e}$ calculados en la aproximación armónica:

$$\Delta_{k,e} = \frac{1}{\sqrt{2}} 2.408 \cdot 10^6 \omega_k^{-3/2} f \cdot M^{-1/2} L_k \tag{48}$$

Donde f es el vector gradiente del estado electrónico excitado *e* evaluados a la geometría de Franck-Condon, M es la matriz diagonal de 3x3 que contiene las masas atómicas, y L_k es la matriz Hessiana asociado al modo vibracional *k*-ésimo.

2.3.2. Cálculo de intensidades de absorción y de dicroísmo circular electrónico.

El tratamiento teórico para el cálculo de espectros de absorción, emisión y dicroísmo circular resueltos vibracionalmente se describe en la bibliografía[45-51] y está implementado en el programa FCclasses[52] desarrollado por el Dr. Fabrizio Santoro y su grupo de investigación. Este método trabaja en la aproximación armónica incluyendo

también el acoplamiento entre modos normales de vibración o rotación en la matriz de Duschinsky y, por tanto, resulta apropiado para moléculas semirrígidas que presentan grupos funcionales o partes de la molécula que pueden rotar.

De forma breve, el programa FCclasses funciona de la siguiente forma: las geometrías de equilibrio, los modos normales y sus frecuencias se leen en los archivos de entrada, procedentes de cálculos mecanocuánticos adecuados. Las transiciones vibrónicas se dividen en clases *Cn*, dependiendo del número "*n*" de modos simultáneamente excitados en el estado final, obteniendo así los factores de Franck-Condon. Para cada clase, se selecciona un valor límite.

FCclasses incluye el efecto de la temperatura y puede tratar tanto las transiciones de Condon (donde los dipolos de transición son independientes de las coordenadas nucleares) como las transiciones de Herzberg-Teller (donde se considera que los dipolos de transición son linealmente dependientes de las coordenadas nucleares). También incluye el efecto del tiempo en el perfil espectral.

2.3.2.1. Absorción.

En primer lugar, se describirá el método independiente del tiempo, y posteriormente se incorporarán las dependencias con la temperatura, el acoplamiento de Herzberg-Teller y el tiempo.

2.3.2.1.1. Método independiente del tiempo a 0K y temperatura finita.

Suponiendo la transición radiativa $|e\rangle \rightarrow |e'\rangle$ entre los estados electrónicos inicial $|e\rangle$ y final $|e'\rangle$, el espectro de líneas se puede calcular de forma general como:

$$\sigma_{abs}(\omega) = \frac{4\pi^2\omega}{3c} \sum_{w',w} N_{w'} \left|\boldsymbol{\mu}_{w',w}\right|^2 \delta(E_{w'} - E_w + \hbar\omega) \qquad (49)$$

Donde $\mu_{w',w} = \langle e'|\langle w'|\mu|w\rangle|e\rangle$ simboliza los momentos dipolares de la transición electrónica, $|w'\rangle$ y $|w\rangle$ los estados vibracionales de los estados $|e'\rangle$ y $|e\rangle$ respectivamente, con energías $E_{w'}$ y E_w. $N_{w'}$ es la población de Boltzmann de los estados $|w'\rangle$ y en este caso tiene valor igual a la unidad, siendo el único término de la sumatoria. ω es la frecuencia angular de la radiación incidente y δ es la función delta de Dirac, la cual selecciona la energía para cada transición. El momento dipolar de la transición electrónica se puede expresar como una serie de potencias en función de las coordenadas normales Q:

$$\boldsymbol{\mu}_{e\prime,e} = \langle e'|\boldsymbol{\mu}|e\rangle = \mu^0 + \sum_k \boldsymbol{\mu}^k \boldsymbol{Q}_k + \sum_{k,l} \boldsymbol{\mu}^{k,l} \boldsymbol{Q}_k \boldsymbol{Q}_l + \cdots \quad (50)$$

Para resolver la parte vibracional de los momentos dipolares de la transición, consideramos que los estados vibracionales $|w'\rangle$ y $|w\rangle$ de dimensión N, siendo N el número de osciladores, se pueden expresar como producto de estados monodimensionales $|w_k\rangle$ para cada modo k:

$$|\boldsymbol{w}\rangle = |w_\mathbf{1}\rangle \otimes |w_\mathbf{2}\rangle \ldots \otimes |\boldsymbol{w_N}\rangle \quad (51)$$

Donde w_k es el número cuántico de $|w_k\rangle$. Los elementos matriciales de los momentos dipolares de la transición se pueden reducir a una combinación de integrales de solapamiento y así obtener los elementos de su matriz. Una transformación lineal que se cumple entre las N coordenadas normales de los estados $|e'\rangle$ y $|e\rangle$ es:

$$\mathbf{Q}' = \mathbf{JQ} + \mathbf{K} \quad (52)$$

Siendo **J** la matriz de Duschinsky y **K** el vector desplazamiento entre las coordenadas $\mathbf{Q}'$ y **Q**. Estas dos matrices se pueden obtener a partir de las coordenadas cartesianas ponderadas en masa:

$$\mathbf{q} = (q_1, q_2, \ldots q_{3N_a}) \quad (53)$$

N_a es el número de átomos del sistema. La relación entre las coordenadas cartesianas ponderadas en masa, la matriz **J** y el vector **K** es:

$$\mathbf{L}'\mathbf{Q}' = (\mathbf{q} - \mathbf{q}'^{\mathrm{eq}}) \quad (54)$$

$$\mathbf{LQ} = (\mathbf{q} - \mathbf{q}^{\mathrm{eq}}) \quad (55)$$

$$\mathbf{J} = \mathbf{L}'^{-\mathbf{1}}\mathbf{L} \quad (56)$$

$$\mathbf{K} = \mathbf{L}'^{-\mathbf{1}}(\mathbf{q}^{\mathrm{eq}} - \mathbf{q}'^{\mathrm{eq}}) \quad (57)$$

Las coordenadas cartesianas ponderadas en masa se obtienen fácilmente a partir de cálculos de frecuencias utilizando códigos mecanocuánticos.

En general, los osciladores no son independientes unos de otros y los factores de Frank-Condon no se pueden aproximar al producto de factores monodimensionales. En su lugar, es necesario utilizar las siguientes fórmulas de recurrencia para las transiciones 0-0 ($\mathfrak{T}_{0',0}$), 0′-w ($\mathfrak{T}_{0',w}$)y w′-w ($\mathfrak{T}_{w',w}$):

$$\mathfrak{T}_{0',0} = (\det \boldsymbol{\Gamma}' \det \boldsymbol{\Gamma})^{1/4} \left(\frac{2^N \det \mathbf{J}}{\det \mathbf{X}}\right)^{1/2} \exp\left[-\frac{1}{2}\mathbf{K}^\dagger \boldsymbol{\Gamma}' \mathbf{K} + \frac{1}{2}\mathbf{Y}^\dagger \mathbf{X}^{-1} \mathbf{Y}\right] \tag{58}$$

$$\mathfrak{T}_{0',w} = \left(\frac{1}{2w_k}\right)^{1/2} A_k \langle 0' | \boldsymbol{w} - 1_k \rangle + \left(\frac{w_k - 1}{w_k}\right)^{1/2} D_{kk} \langle \mathbf{0}' | \boldsymbol{w} - 2_k \rangle + \sum_{l,(l \neq k)} \left(\frac{w_l}{w_k}\right)^{1/2} D_{kl} \langle \mathbf{0}' | \boldsymbol{w} - 1_k - 1_l \rangle \tag{59}$$

$$\mathfrak{T}_{w',w} = \left(\frac{1}{2w'_k}\right)^{1/2} B_k \langle \boldsymbol{w}' - 1_k | \boldsymbol{w} \rangle + \left(\frac{w'_k - 1}{w'_k}\right)^{1/2} E_{kk} \langle \boldsymbol{w}' - 2_k | \boldsymbol{w} \rangle + \sum_{l,(l \neq k)} \left(\frac{w'_l}{w'_k}\right)^{1/2} E_{kl} \langle \boldsymbol{w}' - 1_k - 1_l | \boldsymbol{w} \rangle + \sum_{l} \left(\frac{w_l}{w'_k}\right)^{1/2} F_{kl} \langle \boldsymbol{w}' - 1_k | \boldsymbol{w} - 1_l \rangle \tag{60}$$

Siendo Γ′ y Γ las matrices diagonales de frecuencias reducidas $\omega'_k/\hbar$ y $\omega_k/\hbar$, respectivamente. La notación $|\boldsymbol{w} - 1_k\rangle$ describe un estado en el que todos los números cuánticos de $|\boldsymbol{w}\rangle$ son iguales excepto el del modo *k*. El resto de las matrices se describen a continuación:

$$\mathbf{Y} = \mathbf{J}^\dagger \boldsymbol{\Gamma}' \mathbf{K} \tag{61}$$

$$\mathbf{X} = \mathbf{J}^\dagger \boldsymbol{\Gamma}' \mathbf{J} + \boldsymbol{\Gamma} \tag{62}$$

$$\mathbf{A} = -2\mathbf{K}^\dagger \boldsymbol{\Gamma}' \mathbf{J} \mathbf{X}^{-1} \boldsymbol{\Gamma}^{1/2} \tag{63}$$

$$\mathbf{D} = 2\boldsymbol{\Gamma}^{1/2} \mathbf{X}^{-1} \boldsymbol{\Gamma}^{1/2} - \mathbf{I} \tag{64}$$

$$\mathbf{B} = 2\mathbf{K}^\dagger \boldsymbol{\Gamma}'^{1/2} (1 - \boldsymbol{\Gamma}'^{1/2} \mathbf{J} \mathbf{X}^{-1} \mathbf{J}^\dagger \boldsymbol{\Gamma}'^{1/2}) \tag{65}$$

$$\mathbf{E} = 2\boldsymbol{\Gamma}'^{1/2} \mathbf{J} \mathbf{X}^{-1} \boldsymbol{\Gamma}'^{1/2} - \mathbf{I} \tag{66}$$

$$\mathbf{F} = 2\boldsymbol{\Gamma}'^{1/2} \mathbf{J} \mathbf{X}^{-1} \boldsymbol{\Gamma}^{1/2} \tag{67}$$

Una vez conocidas **K** y **J**, se pueden resolver las ecuaciones 61-67 permitiendo calcular los factores de Frank-Condon (ecuaciones 58-60) y así obtener los momentos dipolares de la transición para finalmente calcular el espectro de línea utilizando la ecuación 49. En este punto, solo se considerará el término de Frank-Condon para la componente electrónica de los momentos dipolares de la transición. La inclusión del término de orden 1 respecto a Q se discutirá en la sección 2.3.2.3, mientras que términos superiores no se tendrán en cuenta.

Para el cálculo de dichos factores de Frank-Condon, se utiliza la siguiente simplificación. Las transiciones vibracionales de los osciladores se clasifican en distintas clases *Cn* atendiendo al número *n* de osciladores que cuyo número cuántico es distinto a cero. Para reducir el coste computacional, solo se considerarán inicialmente las clases C_1 y C_2, y las clases superiores se limitarán en función del resultado obtenido Esto se realiza eligiendo valores umbrales ε_1y ε_2 respectivamente para C_1 y C_2 y encontrando el mayor número cuántico $w_k = w_k^{max}$. Después se calculan y almacenan las matrices $Fc_1^{0'}(k, w_k)$ y $Fc_2^{0'}(k, l, w_{kl})$. La primera de ella almacena los factores de Frank-Condon hasta un número cuántico lo bastante grande para considerar que, a partir de ahí, las integrales son totalmente despreciables. $Fc_2^{0'}(k, l, w_{kl})$ representa:

$$Fc_2^{0'}(k, l, w_{kl}) = |I_2(k, l, w_{kl}|^2 - \frac{Fc_1^{0'}(k, w_{kl})\, Fc_1^{0'}(l, w_{kl})}{\mathfrak{T}_{0',0}} \tag{68}$$

Que es el cuadrado del factor de Frank-Condon C_2 para cada pareja de osciladores menos el producto de los correspondientes factores C_1. Esto permite eliminar cualquier posible efecto de las frecuencias y desplazamientos de posición ya considerados.

Para clases de mayor orden, se define un vector $\mathbf{W_n^{max}}$ cuyo elemento *k* es el número cuántico máximo permitido. De este modo, el número de integrales calculadas está por debajo del umbral definido. El siguiente paso es calcular las combinaciones posibles de *n* osciladores y sus factores de Frank-Condon hasta el valor dictado por $\mathbf{W_n^{max}}$.

Una vez resuelta la parte vibracional, el espectro final se obtiene convolucionando la suma de estados (ecuación 49) con una función de forma de línea normalizada, que puede ser Gaussiana o Lorentziana:

$$G(\omega, \omega_{\omega_{w',w}}) = \frac{1}{\gamma[\pi/\ln(2)]^{1/2}} \exp[-\ln(2)(\omega - \omega_{\omega_{w',w}})^2/\gamma^2] \tag{69}$$

$$L(\omega, \omega_{\omega_{w',w}}) = \frac{\gamma\pi^{-1}}{\gamma^2 + (\omega - \omega_{\omega_{w',w}})^2} \tag{70}$$

Siendo γ la semianchura a la mitad del máximo.

Para incluir el efecto de la temperatura en este procedimiento, se parte de una etapa inicial, a partir de la ecuación 49, donde se trunca el sumatorio extendido a estado vibracionales a aquellos con una población de Boltzmann por debajo de un umbral de corte. Posteriormente, se eligen los llamados "estados madre" teniendo en cuenta que,

dada la naturaleza recursiva de las ecuaciones 58, 59 y 60, un estado $|\boldsymbol{w}'\rangle$ cuyos números cuánticos son superiores en todos los osciladores a otro estado $|\boldsymbol{u}'\rangle$ contiene todos los factores de Frank-Condon necesarios para el espectro de $|\boldsymbol{u}'\rangle$. La opción más eficiente es utilizar estados madres para los estados que tengan el mismo número de osciladores con número cuántico distinto de cero, alcanzando un compromiso para reducir las redundancias y evitar el cálculo de estados poco poblados que contengan varios osciladores activos. La Figura 4 muestra un ejemplo de selección eficaz de "estados madre."

Después, se calculan los mismos estados que eran relevantes a temperatura T = 0K, y posteriormente se amplía a un número superior de estados restringiendo el número de osciladores excitados simultáneamente, lo cual aumenta la eficiencia del cálculo.

2.3.2.1.2. Acoplamiento vibrónico de Herzberg-Teller.

El acoplamiento vibrónico de Herzberg-Teller es en general poco relevante para transiciones intensas, pero puede cobrar gran relevancia para estados poco permitidos y que estén próximos en energía a un estado intenso, dando lugar a una transferencia de intensidad entre estados.

Considerando la ecuación 50 hasta el primer orden, se tiene que el momento dipolar para la transición electrónica es:

$$\boldsymbol{\mu}_{e\prime,e} = \boldsymbol{\mu}^0 + \sum_k \boldsymbol{\mu}^k Q_k \qquad (71)$$

La ecuación 71 puede escribirse de forma matricial de la siguiente manera:

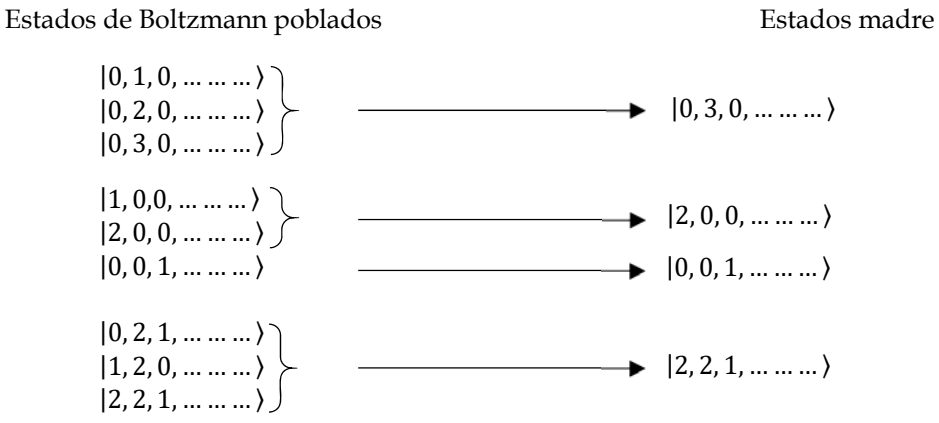

Figura 4. Ejemplo de selección de "estados madre" para incluir en clases superiores debido al efecto de la temperatura.

$$\boldsymbol{\mu}_{e\prime,e} = \boldsymbol{\mu_0} + \mathbf{MQ} \tag{72}$$

Donde M es una matriz de coordenadas cartesianas de dimensión 3xN (siendo N el número de átomos) y $\boldsymbol{\mu}_{e\prime,e}$ y $\boldsymbol{\mu}_0$son vectores columna. Análogamente, si se utilizan las coordenadas $\mathbf{Q}'$ se obtiene:

$$\boldsymbol{\mu}_{e\prime,e} = \boldsymbol{\mu}_\mathbf{0}' + \mathbf{M}'\mathbf{Q}' \tag{73}$$

Reorganizando la ecuación 52 para despejar $\mathbf{Q}$, y sustituyendo en la ecuación 73:

$$\mathbf{Q} = \mathbf{J^T Q}' - \mathbf{J^T K} \tag{74}$$

$$\boldsymbol{\mu}_{e\prime,e} = \boldsymbol{\mu_0} + \mathbf{MJ^T Q}' - \mathbf{MJ^T K} \tag{75}$$

La ecuación 75 proporciona la relación entre el momento dipolar de la transición en la posición de equilibrio del estado electrónico $|e'\rangle$ ($\mathbf{Q}' = 0$) y la posición de equilibrio del estado electrónico $|e\rangle$ ($\mathbf{Q} = 0$). La parte no dependiente de $\mathbf{Q}'$ en la ecuación 75 se corresponde con $\boldsymbol{\mu}_\mathbf{0}'$, de modo que:

$$\boldsymbol{\mu}_\mathbf{0}' = \boldsymbol{\mu_0} - \mathbf{MJ^T K} \tag{76}$$

Esta ecuación es válida siempre y cuando la aproximación lineal de la ecuación 71 sea aceptable. Utilizando el formalismo matemático de segunda cuantización, podemos expresar:

$$\mathbf{Q_k} = \sqrt{\frac{\hbar}{2\omega_k}}(a_k + a_k^\dagger) \tag{77}$$

ω_k es la frecuencia del modo k, a_k y $a_k^\dagger$ son los operadores de aniquilación y creación, respectivamente. Sustituyendo en la ecuación 71 se obtiene:

$$\boldsymbol{\mu}_{e\prime,e} = \boldsymbol{\mu}^0 + \sum_k \mathbf{T}_k\,(a_k + a_k^\dagger) \tag{78}$$

Donde se ha definido $\mathbf{T}_k$ como:

$$\mathbf{T}_k = \sqrt{\frac{\hbar}{2\omega_k}}\boldsymbol{\mu_k} \tag{79}$$

De este modo, el cálculo del momento dipolar de la transición se reduce a una combinación lineal de los solapamientos de Frank-Condon $\langle \boldsymbol{w}'|\boldsymbol{w}\rangle$, que como se ha descrito previamente, en general no se pueden reducir al producto de integrales

monodimensionales, pero se pueden obtener con las fórmulas de recurrencia mostradas en las ecuaciones 58, 59 y 60.

Para calcular las intensidades, se parte de la expresión:

$$I^{tot} = \sum_{w',w} N_{w'} |\langle \boldsymbol{w'} | \boldsymbol{\mu} | \boldsymbol{w} \rangle|^2 = \sum_{w'} N_{w'} \left| \langle \boldsymbol{w'} | \mu^2 | \boldsymbol{w'} \rangle \right| \tag{80}$$

Siendo μ el módulo de $\boldsymbol{\mu}$. Para transiciones Frank-Condon (FC) μ se puede sacar de la integral ya que no depende de la coordenada k. En cambio, en una transición Frank-Condon-Herzberg-Teller (FCHT) la parte independiente de las coordenadas en $\boldsymbol{\mu}$ se extrae, reduciendo esa parte a una suma de productos de integrales monodimensionales de términos lineales $\mathbf{Q}'_k$ y no lineales $\mathbf{Q}'_k \mathbf{Q}'_l$ con $k \neq l$. El producto $\boldsymbol{\mu} \cdot \boldsymbol{\mu}$ se cancela ya que $|\langle \boldsymbol{w}'_k | \boldsymbol{Q}'_k | \boldsymbol{w}'_k \rangle| = 0$. Finalmente, queda que:

$$I^{tot} = \sum_{w',w} N_{w'} \langle \boldsymbol{w'} \left| \boldsymbol{\mu}_{\mathbf{0}}'^{\,2} + \sum_k \boldsymbol{\mu}_{\boldsymbol{k}}'^{\,2} \mathbf{Q}_k'^{\,2} \right| \boldsymbol{w'} \rangle \tag{81}$$

Esta fórmula se puede aplicar para cualquier estado electrónico concreto, por ejemplo, para el estado $|e'\rangle$. El cálculo del valor de expectación de $\mathbf{Q}_k'^{\,2}$ es trivial, y se puede reemplazar:

$$I_{e'}^{tot} = \mu_0'^{\,2} + \sum_{w'} N_{w'} \sum_k \frac{\hbar}{2\omega'_k} \mu_k'^{\,2} (2\, w'_k + 1) = \mu_0'^{\,2} + \sum_{w'} N_{w'} \sum_k |\mathbf{T}'_{\boldsymbol{k}}|^2 (2\, w'_k + 1) \tag{82}$$

$\mathbf{T}'_{\boldsymbol{k}}$ se define de forma análoga al vector $\mathbf{T}_{\boldsymbol{k}}$ ya descrito para el estado $|e\rangle$. Para dicho estado, la intensidad total es:

$$I_e^{tot} = \mu_0^2 + \sum_w N_w \sum_k |\mathbf{T}_{\boldsymbol{k}}|^2 (2\, w_k + 1) = I_e^{FC} + I_e^{HT}(T) \tag{83}$$

Nótese que la componente de Herzberg-Teller de la intensidad depende de la temperatura, al aparecer la población de Boltzmann.

2.3.2.1.3. Dependencia con el tiempo.

La dependencia temporal se incluye de la siguiente manera. En primer lugar, se obtiene la forma de línea omitiendo los prefactores de la ecuación 49.

$$\sigma_{abs}(\omega) = \frac{4\pi^2 \omega}{3c} L(\omega) \tag{84}$$

$$L(\omega) = \sum_{w',w} N_{w'} \left|\boldsymbol{\mu}_{w',w}\right|^2 \delta(E_{w'} - E_w + \hbar\omega) \tag{85}$$

Se sustituye entonces la población de Boltzmann por su expresión completa, y la función delta de Dirac por su correspondiente transformada de Fourier:

$$N_{w'} = \frac{e^{-\beta E_{w'}}}{Z_{vib}} \tag{86}$$

$$\delta(E_{w'} - E_w + \hbar\omega) = \frac{1}{2\pi}\int_{-\infty}^{\infty} dt\, e^{-it\left(\frac{E_{w'} - E_w + \hbar\omega}{\hbar}\right)} \tag{87}$$

$$L(\omega) = \frac{1}{2\pi Z_{vib}}\int_{-\infty}^{\infty} dt \sum_{w',w} e^{-\beta E_{w'}} \left|\boldsymbol{\mu}_{w',w}\right|^2 e^{-it\left(\frac{E_{w'} - E_w + \hbar\omega}{\hbar}\right)} \tag{88}$$

Los exponenciales en la ecuación 88 no dependen de las coordenadas, por lo que se pueden introducir en las integrales del momento dipolar de la transición:

$$L(\omega) = \frac{1}{2\pi Z_{vib}}\int_{-\infty}^{\infty} dt \sum_{w',w} \left\langle w\middle|\, \boldsymbol{\mu}_{w',w} e^{-it\frac{E_w}{\hbar}} \middle| w'\right\rangle \left\langle w'\middle|\, \boldsymbol{\mu}_{w',w} e^{-\beta E_{w'}} e^{-it\frac{E_{w'}}{\hbar}} \middle| w\right\rangle e^{-i\omega t} \tag{89}$$

$$L(\omega) = \frac{1}{2\pi Z_{vib}}\int_{-\infty}^{\infty} dt \sum_{w',w} \left\langle w\middle|\, \boldsymbol{\mu}_{w',w} e^{-iE_w\frac{t}{\hbar}} \middle| w'\right\rangle \left\langle w'\middle|\, \boldsymbol{\mu}_{w',w} e^{-iE_{w'}\left(-\beta - i\frac{t}{\hbar}\right)} \middle| w\right\rangle e^{-i\omega t} \tag{90}$$

$$L(\omega) = \frac{1}{2\pi Z_{vib}}\int_{-\infty}^{\infty} dt \sum_{w',w} \langle w|\boldsymbol{\mu}_{w',w} e^{-iE_w\tau_w}|w'\rangle\langle w'|\boldsymbol{\mu}_{w',w} e^{-iE_{w'}\tau_{w'}}|w\rangle e^{-i\omega t} \tag{91}$$

Donde se ha definido:

$$\tau_w = \frac{t}{\hbar} \tag{92}$$

$$\tau_{w'} = -i\beta - \frac{t}{\hbar} \tag{93}$$

Utilizando las siguientes ecuaciones de los autovalores de los Hamiltonianos vibracionales sobre la ecuación 91, se obtiene:

$$\hat{H}_w|w\rangle = E_w|w\rangle \tag{94}$$

$$\hat{H}_{w'}|w'\rangle = E_{w'}|w'\rangle \tag{95}$$

$$e^{-i\hat{H}_w\tau_w}|w\rangle = e^{-iE_w\tau_w}|w\rangle \tag{96}$$

$$e^{-i\hat{H}_{w'}\tau_{w'}}|w'\rangle = e^{-iE_{w'}\tau_{w'}}|w'\rangle \tag{97}$$

$$L(\omega) = \frac{1}{2\pi Z_{vib}} \int_{-\infty}^{\infty} dt \sum_{w',w} \left\langle w \middle| \boldsymbol{\mu}_{w',w} e^{-i\hat{H}_w \ \tau_w} \middle| w' \right\rangle \left\langle w' \middle| \boldsymbol{\mu}_{w',w} e^{-i\hat{H}_{w'}\tau_{w'}} \middle| w \right\rangle e^{-i\omega t} \quad (98)$$

Los Hamiltonianos no dependen del número cuántico vibracional w', por tanto, las sumatorias se pueden separar:

$$L(\omega) = \frac{1}{2\pi Z_{vib}} \int_{-\infty}^{\infty} dt \sum_{w} \left\langle w \middle| \boldsymbol{\mu}_{w',w} e^{-i\hat{H}_w \ \tau_w} \left[\sum_{w'} |w'\rangle\langle w'| \right] \boldsymbol{\mu}_{w',w} e^{-i\hat{H}_{w'}\tau_{w'}} \middle| w \right\rangle e^{-i\omega t} \quad (99)$$

La sumatoria sobre w' en la ecuación 99 es el operador identidad y la ecuación 99 resulta en:

$$\sum_{w'} |w'\rangle\langle w'| = 1 \quad (100)$$

$$L(\omega) = \frac{1}{2\pi Z_{vib}} \int_{-\infty}^{\infty} dt \, e^{-i\omega t} \sum_{w} \left\langle w \middle| \boldsymbol{\mu}_{w',w} e^{-i\hat{H}_w \ \tau_w} \ \boldsymbol{\mu}_{w',w} e^{-i\hat{H}_{w'}\tau_{w'}} \middle| w \right\rangle \quad (101)$$

Finalmente, introducimos el operador Tr():

$$L(\omega) = \frac{1}{2\pi Z_{vib}} \int_{-\infty}^{\infty} dt \, e^{-i\omega t} Tr\left(\boldsymbol{\mu}_{w',w} e^{-i\hat{H}_w \ \tau_w} \ \boldsymbol{\mu}_{w',w} e^{-i\hat{H}_{w'}\tau_{w'}} \right) \quad (102)$$

$$Tr\left(\boldsymbol{\mu}_{w',w} e^{-i\hat{H}_w \ \tau_w} \ \boldsymbol{\mu}_{w',w} e^{-i\hat{H}_{w'}\tau_{w'}} \right) = \sum_{w} \left\langle w \middle| \boldsymbol{\mu}_{w',w} e^{-i\hat{H}_w \ \tau_w} \ \boldsymbol{\mu}_{w',w} e^{-i\hat{H}_{w'}\tau_{w'}} \middle| w \right\rangle \quad (103)$$

Que representa la suma de los elementos de la diagonal del operador representados en una base completa, que en este caso son los autovectores del Hamiltoniano vibracional. Es interesante resaltar que la traza se puede expresar en cualquier representación que sea una base completa, de modo que sea posible obtener una solución analítica. Esto ocurre si se utilizan las autofunciones del operador posición $|Q\rangle$:

$$Tr\left(\boldsymbol{\mu}_{w',w} e^{-i\hat{H}_w \ \tau_w} \ \boldsymbol{\mu}_{w',w} e^{-i\hat{H}_{w'}\tau_{w'}} \right) = \int_{-\infty}^{\infty} \left\langle w \middle| \boldsymbol{\mu}_{w',w} e^{-i\hat{H}_w \ \tau_w} \ \boldsymbol{\mu}_{w',w} e^{-i\hat{H}_{w'}\tau_{w'}} \middle| w \right\rangle \quad (104)$$

Dado que la posición no está cuantizada, la sumatoria se convierte en una integral. Finalmente, se define la función de correlación $\chi(t,T)$:

$$\chi(t,T) = \frac{1}{Z_{vib}} Tr\left(\boldsymbol{\mu}_{w',w} e^{-i\hat{H}_w \ \tau_w} \ \boldsymbol{\mu}_{w',w} e^{-i\hat{H}_{w'}\tau_{w'}} \right) \quad (105)$$

Y la expresión final de la forma de línea es:

$$L(\omega) = \frac{1}{2\pi}\int_{-\infty}^{\infty} dt\, e^{-i\omega t}\chi(t,T) \tag{106}$$

El espectro es finalmente obtenido como la transformada de Fourier de $\chi(t,T)e^{-i\hbar\omega t}$ y aplicando los prefactores de la ecuación 84. Estos prefactores son la única diferencia en el cálculo de intensidad de emisión, por lo que el tratamiento es el mismo.

2.3.2.2 Dicroísmo circular electrónico.

La variable de interés en dicroísmo circular electrónico es la anisotropía de la absortividad molar ϵ, la cual se define como la diferencia entre las absorciones de la luz circularmente polarizada a izquierda y a derecha, $\Delta\epsilon = \epsilon_L - \epsilon_R$ y se puede expresar como:

$$\Delta\epsilon(\omega) = \frac{64\pi^2\omega N_A}{9\times 1000\times ln(10)\times(4\pi\varepsilon_0)\times\hbar c^2}\times\sum_f\sum_{e'w',ew} L(\omega)\times {}^{e'w'ew}R$$

$$= \frac{64\pi^2\omega N_A}{9\times 1000\times ln(10)\times(4\pi\varepsilon_0)\times\hbar c^2}\times\sum_f {}^{e'e}R\,(\omega) \tag{107}$$

Definimos ${}^{e'e}R$ es la fuerza rotatoria total de la transición ECD $e' \rightarrow e$ y se calcula como:

$${}^{e'e}R = \int_{e'}^{e} {}^{e'e}R(\omega) \tag{108}$$

En la aproximación de Herzberg-Teller, se obtiene para ${}^{e'e}R$:

$${}^{e'e}R = \frac{3}{4}\sum_{w'} N_w\,\Im[\langle e'w'|\hat{\mu}|ew\rangle\cdot\langle ew|\hat{m}|e'w'\rangle] \tag{109}$$

En la que aparecen los momentos dipolares eléctrico (μ) y magnético (m) de la transición. Cada una de las componentes cartesianas (α = x, y, z) de dichos momentos dipolares de la transición pueden expresarse en el marco del acoplamiento vibrónico de Herzberg-Teller como:

$$\mu^{\alpha}_{e'w'ew} = \langle e'w'|\hat{\mu}^{\alpha}|ew\rangle = \mu^{\alpha}_{e'e}(Q_0)\langle w'|w\rangle + \sum_k \frac{\partial\mu^{\alpha}_{e'e}}{\partial Q_k}\langle w'|Q_k|w\rangle \tag{110}$$

$$m^{\alpha}_{e'w'ew} = \langle e'w'|\hat{m}^{\alpha}|ew\rangle = m^{\alpha}_{e'e}(Q_0)\langle w'|w\rangle + \sum_k \frac{\partial m^{\alpha}_{e'e}}{\partial Q_k}\langle w'|Q_k|w\rangle \qquad (111)$$

Siendo el término independiente de las coordenadas normales el de Frank-Condon (FC) y el término de acoplamiento el de Herzberg-Teller (HT). Aquí se realiza la aproximación de que las superficies de energía potencial de las superficies están desplazadas pero la curvatura se puede considerar igual, de modo que los factores de Frank-Condon multidimensionales se pueden expresar como el producto de factores monodimensionales. Por tanto, los efectos del acoplamiento Duschinsky se desprecian, pero son reintroducidos utilizando la metodología descrita en la sección 2.3.2.1.1. Finalmente, los momentos dipolares de la transición se pueden expresar como:

$$\mu^{\alpha}_{e'w'ew} = \mu^{\alpha}_{e'e}(Q_0)\prod_k \langle w'_k|w_k\rangle + \sum_k \frac{\partial \mu^{\alpha}_{e'e}}{\partial Q_k}\langle w'_k|Q_k|w_k\rangle \prod_{l\neq k}\langle w'_l|w_l\rangle \qquad (112)$$

$$m^{\alpha}_{e'w'ew} = m^{\alpha}_{e'e}(Q_0)\prod_k \langle w'_k|w_k\rangle + \sum_k \frac{\partial m^{\alpha}_{e'e}}{\partial Q_k}\langle w'_k|Q_k|w_k\rangle \prod_{l\neq k}\langle w'_l|w_l\rangle \qquad (113)$$

Insertando estas ecuaciones en la ecuación 92 y desarrollando el producto escalar, se obtiene que:

$${}^{e'e}R = \frac{3}{4}\sum_{w'} N_w \Im\left[\langle w'|\left(\mu^{\alpha}_{e'e}(Q_0) + \sum_k \frac{\partial \mu^{\alpha}_{e'e}}{\partial Q_k}Q_k\right)\times\left(m^{\alpha}_{e'e}(Q_0) + \sum_l \frac{\partial m^{\alpha}_{e'e}}{\partial Q_l}Q_l\right)|w\rangle\right] \qquad (114)$$

Los valores de expectación de los términos lineales Q_k y Q_l, así como de los términos bilineales no diagonales del tipo Q_kQ_l con $k \neq l$ se hacen cero, por lo que solo quedan los términos de orden 0 en y cuadráticos en Q_k:

$$\begin{aligned} {}^{e'e}R &= \frac{3}{4}\sum_{w'} N_w \Im\left[\mu^{\alpha}_{e'e}(Q_0)m^{\alpha}_{e'e}(Q_0) + \sum_k\sum_{w'} N_{w'}\frac{\partial \mu^{\alpha}_{e'e}}{\partial Q_k}\frac{\partial m^{\alpha}_{e'e}}{\partial Q_k}\frac{\hbar}{2\omega_k}(2w'_k+1)\right] \\ &= {}^{e'e}R^{\mathrm{FC}} + {}^{e'e}R^{\mathrm{HT}} \end{aligned} \qquad (115)$$

Donde ω_k es la frecuencia armónica del modo k y Q_k^2 se ha reemplazado por su valor de expectación. Las contribuciones vibracionales pueden obtenerse mediante la metodología descrita en el apartado 2.3.2.1.1. Una vez conocido ${}^{e'e}R$ es posible calcular $\Delta\epsilon(\omega)$ y obtener el espectro ECD de la transición $e' \rightarrow e$.

2.4. Método para el cálculo de espectros vibrónicos en espacios de dimensionalidad reducida.

En los apartados V y VI del capítulo de Resultados (capítulo III) se estudian estructuras en conformaciones fuera del equilibrio, pero que serían más parecidas a los sistemas que se pretende estudiar. Los sistemas fuera de equilibrio pueden presentar frecuencias imaginarias en algunos modos normales, lo cual dificulta el cálculo de espectros vibrónicos fiables y de calidad. Por ello, es necesario una metodología para retirar los modos vibracionales que se encuentran fuera de equilibrio, definiendo modelos de dimensionalidad reducida. En esta subsección se detalla el procedimiento utilizado en esta tesis doctoral.

En primer lugar, es necesario trabajar en coordenadas internas curvilíneas, ya que describen apropiadamente las rotaciones moleculares. Se parte de una serie de coordenadas internas no redundantes **s**, que es obtenida a partir de una serie de coordenadas redundantes $\mathbf{s}_r$ la cual incluye todos los N_r enlaces, ángulos y diedros definidos a partir de la estructura molecular. Para ello, se utiliza el método propuesto por Reimers[53] en el que se aplica la rotación de la diagonalización:

$$\mathbf{G_r} = \mathbf{B_r M^{-1} B_r^t} \tag{116}$$

Siendo **M** la matriz diagonal que contiene las masas atómicas en sus elementos diagonales y $\mathbf{B_r}$ la matriz que relaciona las coordenadas cartesianas **x** con las coordenadas internas:

$$\mathbf{s_r} = \mathbf{B_r x} \tag{117}$$

La rotación se define como:

$$\mathbf{s} = \mathbf{A^t s_r} \tag{118}$$

Siendo **A** una matriz rectangular de dimensión $N_r \times (3N\text{-}N_{TrRot})$ con **N** número de átomos y N_{TrRot} el número de grados de libertad traslacionales y rotacionales.

El siguiente paso es definir la matriz Hessiana a partir de la serie de coordenadas internas no redundantes $\mathbf{H_s}$ obtenida a partir de la matriz hessiana en coordenadas cartesianas, empleando la transformación:

$$\mathbf{H_s} = \mathbf{G^{-1} B M^{-1}} (\mathbf{H_x} - \mathbf{g_s^t} \boldsymbol{\beta}) \mathbf{M^{-1} B^t G^{-1}} \tag{119}$$

$\mathbf{B}$ es análoga a $\mathbf{B_r}$ y relaciona la serie no redundante de coordenadas internas $\mathbf{s}$ con las coordenadas cartesianas $\mathbf{x}$. Del mismo modo se relacionan $\mathbf{G}$ se define utilizando la expresión equivalente a la ecuación 116, $\boldsymbol{\beta}$ es la derivada de la matriz $\mathbf{B}$ respecto a las coordenadas $\mathbf{x}$, y $\mathbf{g_s}$ es el vector gradiente en coordenadas internas, obtenido a partir de la expresión:

$$\mathbf{g_s} = \mathbf{G^{-1}BM^{-1}g_x} \tag{120}$$

El siguiente paso es retirar del Hessiano $\mathbf{H_s}$ la contribución de las coordenadas a retirar. Se hace la aproximación de que los modos normales a retirar del espacio (en este caso, torsiones) se pueden considerar "congeladas" con respecto al resto de modos normales con contribución relevant al espectro, ya que las torsiones tienen baja frecuencia y por tanto son vibraciones lentas. Se define entonces la serie de coordenadas internas congeladas $\mathbf{s_f}$ como una combinación lineal de coordenadas internas redundantes:

$$\mathbf{s_f} = \mathbf{Cs_r} \tag{121}$$

Utilizando la ecuación 117, esto resulta en:

$$\mathbf{s_f} = \mathbf{CA^t s} \tag{122}$$

Considérese ahora el caso en el que se retira (proyecta al espacio complementario al Hessiano) una única coordenada congelada $\mathbf{s_{f1}}$. Para ello se requiere el operador de proyección adecuado que se corresponda para dicha coordenada interna. Este operador ha sido definido por Jackels y colaboradores[54] como:

$$\mathbf{P_s^{f1}} = \frac{\mathbf{s_{f1}s_{f1}^t}}{\mathbf{s_{f1}^t G s_{f1}}} \tag{123}$$

Las expresiones para obtener el Hessiano y el gradiente en el espacio complementario, por tanto, son:

$$\mathbf{H_s^{(1)}} = \mathbf{(1 - P_s^{f1}G)H_s(1 - P_s^{f1}G)} \tag{124}$$

$$\mathbf{g_s^{(1)}} = \mathbf{(1 - P_s^{f1}G)g_s} \tag{125}$$

Donde $\mathbf{1}$ es la matriz unitaria. El Hessiano y el gradiente obtenido se pueden utilizar para obtener el espectro sin la contribución de la coordenada congelada $\mathbf{s_{f1}}$. Para generalizar el procedimiento, las ecuaciones 123, 124 y 125 se deben aplicar de forma

iterativa. Pero para hacerlo es necesario actualizar la dimensión de la matriz **G** tras retirar cada coordenada interna. Esto se puede realizar utilizando el proyector:

$$\mathbf{P}_{\mathbf{G}}^{\boldsymbol{f1}} = \frac{\mathbf{s}_{f1}\mathbf{s}_{f1}^{t}}{\mathbf{s}_{f1}^{t}\mathbf{s}_{f1}} \tag{126}$$

Y aplicando la expresión:

$$\mathbf{G}^{(1)} = \left(\mathbf{1} - \mathbf{P}_{\mathbf{G}}^{\boldsymbol{f1}}\right)\mathbf{G}\left(\mathbf{1} - \mathbf{P}_{\mathbf{G}}^{\boldsymbol{f1}}\right) \tag{127}$$

Reemplazando $\mathbf{G}^{(1)}$, $\mathbf{H}_{\mathbf{s}}^{(\mathbf{1})}$ y $\mathbf{g}_{\mathbf{s}}^{(\mathbf{1})}$ por sus análogos en la ecuación 124, y repitiendo el procedimiento propuesto, se pueden obtener los Hessianos y gradientes para N_f coordenadas retiradas ($\mathbf{H}_{\mathbf{s}}^{(Nf)}$ y $\mathbf{g}_{\mathbf{s}}^{(Nf)}$).

Llamando $\mathbf{s}_{\boldsymbol{m}}$ a la serie de coordenadas que quedan en el espacio, las energías potencial y cinética para un estado electrónico genérico "e" se escriben como:

$$\boldsymbol{V}_e(\mathbf{s}) \equiv \boldsymbol{V}_e(\mathbf{s}_{\boldsymbol{m}}) = \boldsymbol{V}_{\boldsymbol{0e}} + (\mathbf{g}_{\boldsymbol{s}}^{\boldsymbol{em}})^{t}\mathbf{s}_{\boldsymbol{m}} + \frac{1}{2}\mathbf{s}_{\boldsymbol{m}}^{t}\mathbf{H}_{\mathbf{s}}^{\boldsymbol{em}}\mathrm{s}_m \tag{128}$$

$$\boldsymbol{T} = \frac{1}{2}\dot{\mathrm{s}}_{\boldsymbol{m}}^{t}(\mathbf{G}_{\boldsymbol{m}})^{-1}\dot{\mathbf{s}}_{\boldsymbol{m}} \tag{129}$$

Donde el acento punto representa las derivadas respecto al tiempo. Y $\mathbf{G}_{\boldsymbol{m}}$, $\mathbf{g}_{\boldsymbol{s}}^{\boldsymbol{em}}$ y $\mathbf{H}_{\mathbf{s}}^{\boldsymbol{em}}$ son las matrices correspondientes definidas en el espacio **m**. El mínimo para cada $\boldsymbol{V}_e(\mathbf{s}_{\boldsymbol{m}})$ se puede obtener[55] como:

$$\Delta\mathbf{s}_{em} = -(\mathbf{H}_{\mathbf{s}}^{\boldsymbol{em}})^{-1}\mathbf{g}_{\mathbf{s}}^{\boldsymbol{em}} \tag{130}$$

Esto permite utilizar el método estándar GF definiendo las $3N\text{-}N_{TrRot}\text{-}N_f$ coordenadas normales $\mathbf{q}_{\boldsymbol{e}}$ con $\mathbf{s}_{\boldsymbol{f}}$ coordenadas congeladas. Definiendo $\mathbf{q}_{\boldsymbol{i}}$ y $\mathbf{q}_{\boldsymbol{f}}$ como las coordenadas normales de la transición electrónica inicial (i) y final (f) se tiene que:

$$\mathbf{s}_{\boldsymbol{m}} - \boldsymbol{\Delta}\mathbf{s}_{\boldsymbol{im}} = \mathbf{L}_i\mathbf{q}_i \tag{131}$$

$$\mathbf{s}_{\boldsymbol{m}} - \boldsymbol{\Delta}\mathbf{s}_{\boldsymbol{fm}} = \mathbf{L}_f\mathbf{q}_f \tag{132}$$

$\mathbf{q}_{\boldsymbol{i}}$ y $\mathbf{q}_{\boldsymbol{f}}$ se pueden relacionar a partir de las ecuaciones es 131 y 132, obteniendo:

$$\mathbf{q}_i = \mathbf{L}_i^{-1}\mathbf{L}_f\mathbf{q}_f + \mathrm{L}_i^{-1}(\boldsymbol{\Delta}\mathbf{s}_{\boldsymbol{fm}} - \boldsymbol{\Delta}\mathbf{s}_{\boldsymbol{im}}) \tag{133}$$

La matriz de Duschinsky y el vector desplazamiento son:

$$\mathbf{J} = \mathbf{L}_i^{-1}\mathbf{L}_f \tag{134}$$

$$\mathbf{K} = \mathbf{L}_i^{-1}(\Delta\mathbf{s}_{fm} - \Delta\mathbf{s}_{im}) \tag{135}$$

El término $\Delta\mathbf{s}_f$ es cero si las optimizaciones se han realizado restringiendo las coordenadas $\mathbf{s}_f$ y se puede utilizar el procedimiento estándar independiente (TI) y dependiente de tiempo (TD) para sistemas armónicos. En esta tesis, hemos seguido el procedimiento TD implementado en la versión en desarrollo del código FCclasses.[52]

2.5. Referencias y notas.

1. L. Goerigk, S. Grimme. *Phys. Chem. Chem. Phys*., **2011**, 13, 6670.
2. Y. Zhao, D. G. Truhlar. *J. Chem. Theory Comput*., **2005**, 1, 415.
3. D. Jacquemin, V. Wathelet, E. A. Perpète, C. Adamo. *J. Chem. Theory Comput*., **2009**, 5, 2420.
4. S. F. Sousa, P. A. Fernandes, M. J. Ramos. *J. Phys. Chem. A*, **2007**, 111, 10439.
5. Y. Zhao, N. González-García, D. G. Truhlar. *J. Phys. Chem. A*, **2005**, 109, 2012.
6. R. Improta, V. Barone. *J. Chem. Phys*., **2006**, 125, 054103.
7. L. A. Burns, A. Vázquez- Mayagoitia, B. G. Sumpter, C. David Sherrill. *J. Chem. Phys*., **2011**, 134, 084107.
8. A. D. Laurent, D. Jacquemin. *Int. J. Quantum Chem*., **2013**, 113, 2019.
9. P. J. Stephens, F. J. Devlin. *Chirality*, **2000**, 12, 172.
10. Y. Katsumoto, T. Tanaka, H. Sato, Y. Ozaki. *J. Phys. Chem. A*, **2002**, 106, 3429.
11. M. Haugk, J. Elsner, Th. Frauenheim, T.E.M. Staab, C.D. Latham, R. Jones, H.S. Leipner, T. Heine, G. Seifert, M. Sternberg. *Phys. Status Solidi B-Basic Solid State Phys*., **2000**, 217, 473.
12. J. Řezáč, K. E. Riley, P. Hobza. *J. Chem. Theory Comput*., **2011**, 7, 2427.
13. K. S. Thanthiriwatte, E. G. Hohenstein, L. A. Burns, C. David Sherrill. *J. Chem. Theory Comput*., **2011**, 7, 88.
14. I. Bâldea. *J. Phys. Chem. A*, **2017**, 121, 2282.
15. D. Jacquemin, T. Le Bahers, C. Adamo, I. Ciofini. *Phys. Chem. Chem. Phys*., *2012*, 14, 5383.
16. Sahar, A. Bari, M. Irfan, Z. Zara, B. Eliasson, K. Ayub, J. Iqbal. *J. Mol. Struct*., **2017**, 1143, 8.
17. Y. Zhao, D. G. Truhlar. *J. Phys. Chem. A*, **2006**, 110, 13126.
18. A. D. Becke. *Phys. Rev. A*, **1988**, 38, 3098.
19. J. P. Perdew. *Phys. Rev. B*, **1986**, 33, 8822.
20. A.D. Becke. *J. Chem. Phys*., **1993**, 98, 5648.
21. P.J. Stephens, F.J. Devlin, C.F. Chabalowski, M.J. Frisch. *J. Phys. Chem*., **1994**, 98, 11623.
22. T. Yanai, D. P. Tew, N. C. Handy. *Chem. Phys. Lett*., **2004**, 393, 51.
23. K. E. Yousaf, K. A. Peterson. *Chem. Phys. Lett*., **2009**, 476, 303.
24. I. Tolvatov, D. M. Chipman. *Theor. Chem. Acc*., **2017**, 82, 2017.

25. A. Szabo, N. S. Ostlund. *Modern Quantum Chemistry: Introduction to Advanced Electronic Structure Theory*. Dover Publications Inc., **1996**.
26. M. V. Putz, D. M. P. Mingos. *Applications of Density Functional Theory to Chemical Reactivity*. Springer, **2012**.
27. E. Engel, R. M. Dreizler. *Density Functional Theory: An Advanced Course. Theoretical and Mathematical Physics*. Springer, **2011**.
28. D. S. Sholl, J. A. Steckel. *Density Functional Theory: A Practical Introduction*. John Wiley & Sons, **2009**.
29. E. K. U. Gross, R. M. Dreizler. *Density Functional Theory. Series B: Physics*. Springer, **2013**.
30. B. O. Roos. *The Complete Active Space Self-Consistent Field Method and its Applications in Electronic Structure Calculations. Advances in Chemical Physics*. John Wiley & Sons, **2007**.
31. A. Kerridge. *The Complete-Active-Space Self-Consistent-Field Approach and Its Application to Molecular Complexes of the f-Elements. Computational Methods in Lanthanide and Actinide Chemistry*. John Wiley & Sons, **2015**.
32. B. O. Roos. *Advances in Chemical Physics; Ab Initio Methods in Quantum Chemistry II*; John Wiley & Sons, **1987**; 69, 399.
33. J. Finley, P.-Å. Malmqvist, B. O. Roos, L. Serrano-Andrés. *Chem. Phys. Lett.* **1998**, 288, 299.
34. K. Anderson, P. Malmqvist, B. Roos, K. Wolinski. *J. Phys. Chem.*, **1990**, 94, 5483.
35. K. Anderson, P. Malmqvist, B. Roos. *J. Chem. Phys.*, **1992**, 95, 1218.
36. F. Avila, D. J. Fernandez, J. F. Arenas, J. C. Otero, J. Soto. *Chem. Commun.*, **2011**, 47, 4210.
37. S. P. Centeno, I. López-Tocón, J. Román-Pérez, J. F. Arenas, J. Soto, J. C. Otero. *J. Phys. Chem. C*, **2012**, 116, 23639.
38. J. Román-Pérez, C. Ruano, S. P. Centeno, I. López-Tocón, J. F. Arenas, J. Soto, J. C. Otero. *J. Phys. Chem. C*, **2014**, 118, 2718.
39. Gaussian 09, Revision C.01, M. J. Frisch, G. W. Trucks, H. B. Schlegel, G. E. Scuseria, M. A. Robb, J. R. Cheeseman, G. Scalmani, V. Barone, B. Mennucci, G. A. Petersson, H. Nakatsuji, M. Caricato, X. Li, H. P. Hratchian, A. F. Izmaylov, J. Bloino, G. Zheng, J. L. Sonnenberg, M. Hada, M. Ehara, K. Toyota, R. Fukuda, J. Hasegawa, M. Ishida, T. Nakajima, Y. Honda, O. Kitao, H. Nakai, T. Vreven, J. A. Montgomery, Jr., J. E. Peralta, F. Ogliaro, M. Bearpark, J. J. Heyd, E. Brothers, K. N. Kudin, V. N.

Staroverov, T. Keith, R. Kobayashi, J. Normand, K. Raghavachari, A. Rendell, J. C. Burant, S. S. Iyengar, J. Tomasi, M. Cossi, N. Rega, J. M. Millam, M. Klene, J. E. Knox, J. B. Cross, V. Bakken, C. Adamo, J. Jaramillo, R. Gomperts, R. E. Stratmann, O. Yazyev, A. J. Austin, R. Cammi, C. Pomelli, J. W. Ochterski, R. L. Martin, K. Morokuma, V. G. Zakrzewski, G. A. Voth, P. Salvador, J. J. Dannenberg, S. Dapprich, A. D. Daniels, O. Farkas, J. B. Foresman, J. V. Ortiz, J. Cioslowski, D. J. Fox, Gaussian, Inc., Wallingford CT, 2010.

40. D. A. Long. *The Raman Effect: A Unified Treatment of the Theory of Raman Scattering by Molecules*. John Wiley & Sons, **2002**.
41. M. Born, R. Oppenheimer. *Ann. Phys.-Berlin*, **1927**, 389, 457.
42. G. Herzberg, E. Teller. *Z. Phys. Chemie-Int. J. Res. Phys. Chem. Chem. Phys*., **1933**, 21B, 410.
43. C. Manneback. *Physica XVII*, **1951**, 10-11, 1001.
44. A. A. Jarzecki. *J. Phys. Chem. A*, **2009**, 113, 2926.
45. F. Santoro, R. Improta, A. Lami, J. Bloino, V. Barone. *J. Chem. Phys*., **2007**, 126, 084509.
46. F. Santoro, R. Improta, A. Lami, V.Barone. *J. Chem Phys*, **2007**, 126, 184102.
47. F. Santoro, R. Improta, A. Lami, J. Bloino, V.Barone. *J. Chem. Phys*., **2008**, 128, 224311.
48. F. Santoro, V. Barone. *Int. J. Quantum. Chem*., **2009**, 110, 476.
49. Roberto Improta, Vincenzo Barone, Fabrizio Santoro. *J. Phys. Chem. B*, **2007**, 111, 14080.
50. N. Lin, Y. Luo, F. Santoro, X. Zhao, A. Rizzo, *Chem. Phys. Lett*., 2008, 464, 144.
51. N. Lin, F. Santoro, X. Zhao, A. Rizzo, V. Barone. *J. Phys. Chem. A*, **2008**, 112, 12401.
52. F. Santoro, *FC*classes, a Fortran 77 code, available online: http://www.pi.iccom.cnr.it/fcclasses, accessed on August 9, 2018.
53. J. R. Reimers. *J. Chem. Phys*., **2001**, 115, 9103.
54. C. F. Jackels, Z. Gu, D. G. Truhlar. *J. Chem. Phys*., **1995**, 102, 3188.
55. J. Cerezo, F. Santoro, *J. Chem. Theory. Comput*., **2016**, 12, 4970.

Capítulo III – Resultados (I).

Analysis of the Potential Dependent Surface-Enhanced Raman Scattering of p-Aminothiophenol on the Basis of MS-CASPT2 Calculations

María R. López-Ramírez, Daniel Aranda, Francisco J. Avila, Silvia P. Centeno, Juan F. Arenas, Juan C. Otero,* and Juan Soto*

The effect of adsorbate concentration on the potential dependent SERS spectra of *p*-aminothiophenol (*p*ATP) recorded on a silver electrode has been studied using $NaClO_4$ as electrolyte. Multiconfigurational second-order perturbation calculations (MS-CASPT2) have been performed in order to help the analysis of the experimental results by computing resonance Raman spectra of selected structural models of the metal-adsorbate surface complex. In order to avoid as far as possible any photochemical reaction, a long wavelength exciting line of 785 nm is used in the experiments. It is found that the spectra are dependent on adsorbate concentration and dominated by a resonant charge transfer (CT) mechanism, where the charge is always transferred from the adsorbate to the metal. The relative SERS enhancements are due to Franck-Condon factors related to the CT process and there are not intensified bands through Herzberg-Teller contributions. Furthermore, the Raman signals of the SERS recorded at low concentration arise from at least three different molecular species: (i) *p*ATP bonded to silver electrode through sulfur atom (Ag_n-S-Ph-NH_2); (ii) *p*ATP bonded to silver electrode through both sulfur and nitrogen atoms (Ag_n-S-$PhNH_2$-Ag_m) and (iii) the azo derivative *p,p'*-dimercaptoazobenzene (or its nitrene precursor).

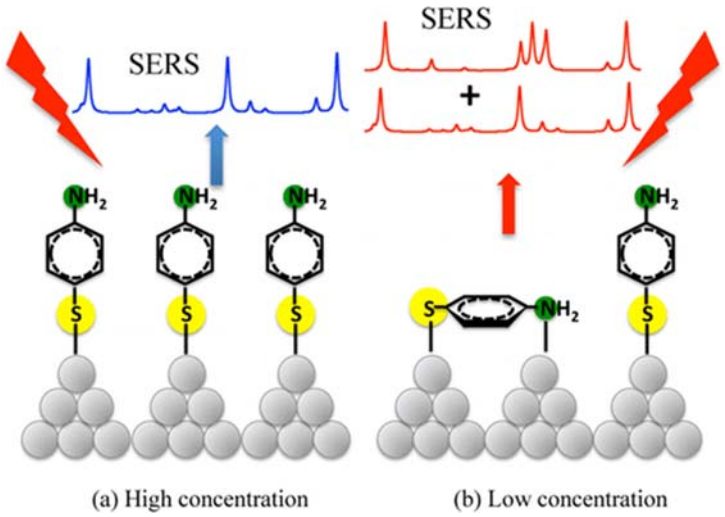

3.1.1. Introduction.

Surface-enhanced Raman Scattering (SERS) has become a widely used spectroscopic technique due to the huge enhancement of the weak Raman signal of a molecule when it is adsorbed on, or close to, metallic nanoparticles.[1] Nowadays it is widely accepted that the plasmonic enhancement mechanism is the main responsible for the phenomenon.[2] This universal contribution of SERS is based on exciting localized surface plasmons of a nanostructured good conductor like silver or gold, however it is not easy at all to account for the selective enhancement of specific SERS bands on the basis of this physical mechanism. In some cases, the plasmonic enhancement can be reinforced by the chemical mechanism (CM), which is very depending on the nature of the metal and the molecule and the particular experimental conditions. This short-range effect can involve resonant Raman processes up to excited states of the molecule (SERRS), new charge transfer (CT) states of the metal-molecule surface complex (CT-SERS) or even excited states of the metal (PL-SERS) able to enhance specific SERS bands of the molecule under particular experimental conditions. As occurs in any resonance Raman process no general selection rules can be derived from the CM contributions and particular vibrations can be enhanced through Franck-Condon (A-term) or Herzberg-Teller (B-term) factors. This makes necessary to predict the effect of the supposed electron resonances for each particular system and conditions which would allow for recognizing the presence of CM in the spectrum.

Pyridine has been the emblematic molecule in SERS due to the phenomenon was discovered from the work by Fleischman *et al*. where the Raman spectrum of this molecule adsorbed on a rough silver electrode was reported.[3-5] More recently, *p*-aminothiophenol (*p*ATP, HS-Ph-NH_2) has become very popular given that this compound is very often used for checking the enhancement capability of each new SERS substrate due to *p*ATP has the property of showing very intense SERS spectra. Several hundreds of papers dealing with the SERS of *p*ATP have been published and most of them have been analyzed by supposing the involvement of the chemical mechanism. Most of the SERS of this molecule are characterized by the very strong intensity of the 1142, 1391, 1438, and 1583 cm^{-1} set of bands, assigned to non-totally symmetric b_2-type modes, by supposing that they took their enhancement through a Herzberg-Teller mechanism of resonance Raman.[6] This conclusion has been assumed in many of the published works but is based mainly on the qualitative and unspecific argument that

Herzberg-Teller contribution is able to intensify non-totally symmetric vibrations in resonance Raman.

More recently, Tian and co-workers,[7-9] among others, have proposed a different interpretation for the selective SERS enhancement of the mentioned b_2-set of bands of *p*ATP. These authors have shown that it is highly probable that such intensified bands correspond to a new chemical species formed by dimerization of *p*ATP during the irradiation of the sample, namely *p,p'*-dimercaptoazobenzene (DMAB). However, the controversy has not ended given that the SERS results are extremely sensitive to small changes of the experimental conditions showing a complex behavior. For instance, Kim *et al.*[10-13] have proposed the opposite chemical reaction in such a way that DMAB monomerizes to *p*ATP when it interacts with the metal surfaces.

SERS of *p*ATP on silver electrode is significantly different from its ordinary Raman spectra. For instance, the Raman in ethanol (Figure S1) is dominated by the very strong intensity of the 1089 cm^{-1} band while the lines at 1600 and 477 cm^{-1} show medium intensities. On the contrary, the SERS is very dependent on the particular conditions of the experiment. The features of the SERS spectra of *p*ATP have been summarized by Tian and co-workers (references 6-8 and quotations therein) finding that they are strongly dependent on the following: (a) irradiation power: as laser power density increases from 8 x 10^2 mW/cm^2 to 2 x 10^7 mW/cm^2, the bands assigned to a_1-modes (1004, 1078, 1176, 1488, and 1595 cm^{-1}) of *p*ATP decrease their intensities while new bands assigned formerly by Osawa *et al.*[6] as b_2-type modes (1142, 1388, 1432 cm^{-1} and a shoulder of the 1595 cm^{-1} band) appear and dominate the spectrum.[8] These changes are even more evident as the electrode potential becomes more positive. When power density is kept at 8 x 10^2 mW/cm^2, only a decreasing of intensity of a_1-modes as electrode potential becomes more positive is observed. (b) Laser wavelength: when using the 1064 nm excitation line, the SERS spectrum is dominated by a_1-modes;[14,15] however, the set of b_2-bands become stronger at excitation wavelengths of 632.8 nm (1.96 eV) or 514.5 nm (2.40 eV). (c) Exposure time. (d) Surface roughness and morphology. (e) Properties of electrolyte solutions. It must be stressed that the SERS spectrum of *p*ATP also strongly depends on the pH of the solution[16-19] given that the so-called b_2-type bands are observed under alkaline conditions and some authors propose that this observation is an irrefutable proof for the formation of the corresponding azobenzene derivative.[17-19]

3.1.2. Methodology.

3.1.2.1 Experimental section.

The chemical reagents (Sigma-Aldrich) were of the highest available purity, and the water employed in all solutions was of Milli-Q quality (resistivity over 18 MΩcm). *p*-Aminothiophenol (*p*ATP) aqueous solutions (10^{-3} M, 10^{-4} M, 10^{-5} M and 10^{-6}M) were prepared from a more concentrated solution of this compound in ethanol-water.

The electrochemical instrument used to record the SERS spectra consists of a CH instrument model 600E potenciostat and a three electrodes cell. Likewise, a platinum counter electrode, an Ag/AgCl/KCl reference electrode to which all the electrode potentials were referred, and a pure silver working electrode were used. The silver surface of the working electrode was polished with 0.30 and 0.05 μm alumina (Buëhler), and then electrochemically activated by using 0.1 M KCl aqueous solution as electrolyte, maintaining the electrode potential at -0.5 V, and then subjecting it to eight 2 s pulses at +0.6 V in order to produce the necessary surface roughness. Finally, the SERS spectra at different concentration of *p*ATP were obtained by using 0.1 M $NaClO_4$ as the electrolyte.

SERS spectra were recorded by using a Renishaw Invia micro-Raman spectrometer and the excitation lines were 514.5 nm and 785 nm from an Ar^+ gas laser and a diode laser, respectively. The microscope was equipped with a macro objective (f: 30mm). Wire 2.0 from Renishaw has been used for spectral data acquisition and manipulation. To avoid overheating during the measurement of Raman spectra neutral density filters with an optical throughput of 0.5% and 1% were used and the laser power aimed at the sample was approximately between 0.1 and 5 mW. The spectral resolution was set at 2 cm^{-1}.

3.1.2.2 Theoretical section.

Multi-state resonance Raman intensities have been calculated according with the vibronic theory[20-22] assuming the small displacement approximation, which allows to treat each vibrational mode *k* as an independent harmonic oscillator (IMDHO model) and, in consequence, the mathematical expression of the polarizability tensor can be simplified. It is assumed as well that the vibrational frequencies for the *k*th mode are the same in all the electronic states. The overlap vibrational integrals are obtained using the

recurrence formulae of Manneback.[23] To be specific, we shell adopt a modified expression of the equation of intensity given by Long,[22] equation (1):

$$I_k = \frac{(2\pi)^4}{h^2} K N_{0^i} \left(\tilde{\nu}_1 - \tilde{\nu}_k\right)^4 \tilde{\nu}_k^2 \sum_e \left(G^e_{\Gamma_{r,k}} \Delta_{k,e}\right)^2 \quad (1)$$

where K is a constant for a given experimental condition and a given irradiance of the incident radiation of wave number $\tilde{\nu}_1$, N_{0^i} is the Boltzmann population of the vibrational ground state, $\tilde{\nu}_k$ is the wave number of *k*th mode, $G^e_{\Gamma_{r,k}}$ is given by equation (2) and depends on the transition dipole moment μ^o_e, the wave number of the energy difference between the excited electronic state *e* and the ground state, $\tilde{\nu}_e$, the wave number $\tilde{\nu}_k$ of *k* mode, and the damping factor $\Gamma_{r,k}$ related to the lifetime of the transition, which is taken as $0.2\tilde{\nu}_k$ in this work.

$$G^e_{\Gamma_{r,k}} = \frac{\left|\mu^0_e\right|^2}{\left[\left(\tilde{\nu}_e - \tilde{\nu}_1\right)^2 + \Gamma^2_{r,k}\right]^{1/2}\left[\left(\tilde{\nu}_e + \tilde{\nu}_k - \tilde{\nu}_1\right)^2 + \Gamma^2_{r,k}\right]^{1/2}} \quad (2)$$

Equation (1) is formally analog to the expression given by Jarzecki,[24] which deals with resonance Raman intensity calculations from multi-state computations as well. $G^e_{\Gamma_{r,k}}$ factor of equation (1) plays the role of weighting factor of Jarzecki; however, the $G^e_{\Gamma_{r,k}}$ parameters are not normalized in equation (1).

The dimensionless shift displacement parameter of Manneback, $\Delta_{k,e}$, has been calculated with the gradient approximation, Eq. (3)

$$\Delta_k = \frac{1}{\sqrt{2}} \cdot 2.408\,10^6\, \omega_k^{-3/2} \boldsymbol{f} \cdot \mathbf{M}^{-1/2} \mathbf{L}_k \quad (3)$$

where $\boldsymbol{f}$ is the force row vector of electronic state *e*, $\mathbf{M}$ is the $3N \times 3N$ diagonal matrix of atomic masses, and $\mathbf{L}_k$ is the column eigenvector of the Hessian matrix for mode *k*th. The vibrational frequencies obtained from quantum-chemical calculations have been scaled by a linear scaling factor obtained for adjusting of modes 1 and 8a.

The quantum-mechanic calculations have been performed with the complete active space self-consistent field (CAS-SCF) method and the multistate extension of the multiconfigurational second-order perturbation (MS-CASPT2) approximation[26,26] as implemented in the MOLCAS 8.0 program.[27,28] These calculations have been performed under C_s symmetry and using the ANO-RCC basis sets[29,30] with the Ag[5s4p3d2f1g]/S[4s3p2d1f]/(C,N)[3s2p1d]/H[2s1p] contraction scheme.

The geometries and molecular orbitals have been analyzed with the help of MacMolPlt[31] and Molden[32] programs.

3.1.3. Results and discussion.

In this work the potential dependent SERS spectra of *p*ATP adsorbed on silver electrode at different concentrations ranging from 10^{-3} to 10^{-6} M is reported. In spite of the effort devoted to the study of SERS of *p*ATP the effect of the concentration of the adsorbate has not received great attention and the low wavenumber region is surprisingly missing in many of the published papers, although the line localized at 388 cm^{-1} can become one of the strongest SERS bands. To avoid as far as possible any photochemical reaction, low power irradiance and 785 nm laser excitation has been applied in our experiments. Within the experimental conditions, it is found that the SERS spectrum of a 10^{-3} M solution are only moderately dependent on electrode potential, but its relative intensities can be very different from its normal Raman spectrum. As it will be demonstrated further, such spectra can be explained on the basis of a unique molecular species adsorbed on silver electrode. To be specific, the molecular species responsible for the observed SERS at high concentration is *p*ATP bonded to the metallic electrode through the sulfur atom. However, it is observed that as adsorbate concentration decreases, new weak bands appear (403 (sh), 439, 803, 1144, 1390, 1434, and 1561(sh) cm^{-1}). As mentioned before, some of them have been assigned in previous works to b_2-types modes of *p*ATP[6] or the DMAB photoproduct,[7-9] but our results point out also to a change in the coordination of *p*ATP with silver.

The experimental SERS have been analyzed in conjunction with MS-CASPT2//CAS-SCF calculations. Nowadays, DFT calculations are very often carried out in order to assist in the analysis of SERS by estimating the effect of the adsorption or by predicting the relative Raman intensities in the ground electronic state[7] or in resonance conditions.[33,34] Opposite to pyridine,[34] for instance, DFT-based predictions of the relative intensities of *p*ATP are very sensitive to the selected functionals and basis sets[7] as can be seen in Figure S2 where the calculated Raman and resonance Raman spectra of the Ag^{+}-*p*ATP^{-} complex (complex C1) by using four different functionals are shown. Moreover, the involvement of resonant processes up to metal-molecule CT states is determined by the energy of such states, which are poorly estimated by standard DFT functionals without long-range correction. For these reasons multiconfigurational SCF calculations have been carried out for the first time in order to analyze the SERS of this system.

Figure 1 shows the potential dependent SERS spectra of *p*ATP on silver electrode registered at two different concentrations of the adsorbate, 10^{-3} and 10^{-6} M, and λ_{exc} = 785 nm (Figure S3 of Supporting Information shows the SERS of the four studied concentrations in this work). The potential was varied from 0.0 to -1.2 V and all the intensities have been normalized with respect to the strong 1080 cm^{-1} band. The assignment of vibrational modes is given in Table S1 (calculated modes are depicted in Figure S4). As can be seen in Figures 1 and S3, the SERS at -1.2 V shows relative intensities very similar to the Raman of *p*ATP in ethanol being dominated by mode 1 recorded at 1080 cm^{-1}. Taking this particular SERS at 10^{-3} M and -1.2 V as a reference, mode 8a and, especially, the ν(AgS) vibration at 388 cm^{-1} becomes enhanced as the electrode potential is made more positive as well as when the concentration is lowered up to 10^{-6} M. In the SERS recorded at 10^{-6} M, the 388 cm^{-1} band is the strongest one and the three a_1-fundamentals ν(AgS), 1 and 8a show similar intensities. This change in the relative intensities points out to the presence of resonant Raman processes from molecules located at a fraction of surface sites. The amount of such sites increases at positive excess of charge. *p*ATP is ionized upon adsorption ($^{-}$S-Ph-NH_2) and the thiolate anion prefers to be bonded to positively charged metal atoms which are in turn the resonant sites. In diluted solutions (10^{-6} M, Figure 1b and S3d) almost all the solute molecules are adsorbed on these positively charged resonant sites which selectively enhances ν(AgS) and 8a modes with respect to vibration 1. In concentrated solutions (10^{-3} M, Figure 1a and S3a) the resonant features are observed at positive potentials, but

the fraction of non-resonant sites is increased at negative potentials. In this last case, the number of non-resonant molecules seems to be much higher than the resonant ones given that the SERS is dominated by the strong intensity of mode 1 and the spectrum looks like the Raman of the solution.

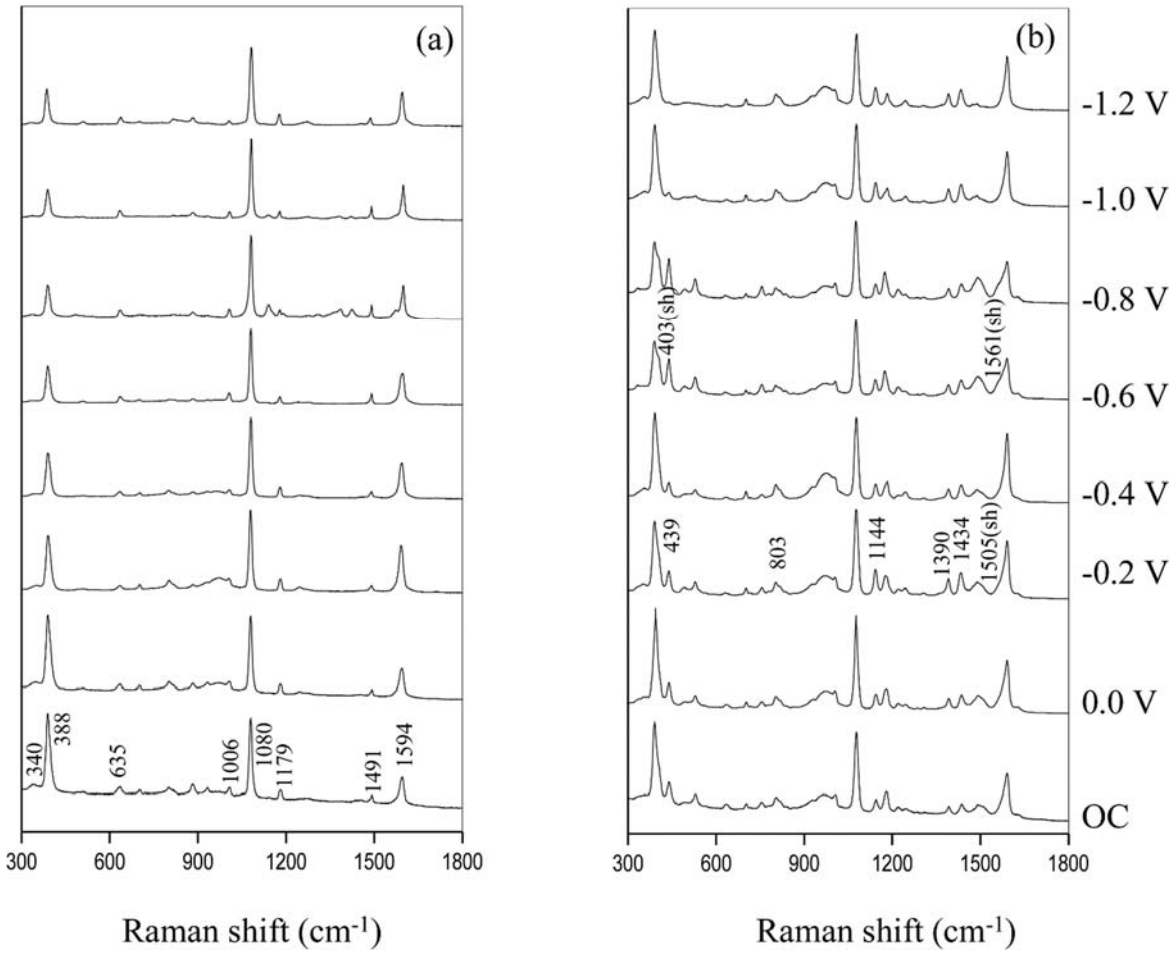

Figure 1. Potential dependent SERS spectra of p-aminothiophenol [(a) 10^{-3}M; (b)10^{-6} M] in $NaClO_4$ on silver electrode at excitation wavelength of 785 nm. Panel (b) shows the wavenumbers of the new observed bands respect to the concentrated solution.

High-level *ab initio* calculations (MS-CASPT2//CAS-SCF) confirm the presence of resonant Raman processes in the SERS of *p*ATP. The potential dependent SERS spectra of *p*ATP have been simulated by convoluting the calculated resonance Raman intensities with a Lorentzian function of HWHM = 10 cm^{-1} for various model complexes where *p*ATP is bonded to stick-like linear clusters of silver atoms $(Ag_n)^q$-S-Ph-NH_2 with different lengths (n) and charges (q=±1,0) (Figure 2). We have shown in previous works that the mean density of charge of these Ag_n^q atomic chains, defined as $q_{eff}=q/n$, controls the electron structure of the complexes in both the ground and the excited electronic states.[32,33] q_{eff} can be envisaged as a microscopic analogue (atomic units/atom of surface)

of the macroscopic surface excess of charge (Coulombs/cm^{-2} of surface) which is controlled in turn by the electrode potential. Therefore, the effect of the electrode potential is modelled through q_{eff} by changing the length or the charge of the silver chains. The complexes $(Ag)^{+1}$-S-Ph-NH_2, $(Ag_2)^{+1}$-S-Ph-NH_2 and $(Ag_3)^{+1}$-S-Ph-NH_2 correspond to *p*ATP bonded to a silver cluster with an effective density of charge of C1(Ag^{+1}), C2($Ag^{+1/2}$), C3($Ag^{+1/3}$), respectively, while the complexes $(Ag_3)^0$-S-Ph-NH_2 and $(Ag)^0$-S-Ph-NH_2 are two different models of *p*ATP bonded to a neutral surface C4/C5(Ag^0) (Figure 2). This set of molecular models have been selected in order to check the reliability of the calculated SERS intensities for *p*ATP bonded to positive or neutral silver clusters.

The calculated resonant Raman spectra upon 785 nm excitation for the five *C-type* complexes are drawn in Figure 2 where the molecular geometries of such complexes are depicted, as well as the overall charge of the systems (Q_T) and the corresponding electron spin multiplicity. As it can be seen, the calculated intensities for *C*-type clusters nicely reproduce the experimental behavior observed at high concentration (10^{-3} M). The spectra obtained at high concentration and positive electrode potentials (10^{-3} M) predict similar relative intensities for modes ν(AgS), 1 and 8a. On the contrary, the 388 cm^{-1} band shows very weak intensity in the calculated spectra for complexes containing neutral silver clusters (C4 and C5). To be specific, the calculated spectra shown in Figure 2 predict that the bands assigned to modes 1 and 8a shall keep their very strong and

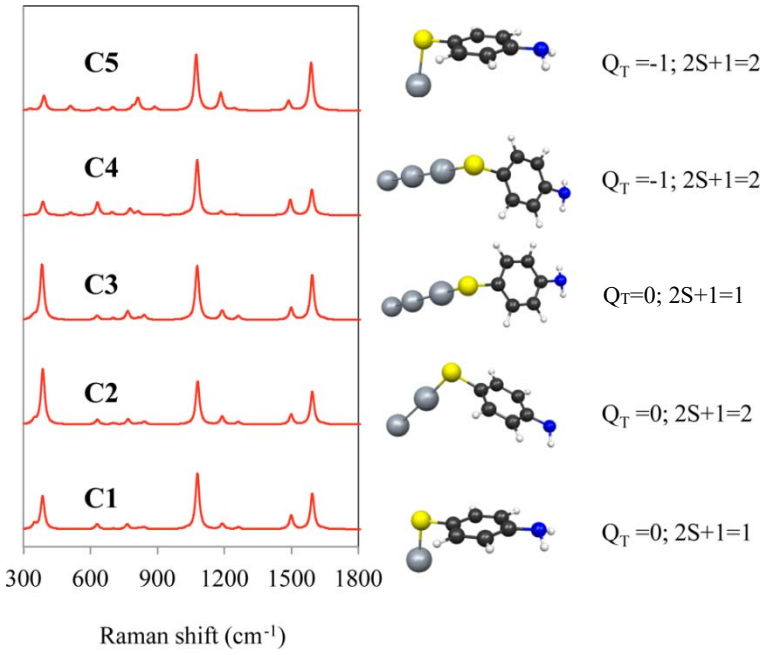

Figure 2. Calculated resonance Raman spectra of p-aminothiophenol for different molecular systems at 785 nm. C1 (q_{eff} = +1); C2 (q_{eff} = +1/2); C3 (q_{eff} = +1/3); C4 (q_{eff} = 0); C5 (q_{eff} = 0).

medium intensities, respectively, at positive or negative potentials, while vibration ν(AgS) will show very strong intensity at positive potentials but will be weakened at negative potentials. Table 1 summarizes the properties of such excited states (symmetry, electron configuration, oscillator strength, vertical energy and weighted contribution of the state to the overall intensity of the multistate resonant spectrum) for each studied complex. The weight of each state has been estimated with the equation of Jarzecki.[24] As can be seen, all the Raman spectra shown in Figure 2 are originated almost exclusively by the resonance up to a single excited state corresponding to a molecule-to-metal CT process with weights very close to the unity. Vertical energies of the resonant CT states lie in the range 1.10-2.79 eV. The largest values (2.79 and 2.65 eV) correspond to *p*ATP bonded to the smaller cluster models of the electrode containing only a single positive or neutral silver atom, respectively. Besides these too small systems, the energies of the CT states (1.10-1.92 eV) are similar to the 1.58 eV of the 785 nm laser line what fulfill the condition of resonance and explain why excitations up to these CT states dominate the SERS relative intensities.

Table 1. Electron configurations and weights of electronic states of the metal-*p*ATP complexes in the calculated SERS spectra at 785 nm (1.58 eV).

Spectrum	*State*	*Electron Configuration*[a]	*Weight*[b]	*Osc.*[c]	DE[d]
C1	2^1A'	$p_2(ring)^1 5s(Ag)^1$	1.00	0.4147	2.79
C2	2^2A'	$p_2(ring)^1 s(Ag)^2$	0.98	0.0930	1.10
	3^2A'	$s(Ag)^0 s^*(Ag)^1$	0.18	0.3901	2.98
C3	2^1A'	np(S)^{1}s*(Ag)^1	1.00	0.6105	1.92
C4	2^2A'	$s(Ag)^1 ns(Ag)^2$	1.00	0.0362	1.49
		$np(S)^1 ns(Ag)^2$			
		$ns(Ag)^0 s^*(Ag)^1$			
C5	2^2A'	$p_2(ring)^1 5s(Ag)^2$	1.00	0.2235	2.65
D1[e]	2^1A'	$np(S)^1 5s_b(Ag)^1$	0.78	0.0510	2.26
	3^1A'	$np(S)^1 5s_a(Ag)^1$	0.62	0.4121	3.36
D2[e]	3^2A'	$np(S)^1 5s_b(Ag)^1$	0.98	0.0525	1.70
		$s5s_a(Ag)^0 5s_b(Ag)^1$			
	4^2A'	$np(S)^1 5s_b(Ag)^1$	0.18	0.0230	1.80
D3[e]	2^2A'	$np(S)^1 s5s_b(Ag)^1$	0.99	0.0185	1.62
	4^2A'	$s5s_b(Ag)^0 s^*5s_b(Ag)^1$	0.07	0.4815	3.08
G1[e]	2^3A"	$np(N)^0 5s_b(Ag)^1$	0.16	0.0049	2.00
	3^3A"	$np(N)^0 5s_a(Ag)^1$	0.50	0.0441	2.26
	4^3A"	$np(S)^1 np(N)^2$	0.85	0.2368	2.70
	1^3A'	$ns(S)^1 np(N)^2$	0.06	0.0024	2.08
G2[e]	3^2A"	$np(N)^0 s^*5s_a(Ag)^1$	1.00	0.0469	1.65

[a]Referred to the ground state configuration given in Table S2 of supporting information. [b]Weight of electron state on the calculated spectrum. [c]Oscillator strength. [d]Vertical transition energy in eV. [e]$5s_a$ and $5s_b$ refer to silver bonded to sulfur or nitrogen, respectively.

Although ionized *p*ATP also bond to negatively charged silver clusters, the complexes are much less stable and the calculated resonant Raman spectra do not agree with any

of the recorded SERS. Moreover, the CT excited states are consequently blue-shifted given that the transferred electron from the molecule is much more difficult when the acceptor is already negatively charged. For instance, the multistate resonance Raman spectrum calculated for the $(Ag_3)^{-1}$-S-Ph-NH_2 (model C6, Figure S5) is characterized by the very strong intensity for a band located at 500 cm^{-1} while the remaining bands show very weak intensity. The calculated SERS in Figure S5 is mainly due to the contribution from the first excited state (3.21 eV, Table S3a), which corresponds to an excitation inside the metal cluster and do not to a molecular or metal-molecule (CT) resonance. This makes unreliable the prediction of the Raman intensities of the molecule from the properties of an electron resonance of the metal. In spite of the negative charge of the Ag_3^{-1} cluster, the lower metal-molecule CT state is localized at 3.50 eV (second excited state), therefore, far away from resonance using 785 nm excitation.

Other weak bands are also observed in the SERS recorded at 10^{-6} M (Figure 1b). As mentioned before, the 1505 (sh), 1434, 1390 and 1144 cm^{-1} lines has been assigned to the dimerized species. But the most interesting feature is a new band at 439 cm^{-1} and a shoulder of the 388 cm^{-1} band recorded at 403 cm^{-1}. These two bands disappear in the spectra recorded at -1.0 and -1.2 V and are missing in Figure 1a. Therefore, in principle, they will not be related to the azo-compound given that their characteristic bands (1390 and 1434 cm^{-1}) are observed in all the spectra compiled in Figure 1b while the 403 and 439 cm^{-1} bands are absent at the most negative potentials. Ab initio force fields point out that the only silver-*p*ATP species able to explain a significant blue-shift of the ν(AgS) vibration is *p*ATP linked to silver through both the sulfur and the nitrogen of the amine group (Ag-S-Ph-NH_2-Ag). Figure 3 shows the calculated multistate resonant Raman spectra for three different complexes D1:$(Ag)^{+1}$-S-Ph-NH_2-$(Ag)^{+1}$, D2:$(Ag)^{+1}$-S-Ph-NH_2-$(Ag_2)^{+1}$ and D3:$(Ag_2)^{+1}$-S-Ph-NH_2-$(Ag)^{+1}$ where *p*ATP acts as a bridging ligand connecting two positively charged silver clusters. For instance, the CASSCF and B3LYP wavenumbers of ν(AgS) fundamental show a blue shift of *ca*. 30 cm^{-1} when the C1 and D1 models are compared (Table S1). The calculated results for C-type and D-type series of spectra are very different (Figures 2 and 3) what demonstrate the very strong dependence of the calculated Raman intensities, *i.e*. of the resonant chemical mechanism to SERS, on the molecular structure. D-type series of spectra is characterized by the strong intensity of the blue-shifted mode ν (AgS) as well as for the very weak intensities of vibrations 1 and 8a what could be the explanation for the shoulder observed at 403 cm^{-1} and the preassigned b_2-type band at 1144 (1142) cm^{-1} which becomes a totally

symmetric mode in the new rearrangement given in Figure 3. The bridging coordination of *p*ATP is only possible at low concentration of the adsorbate because it covers more surface than the monodentate complex and demands more active sites. Moreover, it is very sensitive to the charge of the metal and the nitrogen-silver bond is weakened as the positive charge of the cluster diminishes in such a way that is broken in the $(Ag)^{+1}$-S-Ph-$NH_2\cdots(Ag)^0$ complex where the amine group is bonded to a neutral silver atom (model F1, Figure S6). These could be the reasons why the new low wavenumber band at 403 cm^{-1} disappears in the SERS recorded at negative potentials or at high concentration. The amine and the neutral silver are completely disconnected in model F1 as demonstrates the similarity found between the resonant spectra calculated for monodentate C1 and bridge-broken F1 models.

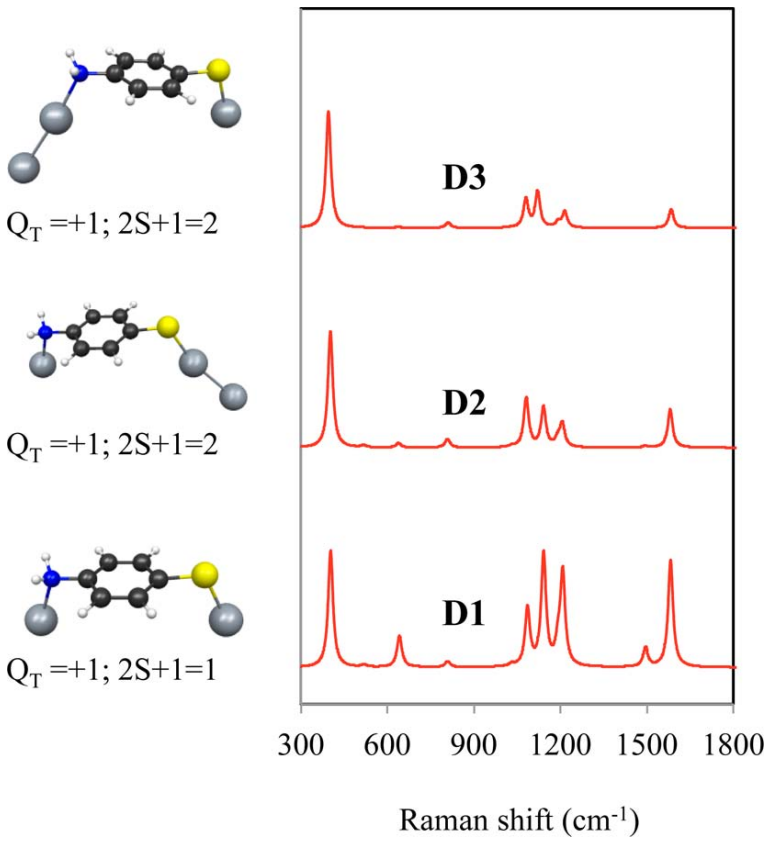

Figure 3. Calculated resonance Raman spectra at 785 nm of p-aminothiophenol bonded to silver through both sulfur and silver atoms for different molecular systems.

The bands localized at 1390 and 1434 cm^{-1} have generated some controversy in the literature with respect to their origins. They were initially assigned to b_2-type modes of *p*ATP[6] activated via the Herzberg-Teller mechanism. However, currently, it seems that there are solid experimental proofs[8,35,36] which support that these bands arise from the azo-dimer (DMAB) which is catalytically generated on the metal surface. It is not clear

at all which is the reaction mechanism through the azo-compound is formed. From our point of view, a plausible mechanism could be one that evolves via the nitrene intermediate. For this reason, we have investigated the resonance Raman spectra of *p*-thiophenyl nitrene bonded to metal clusters. Figure 4 represents the spectra of three complexes: G1:$(Ag)^{+1}$-S-Ph-N-$(Ag)^{+1}$, G2:$(Ag)^{+1}$-S-Ph-N-$(Ag)^{0}$, and singlet G3:$(Ag)^{+1}$-S-Ph-N-$(Ag)^{+1}$. Surprisingly, the calculations predict that triplet nitrene anchored to positively charged silver (Figure 4a) exhibits scaled bands at 428, 1387, 1440, and 1507 cm^{-1} which could be correlated with the observed ones at 439, 1390, 1434, and 1505 cm^{-1}. When charge on the metal becomes more negative the nitrogen atom is disconnected from silver and the calculated spectrum (Figure 4b) notably differs from the experimental one. Figure 4c represents the spectrum of singlet nitrene, which is very different from the triplet species in spite of both spin states are almost isoenergetic.

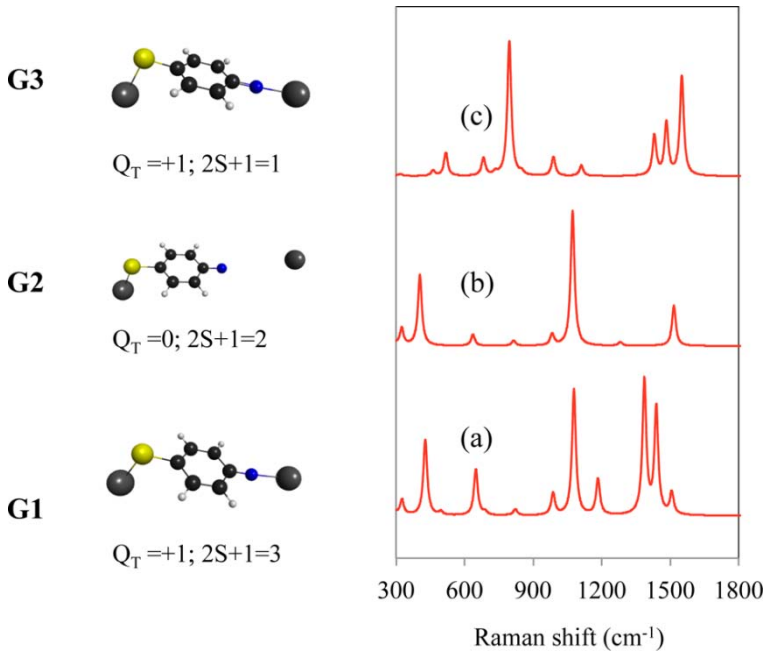

Figure 4. Calculated resonance Raman spectra at 785 nm of *p*-thiophenyl nitrene bonded to silver through both sulfur and silver atoms for different molecular systems. (a) G1 triple; (b) G2 doublet; (c) G3 singlet.

As mentioned before, at first glance, an experienced spectroscopist should conclude that bands localized at 1390 and 1434 cm^{-1} are not related to the low frequency peak of 439 cm^{-1} because the high frequency modes appear in all the recorded spectra at low concentration, but the low frequency band is not present at negative electrode potentials (Figure 1b). This conclusion is reinforced if ones observes the potential dependent SERS series registered at λ_{exc} = 514.5 nm (Figure S7). However, the calculations demonstrate

that the 428 cm^{-1} mode, ν(AgS) of the nitrene derivative, is very sensible to the resonance condition as it is illustrated in Figure S8 for the G1 nitrene species studied in this work. This figure represents the calculated resonance Raman spectra of G1 as a function of excitation line, where is observed that the band corresponding to ν(AgS) disappears as energy of excitation line increases. The weights of the electron states involved in each spectrum are given in Table S4. It is computed that as the energy of excitation raises the weight of 4^3A" state (2.70 eV) on the spectra increases which, in turn, deactivates the low frequency band at 430 cm^{-1}. This effect should operate at negative electrode potentials.

3.1.4. Conclusions.

In summary, it is found that the spectra are dependent on adsorbate concentration and dominated by a resonant charge transfer (CT) mechanism, where the charge is always transferred from the adsorbate to the metal. Our results demonstrate that in the potential dependent SERS of *p*-aminothiophenol are present at least three chemical species. The relative SERS enhancements are due to Franck-Condon factors related to the CT process and there are not intensified bands through Herzberg-Teller contributions.

3.1.5. References and notes.

1. R. Aroca. *Surface-Enhanced Vibrational Spectroscopy*. John Wiley & Sons, **2006**.
2. M. Moskovits. *Phys. Chem. Chem. Phys*., **2013**, 15, 6301.
3. M. Fleischmann, P. J. Hendra, A. McQuillann. *Chem. Phys. Lett*. **1974**, 26, 163.
4. D. L. Jeanmaire, R. P. Van Duyne. *J. Electroanal. Chem. Interfacil Electrochem*., **1977**, 84, 1.
5. M. G. Albrecht, J. A. Creighton. *J. Am. Chem. Soc*., **1977**, 99, 5215.
6. M. Osawa, N. Matsuda, K. Yoshii, I. Uchida. *J. Phys. Chem*., **1994**, 98, 12702.
7. D.-Y Wu, X.-M. Lie, Y.-F. Huang, B. Ren, X. Xu, Z.-Q. Tian. *J. Phys. Chem. C*, **2009**, 113, 18212.
8. Y.-F. Huang, H.-P. Zhu, G.-K- Liu, D.-Y. Wu, B. Ren, Z.-Q. Tian. *J. Am. Chem. Soc*., **2010**, 132, 9244.
9. L.-B. Zhao, Y.-F. Huang, X.-M. Lie, J. R. Anema, D.-Y. Wu, B. Ren, Z.-Q. Tian. *Phys. Chem. Chem. Phys*., **2012**, 14, 12919.
10. K. Kim, D. Shin, J.-Y. Choi, K. L. Kim, k. S. Shin. *J. Phys. Chem. C*, **2011**, 115, 24960.
11. K. Kim, K. L. Kim, S. H. Lee, K. S. Shin. *J. Phys. Chem. C*, **2012**, 116, 11635.
12. K. Kim, K. L. Kim, S. H. Lee, K. S. Shin. *J. Phys. Chem. C*, **2013**, 117, 5975.
13. K. Kim, S. H. Lee, K. L. Kim, K. S. Shin. *J. Raman Spectrosc*., **2013**, 44, 518.
14. Y. Wang, X. Zou, W. Ren, W. Wang, E. Wang. *J. Phys. Chem. C*, **2007**, 111, 3259.
15. A. P. Ritchter, J. R. Lombardi, B. Zhao. *J. Phys. Chem. C*, **2012**, 114, 1610.
16. W. Hil, B. Wehling. *J. Phys. Chem*. **1993**, 97, 9451.
17. M. Sun, Y. Huang, L. Xia, X. Chen, H. Xu. *J. Phys. Chem. C*, **2011**, 115, 9629.
18. A. M. Gabudean, D. Biro, S. Astilean. *J. Mol. Struct*., **2011**, 993, 420.
19. S. Zong, Z. Wang, J. Yang, Y. Cui. *Anal. Chem*., **2011**, 83, 4178.
20. A. C. Albrecht. *J. Chem. Phys*., **1961**, 34, 1476.
21. R. J. H. Clark, T. J. Dines. *Angew. Chem. Int. Ed. Engl*., **1986**, 25, 131.
22. A. D. Long. *The Raman Effect: A Unified Treatment of the Theory of Raman Scattering by Molecules*; John Wiley & Sons, **2002**
23. C. Manneback. *Physica*, **1951**, 10-11, 1001.
24. A. A. Jarzecki. *J. Phys. Chem. A* **2009**, 113, 2926.
25. B. O. Roos. *Advances in Chemical Physics; Ab Initio Methods in Quantum Chemistry II*; John Wiley & Sons, **1987**, 69, 399**.**

26. J. Finley, P.-Å. Malmqvist, B. O. Roos, L. Serrano-Andrés. *Chem. Phys. Lett.* **1998**, 288, 299-306.
27. F. Aquilante, L. De Vico, N. Ferré, G. Ghigo, P.-Å Malmqvist, P. Neogrády, T. B. Pedersen, M. Pitonak, M. Reiher, B. O. Roos, L. Serrano-Andrés, M. Urban, V. Veryazov, R. Lindh. *J. Comput. Chem*., **2010**, 31, 224.
28. V. Veryazov, P-O. Wildmark, L. Serrano-Andrés, R. Lindh, B. O. Roos. *J. Quantum Chem*., **2004**, 100, 626.
29. B. O. Roos, R. Lindh, P.-Å. Malmqvist, V. Veryazov., P.-O. Wildmark. *J. Phys. Chem. A*, **2004**, 108, 2851.
30. B. O. Roos, R. Lindh, P. Å. Malmqvist, V. Veryazov, P.-O. Wildmark. *J. Phys. Chem. A*, **2005**, 109, 6575.
31. B. M. Bode, M. S. Gordon. *J. Mol. Graphics Modell*., **1988**, 16, 133.
32. G. Schaftenaar, J. H. Noordik. *J. Comput.-Aided Mol. Des*., **2000**, 14, 123.
33. F. Avila, D. J. Fernández, J. F. Arenas, J. C. Otero, J. Soto. *Chem. Commun*., **2011**, 47, 4210.
34. F. Avila, C. Ruano, I. López-Tocón, J. F. Arenas, J. F. Soto, J. C. Otero. *Chem. Commun*., **2011**, 4213.
35. S. Y. Ong, Y. P. Chan, P. Zhu, K. H. Leung, D. L. Phillips. *J. Phys. Chem. A*, **2003**, 107, 3858.
36. H.-K Choi, H. K. Shon, H. Yu, T. G. Lee, Z. H. Kim. *J. Phys. Chem. Lett*., **2013**, 4, 1079.

Supporting Information

Table S1. Assignment of normal modes of C1 and D1 complexes (under C_{2v} symmetry). Correlation of CASSCF and B3LYP calculated frequencies according with Duschinsky matrix and normal mode representation.

Assign.[a]	CASSC	B3LYP	CASSCF	B3LYP	Exp.[b]	
C1			**D1**			
ν(C-N)+$\delta(NH_2)$;a_1	1804	1665	1790	1648		
8a;a_1	1744	1639	1730	1622	1594	1561[c]
8b;b_2	1701	1603	1708	1614		
19a;a_1	1631	1524	1626	1516	1491	1505[c]
;b_2	1539	1458	1536	1452		
14;b_2	1429	1352	1431	1361		
ν(C-N);a_1	1355	1308	1303	1310	*	
3;b_2	1292	1309	1293	1225		
9a;a_1	1272	1203	1273	1200	1179	
15;b_2	1171	1146	1176	1160		
1;a_1	1146	1098	1153	1116	1080	
18b;b_2	1143	1073	1162	1103		
12;a_1	1091	1020	1092	1025	1006	
17a;a_2	985	967	996	983		
5;b_1	969	952	977	965		
17b;b_1	880	838	844	838	*	
10b;b_1	853	831	849	815	*	
10a;a_2	840	818	841	822		
4;b_1	730	709	725	710	*	
6b;b_2	687	650	684	651		
6a;a_1	653	650	665	646	635	
b;b_1	536	504	534	620		
16a;a_2	437	420	433	526		
δ(C-N);b_2	423	403	393	412		
ν(Ag-S);a_1	386	379	412	411	388	439[c]
γ(C-N);b_1	350	343	390	372	340	
$\gamma(NH_2)$;b_1	798	533	1216	1079		

[a]Wilson´s nomenclature.
[b]SERS bands assigned to *p*ATP of a 10^{-3} M solution (+0.0 V).
[c]New band in SERS of *p*ATP at 10^{-6} M.

Table S2a. Electron configurations of the ground states for the *p*ATP-silver clusters (MS-CASPT2, C_s symmetry).

Species	Q^a	Active Space	w[b]		Electron Configuration[c]
C1	0	(12*e*, [8a',4a"])	77%	A'	$\pi_1(ring)^2\ \pi_2(ring)^2\ \sigma(CS)^2 n\pi\ (S)^2$
					$\pi_1^*(ring)^0\ \pi_2^*(ring)^0\ \sigma^*(CS)^0\ 5s(Ag)^0$
2*S*+1=1				A"	$n\sigma(S)^2\ \pi_3(ring)^2$
					$\pi_3^*(ring)^0\ 3\delta(\Sigma)^0$
C2	0	(13*e*, [9a',4a"])	61%	A'	$\sigma(CS)^2\ \pi_1(ring)^2\ \pi_2(ring)^2\ \sigma(AgAg)^1\ n\pi\ (S)^2$
					$\sigma^*(CS)^0\ \pi_1^*(ring)^0\ \pi_2^*(ring)^0\ \sigma^*(AgAg)^0$
2*S*+1=2				A"	$\pi_3(ring)^2\ n\sigma(S)^2$
					$3\delta(\Sigma)^0\ \pi_3^*(ring)^0$
			17%	A'	$\sigma(CS)^2\ \pi_1(ring)^2\ \pi_2(ring)^1\ \sigma(AgAg)^2\ n\pi\ (S)^2$
					$\sigma^*(CS)^0\ \pi_1^*(ring)^0\ \pi_2^*(ring)^0\ \sigma^*(AgAg)^0$
				A"	$\pi_3(ring)^2\ n\pi\ (S)^2$
					$3\delta(\Sigma)^0\ \pi_3^*(ring)^0$
C3	0	(14*e*, [10a',3a"])	79%	A'	$\sigma(CS)^2\ \pi_1(ring)^2\ \pi_2(ring)^2\ \sigma(AgAgAg)^2 n\pi\ (S)^2$
2*S*+1=1					$\sigma^*(AgAgAg)^0\ n\sigma(AgAgAg)^0$
					$\sigma^*(CS)^0\ \pi_1^*(ring)^0\ \pi_2^*(ring)^0$
				A"	$\pi_3(ring)^2\ n\pi\ (S)^2$
					$\pi_3^*(ring)^0$
C4	-1	(15*e*, [10a',3a"])	82%	A'	$\sigma(CS)^2\ \pi_1(ring)^2\ n\pi\ (S)^2\ \sigma(AgAgAg)^2\ \pi_2(ring)^2$
					$n\sigma(AgAgAg)^1$
2*S*+1=2					$\sigma^*(AgAgAg)^0\sigma^*(CS)^0\ \pi_1^*(ring)^0\ \pi_2^*(ring)^0$
				A"	$\pi_3(ring)^2\ n\sigma(S)^2$
					$\pi_3^*(ring)^0$
C5	-1	(13*e*, [8a',4a"])	83%	A'	$\pi_1(ring)^2\ \pi_2(ring)^2\sigma(CS)^2 n\pi\ (S)^2$
					$\pi_1^*(ring)^0\ \pi_2^*(ring)^0\ \sigma^*(CS)^0\ 5s(Ag)^1$
2*S*+1=2				A"	$n\sigma(S)^2\ \pi_3(ring)^2$
					$\pi_3^*(ring)^0\ 3\delta(\Sigma)^0$
C6	-2	(16*e*, [10a',3a"])	85%	A'	$\pi_1(ring)^2 n\pi\ (S)^2\sigma(CS)^2\ \pi_2(ring)^2\ \sigma(Ag)^2 n\sigma(Ag)^2$
					$\pi_2^*(ring)^0\ \pi_1^*(ring)^0\sigma^*(CS)^0\sigma^*(Ag)^0$
2*S*+1=1				A"	$\pi_3(ring)^2 n\sigma(S)^2\ \pi_3^*(ring)^0$

[a]Total charge on the complex.
[b]Weight of the reference configuration.
[c]MS-CASPT2 electron configuration.

Table S2b. Electron configurations of the ground states for the bidentate *p*ATP-silver clusters (MS-CASPT2, C_s symmetry).

Species	Q^a	Active Space	w^b		Electron Configuration[c]
D1	+1	(12*e*, [10a',3a"])	82%	A'	$\pi_1(ring)^2\pi_2(ring)^2\sigma(CS)^2\ n\pi(S)^2$
$2S+1=1$					$\pi_2^*(ring)^0 3\delta(\Sigma)^0\sigma^*(CS)^0 5s_b(Ag)^0\pi_1^*(ring)^0$
					$5s_a(Ag)^0$
				A"	$n\sigma(S)^2\pi_3(ring)^2$
					$\pi_3^*(ring)^0$
D2	+1	(11*e*, [8a',3a"])	84%	A'	$\pi_2(ring)^2\ \pi_1(ring)^2 n\pi(S)^2\sigma 5s_a(Ag)^1$
$2S+1=2$					$\pi_2^*(ring)^0\pi_1^*(ring)^0 5s_b(Ag)^0\sigma^* 5s_a(Ag)^0$
				A"	$\pi_3(ring)^2 n\sigma(S)^2$
					$\pi_3^*(ring)^0$
D3	+1	(11*e*, [8a',3a"])	85%	A'	$\pi_2(ring)^2\pi_1(ring)^2 n\pi(S)^2\sigma 5s_b(Ag)^1$
$2S+1=2$					$\pi_1^*(ring)^0 5s_a(Ag)^0\pi_2^*(ring)^0\sigma^* 5s_b(Ag)^0$
				A"	$\pi_3(ring)^2\ n\sigma(S)^2$
					$\pi_3^*(ring)^0$

[a]Total charge on the complex.
[b]Weight of the reference configuration.
[c]MS-CASPT2 electron configuration.

Table S2c. Electron configurations of the ground states for the nitrene derivatives of *p*ATP (MS-CASPT2, C_s symmetry).

Species	Q^a	Active Space	w^b		Electron Configuration[c,d]
G1	+1	(12*e*, [8a',5a"])	80%	A'	$\pi_1(ring)^2\pi_2(ring)^2 n\pi(S)^2 n\pi(N)^1$
$2S+1=3$					$\pi_1^*(ring)^0 5s_b(Ag)^0\pi_2^*(ring)^0 5s_a(Ag)^0$
				A"	$n\sigma(N)^1\pi_3(ring)^2 n\sigma(S)^2$
					$\pi_3^*(ring)^0 3d(S)^0$
G2	0	(13e, [8a',5a"])	71%	A'	$\pi_1(ring)^2\pi_2(ring)^2 n\pi(S)^2 n\pi(N)^1$
$2S+1=2$					$\pi_1^*(ring)^0 5s_b(Ag)^1\pi_2^*(ring)^0\sigma^* 5s_a(Ag)^0$
				A"	$n\sigma(N)^1\pi_3(ring)^2 n\sigma(S)^2$
					$\pi_3^*(ring)^0 3d(S)^0$

[a]Total charge on the complex.
[b]Weight of the reference configuration.
[c]MS-CASPT2 electron configuration.
[d]$5s_a$ and $5s_b$ refer to silver bonded to sulfur or nitrogen, respectively.

Table S3a (continue). MS-CASPT2 vertical transitions in eV of the $Ag_n^{m\pm}$-$SPhNH_2$ complexes (C_s symmetry).

Species	VE (eV)	*OS*[a]	ΔQ[b]	*Configuration*[c]
C1 2S+1=1				
ge→2A'	2.79	0.4147	-0.3	78% $\pi_2(ring)^1$ 5*s*(Ag)^1
ge→3A'	4.51	0.1236	-0.4	73% $n\pi$(S)^1 5*s*(Ag)^1
ge→4A'	6.37	0.32-01	-0.6	40% $\pi_2(ring)^1$ 5*s*(Ag)^1
				20% $\pi_2(ring)^0$ $\pi_2^*(ring)^1$ 5*s*(Ag)^1
ge→1A"	2.43	0.44-02	-0.5	82% $n\sigma$(S)^1 5*s*(Ag)^1
ge→2A"	4.42	0.28-03	-0.4	63% $\pi_3(ring)^1$ 5*s*(Ag)^1
ge→3A"	4.96	0.14-01	+0.1	41% $\pi_2(ring)^1$ $\pi_3^*(ring)^1$
				23% $\pi_3(ring)^1$ $\pi_2^*(ring)^1$
ge→4A"	6.28	0.55-06	-0.5	43% $\pi_2(ring)^1$ $n\sigma$(S)^1 $\pi_2^*(ring)^1$ 5*s*(Ag)^1
				32% $n\sigma$(S)^1 $\pi_3(ring)^1$ $\pi_3^*(ring)^1$ 5*s*(Ag)^1
C2 2S+1=2				
ge→2A'	1.10	0.93-01	-0.39	60% $\pi_2(ring)^1$ σ(Ag)^2
				18% $\pi_2(ring)^2$ σ(Ag)^1
ge→3A'	2.98	0.3901	-0.36	34% σ(Ag)^0 σ^*(Ag)^1
				22% $\pi_2(ring)^0$ σ(Ag)^2 σ^*(Ag)^1
ge→4A'	3.23	0.1067	-0.43	56% σ(Ag)^2 $n\pi$(S)^1
ge→1A"	1.24	0.39-03	-0.52	79% $n\sigma$(S)^1 σ(Ag)^2
ge→2A"	3.00	0.30-02	-0.52	82% $n\sigma$(S)^1 σ^*(Ag)^1
ge→3A"	3.23	0.27-03	-0.56	72% $\pi_3(ring)^1$ σ(Ag)^2
ge→4A"	4.87	0.89-04	-0.56	64% $\pi_3(ring)^1$ σ^*(Ag)^2
C3 2S+1=1				
ge→2A'	1.92	0.6105	-0.33	69% $n\pi$(S)^1 σ^*(Ag)^1
ge→3A'	2.57	0.2979	-0.37	24% σ(Ag)^1 σ^*(Ag)^1
				17% $n\pi$(S)^0 σ^*(Ag)^2
				20% $n\pi$(S)^1 σ(Ag)^1 σ^*(Ag)^2
ge→1A"	1.84	0.17-02	-0.55	79% $n\sigma$(S)^1 σ^*(Ag)^1
ge→2A"	3.03	0.36-03	-0.55	61% $n\sigma$(S)^1 σ(Ag)^1 σ^*(Ag)^2
				17% $n\sigma$(S)^1 $n\sigma$(Ag)^1
ge→3A"	3.82	0.53-03	-0.58	67% $\pi_3(ring)^1$ σ^*(Ag)^1

[a]Oscillator strength.
[b]Increment of CASPT2 Mulliken charge on the silver cluster with respect to the ground state.
[c]MS-CASPT2 electron configurations. Contributions at least greater than 15% are included. Only orbitals with different occupation to the ground state are given.

Table S3a (continuation). MS-CASPT2 vertical transitions in eV of the $Ag_n^{m\pm}$-$SPhNH_2$ complexes (C_s symmetry).

	VE (eV)	*OS*[a]	ΔQ[b]	*Configuration*[c]
C4 2S+1=2				
ge→2A'	1.49	0.36-01	+0.00	46% σ(Ag)^1 *n*σ(Ag)^2
				16% *n*π(S)^1 *n*σ(Ag)^2
				17% *n*σ(Ag)^0 σ*(Ag)^1
ge→3A'	2.42	0.1758	-0.71	60% *n*π(S)^1 *n*σ(Ag)^2
ge→1A"	2.50	0.13-02	-0.85	83% *n*σ(S)^1 *n*σ(Ag)^2
ge→2A"	3.87	0.17-02	+0.06	48% *n*σ(Ag)^0 π_3*(*ring*)^1
				16% π_2(*ring*)^1 π_3*(*ring*)^1
ge→3A"	4.35	0.21-01	+0.05	58% π_2(*ring*)^1 π_3*(*ring*)^1
C5 2S+1=2				
ge→2A'	2.65	0.2223	-0.30	71% π_2(*ring*)^1 5*s*(Ag)^2
ge→3A'	3.72	0.58-01	-0.46	34% π_2(*ring*)^1 π_2*(*ring*)^1
				33% π_2*(*ring*)^1 5*s*(Ag)^0
ge→4A'	4.69	0.17-02	+0.02	54% π_3(*ring*)^1 π_3*(*ring*)^1
ge→1A"	2.97	0.22-02	-0.80	86% *n*σ(S)^1 5*s*(Ag)^2
ge→2A"	3.12	0.27-02	+0.13	63% π_3*(*ring*)^1 5*s*(Ag)^0
				16% π_2(*ring*)^1 π_3*(*ring*)^1
ge→3A"	4.04	0.16-01	+0.05	68% π_2(*ring*)^1 π_3*(*ring*)^1
ge→4A"	5.05	0.21-02	+0.17	42% π_2(*ring*)^1 π_3*(*ring*)^1
C6 2S+1=1				
ge→2A'	3.21	1.9324	+0.07	80% *n*σ(Ag)^{1}σ*(Ag)^1
ge→3A'	3.90	0.23-01	+0.09	57% σ(Ag)^{1}σ*(Ag)^1
				23% *n*σ(Ag)^{0}σ*(Ag)^2
ge→4A'	4.19	0.11-03	+0.03	82% *n*σ(S)^1π_3*(*ring*)^1
ge→1A"	3.50	0.72-02	+0.41	75% *n*σ(Ag)^1π_3*(*ring*)^1
ge→2A"	4.22	0.12-01	+0.32	69% *n*π(S)^1π_3*(*ring*)^1
ge→3A"	4.44	0.18-03	-0.02	80% *n*σ(S)^1π_2*(*ring*)^1
ge→4A"	5.20	0.90-03	+0.65	72% σ(Ag)^1π_3*(*ring*)^1

[a]Oscillator strength.

[b]Increment of CASPT2 Mulliken charge on the silver cluster with respect to the ground state.

[c]MS-CASPT2 electron configurations. Contributions at least greater than 15% are included. Only orbitals with different occupation to the ground state are given.

Table S3b (continue). MS-CASPT2 vertical transitions in eV of the bidentate *p*ATP complexes (C_s symmetry).

Species	VE (eV)	*OS*[a]	ΔQ[b]	*configuration*[c]
D1 2S+1=1				
ge→2A'	2.26	0.51-01	+0.30 -0.93	82% $n\pi(S)^1\ 5s_b(Ag)^1$
ge→3A'	3.36	0.4121	-0.40 +0.00	78% $n\pi(S)^1\ 5s_a(Ag)^1$
ge→4 A'	4.30	0.11-01	+0.25 -0.93	75% $\pi_2(ring)^1\ 5s_b(Ag)^1$
ge→1A"	2.60	0.15-02	+0.24 -0.90	58% $n\sigma(S)^1\ 5s_b(Ag)^1$
				22% $n\sigma(S)^1\ 5s_a(Ag)^1$
ge→2A"	2.73	0.39-02	-0.60 -0.03	22% $n\sigma(S)^1\ 5s_b(Ag)^1$
				54% $n\sigma(S)^1\ 5s_a(Ag)^1$
ge→3A"	3.74	0.11-02	+0.14 -0.91	81% $\pi_3(ring)^1\ 5s_b(Ag)^1$
ge→4A"	4.72	0.17-02	-0.16 -0.01	26% $\pi_3(ring)^1\ 5s_a(Ag)^1$
				35% $n\pi(S)^1\ \pi_3^*(ring)^1$
D2 2S+1=2				
ge→2A'	1.70	0.0525	-0.51 -0.06	61% $n\pi(S)^1\sigma5s_a(Ag)^2$
ge→3A'	1.80	0.0230	+0.30 -0.93	23% $\sigma5s_a(Ag)^0 5s_b(Ag)^1$
				59% $n\pi(S)^1 5s_b(Ag)^1$
ge→4 A'	2.02	0.0338	+0.30 -0.93	77% $n\pi(S)^1 5s_b(Ag)^1$
ge→5A'	3.38	0.20-02	+0.61 -0.82	56% $\sigma5s_a(Ag)^0 5s_b(Ag)^1$
				22% $n\pi(S)^1\sigma5s_a(Ag)^2$
ge→6A'	4.06	0.81-02	+0.07 -0.14	16% $\pi_3(ring)^1\pi_3^*(ring)^1$
				32% $n\pi(S)^1\pi_2^*(ring)^1$
ge→1A"	1.63	0.48-03	-0.41 -0.25	82% $n\sigma(S)^1\sigma5s_a(Ag)^2$
ge→2A"	2.28	0.13-05	+0.16 -0.83	83% $n\sigma(S)^1 5s_b(Ag)^1$
ge→3A"	2.30	0.99-06	+0.10 -0.78	81% $n\sigma(S)^1 5s_b(Ag)^1$
ge→4A"	3.52	0.92-04	+0.13 -0.93	81% $\pi_3(ring)^1 5s_b(Ag)^1$
ge→5A"	3.53	0.78-03	+0.13 -0.93	81% $\pi_3(ring)^1 5s_b(Ag)^1$
ge→6A"	4.19	0.13-03	-0.20 +0.00	20% $\pi_3(ring)^1\sigma5s_a(Ag)^1$
				38% $n\pi(S)^1\pi_3^*(ring)^1$
				14% $\pi_3(ring)^1\pi_2^*(ring)^1$

[a]Oscillator strength.

[b]Increment of CASPT2 Mulliken charge on the silver cluster with respect to the ground state.

[c]MS-CASPT2 electron configurations. Contributions at least greater than 15% are included. Only orbitals with different occupation to the ground state are given.

Table S3b (continuation). MS-CASPT2 vertical transitions in eV of the bidentate *p*ATP complexes (C_s symmetry).

Species	VE (eV)	*OS*[a]	ΔQ[b]	*configuration*[c]
D3 2S+1=2				
ge→2A'	1.62	0.0185	+0.34 -0.96	82% $n\pi(S)^1\sigma 5s_b(Ag)^2$
ge→3A'	2.48	0.31-03	-0.55 -0.00	71% $n\pi(S)^1 5s_a(Ag)^1$
ge→4A'	3.08	0.4815	+0.04 -0.20	74% $\sigma 5s_b(Ag)^0\sigma^* 5s_b(Ag)^1$
ge→5A'	3.46	0.1146	+0.22 -0.65	80% $n\pi(S)^1\sigma^* 5s_b(Ag)^1$
ge→1A"	1.95	0.39-05	+0.34 -0.96	84% $n\sigma(S)^1\sigma 5s_b(Ag)^2$
ge→2A"	2.56	0.13-03	-0.60 +0.01	87% $n\sigma(S)^1 5s_a(Ag)^1$
ge→3A"	2.65	0.50-02	-0.60 +0.01	86% $n\sigma(S)^1 5s_a(Ag)^1$
ge→4A"	3.03	0.15-03	+0.12 -0.95	75% $\pi_3(ring)^1\sigma 5s_b(Ag)^2$
ge→5A"	3.65	0.15-04	+0.33 -0.95	87% $n\sigma(S)^1\sigma^* 5s_b(Ag)^1$

[a]Oscillator strength.

[b]Increment of CASPT2 Mulliken charge on the silver cluster with respect to the ground state.

[c]MS-CASPT2 electron configurations. Contributions at least greater than 15% are included. Only orbitals with different occupation to the ground state are given.

Table S3c. MS-CASPT2 vertical transitions in eV of the nitrene derivatives of *p*ATP complexes (C_s symmetry).

Species	VE (eV)	*OS*[a]	ΔQ[b](a)	ΔQ[c](b)	*Configuration*[d]
G1 2S+1=3					
$ge \rightarrow 2^3A''$	2.00	0.49-02	+0.25	-0.93	76% $n\pi(N)^1 5s_b(Ag)^1$
$ge \rightarrow 3^3A''$	2.26	0.44-01	-0.56	0.00	61% $n\pi(N)^1\ 5s_a(Ag)^1$
$ge \rightarrow 4^3A''$	2.70	0.2367	0.00	0.00	55% $n\pi(S)^1\ n\pi(N)^2$
$ge \rightarrow 1^3A'$	2.08	0.24-02	-0.40	0.00	72% $n\sigma(S)^1\ n\pi(N)^2$
$ge \rightarrow 2^3A'$	2.65	0.51-06	+0.14	0.00	82% $n\pi(S)^1\ n\sigma(N)^2$
$ge \rightarrow 3^3A'$	2.74	0.10-02	0.00	0.00	62% $\pi_3(ring)^1\ n\pi(N)^2$
$ge \rightarrow 4^3A'$	2.83	0.43-02	-0.60	0.00	75% $n\sigma(S)^1\ 5s_a(Ag)^1$
G2 2S+1=2					
$ge \rightarrow 2^2A''$	0.71	0.18-06	0.00	0.00	75% *ground state*[e]
$ge \rightarrow 3^2A''$	1.65	0.47-01	-0.50	0.00	52% $n\pi(N)^0\sigma^*5s_a(Ag)^{1,f}$
$ge \rightarrow 4^2A''$	1.68	0.17-03	-0.40	0.00	55% $n\pi(N)^0\sigma^*5s_a(Ag)^1$
$ge \rightarrow 1^2A'$	1.51	0.0	0.00	0.00	61% $n\pi(N)^0 n\sigma(N)^2$
$ge \rightarrow 2^2A'$	2.23	0.54-03	-0.60	0.00	28% $n\pi(N)^2 n\sigma(S)^1$
					25% $\sigma^*5s_a(Ag)^1 n\sigma(S)^1$
					18% $n\pi(N)^0\sigma^*5s_a(Ag)^2 n\sigma(S)^1$
$ge \rightarrow 3^2A'$	2.25	0.56-03	-0.60	0.00	28% $n\pi(N)^2 n\sigma(S)^1$
					25% $\sigma^*5s_a(Ag)^1 n\sigma(S)^1$
					18% $n\pi(N)^0\sigma^*5s_a(Ag)^2 n\sigma(S)^1$
$ge \rightarrow 4^2A'$	2.38	0.57-02	-0.60	0.00	61% $\sigma^*5s_a(Ag)^1 n\sigma(S)^1$

[a]Oscillator strength.
[b]Increment of CASPT2 Mulliken charge with respect to the ground state on the silver cluster bonded to the sulfur atom.
[c]Increment of CASPT2 Mulliken charge with respect to the ground state on the silver cluster bonded to the nitrogen atom.
[d]MS-CASPT2 electron configurations. Contributions at least greater than 15% are included. Only orbitals with different occupation to the ground state are given.
[e]Configuration differs with respect to ground state in spin pairing.
[f]$5s_a$ and $5s_b$ refer to silver bonded to sulfur or nitrogen, respectively.

Table S4. Electron configurations and weights of electronic states of the G1 complex at different excitation lines.

Spectrum	*eV*[a]	*State*	*Electron Configuration*[b]	*Weight*[c]	*Osc.*[d]	ΔE[e]
785 nm	1.58	2^3A"	$n\pi(N)^0 5s_b(Ag)^{1,e}$	0.16	0.0049	2.00
		3^3A"	$n\pi(N)^0 5s_a(Ag)^1$	0.50	0.0441	2.26
		4^3A"	$n\pi(S)^1 n\pi(N)^2$	0.85	0.2368	2.70
		1^3A'	$n\sigma(S)^1 n\pi(N)^2$	0.06	0.0024	2.08
700 nm	1.77	2^3A"	$n\pi(N)^0 5s_b(Ag)^{1,e}$	0.30	0.0049	2.00
		3^3A"	$n\pi(N)^0 5s_a(Ag)^1$	0.58	0.0441	2.26
		4^3A"	$n\pi(S)^1 n\pi(N)^2$	0.75	0.2368	2.70
		1^3A'	$n\sigma(S)^1 n\pi(N)^2$	0.08	0.0024	2.08
600 nm	2.07	2^3A"	$n\pi(N)^0 5s_b(Ag)^{1,e}$	0.33	0.0049	2.00
		3^3A"	$n\pi(N)^0 5s_a(Ag)^1$	0.81	0.0441	2.26
		4^3A"	$n\pi(S)^1 n\pi(N)^2$	0.42	0.2368	2.70
		1^3A'	$n\sigma(S)^1 n\pi(N)^2$	0.23	0.0024	2.08
500 nm	2.48	3^3A"	$n\pi(N)^0 5s_a(Ag)^1$	0.22	0.0441	2.26
		4^3A"	$n\pi(S)^1 n\pi(N)^2$	0.97	0.2368	2.70
400 nm	3.10	4^3A"	$n\pi(S)^1 n\pi(N)^2$	1.00	0.2368	2.70

[a]Excitation line in eV

[b]Referred to the ground state configuration given in Table S2c of supplementary material.

[c]Weight of electronic state on the calculated spectrum.

[d]Oscillator strength.

[d]Vertical transition energy in eV.

[e]$5s_a$ and $5s_b$ refer to silver bonded to sulfur or nitrogen, respectively.

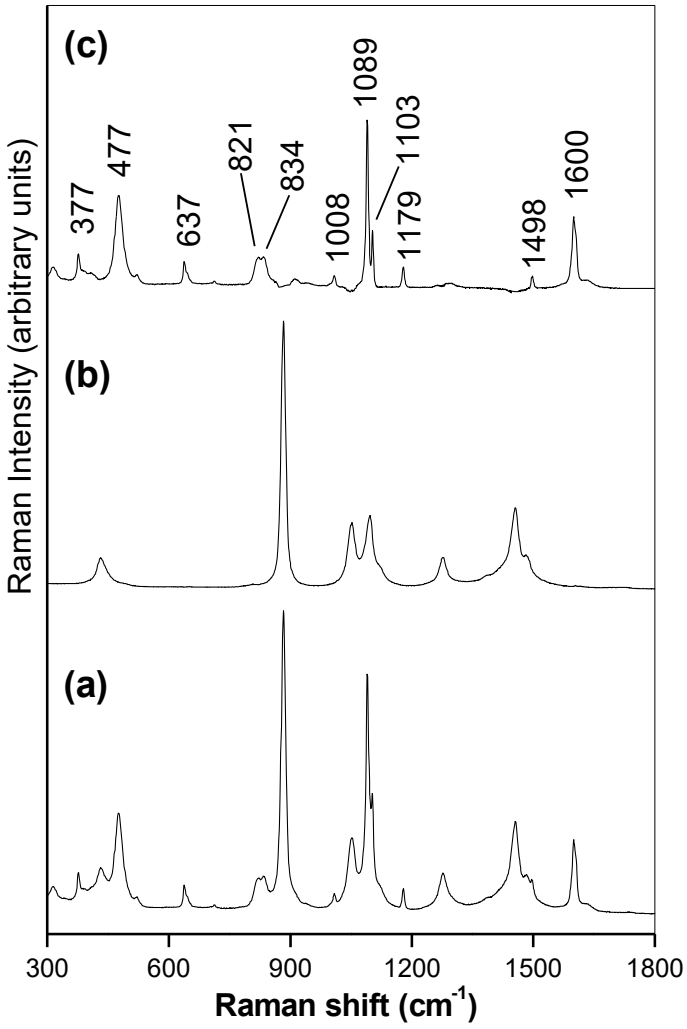

Figure S1. Raman spectra at 785 nm of: (a) 0.5 M of PATP in ethanol solution at pH=7; (b) Ethanol; (c) Spectral difference between a) and b).

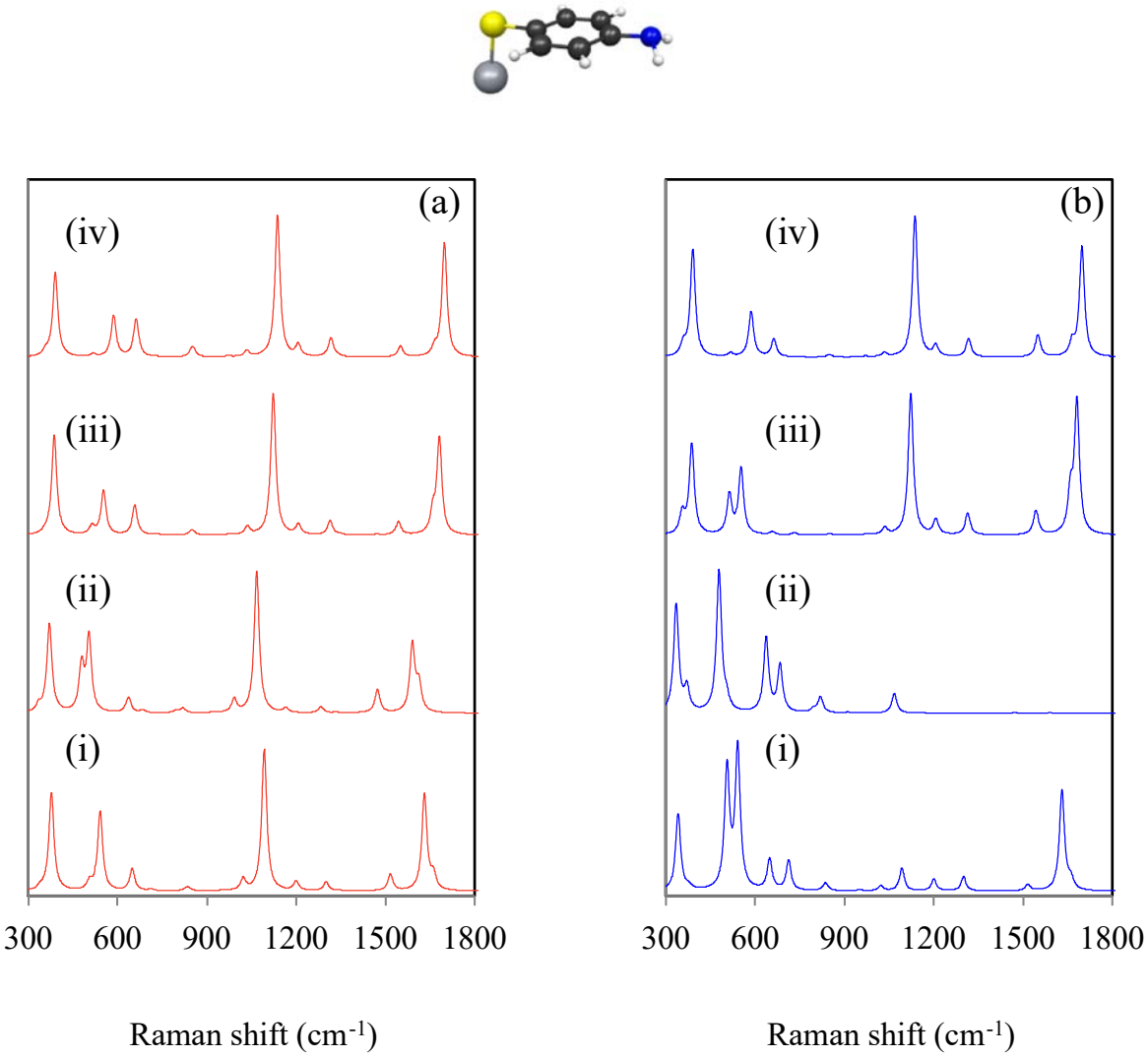

Figure S2. (a) Normal Raman and (b) Resonance Raman spectra of the complex C1 calculated at excitation line of 785 nm with functionals: (i) B3LYP; (ii) PW91PW91; (iii) CAM-B3LYP; (iv) wB97x. Resonance Raman spectra have been calculated with Eq. (1) by including 20 excited states. Basis sets: Lanl2Dz on silver atom; 6-311+G(d,p) on the S, C, N, and H atoms.

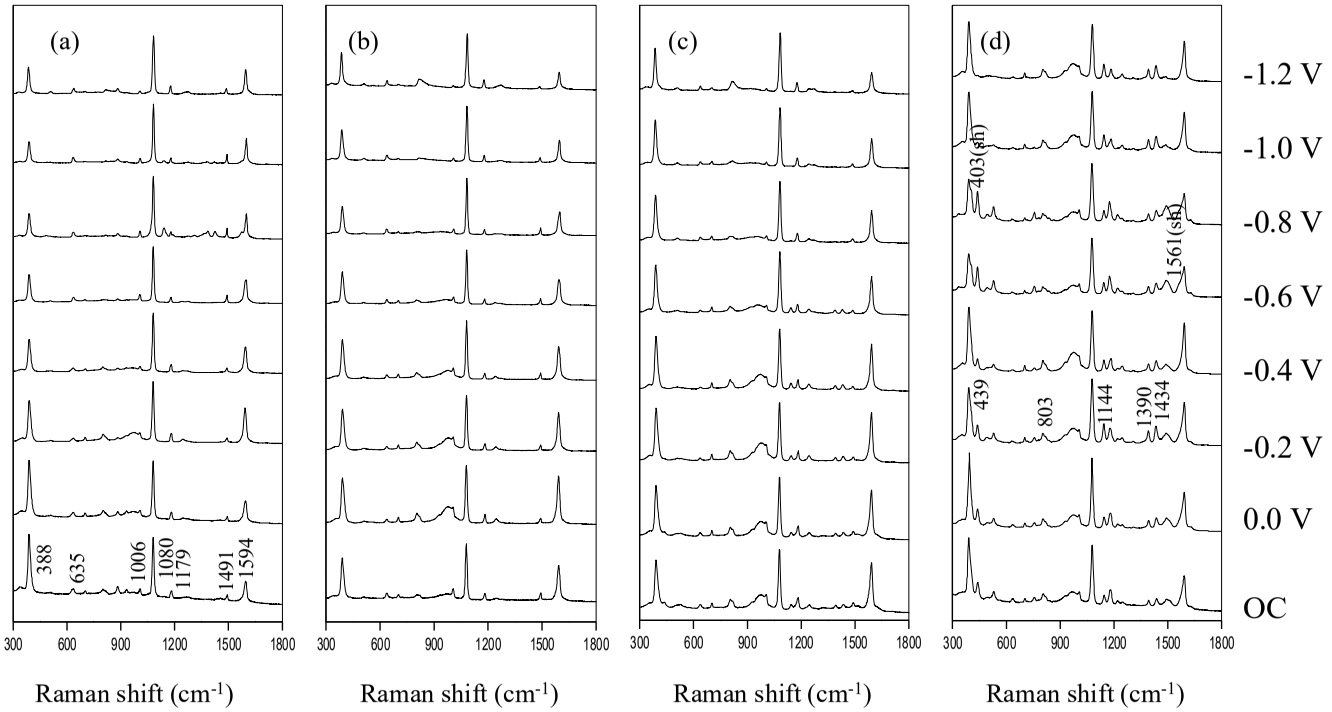

Figure S3. Potential dependent SERS spectra (from open circuit to -1.2 V) of p-aminothiophenol of (a) 10^{-3} M, (b) 10^{-4} M, (c) 10^{-5} M, and (d) 10^{-6} M in $NaClO_4$ on silver electrode at excitation wavelength of 785 nm. Panel (d) shows the wavenumbers of the new observed bands with respect to the concentrated solution

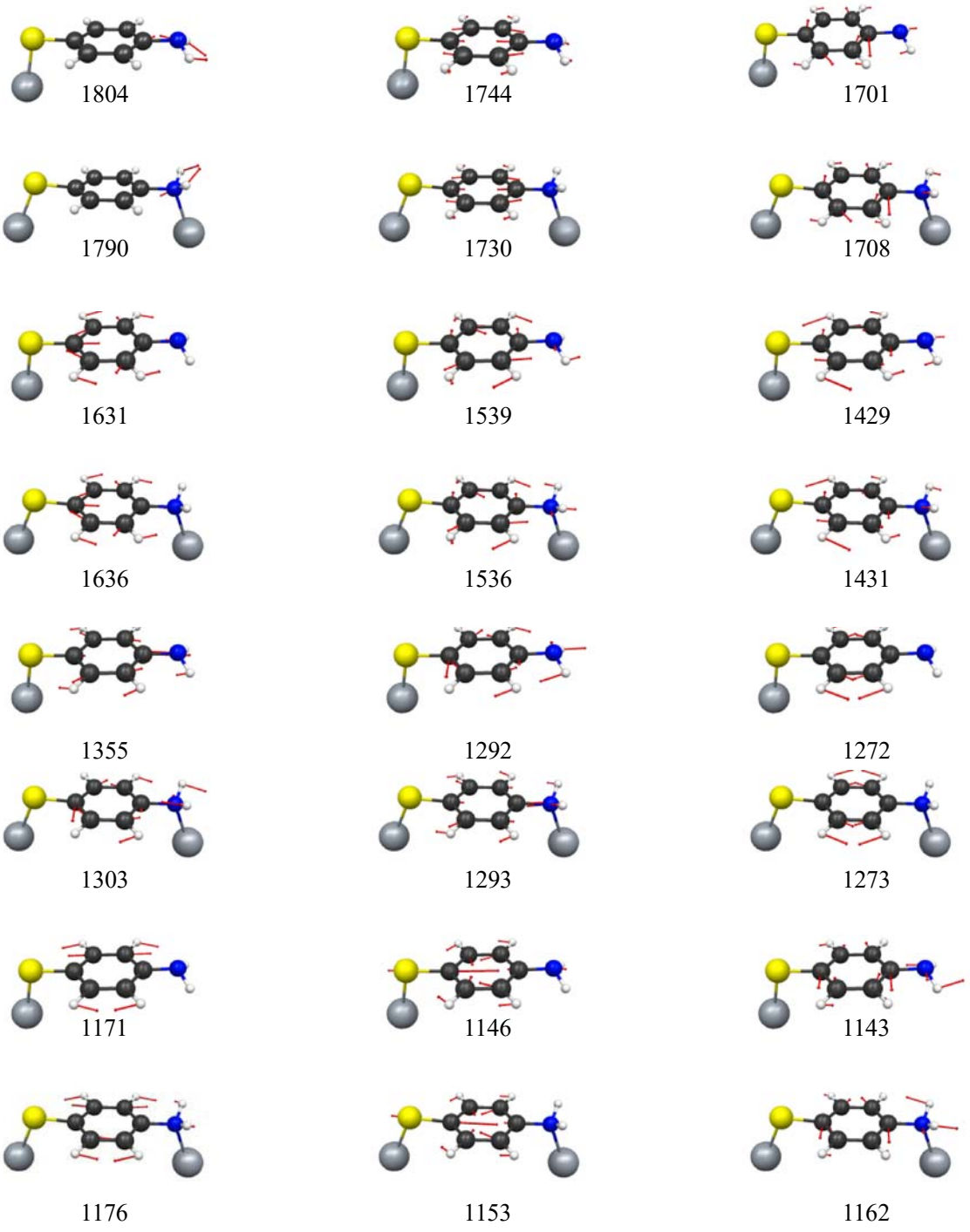

Figure S4 (continue). CASSCF/ANO-RCC frequencies in cm^{-1} of the normal modes of C1 and D1 complexes.

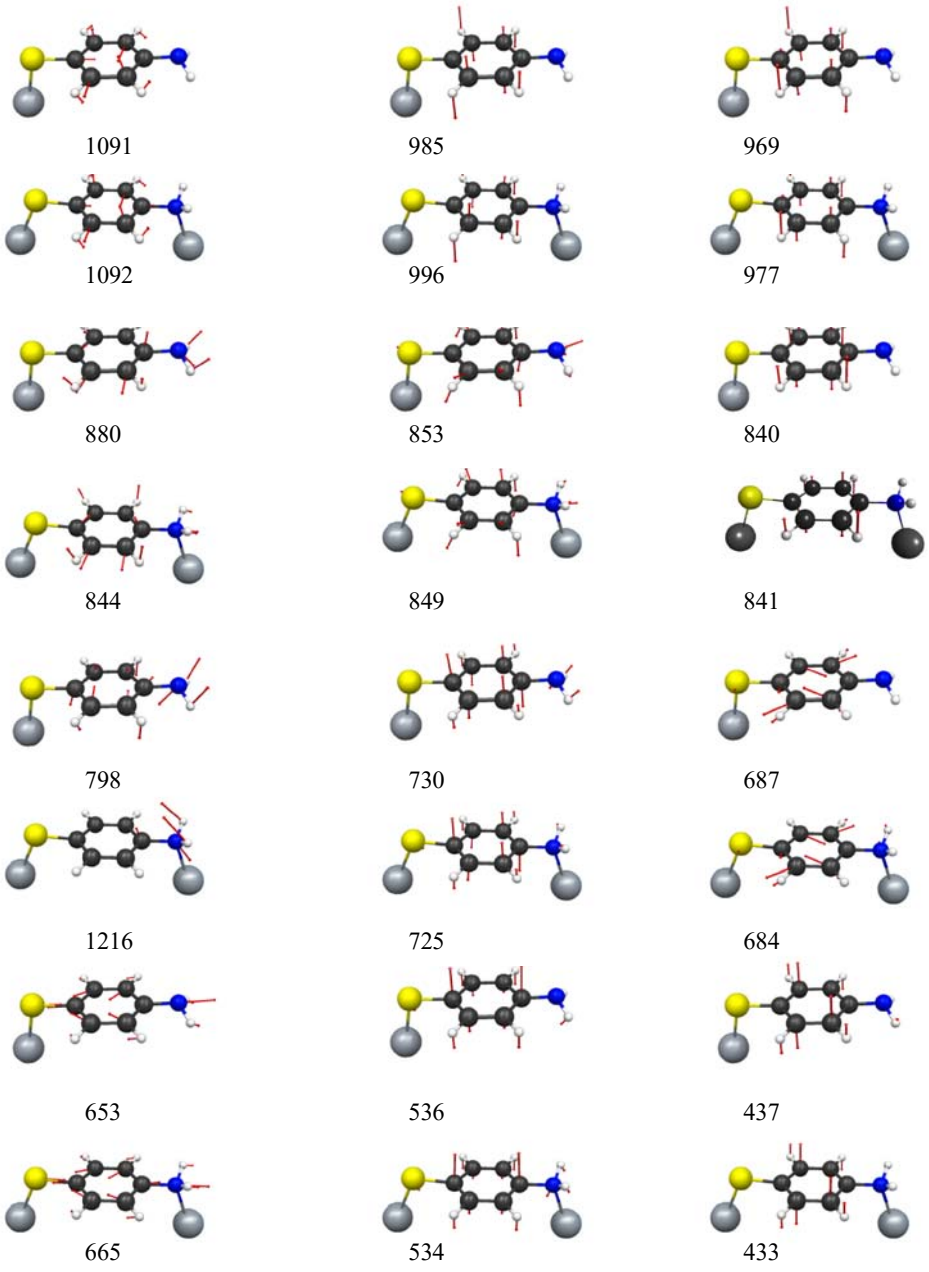

Figure S4 (continuation). CASSCF/ANO-RCC frequencies in cm^{-1} of the normal modes of C1 and D1 complexes.

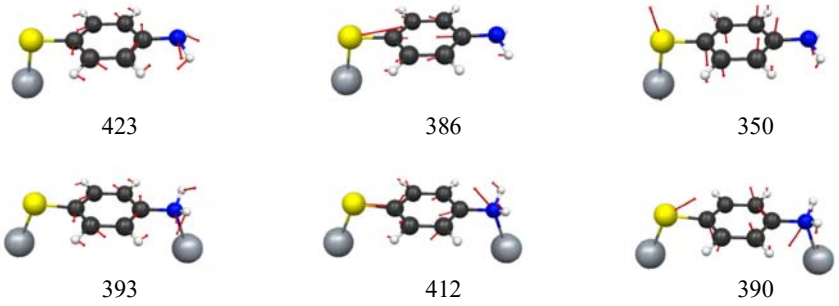

Figure S4 (continuation b). CASSCF/ANO-RCC frequencies in cm^{-1} of the normal modes of C1 and D1 complexes.

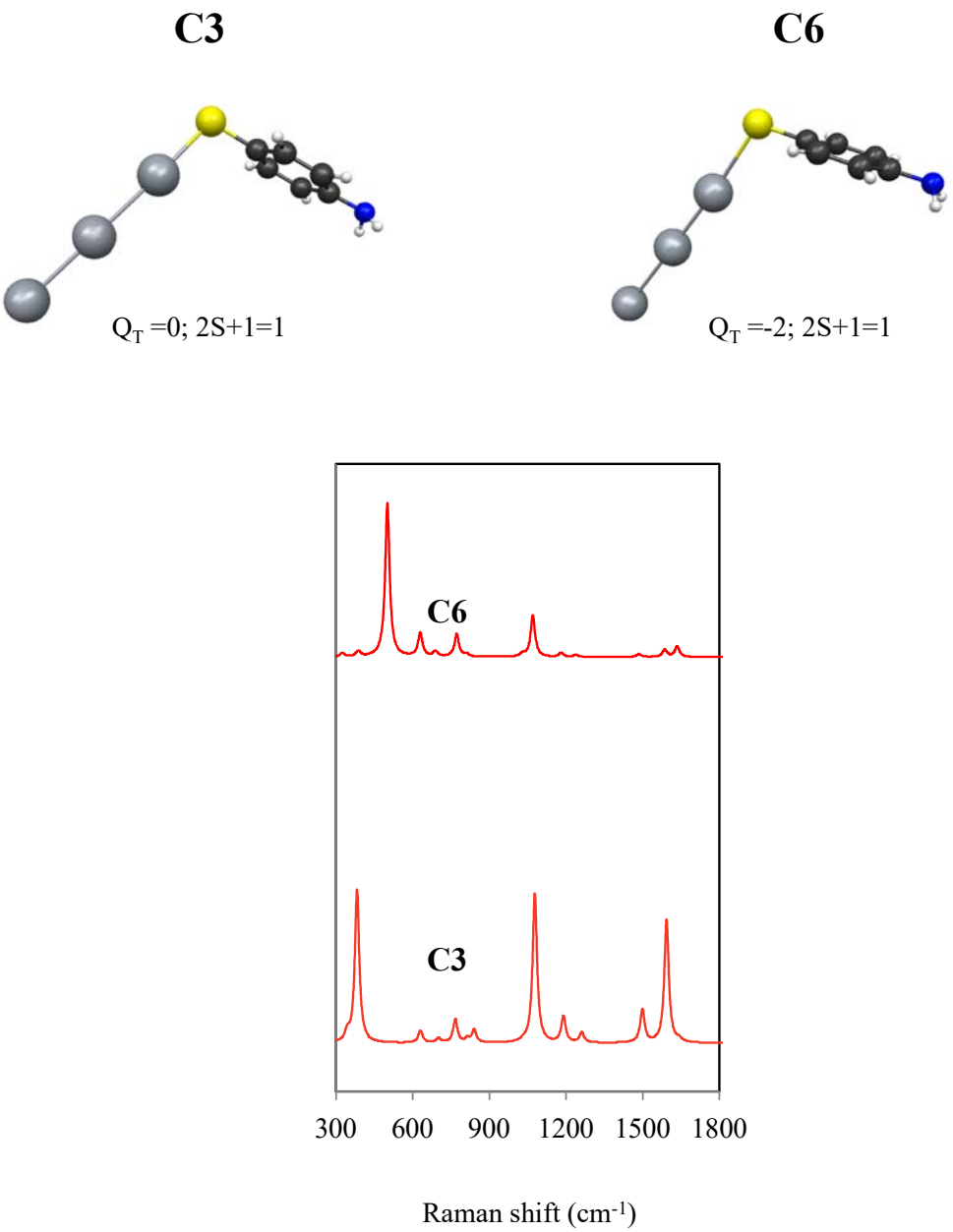

Figure S5. Molecular geometries and multi-state Resonance Raman spectra of C3 and C6 complexes (λ_{exc} = 785 nm). MS-CASPT2/ANO-RCC (eight states in the state average calculations).

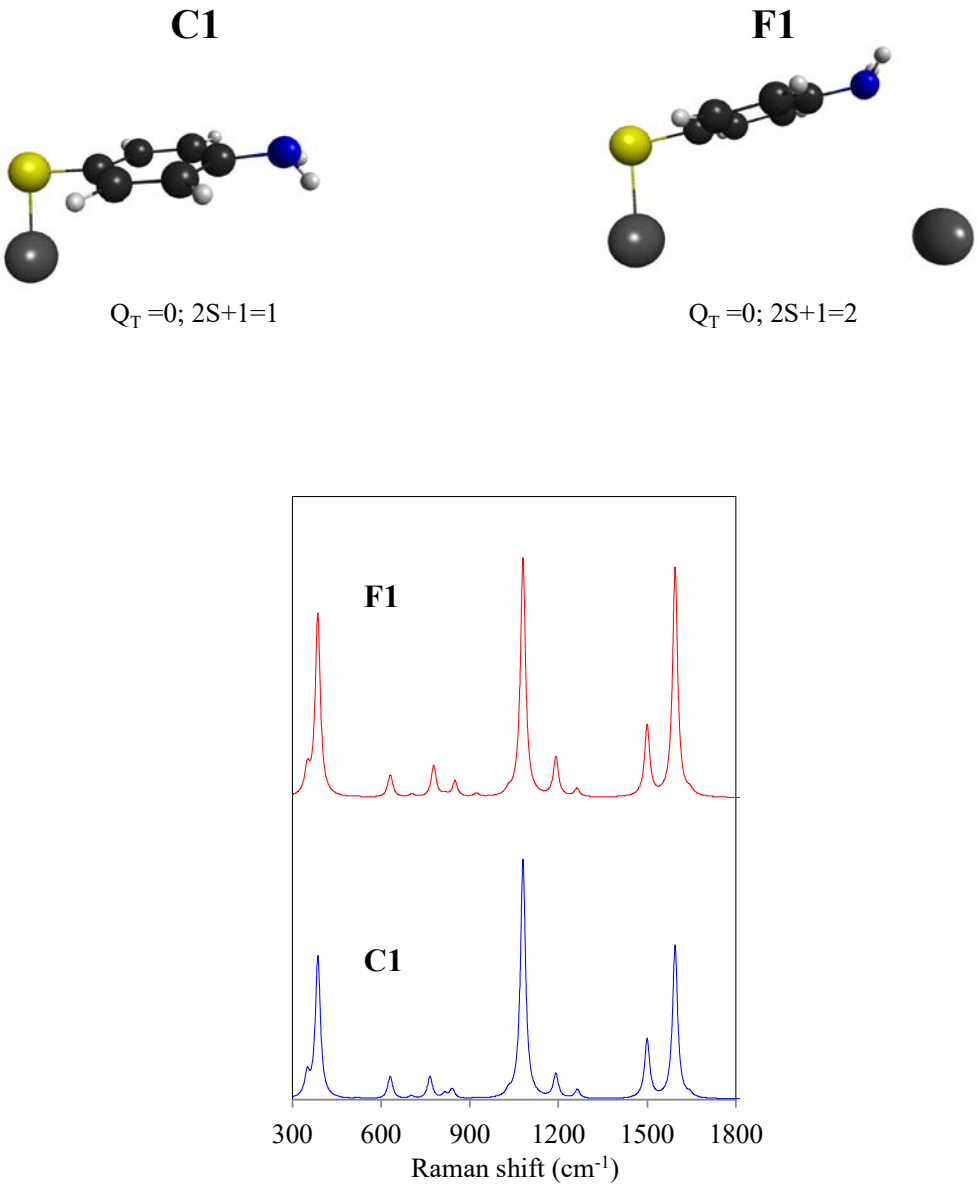

Figure S6. Molecular geometries and multi-state Resonance Raman spectra of C1 and F1 complexes. MS-CASPT2/ANO-RCC (eight states).

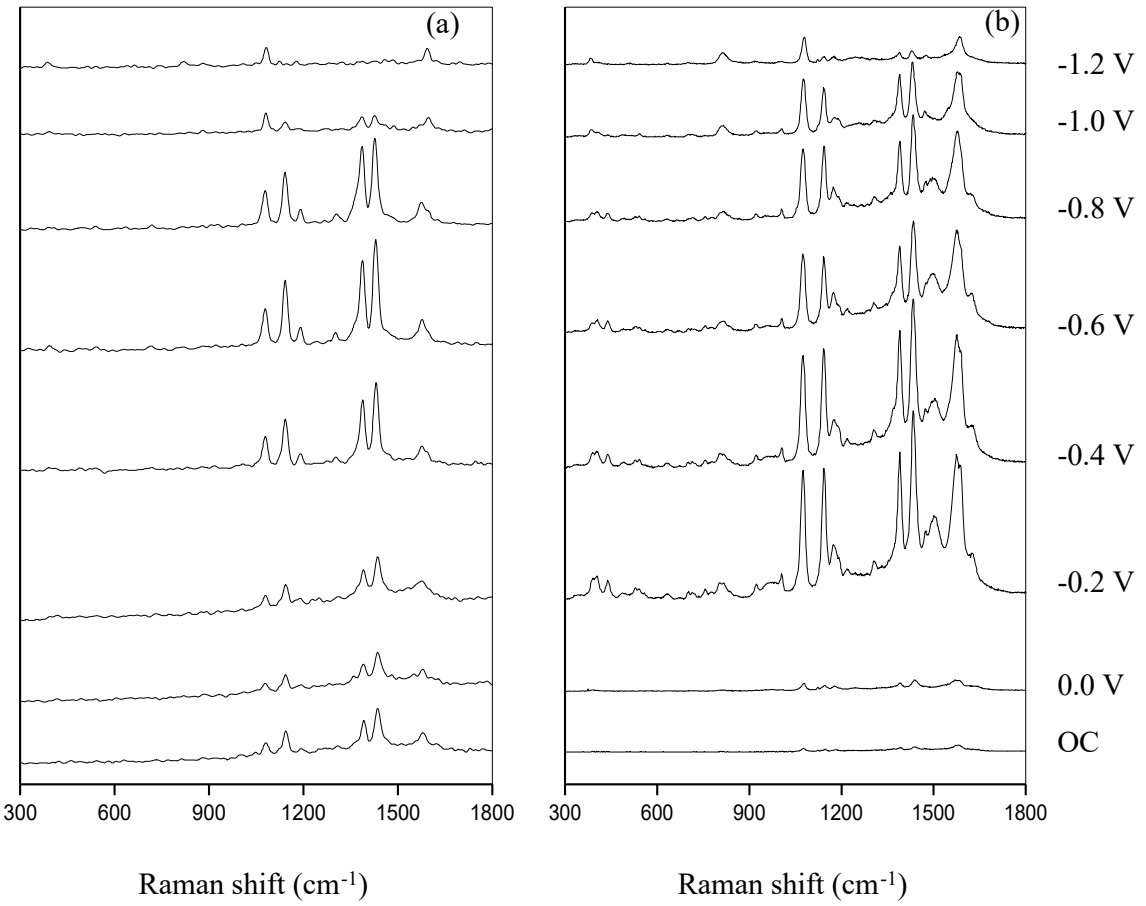

Figure S7. Potential dependent SERS spectra of *p*-aminothiophenol [(a) 10^{-3} M; (b) 10^{-6} M] in $NaClO_4$ on silver electrode at excitation wavelength of 514.5 nm.

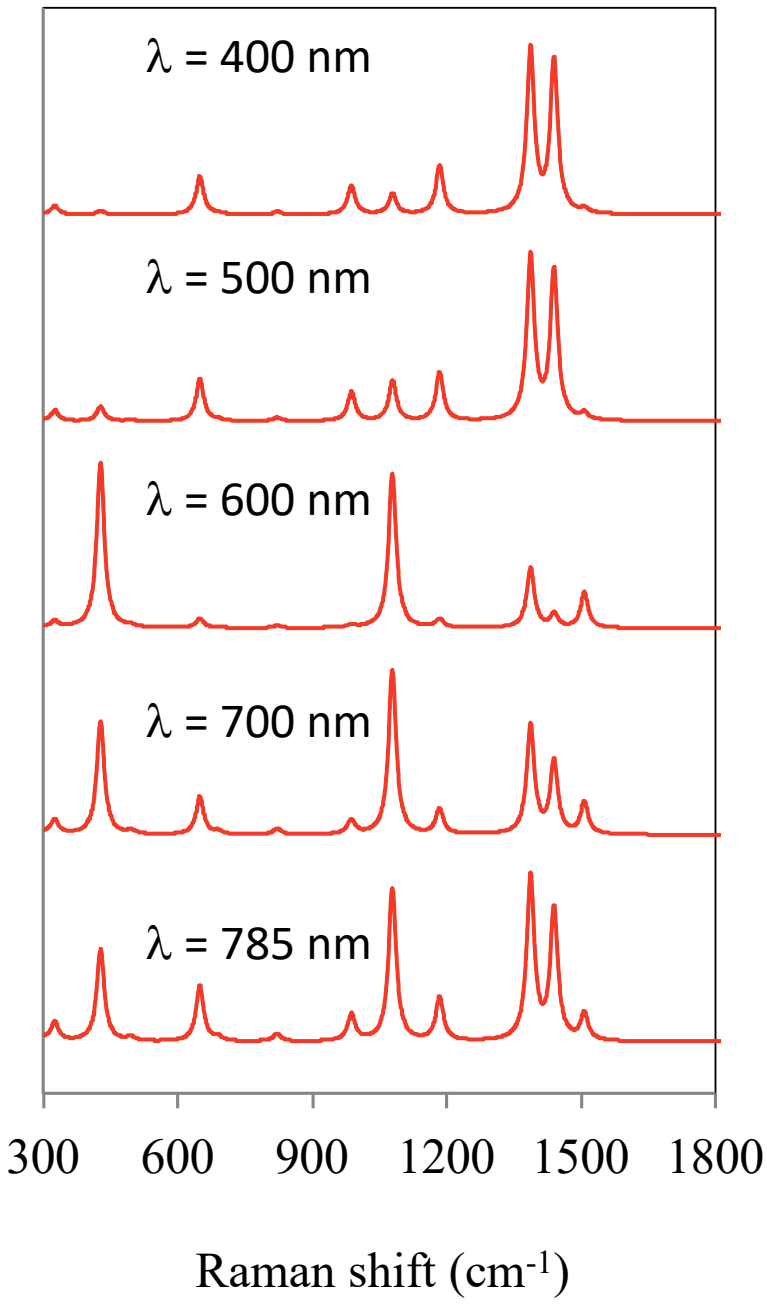

Figure S8. Resonance Raman spectra series of triplet nitrene G1 as a function of excitation line.

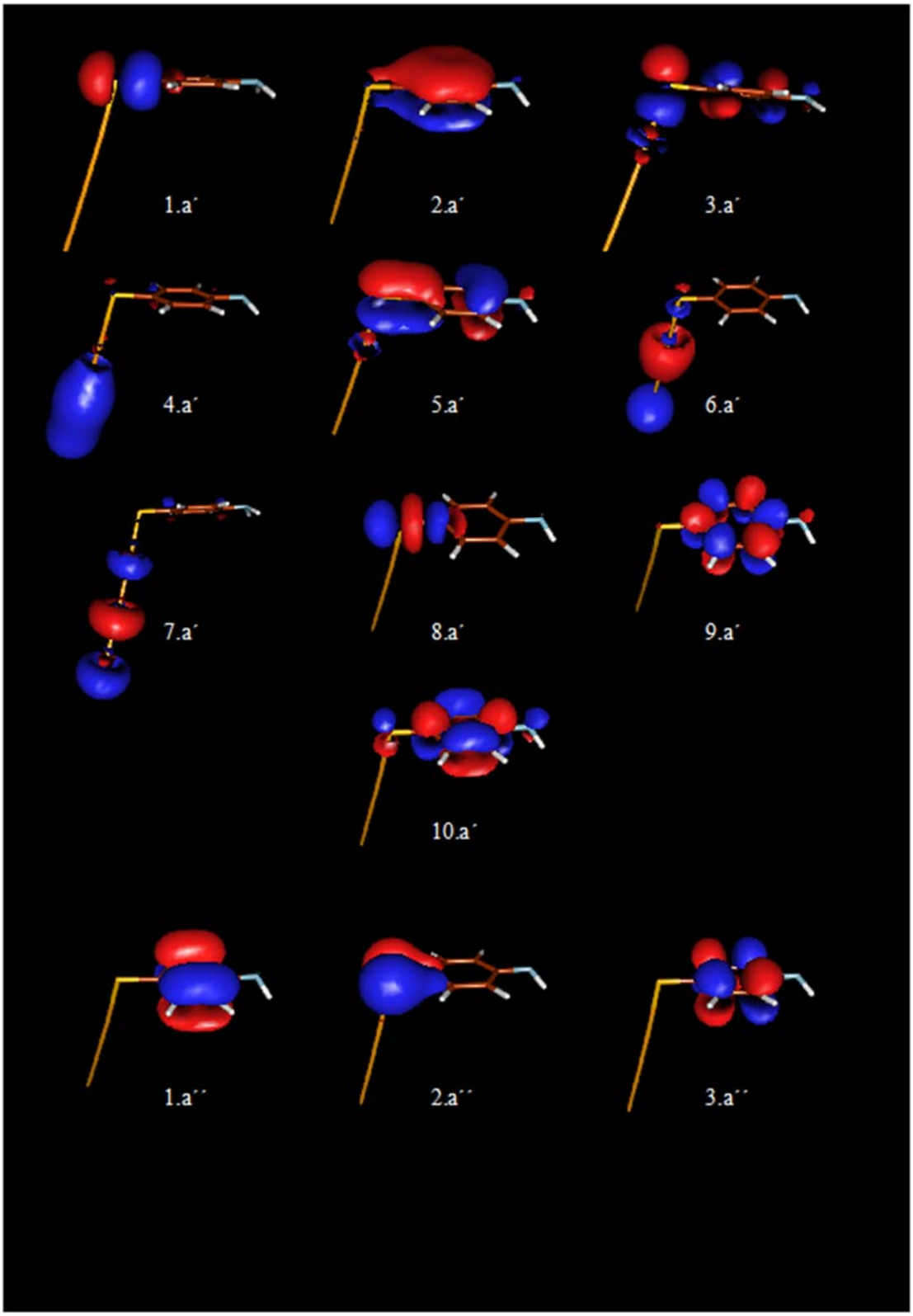

Figure S9. SA-CASSCF molecular orbitals of the Ag_3-$SPhNH_2$ complex.

Capítulo III – Resultados (II).

An MS-CASPT2 Study of the Photodecomposition of 4-Methoxyphenyl Azide: Role of Internal Conversion and Intersystem Crossing.

Daniel Aranda, Francisco J. Avila, Isabel López-Tocón, Juan F. Arenas, Juan C. Otero*, and Juan Soto*.

The photochemical decomposition of 4-methoxyphenyl azide (CH_3O-Ph-N_3) is investigated using multiconfigurational second-order perturbation theory (MS-CASPT2). In addition, the multi-state resonance Raman spectra of the reactant, intermediates, and product are computed with a multi-state version of the vibronic theory of Albrecht. The results support that the key step of the photolysis of the parent azide is a $2^1A'/2^3A''$ intersystem crossing which in a second step decays through a $2^3A''/1^3A''$ conical intersection to give directly the formation of triplet 4-methoxyphenyl nitrene (CH_3O-Ph-N) in its lowest electronic state, $1^3A''$. It is found that the efficiency of the cited intersystem crossing is enhanced by the close presence of a $2^1A'/2^1A''$ conical intersection. On the other hand, the calculated spectra suggest that the only two species which would be observed in the gas phase experiments are the triplet nitrene plus 4,4'-dimethoxyazobenzene.

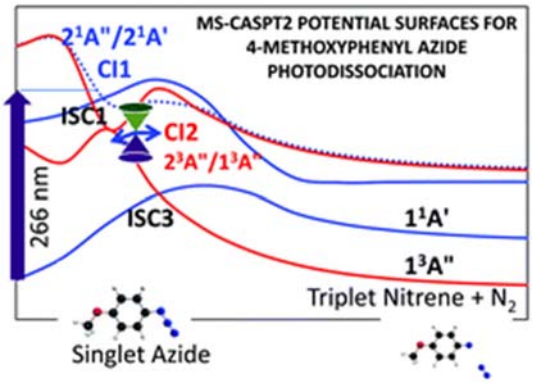

3.2.1. Introduction.

The photochemistry of aryl azide derivatives is interesting from the chemical point of view because the reaction products of the photolysis of these compounds are strongly dependent on the relative position of the substituent in the aromatic ring. Time-resolved resonance Raman (*TR*[3]) spectroscopy has demonstrated that irradiation at 266 nm of *4*-methoxyphenyl azide (1a) yields the azobenzene derivative,[1] 4,4′-dimethoxyazobenzene (1b, c); while photolysis of *3*-methoxy phenyl azide (2a) at the same excitation wavelength forms the dimer of 1,2-didehydroazepine[2] (2b,c) (Scheme 1). It is assumed that the first step of the photolysis of aryl azides is extrusion of molecular nitrogen and formation of the respective arylnitrene.[2] Moreover, it is proposed that the nitrene intermediate is generated in a singlet state and can follow two reaction pathways: one leads to triplet arylnitrene through intersystem crossing (ISC), which subsequently dimerizes to form a stable azobenzene derivative, and the second route is formation of an azirine intermediate that undergoes a ring expansion to give 1,2 didehydroazepine.[2-4] However, the molecular mechanism that governs these processes is not known.

Concerning the formation of azobenzene derivatives, identification by Phillips and co-workers[1,2] of such a compound in the *TR*[3] experiments of *4*-methoxyphenyl azide has played a crucial role in the re-interpretation of SERS (Surface Enhanced Raman Spectroscopy[5]) spectra of *p*-aminothiophenol,[6-8] an emblematic molecule in this kind of spectroscopy.

Furthermore, the chemistry of arylnitrenes and its reaction products are relevant in other practical applications, for example, the ability of azobenzenes for *cis-to-trans* isomerization plays a crucial role in their properties and the applications derived from them.[9] They are used in a wide range of applications such as drugs, dyes, photomobile polymer materials or foldamers.[10,11]

The goal of this work is to study the reaction mechanisms and Resonance Raman spectra of 4-methoxyphenyl azide and its products with the aid of pure *ab initio*

Scheme 1

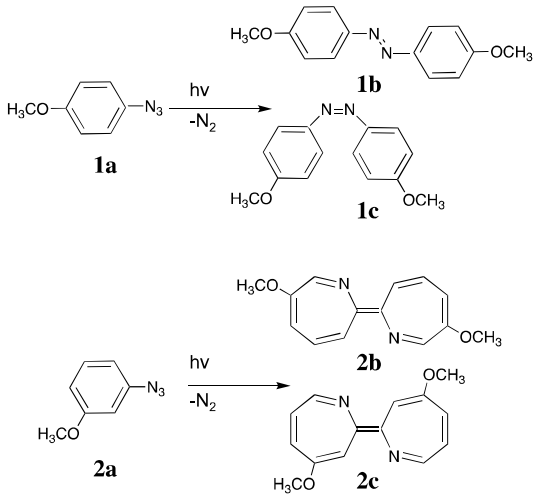

quantum calculations. To be specific, multiconfigurational self-consistent field (MC-SCF) methods with the CAS-SCF and MS-CASPT2 theoretical approximations.[12,13]

3.2.2. Methodology.

The quantum chemical methods applied to the study of the reaction mechanisms of 4-methoxyphenyl azide and its photo dissociation products are based on the Complete Active Space theory, that is, CAS-SCF, CASPT2 and MS-CASPT2[12,13] approximations implemented in MOLCAS 8.2 program.[14,15] MS-CASPT2 calculations for open shell species have been performed with a modified zero-th order Hamiltonian (IPEA=0.25), in contrast, for closed shell systems an IPEA=0 shift has been applied. It must be remarked that special attention has been paid when comparison of energy values has been done, that is, calculations with different IPEA numbers are never compared. Unless other thing is said, all of the calculations have been performed with the ANO-RCC basis sets[16,17] applying the (C,N)[4s3p2d1f]/(H)[3s2p1d] contraction scheme. The analysis of the orbitals, geometries and vibrational modes has been done with the graphical programs MacMolPlt and Molden.[18,19] All of the critical points, minima, intersystem crossings and conical intersections have been optimized in Cartesian coordinates at the CAS-SCF level. Stationary points have been characterized by performing the vibrational analysis from the computed analytical Hessian. Minimum energy geometries for conical intersections has been optimized by calculating the two directions which conform the branching space by means of analytical derivative coupling and gradient

differences vectors for state-average complete-active-space self-consistent field wave functions.[20]

The complex matrix elements $\mathbf{H}_{SO}$ of the spin-orbit coupling between two CAS-SCF states with different multiplicity have been calculated by means of the effective one-electron Fock-type spin-orbit Hamiltonian proposed by Hess and co-workers,[21] and with the RASSI program of MOLCAS. The magnitude of the spin-orbit interaction between states A and A' has been computed according with Equation (1).[22,23]

$$SOC = \left(\sum_{M_S, M_{S'}} \mathrm{Re}^2 \left(\mathbf{H}_{SO} \right)^{IJ}_{M_S, M_{S'}} + \mathrm{Im}^2 \left(\mathbf{H}_{SO} \right)^{IJ}_{M_S, M_{S'}} \right)^{1/2} \quad (1)$$

The reference active space of 4-methoxyphenyl azide (C_s symmetry) includes 14 electrons distributed in 13 orbitals. The ground state configuration is assigned as a': $\pi_\sigma(NN)^2$, $\sigma(NN)^2$, π^*_σ $(NN)^0$, $\sigma^*(NN)^0$; a'': $\pi_1(ring)^2$, $\pi_2(ring)^2$, $\pi_3(ring)^2$, $\pi(NNN)^2$, $\pi^*_1(ring)^0$, $\pi^*_2(ring)^0$, $\pi^*_3(ring)^0$, $\pi^*(NNN)^0$, (Figure S1).

In principle, according with the active space of the parent molecule, the corresponding active space of the nitrene derivatives should comprise 8 electrons in 8 orbitals. However, we have found that in order to maintain the same the active orbitals for the three nitrene derivatives ($1^3A''$, $1^1A''$ and $1^1A'$ states), the active space of each nitrene must be supplemented with the 2*s*(N), σ(CN) and σ*(CN) orbitals, otherwise orbital rotations cannot be avoided. Therefore, the reference active space of *p*-methoxyphenyl nitrene (C_s symmetry) comprises 12 electrons distributed in 11 orbitals. The ground state configuration is assigned as a': $2s(N)^2$, $\pi_\sigma(N)^1$, $\sigma(CN)^2$, $\sigma^*(CN)^2$; a'': $\pi_1(ring)^2$, $\pi_2(ring)^2$, $\pi_3(ring)^2$, $n_\pi(N)^1$ $\pi^*_1(ring)^0$, $\pi^*_2(ring)^0$, $\pi^*_3(ring)^0$, (Figure S2).

The reference active space of 4,4′-dimethoxyazobenzene (C_{2h} symmetry) comprises 16 electrons distributed in 15 orbitals. The ground state configuration is assigned as a_{1g}:

$\sigma(NN)^2$; b_{2g}: $\pi_1(ring)^2$, $\pi_2(ring)^2$, $\pi_3(ring)^2$, $\pi^*_1(ring)^0$, $\pi^*_2(ring)^0$, $\pi^*_3(ring)^0$, $\pi^*(NN)^0$; a_{1u}: $\pi\ (NN)^2$, $\pi_1(ring)^2$, $\pi_2(ring)^2$, $\pi_3(ring)^2$, $\pi^*_1(ring)^0$, $\pi^*_2(ring)^0$, $\pi^*_3(ring)^0$, (Figure S3).

The topology of the potential energy surfaces has been studied performing linear interpolations.[23-25] These interpolations for the dissociation reactions are built in the following manner: electronic energies are represented versus an interpolation vector, $\Delta\boldsymbol{R}$, which connects ground state minima of the initial compound with its respective reaction products, that is, nitrene and molecular nitrogen. This vector is built by calculating the difference between internal coordinates of reactant and reaction products, $\Delta\boldsymbol{R} = \boldsymbol{R}_i - \boldsymbol{R}_j$, where $\boldsymbol{R}_i$ and $\boldsymbol{R}_j$ represent the internal coordinate vectors of the initial and final species, respectively. It must be noted that this interpolation method gives a set of points that are perfectly ordered along a straight line on the potential energy surface. In contrast, a relaxed scan calculation by fixing one or more internal coordinates and relaxing the other ones deviates the points from a straight line. Of course, we can always represent such scanned points on a straight line although they are not actually in it. In addition, it must be remarked as well that the reliability of the interpolation is based on its ability to predict starting points for searching the critical structures on the potential energy surfaces.

Resonance Raman spectra have been calculated as described in previous papers,[8] according with a multi-state version of the vibronic theory of Albrecht.[26-28] It is assumed the small displacement approximation. Each vibrational mode *k* is treated as an independent harmonic oscillator (IMDHO model), which allows a simplified mathematical expression of the polarizability tensor. It is assumed as well that the vibrational frequencies for the *k*-th mode are the same in all the electronic states. The integrals of vibrational overlapping are obtained using the recurrence formulae of Manneback.[29] To be specific, we have implemented a modified expression of the intensity equation given by Long,[28] equation (2)

$$I_k = \frac{(2\pi)^4}{h^2} K N_{0^i} \left(\tilde{\nu}_1 - \tilde{\nu}_k\right)^4 \tilde{\nu}_k^2 \sum_e \left(G^e_{\Gamma_{r,k}} \Delta_{k,e}\right)^2 \qquad (2)$$

where K is a constant for a given experimental condition and a given irradiance of the incident radiation of wave number $\tilde{\nu}_1$, N_{0^i} is the Boltzmann population of the vibrational ground state, $\tilde{\nu}_k$ is the wave number of *k*-th mode, $G^e_{\Gamma_{r,k}}$ is given by equation (3) and depends on the transition dipole moment μ^o_e, the wave number of the energy difference between the excited electronic state *e* and the ground state, $\tilde{\nu}_e$, the wave number $\tilde{\nu}_k$ of *k* mode, and the damping factor $\Gamma_{r,k}$ related to the lifetime of the transition, which is taken as $0.2\tilde{\nu}_k$ in this work.

$$G^e_{\Gamma_{r,k}} = \frac{\left|\mu^0_e\right|^2}{\left[\left(\tilde{\nu}_e - \tilde{\nu}_1\right)^2 + \Gamma^2_{r,k}\right]^{1/2}\left[\left(\tilde{\nu}_e + \tilde{\nu}_k - \tilde{\nu}_1\right)^2 + \Gamma^2_{r,k}\right]^{1/2}} \tag{3}$$

Equation (2) is formally analog to the expression given by Jarzecki,[30] which deals with resonance Raman intensity calculations from multi-state computations as well. $G^e_{\Gamma_{r,k}}$ factor of equation (2) plays the role of weighting factor of Jarzecki, in contrast, the $G^e_{\Gamma_{r,k}}$ parameters are not normalized in equation (2).

The dimensionless shift displacement parameter of Manneback,[29] $\Delta_{k,e}$, has been calculated with the gradient approximation, Eq. (4).

$$\Delta_k = \frac{1}{\sqrt{2}} \cdot 2.408\,10^6 \omega_k^{-3/2} \boldsymbol{f} \cdot \mathbf{M}^{-1/2} \mathbf{L}_k \tag{4}$$

where $\boldsymbol{f}$ is the force row vector of electronic state *e*, $\mathbf{M}$ is the $3N \times 3N$ diagonal matrix of atomic masses, and $\mathbf{L}_k$ is the column eigenvector of the Hessian matrix for mode *k*-th.

The assignments of the resonance Raman spectra have been performed in internal coordinates in accordance with the *GF* method of Wilson implemented in our own programs.[31-35]

3.2.3. Results and discussion.

3.2.3.1. Photodissociation of 4-methoxyphenyl azide

Figure 1 represents a cut of the interpolation lines[23-25] for dissociation of 4-methoxyphenyl azide into phenyl nitrene and N_2 in the ground and low-lying excited states [singlet (blue) and triplet (red), complete interpolation leading to final N-N_2 internuclear distance of 4.70 Å is given in Figure S4]. According with the MS-CASPT2 calculations, excitation of the molecule at 266 nm (4.66 eV) populates the $2^1A'$ (S_2) state (Table 1).

Before discussion of the reaction mechanism, we present in Figure 2 the critical points that have been optimized on the potential energy surfaces depicted in Figure 1. In addition, Figure 3 shows the most relevant active orbitals of such critical points involved in the dissociation mechanism, that is, σ(N-N_2) and σ*(N-N_2) orbitals (Figures S5 to S11 represent the full active space of the intermediates). The S_2 state is non-dissociative. Therefore, the photolysis of the starting species demands that S_2

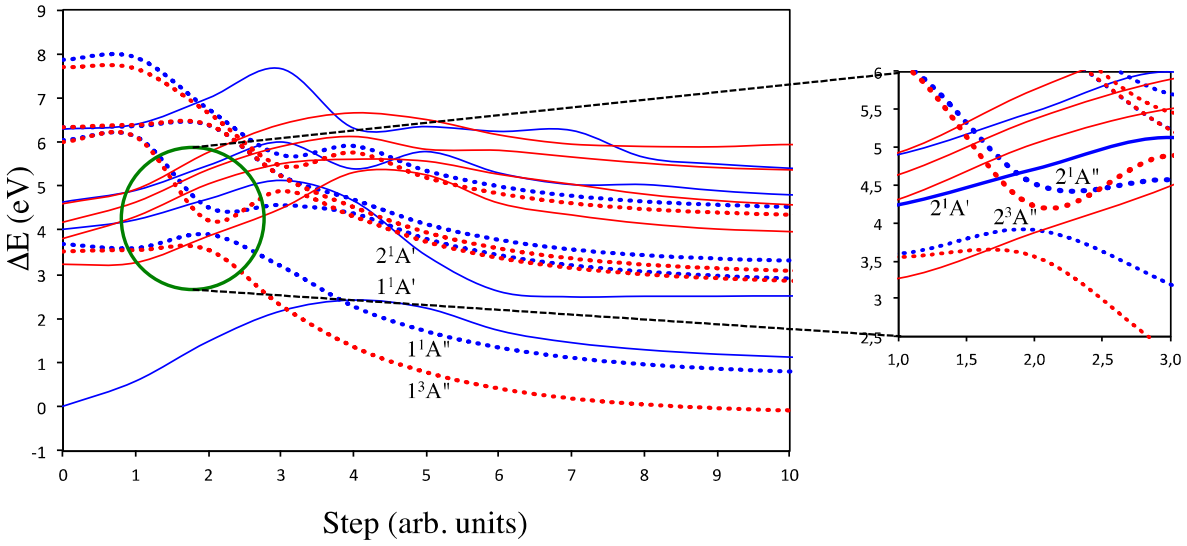

Figure 1. MS-CASPT2/ANO-RCC (C_s symmetry) potential energy curves of the ground and low-lying singlet and triplet excited states of 4-methoxyphenyl azide for dissociation into 4-methoxyphenyl nitrene and N_2. Four state-average CAS-SCF wavefunction in each symmetry block. Blue solid line: singlet A'; red solid line: triplet A'; blue dotted line: singlet A"; red dotted line: triplet A". Inset: expanded view of the 2^1A"/2^1A' and 2^1A'/2^3A" crossings.

crosses with a dissociative surface. There exists a surface crossing with the $2^1A''$ state, which certainly is dissociative. The minimum energy geometry (CI1, Figure 2c) along the seam of crossing of these two singlet surfaces has been localized at 4.5 eV above the azide minimum. However, this $2^1A'/2^1A''$ crossing would involve an upward transition from the lower surface to the upper surface and it should be less likely because there exists a peak in the lower surface that tends to guide trajectories away from the intersection,[36-39] that is, along the adiabatic dissociation route the dominant electronic configuration should change from bonding character (A' symmetry) on the reactant side of the barrier, to repulsive in character (A" symmetry) on the product side; in consequence, the molecule tends to retain its bonding character, which results in a nonadiabatic hop to the upper surface at the conical intersection, that is, a nonadiabatic recrosing.[40-45] On the other hand, according with the potential energy curves plotted in Figure 1, another possible crossing can take place with the $2^3A''$ state.

This process should occur through a $2^1A'/2^3A''$ intersystem crossing whose minimum energy geometry (ISC1, Figure 2f) was able to localised at only 0.2 eV below the excitation line for the *para* isomer, the magnitude of the spin-orbit coupling for this crossing point (Equation 1) is 33 cm^{-1}. In fact, according with the equation of Yarkony[46], the intersystem crossing probability depends on the velocity with which the molecule approaches to the crossing region, that is, as the velocity decreases at such region the probability increases. From this point of view, there are two factors that favor the population of the $2^3A''$ state: (i) the crossing is close to a turning point on the potential energy surface where the molecular velocity tends to zero and (ii) the proximity of the $2^1A'/2^1A''$ conical intersection to this point tends to decelerate the molecule as well. Furthermore, the conjunction of the $2^1A'/2^1A''$ and $2^1A'/2^3A''$ crossings provides a mechanism for ultrafast ISC.[47-51] Afterwards, a very remarkable event occurs, the $2^3A''$ state is driven to a $1^3A''/2^3A''$ conical intersection (CI2, Figure 2d); in consequence, the system decays into the $1^3A''$ state. Once the lowest triplet state of 4-methoxyphenyl azide is generated, the molecule dissociates into N_2 in its ground state and the corresponding arylnitrene in its lowest triplet state, because the system enters in a repulsive path.

There exists a $2^1A'/1^3A''$ intersystem crossing that would lead to direct dissociation of the azide (ISC2, Figure 2g). The minimum energy crossing point of such a crossing is located at ~ 0.5 eV below the vertical excitation and very close to the $2^1A'$ minimum.

It has a relatively small spin-orbit coupling (SOC) constant 9 cm^{-1}, which would lead to a small efficiency of the intersystem crossing process.[52] However, it has been demonstrated that small SOC can induce efficient ISC through vibronic spin-orbit coupling.[53-57] In any case, whether this crossing may drive or not an efficient mechanism of ISC is still an open matter.

Table 1. Vertical transition energies in eV of the singlet states of 4-methoxyphenyl azide (C_s, MS-CASPT2).[a]

Species	ΔE	*f*[b]	*Configuration*[c,d]
1A'→ 2A'	4.04	0.87-01	28% $\pi_3(ring)^1\pi_2^*(ring)^1$ 16% $\pi_2(ring)^1\pi_3^*(ring)^1$ 22% $\pi_3(ring)^1\pi_3^*(ring)^1$
1A'→ 3A'	4.79	0.3406	49% $\pi_3(ring)^1\pi_3^*(ring)^1$
1A'→ 4A'	6.43	0.13-01	18% $n_\pi(NN)^1\pi_3^*(ring)^1$ 21% $\pi_3(ring)^0\pi_3^*(ring)^2$ 16% $\pi_3(ring)^1\pi^*(NNN)^1$
1A'→ 1A"	3.82	0.54-03	80% $\pi_3(ring)^1\pi_\sigma^*(NN)^1$
1A'→ 2A"	6.27	0.0	42% $\pi_2(ring)^1\pi_\sigma^*(NN)^1$ 20% $n_\pi(NN)^1\pi_\sigma^*(NN)^1$
1A'→ 3A"	6.51	0.67-04	20% $\pi_2(ring)^1\pi_\sigma^*(NN)^1$ 42% $n_\pi(NN)^1\pi_\sigma^*(NN)^1$
1A'→ 4A"	8.12	0.0	56% $\pi_2(ring)^1\pi_3(ring)^1\pi_2^*(ring)^1\pi_\sigma^*(NN)^1$

[a]CAS-SCF state average including four roots in each symmetry block (IPEA=0), (Imaginary shift=0.1). [b]Oscillator strength. [c]MS-CASPT2 electron configurations. Only contributions greater than 15% are included and orbitals with different occupation to the ground state are given. [d]Ground state configuration (see text).

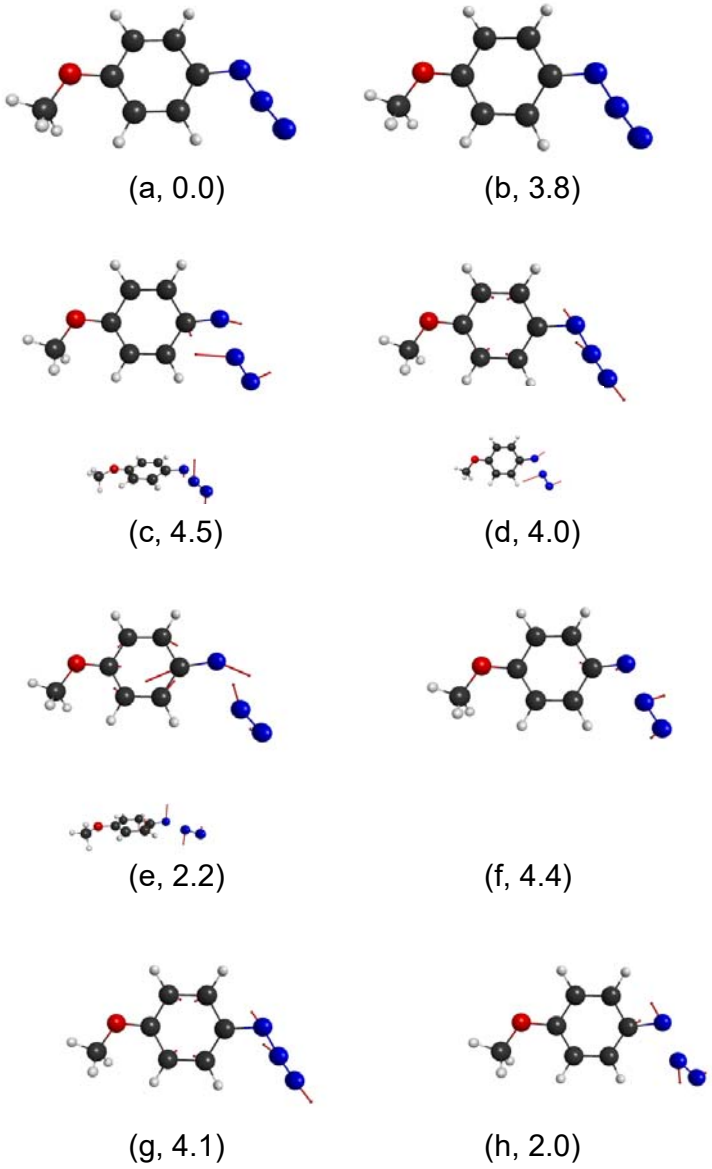

Figure 2. CAS-SCF (14e, 13o)/ANO-RCC optimized geometries. (a) $1^1A'$ minimum, M1; (b) $2^1A'$ minimum, M2; (c) $2^1A''/2^1A'$ conical intersection, CI1; (d) $2^3A''/1^3A''$ conical intersection, CI2; (e) $1^1A''/1^1A'$ conical intersection, CI3; (f) $2^1A'/2^3A''$ intersystem crossing, ISC1; (g) $2^1A'/1^3A''$ intersystem crossing, ISC2; (h) $1^3A''/1^1A'$ intersystem crossing, ISC3. Arrows in figures c-h represent the gradient difference vectors. Arrows in small figures for conical intersections c-e represent the derivative coupling vectors. MS-CASPT2 relative energies with respect to the ground state minimum are given in parenthesis in eV.

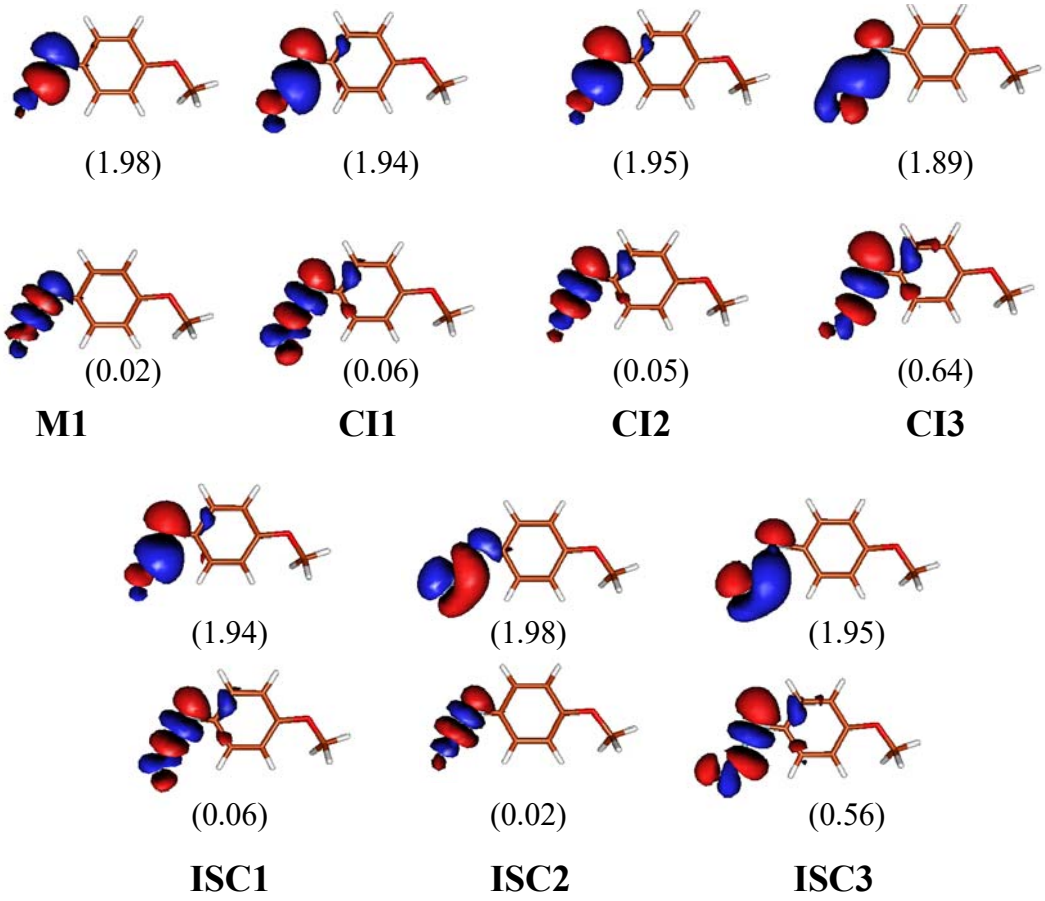

Figure 3. σ(N-N_2) and σ*(N-N_2) active orbitals included in the CAS-SCF of the critical points along the dissociation mechanism. In parenthesis, mean occupation numbers of the state average orbitals.

3.2.3.2. Dissociation of 4-methoxyphenyl azide on the ground state

Dissociation of 4-methoxyphenyl azide on the ground state surface has remarkable characteristics (Figure 1). It dissociates through an intersystem crossing to yield molecular nitrogen plus the nitrene derivative.[53-55] There are two surface crossings which involve the 1^1A' ground state: a 1^1A"/1^1A' conical intersection (CI3, Figure 2e) and a 1^3A"/1^1A' intersystem crossing (ISC3, Figure 2h). It was not possible to find a transition state for dissociation of the azide on the 1^1A' ground state surface under C_s symmetry, the explanation for this fact is that the 1^1A"/1^1A' conical intersection occupies the locus where the hypothetical transition state would be hosted. On the other hand, the 1^3A"/1^1A' intersystem crossing (spin-orbit coupling constant of 41 cm^{-1}) is close to the former conical intersection. In consequence, the efficiency of intersystem crossing is enhanced in analogy with the previous one treated in the precedent subsection, that is, the 2^1A'/2^3A" crossing: (i) the 1^3A"/1^1A' crossing is close to a turning point on the potential energy surface where the molecular velocity tends

to zero; (ii) the proximity of the $1^1A''/1^1A'$ conical intersection to this point tends to decelerate the molecule as well; and (iii) the conjunction of conical intersection and intersystem crossing enhances the efficiency of the singlet-triplet surface hop. In consequence, the probability for dissociation of the molecule into N_2 and triplet 4-methoxyphenyl nitrene is favored with respect to dissociation in the singlet state.

3.2.3.3 Resonance Raman Spectra

Resonance Raman spectroscopy is a valuable technique to identify a chemical species in a particular experiment. The power of this tool increases when is combined with high quality quantum chemical calculations. In this context, we have driven a channel for production of the azo-derivative and and $1^3A''$ triplet nitrene, which is the lowest energy state of 4-methoxyphenyl nitrene. The two lowest minima of singlet nitrene are $1^1A''$ and $1^1A'$, respectively; however, it was not possible to find any evidence for the formation of singlet nitrene in the gas phase dissociation reactions of 4-methoxyphenyl azide. If the $1^1A'$ excited state of nitrene would be formed, it can decay to the $1^3A''$ state via intersystem crossing. In contrast, $1^1A''$ conversion to $1^3A''$ is forbidden by angular momentum conservation law, in other words, electron spin-flip is necessarily accompanied by interchange of the orbitals which occupies the electron.

Figure 4 presents the normalized multi-state Resonance Raman spectra calculated at excitation lines of 320 and 340 nm, respectively, for (i) 4-methoxyphenyl azide, (ii) triplet 4-methoxyphenyl nitrene ($1^3A''$), (iii) singlet 4-methoxyphenyl nitrene ($1^1A''$), (iv) singlet 4-methoxyphenyl nitrene ($1^1A'$), and (v) 4,4'-dimethoxyazobenzene, respectively. The Raman excitation profiles of the active bands for each species are given in SI. Inspection of these profiles shows that the resonance Raman spectra of all of the species excepting the azo derivative are very dependent on the wavelength of the excitation line. The intensities are calculated according with equation 1, by assuming that the experimental constant K is the same for all of the species, the transition dipole moment vectors and the electronic state energy are calculated with the MS-CASPT2 approach, frequencies and gradients of the electronic states with the CAS-SCF method. Within the gradient approach implemented in this work, whose validity has been demonstrated in a wide variety of works (see for example references 56 to 60), the molecules that exhibit the highest emission intensities at 320-340 nm are the triplet nitrene and the azo compound (Figure S12). Furthermore, the calculated

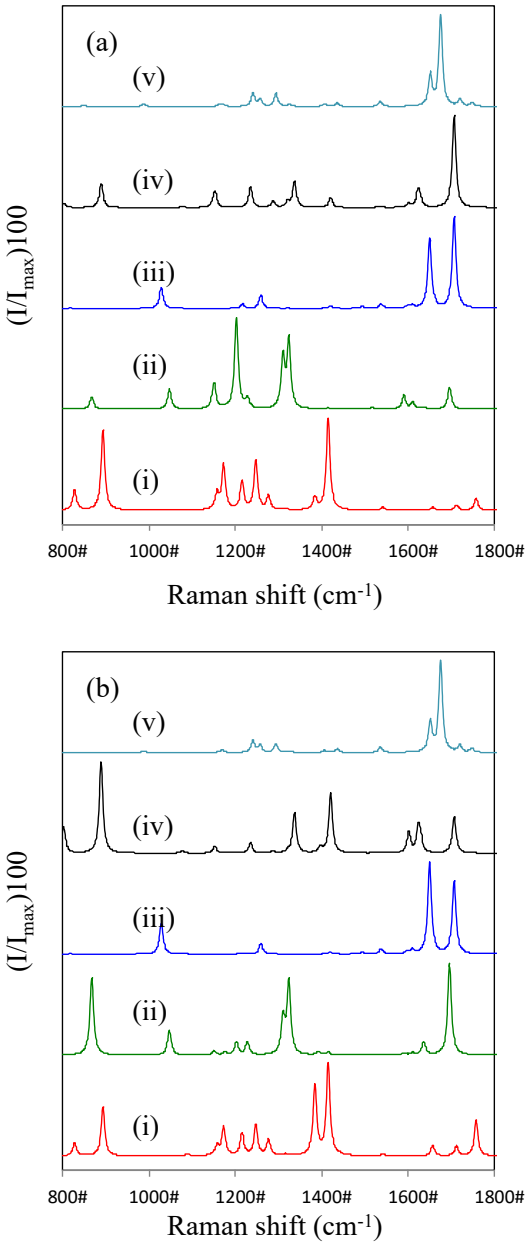

Figure 4. Multi-state Resonance Raman spectra at (a) 320 and (b) 340 nm for (i) 4-methoxyphenyl azide; (ii) 1^3A" triplet 4-methoxyphenyl nitrene; (iii) 1^1A" singlet 4-methoxyphenyl nitrene; (iv) 1^1A' singlet 4-methoxyphenyl nitrene; (v) 4,4'-dimethoxyazobenzene. Raman bands are convoluted with a Lorentzian function of HWHM = 10 cm^{-1}.

intensities of the triplet nitrene are about eight orders of magnitude higher than the two singlet nitrenes. From this point of view, although singlet nitrene was formed it would be difficult to observe its signal in the gas phase spectra. Table 2 and 3 collect the assignment of the predicted bands in the calculated spectra of triplet nitrene and the azo compound, respectively. The calculated spectra of the dimeric species reproduce the bands which are experimentally observed in condensed phase.

However, the open-shell character of the nitrene species makes them strongly dependent on the surrounding environment, it is for this reason that the conclusions derived of this part of our work are only strictly applicable to experiments on the gas phase.

Table 2. Assignment of the calculated Resonance Raman spectrum of triplet 4-methoxyphenyl nitrene at excitation wavelength of 320 nm.[a,b]

CAS-SCF	I_{rel}(320)	I_{rel}(340)	Assignment
1696	25	100	8a
1636	2	15	8b
1611	8	2	δ(C-H)$_{methyl}$
1590	15	3	9b
1516	2	0.3	19b
1324	74	80	δ(C-H)$_{methyl}$
1310	55	39	δ(C-H)$_{methyl}$
1228	0	14	14
1203	100	14	3
1151	28	4	ν(O-CH$_3$)
1047	22	27	19a
868	13	85	1

[a]According with the potential energy distribution matrix (Refs. 34, 35).

[b]Active space: (12e,11o); ANO-RCC[C,N,O/4*s*3*p*2*d*1*f*| |H/3*s*2*p*1*d*]; state average: (4 states A', 4 states A"); IPEA=0.25.

Table 3. Assignment of the calculated Resonance Raman spectrum of 4,4′-dimethoxyazobenzene.[a,b]

CAS-SCF	I_{rel}(320)	I_{rel}(340)	Assignment
1675	100	100	ν(N-N)
1652	34	33	18α+19a
1536	6	6	19b+15
1294	14	9	$\delta(C\text{-}H)_{methyl}$
1257	7	7	9a
1241	15	13	14

[a]According with the potential energy distribution matrix (Refs. 32, 33).
[b]Active space: (16e,15o); ANO-RCC[C,N,O/4*s*3*p*2*d*1*f*||H/3*s*2*p*1*d*]; state average: (4 states A', 4 states A"); IPEA=0.

3.2.4. Conclusions

Non-radiative processes, that is, internal conversion and intersystem crossing, govern the photochemistry of 4-methoxyphenyl azide in the gas phase. After excitation at 266 nm, the system decays to the lowest triplet state through an intersystem crossing ($2^1A'/2^3A''$) and subsequent conical intersection ($2^3A''/1^3A''$) to give triplet 4-methoxyphenyl nitrene and molecular nitrogen. The triplet nitrene dimerizes to give the azo derivative, these two species give the most intense Raman spectra in the gas phase, respectively.

3.2.5. References and notes.

1. S. Y. Ong, P. Y. Chang, P. Zhu, K. H. Leung, D. L. Philipps. *J. Phys. Chem. A,* **2003**, 107, 3858.
2. W. M. Kwok, P. Y.Chan, D. L. Phillips. *J. Phys. Chem. A,* **2005**, 109, 2394.
3. J. Xue, Y. Du, D. L. Phillips, J. Wang, C. Luk, C. M. Hadad, M. S. Platz. *J. Phys. Chem. A,* **2008**, 112, 1502.
4. M. S. Shi, X. Rizk, M. S. Platz. *Biochemistry,* **2006**, 45, 543.
5. J. F. Arenas, J. Soto, D. Peláez, D. J. Fernández, J. C. Otero. *Int. J. Quantum Chem.*, **2005**, 104, 681.
6. Y.-F. Huang, H.-P. Zhu, G.-K. Liu, D.-Y. Wu, B. Ren, Z.-Q. Tian. *J. Am. Chem. Soc.*, **2010**, 132, 9244.
7. L.-B. Zhao, Y.-F. Huang, X.-M. Liu, J. R. Anema, D.-Y. Wu, B. Ren, Z.-Q. Tian. *Phys. Chem. Chem. Phys.,* **2012**, 14, 12919.
8. M. R. Lopez-Ramirez, D. Aranda Ruiz, F. J. Avila Ferrer, S. P. Centeno, J. F. Arenas, J. C. Otero, J. Soto, *J. Phys. Chem. C.* **2016**, 120, 19322.
9. Y.-P. Wang, Z.-X. Zhang, M. Xie, F.-Q. Bai, P.-X. Wang, H.-X. Zhang. *Dyes Pigments*, **2016**, 129, 100.
10. M. Yamada, M. Kondo, J.-I. Mamiya, Y. Yu, M. Kinoshita. C. J. Barrett, T. Ikeda, *Angew. Chem. Int. Ed.* **2008**, 47, 4986.
11. Z. Yu, S. Hecht. *Angew. Chem. Int. Ed.,* **2013**, 52, 13740.
12. B. O. Roos. *Advances in Chemical Physics; Ab Initio Methods in Quantum Chemistry II*; John Wiley & Sons, **1987**; 69, 399.
13. J. Finley, P.-Å. Malmqvist, B. O. Roos, L. Serrano-Andrés. *Chem. Phys. Lett.* **1998**, 288, 299.
14. V. Veryazov, P.-O. Widmark, L. Serrano-Andrés, R. Lindh, B. O. Roos. Int. *J. Quantum Chem.*, **2004**, 100, 626.
15. F. Aquilante, J. Autschbach, R. K. Carlson, L. F. Chibotaru, M. G. Delcey, L. De Vico, I. Fdez. Galván, N. Ferré, L. M. Frutos, L. Gagliardi, M. Garavelli, A. Giussani, C. E. Hoyer, G. Li Manni, H. Lischka, D. Ma, P. Å. Malmqvist, T. Müller, A. Nenov, M. Olivucci, T. B. Pedersen, D. Peng, F. Plasser, B. Pritchard, M. Reiher, I. Rivalta, I. Schapiro, J. Segarra-Martí, M. Stenrup, D. G. Truhlar, L. Ungur, A. Valentini, S. Vancoillie, V. Veryazov, V. P. Vysotskiy, O. Weingart, F. Zapata, R. Lindh. *J. Comp. Chem.*, **2016**, 37, 506.

16. B. O. Roos, R. Lindh, P.-Å. Malmqvist, V. Veryazov, P.-O. Widmark. *J. Phys. Chem. A*, **2004**, 108, 2851.
17. B. O. Roos, R. Lindh, P.-Å. Malmqvist, V. Veryazov, P.-O. Widmark. *J. Phys. Chem. A*, **2005**, 109, 6575.
18. B. M. Bode, M. S. Gordon. *J. Mol. Graphics and Modeling*, **1998**, 16, 133.
19. G. Schaftenaar, J. H. Noordik. *J. Comput.-Aided Mol. Design*, **2000**, 14, 123.
20. I. Fdez. Galván, M. G. Delcey, T. B. Pedersen, F. Aquilante, R. Lindh. *J. Chem. Theory Comput.,* **2016**, 12, 3636.
21. B. A. Hess, C. Marian, U. Wahlgren, O. Gropen. *Chem. Phys. Lett.,* **1996**, 251, 365.
22. J. F. Arenas, J. C. Otero, D. Peláez, J. Soto. *J. Chem. Phys.,* **2003**, 119, 7814.
23. J. F. Arenas, J. C. Otero, D. Peláez, J. Soto. *J. Chem. Phys.,* **2005**, 122, 084324.
24. J. F. Arenas, F. J. Avila, J. C. Otero, D. Peláez, J. Soto. *J. Phys. Chem. A,* **2008**, 112, 249.
25. J. Soto, D. Peláez, J. C. Otero, F. J. Avila, J. F. Arenas. *Phys. Chem. Chem. Phys.*, **2009**, 11, 2631.
26. A. C. Albrecht. *J. Chem. Phys.*, **1961**, 34**,** 1476.
27. R. J. H. Clark, T. J. Dines. *Angew. Chem. Int. Ed. Engl.*, **1986**, 25, 131.
28. D. A. Long. *The Raman Effect: A Unified Treatment of the Theory of Raman Scattering by Molecules*, John Wiley & Sons, **2002**.
29. C. Manneback. *Physica XVII*, **1951**, 10-11, 1001.
30. A. A. Jarzecki. *J. Phys. Chem. A,* **2009**, 113, 2926.
31. E. B. Wilson, Jr., J. C. Decius, P. C. Cross. *Molecular Vibrations*, McGraw-Hills, **1955**.
32. J. F. Arenas, J. T. López-Navarrete, J. I. Marcos, J. C. Otero. *Specstrochim. Acta A,* **1986**, 42A, 1343.
33. J. F. Arenas, S. P. Centeno, J. I. Marcos, J. C. Otero, J. Soto. *J. Chem. Phys.,* **2000**, 113, 8472.
34. G. Keresvtury, Jalsovsky. *J. Mol. Struct.*, **1971**, 10, 304.
35. P. Pulay, G. Fogarasi, G. Pongor, J. E. Boggs, A. Vargha. *J. Am. Chem. Soc.,* **1983**, 105, 7037.
36. G. J. Atchity, S. S. Xantheas, K. Ruedenberg. *J. Chem. Phys.,* **1991**, 95, 1862.
37. U. Manthe, H. Köppel. *J. Chem. Phys.*, **1990**, 93, 1658.
38. T. J. Martínez. *Chem. Phys. Lett.,* **1997**, *272*, 139.
39. J. Soto, J. F. Arenas, J. C. Otero, D. Peláez. *J. Phys. Chem. A,* **2006**, 110, 8221.

40. J. L. Miller, L. R. McCunn, M. J. Krisch, L. J. Butler, J. Shu. *J. Chem. Phys.* **2004**, 121, 1830.
41. M. L. Morton, D. E. Szpunar, L. J. Butler. *J. Chem. Phys.,* **2001**, 115, 204.
42. L. Blancafort, P. Hunt, M. A. Robb. *J. Am. Chem. Soc.*, **2005**, 127, 3391.
43. G. C. G. Waschewsky, P. W. Kash, T. L. Myers, D. C. Kitchen, L. J. Butler. *J. Chem. Soc. Faraday Trans.*, **1994**, 90, 1581.
44. N. R. Forde, T. L. Myers, J. L. Butler. *Faraday, Discuss.*, **1997**, 108, 221.
45. P. W. Kash, G. C. G. Waschewsky R. E. Morss, L. J. Butler, M. M. Francl. *J. Chem. Phys.,* **1994**, 100, 3463.
46. D. R. Yarkony. *J. Am. Chem. Soc.,* **1992**, 114, 5406.
47. T. J. Penfold, G. A. Worth. *Chem. Phys.*, **2010**, 375, 58.
48. S. Cogan, Y. Haas, S. Zilberg. *J. Photochem. Photobiol. A*, **2007**, 190, 200.
49. C. M. Marian. *WIREs Comput. Mol. Sci.*, **2012**, **2,** 187.
50. F. F. de Carvalho, B. F. E. Curchod, T . J. Penfold, I. Tavernelli. *J. Chem. Phys.*, **2014**, **140,** 144103.
51. J. Tatchen, N. Gilka, C. M. Marian. *Phys.Chem.Chem.Phys.*, **2007**, 9, 5209.
52. A. C. Borin, S. Mai, P. Marquetand, L. Gonzalez. *Phys.Chem.Chem.Phys.*, **2017**, 19, 5888.
53. J. F. Arenas, J. I. Marcos, J. C. Otero, A. Sanchez-Galvez, J. Soto. *J. Chem. Phys.,* **1999**, 111, 551.
54. J. F. Arenas, J. I. Marcos, I. López-Tocón, J. C. Otero, J. Soto. *J. Chem. Phys.,* **2000**, 113, 2282.
55. J. F. Arenas, J. I. Marcos, J. C. Otero, I. López-Tocón, J. Soto. *Int. J. Quantum Chem.*, **2001**, 84, 241.
56. F. Avila, C. Ruano, I. López-Tocón, J. F. Arenas, J. Soto, J. C. Otero. *Chem. Comm.*, **2011**, 47, 4213.
57. S. P. Centeno, I. López-Tocón, J. Román-Pérez, J. F. Arenas, J. Soto, J. C. Otero. *J. Phys. Chem. C*, **2012**, 116, 23639.
58. F. Avila, J. Soto, J. F. Arenas, J. A. Rodríguez, D. Peláez, J. C. Otero. *J. Phys. Chem. C*, **2009**, 113, 105.
59. J. Román-Pérez, I. López-Tocón, J. L. Castro, J. F. Arenas, J. Soto, J. C. Otero. *Phys. Chem. Chem. Phys.,* **2015**, 17, 2326.
60. M. Sardo, C. Ruano, J. L. Castro, I. López-Tocón, J. Soto, P. Ribeiro-Claro, J. C. Otero. *Phys. Chem. Chem. Phys.,* **2009**, 11, 7437.

Supporting Information

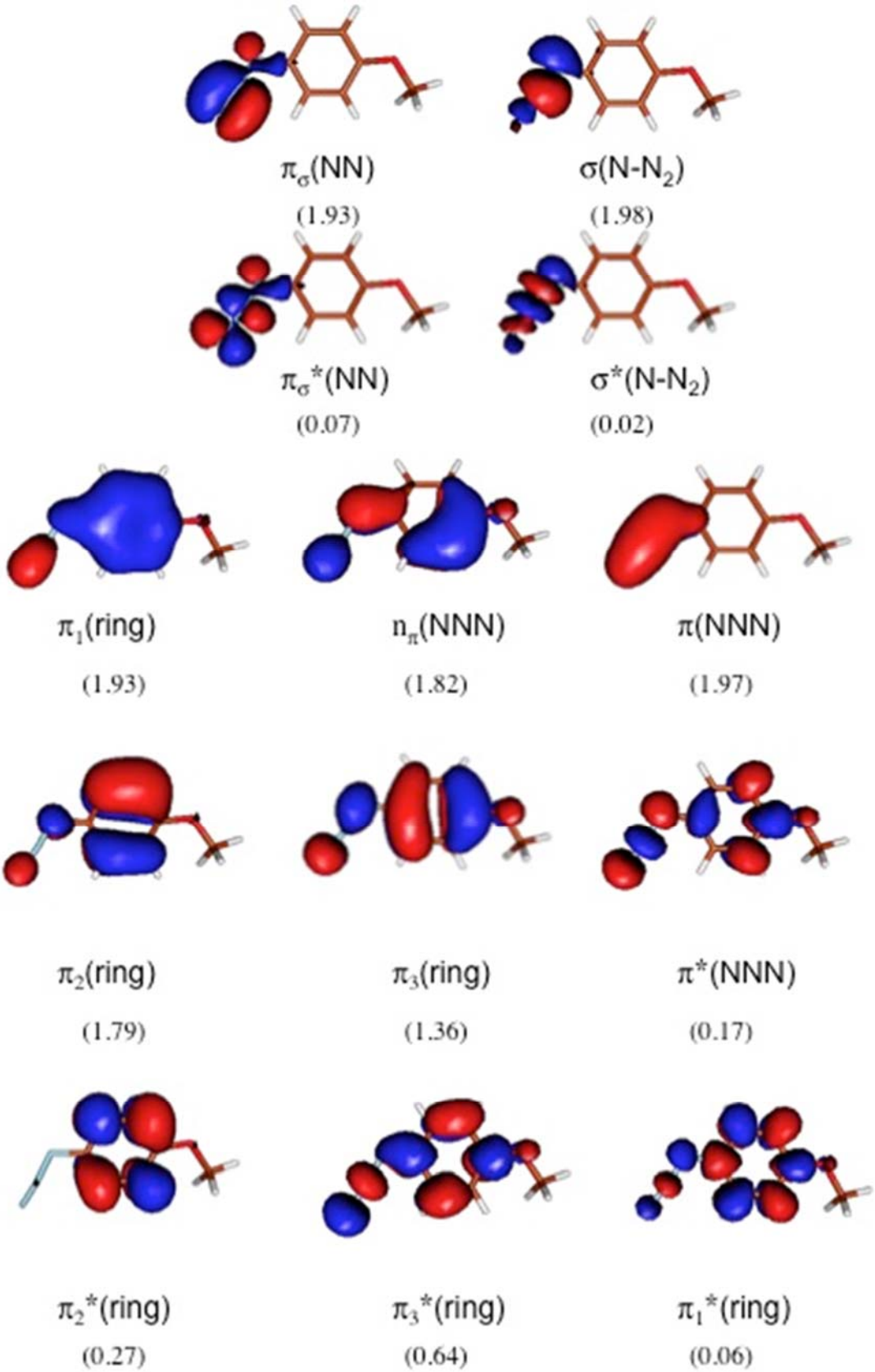

Figure S1. State average active orbitals included in the CAS-SCF wavefunction of 4-methoxyphenyl azide. In parenthesis, mean occupation numbers of the state average orbitals.

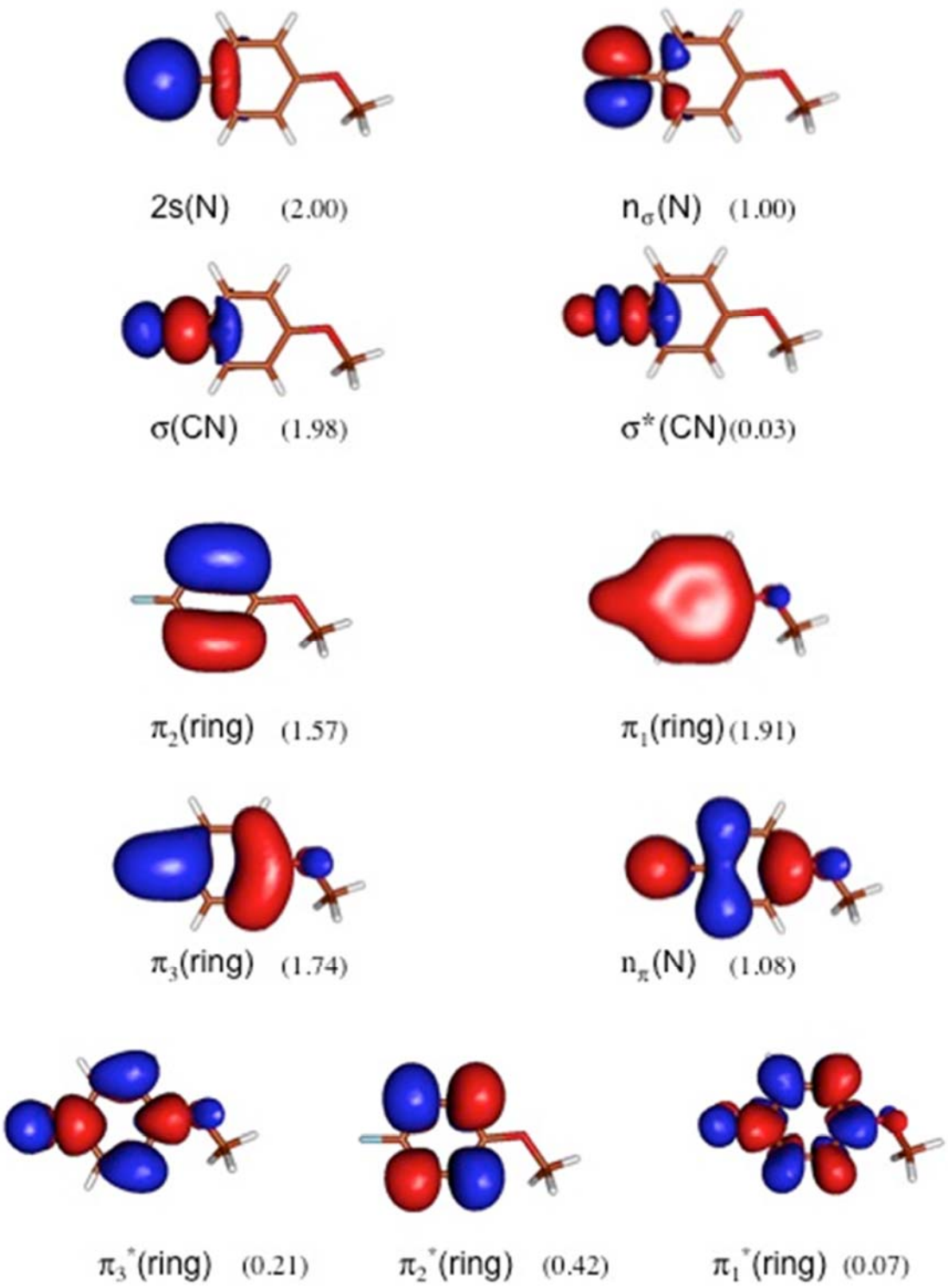

Figure S2. Active orbitals included in the CAS-SCF wavefunction of 4-methoxyphenyl nitrene. In parenthesis, mean occupation numbers of the state average orbitals.

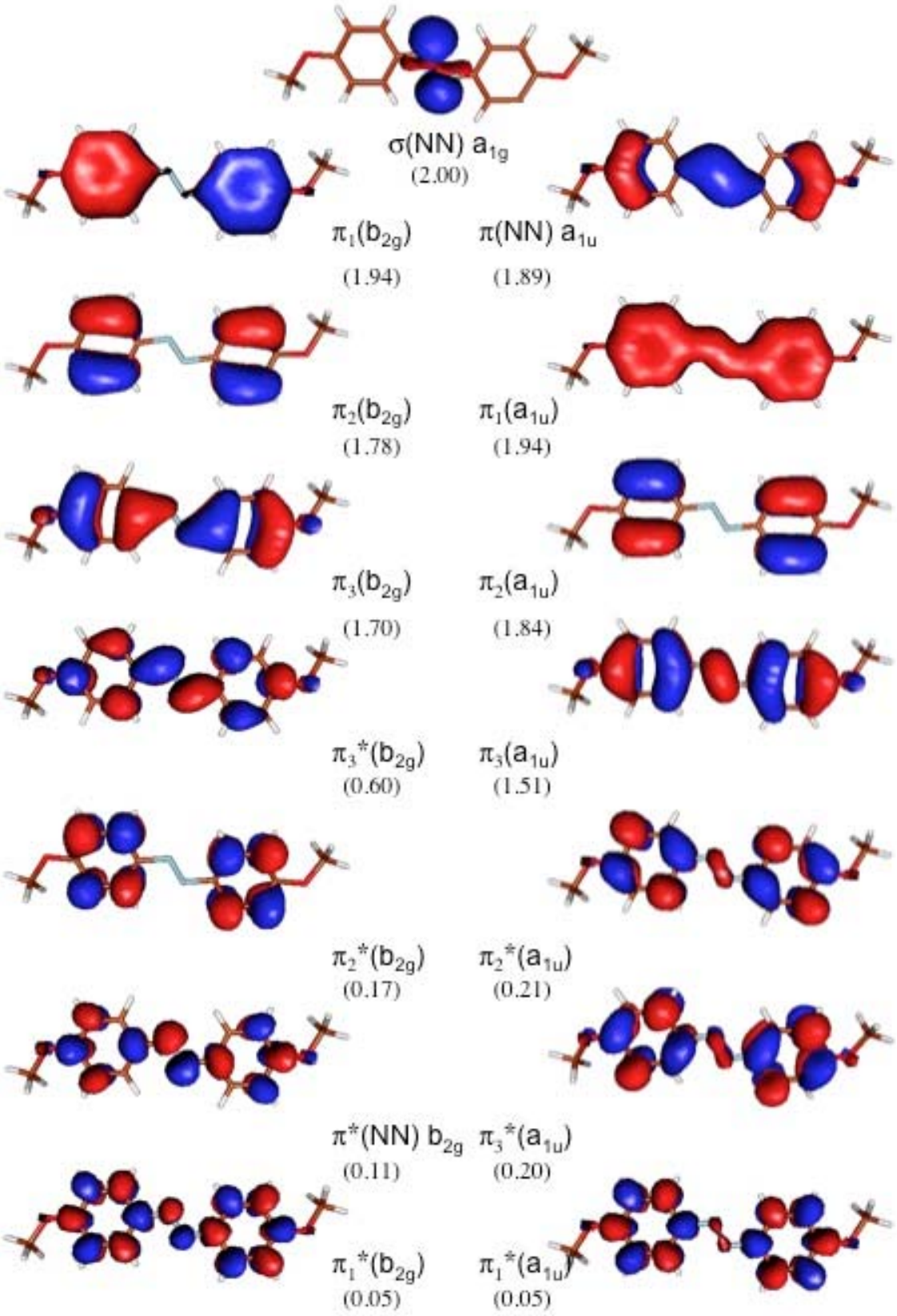

Figure S3. Active orbitals included in the CAS-SCF wavefunction of 4,4'dimethoxyazobenzene. In parenthesis, mean occupation numbers of the state average orbitals.

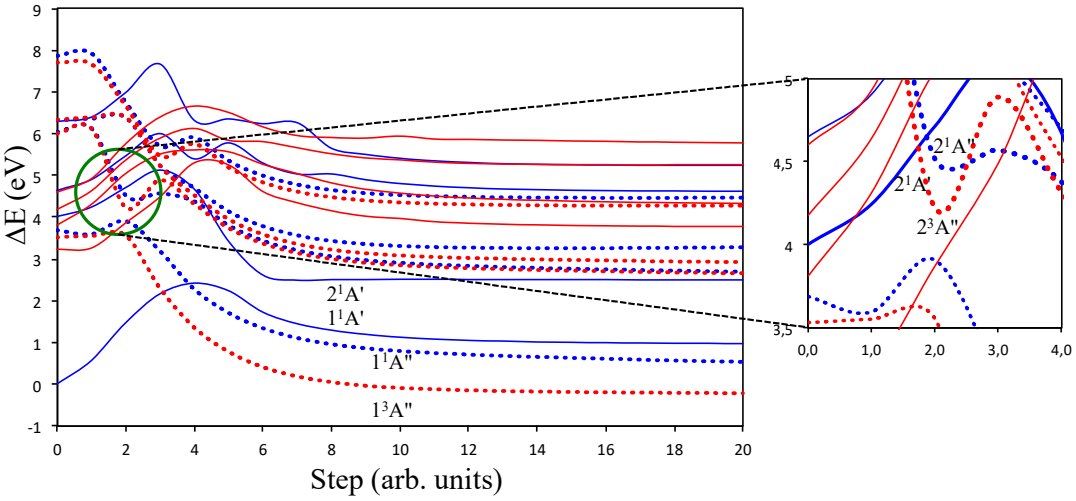

Figure S4. MS-CASPT2/ANO-RCC (C_s symmetry) potential energy curves of the ground and low-lying singlet and triplet excited states of 4-methoxyphenyl azide for dissociation into 4-methoxyphenyl nitrene and N_2. Four state-average CAS-SCF wavefunction in each symmetry block. Blue solid line: singlet A'; red solid line: triplet A'; blue dotted line: singlet A"; red dotted line: triplet A". Inset: expanded view of the $2^1A"/2^1A'$ and $2^1A'/2^3A"$ crossings. Final $\boldsymbol{R}(N\text{-}N_2)$ = 4.7 Å.

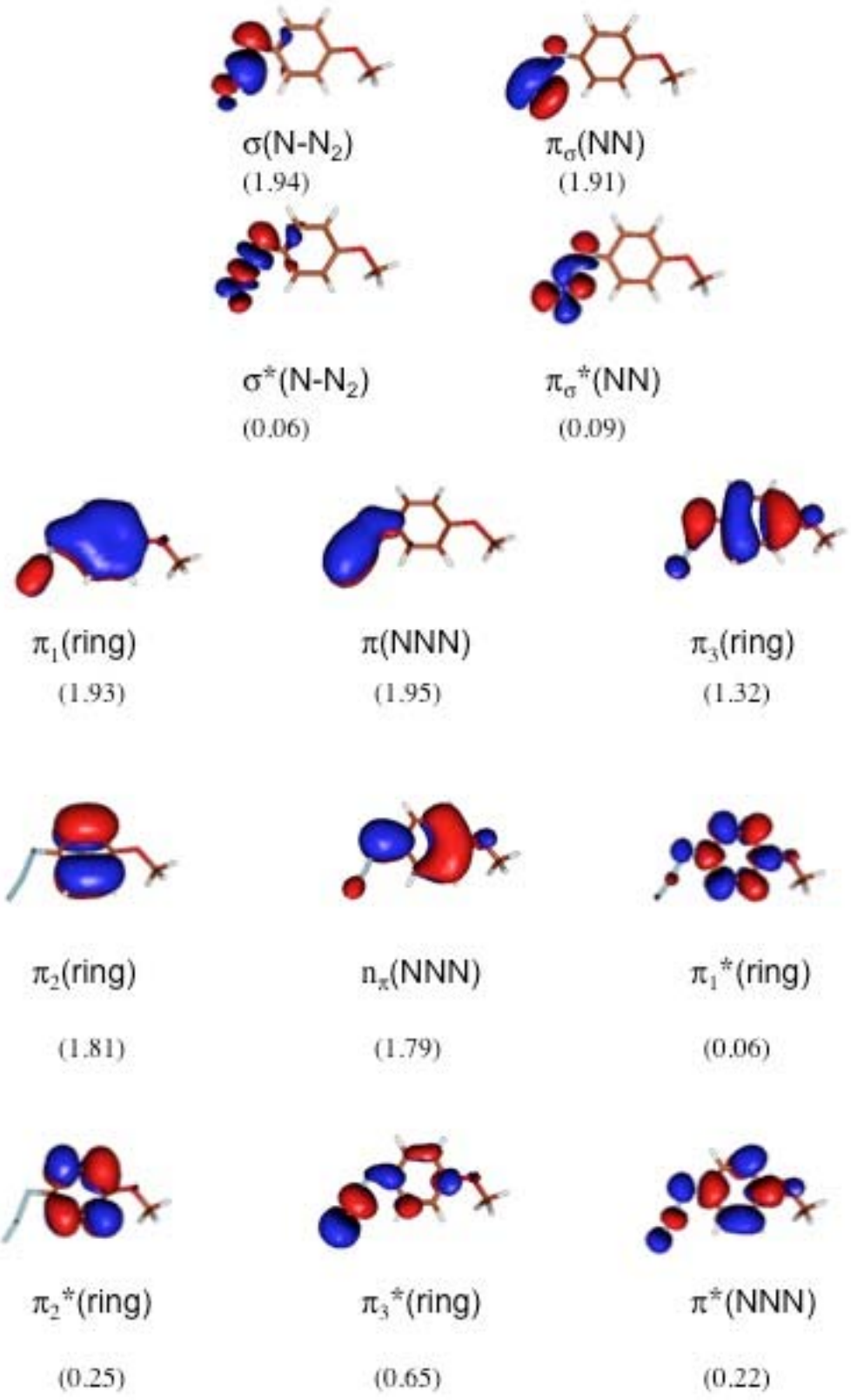

Figure S5. Active orbitals included in the CAS-SCF wavefunction of CI1. In parenthesis, mean occupation numbers of the state averaged orbitals.

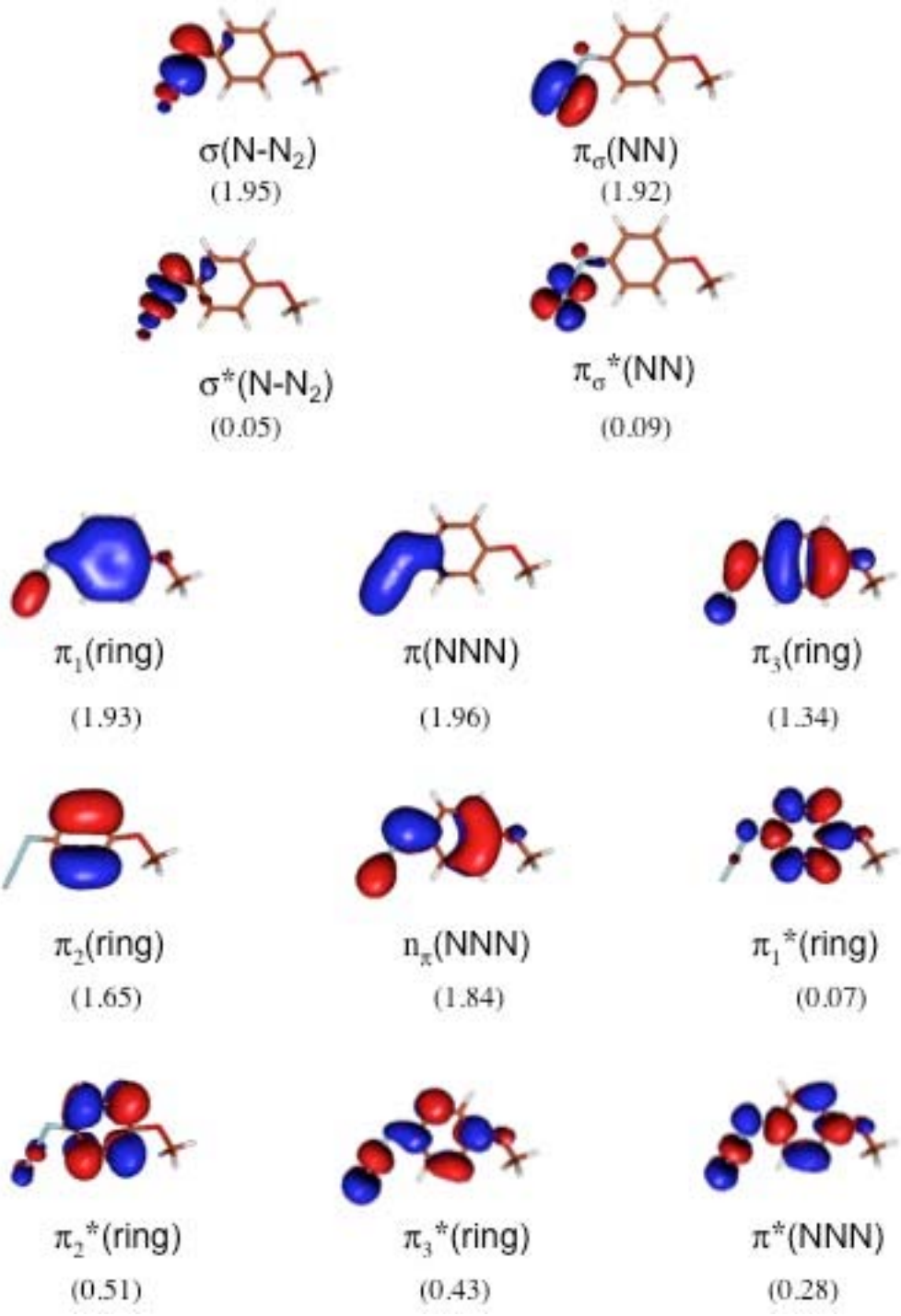

Figure S6. Active orbitals included in the CAS-SCF wavefunction of CI2. In parenthesis, mean occupation numbers of the state average orbitals.

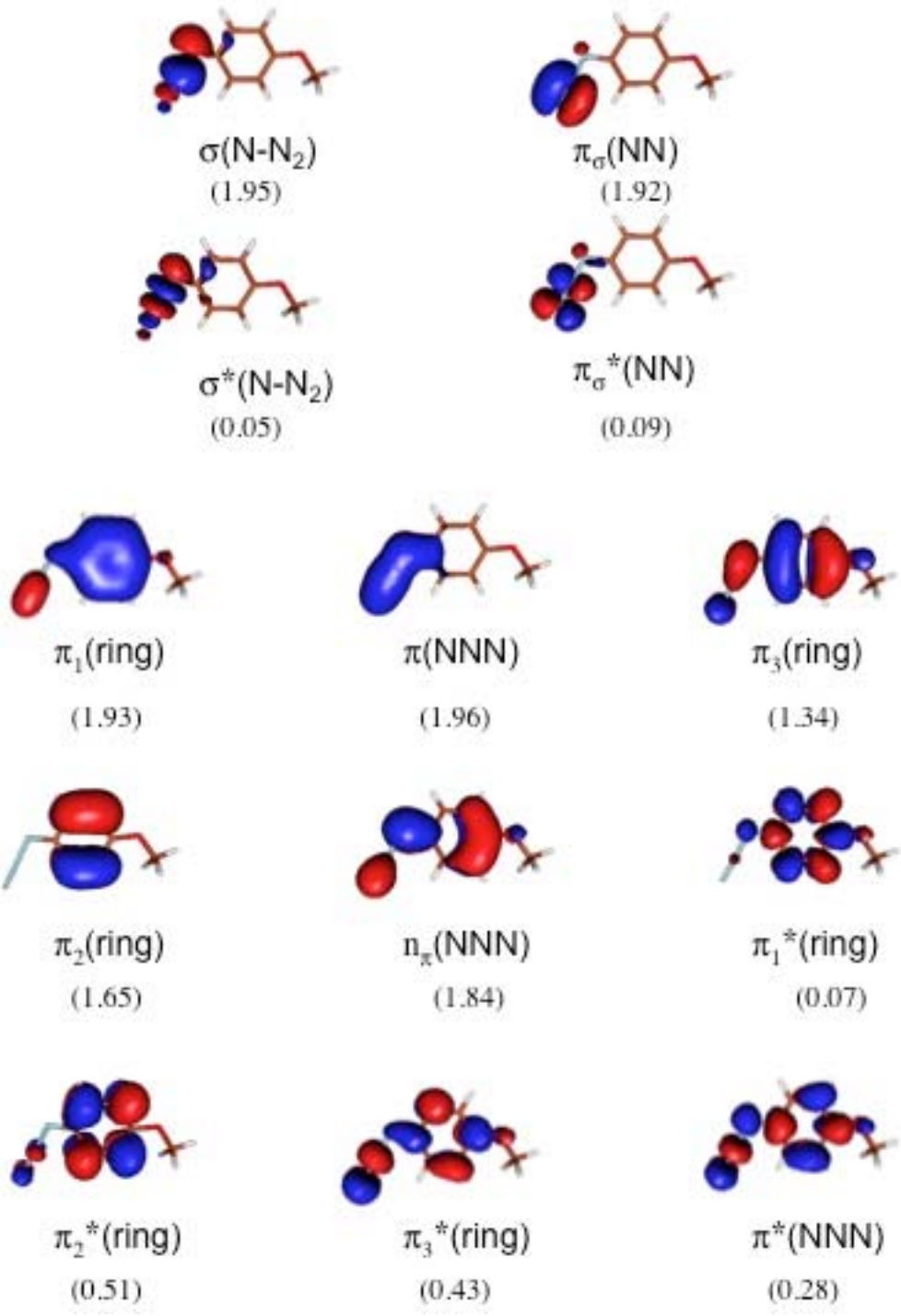

Figure S7. Active orbitals included in the CAS-SCF wavefunction of CI2. In parenthesis, mean occupation numbers of the state averaged orbitals.

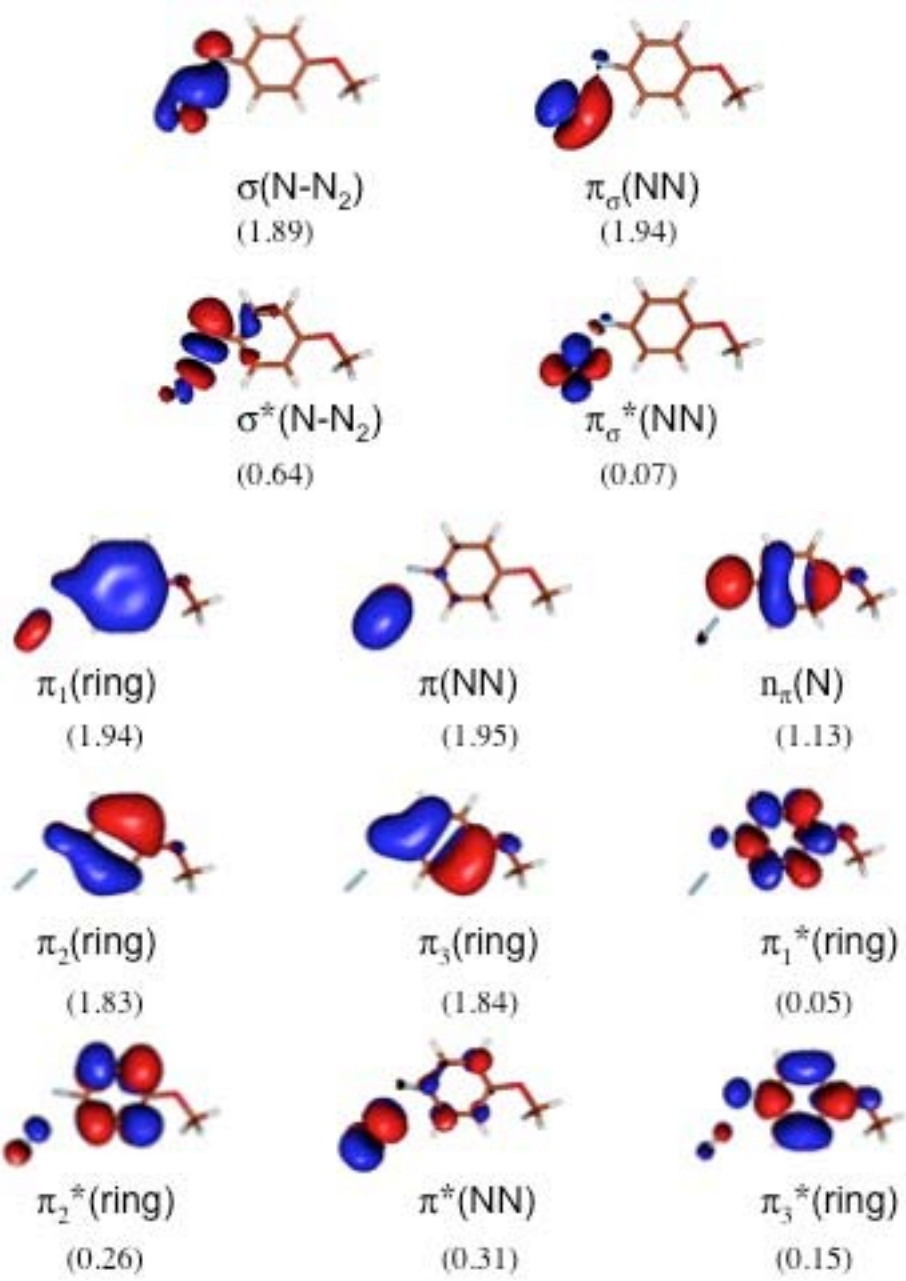

Figure S8. Active orbitals included in the CAS-SCF wavefunction of CI3. In parenthesis, mean occupation numbers of the state average orbitals.

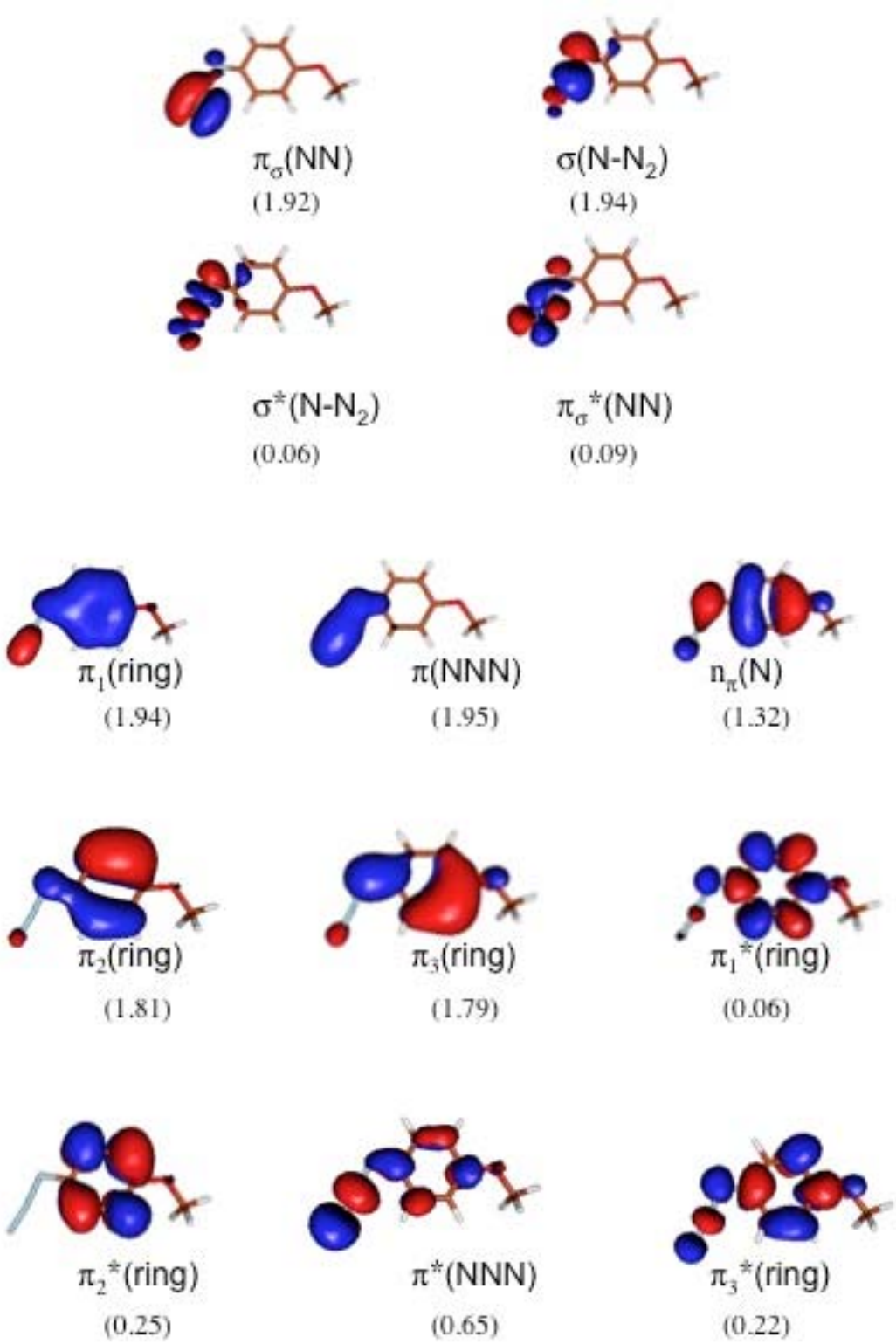

Figure S9. Active orbitals included in the CAS-SCF wavefunction of ISC1. In parenthesis, mean occupation numbers of the state average orbitals.

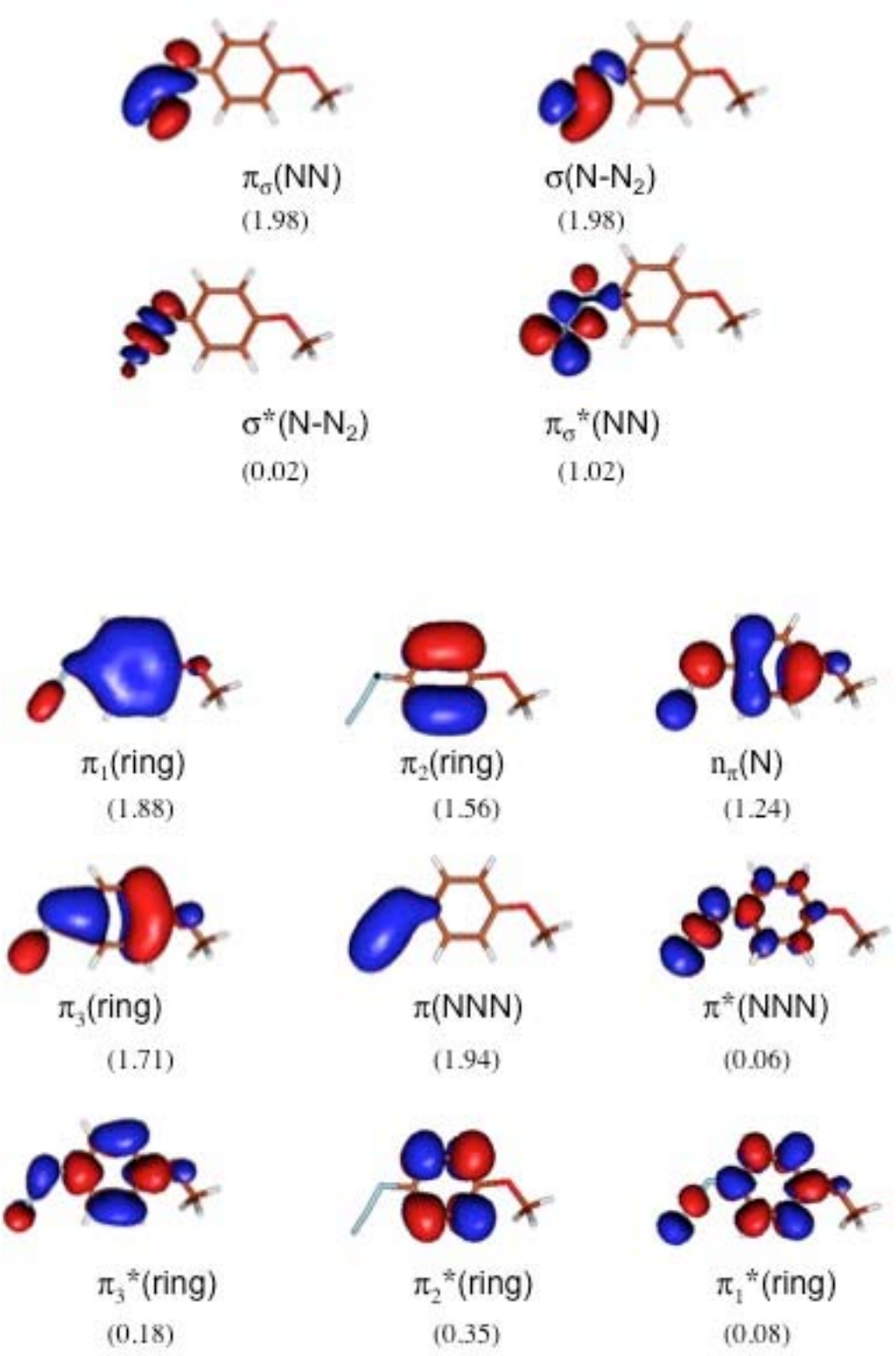

Figure S10. Active orbitals included in the CAS-SCF wavefunction of ISC2. In parenthesis, mean occupation numbers of the state average orbitals.

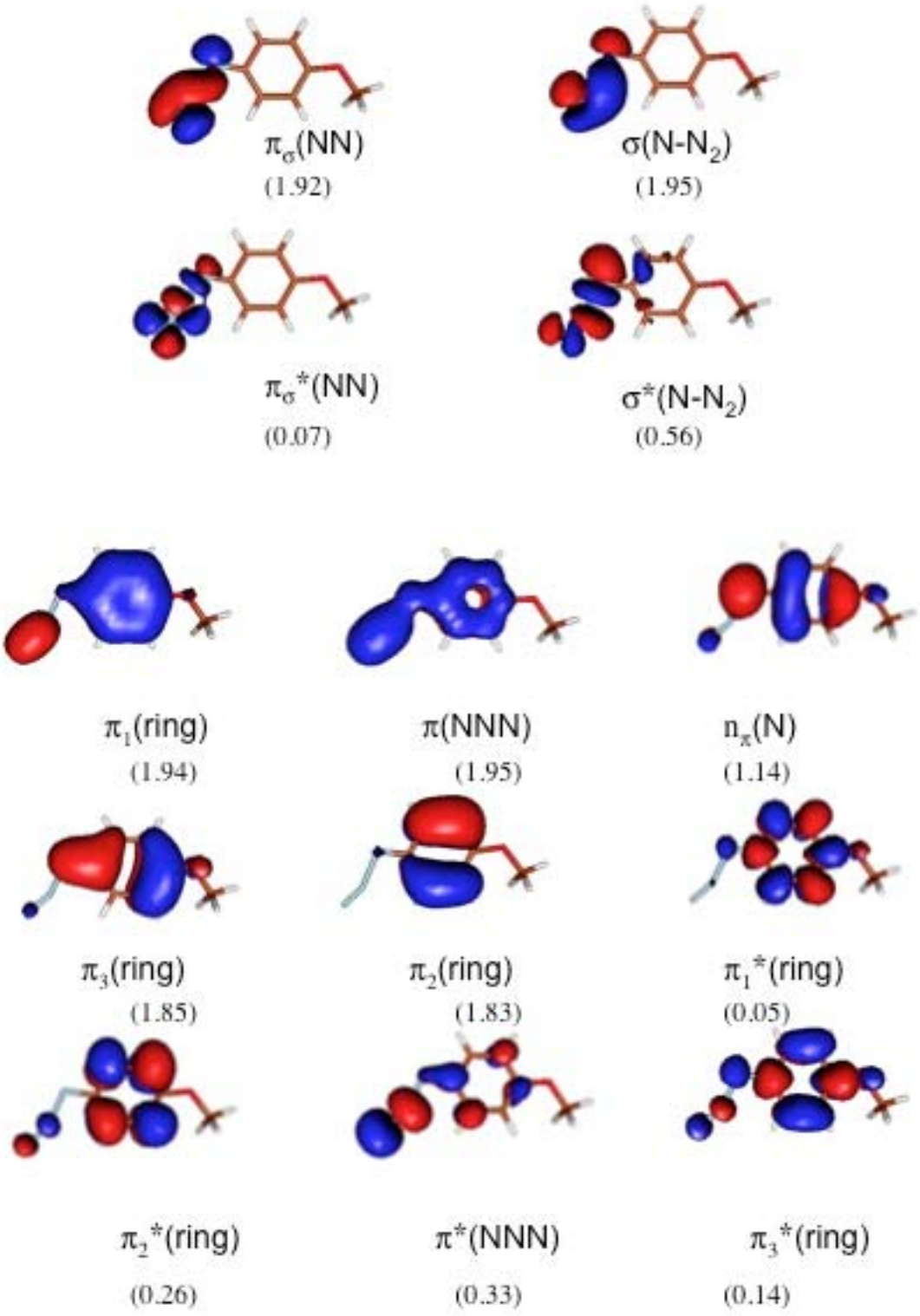

Figure S11. Active orbitals included in the CAS-SCF wavefunction of ISC3. In parenthesis, mean occupation numbers of the state average orbitals.

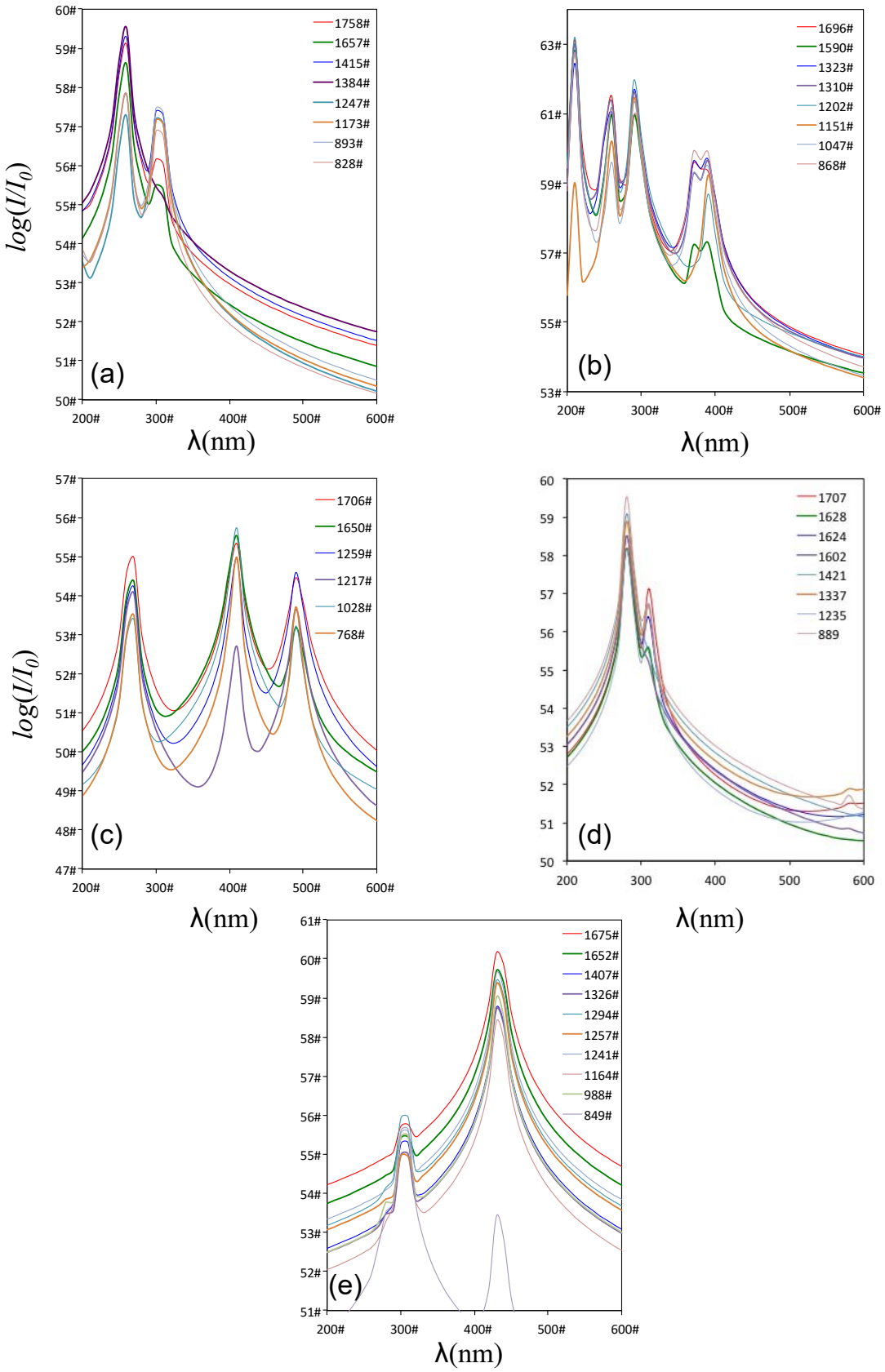

Figure S12. Multi-state Raman excitation profiles of (a) 4-methoxyphenyl azide; (b) triplet 4-methoxyphenyl nitrene; (c) $1^1A''$ 4-methoxyphenyl nitrene; (d) $1^1A'$ 4-methoxyphenyl nitrene; (e) 4,4'-dimethoxyazobenzene.

CAS-SCF Cartesian Coordinates in Ångstroms of the Critical Points on the Potential Energy Surfaces of *p*-Methoxyphenyl Azide:

M1 (S_0 Ground State Minimum, $1^1A'$)			
N1	2.496888	0.0000000	0.8149510
C2	1.199553	0.0000000	0.2409398
C3	1.152921	0.0000000	-1.1568965
C4	0.013275	0.0000000	0.9544298
C5	-0.059220	0.0000000	-1.8147732
C6	-1.218257	0.0000000	0.2891129
C7	-1.258469	0.0000000	-1.0944310
O8	-2.389936	0.0000000	-1.8340958
C9	-3.630787	0.0000000	-1.1977521
H10	2.072194	0.0000000	-1.7076011
H11	0.014276	0.0000000	2.0272770
H12	-0.101289	0.0000000	-2.8856678
H13	-2.115369	0.0000000	0.8720036
H14	-4.375124	0.0000000	-1.9779406
H15	-3.763854	0.8841296	-0.5839424
H16	-3.763854	-0.8841296	-0.5839424
N17	2.532838	0.0000000	2.0449088
N18	2.658747	0.0000000	3.1652800

M2 (S_2 Excited State Minimum, $2^1A'$)			
N1	2.485976	0.000000	0.814358
C2	1.217158	0.000000	0.244241
C3	1.192731	0.000000	-1.180046
C4	0.004198	0.000000	1.004959
C5	-0.062189	0.000000	-1.860509
C6	-1.245474	0.000000	0.321636
C7	-1.263230	0.000000	-1.105009
O8	-2.394033	0.000000	-1.829533
C9	-3.643499	0.000000	-1.203817
H10	2.118182	0.000000	-1.715010
H11	0.022567	0.000000	2.074550
H12	-0.119245	0.000000	-2.927883
H13	-2.151363	0.000000	0.886372
H14	-4.377579	0.000000	-1.993531
H15	-3.782428	0.884491	-0.593575
H16	-3.782428	-0.884491	-0.593575
N17	2.534456	0.000000	2.051281
N18	2.692161	0.000000	3.167318

ISC1 (Intersystem Crossing Minimum, $2^1A'/2^3A''$)			
N1	0.109002	0.000000	0.052497
C2	0.012060	0.000000	1.348920
C3	1.284522	0.000000	2.047777
C4	-1.181582	0.000000	2.141092
C5	1.327598	0.000000	3.405038
C6	-1.098002	0.000000	3.529753
C7	0.133753	0.000000	4.176952
O8	0.313413	0.000000	5.507602
C9	-0.794456	0.000000	6.360949
H10	2.181675	0.000000	1.462781
H11	-2.135683	0.000000	1.665000
H12	2.265821	0.000000	3.922913
H13	-2.008950	0.000000	4.091081
H14	-0.404222	0.000000	7.365501
H15	-1.403541	-0.884744	6.217023
N17	-1.379205	0.000000	-0.517833
N18	-2.389649	0.000000	-1.087849

ISC2 (Intersystem Crossing Minimum, $2^1A'/1^3A''$)			
N1	-0.046870	0.000000	-0.035160
C2	-0.067425	0.000000	1.370368
C3	1.230934	0.000000	1.981305
C4	-1.262484	0.000000	2.150627
C5	1.327482	0.000000	3.419856
C6	-1.161130	0.000000	3.582635
C7	0.143862	0.000000	4.195100
O8	0.323997	0.000000	5.525975
C9	-0.766944	0.000000	6.399173
H10	2.100348	0.000000	1.360804
H11	-2.229192	0.000000	1.693046
H12	2.274838	0.000000	3.914401
H13	-2.050271	0.000000	4.172201
H14	-0.356085	0.000000	7.396097
H15	-1.379320	-0.884620	6.271566
H16	-1.379320	+0.884620	6.271566
N17	-1.160736	0.000000	-0.590386
N18	-2.107511	0.000000	-1.156899

ISC3 (Intersystem Crossing Minimum, $1^1A'/1^3A''$)			
N1	0.044289	0.000000	-0.004226
C2	-0.061996	0.000000	1.392499
C3	1.193011	0.000000	2.033153
C4	-1.201802	0.000000	2.181997
C5	1.281888	0.000000	3.409457
C6	-1.108348	0.000000	3.580825
C7	0.127923	0.000000	4.200130
O8	0.327710	0.000000	5.540643
C9	-0.771167	0.000000	6.396531
H10	2.086664	0.000000	1.439973
H11	-2.177959	0.000000	1.741203
H12	2.239238	0.000000	3.891562
H13	-2.015064	0.000000	4.149162
H14	-0.378956	0.000000	7.401291
H15	-1.385010	-0.883882	6.258838
N17	-1.557602	0.000000	-0.640866
N18	-2.319412	0.000000	-1.427699

CI1 (Conical Intersection, $2^1A''/2^1A'$)			
N1	0.116642	-0.000004	0.053027
C2	0.015401	-0.000001	1.352259
C3	1.290426	-0.000000	2.049433
C4	-1.179689	0.000001	2.146523
C5	1.332594	0.000001	3.407092
C6	-1.100892	0.000001	3.533843
C7	0.133552	0.000001	4.178755
O8	0.316580	0.000002	5.511524
C9	-0.794522	-0.000001	6.366161
H10	2.188600	-0.000001	1.461989
H11	-2.135456	0.000001	1.667525
H12	2.270576	0.000003	3.929544
H13	-2.014355	0.000002	4.094879
H14	-0.401895	-0.000003	7.372171
H15	-1.402697	-0.887118	6.221067
H16	-1.402699	0.887116	6.221071
N17	-1.405592	-0.000001	-0.525665
N18	-2.397561	0.000001	-1.134977

CI2 (Conical Intersection, $2^3A''/1^3A''$)			
N1	0.089811	-0.000000	0.041534
C2	0.005621	-0.000000	1.368872
C3	1.269017	-0.000000	2.047899
C4	-1.178269	-0.000000	2.158988
C5	1.326696	0.000000	3.415014
C6	-1.100829	-0.000000	3.542028
C7	0.141168	-0.000000	4.182612
O8	0.317123	0.000000	5.515214
C9	-0.795116	0.000000	6.369625
H10	2.163659	-0.000000	1.454914
H11	-2.135389	-0.000000	1.678503
H12	2.268481	0.000000	3.930343
H13	-2.011586	-0.000000	4.107093
H14	-0.401842	0.000000	7.375312
H15	-1.402982	-0.887189	6.225049
H16	-1.402982	0.887189	6.225049
N17	-1.328901	0.000000	-0.586309
N18	-2.389034	0.000000	-1.075055

CI3 (S_1/S_0 Conical Intersection, $1^1A''/1^1A'$)			
N1	0.113242	0.000015	-0.013592
C2	-0.042387	0.000009	1.399568
C3	1.209017	0.000003	2.041134
C4	-1.182885	0.000010	2.157863
C5	1.281966	-0.000007	3.420365
C6	-1.105073	0.000006	3.567969
C7	0.119094	-0.000005	4.197188
O8	0.310075	-0.000006	5.543704
C9	-0.801670	-0.000002	6.387192
H10	2.113654	0.000006	1.459881
H11	-2.154019	0.000017	1.703528
H12	2.236427	-0.000015	3.912663
H13	-2.021542	0.000009	4.124500
H14	-0.419725	-0.000001	7.398303
H15	-1.413290	-0.886111	6.240766
H16	-1.413284	0.886111	6.240763
N17	-1.740350	0.000002	-0.759781
N18	-2.598489	-0.000040	-1.436976

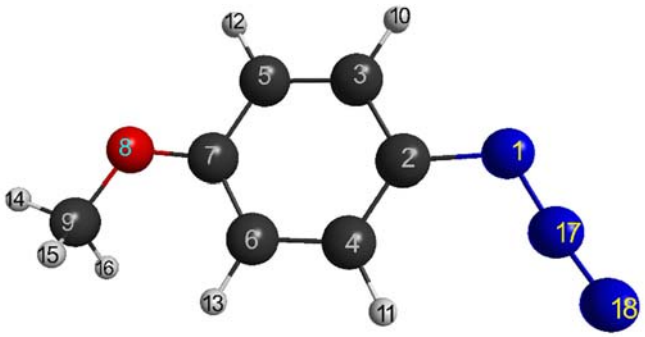

Table S1 (continue). CAS-SCF internal coordinates of 4-methoxyphenyl azide.[a]

Coor.	**M1**[b]	**M2**[b]	**CI1**[c]	**CI2**[c]	**CI3**[c]	**ISC1**[b]	**ISC2**[b]	**ISC3**[b]
$R_{1,2}$	1.419	1.391	1.303	1.334	1.422	1.300	1.406	1.401
$R_{3,2}$	1.399	1.424	1.453	1.429	1.406	1.452	1.435	1.409
$R_{4,2}$	1.384	1.432	1.435	1.423	1.370	1.433	1.427	1.387
$R_{5,3}$	1.379	1.428	1.358	1.371	1.381	1.358	1.442	1.379
$R_{6,4}$	1.400	1.424	1.390	1.387	1.412	1.391	1.436	1.402
$R_{7,5}$	1.399	1.419	1.426	1.412	1.398	1.422	1.415	1.399
$R_{8,7}$	1.352	1.343	1.345	1.344	1.360	1.343	1.343	1.355
$R_{9,8}$	1.395	1.397	1.402	1.402	1.396	1.398	1.397	1.393
$R_{10,3}$	1.072	1.069	1.073	1.073	1.075	1.071	1.068	1.073
$R_{11,4}$	1.073	1.070	1.069	1.071	1.072	1.066	1.070	1.071
$R_{12,5}$	1.072	1.069	1.074	1.073	1.074	1.072	1.069	1.072
$R_{13,6}$	1.070	1.068	1.072	1.072	1.072	1.070	1.067	1.070
$R_{14,9}$	1.078	1.078	1.080	1.080	1.081	1.078	1.078	1.079
$R_{15,9}$	1.085	1.084	1.085	1.085	1.087	1.084	1.083	1.085
$R_{16,9}$	1.085	1.084	1.085	1.085	1.087	1.084	1.083	1.085
$R_{17,1}$	1.230	1.238	1.629	1.558	1.998	1.594	1.245	1.724
$R_{18,17}$	1.127	1.127	1.164	1.171	1.093	1.160	1.103	1.095
$A_{3,2,1}$	115.778	115.178	114.214	114.638	110.859	114.500	114.361	112.692
$A_{4,2,1}$	125.108	123.710	128.064	127.256	129.904	127.847	123.979	129.060
$A_{5,3,2}$	120.401	119.451	120.449	120.693	120.171	120.594	119.039	120.738
$A_{6,4,2}$	120.596	119.236	120.357	120.470	120.461	120.126	119.092	120.887
$A_{7,5,4}$	60.508	59.156	59.410	59.593	60.865	59.622	59.331	60.717
$A_{8,7,5}$	115.835	115.180	114.944	115.372	115.671	115.196	115.516	115.941
$A_{9,8,7}$	119.676	120.751	119.747	119.968	119.115	119.916	120.966	119.437
$A_{10,3,2}$	119.014	119.048	118.144	118.293	120.135	118.117	119.285	119.382
$A_{11,4,2}$	120.971	121.110	119.773	119.700	121.309	119.910	121.529	120.989

[a]Internuclear distance in Ångstroms, valence bond and dihedral angles in degrees. [b]ANO-RCC (C,N,O[4s3p2d1f]/H[3s2p1d]). [c]ANO-RCC (C,N,O[3s2p1d]/H[2s1p]).

Table S1 (continuation).

Coor.	**M1**[b]	**M2**[b]	**CI1**[c]	**CI2**[c]	**CI3**[c]	**ISC1**[b]	**ISC2**[b]	**ISC3**[b]
$A_{12,5,7}$	118.742	119.112	118.118	118.443	118.972	118.217	119.210	118.853
$A_{13,6,7}$	121.349	121.227	120.858	120.930	121.528	120.640	121.311	121.312
$A_{14,9,8}$	106.503	106.308	106.247	106.178	106.494	106.376	106.276	106.591
$A_{15,9,8}$	111.558	111.521	111.264	111.292	111.529	111.359	111.572	111.617
$A_{16,9,8}$	111.558	111.521	111.264	111.292	111.528	111.359	111.572	111.617
$A_{17,1,2}$	115.541	116.440	106.359	110.317	105.643	106.692	115.657	107.323
$A_{18,17,1}$	175.262	174.201	169.255	179.138	163.649	171.540	175.600	155.749
$D_{4,2,1,3}$	180.000	180.000	180.000	-180.000	180.000	180.000	180.000	180.000
$D_{5,3,2,4}$	0.000	0.000	0.000	0.000	0.000	0.000	0.000	0.000
$D_{6,4,2,3}$	0.000	0.000	0.000	0.000	0.000	0.000	0.000	0.000
$D_{7,5,4,2}$	180.000	180.000	180.000	180.000	180.000	180.000	180.000	180.000
$D_{8,7,5,6}$	180.000	180.000	180.000	180.000	180.000	180.000	180.000	180.000
$D_{9,8,7,6}$	0.000	0.000	0.000	0.000	0.000	0.000	0.000	0.000
$D_{10,3,2,5}$	180.000	180.000	180.000	-180.000	180.000	180.000	180.000	180.000
$D_{11,4,2,6}$	180.000	180.000	180.000	180.000	180.000	180.000	180.000	180.000
$D_{12,5,7,3}$	180.000	180.000	180.000	-180.000	180.000	180.000	180.000	180.000
$D_{13,6,7,4}$	180.000	180.000	180.000	180.000	180.000	180.000	180.000	180.000
$D_{14,9,8,7}$	180.000	180.000	180.000	180.000	-180.000	180.000	180.000	180.000
$D_{15,9,8,14}$	-118.770	-118.660	-118.706	-118.661	-118.760	-118.766	-118.599	-118.795
$D_{16,9,8,14}$	118.770	118.660	118.706	118.661	118.760	118.766	118.599	118.795
$D_{17,1,2,3}$	180.000	180.000	180.000	180.000	179.999	180.000	180.000	180.000
$D_{18,17,1,2}$	180.000	180.000	180.000	179.995	-179.993	180.000	180.000	180.000

[a]Internuclear distance in Ångstroms, valence bond and dihedral angles in degrees.
[b]ANO-RCC (C,N,O[4s3p2d1f]/H[3s2p1d]).
[c]ANO-RCC (C,N,O[3s2p1d]/H[2s1p]).

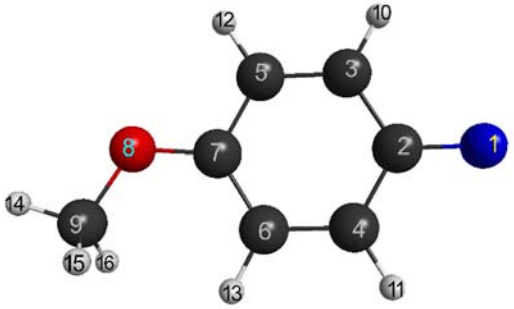

Table S2 (continue). CAS-SCF internal coordinates of 4-methoxyphenyl nitrene.[a]

Coor.	**$1^3A''$**[b]	**$1^1A''$**[b]	**$1^1A'$**[b]	**$2^1A'$**	**$2^1A'/2^3A''$**	**$4^1A/3^1A$**
$R_{1,2}$	1.345	1.290	1.346	1.388	1.337	1.330
$R_{3,2}$	1.428	1.469	1.426	1.406	1.421	1.433
$R_{4,2}$	1.419	1.468	1.417	1.393	1.436	1.437
$R_{5,3}$	1.371	1.354	1.370	1.382	1.410	1.419
$R_{6,4}$	1.386	1.368	1.381	1.396	1.410	1.417
$R_{7,5}$	1.409	1.430	1.407	1.396	1.400	1.393
$R_{8,7}$	1.347	1.344	1.330	1.355	1.353	1.354
$R_{9,8}$	1.397	1.398	1.403	1.394	1.394	1.394
$R_{10,3}$	1.072	1.071	1.072	1.072	1.070	1.070
$R_{11,4}$	1.072	1.071	1.072	1.072	1.070	1.070
$R_{12,5}$	1.072	1.072	1.072	1.072	1.071	1.071
$R_{13,6}$	1.070	1.070	1.069	1.070	1.070	1.069
$R_{14,9}$	1.078	1.078	1.077	1.078	1.078	1.078
$R_{15,9}$	1.084	1.084	1.083	1.085	1.085	1.085
$R_{16,9}$	1.084	1.084	1.083	1.085	1.085	1.085
$A_{3,2,1}$	120.818	121.399	121.708	119.600	120.796	121.044
$A_{4,2,1}$	120.835	121.483	120.930	120.788	120.806	120.869
$A_{5,3,2}$	120.207	120.221	121.242	119.581	119.876	119.811
$A_{6,4,2}$	120.709	120.726	121.898	120.002	120.082	120.201
$A_{7,5,4}$	59.627	58.789	59.141	60.672	60.131	60.250
$A_{8,7,5}$	115.431	115.096	115.226	115.898	115.533	115.733
$A_{9,8,7}$	120.016	120.125	120.943	119.562	119.747	119.862
$A_{10,3,2}$	119.023	118.271	117.599	120.287	119.773	119.736
$A_{11,4,2}$	119.023	118.217	117.398	120.358	119.646	119.603
$A_{12,5,7}$	118.274	117.671	118.199	118.789	118.876	118.947
$A_{13,6,7}$	120.925	120.436	120.905	121.251	121.165	121.174
$A_{14,9,8}$	106.394	106.390	106.069	106.543	106.486	106.466

Table S2. (**continuation**).

Coor.	**$1^3A''$**[b]	**$1^1A''$**[b]	**$1^1A'$**[b]	**$2^1A'$**	**$2^1A'/2^3A''$**	**$4^1A/3^1A$**
$A_{15,9,8}$	111.496	111.449	111.229	111.607	111.590	111.627
$A_{16,9,8}$	111.496	111.449	111.229	111.607	111.590	111.627
$D_{4,2,1,3}$	180.000	180.000	180.000	180.000	180.000	180.000
$D_{5,3,2,4}$	0.000	0.000	0.000	0.000	0.000	0.000
$D_{6,4,2,3}$	0.000	0.000	0.000	0.000	0.000	0.000
$D_{7,5,4,2}$	180.000	180.000	180.000	180.000	180.000	180.000
$D_{8,7,5,6}$	180.000	180.000	180.000	180.000	180.000	180.000
$D_{9,8,7,6}$	0.000	0.000	0.000	0.000	0.000	180.000
$D_{10,3,2,5}$	180.000	180.000	180.000	180.000	180.000	0.000
$D_{11,4,2,6}$	180.000	180.000	180.000	180.000	180.000	180.000
$D_{12,5,7,3}$	180.000	180.000	180.000	180.000	180.000	180.000
$D_{13,6,7,4}$	180.000	180.000	180.000	180.000	180.000	180.000
$D_{14,9,8,7}$	180.000	180.000	180.000	180.000	180.000	180.000
$D_{15,9,8,14}$	-118.721	-118.727	-118.683	-118.769	-118.741	-118.707
$D_{16,9,8,14}$	118.721	118.727	118.683	118.769	118.741	118.707

[a]Intenuclear distance in Ångstrom, valence bond and dihedral angles in degrees.
[b]ANO-RCC (C,N,O[4s3p2d1f]/H[3s2p1d]).

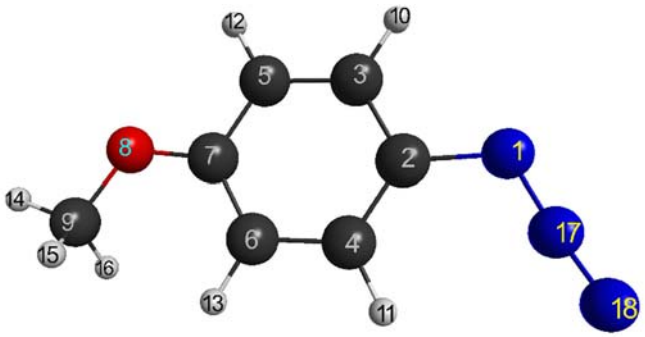

Table S3 (continue). Definition of redundant internal coordinates of 4,4′-dimethoxyazobenzene.

Nº	*Coor.*	*Connectivity*	*type*
1	r_1	9–14	$\nu(C\text{-}H)_{methyl}$
2	r_2	9–15	$\nu(C\text{-}H)_{methyl}$
3	r_3	9-16	$\nu(C\text{-}H)_{methyl}$
4	r_4	3-10	$\nu(C\text{-}H)_{ring}$
5	r_5	4-11	$\nu(C\text{-}H)_{ring}$
6	r_6	5-12	$\nu(C\text{-}H)_{ring}$
7	r_7	6-13	$\nu(C\text{-}H)_{ring}$
8	r_8	7-8	$\nu(C\text{-}O)$
9	r_9	8-9	$\nu(O\text{-}CH_3)$
10	r_{10}	2-1	$\nu(N\text{-}C_{ring})$
11	r_{11}	1-17	$\nu(N\text{-}N)$
12	r_{12}	17-18	$\nu(N\text{-}N)$
13	P_1	2-3	$\nu(C\text{-}C)$
14	P_2	3-5	$\nu(C\text{-}C)$
15	P_3	5-7	$\nu(C\text{-}C)$
16	P_4	7-6	$\nu(C\text{-}C)$
17	P_5	4-2	$\nu(C\text{-}C)$
18	P_6	6-4	$\nu(C\text{-}C)$
19	β_1	[10-3-2]-[10-3-5]	$\delta(C\text{-}H)_{ring}$
20	β_2	[12-5-7]-[12-5-3]	$\delta(C\text{-}H)_{ring}$
21	β_3	[13-6-7]-[13-6-4]	$\delta(C\text{-}H)_{ring}$
22	β_4	[11-4-2]-[11-4-6]	$\delta(C\text{-}H)_{ring}$
23	β_5	[8-7-5]-[8-7-6]	$\delta(O\text{-}C\text{-}C)$
24	β_6	[1-2-3]-[1-2-4]	$\delta(N\text{-}C\text{-}C)$

Table S3 (continuation.)

25	β_7	9-8-7	δ(C-O-C)
26	β_8	2-1-17	δ(C-N-N)
27	β_9	1-17-18	δ(N-N-N)
28	α_1	15-9-16	$\delta(H\text{-}C\text{-}H)_{methyl}$
29	α_2	14-9-16	$\delta(H\text{-}C\text{-}H)_{methyl}$
30	α_3	14-9-15	$\delta(H\text{-}C\text{-}H)_{methyl}$
31	$\alpha э_1$	14-9-8	$\delta(O\text{-}C\text{-}H)_{methyl}$
32	$\alpha э_2$	15-9-8	$\delta(O\text{-}C\text{-}H)_{methyl}$
33	$\alpha э_3$	16-9-8	$\delta(O\text{-}C\text{-}H)_{methyl}$
34	α_4	5-7-6	$\delta(C\text{-}C\text{-}C)_{ring}$
35	α_5	7-6-4	$\delta(C\text{-}C\text{-}C)_{ring}$
36	α_6	6-4-2	$\delta(C\text{-}C\text{-}C)_{ring}$
37	α_7	4-2-3	$\delta(C\text{-}C\text{-}C)_{ring}$
38	α_8	2-3-5	$\delta(C\text{-}C\text{-}C)_{ring}$
39	α_9	3-5-7	$\delta(C\text{-}C\text{-}C)_{ring}$
40	γ_1	13-6-7-4	γ(C-H)
41	γ_2	11-4-6-2	γ(C-H)
42	γ_3	10-3-2-5	γ(C-H)
43	γ_4	12-5-3-7	γ(C-H)
44	γ_5	1-2-4-3	γ(C-N)
45	γ_6	8-7-5-6	γ(O-C)
46	Γ_1	(5,8)-7-6-(4-13)	Γ(CC)
47	Γ_2	(7,13)-6-4-(11-2)	Γ(CC)
48	Γ_3	(6,11)-4-2-(3-1)	Γ(CC)
49	Γ_4	(4,1)-2-3-(5-10)	Γ(CC)
50	Γ_5	(2,10)-3-5-(7-12)	Γ(CC)
51	Γ_6	(3,12)-5-7-(6-8)	Γ(CC)
52	Γ_7	(5,6)-7-8-(9)	Γ(OC)
53	Γ_8	(14,15,16)-9-8-(7)	Γ(CO)
54	Γ_9	(3,4)-1-2-(17)	Γ(CN)
55	Γ_{10}	(2)-1-17-(18)	Γ(NN)

Table S3b (continue). Non-redundant internal coordinates of 4-methoxyphenyl nitrene.

Coordinate	*type*	*Definition*	Wilson
$q_1 \ldots q_3$	$\nu(C\text{-}H)_{methyl}$	$r_1 \ldots r_3$	
$q_4 \ldots q_7$	$\nu(C\text{-}H)_{ring}$	$r_4 \ldots r_7$	
q_8	$\nu(C\text{-}O)$	r_8	
q_9	$\nu(O\text{-}CH_3)$	r_9	
q_{10}	$\nu(N\text{-}C_{ring})$	r_{10}	
q_{11}	$\nu(N\text{-}N)$	r_{11}	
q_{12}	$\nu(N\text{-}N)$	r_{12}	
q_{13}	$\nu(C\text{-}C)$	$6^{-1/2}(P_1+P_2+P_3+P_4+P_5+P_6)$	1
q_{14}	$\nu(C\text{-}C)$	$12^{-1/2}(-P_1+2P_2-P_3-P_4+2P_5-P_6)$	8a
q_{15}	$\nu(C\text{-}C)$	$2^{-1}(-P_1+P_3-P_4+P_6)$	8b
q_{16}	$\nu(C\text{-}C)$	$6^{-1/2}(P_1-P_2+P_3-P_4+P_5-P_6)$	14
q_{17}	$\nu(C\text{-}C)$	$2^{-1}(P_1-P_3-P_4+P_6)$	19a
q_{18}	$\nu(C\text{-}C)$	$2^{-1/2}(P_2-P_6)$	19b
q_{19}	$\delta(C\text{-}H)_{ring}$	$2^{-1}(\beta_1+\beta_2+\beta_3+\beta_4)$	9a
q_{20}	$\delta(C\text{-}H)_{ring}$	$2^{-1}(\beta_1+\beta_2-\beta_3-\beta_4)$	15
q_{21}	$\delta(C\text{-}H)_{ring}$	$2^{-1}(\beta_1-\beta_2+\beta_3-\beta_4)$	3
q_{22}	$\delta(C\text{-}H)_{ring}$	$2^{-1}(\beta_1-\beta_2-\beta_3+\beta_4)$	18a
q_{23}	$\delta(O\text{-}C\text{-}C)$	β_5	
q_{24}	$\delta(N\text{-}C\text{-}C)$	β_6	
q_{25}	$\delta(C\text{-}O\text{-}C)$	β_7	
q_{26}	$\delta(C\text{-}N\text{-}N)$	β_8	
q_{27}	$\delta(N\text{-}N\text{-}N)$	β_9	
q_{28}	$\delta(C\text{-}H)_{methyl}$	$6^{-1/2}(\alpha_1+\alpha_2+\alpha_3+\alpha'_1-\alpha'_2-\alpha'_3)$	
q_{29}	$\delta(C\text{-}H)_{methyl}$	$6^{-1/2}(2\alpha_1-\alpha_2-\alpha_3)$	
q_{30}	$\delta(C\text{-}H)_{methyl}$	$2^{-1/2}(\alpha_2-\alpha_3)$	
q_{31}	$\delta(C\text{-}H)_{methyl}$	$6^{-1/2}(2\alpha'_1-\alpha'_2-\alpha'_3)$	
q_{32}	$\delta(C\text{-}H)_{methyl}$	$2^{-1/2}(\alpha'_2-\alpha'_3)$	
q_{33}	$\delta(C\text{-}C\text{-}C)$	$6^{-1/2}(\alpha_4-\alpha_5+\alpha_6-\alpha_7+\alpha_8-\alpha_9)$	12
q_{34}	$\delta(C\text{-}C\text{-}C)$	$12^{-1/2}(2\alpha_4-\alpha_5-\alpha_6+2\alpha_7-\alpha_8-\alpha_9)$	6a
q_{35}	$\delta(C\text{-}C\text{-}C)$	$2^{-1}(\alpha_5-\alpha_6+\alpha_8-\alpha_9)$	6b
$q_{36\ldots39}$	$\gamma(C\text{-}H)$	$\gamma_1 \ldots \gamma_4$	
q_{40}	$\gamma(C\text{-}N)$	γ_5	
q_{41}	$\gamma(O\text{-}C)$	γ_6	
q_{42}	$\Gamma(CC)$	$6^{-1/2}(\Gamma_1-\Gamma_2+\Gamma_3-\Gamma_4+\Gamma_5-\Gamma_6)$	
q_{43}	$\Gamma(CC)$	$2^{-1}(\Gamma_1+\Gamma_3+\Gamma_4+\Gamma_6)$	

Table S3b *(c*ontinuation).

q_{44}	Γ(CC)	$12^{-1/2}(-\Gamma_1+2\Gamma_2-\Gamma_3-\Gamma_4+2\Gamma_5-\Gamma_6)$
q_{45}	Γ(OC)	Γ_7
q_{46}	Γ(CO)	Γ_8
q_{47}	Γ(CN)	Γ_9
q_{48}	Γ(NN)	Γ_{10}

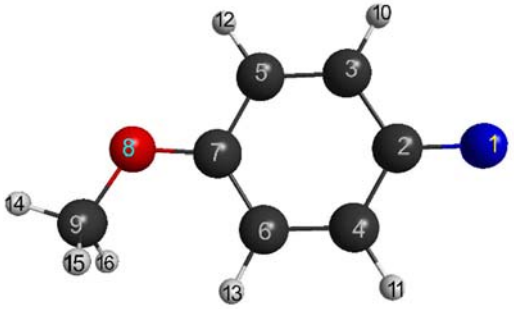

Table S4(continue). Definition of redundant internal coordinates of 4-methoxyphenyl nitrene.

Nº	*Coor.*	*Connectivity*	*type*
1	r_1	9–14	$\nu(C\text{-}H)_{methyl}$
2	r_2	9–15	$\nu(C\text{-}H)_{methyl}$
3	r_3	9-16	$\nu(C\text{-}H)_{methyl}$
4	r_4	3-10	$\nu(C\text{-}H)_{ring}$
5	r_5	4-11	$\nu(C\text{-}H)_{ring}$
6	r_6	5-12	$\nu(C\text{-}H)_{ring}$
7	r_7	6-13	$\nu(C\text{-}H)_{ring}$
8	r_8	7-8	$\nu(C\text{-}O)$
9	r_9	8-9	$\nu(O\text{-}CH_3)$
10	r_{10}	2-1	$\nu(N\text{-}C_{ring})$
11	R_1	2-3	$\nu(C\text{-}C)$
12	R_2	3-5	$\nu(C\text{-}C)$
13	R_3	5-7	$\nu(C\text{-}C)$
14	R_4	7-6	$\nu(C\text{-}C)$
15	R_5	4-2	$\nu(C\text{-}C)$
16	R_6	6-4	$\nu(C\text{-}C)$
17	β_1	[10-3-2]-[10-3-5]	$\delta(C\text{-}H)_{ring}$
18	β_2	[12-5-7]-[12-5-3]	$\delta(C\text{-}H)_{ring}$
19	β_3	[13-6-7]-[13-6-4]	$\delta(C\text{-}H)_{ring}$
20	β_4	[11-4-2]-[11-4-6]	$\delta(C\text{-}H)_{ring}$
21	β_5	[8-7-5]-[8-7-6]	$\delta(O\text{-}C\text{-}C)$
22	β_6	[1-2-3]-[1-2-4]	$\delta(N\text{-}C\text{-}C)$
23	β_7	[9-8-7]	$\delta(C\text{-}O\text{-}C)$

Table S4 (continuation).

24	α_1	[15-9-16]	$\delta(H\text{-}C\text{-}H)_{methyl}$
25	α_2	[14-9-16]	$\delta(H\text{-}C\text{-}H)_{methyl}$
26	α_3	[14-9-15]	$\delta(H\text{-}C\text{-}H)_{methyl}$
27	α'_1	[14-9-8]	$\delta(O\text{-}C\text{-}H)_{methyl}$
28	α'_2	[15-9-8]	$\delta(O\text{-}C\text{-}H)_{methyl}$
29	α'_3	[16-9-8]	$\delta(O\text{-}C\text{-}H)_{methyl}$
30	α_4	[5-7-6]	$\delta(C\text{-}C\text{-}C)_{ring}$
31	α_5	[7-6-4]	$\delta(C\text{-}C\text{-}C)_{ring}$
32	α_6	[6-4-2]	$\delta(C\text{-}C\text{-}C)_{ring}$
33	α_7	[4-2-3]	$\delta(C\text{-}C\text{-}C)_{ring}$
34	α_8	[2-3-5]	$\delta(C\text{-}C\text{-}C)_{ring}$
35	α_9	[3-5-7]	$\delta(C\text{-}C\text{-}C)_{ring}$
36	γ_1	{13-6-7-4}	$\gamma(C\text{-}H)$
37	γ_2	{11-4-6-2}	$\gamma(C\text{-}H)$
38	γ_3	{10-3-2-5}	$\gamma(C\text{-}H)$
39	γ_4	{12-5-3-7}	$\gamma(C\text{-}H)$
40	γ_5	{1-2-4-3}	$\gamma(C\text{-}N)$
41	γ_6	{8-7-5-6}	$\gamma(O\text{-}C)$
42	Γ_1	(5,8)-7-6-(4-13)	$\Gamma(CC)$
43	Γ_2	(7,13)-6-4-(11-2)	$\Gamma(CC)$
44	Γ_3	(6,11)-4-2-(3-1)	$\Gamma(CC)$
45	Γ_4	(4,1)-2-3-(5-10)	$\Gamma(CC)$
46	Γ_5	(2,10)-3-5-(7-12)	$\Gamma(CC)$
47	Γ_6	(3,12)-5-7-(6-8)	$\Gamma(CC)$
48	Γ_7	(5,6)-7-8-(9)	$\Gamma(C\text{-}OCH_3)$
49	Γ_8	(14,15,16)-9-8-(7)	$\Gamma(O\text{-}CH_3)$

Table S4b. Non redundant internal coordinates of 4-methoxyphenyl nitrene.

Coordinate	*Type*	*Definition*	Wilson
$q_1 \ldots q_3$	$\nu(C\text{-}H)_{methyl}$	$r_1 \ldots r_3$	
$q_4 \ldots q_7$	$\nu(C\text{-}H)_{ring}$	$r_4 \ldots r_7$	
q_8	$\nu(C\text{-}O)$	r_8	
q_9	$\nu(O\text{-}CH_3)$	r_9	
q_{10}	$\nu(N\text{-}C_{ring})$	r_{10}	
q_{11}	$\nu(C\text{-}C)$	$6^{-1/2}(R_1+R_2+R_3+R_4+R_5+R_6)$	1
q_{12}	$\nu(C\text{-}C)$	$12^{-1/2}(-R_1+2R_2-R_3-R_4+2R_5-R_6)$	8a
q_{13}	$\nu(C\text{-}C)$	$2^{-1}(-R_1+R_3-R_4+R_6)$	8b
q_{14}	$\nu(C\text{-}C)$	$6^{-1/2}(R_1-R_2+R_3-R_4+R_5-R_6)$	14
q_{15}	$\nu(C\text{-}C)$	$2^{-1}(R_1-R_3-R_4+R_6)$	19a
q_{16}	$\nu(C\text{-}C)$	$2^{-1/2}(R_2-R_5)$	19b
q_{17}	$\delta(C\text{-}H)_{ring}$	$2^{-1}(\beta_1+\beta_2+\beta_3+\beta_4)$	9a
q_{18}	$\delta(C\text{-}H)_{ring}$	$2^{-1}(\beta_1+\beta_2-\beta_3-\beta_4)$	15
q_{19}	$\delta(C\text{-}H)_{ring}$	$2^{-1}(\beta_1-\beta_2+\beta_3-\beta_4)$	3
q_{20}	$\delta(C\text{-}H)_{ring}$	$2^{-1}(\beta_1-\beta_2-\beta_3+\beta_4)$	18a
q_{21}	$\delta(O\text{-}C\text{-}C)$	β_5	
q_{22}	$\delta(N\text{-}C\text{-}C)$	β_6	
q_{23}	$\delta(C\text{-}O\text{-}C)$	β_7	
q_{24}	$\delta(C\text{-}H)_{methyl}$	$6^{-1/2}(\alpha_1+\alpha_2+\alpha_3+\alpha_{э1}-\alpha_{э2}-\alpha_{э3})$	
q_{25}	$\delta(C\text{-}H)_{methyl}$	$6^{-1/2}(2\alpha_1-\alpha_2-\alpha_3)$	
q_{26}	$\delta(C\text{-}H)_{methyl}$	$2^{-1/2}(\alpha_2-\alpha_3)$	
q_{27}	$\delta(C\text{-}H)_{methyl}$	$6^{-1/2}(2\alpha'_1-\alpha'_2-\alpha'_3)$	
q_{28}	$\delta(C\text{-}H)_{methyl}$	$2^{-1/2}(\alpha'_2-\alpha'_3)$	
q_{29}	$\delta(C\text{-}C\text{-}C)$	$6^{-1/2}(\alpha_4-\alpha_5+\alpha_6-\alpha_7+\alpha_8-\alpha_9)$	12
q_{30}	$\delta(C\text{-}C\text{-}C)$	$12^{-1/2}(2\alpha_4-\alpha_5-\alpha_6+2\alpha_7-\alpha_8-\alpha_9)$	6a
q_{31}	$\delta(C\text{-}C\text{-}C)$	$2^{-1}(\alpha_5-\alpha_6+\alpha_8-\alpha_9)$	6b
$q_{32 \ldots 35}$	$\gamma(C\text{-}H)$	$\gamma_1 \ldots \gamma_4$	
q_{36}	$\gamma(C\text{-}N)$	γ_5	
q_{37}	$\gamma(O\text{-}C)$	γ_6	
q_{38}	$\Gamma(CC)$	$6^{-1/2}(\Gamma_1-\Gamma_2+\Gamma_3-\Gamma_4+\Gamma_5-\Gamma_6)$	
q_{39}	$\Gamma(CC)$	$2^{-1}(\Gamma_1+\Gamma_3+\Gamma_4+\Gamma_6)$	
q_{40}	$\Gamma(CC)$	$12^{-1/2}(-\Gamma_1+2\Gamma_2-\Gamma_3-\Gamma_4+2\Gamma_5-\Gamma_6)$	
q_{41}	$\Gamma(CO)$	Γ_7	
q_{42}	$\Gamma(OCH_3)$	Γ_8	

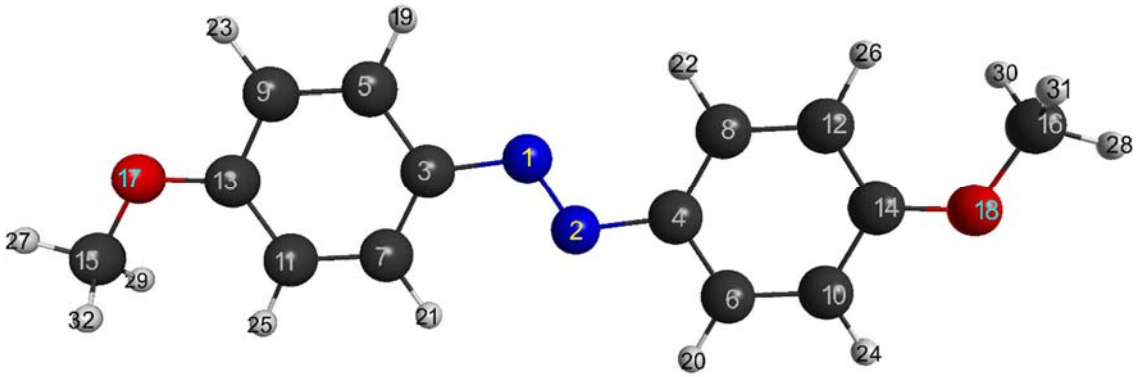

Table S5 (continue). Definition of redundant internal coordinates of 4,4′-dimethoxyazobenzene.

Nº	*Coor.*	*Connectivity*	*type*
1	r_1	15-27	$\nu(C\text{-}H)_{methyl}$
2	r_2	16 -28	$\nu(C\text{-}H)_{methyl}$
3	r_3	15-29	$\nu(C\text{-}H)_{methyl}$
4	r_4	16-30	$\nu(C\text{-}H)_{ring}$
5	r_5	15-32	$\nu(C\text{-}H)_{ring}$
6	r_6	16-31	$\nu(C\text{-}H)_{ring}$
7	r_7	5-19	$\nu(C\text{-}H)_{ring}$
8	r_8	6-20	$\nu(C\text{-}H)_{ring}$
9	r_9	7-21	$\nu(C\text{-}H)_{ring}$
10	r_{10}	8-22	$\nu(C\text{-}H)_{ring}$
11	r_{11}	9-23	$\nu(C\text{-}H)_{ring}$
12	r_{12}	10-24	$\nu(C\text{-}H)_{ring}$
13	r_{13}	11-25	$\nu(C\text{-}H)_{ring}$
14	r_{14}	12-26	$\nu(C\text{-}H)_{ring}$
15	r_{15}	13-17	$\nu(C\text{-}O)$
16	r_{16}	14-18	$\nu(C\text{-}O)$
17	r_{17}	15-17	$\nu(O\text{-}CH_3)$
18	r_{18}	16-18	$\nu(O\text{-}CH_3)$
19	r_{19}	1-2	$\nu(N\text{-}N)$
20	r_{20}	1-3	$\nu(N\text{-}C_{ring})$
21	r_{21}	2-4	$\nu(N\text{-}C_{ring})$
22	R_1	3-5	$\nu(C\text{-}C)$
23	R_2	5-9	$\nu(C\text{-}C)$
24	R_3	9-13	$\nu(C\text{-}C)$
25	R_4	13-11	$\nu(C\text{-}C)$
26	R_5	11-7	$\nu(C\text{-}C)$
27	R_6	7-3	$\nu(C\text{-}C)$

Table S5 (continuation).

28	R_7	4-6	ν(C-C)
29	R_8	6-10	ν(C-C)
30	R_9	10-14	ν(C-C)
31	R_{10}	14-12	ν(C-C)
32	R_{11}	12-8	ν(C-C)
33	R_{12}	8-4	ν(C-C)
34	β_1	[19-5-3]-[19-5-9]	$\delta(C\text{-}H)_{ring}$
35	β_2	[23-9-13]-[23-9-5]	$\delta(C\text{-}H)_{ring}$
36	β_3	[25-11-13]-[25-11-7]	$\delta(C\text{-}H)_{ring}$
37	β_4	[21-7-3]-[21-7-11]	$\delta(C\text{-}H)_{ring}$
38	β_5	[20-6-4]-[20-6-10]	$\delta(C\text{-}H)_{ring}$
39	β_6	[24-10-14]-[24-10-6]	$\delta(C\text{-}H)_{ring}$
40	β_7	[26-12-14]-[26-12-8]	$\delta(C\text{-}H)_{ring}$
41	β_8	[22-8-4]-[22-8-12]	$\delta(C\text{-}H)_{ring}$
42	β_9	[17-13-9]-[17-13-11]	δ(O-C-C)
43	β_{10}	[18-14-10]-[18-14-12]	δ(O-C-C)
44	β_{11}	[1-3-5]-[1-3-7]	δ(N-C-C)
45	β_{12}	[2-4-6]-[2-4-8]	δ(N-C-C)
46	β_{13}	[3-1-2]	δ(N-N-C)
47	β_{14}	[1-2-4]	δ(N-N-C)
48	β_{15}	[15-17-13]	δ(C-O-C)
49	β_{16}	[16-18-14]	δ(C-O-C)
50	α_1	[27-15-29]	$\delta(H\text{-}C\text{-}H)_{methyl}$
51	α_2	[29-15-32]	$\delta(H\text{-}C\text{-}H)_{methyl}$
52	α_3	[32-15-27]	$\delta(H\text{-}C\text{-}H)_{methyl}$
53	α'_1	[27-15-17]	$\delta(O\text{-}C\text{-}H)_{methyl}$
54	α'_2	[29-15-17]	$\delta(O\text{-}C\text{-}H)_{methyl}$
55	α'_3	[32-15-17]	$\delta(O\text{-}C\text{-}H)_{methyl}$
56	α_4	[28-16-30]	$\delta(H\text{-}C\text{-}H)_{methyl}$
57	α_5	[30-16-31]	$\delta(H\text{-}C\text{-}H)_{methyl}$

Table S5 (continuation).

58	α_6	[31-16-28]	$\delta(H\text{-}C\text{-}H)_{methyl}$
59	α'_4	[28-16-18]	$\delta(O\text{-}C\text{-}H)_{methyl}$
60	α'_5	[30-16-18]	$\delta(O\text{-}C\text{-}H)_{methyl}$
61	α'_6	[31-16-18]	$\delta(O\text{-}C\text{-}H)_{methyl}$
62	α_7	[7-3-5]	$\delta(C\text{-}C\text{-}C)_{ring}$
63	α_8	[3-5-9]	$\delta(C\text{-}C\text{-}C)_{ring}$
64	α_9	[5-9-13]	$\delta(C\text{-}C\text{-}C)_{ring}$
65	α_5	[9-13-11]	$\delta(C\text{-}C\text{-}C)_{ring}$
66	α_{10}	[13-11-7]	$\delta(C\text{-}C\text{-}C)_{ring}$
67	α_{11}	[11-7-3]	$\delta(C\text{-}C\text{-}C)_{ring}$
68	α_{12}	[8-4-6]	$\delta(C\text{-}C\text{-}C)_{ring}$
69	α_{13}	[4-6-10]	$\delta(C\text{-}C\text{-}C)_{ring}$
70	α_{14}	[6-10-14]	$\delta(C\text{-}C\text{-}C)_{ring}$
71	α_{15}	[10-14-12]	$\delta(C\text{-}C\text{-}C)_{ring}$
72	α_{16}	[14-12-8]	$\delta(C\text{-}C\text{-}C)_{ring}$
73	α_{17}	[12-8-4]	$\delta(C\text{-}C\text{-}C)_{ring}$
74	γ_1	{19-5-4-9}	$\gamma(C\text{-}H)$
75	γ_2	{20-6-4-10}	$\gamma(C\text{-}H)$
76	γ_3	{21-7-11-3}	$\gamma(C\text{-}H)$
77	γ_4	{22-8-12-4}	$\gamma(C\text{-}H)$
78	γ_5	{23-9-13-5}	$\gamma(C\text{-}H)$
79	γ_6	{24-10-14-6}	$\gamma(C\text{-}H)$
80	γ_7	{25-11-13-7}	$\gamma(C\text{-}H)$
81	γ_8	{26-12-14-8}	$\gamma(C\text{-}H)$
82	γ_9	{1-3-7-5}	$\gamma(C\text{-}N)$
83	γ_{10}	{2-4-8-6}	$\gamma(C\text{-}N)$
84	γ_{11}	{17-13-9-11}	$\gamma(O\text{-}C)$
85	γ_{12}	{18-14-10-12}	$\gamma(O\text{-}C)$
86	Γ_1	(1,7)-3-5-(19,9)	$\Gamma(CC)$
87	Γ_2	(19,3)-5-9-(23,13)	$\Gamma(CC)$
88	Γ_3	(23,5)-9-13-(17,11)	$\Gamma(CC)$
89	Γ_4	(17,9)-13-11-(25,7)	$\Gamma(CC)$
90	Γ_5	(25,13)-11-7-(21,3)	$\Gamma(CC)$
91	Γ_6	(21,11)-7-3-(1,5)	$\Gamma(CC)$

Table S5 (continuation).

92	Γ_7	(2,8)-4-6-(20,10)	Γ(CC)
93	Γ_8	(20,4)-6-10-(24,14)	Γ(CC)
94	Γ_9	(24,6)-10-14-(18,12)	Γ(CC)
95	Γ_{10}	(18,10)-14-12-(26,8)	Γ(CC)
96	Γ_{11}	(26,14)-12-8-(22 ,4)	Γ(CC)
97	Γ_{12}	(22,12)-8-4-(2,6)	Γ(CC)
99	Γ_{13}	(3)-1-2-(4)	Γ(NN)
100	Γ_{14}	(2)-1-3-(7,5)	Γ(CN)
101	Γ_{15}	(1)-2-4-(8,6)	Γ(CN)
102	Γ_{16}	(15)-17-13-(11,9)	Γ(C-OCH_3)
103	Γ_{17}	(16)-18-14-(12,10)	Γ(C-OCH_3)
104	Γ_{18}	(13)-17-15-(27,29,32)	Γ(O-CH_3)
105	Γ_{19}	(14)-18-16-(28,30,31)	Γ(O-CH_3)

Table S5b. Non redundant internal coordinates of 4,4′-dimethoxyazobenzene.

Coordinate	*Type*	*Definition*	Wilson
$q_1 \ldots q_6$	ν(C-H)$_{methyl}$	$r_1 \ldots r_6$	
$q_7 \ldots q_{14}$	ν(C-H)$_{ring}$	$r_7 \ldots r_{14}$	
$q_{15,16}$	ν(C-O)	$r_{15,16}$	
$q_{17,18}$	ν(O-CH$_3$)	$r_{17,18}$	
q_{19}	ν(N-N)	r_{19}	
$q_{20,21}$	ν(N-C$_{ring}$)	r_{20}, r_{21}	
$q_{22,23}$	ν(C-C)	$6^{-1/2}(R_{1,7}+R_{2,8}+R_{3,9}+R_{4,10}+R_{5,11}+R_{6,12})$	1
$q_{24,25}$	ν(C-C)	$12^{-1/2}(-R_{1,7}+2R_{2,8}-R_{3,9}-R_{4,10}+2R_{5,11}-R_{6,12})$	8a
$q_{26,27}$	ν(C-C)	$2^{-1}(-R_{1,7}+R_{3,9}-R_{4,10}+R_{6,12})$	8b
$q_{28,29}$	ν(C-C)	$6^{-1/2}(R_{1,7}-R_{2,8}+R_{3,9}-R_{4,10}+R_{5,11}-R_{6,12})$	14
$q_{30,31}$	ν(C-C)	$2^{-1}(R_{1,7}-R_{3,9}-R_{4,10}+R_{6,12})$	19a
$q_{32,33}$	ν(C-C)	$2^{-1/2}(R_{2,8}-R_{5,11})$	19b
$q_{34,35}$	δ(C-H)$_{ring}$	$2^{-1}(\beta_{1,5}+\beta_{2,6}+\beta_{3,7}+\beta_{4,8})$	9a
$q_{36,37}$	δ(C-H)$_{ring}$	$2^{-1}(\beta_{1,5}+\beta_{2,6}-\beta_{3,7}-\beta_{4,8})$	15
$q_{38,39}$	δ(C-H)$_{ring}$	$2^{-1}(\beta_{1,5}-\beta_{2,6}+\beta_{3,7}-\beta_{4,8})$	3
$q_{40,41}$	δ(C-H)$_{ring}$	$2^{-1}(\beta_{1,5}-\beta_{2,6}-\beta_{3,7}+\beta_{4,8})$	18a
$q_{42,43}$	δ(O-C-C)	$\beta_{9,10}$	
$q_{44,45}$	δ(N-C-C)	$\beta_{11,12}$	
$q_{46,47}$	δ(N-N-C)	$\beta_{13,14}$	
$q_{48,49}$	δ(C-O-C)	$\beta_{15,16}$	
$q_{50,51}$	δ(C-H)$_{methyl}$	$6^{-1/2}(\alpha_{1,4}+\alpha_{2,5}+\alpha_{3,6}+\alpha'_{1,4}-\alpha'_{2,5}-\alpha'_{3,6})$	
$q_{52,53}$	δ(C-H)$_{methyl}$	$6^{-1/2}(2\alpha_{1,4}-\alpha_{2,5}-\alpha_{3,6})$	
$q_{54,55}$	δ(C-H)$_{methyl}$	$2^{-1/2}(\alpha_{2,5}-\alpha_{3,6})$	
$q_{56,57}$	δ(C-H)$_{methyl}$	$6^{-1/2}(2\alpha'_{1,4}-\alpha'_{2,5}-\alpha'_{3,6})$	
$q_{58,59}$	δ(C-H)$_{methyl}$	$2^{-1/2}(\alpha'_{2,5}-\alpha'_{3,6})$	
$q_{60,61}$	δ(C-C-C)	$6^{-1/2}(\alpha_{7,13}-\alpha_{8,14}+\alpha_{9,15}-\alpha_{10,16}+\alpha_{11,17}-\alpha_{12,18})$	12
$q_{62,63}$	δ(C-C-C)	$12^{-1/2}(2\alpha_{7,13}-\alpha_{8,14}-\alpha_{9,15}+2\alpha_{10,16}-\alpha_{11,17}-\alpha_{12,18})$	6a
$q_{64,65}$	δ(C-C-C)	$2^{-1}(\alpha_{8,14}-\alpha_{9,15}+\alpha_{11,17}-\alpha_{12,18})$	6b
$q_{66 \ldots 73}$	γ(C-H)	γ_1,γ_8	
$q_{74,75}$	γ(C-N)	$\gamma_{9,10}$	
$q_{76,77}$	γ(O-C)	$\gamma_{11,12}$	
$q_{78,79}$	Γ(CC)	$6^{-1/2}(\Gamma_{1,7}-\Gamma_{2,8}+\Gamma_{3,9}-\Gamma_{4,10}+\Gamma_{5,11}-\Gamma_{6,12})$	
$q_{80,81}$	Γ(CC)	$2^{-1}(\Gamma_{1,7}+\Gamma_{3,9}+\Gamma_{4,10}+\Gamma_{6,12})$	
$q_{82,83}$	Γ(CC)	$12^{-1/2}(-\Gamma_{1,7}+2\Gamma_{2,8}-\Gamma_{3,9}-\Gamma_{4,10}+2\Gamma_{5,11}-\Gamma_{6,12})$	
q_{84}	Γ(NN)	Γ_{13}	
$q_{85,86}$	Γ(CN)	$\Gamma_{14,15}$	
$q_{87,88}$	Γ(C-OCH$_3$)	$\Gamma_{16,17}$	
$q_{89,90}$	Γ(O-CH$_3$)	$\Gamma_{18,19}$	

Table S6 (continue). Assignment of the CAS-SCF vibrational frequencies of 4-methoxyphenyl azide.[a,b]

N°	*Freq*(cm^{-1})	*PED*[c]	Assignment
1	3364	93 q_7	ν(C-H)$_{ring}$
2	3354	52 q_4 + 46 q_6	ν(C-H)$_{ring}$
3	3337	47 q_4 + 53 q_6	ν(C-H)$_{ring}$
4	3325	94 q_5	ν(C-H)$_{ring}$
5	3268	91 q_1	ν(C-H)$_{methyl}$
6	3207	50 q_2 + 50 q_3	ν(C-H)$_{methyl}$
7	3152	46 q_2 + 46 q_3	ν(C-H)$_{methyl}$
8	2191	20 q_{11}+ 79 q_{12}	ν(N-N)
9	1758	36 q_{14}+15 q_{19}+26 q_{34}+18 q_{35}	8a
10	1712	62 q_{15}+ 13 q_{19}	8b
11	1657	35 q_{17}+ 14 q_{18}+ 32 q_{22}	19a+18a
12	1630	89 q_{29}	δ(C-H)$_{methyl}$
13	1622	93 q_{30}	δ(C-H)$_{methyl}$
14	1606	85 q_{28}	δ(C-H)$_{methyl}$
15	1541	49 q_{18}+ 35 q_{20}	19b+15
16	1440	76 q_{21}	3
17	1415	28 q_8+ 12 q_{10}+ 10 q_{13}	ν(C-O)
18	1384	12q_8+ 26q_{10}+22 q_{11}+12q_{22}+10q_{33}	ν(N-C$_{ring}$)
19	1316	52 q_{31}	δ(C-H)$_{methyl}$
20	1282	95 q_{32}	δ(C-H)$_{methyl}$
21	1277	21 q_{14}+55q_{19}	9a
22	1247	53 q_{16}+ 14 q_{20}	14
23	1216	27 q_{11}+ 10 q_{17}+ 13 q_{33}	ν(N-N)
24	1173	34 q_{16}+ 45 q_{18}+ 10 q_{20}	19b+15
25	1157	28 q_9+ 12 q_{13}+ 26 q_{16}	ν(O-CH$_3$)
26	1090	44 q_{17}+ 20 q_{18}+ 28 q_{33}	12
27	997	34 q_{38}+26 q_{39}+ 26 q_{44}	γ(C-H)
28	953	26 q_{36}+26 q_{37}+21q_{42}+12q_{43}+11q_{44}	γ(C-H)
29	894	22 q_{13}+ 28 q_{34}+ 18 q_{35}	1
30	861	28 q_{38}+ 30 q_{39}+ 23 q_{43}	γ(C-H)
31	832	41 q_{36}+ 37 q_{37}	γ(C-H)
32	828	20 q_{34}+ 16 q_{35}+ 10 q_{26}	6a
33	733	19 q_{40}+ 23 q_{41}+ 40 q_{42}	Γ(CC)
34	688	74 q_{35}	6b
35	674	12 q_{27}+ 34 q_{34}	δ(N-N-N)
36	575	96 q_{48}	Γ(NN)
37	545	23 q_{23}+ 35 q_{25}+ 35 q_{34}	δ(C-O-C)
38	544	37 q_{40}+ 39 q_{41}	γ(C-N)
39	450	10 q_{27}+31 q_{34}+ 41 q_{35}	δ(N-N-N)
40	444	19 q_{43}+ 56 q_{44}	Γ(CC)

Table S6 (continuation).

41	381	16 q_{40}+ 10 q_{41}+ 29 q_{42}+ 23 q_{43}	Γ(CC)
42	366	13 q_{24}+ 43 q_{34}+ 22 q_{45}	δ(N-C-C)
43	263	87 q_{46}	Γ(O-CH_3)
44	257	35 q_{23}+ 28 q_{25}+ 12 q_{26}+ 11 q_{27}	δ(O-C-C)
45	165	61 q_{43}	Γ(CC)
46	132	24 q_{24}+ 42 q_{26}+ 20 q_{27}	δ(C-N-N)
47	67	65 q_{45}+ 31 q_{46}	Γ(OC_{ring})
48	53	80 q_{47}	Γ(CN)

[a]According with the potential energy distribution matrix (Refs. 32, 33).
[b]Active space: (12e,11o); ANO-RCC[C,N,O/4*s*3*p*2*d*1*f*| |H/3*s*2*p*1*d*].
[c]Potential energy distribution.

Table S7. Assignment of the CAS-SCF vibrational frequencies of triplet 4-methoxyphenyl nitrene.[a,b]

N°	*Freq*(cm^{-1})	*PED*[c]	Assignment
1	3365	85 q_7	ν(C-H)$_{ring}$
2	3353	45 q_4 + 53 q_6	ν(C-H)$_{ring}$
3	3339	85 q_5	ν(C-H)$_{ring}$
4	3335	53 q_4 + 45 q_6	ν(C-H)$_{ring}$
5	3273	90 q_1	ν(C-H)$_{methyl}$
6	3214	50 q_2 + 50 q_3	ν(C-H)$_{methyl}$
7	3156	46 q_2 + 46 q_3	ν(C-H)$_{methyl}$
8	1696	28 q_{12}+ 15 q_{19}+ 21 q_{30}+ 13 q_{31}	8a
9	1636	46 q_{13}+15 q_{17}+ 12 q_{31}	8b
10	1630	86 q_{25}	δ(C-H)$_{methyl}$
11	1623	93 q_{26}	δ(C-H)$_{methyl}$
12	1611	72 q_{24}	δ(C-H)$_{methyl}$
13	1590	16 q_{15}+ 45 q_{18}+ 13 q_{24}	9b
14	1516	41 q_{16}+ 30 q_{20}	19b
15	1415	35 q_8	ν(C-O)
16	1393	18 q_{13}+ 44 q_{17}	9a
17	1324	21 q_{10}+ 14 q_{19}+ 24 q_{27}	ν(N-C$_{ring}$)
18	1310	17 q_{10}+ 12 q_{19}+ 35 q_{27}	δ(C-H)$_{methyl}$
19	1282	95 q_{28}	δ(C-H)$_{methyl}$
20	1228	65 q_{14}	14
21	1203	14 q_{10}+ 14 q_{12}+ 18 q_{19} + 14 q_{30}	3
22	1176	23 q_{14}+ 53 q_{16}+ 20 q_{20}	19b
23	1151	38 q_9+ 13 q_{30}	ν(O-CH$_3$)
24	1047	39 q_{15}+ 27 q_{29}	19a
25	991	28 q_{34}+ 32 q_{35}	γ(C-H)
26	962	31 q_{32}+ 22 q_{33}	γ(C-H)
27	868	45 q_{11}+21 q_{30}+ 15 q_{31}	1
28	846	32 q_{34}+ 18 q_{35}+ 16 q_{39}	γ(C-H)
29	818	24 q_{32}+ 33 q_{33}+ 14 q_{34}+ 15 q_{39}	γ(C-H)
30	778	21 q_8+ 21 q_{29}	12
31	728	22 q_{36}+ 27 q_{37}+ 29 q_{38}	γ(C-N)
32	669	76 q_{31}	6b
33	555	24 q_{23}+ 43 q_{30}	6a + δ(C-O-C)
34	527	33 q_{36}+ 43 q_{37}	γ(O-C)
35	445	40 q_{30}+ 47 q_{31}	6b
36	427	15 q_{39}+ 55 q_{40}	Γ(CC)
37	390	53 q_{22}+ 14 q_{23}	δ(N-C-C)
38	352	32 q_{38}+ 21 q_{39}	Γ(CC)
39	257	80 q_{42}	Γ(OCH$_3$)
40	246	44 q_{21}+ 34 q_{23}	δ(O-C-C)
41	151	60 q_{39}+ 20 q_{41}	Γ(CC)
42	69	66 q_{41}+ 32 q_{42}	Γ(CO)

[a]According with the potential energy distribution matrix (Refs. 34, 35).
[b]Active space: (12e,11o); ANO-RCC[C,N,O/4*s*3*p*2*d*1*f*| |H/3*s*2*p*1*d*].
[c]Potential energy distribution.

Table S8. Assignment of the CAS-SCF vibrational frequencies of $1^1A''$ 4-methoxyphenyl nitrene.[a,b]

N°	*Freq*(cm^{-1})	*PED*[c]	Assignment
1	3365	43 q_5+ 55 q_7	ν(C-H)$_{ring}$
2	3358	72 q_4 + 26 q_7	ν(C-H)$_{ring}$
3	3346	56 q_5 + 26 q_6	ν(C-H)$_{ring}$
4	3337	23 q_4 + 73 q_6	ν(C-H)$_{ring}$
5	3275	90 q_1	ν(C-H)$_{methyl}$
6	3217	50 q_2 + 50 q_3	ν(C-H)$_{methyl}$
7	3158	45 q_2 + 45 q_3	ν(C-H)$_{methyl}$
8	1707	28 q_{12}+ 15 q_{17}+ 25 q_{30}+ 17 q_{31}	8a
9	1650	32 q_{10}+17 q_{15}+ 23 q_{20}	ν(N-C$_{ring}$)
10	1630	88 q_{25}	δ(C-H)$_{methyl}$
11	1623	93 q_{26}	δ(C-H)$_{methyl}$
12	1610	18 q_{16}+ 52 q_{24}	δ(C-H)$_{methyl}$
13	1598	28 q_{16}+ 18 q_{24}	19b
14	1537	27 q_{10}+ 11 q_{19}+ 26 q_{20}	18a
15	1494	13 q_{16}+ 12 q_{18}+ 44 q_{19}	3
16	1420	39 q_8+ 15 q_{20}+ 10 q_{27}	ν(C-O)
17	1346	24 q_{13}+ 14 q_{14}+ 21 q_{18}+ 24 q_{19}	8b+3
18	1322	17 q_{10}+ 12 q_{19}+ 35 q_{27}	δ(C-H)$_{methyl}$
19	1281	95 q_{28}	δ(C-H)$_{methyl}$
20	1259	23 q_{14}+ 32 q_{17}	9a
21	1217	45 q_{14}+ 13 q_{16}+ 11 q_{17}	14
22	1175	23 q_{14}+ 39 q_{16}+ 39 q_{18}	19b+15
23	1153	59 q_9	ν(O-CH$_3$)
24	1029	36 q_{15}+ 51 q_{29}	12
25	979	19 q_{34}+ 47 q_{35}+ 23 q_{40}	γ(C-H)
26	952	50 q_{32}+ 12 q_{33}+ 12 q_{38}+ 17 q_{40}	γ(C-H)
27	818	50 q_{11}+12 q_{15}+ 14 q_{30}	1
28	800	16 q_{33}+ 41 q_{34}+ 23 q_{36}	γ(C-H)
29	768	18 q_8+ 20 q_{15}+ 17 q_{29}	19a+12
30	744	39 q_{33}+ 13 q_{34}+ 15 q_{35}+ 15 q_{39}	γ(C-H)
31	683	21 q_{32}+ 12 q_{35}+ 22 q_{36}+ 17 q_{38}	γ(C-N)
32	640	20 q_{13}+ 68 q_{31}	6b
33	547	12 q_{21}+ 24 q_{23}+ 45 q_{30}	6a + δ(C-O-C)
34	462	31 q_{36}+ 41 q_{37}+ 11 q_{30}	γ(O-C)
35	442	39 q_{30}+ 47 q_{31}	6a+6b
36	397	32 q_{22}+ 11 q_{23}+ 34 q_{30}+ 12 q_{31}	δ(N-C-C)
37	364	12 q_{32}+ 12 q_{33}+ 10 q_{35}+ 45 q_{40}	Γ(CC)
38	294	15 q_{37}+ 16 q_{38}+ 13 q_{39}+ 43 q_{42}	Γ(OCH$_3$)
39	244	47 q_{21}+ 33 q_{23}	δ(O-C-C)
40	231	17 q_{37}+ 25 q_{38}+ 16 q_{39}+ 29 q_{42}	Γ(CC)
41	110	14 q_{38}+ 27 q_{39}+ 33 q_{41}	Γ(CC)
42	62	61 q_{41}+ 32 q_{42}	Γ(CO)

[a]According with the potential energy distribution matrix (Refs. 34, 35).
[b]Active space: (12e,11o); ANO-RCC[C,N,O/4*s*3*p*2*d*1*f*| |H/3*s*2*p*1*d*].
[c]Potential energy distribution.

Table S9. Assignment of the CAS-SCF vibrational frequencies of $1^1A'$ 4-methoxyphenyl nitrene.[a,b]

N°	*Freq*(cm^{-1})	*PED*[c]	Assignment
1	3372	24 q_5+ 74 q_7	$\nu(C\text{-}H)_{ring}$
2	3362	71 q_4 + 27 q_6	$\nu(C\text{-}H)_{ring}$
3	3351	75 q_5 + 24 q_7	$\nu(C\text{-}H)_{ring}$
4	3343	28 q_4 + 72 q_6	$\nu(C\text{-}H)_{ring}$
5	3287	89 q_1	$\nu(C\text{-}H)_{methyl}$
6	3236	50 q_2 + 50 q_3	$\nu(C\text{-}H)_{methyl}$
7	3170	45 q_2 + 45 q_3	$\nu(C\text{-}H)_{methyl}$
8	1707	35 q_{12}+ 15 q_{17}+ 22 q_{30}+ 15 q_{31}	8a
9	1667	57 q_{13}+14 q_{19}+ 23 q_{20}	8b
10	1629	70 q_{25}	$\delta(C\text{-}H)_{methyl}$
11	1625	93 q_{26}	$\delta(C\text{-}H)_{methyl}$
12	1624	21 q_{24}+ 18 q_{25}	$\delta(C\text{-}H)_{methyl}$
13	1602	25 q_{20}+ 57 q_{24}	18a
14	1534	47 q_{16}+ 28 q_{18}	19b
15	1421	37 q_8+ 13 q_{20}	$\nu(C\text{-}O)$
16	1396	12 q_{13}+ 58 q_{19}	3
17	1337	42 q_{10}	$\nu(N\text{-}C_{ring})$
18	1321	25 q_{14}+ 23 q_{27}	$\delta(C\text{-}H)_{methyl}$
19	1287	62 q_{14}+ 19 q_{16}+ 37 q_{17}	14
20	1282	95 q_{28}	$\delta(C\text{-}H)_{methyl}$
21	1235	13 q_{10}+ 15 q_{12}+ 37 q_{17}	9a
22	1185	38 q_{16}+ 47 q_{18}	15
23	1152	72 q_9	$\nu(O\text{-}CH_3)$
24	1078	41 q_{15}+ 14 q_{20}+ 44 q_{29}	12
25	1042	49 q_{34}+ 18 q_{35}+ 16 q_{38}	$\gamma(C\text{-}H)$
26	1038	14 q_{32}+ 46 q_{33}+ 22 q_{40}	$\gamma(C\text{-}H)$
27	889	40 q_{11}+26 q_{30}+ 19 q_{31}	1
28	889	20 q_{32}+ 30 q_{35}+ 14 q_{37}	$\gamma(C\text{-}H)$
29	846	45 q_{32}+ 14 q_{33}+ 20 q_{35}	$\gamma(C\text{-}H)$
30	802	17 q_8+ 21 q_{15}+ 22 q_{29}+ 12 q_{30}	
31	783	16 q_{36}+ 37 q_{37}+ 27 q_{38}	$\gamma(O\text{-}C)$
32	674	15 q_{13}+ 70 q_{31}	6b
33	569	27 q_{21}+ 27 q_{36}+ 48 q_{37}	$\gamma(N\text{-}C)$
34	562	13 q_{21}+ 26 q_{23}+ 42 q_{30}	$\delta(C\text{-}O\text{-}C)$
35	454	36 q_{30}+ 48q_{31}	6a
36	427	15 q_{39}+ 61 q_{40}	$\Gamma(CC)$
37	410	43 q_{22}+ 28 q_{30}	$\delta(N\text{-}C\text{-}C)$
38	312	29 q_{38}+ 30 q_{39}+ 18 q_{42}	$\Gamma(CC)$
39	254	44 q_{21}+ 42 q_{23}	$\delta(O\text{-}C\text{-}C)$
40	237	20 q_{38}+ 17 q_{39}+ 49 q_{42}	$\Gamma(OCH_3)$
41	127	20 q_{36}+ 15 q_{38}+ 36 q_{41}	$\Gamma(CC)$
42	80	44 q_{41}+ 18 q_{42}	$\Gamma(CO)$

[a]According with the potential energy distribution matrix (Refs. 32, 33).
[b]Active space: (12e,11o); ANO-RCC[C,N,O/4*s*3*p*2*d*1*f*| |H/3*s*2*p*1*d*].
[c]Potential energy distribution.

Table S10 (continue). Assignment of the CAS-SCF vibrational frequencies of 4,4′-DMAB.[a,b]

N°	*Freq*(cm^{-1})	*PED*[c]	Assignment
1	3376	40 q_9+ 40 q_{10}	ν(C-H)$_{ring}$
2	3376	40 q_9+ 40 q_{10}	ν(C-H)$_{ring}$
3	3355	39 q_{13}+ 39 q_{14}	ν(C-H)$_{ring}$
4	3355	39 q_{13}+ 39 q_{14}	ν(C-H)$_{ring}$
5	3352	21 q_7+ 21 q_8+ 28 q_{11}+ 28 q_{12}	ν(C-H)$_{ring}$
6	3352	21 q_7+ 21 q_8+ 28 q_{11}+ 28 q_{12}	ν(C-H)$_{ring}$
7	3335	28 q_7+ 28 q_8+ 22 q_{11}+ 22 q_{12}	ν(C-H)$_{ring}$
8	3335	28 q_7+ 28 q_8+ 22 q_{11}+ 22 q_{12}	ν(C-H)$_{ring}$
9	3269	47 q_1+ 47 q_2	ν(C-H)$_{methyl}$
10	3269	47 q_1+ 47 q_2	ν(C-H)$_{methyl}$
11	3211	25 q_3+ 25 q_4+ 25 q_5+ 25 q_6	ν(C-H)$_{methyl}$
12	3211	25 q_3+ 25 q_4+ 25 q_5+ 25 q_6	ν(C-H)$_{methyl}$
13	3154	23 q_3+ 23 q_4+ 23 q_5+ 23 q_6	ν(C-H)$_{methyl}$
14	3154	23 q_3+ 23 q_4+ 23 q_5+ 23 q_6	ν(C-H)$_{methyl}$
15	1748	26 q_{24}+ 23 q_{25}	8a
16	1746	29 q_{24}+ 29 q_{25}	8a
17	1720	28 q_{26}+ 28 q_{27}	8b
18	1710	34 q_{26}+ 34 q_{27}	8b
19	1675	64 q_{19}	ν(N-N)
20	1659	23 q_{40}+ 23 q_{41} +16 q_{30}+16 q_{31}	18a+19a
21	1652	22 q_{40}+ 22 q_{41} +14 q_{30}+14 q_{31}	18a+19a
22	1630	33 q_{34}+ 33 q_{35}	9a
23	1630	33 q_{34}+ 33 q_{35}	9a
24	1622	35 q_{52}+ 35 q_{53}	δ(C-H)$_{methyl}$
25	1622	35 q_{52}+ 35 q_{53}	δ(C-H)$_{methyl}$
26	1606	44 q_{50}+ 44 q_{51}	δ(C-H)$_{methyl}$
27	1606	43 q_{50}+ 43 q_{51}	δ(C-H)$_{methyl}$
28	1536	25 q_{32}+ 25 q_{33}+ 17 q_{36}+ 17 q_{37}	19b
29	1536	24 q_{32}+ 24 q_{33}+ 16 q_{36}+ 16 q_{37}	19b+15
30	1436	38 q_{38}+ 38 q_{39}	3
31	1429	39 q_{38}+ 39 q_{39}	3
32	1406	21 q_{15}+ 21 q_{16}	ν(O-C$_{ring}$)
33	1402	21 q_{15}+ 21 q_{16}	ν(O-C$_{ring}$)
34	1338	25 q_{20}+ 25 q_{21}	ν(N-C$_{ring}$)
35	1326	14 q_{56}+ 14 q_{57}	δ(C-H)$_{methyl}$
36	1317	23 q_{56}+ 23 q_{57}	δ(C-H)$_{methyl}$
37	1294	12 q_{56}+ 12 q_{57}	δ(C-H)$_{methyl}$
38	1282	48 q_{58}+ 48 q_{59}	δ(C-H)$_{methyl}$
39	1282	48 q_{58}+ 48 q_{59}	δ(C-H)$_{methyl}$
40	1264	14 q_{28}+ 14 q_{29}+ 18 q_{34}+ 18 q_{35}	9a
41	1258	25 q_{34}+ 25 q_{35}	9a
42	1243	24 q_{28}+ 24 q_{29}	14
43	1241	23 q_{28}+ 23 q_{29}	14
44	1173	16 q_{28}+ 16 q_{29}+ 16 q_{32}+ 16 q_{33}	19b
45	1170	18 q_{28}+ 18 q_{29}+ 22 q_{32}+ 22 q_{33}	19b
46	1164	13 q_{17}+ 13 q_{18}+ 18 q_{32}+ 18 q_{33}	ν(O-CH$_3$)
47	1164	25 q_{17}+ 25 q_{18}	ν(O-CH$_3$)

Table S10(continuation).

48	1088	21 q_{30}+ 21 q_{31}+ 22 q_{60}+ 22 q_{61}	19a+12
49	1088	21 q_{30}+ 21 q_{31}+ 22 q_{60}+ 22 q_{61}	19a +12
50	1003	11 q_{67}+ 17 q_{82}+ 17 q_{83}	γ(C-H)
51	1003	11 q_{67}+ 17 q_{82}+ 17 q_{83}	γ(C-H)
52	992	13 q_{68}+ 13 q_{60}+ 14 q_{78}+ 14 q_{79}	γ(C-H)
53	989	13 q_{68}+ 13 q_{60}+ 14 q_{78}+ 14 q_{79}	γ(C-H)
54	988	11 q_{22}+ 11 q_{23}+ 20 q_{46}+ 20 q_{47}	δ(N-N-C)
55	891	27 q_{22}+ 27 q_{23}	1
56	876	17 q_{70}+ 15 q_{71}	γ(C-H)
57	869	19 q_{70}+ 17 q_{71}	γ(C-H)
58	849	13 q_{22}+ 13 q_{23}+ 11 q_{62}+ 11 q_{63}	1
59	847	18 q_{72}+ 16 q_{73}+ 21 q_{80}+ 14 q_{81}	γ(C-H)
60	846	18 q_{72}+ 16 q_{73}+ 21 q_{80}+ 14 q_{81}	γ(C-H)
61	800	11 q_{15}+ 11 q_{16}+ 13 q_{60}+ 13 q_{61}	12
62	758	11 q_{76}+ 11 q_{77}+ 15 q_{78}+ 15 q_{79}	γ(O-C)
63	741	12 q_{76}+ 12 q_{77}+ 18 q_{78}+ 18 q_{79}	γ(O-C)
64	695	31 q_{64}+ 31 q_{65}	6b
65	682	38 q_{64}+ 38 q_{65}	6b
66	638	17 q_{62}+ 17 q_{63}	6a
67	588	9q_{44}+ 9q_{45}+ 7 q_{46}+ 9 q_{46}+ 13 q_{64}+ 13 q_{65}	δ(N-C-C)+δ(N-N-C)
68	585	16 q_{74}+ 14 q_{75}+ 17 q_{76}+ 18 q_{77}	γ(C-N)
69	542	18 q_{74}+ 15 q_{75}+ 18 q_{76}+ 18 q_{77}	γ(C-N)
70	531	12 q_{48}+ 12 q_{49}+ 11 q_{62}+ 11 q_{63}	δ(C-O-C)
71	522	15 q_{42}+ 15 q_{43}+ 16 q_{48}+ 16 q_{49}	δ(C-O-C)
72	450	26 q_{82}+ 26 q_{83}	Γ(CC)
73	450	20 q_{80}+ 14 q_{81}+ 15 q_{82}+ 15 q_{83}	Γ(CC)
74	443	19 q_{62}+ 19 q_{63}	6a
75	443	12 q_{78}+ 12 q_{79}	Γ(CC)
76	383	13 q_{74}+ 11 q_{75}+ 13 q_{78}+ 13 q_{79}+ 11 q_{80}	Γ(CC)
77	325	19 q_{44}+ 19 q_{45}+ 17 q_{48}+ 17 q_{49}	δ(N-C-C)
78	274	42 q_{89}+ 42 q_{90}	Γ(O-CH_3)
79	263	49 q_{89}+ 40 q_{90}	Γ(O-CH_3)
80	263	20 q_{42}+ 20 q_{43}+ 20 q_{48}+ 20 q_{49}	δ(O-C-C)
81	249	10 q_{42}+ 10 q_{43}+ 13 q_{62}+ 13 q_{63}	δ(O-C-C)
82	204	11 q_{80}+ 21 q_{84}	Γ(CC)
83	190	13 q_{80}+ 29 q_{85}+ 12 q_{86}	Γ(NN)
84	161	16 q_{44}+ 16 q_{45}	δ(N-C-C)
85	88	24 q_{66}+ 20 q_{85}+ 13 q_{87}+ 13 q_{88}	Γ(CN)
86	77	30 q_{87}+ 30 q_{88}+ 14 q_{89}+ 13 q_{90}	Γ(C-OCH_3)
87	59	13 q_{66}+ 21 q_{87}+ 21 q_{88}+ 12 q_{89}+ 12 q_{90}	Γ(C-OCH_3)
88	58	15 q_{44}+ 15 q_{45}+ 28 q_{46}+ 28 q_{47}	δ(N-N-C)+δ(N-C-C)
89	33	35 q_{66}+ 14 q_{80}+ 10 q_{84}	Γ(CC)
90	20	50 q_{85}+ 20 q_{86}	Γ(CN)

[a]According with the potential energy distribution matrix (Refs. 32, 33).
[b]Active space: (16e,15o); ANO-RCC[C,N,O/4*s*3*p*2*d*1*f*| |H/3*s*2*p*1*d*].
[c]Potential energy distribution.

Table S11. Assignment of the calculated Resonance Raman spectrum of singlet 4-methoxyphenyl nitrene and 4-methoxyohenyl azide.[a,b]

CAS-SCF[c]	I_{rel}(320)	I_{rel}(340)	Assignment
1707	100	80	8a
1650	76	100	ν(N-C_{ring})
1259	14	12	9a
1029	23	34	12
CAS-SCF[d]	I_{rel}(320)	I_{rel}(340)	Assignment
1707	100	40	8a
1629	4	11	δ(C-H)$_{methyl}$
1624	19	27	δ(C-H)$_{methyl}$
1602	4	22	18a
1421	11	65	ν(C-O)
1337	28	44	ν(N-C_{ring})
1235	23	11	9a
1152	19	7	ν(O-CH_3)
889	27	100	1
562	44	13	δ(C-O-C)
454	85	34	6a
CAS-SCF[e]	I_{rel}(320)	I_{rel}(340)	Assignment
1758	12	39	8a
1712	6	10	8b
1657	3	11	19a+18a
1415	100	100	ν(C-O)
1384	14	76	ν(N-C_{ring})
1277	15	18	9a
1247	54	33	14
1216	31	24	ν(N-N)
1173	49	31	19b+15
1157	18	12	ν(O-CH_3)
894	87	54	1
828	22	14	6a

[a]According with the potential energy distribution matrix (Refs. 32, 33).
[b]Active space: (12e,11o); ANO-RCC[C,N,O/4*s*3*p*2*d*1*f*| |H/3*s*2*p*1*d*]; state average: (4 states A', 4 states A"); IPEA=0.25. [c]1^1A" 4-methoxyphenyl nitrene. [d]1^1A' 4-methoxyphenyl nitrene. [e]4-methoxyohenyl azide.

Table S12. Vertical transition energies in eV of triplet 4-methoxyphenyl nitrene (MS-CASPT2), C_s-symmetry.[a]

Transition	VE[b]	*OS*[c]	*Configuration*[d]
1^3A"→2^3A"	3.16	0.20-02	29% $n_\sigma(N)^1\ n_\pi(N)^0\ \pi_2^*(ring)^1$ 36% $n_\sigma(N)^1\ \pi_2(ring)^1\ n_\pi(N)^2$
1^3A"→3^3A"	3.31	0.84-02	43% $n_\sigma(N)^1\ n_\pi(N)^2\ \pi_3\ (ring)^1$ 24% $n_\sigma(N)^1\ \pi_3(ring)^1\ n_\pi(N)^0$
1^3A"→4^3A"	4.80	0.61-03	73% $n_\sigma(N)^1\ \pi_2(ring)^1\ n_\pi(N)^1\ \pi_2^*(ring)^1$
1^3A"→1^3A'	4.22	0.11-04	76% $n_\sigma(N)^2\ n_\pi(N)^1\ \pi_3(ring)^1$
1^3A"→2^3A'	4.24	0.83-02	76% $n_\sigma(N)^1\ \sigma(CN)^1\ n_\pi(N)^2$
1^3A"→3^3A'	4.85	0.19-04	68% $n_\sigma(N)^2\ \pi_2\ (ring)^1\ n_\pi(N)^1$
1^3A"→4^3A'	5.88	0.00	72% $n_\sigma(N)^2\ \pi_2\ (ring)^1\ n_\pi(N)^0\ \pi_2^*(ring)^1$

[a]Four state-average CAS-SCF reference wavefunction: (12e, 11o). ANO-RCC, (C,N)[4s3p2d1f]/(H)[3s2p1d].
[b]Vertical excitation energy in eV.
[c]Oscillator strength, dipole-length formula.
[d]MS-CASPT2 electron configurations. Only contributions greater than 15% are included. Only orbitals with different occupation to the ground state are given.

Table S13. Vertical transition energies in eV of 1^1A" 4-methoxyphenyl nitrene (MS-CASPT2), C_s-symmetry.[a]

Transition	VE[b]	*OS*[c]	*Configuration*[d]
1^1A"→2^1A"	2.52	0.93-03	34% $n_\sigma(N)^1$ $n_\pi(N)^0$ π_2*(ring)^1 40% $n_\sigma(N)^1$ $\pi_2(ring)^1$ $n_\pi(N)^0$
1^1A"→3^1A"	3.04	0.30-02	44% $n_\sigma(N)^1$ $\pi_3(ring)^1$ $n_\pi(N)^2$ 32% $n_\sigma(N)^1$ $n_\pi(N)^0$ π_2*(ring)^1
1^1A"→4^1A"	4.67	0.22-02	25% $n_\sigma(N)^1$ $n_\pi(N)^2$ $\pi_1(ring)^1$ 28% $n_\sigma(N)^1$ $n_\pi(N)^1$ $\pi_1(ring)^1$ π_2*(ring)^1
1^1A"→1^1A'	0.47	0.0	83% $n_\sigma(N)^2$ $n_\pi(N)^0$
1^1A"→2^1A'	1.92	0.0	71% $n_\sigma(N)^2$ $n_\pi(N)^2$
1^1A"→3^1A'	4.55	0.51-04	53% $n_\sigma(N)^2$ $n_\pi(N)^1$ $\pi_2(ring)^1$
1^1A"→4^1A'	4.95	0.0	63% $n_\sigma(N)^2$ π_3 $(ring)^1$ $n_\pi(N)^1$

[a]Four state-average CAS-SCF reference wavefunction: (12e, 11o). ANO-RCC, (C,N)[4s3p2d1f]/(H)[3s2p1d].
[b]Vertical excitation energy in eV.
[c]Oscillator strength, dipole-length formula.
[d]MS-CASPT2 electron configurations. Only contributions greater than 15% are included. Only orbitals with different occupation to the ground state are given.

Table S14. Vertical transition energies in eV of $1^1A'$ 4-methoxyphenyl nitrene (MS-CASPT2), C_s-symmetry.[a]

Transition	VE[b]	*OS*[c]	*Configuration*[d]
$1^1A' \rightarrow 2^1A'$	1.42	0.16-01	74% $n_\sigma(N)^0\ n_\pi(N)^2$
$1^1A' \rightarrow 3^1A'$	3.97	0.26-01	55% $n_\sigma(N)^2\ \pi_2(ring)^1\ n_\pi(N)^1$
$1^1A' \rightarrow 4^1A'$	4.39	0.3829	60% $n_\sigma(N)^2\ \pi_3(ring)^1\ n_\pi(N)^1$
$1^1A' \rightarrow 1^1A''$	-0.30	0.0	84% $n_\sigma(N)^1\ n_\pi(N)^1$
$1^1A' \rightarrow 2^1A''$	2.13	0.24-04	33% $n_\sigma(N)^1\ \pi_2^*(ring)^1$ 40% $n_\sigma(N)^1\ \pi_2(ring)^1\ n_\pi(N)^2$
$1^1A' \rightarrow 3^1A''$	2.50	0.00	46% $n_\sigma(N)^1\ n_\pi(N)^1$ 31% $n_\sigma(N)^1\ \pi_3^*(ring)^1$
$1^1A' \rightarrow 4^1A''$	3.97	0.0	18% $n_\sigma(N)^2\ \pi_1(ring)^1\ n_\pi(N)^2$ 34% $n_\sigma(N)^1\ \pi_1(ring)^1\ n_\pi(N)^1\ \pi_2^*(ring)^1$

[a]Four state-average CAS-SCF reference wavefunction: (12e, 11o). ANO-RCC, (C,N)[4s3p2d1f]/(H)[3s2p1d].
[b]Vertical excitation energy in eV.
[c]Oscillator strength, dipole-length formula.
[d]MS-CASPT2 electron configurations. Only contributions greater than 15% are included. Only orbitals with different occupation to the ground state are given.

Table S15. Vertical transition energies in eV of 4,4′-dimethoxyazobenzene C_{2h} (MS-CASPT2).

Species	VE[a]	*OS*[b]	*Configuration*[c]
$1A_g \rightarrow 2A_g$	4.05	0.0000	24% $\pi_3(b_g)^1\pi^*(NN)^1$
$1A_g \rightarrow 3A_g$	4.76	0.0000	22% HF 25% $\pi_3(b_g)^1\pi^*(NN)^1$
$1A_g \rightarrow 1B_g$	2.02	0.0000	75% $\sigma(NN)^1\pi^*(NN)^1$
$1A_g \rightarrow 2B_g$	4.22	0.0000	42% $\sigma(NN)^1\pi_2^*(b_g)^1\pi^*(NN)^2$
$1A_g \rightarrow 3B_g$	5.00	0.0000	22% $\sigma(NN)^1\pi_2(b_g)^1$ 17% $\sigma(NN)^1\pi_3^*(b_g)^1$
$1A_g \rightarrow 1A_u$	4.10	0.72-03	22% $\sigma(NN)^1\pi_3(a_u)^1\pi^*(NN)^2$ 23% $\sigma(NN)^1\pi_2^*(a_u)^1$
$1A_g \rightarrow 2A_u$	4.49	0.45-03	15% $\sigma(NN)^1\pi_3(a_u)^1\pi^*(NN)^2$ 18% $\sigma(NN)^1\pi_2^*(b_g)^1$
$1A_g \rightarrow 3A_u$	5.75	0.0000	25% $\sigma(NN)^1\pi^*_2(b_g)^1\pi^*(NN)^1\pi_2(a_u)^1$ 22% $\sigma(NN)^1\pi_2(b_g)^1\pi^*(NN)^1\pi_2^*(a_u)^1$
$1A_g \rightarrow 1B_u$	2.83	0.4982	73% $\pi_3(b_g)^1\pi_3(a_u)^1\pi^*(NN)^2$
$1A_g \rightarrow 2B_u$	4.04	0.16-01	26% $\pi_2(a_u)^1\pi^*(NN)^1$ 17% $\pi_3(a_u)^1\pi^*_2(b_g)^1$
$1A_g \rightarrow 3B_u$	6.20	0.21-02	15% $\pi(NN)^1\pi^*(NN)^1$

[a]Vertical excitation energy in eV.
[b]Oscillator strength.
[c]MS-CASPT2 electron configurations. Only contributions greater than 15% are included. Only orbitals with different occupation to the ground state are given.

Capítulo III – Resultados (III).

Comment on "Elucidation of the charge-transfer SERS selection rules by considering the excited state properties and the role of electrode potential" by M. Mohammadpour, M. H. Khodabandeh, L. Visscher and Z. Jamshidi, *Phys. Chem. Chem. Phys*. 2017, 19, 7833. †

D. Aranda, J. Román-Pérez, I. López-Tocón, J. Soto, F. Avila* and J. C. Otero.

The differences between alternative approaches for quantifying the complex effect of the electronic structure of charged metal-molecule hybrids in SERS (the so-called chemical enhancement mechanism) are highlighted. The discussion is focused on the predictions obtained by using different methodological tools for modelling the role of the electrode potential in the SERS relative intensities. Finite electric fields are used in the commented paper for this purpose, but we have found some inconsistences in the results and the method for calculating the Raman intensities is not made sufficiently clear, which prevents the assessment of the results.

3.3.1. Introduction.

Mohammadpour et *al*.[1] have recently published a theoretical work studying he effect of the electrode potential on surface-enhanced Raman scattering (SERS). The method consists of calculating resonance Raman (RR) intensities (eqn (3) in ref. 1) with the parameters provided by DFT electronic structure calculations (BP86 and BHandHLYP/Def2-TZVP) of a system containing a pyridine (Py) bounded to a Ag_6 silver cluster (Figure S1, ESI†). The role of the electrode potential has been taking into account in the calculations by applying finite electric fields ranging between -0.009 and +0.003 a.u. The main achievement is the general agreement between the theoretically estimated relative intensities (Figure 1a) and the experimental SERS previously recorded by us[2,3] at different electrode potentials (Figure 1b), however we have detected inconsistences when different sets of results are labelled with respect to the sign of the respective electric fields.

3.3.2. Methodology.

Electronic calculations were performed using Density Functional Theory (DFT) at the same level than the authors of ref. 1 did. For spectra calculations, several approaches are given in the subsequent sections and discussed therein.

3.3.3. Results and discussion.

3.3.3.1. Labelling calculated results according to the electric field.

The potential of zero charge (PZC, V_{PZC}) of a polycrystalline silver electrode lies at *ca.* -0.8/-0.9V.[4] Therefore, more positive potentials than PZC (called +V henceforth) induce positive excess of charge in the metal surface, which favors the amount of transferred charge from the nitrogen of pyridine to the silver cluster ($\Delta q_{s0}^{cluster}$), giving a more stable Ag-Py surface complex with larger binding energy (ΔE_b) and shorter $N_{Py\text{-}Ag}$ distance ($R_{N\text{-}Ag}$) (Table 2 in ref. 1). The situation is just the opposite with electrode potentials more negative than PZC (-V). The last column of this Table 2[1] labelled -0.009 a.u. summarizes $\Delta q_{s0}^{cluster}$, ΔE_b and $R_{N\text{-}Ag}$ values corresponding undoubtedly to the +V case. The same column contains also the calculated SERS intensities I_k of modes 6a, 1, 12, 9a and 8a amounting to 67.4, 100, 5.2, 117.8 and 6.3, respectively, but this spectrum (Figure 1a, top) characterized by the strong enhancement of mode 9a, has been correlated with the SERS recorded at -1.2V, (Figure 1b), *i.e.*, to -V. Therefore, calculated properties related to

positive +V ($\Delta q_{s0}^{cluster}$, $\Delta E_b$and $R_{\text{N-Ag}}$) and negative -V (I_k, SERS spectrum) potentials are labelled with the same negative field of -0.009 a.u. Finally, some misplaced results cannot be relocated in the table given that, for instance, +0.009 and +0.006 a.u. columns are missing.

The described inconsistences in labelling incompatible sets of results under the same sign of the electric field are schematized in Figures S2a and b for negative and positive fields, respectively (see note 5). This is one of the key issues of this comment and raises the question of whether the calculated SERS are displayed suitably in Figure 1a or should be drawn in the reverse order, losing the apparent agreement with the experimental behavior.

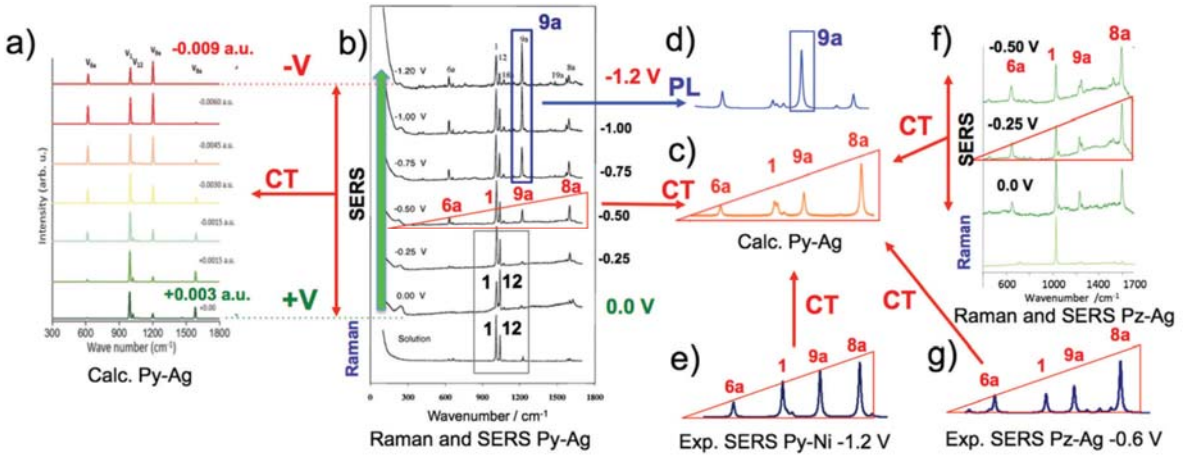

Figure 1. (a) Effect of the electric field on the calculated SERS-CT intensities of pyridine (Py) reported by Mohmmadpour.[1] (b) Raman and SERS spectra of Py recorded on Ag at different electrode potentials (*vs.* Ag/AgCl/KCl saturated electrode) under 514.5 nm excitation.[2] (c) Calculated pre-resonance intensities of Py with the first charge transfer (CT)[8] and (d) the plasmon-like (PL)[3] excited states of [Py-Ag_n]q complexes. (e) SERS of Py adsorbed on Ni at -1.2 V.[10] (f) SERS of pyrazine (Pz) recorded under the same conditions as (b).[8] (g) SERS of Pz recorded on Ag at -0.6 V.[11]

3.3.3.2. Calculating SERS intensities: single-state vs. multi-state approaches.

Only the authors are in a position to address this issue given that the methodology used for predicting the resonant Raman I_k of each particular mode k at different electrode potentials is not clearly specified in the article. In the simplest case, only a single S_0-S_i resonant transition can be considered in the calculation (SS: single-state $I_{k,\text{SS}}$) and the so obtained state, spectrum must be assigned to the corresponding excited state, I_{k,S_i}. it is stated in the article that the intensities have been calculated according to eqn (3)[1] which takes into account the weighted contributions of a set of electronic states S_n (MS: multi-state $I_{k,\text{MS}}$). Therefore, it seems that the results correspond to MS calculations, but this

approach requires the selection of a particular photon energy E_L and the homogeneous linewidths Γ_n, which are not specified in the paper. Each MS spectrum should be assigned to the selected E_L value $I_{k,\mathrm{E_L}}$, which prevents the use of a single S_0-S_i transition in labelling the results as is carried out in Figure2 of ref. 1. This is also the case for the most relevant results of the article summarized in Figure 6 and 7 of ref. 1 showing the dependence of the so-called "SERS-CT" spectra on the electric field. According to the article, "SERRS-CT" refers to a single $S_0 - S_{CT_1}$ metal-to-molecule charge transfer transition up to the selected CT1 state, called CT_{A1} henceforth, which suggest a single-state approach. The reading of the almost simultaneously published and very related ref. 6 and 7 does not solve this apparent contradiction. A possible explanation for this would be to carry out an MS calculation with E_L matching the energy of a particular S_i state $E_{L,\mathrm{CT_{A1}}}$ which could then be used for labelling the $I_{k,\mathrm{E_L}}$ multi-state intensities: $I_{k,\mathrm{E_L=S}_i} \equiv I_{k,\mathrm{S}_i}$. The electric field tunes the energies of the states, especially the CT ones, and therefore, each multi-state "SERS-CT" spectrum of Figure 1a must be calculated at a different $E_{L,\mathrm{CT_{A1}}}$ corresponding to the CT_{A1} energy at the particular field (see Figure 2). Anyway, the method used for calculating the intensities should be clearly specified.

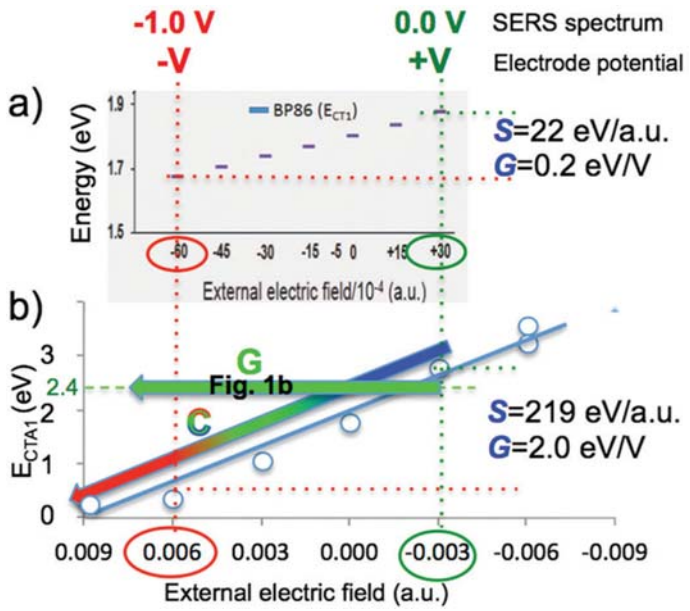

Figure 2. Effect of the electric field on the calculated 8a) BP86/Def2-TZVP energies of the CT excitation reported in ref. 1 and (b) TD-BP86/Def2-TZVP vertical energies of the CT_{A1} state (see the text). Note that the sign of the electric fields is reversed in both figures.

Finally, the trivial alternative that "SERS-CT" spectra in Figure 1a are dealing with single-state $S_0 - S_{\mathrm{CT_{A1}}}$ transitions seems to be discarded as explained below.

3.3.3.3. Calculating SERS intensities: resonance *vs*. pre-resonance conditions.

MS or SS spectra can be obtained under either resonance Raman (RR: eqn (11) in ref. 6) or pre-resonance Raman (preRR: eqn (10) in ref. 6) conditions. In both cases the calculated intensities depend on the calculated dimensionless displacements Δ_{k,S_i} which are reported in Table 1 of ref. 1 (with k = 6a, 1, 12, 9a and 8a modes) for some S_i states (with S_i = IC (intracluster), CT_{A1}/CT_2 (charge transfer) or IC + CT (combination)) of the unperturbed Ag-Py complex. The effect of the electric field on Δ_{k,S_i}can be seen in Table S3 of ref. 1 (with k = 6a, 9a and 8a modes) and it seems to correspond to the $S_{CT_{A1}}$ state, although this is not sufficiently clear either.

The last set of $\Delta_{k,CT_{A1}}$ would have to be closely related to the "SERS-CT" set of spectra of Figure 1a which shows a complex behavior. It is evident that such spectra have not been calculated in pre-resonance with this single CT_{A1} state (SS-preRR) given that, in this case, the intensity $I_{k,CT_{A1}}^{preRR(1)}$ of a mode with wavenumber ω_k is only dependent of the respective $\Delta_{k,CT_{A1}}$ and be roughly estimated through the simple relationship:

$$I_{k,CT_{A1}}^{preRR(1)} \sim {\Delta_{k,S_i}}^2 \omega_k^2 \quad (1)$$

According to this equation, $I_{k,CT_{A1}}^{preRR(1)}$ intensities of modes 6a, 9a and 8a should not be dependent at all on the electric field given that the respective $\Delta_{k,CT_{A1}}$ are almost insensitive to the electric field (Table S3 in ref. 1). We have simulated the corresponding $I_{k,CT_{A1}}^{preRR(1)}$ spectra from the reported $\Delta_{k,CT_{A1}}$ and all of them (Figure. S3, ESI†) look like the calculated CT spectrum previously reported by us[8] shown in Figure 1c. This spectrum has been calculated in pre-resonance with a single CT state of a Py molecule bonded to linear stick-line silver cluster with different sizes and charges $[Ag_{n=2,3,5,7} - Py]^{q=0,\pm1}$ using long-range corrected DFT methods.[8] The effect of the electrode potential is simulated in our case through $q_{eff} = q/n$, a parameter which quantifies the effective average charge of $[Ag_n]^q$ clusters and mimics the surface excess of charge of the metal which is tuned by the electrode potential.[9]

Therefore, single-state $S_0 - S_{CT_{A1}}$ pre-resonance calculations are unable to account for the "SERS-CT" intensities of Figure 1a where the spectra are very sensitive to the field being dominated by the strong bands of modes 1 and 9a.

Single state-resonance Raman calculations could account for the complex behavior shown in Figure 1a since the intensity a mode k, I_{k,S_i}^{RR}, is now dependent on E_L, on the respective Δ_{k,S_i} as well as on the $\Delta_{j\neq k,S_i}$ of the remaining totally symmetric modes.[6] But $I_{k,CT_{A1}}^{RR}$ intensities cannot be reproduced from the incomplete set of data summarized in Table S3 of ref. 1 which is restricted to 6a, 9a and 8a fundamentals.

All the SERS in Figure 1b are compared in the commented article[1] with a single series of calculated spectra called "SERS-CT" (Figure 1a), which explains the title of the paper. However, our methodology based on charged clusters requires the use of three different contributions, non-resonant (modes 1 and 12 at more positive potentials), charge-transfer (CT) (modes 6a, 1, 9a, and 8a at medium potentials, Figure 1c) and plasmon-like (PL called IC in ref. 1) (mode 9a at very negative potentials, Figure 1d) in order to account for the experimental SERS enhancement. [3,8] On the other hand, the relative intensities in these three figures are very similar to the calculated on in Figure S3 (ESI†) and agree with the triangle-shaped SS-preRR calculated spectra of Pz or Py reported by us.[3,8] (Figure 1c). Therefore, the question arises as to whether the presence of CT resonances in the SERS of benzene-like molecules is characterized by the triangle-shaped enhancement of vibrations 6a, 1, 9a and 8a, or, conversely, is the solely responsible for the complex behavior shown in Figure 1b.

3.3.3.4. Dependence of the energies of the selected CT state $E_{CT_{A1}}$ on the electrode potential.

There is another issue in ref. 1 concerning the dependence of the DFT calculated energies of the metal-to-molecule charge transfer process on the electric field. The data shown in Figure 4 (left) of ref. 1 have been re-drawn in Figure 2a. They are called CT excitation and seem to be obtained by considering exclusively the dependence of the Fermi level (E_F) of the metal on the applied field (Figure 4 (right) or ref. 1). It increases at +V given that positive potentials +B and -V to negative electric fields, respectively. The slope S in Figure 2a quantifies the effectiveness of the applied field in tuning the energy of the CT excitations amounting to *ca*. S = 22 eV a.u.$^{-1}$. The effectiveness of the electrode potential (G) can be derived from the dependence on the field (S) by correlating the calculated

spectra at -0.006 and +0.003 a.u. to the experimental SERS recorded at -1.0 and 0.0 V, respectively as has been carried out in Fig 1a and b. The so obtained energy gain is only G=0.2 eV·V^{-1} which does not account for the huge efficiency of the electrode potential in tuning CT processes observed in electrochemical SERS or reflectance experiments amounting up to ca. G = 3-5 eV V^{-1}.[12] We have recalculated the TD-BP86/Def2-TZVP vertical energies of the first twenty excited states of the same Py-Ag complex used in ref. 1 under applied fields by using the Gaussian 09 program package.[13] Table S1 and Figure S4 (ESI†) summarize the results for the two low-lying CT_{B1} and CT_{A1} states, respectively. The energies of the CT_{A1} state ($E_{CT_{A1}}$) can be compared in Figure 2 with the CT excitations of ref. 1 where it can be seen that the sign convention of the fields is just the opposite[5] than in ref. 1. The slope of CT states is now some ten times higher ($G_{CT_{A1}}$= 2.0, $G_{CT_{B1}}$=1.8 eV V^{-1} *vs*. 0.2 eV V^{-1}), in better agreement with the experimental evidence. The origin of this unexpected energy gain G is discussed in ref. 12 and should be very relevant in molecular electronics given that G controls the involvement of molecular levels (resonant mechanism)[14] in the electronic transport.[12,15]

G = 1 eV V^{-1} is the expected value from simple electrochemical considerations. Very large G implies that the effect of changing the laser excitation energy E_L in SERS spectroscopy is not at all equivalent to modify the electrode potential, given that both variables are related to different Y- and X-axes in Figure 2, respectively. The SERS spectra of Py in Figure 1b have been obtained under E_L = 2.4 eV excitation (514.5 nm, green Ar^+ laser line) at different electrode potentials, *i.e.*, along the green arrow "G" of Figure 2b. Therefore, they can be only compared with theoretical results obtained using a multi-state approach at fixed E_L of 2.4 eV for instance. If the energy of the CT state is very dependent on the electric field, the complete series of multi-state spectra cannot be called "SERS-CT". Only some particular spectra of the series could be called "SERS-CT" if the weighted contribution of the S_0-S_{CT} excitation dominates the multi-state spectrum at a particular electric field. For this, the two following conditions have to be fulfilled: (i) $E_{CT_{A1}}$ matches or is sufficiently close to EL (resonant condition). (ii) The $S_0 - S_{CT_{A1}}$ electronic transition is strong enough.

A series of spectra calculated at different fields along the colored arrow "C" of Figure 2b correspond to either single-state calculations carried out for each one of the CT_{A1} states ($I_{k,CT_{A1}}$, Figure S3, ESI†)[8] or to multi-state calculations where the E_L equals the corresponding $E_{CT_{A1}}$ energy at each field ($I_{k,E_L=CT_{A1}}$). Both kinds of calculations ca be

called SERS-CT but neither of them can be directly compared to the experimental SERS of Figure 1b.

This is why it is so important to dispel the doubts about the methodology used in ref. 1 for calculating the SERS intensities.

3.3.4. Conclusions.

It is to be stressed that, once the raised questions have been clarified, very valuable conclusions can be extracted from the methodology followed by Mohammadpour *et al*.[1] in order to improve theoretical tools to detect and quantify the presence of the so-called chemical enhancement mechanism of SERS, which is an unresolved and controversial challenge.[16] Uniform finite fields or charged metallic clusters are rough approaches to real electrochemical interfaces but can provide invaluable support for correlating the subtle electronic structure of charged metal-molecule systems and SERS spectra. This would make SERS spectroscopy a powerful technique to gain insight about key processes in electrochemistry, heterogeneous adsorption, catalysis or electron transport through molecular junctions.

3.3.5. References and notes.

1. M. Mohammadpour, M. H. Khodabandeh, L. Visscher and Z. Jamshidi, *Phys. Chem. Chem. Phys.*, **2017**, 19, 7833.
2. J. F. Arenas, I. López Tocón, J. C. Otero and J. I. Marcos, *J. Phys. Chem.*, **1996**, 100, 9254.
3. J. Román-Pérez, I. López-Tocón, J. L. Castro, J. F. Arenas, J. Soto and J. C. Otero, *Phys. Chem. Chem. Phys.*, **2015**, 17, 2326.
4. J. T. Hupp, D. Larkin and M. J. Weaver, Surf. Sci., 1983, 125, 429; Y.-X. Chen and A. Otto, *J. Raman Spectrosc.*, **2005**, 36, 736.
5. The sign of the electric field depends on the arbitrary orientation of the system with respect to the Cartesian axes and on how each particular program introduces the field. Gaussian13 warns that care must be taken regarding the sign convention when interpreting the results (http://gaussian.com/field/) (see Figure S1, ESI†). Mohammadpour et al.1 use two programs, Gaussian 03 and ORCA 3.0, for estimating different properties what complicates the situation. Furthermore, the sign convention in finite field calculations has been modified in ORCA 4.0 with respect to the 3.0.3version (see page XXII of the ORCA 4.0 manual, https://orcaforum.cec.mpg.de/OrcaManual.pdf).
6. M. Mohammadpour and Z. Jamshidi, *J. Phys. Chem. C*, **2017**, 121, 2858.
7. M. Mohammadpour and Z. Jamshidi, *J. Chem. Phys.*, **2016**, 144, 194302.
8. F. Avila, C. Ruano, I. López-Tocón, J. F. Arenas, J. Soto and J. C. Otero, *Chem. Commun.*, **2011**, 47, 4213.
9. F. Avila, D. J. Fernández, J. F. Arenas, J. C. Otero and J. Soto, *Chem. Commun.*, **2011**, 47, 4210.
10. Q. J. Huang, X. F. Lin, Z. L. Yang, J. W. Hu and Z. Q. Tian, *J. Electroanal. Chem.*, **2004**, 563, 121.
11. Q. J. Huang, J. L. Yao, B. W. Mao, R. A. Gu and Z. Q. Tian, *Chem. Phys. Lett.*, **1997**, 271, 101.
12. J. Román-Pérez, C. Ruano, S. P. Centeno, I. López-Tocón, J. F. Arenas, J. Soto and Juan C. Otero, *J. Phys. Chem. C*, **2014**, 118, 2718 and references therein.
13. M. J. Frisch, et al., *Gaussian 09, Revision A.02*, Gaussian Inc., **2009**.
14. J. C. Cuevas and E. Scheer. *Molecular electronics: an introduction to theory and experiment*. World Scientific, Singapore, **2010**.

15. D. Aranda, I. López-Tocón, J. Soto, J. C. Otero and F. Avila, *Phys. Chem. Chem. Phys.*, **2016**, 18, 27179.
16. M. Moskovits, *Phys. Chem. Chem. Phys.*, **2013**, 15, 5301.

Supporting Information

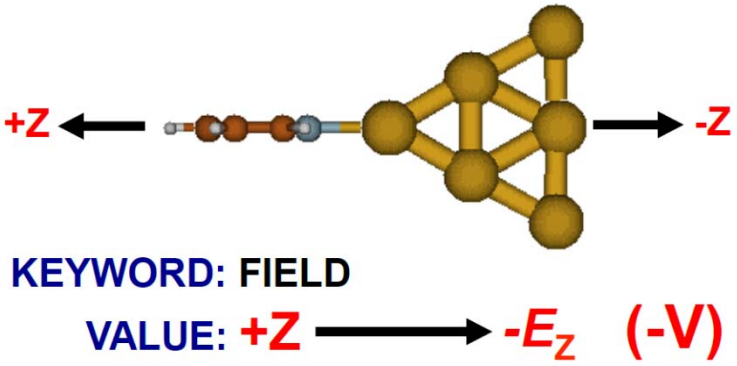

Figure S1. Py-Ag_6 perpendicular complex used in ref. 1 for modeling the pyridine bonded to the silver electrode, with the molecule pointing towards positive +z-axis. Gaussian09 sign convention for finite fields: When a +Z value is introduced in the FIELD keyword an electric field is applied in the opposite direction -E_z, *i.e.*, pointing towards the metal, which corresponds to negative electrode potentials (-V).

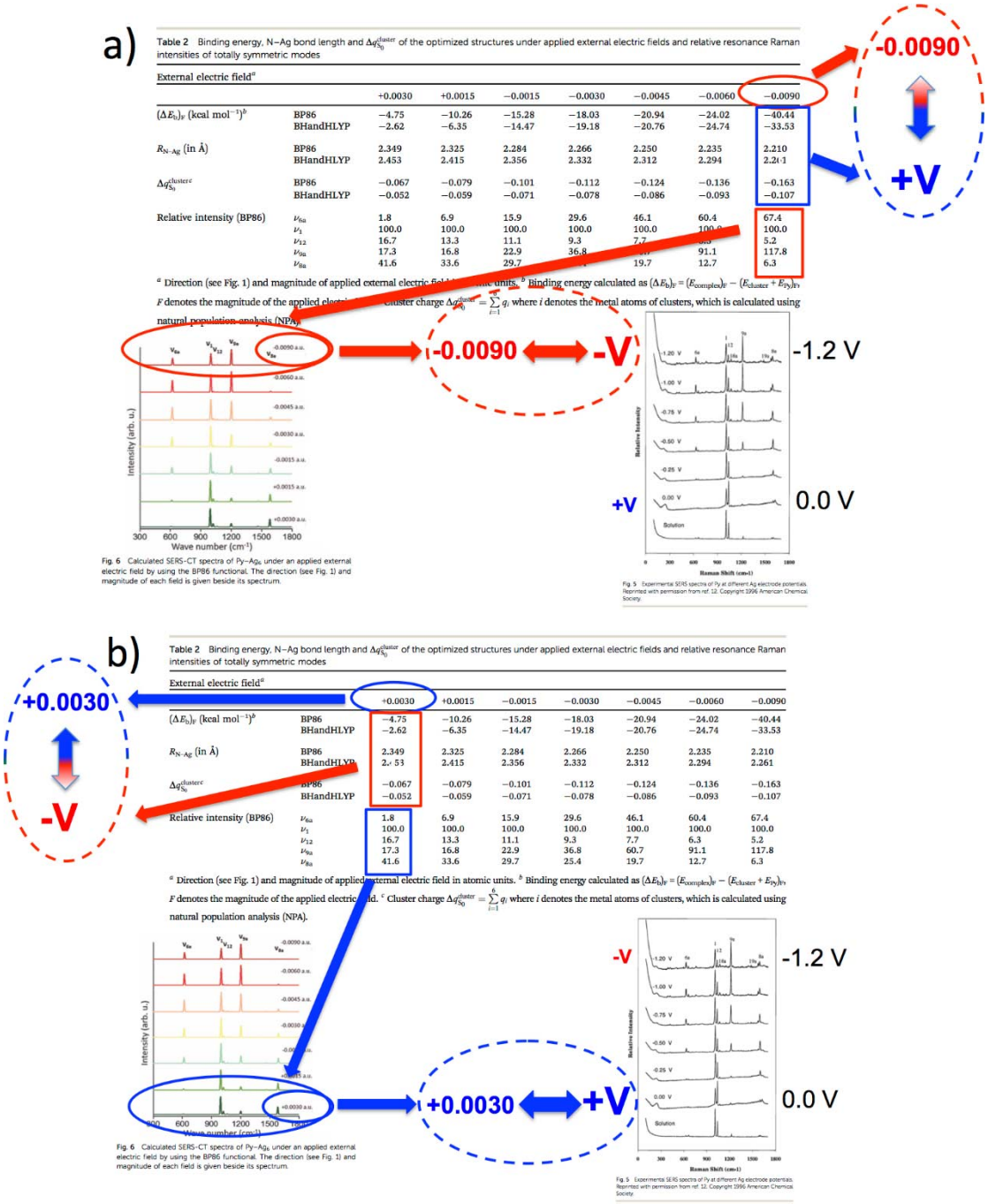

Figure S2. Schemes showing how set of results reported in Table 2 of ref. 1 corresponding to positive (+V) and negative (-V) electrode potentials are both labelled as a) negative (-0.0090 a.u.) or b) positive electric fields (+0.0030 a.u.).

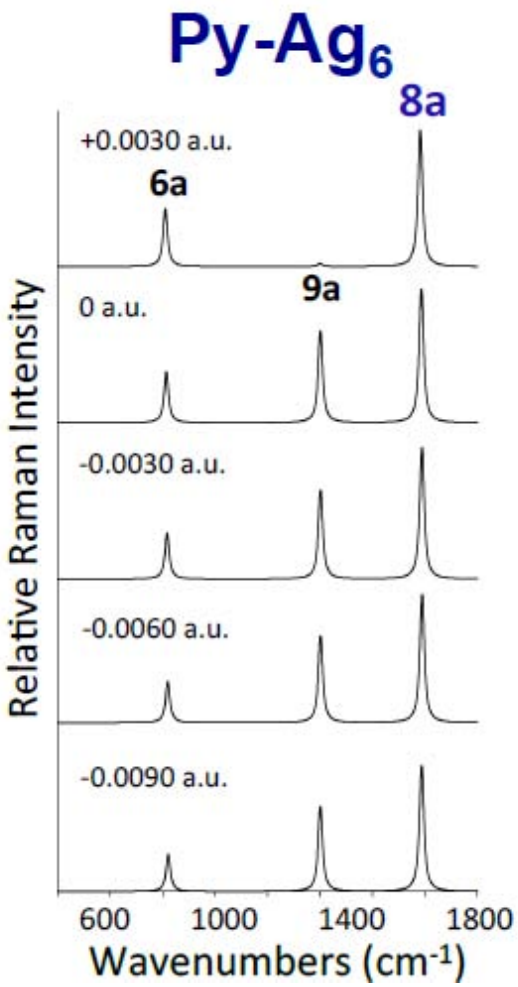

Figure S3. Effect of the electric field on the $\boldsymbol{I_{k,CT}^{preRR(1)}}$ intensities of Py-Ag_6 calculated by using the dimensionless displacements $\boldsymbol{\Delta_{k,CTA1}}$ reported in Table S3 of ref. 1 for the 6a, 9a and 8a modes. Electric fields labelled according to ref. 1. The value of $\boldsymbol{\Delta_{9a,CTA1}}$=0.01606 for +0.0030 a.u. seems to be wrong.

Table S1 Dependence of the TD-BP86/DEF2TZVPP calculated properties of the $CT_1;B_2$ and $CT_{A1};A_1$ states of Py-Ag_6 under applied electric field (Gaussian09 sign convention).

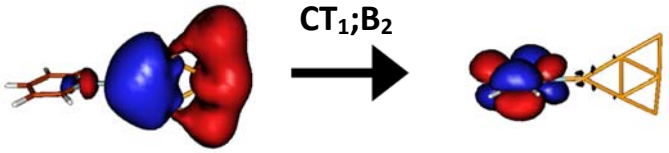

$HOMO_{Ag6};A_1$ $LUMO_{Py};B_2$

	Field (a.u.)[a]	Root[b]	Energy (eV)	Weight[c]	$\Delta q_{S0\rightarrow Sn}^{cluster}$[d]	f[e]
-V	0.009[f]	1	0.1382	0.71152	-0.134037	0.0001
	0.006	1	0.3990	0.70712	-0.712093	0.0001
	0.003	1	1.0065	0.70675	-0.759865	0.0002
	0.000	1	1.6424	0.70476	-0.736756	0.0006
	-0.003	2	2.2408	0.21700	-0.47096	0.0015
		3	2.4573	0.61045	-0.220648	0.0018
	-0.006	4	2.9467	0.47110	-0.339069	0.2511
+V		7	3.0574	-0.47958	-0.237323	0.3675
	-0.009	17	3.6195	0.69274	-0.474918	0.0137

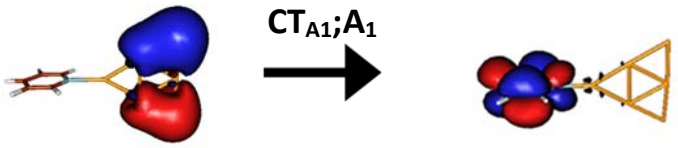

$HOMO\text{-}1_{Ag6};A_1$ $LUMO_{Py};B_2$

	Field (a.u.)[a]	Root[b]	Energy (eV)	Weight[c]	$\Delta q_{S0\rightarrow Sn}^{cluster}$[d]	f[e]
-V	0.009[f]	2	0.2784	0.84796	0.056396	0.0163
	0.006	2	0.4103	0.70711	-0.666809	0.0036
	0.003	2	1.0874	0.70675	-0.779839	0.0018
	0.000	2	1.8005	0.70473	-0.761208	0.0017
	-0.003	4	2.4944	0.32150	-0.595706	0.0049
		5	2.7730	0.54816	-0.136401	0.0051
	-0.006	9	3.2480	0.40409	-0.179755	0.2871
+V		10	3.3704	0.55555	-0.358009	0.3661
	-0.009[g]	>20	-	-	-	-

[a]Applied electric field (Gaussian 09 sign convention). [b]Root showing the largest weight of the corresponding CT monoelectronic configuration. At -0.003 and -0.006 a.u. the CT configuration is mixed with intracluster excitations (IC) and is missing in the first 20 excited states calculated at -0.009 a.u. [c]Weight of the CT configuration. [d]Transferred Mulliken´s charges (a.u.) from Py to Ag_6 in the $S_0 \rightarrow S_{CT}$ transition. [e]Oscillator strength. [f]CT states are too close to the ground electronic state at this particular field. This is why the corresponding $\Delta q_{S0\rightarrow Sn}^{cluster}$ deviated from the remaining ones. [g]CT_{A1} state does not appear in the first twenty excited states at this field.

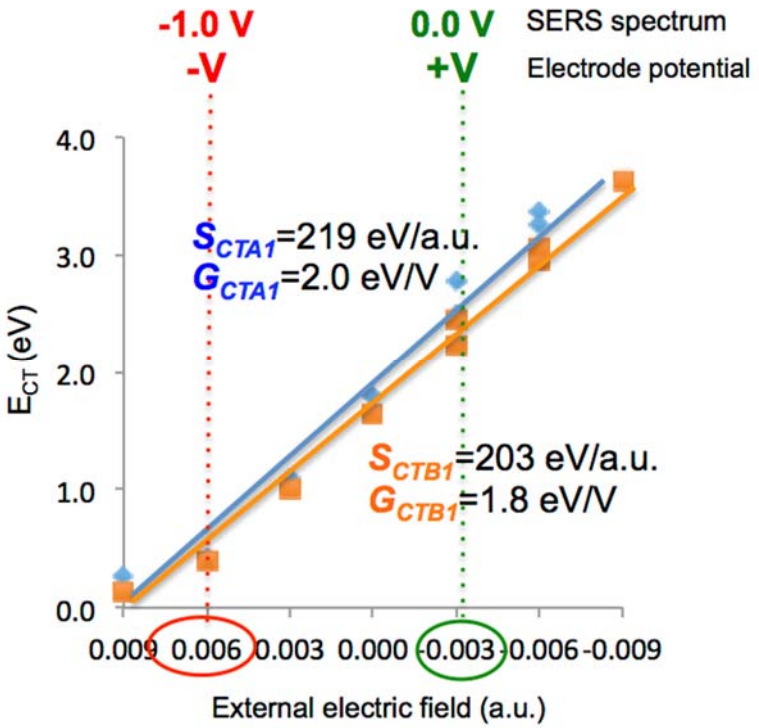

Figure S4. Dependence of the TD-BP86/DEF2TZVPP calculated energies of the CT_1;B_2 (orange) and CT_{A1};A_1 (blue) states of Py-Ag_6 under applied electric field (Gaussian09 sign convention).

Capítulo III – Resultados (IV).

An approach to the electronic structure of molecular junctions with metal clusters of atomic thickness. †

Daniel Aranda, Isabel López-Tocón, Juan Soto, Juan C. Otero* and Francisco Avila*.

TD-DFT calculations predict a linear dependence of the energies of charge transfer states of Ag_n-pyrazine-Ag_n molecular junctions on the inverse of the size (1/n) of the linear metal chains. The density of charge (q_{eff} = q/n) in the metal-to-meal charge transfer excited states (CT_{MM}: $Ag_n^q - \text{pyrazine} - Ag_n^{-q}$) smoothly tunes the electronic structure of the junction, especially the metal-to-molecule charge transfer states (CT_0 and CT_1) and the first excited single of pyrazine ($S_{1,Pz}$). In enlarged junctions, pyrazine bonds preferable to one of the Ag_n clusters and this weak adsorption produces a significant unexpected asymmetry for forward and reverse charge transfer processes.

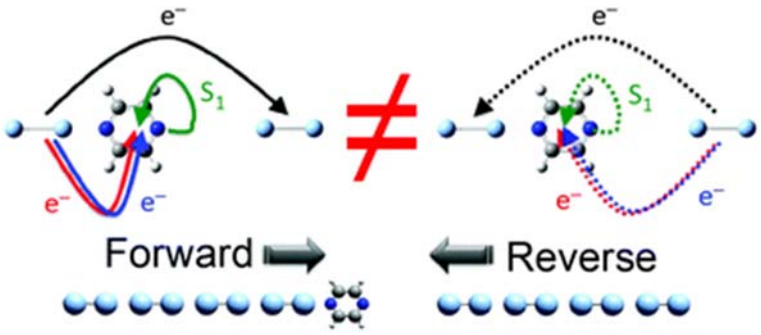

3.4.1. Introduction

A deep understanding of the electronic transport through molecular junctions is the key for the development of molecular electronics.[1,2] Molecular junctions consist of a single molecule (A) placed between two metallic electrodes (M_n) where the transmission event can be non-resonant or resonant if metal-to-molecule (M^+-A^-) or molecule-to-metal (A^+-M^-) charge transfer states (CT) or excited state of the molecule (A*) are intermediate steps in the conduction. In this case, the conductance undergoes a dramatic enhancement and the electronic structure of the molecule and its chemical anchoring to the metal electrodes control the electric transport. A resonant conduction channel can be enabled if these metal-molecule or molecular states lie inside the window between the Fermi levels (FLs) of both metals in the case of large conductions, or between the corresponding $HOMO_M$ and $LUMO_{M'}$ orbitals of small insulating or semiconductor metal clusters. But the relative energies of these states are tuned in a complex way by the applied electric potential (EV) making necessary the use of simplified schemes, as shown in Figure 1a, where EV shifts only both FLs with respect the energies of the $HOMO_A$ and $LUMO_A$ orbitals of the molecule which remain unaltered. Subtle chemical contributions are missing in these schemes and the complex dependence of the electronic states of the overall M-A-M' system on the applied bias is not taken into account.

In this work, a strategy based on time-dependent DFT calculations (TD-DFT) to model the effect of the size, the density of charge and the inter-cluster distance on the overall electronic structure of molecular junctions containing two silver nanowires with

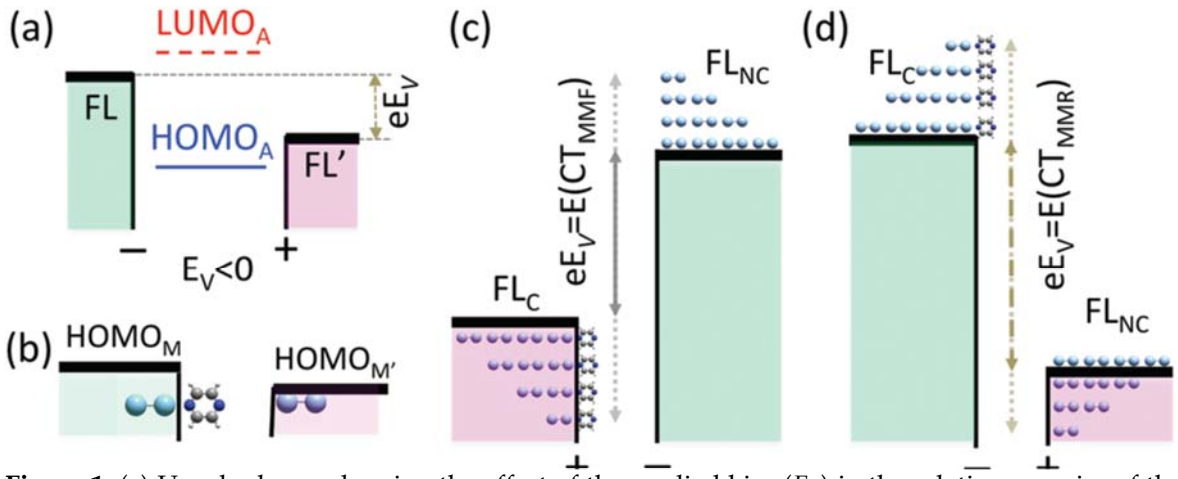

Figure 1. (a) Usual scheme showing the effect of the applied bias (E_V) in the relative energies of the Fermi levels (FL) of the electrodes with respect to the $HOMO_A$ and $LUMO_A$ orbitals of the molecule. (b) Shift of the $HOMO_M$ induced by the molecular adsorption. (c and d) Fermi levels under positive or negative electrode potentials related to the metal-to-metal forward (CT_{MMF}) and reverse (CT_{MMR}) charge transfer states of Ag_n-Pz-Ag_n with different sizes.

monoatomic thickness is introduced. A very symmetric D_{2h} molecule (pyrazine, Pz) has been selected, which is N-linked to the electrodes (Figure 2). Nowadays, scanning tunneling microscopy techniques are able to build these molecular junctions with linear chains of noble metal atoms and to carry out spectroscopy measurements.[3-5] A Pz molecule is placed between the two silver linear clusters in a planar collinear configuration Ag_n-Pz-Ag_n. With n = 2, 4, 6 and 8, in order to study the effect of the metal cluster size in the electronic structure of the junction (Figure 2). Guidez and Aikens[6,7] have reported TD-DFT calculates on the effect of the size of the electronic structure of single silver and gold atomic nanowires. In this work, these systems have been extended by adding a second metal chain and an organic molecule which connects both the metal clusters. This allows for studying metal-to-metal and metal-to-metal CT states as well as electronic excitations of the bridge molecule which are absent in a single metal cluster.

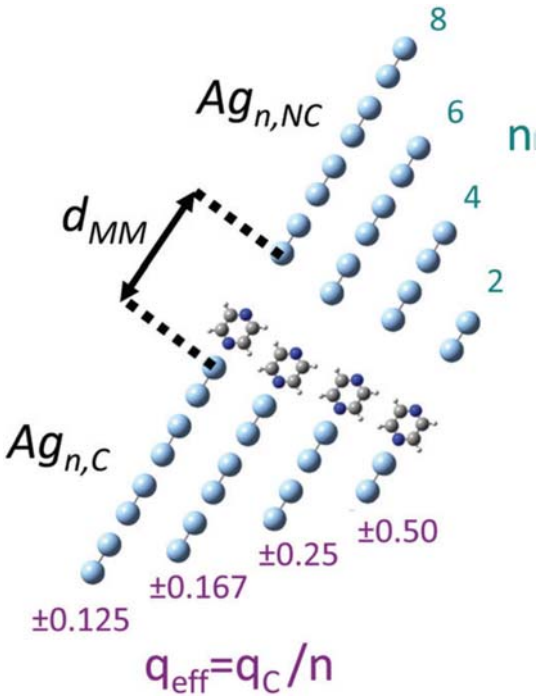

Figure 2. Structures of Ag_n-pyrazine-Ag_n molecular junctions and the corresponding effective density of charges ($q_{eff} = q_c/n$) of the contact metal electrode in the forward (q_c = +1) and reverse (q_c = -1) metal-to-metal CT_{MM} charge transfer states.

3.4.2. Methodology

To compute the ground and single excited states energies, *Gaussian09* implementation of the long-range corrected M06HF[9] functional in combination with the LanL2DZ[10] basis set has been used. This functional contains the full HF exchange and provides good estimations of the energies of CT states.[11] Excited state calculations haven been restricted to the Franck-Condon (FC) point. Although some amount of charge is transferred between both metals or between the metals and the molecule in the ground and excited states, charge transfer states (CT) are easily recognized by checking the Mulliken's charges of the moieties and the CI expansion. The transferred charge in CT states usually lies in the range of 0.6-0.9 a.u., while it is less than 0.10 a.u. in the remaining non-CT states.

3.4.3. Results and discussion.

Equilibrium ground state structures with D_{2h} symmetry have been found for all the investigated closed shell systems, with the distance between the two closest silver atoms of each cluster amounting to $d_{MM,eq} \approx 7.5$ Å. At the respective equilibrium geometries, it is not possible to find electronic excited states with metal-to-metal CT character (CT_{MM}) because the metallic molecular orbitals are symmetrically delocalized along both clusters under D_{2h}.

The effect of the inter-electrode distance (d_{MM}) on the electronic structure has been investigated by computing the respective optimized geometries and TD-DFT vertical energies in the range d_{MM} = 7.0-11.0 Å in steps of 0.5 Å. It is found that for d_{MM} distances larger than 8.0 Å the symmetric D_{2h} structure is lost because Pz preferably links to one of the clusters (M_C: contact metal, M_{NC}: non-contact metal) giving a C_{2v} M_C-Pz$\cdots$$M_{NC}$ junction. When pyrazine is bonded and closer to one of the metals, the electrodes become non-equivalent. The interaction of the nonbonding electrons of the nitrogen with the bonded metal produces the injection of a small Mulliken's charge amounting to 0.09-0.10 a.u. for n = 2-8, respectively, in the contact cluster. This slightly raises the $HOMO_M$ (FL_C) of the metal to which the molecule is adsorbed (Figure 1b) and the symmetry of the system is reduced to C_{2v}. This small charge transfer process in the ground electronic state of the systems corresponds to the charge transfer induced potential of Ratner *et at*.[12] The confinement of the metallic molecular orbitals inside each cluster allows for the emergence of localized metal-to-metal CTMM electronic states.

Although the adsorption process is weak (M_C-A bond energy is only 0.5 eV, Figure S1, ESI†) it has important consequences in the electronic structure of Ag_n-Pz$\cdots$$Ag_n$ junctions, as can be seen in Figure 3. This figure shows the linear dependence of the vertical energies of selected CT excited states of these systems at d_{MM} = 9.0 Å on the inverse of the length of the chains (or the number of silver atoms, $1/n$),[13] depending on whether the transferred electron comes from the contact (right panel) or the non-contact (left panel) metals.

CT_{MM} are excited states of the junctions which can be electrified in the forward (CT_{MMF}: $HOMO_C \rightarrow LUMO_{NC}$, M_C^+-A$\cdots$$M_{NC}^-$) or reverse ($CT_{MMR}$: $HOMO_{NC} \rightarrow LUMO_C$, M_C^--A$\cdots$$M_{NC}^+$) directions (Figures 1c and d) respectively. Metal-to-metal CT states arise from electron transfer from the FL of the metal ($HOMO_M$) to vacant orbitals of the pyrazine (CT_0; B_1: $HOMO_M \rightarrow LUMO_A$; CT_1; A_2: $HOMO_M \rightarrow LUMO_A$+1, *etc.*) and are also labelled as forward or reverse, $CT_{0,1F}$ (M_C^+-$A^-\cdots M_{NC}$) or $CT_{0,1R}$ (M_C-$A^+\cdots M_{NC}^-$), depending on the M_C or M_{NC} cluster from which the electron is transferred, respectively. Molecule-to-metal CT processes are very energetic in silver-pyrazine systems and have not been discussed.

By comparing the left and right panels it is concluded that the forward and reverse CT processes are not equivalent at all, which would allow for current rectification. Rectification is an important property of molecular junctions able to produce asymmetric currents when potentials of equal magnitude, but opposite sign are applied.[2] The chemical adsorption slightly enriches the density of negative charge of the contact electrode, which favors the forward $M_C \rightarrow M_{NC}$ and $M_C \rightarrow$ A CT processes but blue-shifts

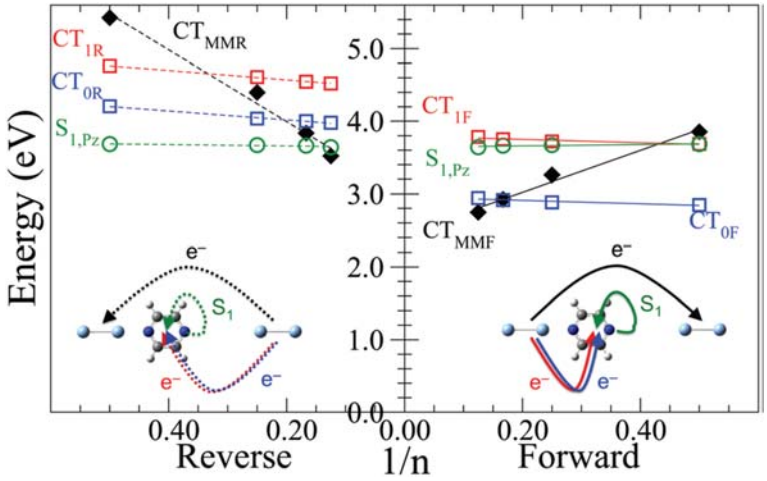

Figure 3. M06-HF/LanL2DZ vertical excitation energies of metal-metal CT_{MM} metal-molecule $CT_{0,1}$ and molecular $S_{1,Pz}$ states with respect to the inverse of the number of atoms ($1/n$) of silver clusters in Ag_n-Pz-Ag_n molecular junctions with d_{MM} = 9.0 Å.

the reverse $CT_{0,1R}$ states 0.5-1 eV with respect the forward ones. Moreover, only CT_{MM} states depend on $1/n$, with a larger slope in the case of CT_{MMR}, while $CT_{0,1}$ remains almost insensitive to the length of the chains as occurring with the first single excited state of Pz (A^*, $S_{1,Pz}$;B_1) also shown in Figure 3.

All the states in this figure lie in the range 2.5-5.5 eV but their energies and relative positions depend also on d_{MM}, as can be seen in Figure 4 and Figure S2 (ESI†). Two regions can be differentiated in these plots. All the states show degenerate energies for the respective forward and reverse processes in the compressed region at short distances $d_{MM} \leq 8$ Å where the weaker $(M_CA)\cdots M_{NC}$ bond is not significantly stretched near this critical value. This can be seen in Figure S1 (ESI†) where the respective Ag_C-N_{Pz} and N_{Pz}-Ag_{NC} distances are represented *vs*. d_{MM}. Both bonds enlarge almost symmetrically until 8 Å, but once this critical point is overpassed, the Ag_C-N_{Pz} bond is again shortened to its equilibrium distance (ca. 2.36 Å), while the $N_{Pz}\cdots Ag_{NC}$ distance stretches progressively, being the only recipient of additional Δd_{MM} increments.

CT_{MMF} and CT_{MMR} are not charged in the compressed region,[14] but forward and reverse branches appear differentiated in enlarged junctions (d_{MM} > 8 Å) showing smaller splitting as the size of the chains increases (1.8 and 0.9 eV for n = 2 and 8, respectively, in the range d_{MM} = 9-11 Å). Concerning the metal-molecules CT states, CT_1 is 1 eV above CT_0 in compressed junctions, where both are strongly stabilized *ca*. 0.8 eV (30%) when

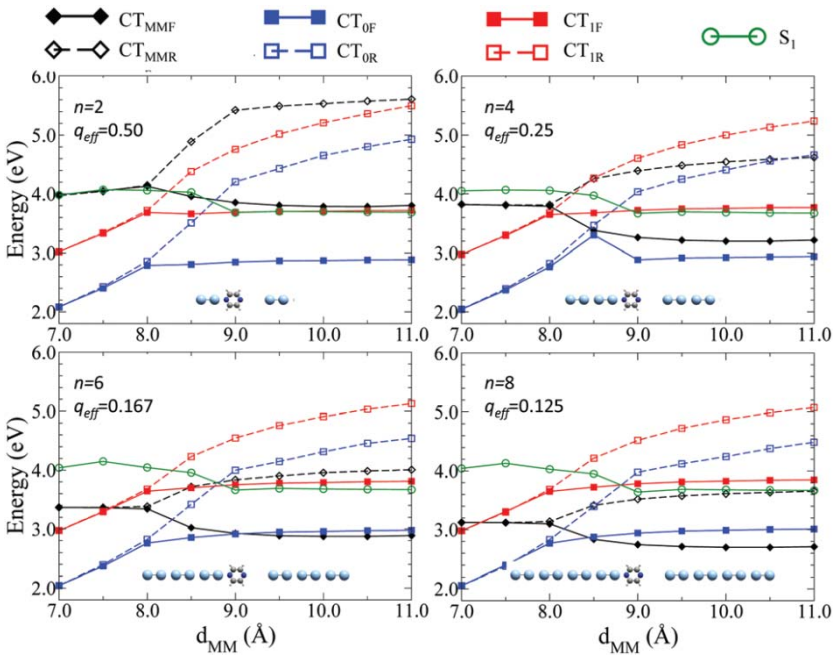

Figure 4. Effect of the intercluster distance (d_{MM}) on the vertical energies of the CT_{MM}, CT_0 and CT_1, and $S_{1,Pz}$ electronic states of Ag_n-Pz-Ag_n with n = 2, 4, 6 and 8.

d_{MM} shortens from 9 to 7 Å. In contrast, the energy of $S_{1,Pz}$ (ca. 3.7 eV) remains almost constant at large distances, irrespective of the size, but slightly destabilizes under compressions (0.3-0.4 eV).

The forward and reverse CT_0 and CT_1 states also split in the enlarged region (d_{MM} > 8-9 Å) mainly due to the respective reverse branches $CT_{0,1R}$ (M_C-$A^-\cdots M_{NC}^+$), whose energies increase as the positively charged donor cluster M_{NC}^+ progressively moves away from the negatively charged acceptor M_C-A^-. As expected, the $CT_{0,1F}$ forward processes do not depend on the position of the neutral M_{NC} cluster at d_{MM} > 8 Å given that is not involved in the $CT_{0,1F}$ (M_C^+-$A^-\cdots M_{NC}$) electron transfer.

Standard conductance experiments in molecular junctions containing large metal electrodes are carried out under an applied bias but charge transfer transport can be also induced by light excitation.[15] Analogously, the discussed CT_{MM} electrified states ($M^+ - A - M^-$) can be taken as the starting point for electron transport across these simple chain-like systems. In our models, CT_{MM} states can be reached, for instance, by photoexcitation, with very different energies for forward and reverse directions depending on both, $1/n$ and d_{MM}, as shown in Figures 3 and 4:

$$S_0\text{: } M_C\text{-}A\cdots M_{NC} + h\nu \rightarrow CT_{MMF}\text{: } M_C^+\text{-}A\cdots M_{NC}^-$$

$$S_0\text{: } M_C\text{-}A\cdots M_{NC} + h\nu' \rightarrow CT_{MMR}\text{: } M_C^-\text{-}A\cdots M_{NC}^+$$

These polarized states act as energy reservoirs and can be taken as the origins of the energies for processes subsequent to electrization CT_{MM} would play the role of the "injecting energy" in the "extended molecule" of Ratner *et al.*[4,16] corresponding to our Ag_n-$A\cdots Ag_n$ linear complexes.

Charge separation in CT_{MM} states can recombine through different mechanisms. Direct electronic transport across the junction is the opposite process where CT_{MM} decays to the S_0 ground state.

$$CT_{MMR}\text{: } M_C^-\text{-}A\cdots M_{NC}^+ \rightarrow S_0\text{: } M_C\text{-}A\cdots M_{NC}$$

$$CT_{MMF}\text{: } M_C^+\text{-}A\cdots M_{NC}^- \rightarrow S_0\text{: } M_C\text{-}A\cdots M_{NC}$$

Molecule mediated conduction produces enhanced electron transport and is allowed if metal-molecule $CT_{0,1}$ states lie below CT_{MM}. The fulfilment of this condition depends on both $1/n$ and d_{MM} and can be checked in Figure 5. This figure shows the relative energies of $CT_{0,1}$ and $S_{1,Pz}$ states in enlarged structure with d_{MM} = 8.5, 9.0 and 11 Å with respect to the CT_{MMF} or CT_{MMR} states which are taken as the origin of the energies. Figure 5 shows that $CT_{0,1F}$ remains almost insensitive to the position of the M_{NC}^{-} donor group:

$$CT_{MMF}: M_C^{+}\text{-}A\cdots M_{NC}^{-} \rightarrow CT_{0,1F}: M_C\text{-}A^{-}\cdots M_{NC}^{+} \rightarrow S_0: M_C\text{-}A\cdots M_{NC}$$

It can be seen that the conduction channel through CT_0 is available in the case of forward polarization at any distance, except for n = 8, while an equivalent situation is only found at short distances (d_{MM} = 8.5 Å) when the sign of electrization is reversed.

Emission of electroluminescence from A* excited states of the molecule is also possible. Figure 5 points out that A*, $S_{1,Pz}$ is available at d_{MM} = 8 or 9 Å from the more energy demanding CT_{MMR} polarization:

$$CT_{MMR}: M_C^{-}\text{-}A\cdots M_{NC}^{+} \rightarrow S_{1,Pz}: M_C\text{-}A*\cdots M_{NC} \rightarrow S_0: M_C\text{-}A\cdots M_{NC} + h\upsilon$$

This mechanism is not allowed in the forward panels of Figure 5 because the energy of $S_{1,Pz}$ always remains above CT_{MMF}.

Figure 5 and Figure S3 (ESI†) summarize the required conditions for each particular process and distance. The variable used in the x-axis ($1/n$, bottom) has been replaced by another one (q_{eff}, top) defined in the respective charged CT_{MM}: $M_C^{q}\text{-}A\cdots M_{NC}^{-q}$ excited states of the junctions, with forward (q = +1) and reverse (q = -1) polarizations, as:

$$q_{eff} = q_{eff,C} = -q_{eff,NC} = q/n$$

q_{eff} quantifies the average of the density of charge per atom in the CT_{MM} states of the respective Ag_n clusters and ranges from ±0.5 (n = 2) to ±0.125 (n = 8) a.u. per silver atom. Therefore, the size of silver chains modulates the effective density of charge of the metal and, consequently, Figure 5 can also be seen as showing dependence of the relative energies of the $CT_{0,1}$ and $S_{1,Pz}$ states on qeff, the charge density of the clusters. The ESI† file contains the molecular orbitals involved ibn the discussed electronic states (Figures S4-S7) and Table S1 summarizes single-electron excitations related to forward and reverse CT_{MM} and CT_0 charge transfer states.

q_{eff} (electron per atom) can be considered as a microscopic analogue of the macroscopic excess of the surface charge of a metal (q', Coulumb per cm^2), which is controlled in a continuous way by the electric potential through the capacitance ($C = q'/E_V$). CT_{MM} states in these chain-like systems would be considered in turn as the microscopic analogue of a large molecular junction under applied electric potential, where the energy of the CT_{MM} state corresponds to the energy difference between the respective Fermi levels of the macro/microscopic electrodes ($E(CT_{MM}) \approx E(FL_{NC}) - E(FLC) = eE_V$) (Figures 1c and d).

Electron transport studies usually report statistical measurements using large electrodes where it is very difficult to control the experimental conditions at the nanometer-size or atomic level. Conductance is controlled by the electronic structure of the overall junction,

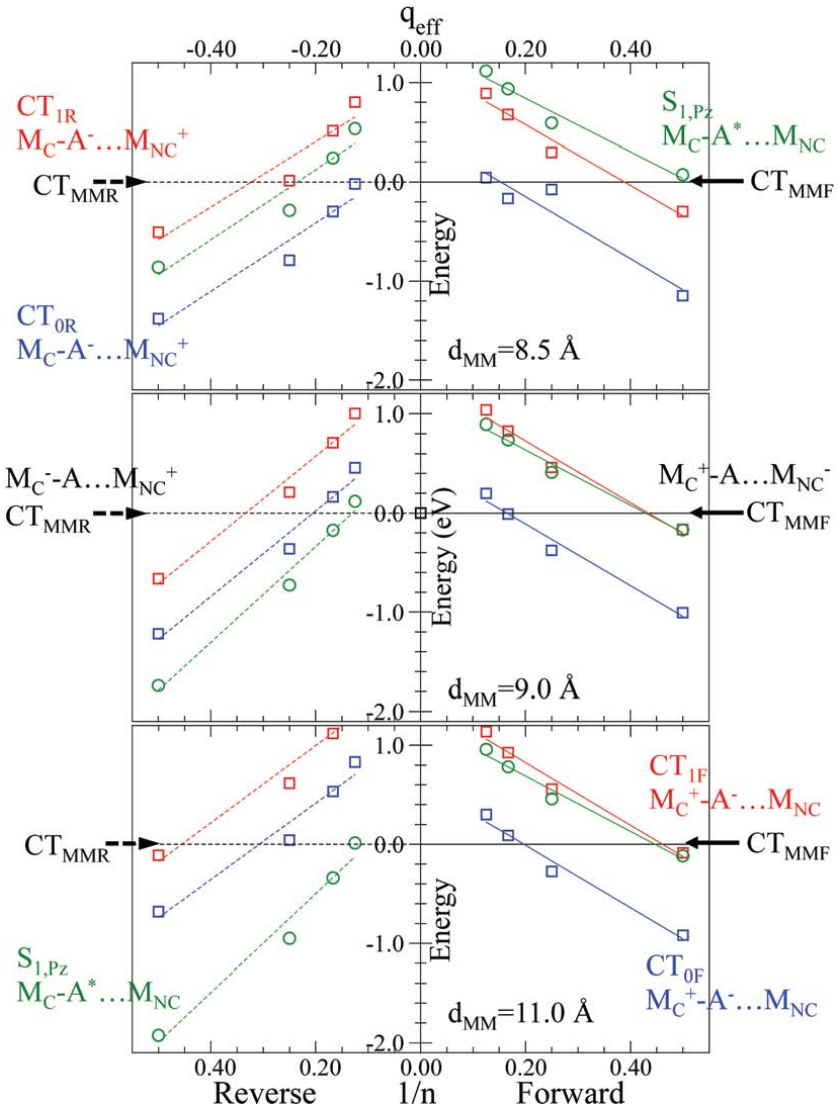

Figure 5. Relative energies of metal-molecule $CT_{0,1}$ and molecular $S_{1;Pz}$ states referred to the energies of forward and reverse CT_{MM} status *versus* the inverse of the number of atoms ($1/n$, bottom) or the density of charge ($q$eff = q/n, top) of the silver cluster in $Ag_n{}^{q}$-$A\cdots Ag_n{}^{-q}$ molecular juntions at d_{MM} = 8.5, 9.0 and 11.0 Å.

which is very sensitive to the particular geometry of the system. Concerning the metal, Gao *et al*.[17] have reported the strong dependence of the electronic excitations of silver clusters on the shape of the atomic chains. HOMO and LUMO energies of the metal can be tuned by geometric parameters of the cluster, but these frontier orbitals are involved in the metal-metal ad metal-molecule CT states of the junction and therefore, the shape of the metal controls the energies of the processes. Moreover, there is a general consensus on the critical role of the atomic-scale metal-molecule contact geometries and chemistry in the transport.[18] The presence of surface irregularities at these scales are unavoidable, which implies geometrical uncertainties of the systems to be modelled. Each particular adsorption site is characterized by an unknown nanometer/atomic density of charge which determines the line-up of the relevant electronic states as Figure 5 shows. This introduces an almost unaffordable number of variables to be taken into account when modelling standard junctions containing large metal electrodes and complicates enormously any theoretical calculation. Therefore, it is very difficult to include the effect of the bias in large clusters and is almost unavoidable to discuss the results on the basis of molecular orbitals and metal levels (Figure 1a) an does not on the stationary states of the overall system (Figure 5). Although the obtained results for chain-like molecular bridges cannot be directly extrapolated to junctions with large metals, they can be useful to understand the complex dependence of the electronic building on the electric potential. In this regard, Figure 5 would show how the electronic structure of a standard junction is tuned by an applied bias able to induce a partial charge q_{eff} in the metal atom directly bonded to the molecule in the surface of a micro/macroscopic electrode.

This situation is very similar to that of surface-enhanced Raman scattering (SERS) which consists in the huge enhancement of the Raman signal of molecules on the surface of nanometer-size metal clusters.[19] SERS is a very complex phenomenon very dependent on the same factors mentioned above, particularly the electric potential of the interface. DFT calculations on metal-molecule systems including large metal clusters or slab models are very often used to support the discussion of both molecular junctions[2] or SERS results.[20] The likeness of a molecular junction and the proposed models for hot spots in SERS[21] proves the close relationship[22-25] between both kinds of experiments. We have previously shown the usefulness of DFT calculations in stick-like $\mathrm{Ag}_n^{\mathrm{q}} - \mathrm{A}$ complexes with different charges and sizes (n = 3, 5, 7 with q = ±1, n = 2 with q = 0) in order to model the effect of the electrode potential in SERS. These $\mathrm{Ag}_n^{\mathrm{q}} - \mathrm{A}$ charged systems are similar to the $\mathrm{CT_{MM}}$ states of the $\mathrm{Ag}_n - \mathrm{A} \cdots \mathrm{Ag}_n$ junctions at infinite

separation. We have shown that q_{eff} accounts for the experimental shifts observed in the SERS wavenumbers induced by the electrode potential.[26] It tunes linearly the CT states of the $Ag_n^q - A$ complexes[27] and smoothly modifies the relative intensities of the Raman bands.[28] This has allowed to detect resonant Raman processes involving CT metal-molecule (CT-SERS)[29] or plasmonic metal-metal (PL-SERS)[30] excited states in particular SERS, as well as to propose a comprehensive explanation for the unexpected effectiveness of the electrode potential in tuning the energy of the metal-molecule CT states.[31] Simple schemes, like the one shown in Figure 1a imply the equivalence between the applied bias (ΔE_V) and the corresponding shift of the energy of the CT states (ΔE_{CT}) ($G = \Delta E_{CT}/\Delta E_V = 1$ eV V^{-1})[32] but huge energy gains up to G = 4-5 eV V^{-1} have been measured from SERS and others experiments.[31,33-35] On the basis of these simple chain-like models, we have shown that the energy gain contains two different contributions $G = SC$. $C = q_{eff}/E_V$ is the electrical capacitance of the metal which quantifies its capability for converting the applied bias in surface excess of charge (q_{eff} in out model). $S = E_{CT}/q_{eff}$ is the dependence of the energy of each CT state on the surface charge q_{eff}. S is quantified through the slope of a particular state in Figure 5. The gain is not uniform along the metal surface but is mainly located at large curvature sites[32] corresponding to hot spot in SERS or the tips of the electrodes in molecular junction devices. Therefore, it should be also relevant in conductance experiments and would invalidate any estimation of the required bias for molecule-mediated electron transport deduced from schemes like shown in Figure 1.

Although the DFT calculations reported here must be taken as qualitative and restricted to atomic thickness junctions like those built by Ho *et al.*[4] they can be useful in order to understand the complex electronic structure of charge molecular junctions containing large metal electrodes. The non-equivalence between forward and reverse CT processes should be only significant in small metal clusters, but it could play a relevant role in some experiments using larger electrodes. Recently published works [36,37] discuss the formation of hybrid junctions where a single organic molecule is connected to chains of metal atoms like discussed here, formed at the end of large electrodes when the systems is under tensile stress. It has been proposed that these hybrid junctions are a new type of atomic scale interfaces[38] and can be responsible for the anomalous enhancement of the conductance detected in particular experiments.[39]

3.4.4. Conclusions.

Summarizing, on the basis of (TD)-DFT calculations the effect of the cluster size (n) and the distance between metals (d_{MM}) on the electronic structure of $Ag_n - Pz \cdots Ag_n$ chain-like molecular junctions have been investigated. The electronic structure shows a dual behavior at short and large inter-cluster distances. In the last case, forward and reverse processes become non-equivalent due to the asymmetry induced by the adsorption of the molecule on one of the metals. As a result, a microscopic model to discuss the effect of the density of charge of the metal chains (q_{eff}) in the electronic states where the molecule is involved ($CT_{0,1}$ and $S_{1,Pz}$) has been proposed. It has been found that the relative energies of these electronic states depend linearly on the charge density of the metals, q_{eff}.

3.4.5. References and notes.

1. A. Nitzan, M. A. Ratner. *Science*, **2003**, 300, 1384.
2. J. C. Cuevas, E. Scheer. *Molecular Electronics: An introduction to theory and experiment*. World Scientific, Singapore, **2010**.
3. N. Nilius, T. Wallis, W. Ho. *Science*, **2002**, 297, 1853.
4. G. Nazin, X. Qiu, W. Ho. *Science*, **2003**, 302, 77.
5. D. R. Belcher, M. W. Radny, S. R. Schofield, P. V. Smith, O. Warschkow. *J. Am. Chem. Soc.*, **2012**, 134, 15312.
6. E. B. Guidez, C. M. Aikens. *Nanoscale*, **2012**, 4, 4190.
7. E. B. Guidez, C. M. Aikens. *Nanoscale*, **2014**, 6. 11512.
8. M. J. Frisch, et al. *Gaussian 09, Revission A.02*, Gaussian, Inc., **2009**, and references therein.
9. Y. Zhao, D. G. Truhlar. *J. Phys. Chem. A*, **2006**, 110, 13126.
10. P. J. Hay, W. R. Wadt. *J. Chem. Phys.*, **1985**, 82, 270.
11. D. Jacquemin, E. A. Perpète, I. Ciofini, C. Adamo, R. Valero, Y. Zhao, D. G. Truhlar. *J. Chem. Theory Compu*t., **2010**, 6, 2017.
12. Y. Q. Xue, M. A. Ratner. *Phys. Rev. B: Condens. Matter Mater. Phys.*, **2003**, 68, 115406.
13. The particle in a box model predicts that the $HOMO_M$ energy of linear clusters with even number of atoms is not dependent on the size while the $LUMO_M$ energy is inversely proportional to the length of the chains.
14. CT_{MM} states at $d_{MM} \leq 8$ Å are degenerate and correspond to symmetric and antisymmetric combinations of the forward and reverse electrified configurations: $(M^+ - A - M^-) \pm (M^- - A - M^+)$.
15. Z. Hu, M. A. Ratner, T. Seideman. *J. Chem. Phys.*, **2014**, 141, 224104.
16. S. N. Yaliraki, A. E. Robert, C. Gonzalez, V. Mujica, M. A. Ratner. *J. Chem. Phys.*, **1999**, 111, 6997.
17. B. Gao, K. Ruud, Y. Liu. *J. Phys. Chem. C*, **2014**, 118, 13059.
18. M. Di Ventra, S. T. Pantelides, N. D. Lang. *Phys. Rev. Lett.*, **2000**, 84, 979.
19. R. Aroca. *Surface-enhanced vibrational spectroscopy*. John Wiley & Sons Ltd, Chichester, **2006**.
20. L. Jensen, C. M. Aikens, G. C. Schatz. *Chem. Soc. Rev.*, **2008**, 37, 1061, and references therein.
21. D. V. Chulhai, X. Chen, L. Jensen. *J. Phys. Chem. C*, **2016**, 120, 20833.

22. M. Oren, M. Galperin, A. Nitzan. *Phys. Rev. B: Condens. Matter Mater. Phys.*, **2012**, 85, 115435.
23. T.-H. Park, M. Galperin. *Phys. Rev. B: Condens. Matter Mater. Phys.*, **2011**, 84, 075447.
24. F. Mirjani, J. M. Thijssen, M. A. Ratner. *J. Phys. Chem. C*, **2012**, 116, 23120.
25. Y. Li, P. Doak, L. Kronik, J. B. Neaton, D. Natelson. *Proc Natl. Acad. Sci. U. S. A.*, **2014**, 111, 1282.
26. J. Soto, D. J. Fernández, S. P. Centeno, I. López-Tocón, J. C. Otero. *Langmuir*, **2002**, 18, 3100.
27. F. Avila, D. J. Fernández, J. F. Arenas, J. C. Otero, J. Soto. *Chem. Commun.*, **2011**, 47, 4210.
28. F. Avila, C. Ruano, I. López-Tocón, J. F. Arenas, J. Soto, J. C. Otero. *Chem. Commun.*, **2011**, 47, 4212.
29. S. P. Centeno, I. López-Tocón, J. Román-Pérez, J. F. Arenas, J. Soto, J. C. Otero. *J. Phys. Chem. C*, **2012**, 116, 23639.
30. J. Román-Pérez, I. López-Tocón, J. L. Castro, J. F. Arenas, J. Soto, J. C. Otero. *Phys. Chem. Chem. Phys.*, **2015**, 17, 2326.
31. J. Román-Pérez, C. Ruano, S. P. Centeno, I. López-Tocón, J. F. Arenas, J. Soto, J. C. Otero. *J. Phys. Chem. C*, **2014**, 118, 2718.
32. According to Figure 1a, the applied bias E_V shifts symmetrically the FLs of both electrodes and therefore, the expected gain is $G = 1/2$ eV V^{-1}.
33. L. Cui, D. W. Wu, A. Wang, B. Ren, Z. Q. Tian. *J. Phys. Chem. C*, **2010**, 114, 16588.
34. A. Otto, J. Billmann, J. Eickmans, U. Ertürk, C. Pettenkofer. *Surf. Sci.*, **1984**, 138, 319.
35. D. M. Kolb. *Angew. Chem., Int. Ed.*, **2001**, 40, 1162.
36. W. R. French, C. R. Iacovella, I. Rungger, A. M. Souza, S. Sanvito, P. T. Cummings. *Nanoscale*, **2013**, 5, 3654.
37. A. Saffarzadeh, F. Demir, G. Kirczenow. *Phys. Rev. B: Condens. Matter Mater. Phys.*, **2014**, 89, 045431.
38. T. Yelin, R. Vardimon, N. Kuritz, R. Korytar, A. Bagrets, F. Evers, L. Kronik, O. Tal. *Nano Lett.*, **2013**, 13, 1956.
39. C. Bruot, J. Hihath, N. Tao. *Nat. Nanotechnol.*, **2012**, 7. 35.

Supporting Information

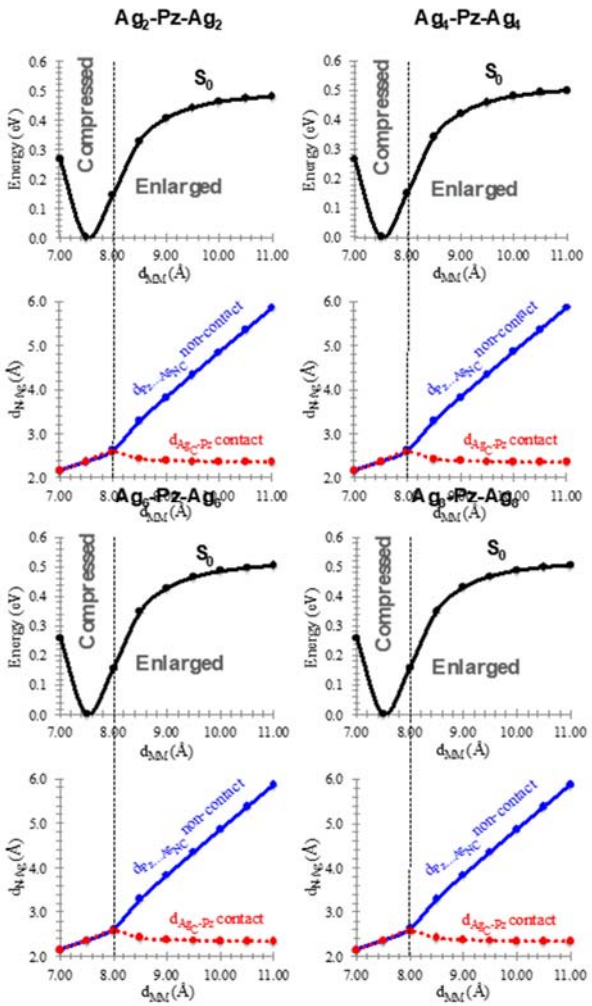

Figure S1. Effect of the inter-cluster distance (d_{MM}) on the M06-HF/LanL2DZ stabilization energy of the bond formed between pyrazine and the non-contact silver cluster in the ground electronic state S_0 (top) of Ag_n-Pz-Ag_n junctions. N-Ag bond lengths of pyrazine linked to the contact ($d_{AgC\text{-}Pz}$) and non-contact ($d_{Pz\ldots AgNC}$) silver clusters versus the intercluster distance (bottom).

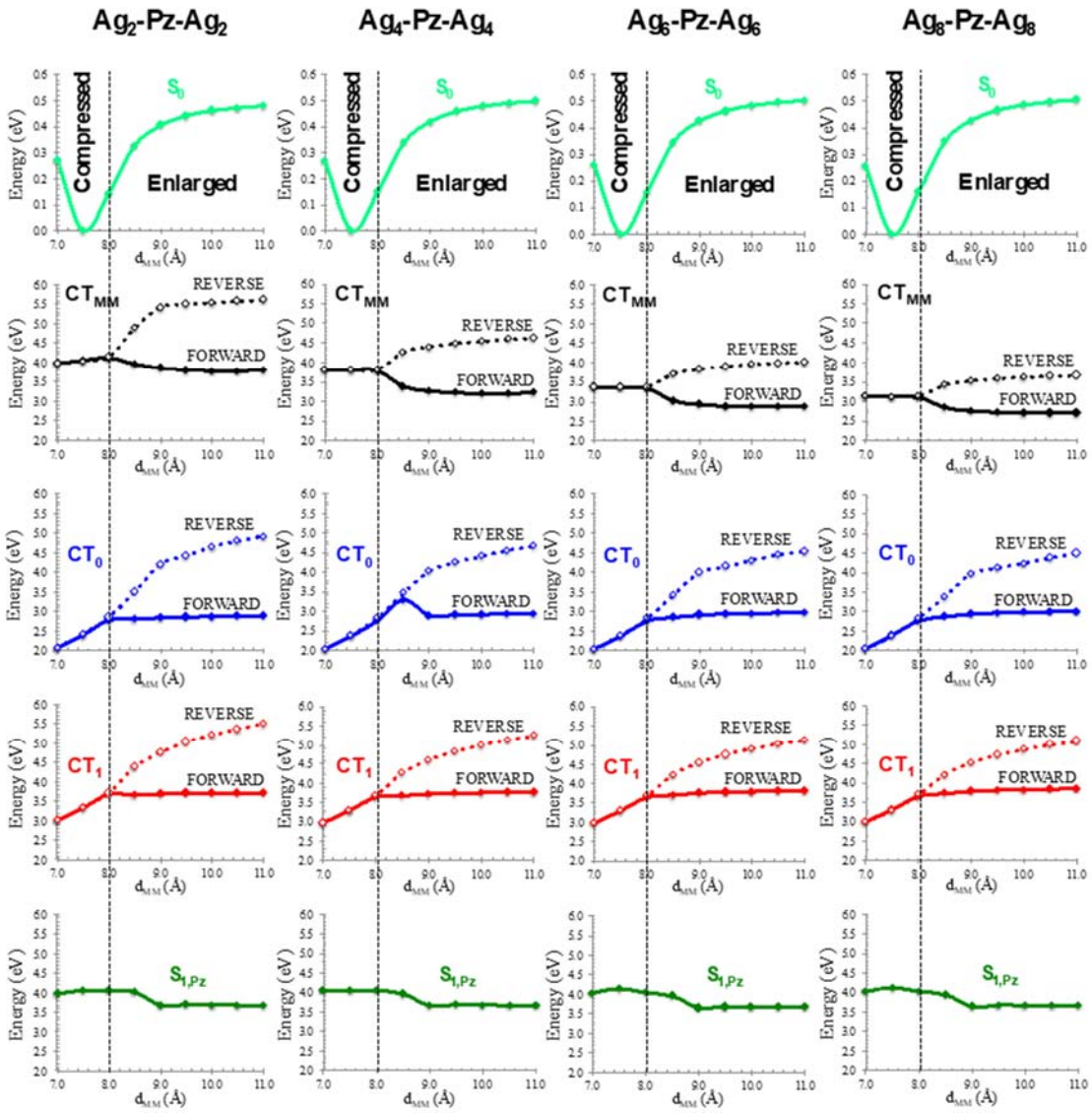

Figure S2. Effect of the inter-cluster distance (d_{MM}) on the M06-HF/LanL2DZ stabilization energy of the bond formed between pyrazine and the non-contact silver cluster in the ground electronic state S_0 (top) and on the corresponding vertical energies of the metal-metal (CT_{MM}), metal-molecule ($CT_{0,1}$) and molecular ($S_{1,Pz}$) excited states of Ag_n-Pz-Ag_n junctions.

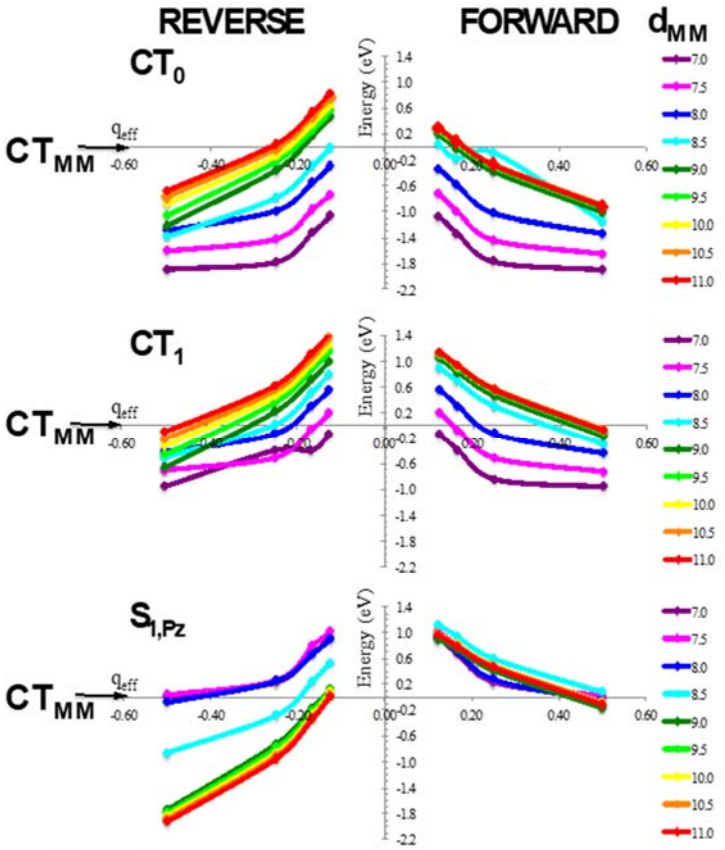

Figure S3. M06-HF/LanL2DZ relative energies of the $CT_{0,1}$ and $S_{1,Pz}$ states referred to the corresponding forward (q=+1) and reverse (q=-1) CT_{MM} polarized states plotted versus the density of charge (q_{eff}=q/n) of the silver clusters in charged Ag_n^q-Pz-Ag_n^{-q} junctions at different inter-cluster distances (d_{MM}).

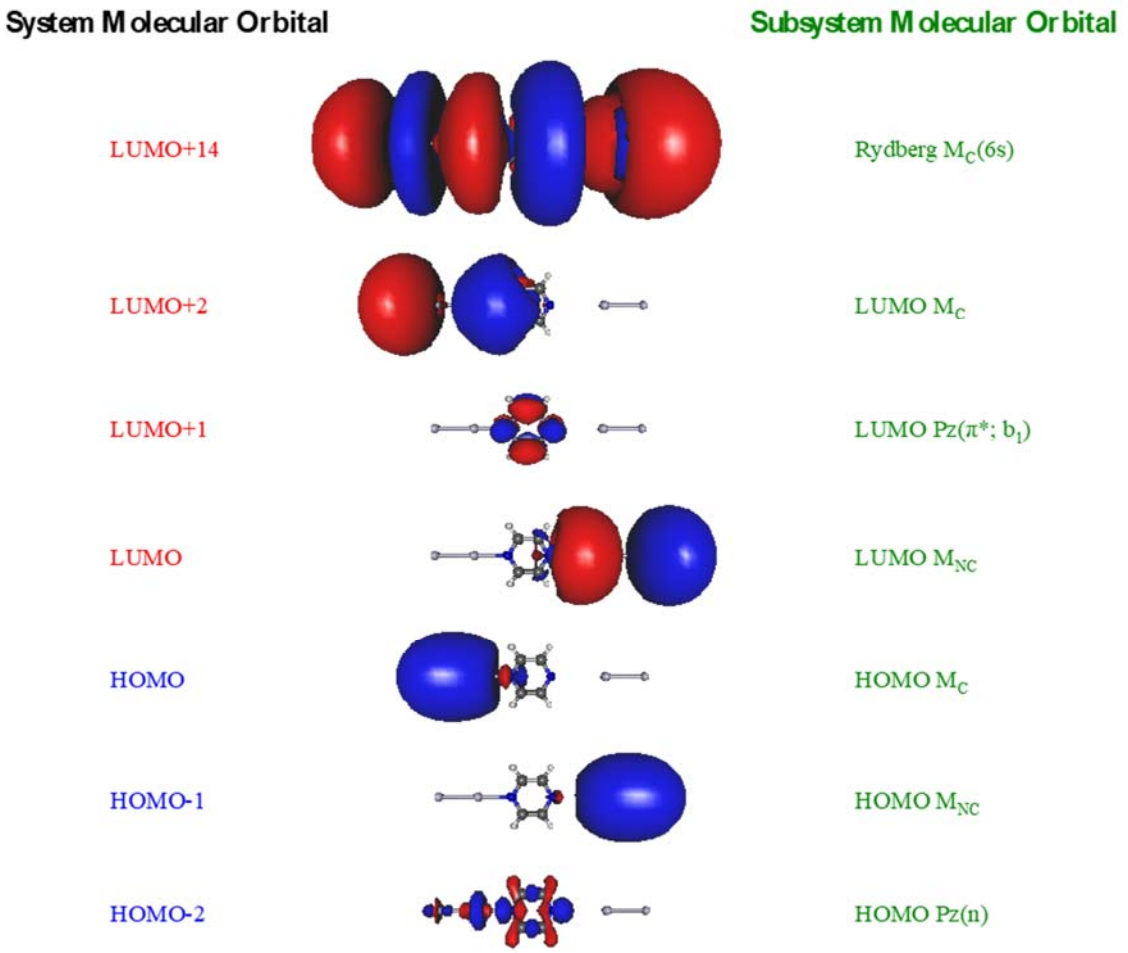

Figure S4. Relevant Kohn-Sham molecular orbitals involved in the forward and reverse CT_{MM} and CT_0 charge transfer states of the Ag_2-Pz$\cdots$$Ag_2$ junction at an intercluster distance of 9.0 Å. Orbitals labelled according to the energies for the whole M_C-Pz$\cdots$$M_{NC}$ system (left) or for each subsystem: the contact metal (M_C), the molecule (Pz) and the non-contact metal (M_{NC}) (right) (see Table S1).

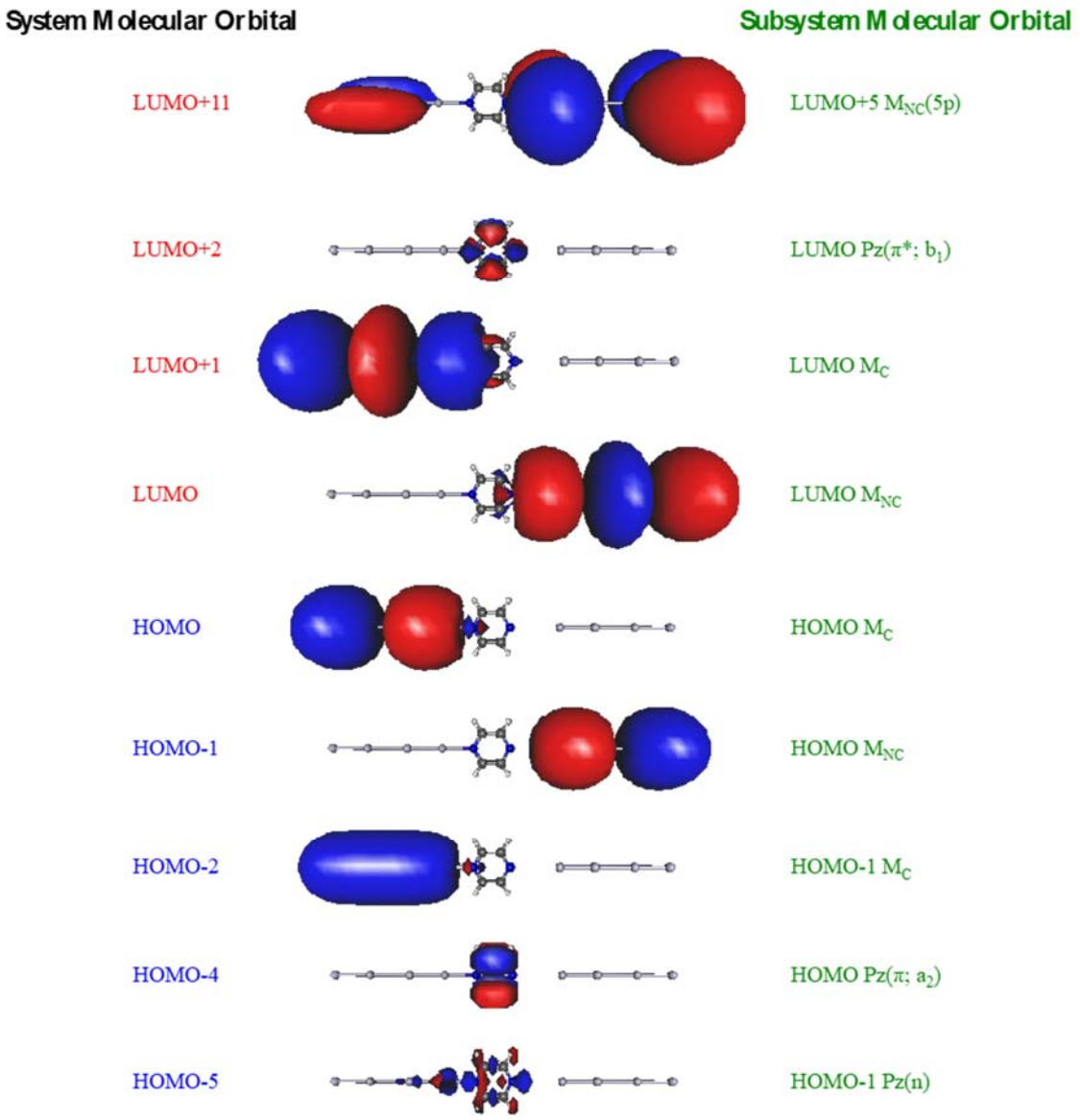

Figure S5. Relevant Kohn-Sham molecular orbitals involved in the forward and reverse CT_{MM} and CT_0 charge transfer states of the Ag_4-Pz$\cdots$$Ag_4$ junction at an intercluster distance of 9.0 Å. Orbitals labelled according to the energies for the whole M_C-Pz$\cdots$$M_{NC}$ system (left) or for each subsystem: the contact metal (M_C), the molecule (Pz) and the non-contact metal (M_{NC}) (right) (see Table S1).

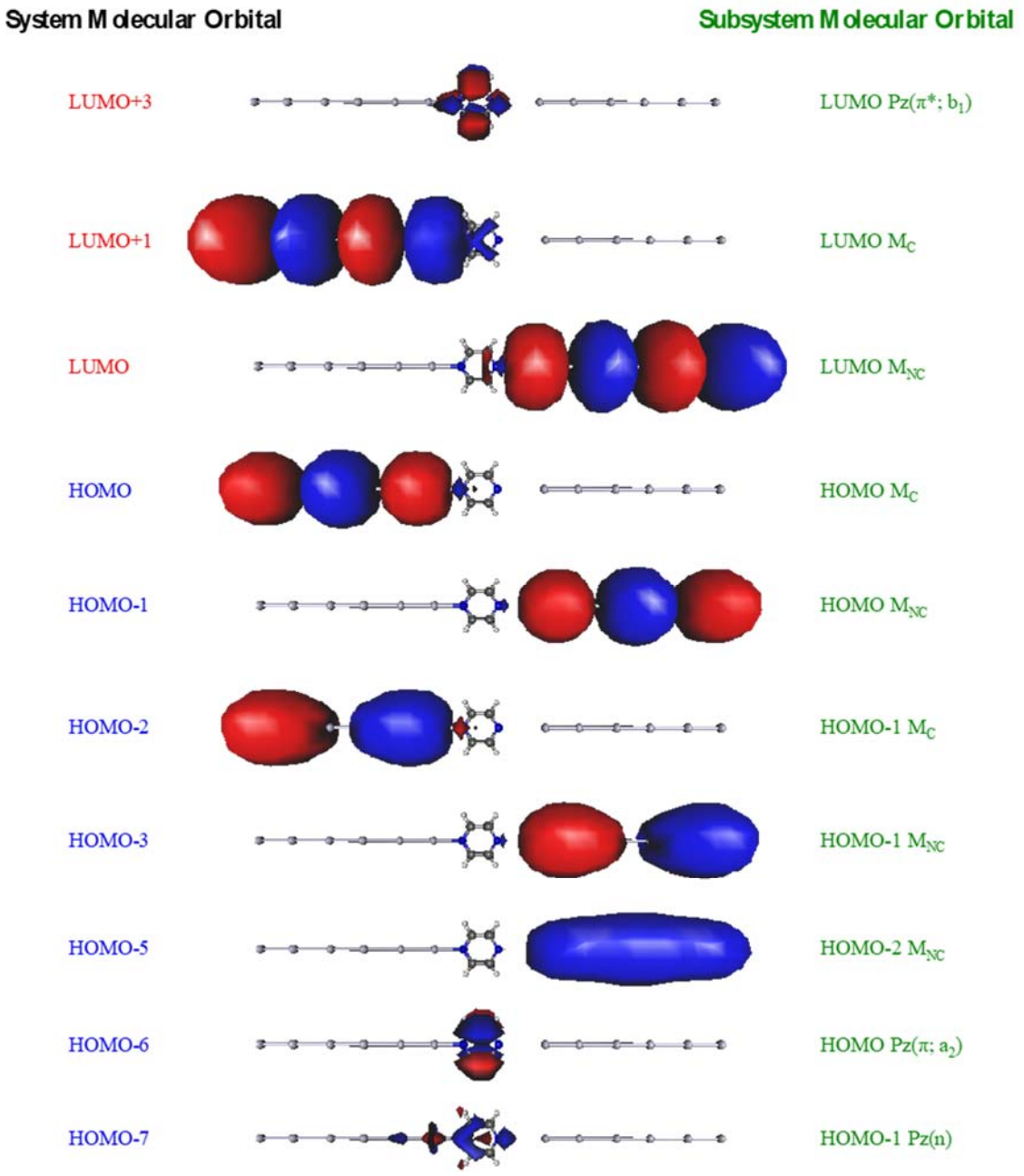

Figure S6. Relevant Kohn-Sham molecular orbitals involved in the forward and reverse CT_{MM} and CT_0 charge transfer states of the Ag_6-Pz$\cdots$$Ag_6$ junction at an intercluster distance of 9.0 Å. Orbitals labelled according to the energies for the whole M_C-Pz$\cdots$$M_{NC}$ system (left) or for each subsystem: the contact metal (M_C), the molecule (Pz) and the non-contact metal (M_{NC}) (right) (see Table S1).

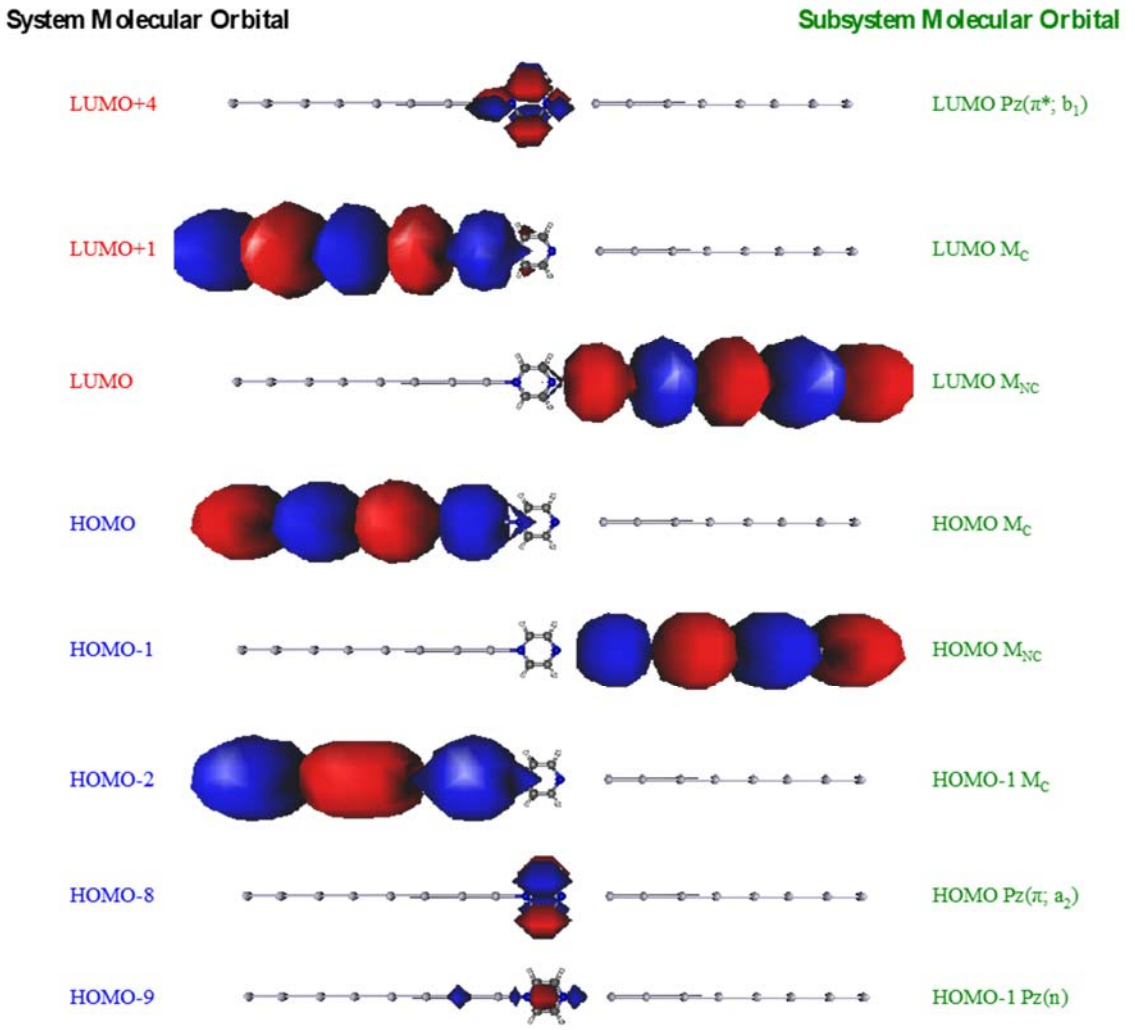

Figure S7. Relevant Kohn-Sham molecular orbitals involved in the forward and reverse CT_{MM} and CT_0 charge transfer states of the Ag_8-Pz$\cdots$$Ag_8$ junction at an intercluster distance of 9.0 Å. Orbitals labelled according to the energies for the whole M_C-Pz$\cdots$$M_{NC}$ system (left) or for each subsystem: the contact metal (M_C), the molecule (Pz) and the non-contact metal (M_{NC}) (right) (see Table S1).

Table S1 M06-HF/LanL2DZ vertical energies (VE/eV) and wave function for CT_{MM} metal-to-metal and CT_0 metal-to-molecule forward and reverse charge transfer states of Ag_n-Pz-Ag_n junctions (n=2,4,6 and 8) at 9.0 Å intercluster distance (d_{MM}).

CT_{MMF} : M_C^+-A…M_{NC}^-			
n[a]	**Configurations**[b]	**Coeff.**[c]	**VE**[d]
2	HOMO(M_C) → LUMO(M_{NC})	0.66	3.85
4	HOMO(M_C) → LUMO(M_{NC})	0.68	3.26
6	HOMO(M_C) → LUMO(M_{NC}) HOMO-2(M_{NC}) → LUMO(M_{NC})	0.55 -0.41	2.92
8	HOMO(M_C) → LUMO(M_{NC})	0.67	2.75

CT_{MMR} : M_C^--A…M_{NC}^+			
n[a]	**Configurations**[b]	**Coeff.**[c]	**VE**[d]
2	HOMO(M_{NC}) → LUMO(M_C) HOMO(M_{NC}) → Rydberg(M_{NC}; 6s)	0.50 -0.37	5.42
4	HOMO(M_{NC}) → LUMO(M_C)	0.68	4.40
6	HOMO(M_{NC}) → LUMO(M_C)	0.67	3.84
8	HOMO(M_{NC}) → LUMO(M_C)	0.69	3.52

CT_{0F} : M_C^+-A^-…M_{NC}			
n[a]	**Configuration**[b]	**Coeff.**[c]	**VE**[d]
2	HOMO(M_C) → LUMO(Pz; π*, b_1)	0.68	2.85
4	HOMO(M_C) → LUMO(Pz; π*, b_1) HOMO-1(M_C) → LUMO(Pz; π*, b_1)	0.61 -0.29	2.88
6	HOMO(M_C) → LUMO(Pz; π*, b_1) HOMO-1(M_C) → LUMO(Pz; π*, b_1)	0.55 -0.36	2.92
8	HOMO(M_C) → LUMO(Pz; π*, b_1) HOMO-1(M_C) → LUMO(Pz; π*, b_1)	0.49 0.38	2.94

CT_{0R} : M_C-A^-…M_{NC}^+			
n[a]	**Configurations**[b]	**Coeff.**[c]	**VE**[d]
2	HOMO(M_{NC}) → LUMO(Pz; π*, b_1)	0.64	4.21
4	HOMO(M_{NC}) → LUMO(Pz; π*, b_1) HOMO(M_{NC}) → LUMO+5(M_{NC}; 5p, b_1) HOMO-1(Pz; n, a_1) → LUMO(Pz; π*, b_1)	0.48 0.30 -0.26	4.04
6	HOMO(M_{NC}) → LUMO(Pz; π*, b_1) HOMO-1(Pz; n, a_1) → LUMO(Pz; π*, b_1) HOMO-1(M_{NC}) → LUMO(Pz; π*, b_1)	0.51 -0.32 0.27	4.00
8	HOMO(M_{NC}) → LUMO(Pz; π*, b_1) HOMO-1(Pz; n, a_1) → LUMO(Pz; π*, b_1)	0.39 0.28	3.98

[a]Number of silver atoms of each silver cluster; [b]Configurations with weights larger than 7%. Molecular orbitals are labelled for the contact metal (M_C), the molecule (Pz) and the non-contact metal (M_{NC}) subsystems (see Figs. S4-S7); [c]Coefficient of the corresponding configuration; [d]Vertical excitation energies at S_0 geometries.

Capítulo III – Resultados (V).

A Computational Study of the Vibrationally-Resolved Electronic Circular Dichroism Spectra of Single-Chain Transoid and Cisoid Oligothiophenes in Chiral Conformation.

Daniel Aranda, Javier Cerezo, Gennaro Pescitelli, Francisco J. Avila Ferrer, Juan Soto, Fabrizio Santoro*

We simulate the vibronic profile of the electronic circular dichroism (ECD) spectra of oligothiophenes in *cisoid* and *transoid* chiral arrangements. We consider oligomers of different lenghts, from two to fifteen units, and investigate extensively how the ECD spectral shapes depend on the inter-ring torsions. In general, the molecular structures we consider are not stationary points of the ground state potential enegy surface. Therefore in order to perform vibronic calculations we present a new computational protocol able to define reduced-dimensionality models where the effect of the off-equilibrium is removed. This is done adopting a description of the vibrational motions in curvilinear internal coordinates, and vertical harmonic models coupled with an iterative application of projectors to define energy Hessians, and therefore effective normal modes, in the space complementary to the one of the off-equilibrim coordinates. Although we consider both Franck-Condon and Herzberg-Teller contributions, the results show that *transoid* twisted ribbons always give rise to monosignated ECD spectra, while bi-signated and multi-signated spectra are expected for *cisoid* helices. These findings are explained on the basis of the different transition strenghts of the lowest electronic states imparted by the different spatial arrangment, that is almost linear for *transoid* structures and more globular for *cisoid* ones. We predicted the chiroptical response of large number of possible molecular arrangments. These data are employed to critically discuss the experimental ECD of polythiophenes in different experimental conditions, forming either aggregates or host-guest complexes. The method here proposed to perform vibronic calculations in reduced-dimensionality models is of general applicability and its potential interest goes beyond the practical application presented here.

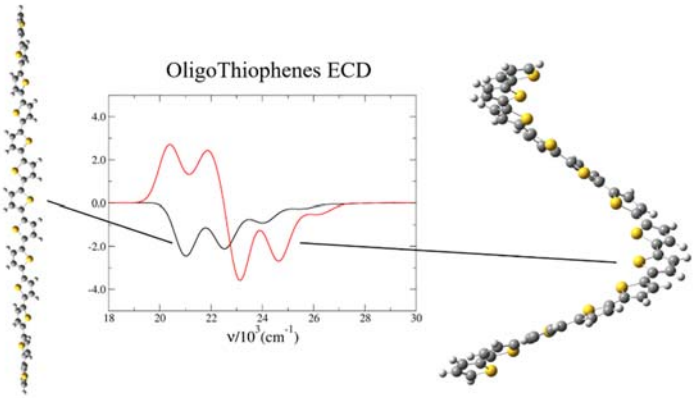

3.5.1. Introduction.

π-Conjugated oligomers and polymers are widely-used building blocks for optoelectronic materials such as sensors, transistors, solar cells and light-emitting devices.[1,2] The properties of such materials depend not only on the molecular skeleton but also on the supramolecular organization.[3,4] For the specific category of chiral materials,[5,6] Electronic Circular Dichroism (ECD) is a powerful tool to study such organization since it is very sensitive to supramolecular ordering (e.g. helices and helical packings).[7] In many cases, however, the interpretation of the ECD of these systems is mostly based on qualitative arguments[8] and the availability of suitable models to improve and make more robust the understanding of the relation between structure and chiroptical response is desirable. Chiral polythiophenes (PTs) have been widely investigated for their optoelectronic properties. In aggregated phases they often exhibit ECD spectra in the energy region of ππ* bright transition, characterized by a couplet feature with clear vibronic signatures.[9-24] In principle the chiroptical response of PTs observed in the aggregate state can arise from intramolecular or intermolecular chiral structures (Figure 1). Chiral intramolecular structures are both twisted transoid (Figure 1a) and helical cisoid (Figure 1b) arrangements of the single polymer chain. A chiral supramolecular assembly may originate from a helical packing of several approximately-planar chains (Figure 1c). In all cases, the chirality is transferred from covalently attached chiral pendants to the polymer chains and/or their packings. For simple alkyl- or alkoxy-substituted chiral PTs aggregates, Janssen and co. presented evidence that the ECD response mainly arises from a supramolecular helical packing (intermolecular mechanism).[14]

Recently[25] we have shown that a vibronic/exciton model, applied to a dimeric system made up of two planar stacked oligothiophenes in a twisted arrangement, provides ECD vibronic spectra in nice agreement with experiment, thus supporting the conclusions reached by Janssen et al.[14]

However, a detailed description of the ECD signatures corresponding to twisted *transoid* and/or helical *cisoid* arrangements of single PT polymer chain is still lacking. On the one hand, this information will clarify whether the intramolecular chiral arrangements could

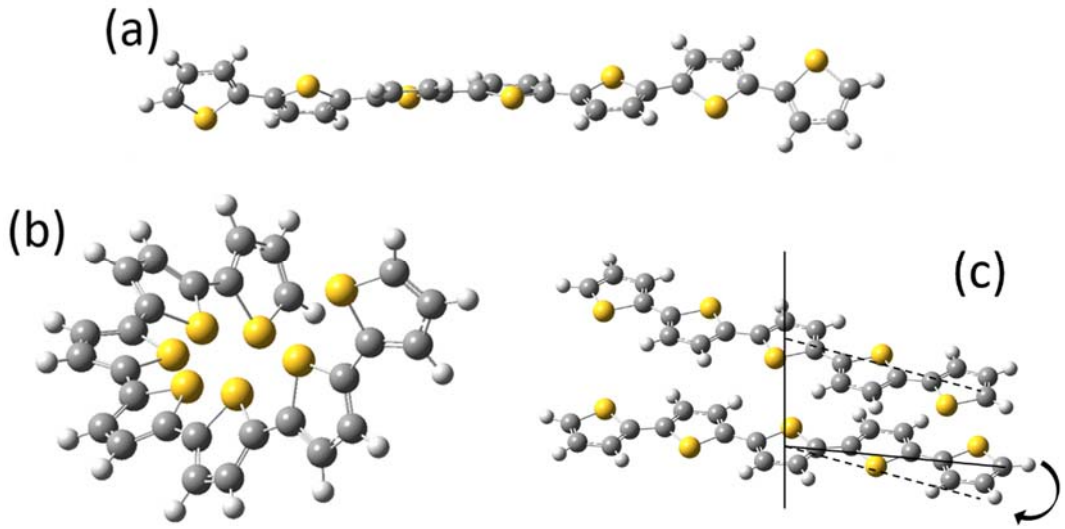

Figure 1. Single-chain chiral structures (a, twisted-ribbon *transoid*; b, helical *cisoid*), and supramolecular (c) chiral arrangement exhibited by PTs.

also play a role determining the chiral response of PT aggregates, thus providing a definitive answer in this respect. On the other hand, the detailed description of the ECD responses arising from both structural motifs will provide a rationale to elucidate the actual chiral arrangements adopted by single PT chains, which have been reported in some conditions. In one example, an "exciton-couplet feature" (although with no vibronic resolution) was detected in the ECD of an achiral PT interacting with a polysaccharide, schizophyllan.[26] The authors concluded that the single PT chains were insulated in the PT/polysaccharide complex where they adopted a transoid twisted ribbon conformation. More recently, it has been shown that, when achiral PTs interact with cellulose nanocrystals that form a nematic liquid crystal, a chirality transfer occurs, and PTs show a distinctive ECD signal with vibronic features.[27] The authors suggest that in this case the PT follows the helicoidal twist of the chiral host but, notably, in this case the ECD is monosignated. Weak monosignated ECD signals have been also observed for disubstituted poly-3,4di[(S)methylbutyl]-thiophene, concluding that a supramolecular organization was missing.[28]

In principle, classical Molecular Dynamics (MD) simulations with accurate force fields may help rationalizing these findings. Beside the challenge due to the complexity of the systems, such MD studies need in any case to be coupled with explicit ECD calculations with methods able to take into account vibronic resolution (i.e. the quantum nature of molecular vibrations). Vibronic methods are nowadays rather standard for rigid systems,[29-42] and have been also specialized

for ECD calculations,[34,40,43-48] while developments are currently ongoing for molecules showing some flexibility.[49-57] Among them the absorption and emission (but not the ECD) of oligothiophenes have been deeply investigated.[58-60] However, no straightforward computational approach is currently available for such complex systems as the ones described in this introduction.

On these grounds, we decided to perform a model study of the absorption (Abs) and ECD spectra of oligothiophenes in twisted transoid and helical cisoid arrangements. Since, in the different physical situations, the conjugation length and the actual helical structure (i.e. the torsional angles between adjacent units) of the PTs will be dictated by the interaction within the aggregate or with the host species, we present here an extensive analysis of the ECD response as a function of the length of the oligomer and the torsional angles. These latter in particular are considered as parameters and we investigate how the ECD response depends on them.

The idea behind such an exploration is that different dihedral angles between the thiophene units may mimic different PT conformations realized in different environments, where they are blocked by intermolecular interactions with chiral hosts. However, in order to make the vibronic calculations doable, the explicit description of the environment is not included in the model. The consequence is that the investigated chiral transoid and cisoid structures with fixed inter-ring torsions are in general not stationary structures of the oligothiophenes either in the ground or in the excited electronic states. In order to perform a meaningful computation of vibronic spectra we need to properly deal with these off-equilibrium cases. Here we propose a novel computational strategy that adopts vertical vibronic models[61] in the space of internal[62-66] and curvilinear[67,68] coordinates and an iterative procedure to project out the inter-ring torsions. This protocol allows to compute effective normal coordinates for both ground and excited electronic states, that are coherently defined in the space complementary to the one defined by the inter-ring torsions. Once this is done, effective vibrational states can be computed for both states and a Duschinsky relation can be written to connect them so that standard methods for the computation of vibronic spectra can be applied, including the effects of equilibrium geometry displacements, frequency changes and normal-mode mixings.

3.5.2. Methodology.

3.5.2.1. Molecular models.

We consider *cisoid* and *transoid* structures of oligothiophenes T_n of different length, up to n = 15. As we do not introduce chiral pendants in our model, each system may equivalently assume P or M helical arrangements, with exactly opposite chiral response. We selected right-handed (P) *cisoid* and left-handed (M) *transoid* structures because they deliver spectra with signs in agreement with the experimental spectra we will compare with.

We mainly focused our analysis on members of the series with an odd number of units since this allowed us to save computational time and cover, at the same time, a large interval of molecular dimensions. However, in order to exclude any odd-even effect, we also considered the "even" species T_{14}. For both *cisoid* and *transoid* arrangements it is possible to locate stable equilibrium structures in the ground electronic state. However, it cannot be taken for granted that the equilibrium helical structures of isolated oligothiophenes are representative of what happens in PT aggregates or in host-guest structures, where the actual values of the inter-ring torsions will depend on intermolecular interactions. Therefore, we studied two different classes of structures. In the first class (*I*), we consider oligomers of different length in their GS helical minima in isolated phase, while in the second class (*II*) we include oligomers of different lengths with predetermined (and all equal) values of the inter-ring torsions. Class *II cisoid* and *transoid* structures will be defined hereafter giving the value of the inter-ring S-C-C-S and S-C-C-C angles, respectively, generically indicated as θ. Notice that for the considered M *transoid* twisted ribbons S-C-C-C angles are all negative but, for simplicity, in the following they will be given in absolute values. All structures considered in this work belong to the C_2 symmetry point group.

3.5.2.2 Electronic structure calculations.

Electronic calculations were performed in gas-phase with Density Functional Theory (DFT) for the ground state and with Time Dependent (TD)-DFT for excited states, using Gaussian 16 suite of programs.[69] Plots of Kohn-Sham molecular orbitals were performed with Avogadro[70] version 1.2.0. We employed the CAM-B3LYP functional in combination with the 6-31G(d) basis set. The choice of a rather

small basis set was convenient for the extended investigation presented in this work, since it allowed us to compute in reasonable time the energy gradient and Hessians, and the transition dipole derivatives with respect to the Cartesian coordinates that are necessary for the computation of vibronic spectra, also in large oligomers like T_{15}. CAM-B3LYP was chosen for its better performance in the description of systems with extended π-delocalization.[71-75] In a previous paper,[49] some of us reported an extended investigation of the performance of different functionals and different basis sets on the position and shape of the absorption spectra of T_2 showing that CAM-B3LYP/6-31G(d) provides good spectral shapes, the main focus of this contribution, blue-shifted by ~0.2 eV with respect to those computed with the larger 6-311+G(2d,2p) basis set. In a subsequent paper we also showed that this level of theory provides Abs spectra in good agreement with experiment for T_3-T_7 *trans* oligomers.[51] Here we further checked the performance of the limited 6-31G(d) basis set on the more extended oligomer T_{13}, both in cisoid and transoid arrangement. In the Tables S1a and S1b in the ESI we show that increasing the basis set from 6-31G(d) to 6-311+G(2d,2p) the vertical excitations energies of the three states relevant for our analysis, namely S1, S2 and S3, exhibit a red-shift within 0.14 eV while their oscillator and rotatory strengths change only modestly. Therefore, for this specific application CAM-B3LYP/6-31G(d) represents a good compromise between accuracy and computational costs. Class *I* and class *II* structures were determined respectively by full optimizations and constrained optimizations (freezing the inter-ring torsions) in the ground state.

3.5.2.3 Vibronic calculations in reduced-dimensionality spaces.

Vibronic spectra were computed in harmonic approximation adopting vertical models, where both the initial and final states are quadratically expanded around the initial-state equilibrium geometry. We adopted both Vertical Gradient (VG) and Vertical Hessian (VH) models.[61] The Hessians of the final states are assumed to be equal to the one in the initial state in VG, while they are explicitly computed in VH. For class *II* structures, we consider initial-state geometries that do not correspond to stationary structures. Therefore, in order to compute the spectra, the contribution of the coordinates that are off-equilibrium (the inter-ring torsions) must be removed, defining reduced-dimensionality models. This requires a generalization of the standard VG and VH models. First it is necessary

to adopt curvilinear internal coordinates since they provide the correct framework to remove the contributions of molecular rotations at non-stationary points.[67] We use a set of non-redundant internal coordinates, $\mathbf{s}$, that is obtained from a redundant set, $\mathbf{s_r}$, that includes all the N_r bonds, angles and dihedrals arising from connectivity. In order to do that we apply the same rotation that diagonalizes $\mathbf{G_r} = \mathbf{B_r M^{-1} B_r^t}$, taking only the eigenvectors with non-zero eigenvalues, as proposed by Reimers.[76] In the previous expression, $\mathbf{B_r}$ is the matrix that relates Cartesian ($\mathbf{x}$) and internal coordinates, $\mathbf{s_r} = \mathbf{B_r x}$ and $\mathbf{M}$ is a diagonal matrix with atomic masses as diagonal elements. The rotation is then defined as $\mathbf{s} = \mathbf{A^t s_r}$ where $\mathbf{A}$ is a $N_r \times (3N\text{-}N_{TrRot})$ rectangular matrix, N is the number of atoms and N_{TrRot} is the number of translational and rotational degrees of freedom, i.e., 6 for non-linear and 5 for linear molecules.

The Hessian in terms of the nonredundant set of internal coordinates ($\mathbf{H_s}$), is obtained from the one in Cartesian coordinates ($\mathbf{H_x}$) with the following transformation,

$$\mathbf{H_s} = \mathbf{G^{-1} B M^{-1} (H_x - g_s^t \boldsymbol{\beta}) M^{-1} B^t G^{-1}} \quad (1)$$

where $\mathbf{B}$ is the matrix that relates Cartesian $\mathbf{x}$ and internal $\mathbf{s}$ coordinates, $\boldsymbol{\beta}$ is its derivative with respect to $\mathbf{x}$, $\mathbf{G} = \mathbf{B M^{-1} B^t}$, and $\mathbf{g_s}$ is the gradient in terms of $\mathbf{s}$, which is obtained from the one in Cartesian coordinates as $\mathbf{g_s} = \mathbf{G^{-1} B M^{-1} g_x}$.

As a second step to build up our reduced-dimensionality model it is necessary to remove from the Hessian the contributions of the "frozen" coordinates. In order to do that it is necessary to define the space spanned by these coordinates and project the gradient and Hessian in the complementary space. Let us define the sub-set of frozen internal coordinates $\mathbf{s_f}$ which are in general linear combinations of the redundant internal coordinates $\mathbf{s_r}$. ($\mathbf{s_f} = \mathbf{C s_r}$). We then write them on the basis of the nonredundant coordinates $\mathbf{s}$, $\mathbf{s_f} = \mathbf{C A^t s}$. Curvilinear internal coordinates define a non-orthogonal and non-Euclidean space, and this makes less trivial the definition of projectors. Let us first consider the particular case where the number of frozen coordinates $N_f = 1$, where we want to project the Hessian in the space complementary to a single coordinate $\mathbf{s_{f1}}$. The

component of the projection operator corresponding to such internal coordinate has been defined by Jackels et al[77] and is

$$\mathbf{P}_{\mathbf{s}}^{\boldsymbol{f1}} = \frac{\mathbf{s}_{f1}\mathbf{s}_{f1}^{t}}{\mathbf{s}_{f1}^{t}\mathbf{G}\mathbf{s}_{f1}} \tag{2}$$

and the Hessian projected onto the complementary space is,

$$\mathbf{H}_{\mathbf{s}}^{(\mathbf{1})} = (\mathbf{1} - \mathbf{P}_{\mathbf{s}}^{\boldsymbol{f1}}\mathbf{G})\mathbf{H}_{\mathbf{s}}(\mathbf{1} - \mathbf{P}_{\mathbf{s}}^{\boldsymbol{f1}}\mathbf{G}) \tag{3}$$

where $\mathbf{1}$ is the identity matrix. Equivalently, the gradient can also be projected on the complementary space as,

$$\mathbf{g}_{\mathbf{s}}^{(\mathbf{1})} = (\mathbf{1} - \mathbf{P}_{\mathbf{s}}^{\boldsymbol{f1}}\mathbf{G})\mathbf{g}_{\mathbf{s}} \tag{4}$$

In order to generalize this procedure to a case where N_f>1 we apply Eq. 2,3 and 4 in an iterative manner. However, we have to take into account that, after each coordinate is removed, the internal space is modified and so is the $\mathbf{G}$ matrix, which must be updated since it enters into the definition of both the projector and the projected Hessian and gradient. The operator that picks the coordinate $\mathbf{s}_{\boldsymbol{f1}}$ from $\mathbf{G}$ is simply,

$$\mathbf{P}_{\mathbf{G}}^{\boldsymbol{f1}} = \frac{\mathbf{s}_{f1}\mathbf{s}_{f1}^{t}}{\mathbf{s}_{f1}^{t}\mathbf{s}_{f1}} \tag{5}$$

and the updated matrix is $\mathbf{G}^{(\mathbf{1})} = \left(\mathbf{1} - \mathbf{P}_{\mathbf{G}}^{\boldsymbol{f1}}\right)\mathbf{G}\left(\mathbf{1} - \mathbf{P}_{\mathbf{G}}^{\boldsymbol{f1}}\right)$. By replacing $\mathbf{G}$, $\mathbf{H}_{\mathbf{s}}$ and $\mathbf{g}_{\mathbf{s}}$ by $\mathbf{G}^{(\mathbf{1})}$, $\mathbf{H}_{\mathbf{s}}^{(1)}$ and $\mathbf{g}_{\mathbf{s}}^{(1)}$, it is now possible to project out a second coordinate $\mathbf{s}_{\boldsymbol{f2}}$, generating a new Hessian $\mathbf{H}_{\mathbf{s}}^{(\mathbf{2})}$ and gradient $\mathbf{g}_{\mathbf{s}}^{(\mathbf{2})}$, as well as a new $\mathbf{G}^{(\mathbf{2})}$. At this point the procedure

can be straightforwardly repeated until the last coordinate $\mathbf{s}_{Nf}$ is projected out. In this way we achieve the definition of the Hessian matrix and gradient vector projected in the space complementary to $\mathbf{s}_f$ set of coordinates, $\mathbf{H}_s^{(Nf)}$ and $\mathbf{g}_s^{(Nf)}$, and the corresponding **G** matrix $\mathbf{G}^{(Nf)}$.

The dimensionality of the projected space is $3N\text{-}N_{TrRot}\text{-}N_f$ and let us call $\mathbf{s}_m$ the set of coordinates that span such space. If we now consider the $\mathbf{s}_f$ coordinates as frozen, the quadratic potential and the kinetic energy for the generic electronic state "e" can be written as,

$$V_e(\mathbf{s}) \equiv V_e(\mathbf{s}_m) = V_{0e} + (\mathbf{g}_s^{em})^t \mathbf{s}_m + \frac{1}{2}\mathbf{s}_m^t \mathbf{H}_s^{em} \mathbf{s}_m \tag{6}$$

$$T = \frac{1}{2}\dot{\mathbf{s}}_m^t (\mathbf{G}_m)^{-1} \dot{\mathbf{s}}_m \tag{7}$$

where the dot indicates derivative with respect to time and $\mathbf{G}_m$, $\mathbf{g}_s^{em}$ and $\mathbf{H}_s^{em}$ correspond to the $\mathbf{G}^{(Nf)}$, $\mathbf{g}_s^{(Nf)}$ and $\mathbf{H}_s^{(Nf)}$ matrices defined above. Notice that the definition of $\mathbf{G}_m$ does not depend on the electronic state, but only on the reference geometry used to expand the internal coordinates in terms Cartesian coordinates. At this point, the minimum for each $V_e(\mathbf{s}_m)$ can be obtained,[67] as $\Delta\mathbf{s}_{em} = -(\mathbf{H}_s^{em})^{-1}\mathbf{g}_s^{em}$ and the standard GF method can be used for defining $\mathbf{q}_e$, the effective $3N\text{-}N_{TrRot}\text{-}N_f$ normal coordinates when $\mathbf{s}_f$ coordinates are frozen.

In summary for the normal coordinates $\mathbf{q}_i$ and $\mathbf{q}_f$ of the initial (i) and a final (f) states of the electronic transition we have

$$\mathbf{s}_m - \Delta\mathbf{s}_{im} = \mathbf{L}_i \mathbf{q}_i \tag{8a}$$

$$\mathbf{s}_m - \Delta\mathbf{s}_{fm} = \mathbf{L}_f \mathbf{q}_f \tag{8b}$$

A Duschinsky relationship between $\mathbf{q}_i$ and $\mathbf{q}_f$ can be established from Eqs 8

$$\mathbf{q}_i = \mathbf{L}_i^{-1}\mathbf{L}_f\mathbf{q}_f + \mathbf{L}_i^{-1}(\Delta\mathbf{s}_{fm} - \Delta\mathbf{s}_{im}) \quad (9)$$

so that the Duschinsky matrix is $\mathbf{J} = \mathbf{L}_i^{-1}\mathbf{L}_f$ and is orthogonal (for vertical models only)[67] and the displacement vector is $\mathbf{K} = \mathbf{L}_i^{-1}(\Delta\mathbf{s}_{fm} - \Delta\mathbf{s}_{im})$. Notice further that if the spectra are computed from molecular structures obtained from constrained optimizations freezing s_f coordinates, the gradient $\mathbf{g}_{im}$ along $\mathbf{s}_m$ coordinates is zero and therefore also $\Delta\mathbf{s}_m$ vanishes. Once the Duschinsky relation is established, the spectra can be computed with standard time-independent (TI) and time dependent (TD) procedures developed for harmonic systems. We adopted the TD procedure implemented in the development version of our code FCclasses[78] at 0K.

In the following, the above protocol is adopted to remove the contributions of the inter-ring torsions, defined as linear combinations of all dihedrals along the rotated bond, all with identical coefficients.

This protocol is the main methodological novelty introduced in this work for the computation of vibronic spectra. On the other side, there is a vast literature on methods to compute the spectra of oligomers.[25,79-87] Most of them start from a diabatic (localized) picture, based on the Hamiltonians of the monomers and their couplings, and compute the spectra solving the challenging non-adiabatic problem in approximate ways[85,86] or reducing the space of the possible vibronic states (e.g. limiting the number of modes or their maximum excitation).[79-84] Such a reduction can also be performed in a rigorous framework, employing hierarchical representations of the Hamiltonians to obtain effective modes,[88-90] and we previously adopted these methodologies to compute the ECD of exciton coupled dimers,[25,87] like the stacked dimer of oligothiophenes reported in Figure 1c.[25] Using these non-adiabatic approaches would be a formidable task for the long oligomers investigated here. Therefore, we employed an "adiabatic" approach, considering directly the electronic adiabatic states of the covalently-bound multimers, each independent from the others, dressed by vibrational states described in terms of normal modes of the entire molecular structure. The effects of the couplings among the electronic states are then introduced in a perturbative way through the HT effects. This approach is similar to what done by Wykes et al for dimers in crystals[83] and it allows us to use the efficient all-coordinates methodologies developed for systems with harmonic potential energy surfaces and implemented in our code FCclasses.[78]

3.5.3. Results and discussion.

In order to compute the vibronic Abs and ECD spectra of the *transoid* and *cisoid* oligomers we need to perform a vibrational analysis of their ground state (S_0) and all the relevant excited-states [S_n with n=1,2,3 or generically ES]. In principle, structures of class *II* do not correspond to stable minima in the isolated species, neither in S_0 nor in ES. Additionally, twisted minima in the S_0 of the class *I* do not have a counterpart in the ES, where isolated oligothiophenes tend to get a planar arrangement.[51] In such a situation it is expected that a frequency analysis performed on the full internal coordinate space may predict the existence of a number of imaginary frequencies in GS and/or ES. For both classes of structures, the problem is solved by performing the vibrational analysis only in the space complementary to the inter-ring torsions, assuming that in the real scenarios we want to mimic, an aggregate or a host-guest complex, they are "practically" blocked and therefore "silent" for vibronic spectra (at least for low-resolution ones). Table 1 shows the results of this procedure by reporting the five lowest frequencies for cis-T_5 and trans-T_5 for a constrained GS minimum (class *II* structures) where all inter-ring torsions are fixed at $\theta = 10°$.

Table 1. Five lowest-frequency normal modes (in cm^{-1}) of S_0 and S_1 for cis-T_5 helices and trans-T_5 twisted ribbons of class II with $\theta = 10°$ computed from (a) the full-dimensionality Hessian, and (b) the reduced dimensionality Hessian obtained projecting out the inter-ring torsions. Letter "i" denotes imaginary frequencies.

	(a)				(b)			
	cis-T_5		trans-T_5		cis-T_5		trans-T_5	
Normal Mode	S_0	S_1	S_0	S_1	S_0	S_1	S_0	S_1
1	41.06i	19.87	18.23i	14.28	25.24	23.96	28.99	27.58
2	34.46i	19.98	17.28i	26.36	33.97	29.54	36.76	31.83
3	23.66i	24.76	9.03i	27.33	51.87	46.13	53.10	47.17
4	12.44i	32.14	1.47i	34.03	65.74	62.80	71.46	67.01
5	25.07	37.44	25.26	40.28	89.98	79.73	90.92	79.10

VH model accounts for both the effects of equilibrium geometry displacements and the effect of frequency changes and Duschinsky mixings. For helical oligothiophenes, the latter have a moderate effect on the position and the shape of the absorption spectra. This is illustrated in Figure 2 by comparing VH and VG predictions for $S_0 \rightarrow S_1$ ECD spectra of trans-T_2 and trans-T_5 species from their isolated minima in S_0 (class *I* structures). VG model only considers geometry displacements. The shapes of the spectra

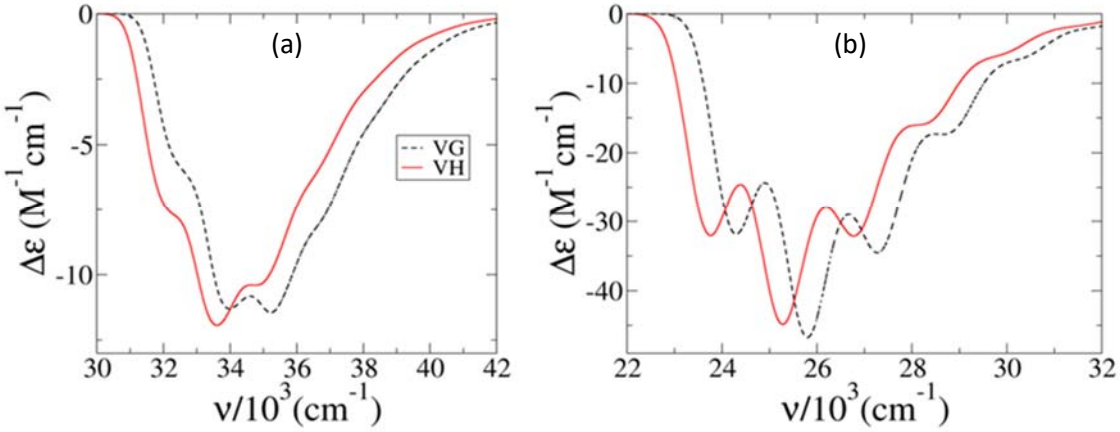

Figure 2. Comparison of the FC ECD spectra of (a) trans T_2 and (b) trans T_5 (class *I* structures), computed with VG and VH models at 0K and broadened with a Gaussian with HWHM=450 cm^{-1}. Inter-ring torsion angles are considered frozen during the transition.

are similar, meaning that Duschinsky effects are minor. The VH spectra are only slightly red-shifted due to the changes of the frequencies from S_0 to S_1. The frequency shift is not important in our simulations since we mainly focus on the shape of the spectra rather than on their position.

Notwithstanding the similarity of VG and VH predictions for the ECD of short oligomers, it is important to highlight that the analysis of the ES Hessians, a prerequisite for VH calculations, is useful to unveil the existence of inter-state electronic couplings which would be undetected by a simple application of the VG model. We found that for systems with more than 7 units, even after removing all the inter-ring torsions, a sizable imaginary frequency is predicted for S_1 state, along a non-total symmetric (*b* irreps) mode, corresponding to a stretching of the backbone. Table 2 shows the value of such frequency for systems with an odd number of units from T_9 to T_{13}, for inter-ring torsions fixed at a dihedral angle $\theta = 25°$ (class *II* structures). T_{14} was also included to show that members of the series T_n with odd and even "n" have similar behaviors. Analysis of the Hessian of S_2 state reveals that these imaginary frequency modes (or, more precisely, the modes of S_2 that mostly resemble them) exhibit an anomalously large (> 2000 cm^{-1}) real frequency. This is a signature of a coupling between the S_1 (B symmetry) and S_2 (A symmetry) states promoted by these b modes. Distortion along these modes activates the coupling, causing a repulsion of S_1 and S_2 energies that increases the frequency on the upper-energy state, and, if it is strong enough, produces an imaginary frequency on the lower-energy state.

Table 2. Imaginary frequency on S_1 at the constrained helixes with all inter-ring torsions set to θ = 25° (class *II* structures). The frequency of the most similar S_2 mode (projection always larger than 0.6) is also reported. Values in cm^{-1}.

	cis-T_n				trans-T_n			
	T_9	T_{11}	T_{13}	T_{14}	T_9	T_{11}	T_{13}	T_{14}
S_1	343.23i	706.30i	960.74i	1063.91i	496.68i	815.24i	1029.82i	1116.60i
S_2	2038.47	2123.89	2203.47	2241.54	2088.17	2170.14	2239.14	2270.63

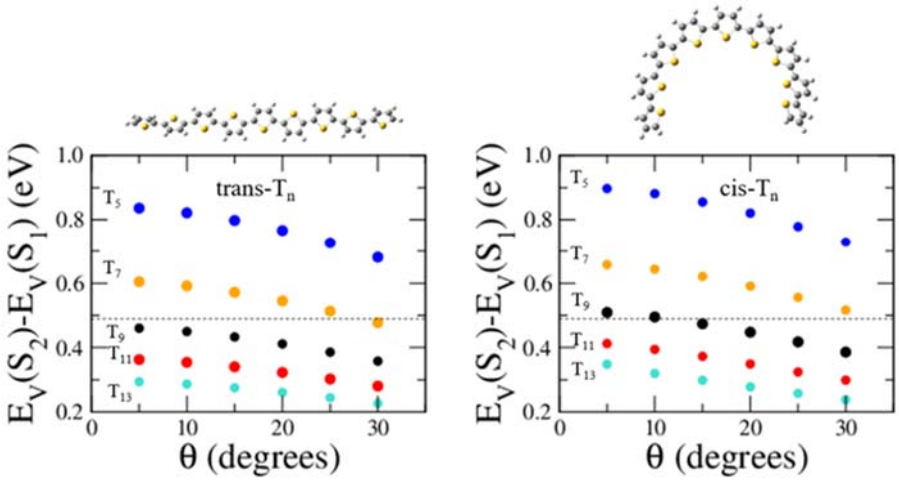

Figure 3. Vertical transition energy difference between S_1 and S_2. for class *II* systems (symmetry C_2) with transoid (left) or cisoid (right) arrangements (for a fast identification, the structures of *transoid* and *cisoid* T_9 are sketched above the two panels). In systems with an energy gap below the threshold close to 0.5 eV, indicated by the horizontal line, an imaginary frequency was computed along an anti-symmetric stretching mode (b symmetry).

Such a coupling becomes more effective for long oligomers since in these systems S_1 and S_2 get closer in energy. To highlight this phenomenon, in Figure 3 we report the difference on the vertical transition energies for both S_1 and S_2 for class *II* transoid twisted ribbons and cisoid helices of odd oligomers (from T_5 to T_{13}), as a function of the fixed inter-ring twist angle θ. The energy gap between S_2 and S_1 decreases upon increasing the length of the chain or twist angle. Interestingly, in all the cases in which the energy gap decreases below a threshold value, determined to be slightly below 0.5 eV, an imaginary frequency is observed on S_1.

From the point of view of the computation of vibronic spectra, the occurrence of inter-state couplings poses an additional challenge. Generalizations to include such coupling in the vertical models described in the Section 2 are possible, adopting the so called linear (LVC) and quadratic vibronic coupling (QVC) models,[91] but they require a completely different computational approach, based on the numerical propagation of nuclear wavepackets on the coupled surfaces. Such accurate calculations are challenging and time-consuming (although remarkable progresses have been made with the

multiconfigurational time dependent Hartree method[92]) and are out of the scope of the present investigation. Therefore in the following, for long oligomers, we base our discussion on the simple VG model. Like VH, it neglects the effect of inter-state couplings, but it is more robust than VH since it does not suffer from the technical problems connected to the occurrence of imaginary frequencies in the ES that, if not properly treated, can generate remarkable artefacts in the spectra simulation. Clearly, inter-state couplings may have an impact on the spectral shape. Therefore our VG results will be mainly used for a qualitative discussion.

By theory, in FC approximation ECD spectra involving only one final electronic state are monosignated. An alternation of signs can arise from intensity borrowing mechanisms, and it can be straightforwardly described at perturbative level within the so called Herzberg-Teller (HT) theory.[43,45-48] Since in different experimental conditions the ECD spectra of PTs are bisignated, in the following we perform FC+HT (FCHT) calculations. We are aware that, when the inter-state couplings are large and the coupled states are close in energy, the perturbative HT treatment can give rise to remarkable artefacts (and a proper description would require the QVC or LVC Hamiltonians described above). The problems manifest with an anomalous increase of the intensity of the spectrum, often accompanied by a drastic change of its shape.[52] Since for almost all the investigated molecular structures, HT effects are predicted to be extremely small, so that FC and FCHT predictions are hardly distinguishable, we can confidently trust our FCHT results.

3.5.3.1. Transoid Twisted Ribbon.

In this section we focus on oligomers adopting a transoid twisted ribbon arrangments. As reported in the Electronic Supplementary Information (ESI), for trans species we can consider the lowest exicted state only, S_1 , since both in the totally relaxed S_0 geometry (Figure S1 in the ESI) and in any considered constrained-minimum with fixed dihedral angles θ (Figures S2-S4 in the ESI), S_1 is the only bright state for either absorption or ECD. Figure 4 reports the predicted absortion and ECD spectra of T_9 , T_{11} and T_{13} oligomers, starting from totally relaxed structures on S_0 (class *I*). The spectra of T_5 and T_7 are plotted in Figure S5 in the ESI. For the investigated species the S-C-C-C inter-ring torsions range from -18 to -22 degrees. HT contributions to both Abs and ECD spectra are negligible. This fact has two main consequences: (i) the ECD spectra are predicted to be monosignated, with negative sign for negative S-C-C-C angles and (ii) Abs and ECD

spectra exhibit superimposable shapes. A variation of the spectral shape with the chain length is observed: the relative intensity of the 0-0 transition in fact becomes progressively larger for longer oligomers. The overall ECD intensity also increases for longer systems, as expected, since every additional ring increases both the electric transition dipole and the chiral response of the helix. Finally, in agreement with experiment, a red shift is also observed at the increase of "n" since the HOMO and the LUMO get closer in energy.

Next, we focus on systems of the class *II*, i.e., with fixed and equal torsional angles. We report the Abs and ECD spectra dependence on the inter-ring torsion angle for T_9 ,T_{11} and T_{13} in Figure 5. Results for T_5 and T_7 are given in Figures S6-S7 of the ESI. Even for class *II* structures the HT contribution is very small for Abs and vanishingly small for ECD. The overall intensity of the Abs spectra is almost constant with the torsion angle. The spectral shape changes remarkably with the length on the oligomer, since the relative intensity of the 0-0 transition becomes larger, while a smaller dependence with the torsional angle is seen. At variance with Abs, the ECD intensity remarkably increases at the increase of the twist angle. This was expected since, for the same molecule, a larger twist angle implies a higher number of turns which results in an increase of the chiral response. Finally, a blue shift of the Abs and ECD spectra with the increase of θ is observed: the red-most spectrum is predicted for planar structures, where the S_1 energy is minimum, while moving away from planarity the S_1-S_0 energy gap increases since the S_1 energy profile is steeper than the S_0 one.[51] Figure S8 in the ESI reports the results for T_{14} at θ = 10° and θ = 15° showing that there is no significant difference with respect to systems with odd number of units.

3.5.3.2. Cisoid Helix.

The cisoid helical conformers show a spectral behaviour much more complicated than the transoid species. Both S_1 and S_2 are bright and have rotatory strengths with opposite sign, whereas the intensity of S_3 is strongly dependent on the length and the torsion angles for both Abs and ECD. This dependence is analysed in the ESI, Figures S9-S11. FC and FCHT Abs and ECD spectra are shown in Figure 6 for class *I* cisoid helices of T_9, T_{11} and T_{13}. T_5 and T_7 spectra are reported in Figure S12 in the ESI and T_{15} in Figure S13. The contribution of each state and their sum is shown. Some similarities with the

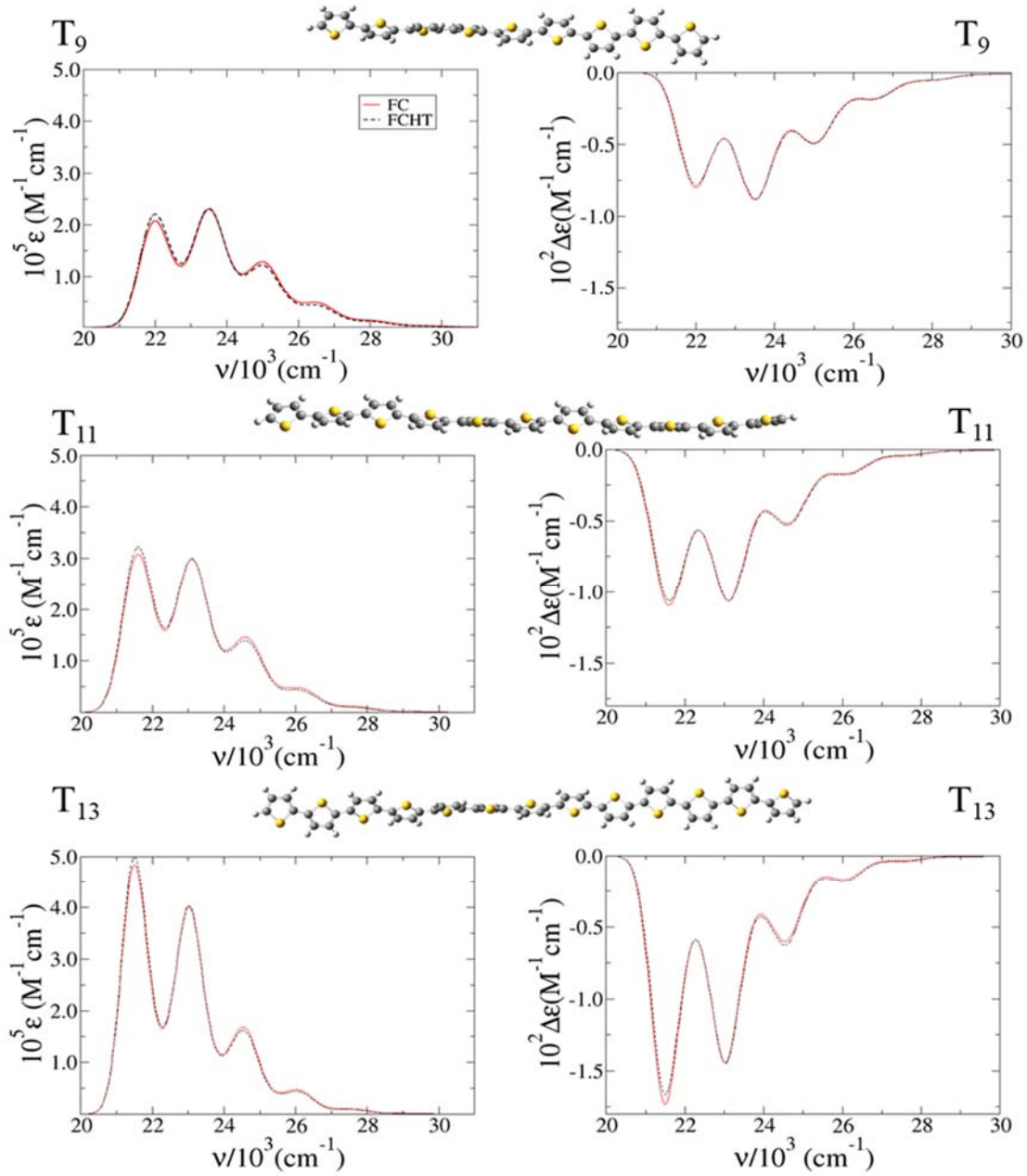

Figure 4. FC and FCHT absorption (left) and ECD (right) spectra computed for the *class I* structure of T_9, T_{11} and T_{13} transoid twisted ribbons (structures shown above the figures) at 0K and broadened with a Gaussian with HWHM=450 cm^{-1}. Inter-ring torsion angles are considered frozen during the transition.

findings for transoid structures are observed: HT contribution is small for Abs (apart from some remarkable effect on S_2 for T_{11} and T_{13}) and negligible for the ECD. Moreover, in relative terms, the ECD intensity of S_1 progressively increases with respect to S_2 with the length of the oligomer: the most intense state for the shortest system is S_2, while it is S_1 for T_{13}. The energy difference among the different states decreases with the length of the oligomer so that their contribution overlap increasingly. Therefore the contributions of different states cumulate in Abs and give rise to partial cancelations in ECD. The

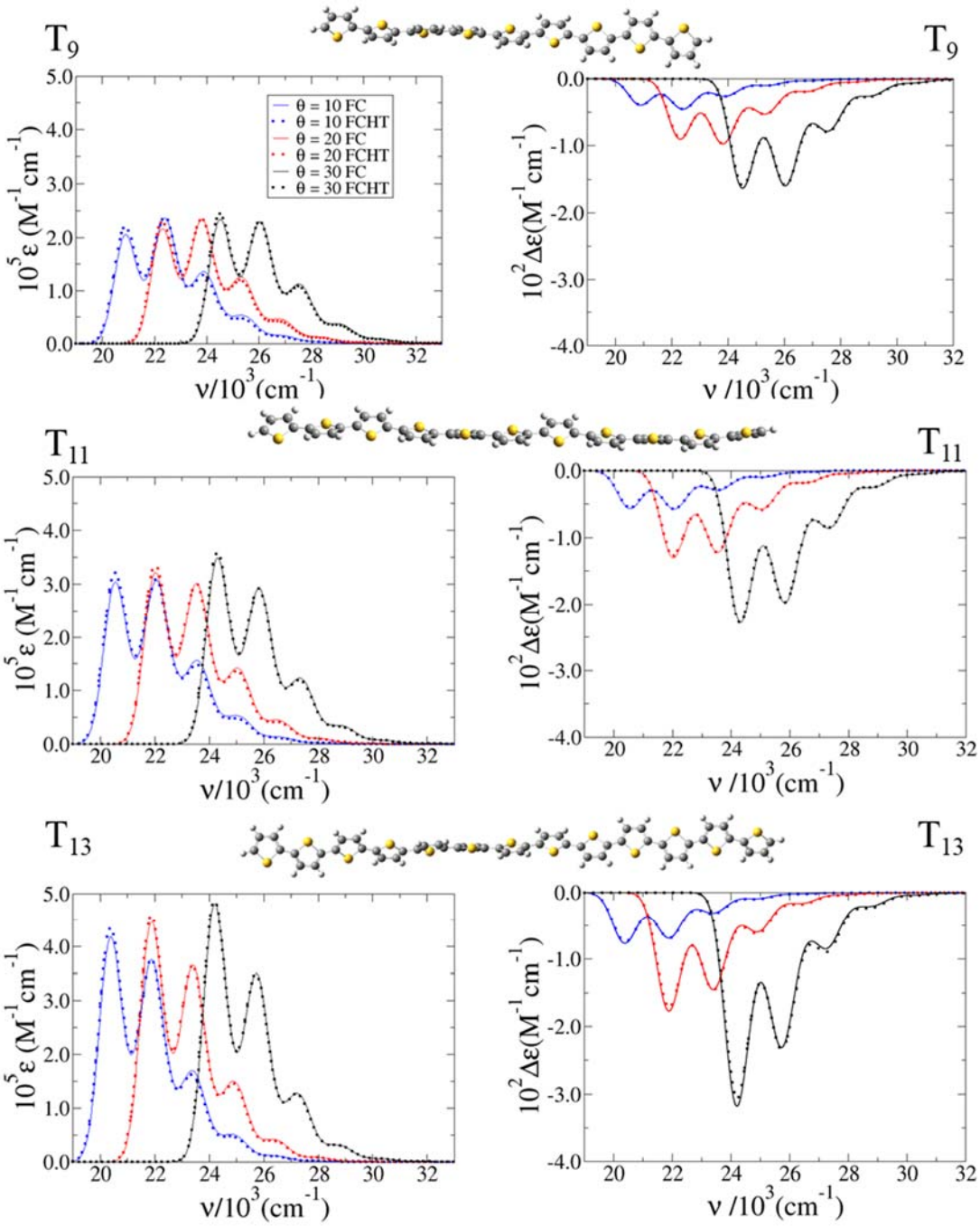

Figure 5. FC absorption (left) and ECD (right) spectra computed for the *class II* structure of T_9, T_{11} and T_{13} transoid twisted ribbons at 0K and broadened with a Gaussian with HWHM=450 cm^{-1} at different torsion angles (considered frozen during the transition).

resulting exciton-like ECD couplets have positive short-frequency component for right-handed helices. Notice in this respect that, at the same time, the couplings among the different states becomes more effective (see beginning of the Section 3) so that it is expected that their proper inclusion in the model would lead to a modulation of the predicted spectral shapes.

Results for class *II* molecules T_9, T_{11} and T_{13} are reported in Figure 7. Here, for clarity, only the sum of the contributions of the S_1-S_3 states and only FC spectra are shown. FCHT

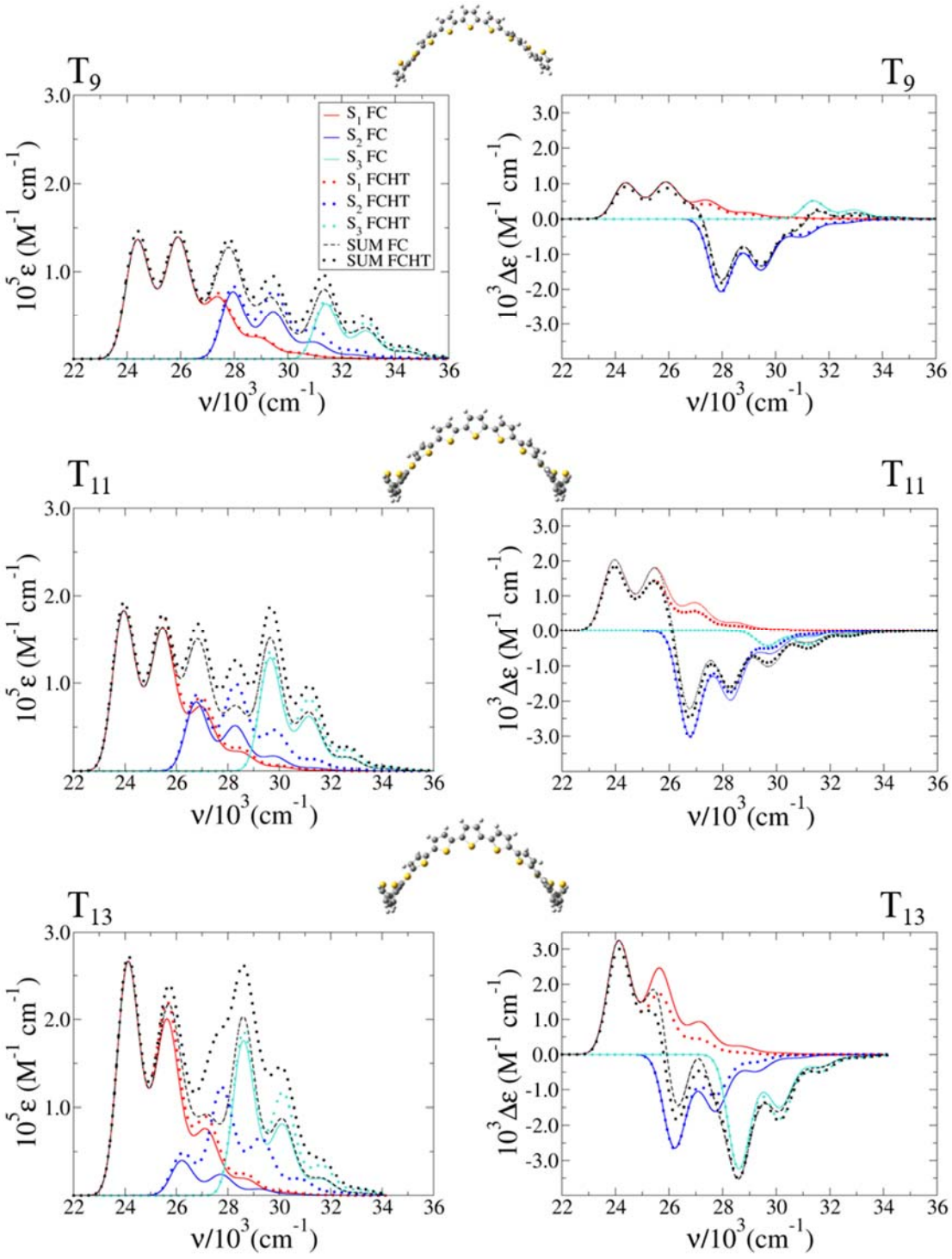

Figure 6. FC and FCHT absorption (left) and ECD (right) spectra computed for the *class I* structure of T_9, T_{11} and T_{13} cisoid helices (structures shown above the figures) at 0K and broadened with a Gaussian with HWHM=450 cm^{-1}. Inter-ring torsion angles are considered frozen during the transition.

results are very similar and are shown in the ESI, together with the individual contributions of each system, also for T_5, T_7 and T_{15} in Figures S14-S25.

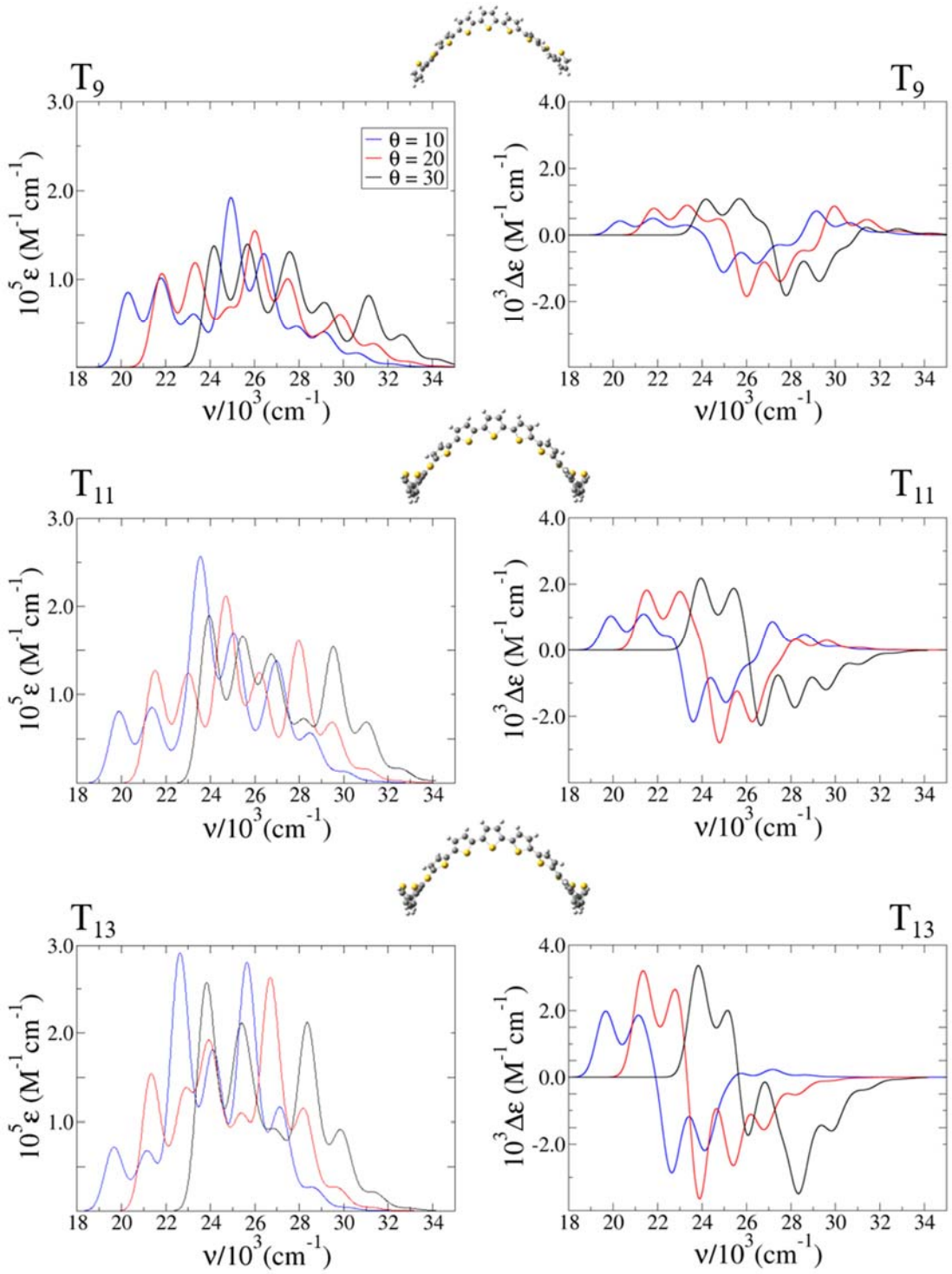

Figure 7. FC absorption (left) and ECD (right) spectra computed for the *class II* structure of T_9, T_{11} and T_{13} cisoid helices at 0K and broadened with a Gaussian with HWHM=450 cm^{-1} at different torsion angles (considered frozen during the transition).

For Abs, the intensity of S_1 is barely affected by the length of the oligomer in absolute terms, but the dependence on θ is steeper. On the contrary, S_2 intensity steadily increases with the length, but it decreases for larger twisting angles. Finally, S_3 intensity rises with the length, while it is less sensitive to the torsion angle than for the other two states.

For all the states, the oligomer length modifies the dependence of the ECD intensity with the torsional angle. More specifically, the ECD intensity is basically constant with θ for short systems, it increases approximately linearly with θ for T_9 and finally it exhibits a non-linear behaviour for longer systems like T_{11} and T_{13}. In summary, due to the simultaneous contribution of three excited states, the Abs spectrum for cisoid helices is predicted to be very broad and the ECD spectrum is predicted to be bisignated, or even trisignated (see for instance the results for class *II* structures of T_9 and T_{11} with θ=10°). The number and relative intensity of vibronic peaks in the positive and negative parts of the ECD spectra strongly depend on the length of the oligomer and the dihedral angle θ. If we focus on the lowest-energy positive part, it is composed by three peaks in T_7 and T_9 and two peaks in T_{11} and T_{13}, and the relative intensity of the lowest-energy peak increases with the length of the oligomer. As in the case of *transoid* species, no odd-even effect was observed by the analysis of the spectra of cisoid T_{14}.(Figure S26). Before closing this section, we notice that we investigated limiting regular structures, either all *cisoid* or all *transoid*. In some cases a combination of both may be expected, as well as mixtures of segments with left-handed and right-handed helices, although these structures may contrast or even disrupt supramolecular organization. In the ESI we report a test calculation for a T_{13} oligomer made up by two T_7 segments (the central T unit is shared between the two), respectively with transoid and cisoid arrangments. Both Abs and ECD spectra of this mixed structure are placed in the same energy range of fully *cisoid* and *transoid* T_{13} species (and not where T_7 spectra are). The spectral shapes are more similar to those of *cisoid* than *transoid* structures, and to those of T_{13} than T_7. In particular the ECD is bisignated and, when properly scaled, it is practically superimposed to the one of cisoid T_{13}. However some effect of the transoid moiety is noticed both in the relative intensity of the Abs vibronic peaks and in the overall intesity of the ECD that is remarkably smaller than for pure cisoid T_{13}. See Figures S27-S29 in the ESI.

3.5.3.3. Comparison with experimental results.

The results reported in the previous sections indicate that the ECD spectra of *transoid* twisted ribbons are always monosignated while those of *cisoid* helices may be bi- or tri-signated. This drastic difference arises from the fact that the spectra of *transoid* structures are dominated by a single state, S_1, while the spectra of *cisoid* helices arise from the comparable contributions of two or three different electronic states. In the ESI we analyse this different behaviour, focusing on the electric transition dipole of T_7 and T_{13}, and considering both the Kohn-Sham molecular orbitals (MOs) involved in the transitions (Figures S30-S33) and the transition densities (Figures S34-S39). The lowest energy states of these systems arise from transitions between very similar MOs in both *cisoid* helices and *transoid* twisted ribbons, and also the transition densities look pretty similar. However, the different spatial arrangments of the two structures have a deep impact on the Cartesian components of the transition dipoles. Transoid structures, in fact, mostly extend in the direction of the non-total symmetric Y axis. On the contrary, cisoid helices extend along all the three axes. S_2 belongs to A irreps, and the extension of the cisoid helices along the Z axis gives rise to a strong Z component of the transition dipole, not possible in the transoid structure. As far as S_3 (B symmetry) is concerned, with respect to the T_7 structure, longer cisoid species, like T_{13}, have left and right wings that elongate in the X and Y directions. We show that these wings give the largest contribution to the X component of the transition dipole explaining why the transition is strong for T_{13} and weak for T_7. In the following discussion, the different predictions for the ideal regular *cisoid* helices and *transoid* twisted ribbons investigated above will be exploited to qualitatively discuss the experimental Abs and ECD spectra of PTs in different aggregation phase or in host/guest complexes. Quantitative comparisons are not possible due to the lack in our idealized models of several ingredients, like the environment (e.g. the host nanostructures), or the substituents. However, it is worthy to recall that although the substituents are necessary to help solubilization[26,27] or to introduce a stereodefined element of chirality, in most cases they are alkyl or alkoxy groups which are not expected to introduce large changes in the low-lying electronic states. To test the impact of substituent, we modelled a T_{13} species with all thiophene units methylated at position 3. For this model, the S1-S3 states are shifted by less than 0.05 eV (see Table S2 in ESI) with respect to T_{13}. Another source of substantial difference between our idealized structures and real PT systems lies in the oligomer length, because

the largest species we investigated here is T_{15}. In some cases, the length of the experimental chains we discuss below is longer. However, it is known for PTs that the effective limit of the conjugation length for the lowest electronic state is already reached for oligomers with n=20,[93] i.e. only slightly larger than those investigated here. The fact that the conjugation length for S1 is close to reach its limit could be also inferred from the inspection of the orbitals invovled in the transition. In fact already for T_{13} HOMO and LUMO start being rather confined in the central molecular portion (see ESI, Figure S31 and Figure S33). For the higher states S_2 and S_3 (relevant for Abs or ECD, especially in cisoid structures) the discussion is less straightforward. In fact, although also the orbitals involved in these transitions do not uniformly spread over the whole molecular structure, they tend to have a small density on the central part and be more concentrated on the two extremes of the molecular structure. However, as a matter of fact our predictions for the longest investigated species (from T_{13} to T_{15}) are quite similar. On these grounds, we will extrapolate our results to qualitatively discuss also the behaviour of longer PT species. From the technical point of view, it is possible to foresee that an attempt to simulate the spectra of remarkably longer chains (dozens of units) might require the inclusion of a larger number of states and be challenged by the occurrence of larger inter-state couplings.

3.5.3.3.1. Aggregate states of chiral PTs.

In Figure 8 (top) we report the Abs and ECD experimenal spectra of an aggregate of a poly[3,4-bis((S)-2-methylbutoxy)thiophene] (PBMBT) with an average chain length of ~60 units in CH_2Cl_2 at 243 K. Similar experimental spectra have been observed in other aggregate states, e.g. thin films or solvent/non-solvent mixtures.[14] The ECD is bisignated and therefore, according to the results in the previous section, it is not compatible with a transoid twisted ribbon arrangment. At variance, we showed that cisoid helices can give rise to bisignated spectra. In Figure 8 (top panel) the experimental spectra are compared with those predicted for a cisoid helix of T_{13} with $\theta = 15°$, a case that provides a quite nice agreement for ECD. For completeness Figure 8 also reports the spectrum computed for a stacked dimer of T_{13} ($T13_2$) with a vibronic exciton model from ref. [25] which fits very well the experiments. Therefore, based on the analysis of ECD only, two completely different molecular arrangments seem compatible with the experiment. In order to discriminate between the two possibilities we notice that in ref. [25] we showed that results are similar for dimers of oligomers of different length. At variance, apart

from T_{13} with θ = 15°, only a few other combinations of length and torsion fits reasonably well the experimental spectrum of PBMBT (for example T_{15} with θ = 10°). For instance,

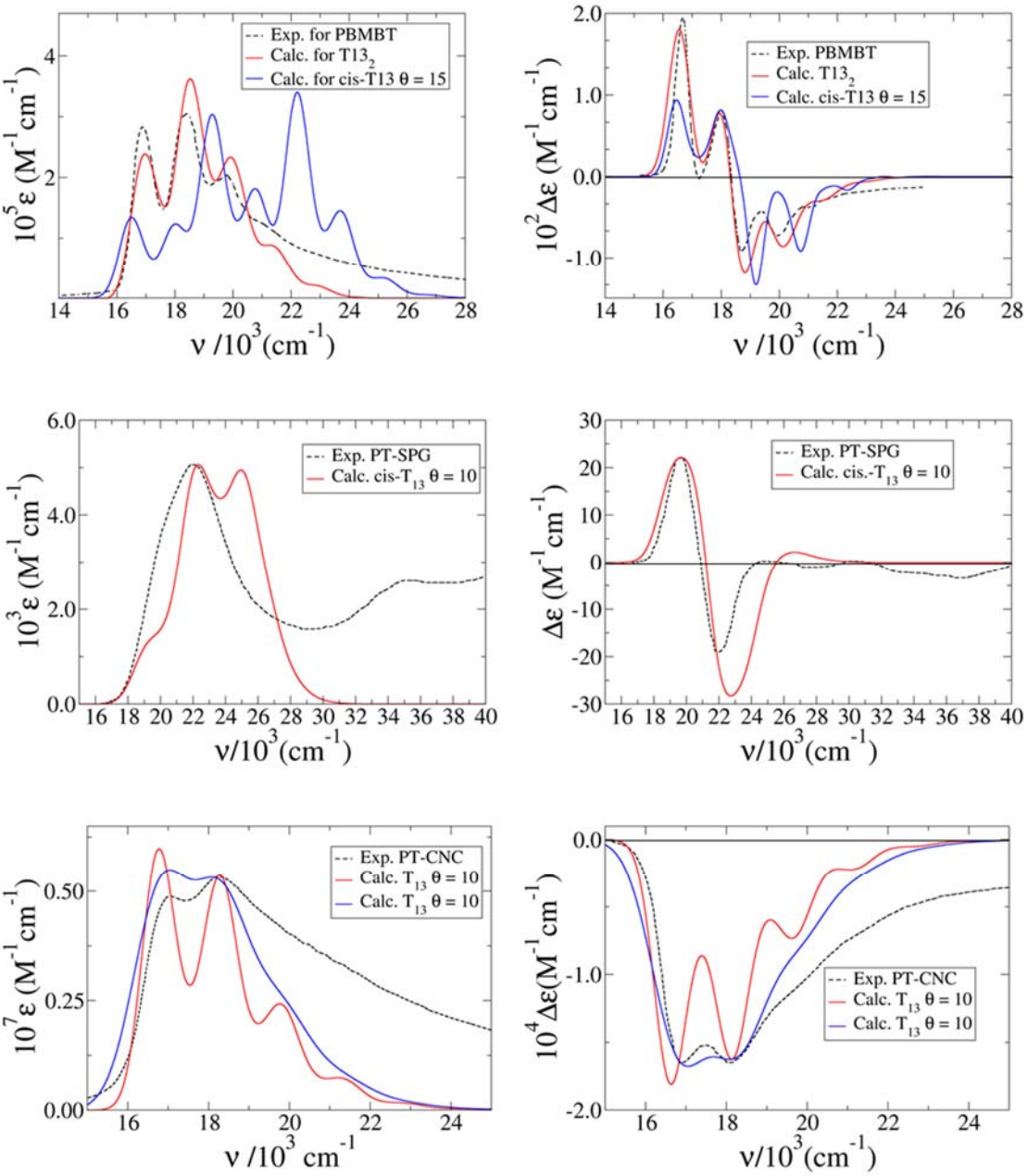

Figure 8. Comparison of experimental and calculated absorption (left) and ECD (right) results. Top panels compare the experimental spectra of PBMBT with a FC spectrum of cisoid T_{13} class *II* structure with θ = 15° shifted by ~3900 cm^{-1} and broadened with an HWHM=320 cm^{-1}. For completeness, results for an exciton dimer $(T_{13})_2$ from ref. 25 are also included. Central panels report the experimental spectra of a PT-SPG supramolecular complex compared with the results of a cisoid T_{13} with θ = 10° shifted by ~4800 cm^{-1} and broadened with an HWHM=970 cm^{-1}. Finally, bottom panels compares the experimental spectra of PPBT over CNC with the results for a transoid class *II* structure of T_{13} with θ = 10° redshifted by ~3600 cm^{-1} and broadened with an HWHM=770 cm^{-1} (blue) and a narrower (red) HWHM of 450 cm^{-1}. In all cases, the calculated intensities were rescaled so to fit with experiment.

cisoid-T_9 (Figure S19) shows a high-frequency positive series of peaks not observed in experiments.

It appears unlikely that a polymer aggregate is so ordered that only cisoid helices with a specific conjugation length and a specific value of the inter-ring torsion occur. Therefore, the large variability of the predicted ECD spectra of cisoid helices with the length and the twist angle suggest that they cannot satisfactorily explain the ECD spectra commonly observed for chiral PT aggregates.[14] A strong support to this conclusion comes from fact that the Abs spectrum predicted for cis-T_{13} and cis-T_{15} (see ESI, Figure S22 and Figure S24) helices is much broader than in the experiment, while the one predicted for the stacked dimer nicely fits the observation. Finally, even for cis-T_{13} and cis-T_{15} helices the ECD envelope is actually wider than the experimental one. Thus, the present results reinforce the previous findings[14,25] that the vibronic ECD couplets seen for chiral PT aggregates are a signature of intermolecular exciton coupling between quasi-planar PT chains arranged in helical stacks.

3.5.3.3.2. Achiral PT bound to schizophyllan.

As discussed in the previous sections, all spectra computed for transoid twisted ribbons are monosignated, irrespective of their conjugation length and inter-ring torsion. On these grounds it seems unlikely that the water-soluble PT poly[3-(3-trimethylammonium chloride)propoxy-4-methyl-thiophene] bound to chiral schizophyllan in DMSO/water mixture at 293K, as reported in ref. [26], assumes a transoid twisted ribbon arrangement, as inferred by the authors. In fact, the observed ECD spectrum is markedly bisignated (Figure 8, middle panel). Additionally, in those experiments the PT are not expected to form aggregates like supramolecular helical stacks. For these reasons, we decided to investigate if single chain cisoid helices can give rise to signals compatible with the experimental findings. In Figure 8 (middle panel) we compare the experimental Abs and ECD spectra with those predicted for the cisoid helix of T_{13} (class *II*) with θ=10° which provides the best agreement with the experimental ECD. We adopted a large broadening that washes out the progressions as it happens in the experiment, where this phenomenon is likely due to inhomogeneous broadening mechanisms. The computed ECD spectrum of the cisoid helix is qualitatively in agreement with experiment, showing a clear bisignated spectrum. Because of the broadening, in fact, the positive contribution at high-frequencies due to S_3 state is almost

completely cancelled by the S_2 one. Actually, a very weak positive signal on the blue side of the couplet is seen in the experiment and it has a counterpart (due to S_3 contribution) also in the computation. From the quantitative point of view, the computed Davydov splitting (couplet width) is overestimated and the Abs spectrum is too broad. These discrepancies can be due to several factors, like for instance, the absence in our calculations of an explicit model of the chiral environment, or computational errors on the relative oscillator and rotatory strengths of the different states or on their energy gaps, or the fact that inter-state couplings have been neglected. It is also likely that longer oligomers should be used for a more reliable comparison, even though no improvement is predicted by our calculations on the shape of the spectra when moving from T_{13} to T_{15}. Therefore, our results suggest that the formation of cisoid helices, possibly due to the interaction with the triple helix of schizophyllan, may lead to the observed ECD signal. Since the agreeement we got is only qualitative it is also possible that more complicated structures are formed which only locally assume a cisoid character. In any case, the helices should be characterized by small inter-ring torsions. In fact: (i) the experimental spectra are remarkably red-shifted with respect to those in solution, and our results confirm that the spectrum blue-shifts upon increasing θ; (ii) the positive contribution due to S_3, which is only scarcely visible in the experiment, is predicted to increase with θ. In summary, on the grounds of the above analysis, the PT interacting with schizophyllan is more likely to form cisoid-like helices, e.g. by wrapping around or together with the schizophyllan triple helix, rather than elongated transoid twisted ribbons encapsulated in the triple helix, as inferred in the original paper.[26]

A similar conclusion might also be viable for another achiral PT, poly(thiopheneboronic acid), encapsulated into soft nanotubes based on glycolipids.[94] In one case discussed in that paper, an isolated PT chain was argued to form with transoid twisted ribbon arrangement. The corresponding chiroptical response was once again a bisignated non-structured ECD profile, which, according to our findings, is incompatible with the suggested arrangement.

3.5.3.3.3. Achiral PT interacting with cellusole nanocrystals.

PTs interacting with chiral cellulose nanocrystals in water exhibit a negative monosignated ECD spectrum.[27] In Figure 8 (bottom panel) we compare the experimental Abs and ECD spectra of the commercially available poly[3-(potassium-4-butanoate)

thiophene-diyl] with an average length of 78 units, with those computed for a transoid twisted ribbon (class *II*) of T_{13} with with θ=10°. The low resolution of the experimental spectrum in such a complicated system may be dictated by many physical factors, including the inhomogeneous broadening due to the interaction with the crystals and/or with the solvent (water), and a limited, but not null mobility of inter-ring torsions. Notice in fact that a mobility of these comparable to the one expected in solution would erase all the vibronic structures.[51] Therefore, we report computed spectra with both the narrow broadening adopted in the previous sections and also with a larger one. The nice agreement of computed and experimental spectra suggest that when interacting with cellulose nanocrystals the single chains of PTs can actually assume a transoid twisted ribbon arrangement, in keeping with the authors' picture.[27] Interestingly enough, a transoid twisted ribbon arrangement has been also postulated for chiral PT block copolymers in mixtures of solvent and non-solvent, also displaying monosignate ECD spectra.[95] In fact, in conditions promoting extensive aggregation, the polymer chains are packed in a parallel fashion rather than in the most common helical one. Other monosignated ECD spectra, like those observed for some disubstituted chiral PTs,[28] seem similarly compatible with *transoid* twisted ribbon structures of the PT.

3.5.4. Conclusions.

In this contribution we have investigated the expected line shapes of the Abs and ECD spectra for oligothiophenes in *transoid* and *cisoid* chiral arrangements. We studied ribbon-like and helical oligomers of different lengths and characterized by several different inter-ring twists. In this way we explored the chiroptical response of several possible molecular structures that may mimic the arrangements assumed in different physical situations, like aggregates or host/guest complexes. We have shown that any transoid twisted ribbon, independently of the length of the oligomer and the extent of the inter-ring twist, i.e. ribbons with small or very long steps, is expected to have a monosignated ECD, with a shape very similar to the Abs one. This is due to the fact that only the first excited state has a strong oscillator and rotatory strength, and that HT contributions are negligible. At variance, *cisoid* helices can give rise to (at least) bisignated ECD spectra, since higher-excited state beyond S_1 contribute to the

signal. The spacing between the positive and negative components depend on the energy gap between the excited states, and therefore on the length of the oligomer.

As for the interpretation of the different ECD lineshapes of polythiophenes observed in different environments, our model study provides some qualitative conclusions. Concerning chiral polythiophenes aggregates in solutions or thin films, our results exclude that their typical chiroptical response can be due to transoid-like single chain PTs. The spectrum predicted for a cisoid helix of T_{13} or T_{15} resembles the aggregate ECD spectra, but it remarkably deviates from it for shorter oligomers, while the agreement of the Abs spectrum is always rather poor. In summary, the results support the conclusion, already reached on the ground of experimental arguments,[14] and confirmed by our calculations on a dimeric exciton model,[25] that the ECD arises from a supramolecular chiral packing

Our results also indicate that the ECD spectrum of an achiral PT bound to the triple helix of schizophyllan[26] is not compatible with a transoid twisted ribbon of the PT and suggest that it might be due to structures with some cisoid-like arrangement. On the contrary, the monosignated ECD profile reported for a PT interacting with chiral cellulose nanocrystals[27] is in keeping with the suggested intra-chain mechanism for a transoid twisted ribbon. These qualitative or semi-quantitative conclusions were based on predictions made for isolated helical structures. It would be interesting to investigate if the ideal, isolated structures here studied are sufficiently accurate to mimic the actual ones encountered in host/guest complexes. Since the electronic transitions of the PT chains are well separated from those of any chiral host described above, it is not plausible that the specific interactions will revert the response of the isolated species from monosignated to bisignated or vice-versa. Still, environmental factors will surely impact on the spectral profiles.

From the methodological point of view, the presented investigation required the development of a suitable protocol to compute vibronic spectra starting from partially-constrained structures --which therefore do not correspond to true stable conformers of the system considered in isolated form-- removing the contribution of the frozen coordinates. Such a method has been worked out in a vertical framework, adopting curvilinear internal coordinates and iterative projection

schemes. The proposed computational approach is expected to have a rather general applicability, well beyond the specific systems investigated here. In fact, for the computation of electronic spectra in flexible systems, it provides a proper framework to separate stiff and soft molecular modes and to apply advanced hybrid quantum/classical approaches, where the soft modes are not considered frozen but treated at an approximated classical level.[51,52,55-57] These approaches can represent the basis to open the route to the vibronic simulation of the molecular (chiro)optical response in diverse complex environments, like dyes in homogeneous and heterogeneous media, and chromophores grafted on nanoparticles or surfaces, or bound to protein scaffolds.

3.5.5. References and notes.

1. P. Bujak, I. Kulszewicz-Bajer, M. Zagorska, V. Maurel, I. Wielgus, A. Pron, *Chem. Soc. Rev.*, **2013**, 42, 8895.
2. O. Ostroverkhova, *Chem. Rev.*, **2016**, 116, 13279.
3. A. Salleo, R.J. Kline, D.M. DeLongchamp, M.L. Chabinyc, *Adv. Mater.*, **2010**, 22, 3812.
4. P.M. Beaujuge, J.M.J. Frechet, *J. Am. Chem. Soc.*, **2011**, 133, 20009.
5. Y. Yang, B. Rice, X. Shi, J.R. Brandt, R. Correa da Costa, G.J. Hedley, D.M. Smilgies, J.M. Frost, I.D.W. Samuel, A. Otero-de-la-Roza, E.R. Johnson, K.E. Jelfs, J. Nelson, A.J. Campbell, M.J. Fuchter, *ACS Nano*, **2017**, 11, 8329.
6. J.R. Brandt, F. Salerno, M.J. Fuchter, *Nat. Rev. Chem.*, **2017**, 1, 0045.
7. G. Pescitelli, L. Di Bari, N. Berova, *Chem. Soc. Rev.*, **2014**, 43 5211.
8. P. A. Korevaar, T. F. A. de Greef, E. W. Meijer, *Chem. Mater.*, **2013**, **26**, 576.
9. T. Shiraki, A. Dawn, Y. Tsuchiya, T. Yamamoto, S. Shinkai, *Chem. Commun.*, **2012**, 48, 7091.
10. H. Goto, Y. Okamoto, E. Yashima, *Chem.–Eur. J.*, **2002**, 8, 4027.
11. H. Goto, Y. Okamoto, E. Yashima, *Macromolecules*, **2002**, 35, 4590.
12. B. M. W. Langeveld-Voss, D. Beljonne, Z. Shuai, R. A. J. Janssen, S. C. J. Meskers, E. W. Meijer, J.-L. Brédas, *Adv. Mater.*, **1998**, 10, 1343.
13. B. M. W. Langeveld-Voss, E. Peeters, R. A. J. Janssen, E. W. Meijer, *Synth. Met.*, **1997**, 84, 611.
14. B. M. W. Langeveld-Voss, R. A. J. Janssen, E. W. Meijer, J. *Mol. Struct.*, **2000**, 521, 285.
15. C. R. G. Grenier, S. J. George, T. J. Joncheray, E. W. Meijer, J. R. Reynolds, *J. Am. Chem. Soc.*, **2007**, 129, 10694.
16. T. Minami, Y. Kubo, *Supramol. Chem.*, **2011**, 23, 13.
17. K. Watanabe, I. Osaka, S. Yorozuya, K. Akagi, *Chem. Mater.*, **2012**, 24, 1011.

18. B. M. W. Langeveld-Voss, R. A. J. Janssen, M. P. T. Christiaans, S. C. J. Meskers, H. P. J. M. Dekkers, E. W. Meijer, *J. Am. Chem. Soc*., **1996**, 118, 4908.

19. M. M. Bouman, E. W. Meijer, *Adv. Mater*., **1995**, 7, 385.

20. G. Bidan, S. Guillerez, V. Sorokin, *Adv. Mater*., **1996**, 8, 157.

21. B. M. W. Langeveld-Voss, R. J. M. Waterval, R. A. J. Janssen, E. W. Meijer, *Macromolecules*, **1999**, 32, 227.

22. Y. Takeoka, F. Saito, M. Rikukawa, *Langmuir*, **2013**, 29, 8718.

23. F. Brustolin, F. Goldoni, E. W. Meijer, N. A. J. M. Sommerdijk, *Macromolecules*, **2002**, 35, 1054.

24. C. Li, M. Numata, M. Takeuchi, S. Shinkai, *Chem.–Asian J*., **2006**, 1, 95.

25. D. Padula, F. Santoro, G. Pescitelli, *RSC Advances*, **2016**, 6, 37938.

26. C. Li, M. Numata, A. Bae, K. Sakurai, S. Shinkai, *J. Am. Chem. Soc*., **2005**, 127, 4548.

27. B. Risteen, A. Blake, M. A. McBride, C. Rosu, J. Park, M. Srinivasarao, P. S. Russo, E. Reichmanis, *Biomacromolecules*, **2017**, 18, 1556.

28. F. Le Bron, G. Longhi, S. Abbate, M. Catellani, F. Wang, P. L. Polavarapu, *Enantiomer*, **2002**, 7, 207.

29. M. Dierksen, S. Grimme, *J Chem. Phys.*, **2005**, 122, 244101.

30. A. Hazra, M. Nooijen, *J. Chem. Phys*. **2005**, 122, 204327.

31. F. Santoro, R. Improta, A. Lami, J. Bloino, V. Barone, *J. Chem. Phys*., **2007**, 126, 084509.

32. H. C. Jankowiak, J.L. Stuber, R. Berger, *J. Chem. Phys*., **2007**, 127, 234101.

33. F. Santoro, A. Lami, R. Improta, J. Bloino, V. Barone, *J. Chem*. Phys., **2008**, 128, 224311.

34. F. Santoro, V. Barone, *Int. J. Quantum Chem*., **2010**, 110, 476.

35. J. Bloino, M. Biczysko, F. Santoro, V. Barone, *J. Chem. Theory Comput*., **2010**, 6, 1256.

36. J. Tatchen, E. Pollak, J. Chem. Phys., **2008**, 128, 164303.

37. Q. Peng, Y. Niu, C. Deng, Z. Shuai, *Chem Phys*., **2010**, 370, 215.

38. J. Huh, R. Berger, *J. Phys. Conf. Ser*., **2012**, 380, 012019.

39. R. Borrelli, A. Capobianco, A. Peluso, *J. Phys. Chem. A*, **2012**, 116, 9934.

40. A. Baiardi, J. Bloino, V. Barone, *J. Chem. Theory Comput*., **2013**, 9, 4097.

41. F. J. Avila Ferrer, J. Cerezo, J. Soto, R. Improta, F. Santoro, *Comput. Theoret. Chem*., **2014**, 1040, 328.

42. F. Santoro, D. Jacquemin, *WIREs Comput. Mol. Sci*., **2016**, 6, 460.

43. M. Dierksen, S. Grimme, *J. Chem. Phys.* **2006**, 124, 174301.

44. M. Nooijen, *Int. J. Quantum Chem*., **2006**, 106, 2489.

45. G. Pescitelli, V. Barone, L. Di Bari, A. Rizzo, F. Santoro, *J. Org. Chem*., **2013**, 78, 7398.

46. N. Lin, Y. Luo, F. Santoro, X. Zhao, A. Rizzo, *Chem. Phys. Lett.* **2008**, 464, 144.

47. N. Lin, F. Santoro, X. Zhao, A. Rizzo, V. Barone. *J. Phys. Chem. A*, **2008**, 112, 12401.

48. N. Lin, F. Santoro, A. Rizzo, Y. Luo, X. Zhao, V. Barone, *J. Phys. Chem. A*, **2009**, 113, 4198.

49. E. Stendardo, F. Avila Ferrer, F. Santoro, R. Improta, *J. Chem. Theory Comput*., **2012**, 8, 4483.

50. A. Baiardi, J. Bloino, V. Barone, *J. Chem. Theory Comput*., **2017**, 13, 2804.

51. R. Improta, F.J.A. Ferrer, E. Stendardo, F. Santoro, *ChemPhysChem*, **2014**, 15, 3320.

52. Y. Liu, J. Cerezo, F. Santoro, A. Rizzo, N. Lin, X. Zhao, *Phys. Chem. Chem. Phys*., **2016**, 18, 22889.

53. M. D'Abramo, M. Aschi, A. Amadei, *J. Chem. Phys.*, **2014**, 140, 164104.

54. R. Zalensy, N. A. Murugan, F. Gelmukhanov, Z. Rinkevicius, B. Ośmialowski, W. Bartkowiak, H. Ågren, *J. Phys. Chem. A*, **2015**, 119, 5145.

55. J. Cerezo, G. Mazzeo, G. Longhi, S. Abbate, F. Santoro, *J. Phys. Chem. Lett.*, **2016**, 7, 4891.

56. D. Padula, J. Cerezo, G. Pescitelli, F. Santoro, *Phys. Chem. Chem. Phys.*, **2017**, 19, 32349.

57. J. Cerezo, D. Aranda, F. J. Avila Ferrer, G. Prampolini, G. Mazzeo, G. Longhi, S. Abbate, F. Santoro, *Chirality* **2018**, 30, 730.

58. J. Gierschner, H.-G. Mack, H.-J. Egelhaaf, S. Schweizer, B. Doser, D. Oelkrug, *Synthetic Metals*, **2003**, 138, 311.

59. G. Macchi, B. Milián Medina, M. Zambianchi, R. Tubino, J. Cornil, G. Barbarella, J. Gierschner, F. Meinardia, *Phys. Chem. Chem. Phys.*, **2009**, 11, 984.

60. B. Milián Medina, D. Wasserberg, S. C. J. Meskers, E. Mena-Osteritz, P. Baüerle, J. Gierschner, *J. Phys. Chem. Lett.*, **2008**, 112, 13282.

61. F.J. Avila Ferrer, F. Santoro, *Phys. Chem. Chem. Phys.*, **2012**, 14, 13549.

62. R. Borrelli, A. Peluso, *J. Chem. Phys.*, **2006**, 125, 194308.

63. J. Cerezo, J. Zúñiga, A. Requena, F.J. Avila Ferrer, F. Santoro, *J. Chem. Theory Comput.*, **2013**, 9, 4947.

64. J. P. Götze, B. Karasulu, W. Thiel, *J. Chem. Phys.*, **2013**, 139, 234108.

65. B. Karasulu, J.P. Götze, W. Thiel, *J. Chem. Theory Comput.*, **2014**, 10, 5549.

66. A. Baiardi, J. Bloino, V. Barone, *J. Chem. Theory Comput.*, **2015**, 11, 3267.

67. J. Cerezo, F. Santoro, *J. Chem. Theory. Comput.*, **2016**, 12, 4970.

68. A. Baiardi, J. Bloino, V. Barone, *J. Chem. Phys.*, **2016**, 144, 084114.

69. Gaussian 16, Revision A.03, M. J. Frisch, G. W. Trucks, H. B. Schlegel, G. E. Scuseria, M. A. Robb, J. R. Cheeseman, G. Scalmani, V. Barone, G. A. Petersson, H. Nakatsuji, X. Li, M. Caricato, A. V. Marenich, J. Bloino, B. G. Janesko, R. Gomperts, B. Mennucci, H. P. Hratchian, J. V. Ortiz, A. F. Izmaylov, J. L. Sonnenberg, D. Williams-Young, F. Ding, F. Lipparini, F. Egidi, J. Goings, B. Peng, A. Petrone, T. Henderson, D. Ranasinghe, V. G. Zakrzewski, J. Gao, N. Rega, G. Zheng, W. Liang, M. Hada, M. Ehara, K.

Toyota, R. Fukuda, J. Hasegawa, M. Ishida, T. Nakajima, Y. Honda, O. Kitao, H. Nakai, T. Vreven, K. Throssell, J. A. Montgomery, Jr., J. E. Peralta, F. Ogliaro, M. J. Bearpark, J. J. Heyd, E. N. Brothers, K. N. Kudin, V. N. Staroverov, T. A. Keith, R. Kobayashi, J. Normand, K. Raghavachari, A. P. Rendell, J. C. Burant, S. S. Iyengar, J. Tomasi, M. Cossi, J. M. Millam, M. Klene, C. Adamo, R. Cammi, J. W. Ochterski, R. L. Martin, K. Morokuma, O. Farkas, J. B. Foresman, and D. J. Fox, Gaussian, Inc., Wallingford CT, 2016.

70. Avogadro: an open-source molecular builder and visualization tool. Version 1.2.0. http://avogadro.cc/;Marcus D Hanwell, Donald E Curtis, David C Lonie, Tim Vandermeersch, Eva Zurek and Geoffrey R Hutchison; "Avogadro: An advanced semantic chemical editor, visualization, and analysis platform" *Journal of Cheminformatics* **2012**, 4, 17.

71. M. J. G. Peach, E. I. Tellgren, P. Salek, T. Helgaker, D. J. Tozer, *J. Phys. Chem. A*, **2007**, 111, 11930.

72. P. A. Limacher, K. V. Mikkelsen, H. P. Lüthi, *J. Chem. Phys.*, **2009**, 130, 194114.

73. D. Jacquemin, V. Wathelet, E. A. Perpète, C. Adamo, *J. Chem. Theory Comput.*, **2009**, 5, 2420.

74. J. Zhang, X. Guo, Z. Cao, *J. Chem. Phys.*, **2009**, 131, 144307.

75. S. Borini, P. A. Limacher, H. P. Lüthi, *J. Phys. Chem. A*, **2010**, 114, 2221.

76. J. R. Reimers, *J. Chem. Phys.*, **2001**, 115, 9103.

77. C. F. Jackels, Z. Gu, D. G. Truhlar, *J. Chem. Phys.*, **1995**, 102, 3188.

78. F. Santoro, FCclasses, a Fortran 77 code, available online: http://www.pi.iccom.cnr.it/fcclasses, accessed on February 15, 2018.

79. A. Myers Kelley, *J. Chem. Phys.*, **2003**, 119, 3320.

80. J. Guthmuller, F. Zutterman, B. Champagne, *J. Chem. Phys.*, **2009**, 131, 154302.

81. J. Roden, A. Eisfeld, M. Dvořák, O. Bünermann, F. Stienkemeier, *J. Chem. Phys.*, **2011**, 134, 054907.

82. B. Nebgen, F. L. Emmert III, L. V. Slipchenko, *J. Chem. Phys.*, **2012**, 137, 084112.

83. M. Wykes, R. Parambil, D. Beljonne, and J. Gierschner, *J. Chem. Phys*., **2015**, 143, 114116.

84. J. Guthmuller, F. Zutterman, B. Champagne, *J. Chem. Theory Comput.,* **2008**, 4, 2094.

85. A.Eisfeld, J.S.Briggs, *Chem. Phys*., **2006**, 324, 376.

86. M. Andrzejak, P. Petelenz, *Chem. Phys*., **2007**, 335, 155.

87. D. Padula, D. Picconi, A. Lami, G. Pescitelli, F. Santoro, *J. Phys. Chem. A*, **2013**, 117, 3355.

88. L. S. Cederbaum, E. Gindensperger, I. Burghardt, *Phys. Rev. Lett*., **2005**, 94, 113003.

89. E. Gindensperger, I. Burghardt, L. S. Cederbaum, *J. Chem. Phys*., **2006**, 124, 144103.

90. D. Picconi, A. Lami, F. Santoro, *J. Chem. Phys*., **2012**, 136, 244104.

91. H. Köppel, W. Domcke, L. Cederbaum, *Electronic Structure Dynamics and Spectroscopy*, **2004**, 15, 323.

92. M. H. Beck, A. Jäckle, G. A. Worth, H.-D. Meyer, *Phys. Rep*., **2000**, 324, 1.

93. J. Gierschner, J. Cornil, H.-J. Egelhaaf, *Adv. Mater*., **2007**, 19, 173.

94. N. Kameta, M. Masuda, T. Shimizu, *Chem. Commun*., **2016**, 52, 1346.

95. K. Van den Bergh, I. Cosemans, T. Verbiest, G. Koeckelberghs, *Macromolecules*, **2010**, 43, 3794.

Supporting Information

Table S1a. Oscillator strength (OS), vertical energy (VE) and rotatory strength (RS) for the three first excited states of transoid T_{13} at θ=15º with different basis sets.

	S1			S2			S3		
	OS	VE (eV)	RS (10^{-40} cgs)	OS	VE (eV)	RS (10^{-40} cgs)	OS	VE (eV)	RS (10^{-40} cgs)
6-31G(d)	4.9906	2.7657	338	0.0000	3.0409	0	0.3856	3.3382	29
6-311G(d,p)	4.8447	2.7309	340	0.0000	2.9959	0	0.3707	3.2803	29
6-311+G(2d,p)	4.6701	2.6755	380	0.0000	2.929	0	0.3469	3.1974	32
6-311+G(2d,2p)	4.6621	2.6739	381	0.0000	2.9272	0	0.3464	3.1954	32

Table S1b. Oscillator strength (OS), vertical energy (VE) and rotatory strength (RS) for the three first excited states of cisoid T_{13} at θ=15º with different basis sets.

	S1			S2			S3		
	OS	VE (eV)	RS (10^{-40} cgs)	OS	VE (eV)	RS (10^{-40} cgs)	OS	VE (eV)	RS (10^{-40} cgs)
6-31G(d)	1.3158	2.6940	8011	1.8776	2.9922	-9400	1.7222	3.3247	591
6-311G(d,p)	1.2810	2.6574	7831	1.8125	2.9479	-9114	1.6555	3.2711	579
6-311+G(2d,p)	1.2265	2.6070	7642	1.7031	2.8857	-8750	1.5319	3.1926	481
6-311+G(2d,2p)	1.2246	2.6055	7629	1.7011	2.8839	-8715	1.5304	3.1905	482

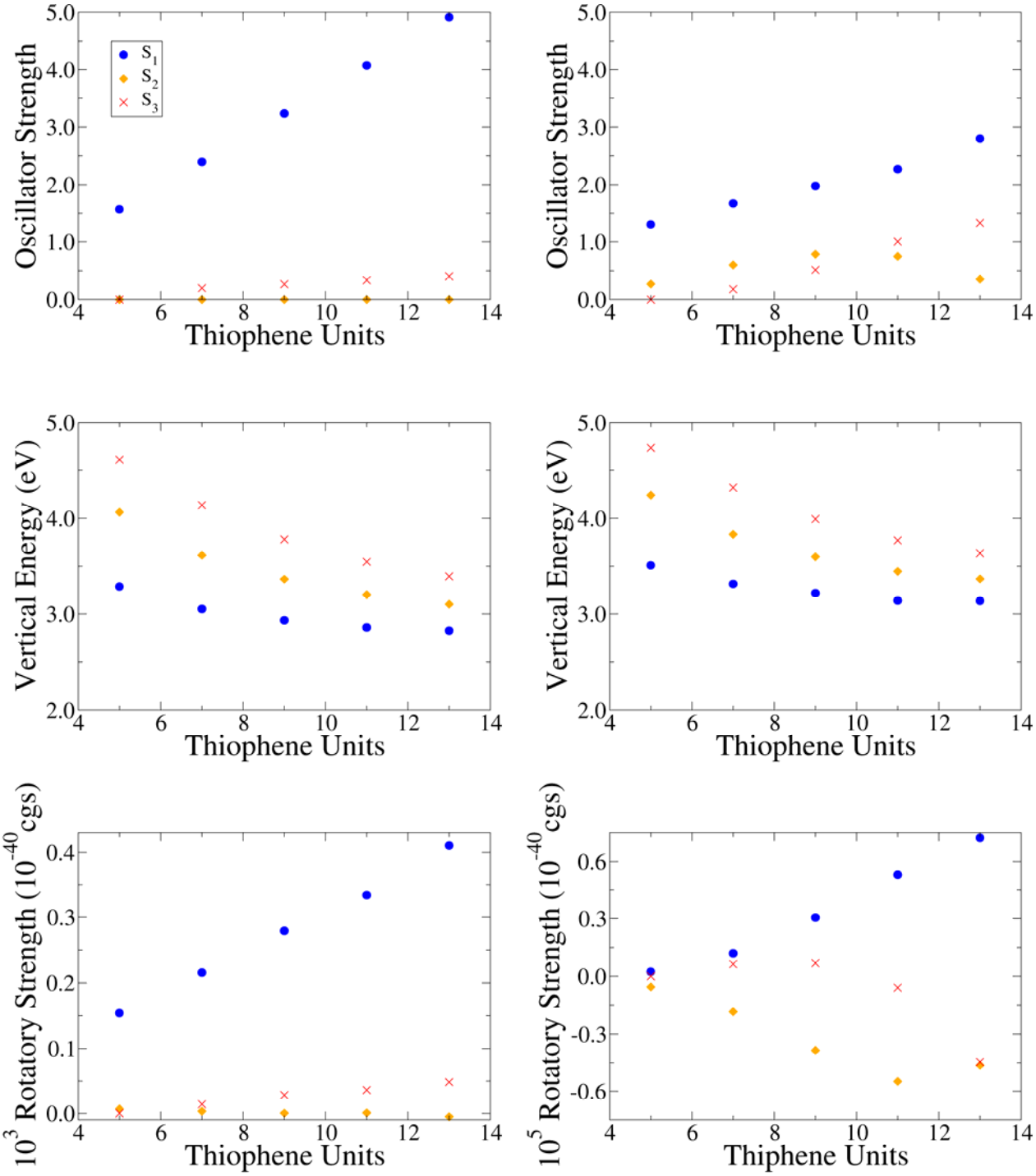

Figure S1. Oscillator Strength (top), Vertical Transition Energy (middle) and Rotatory Strength (bottom) dependence with the number of thiophene units for the all-trans (left) and all-cis (right) molecules of class *I*.

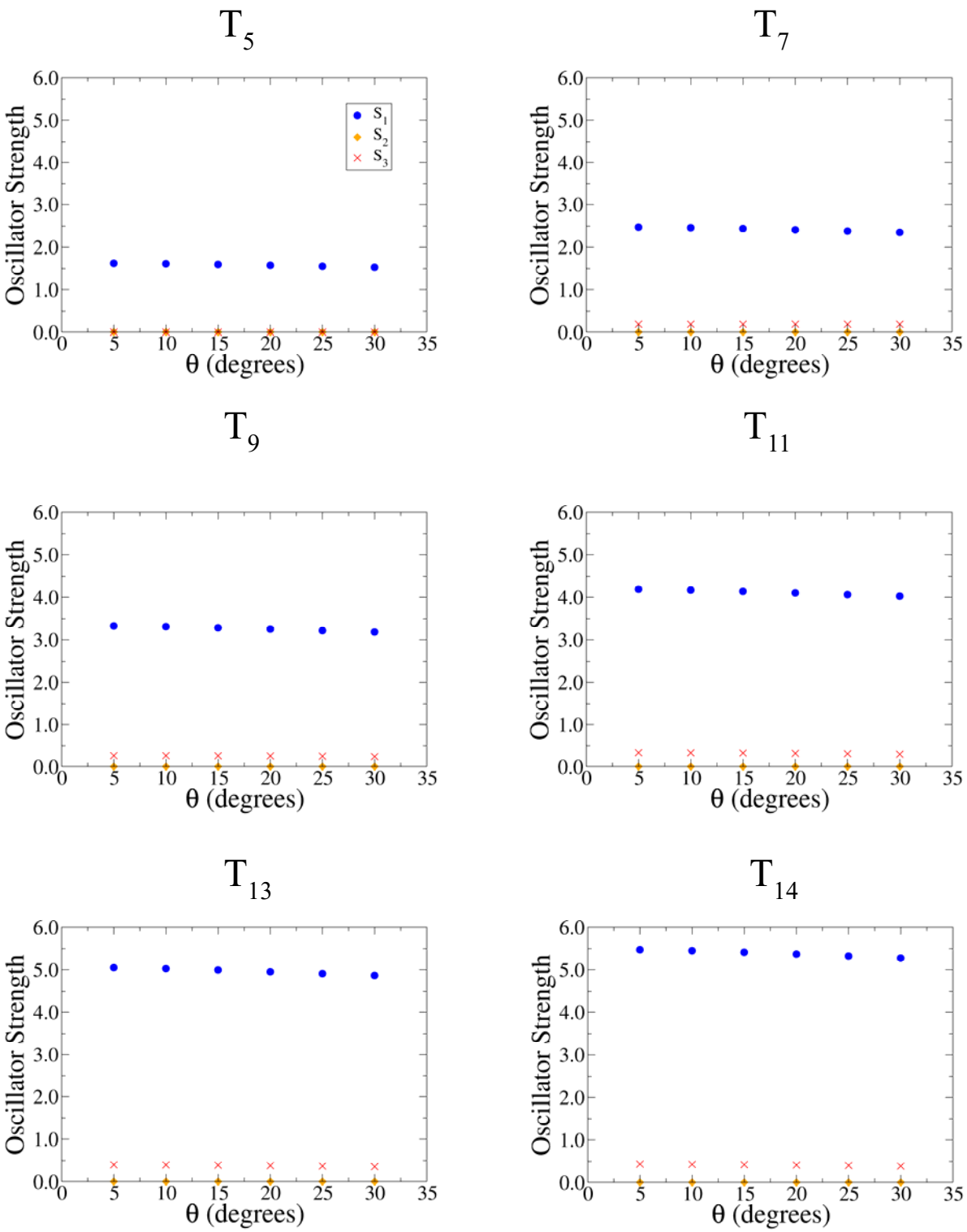

Figure S2. Oscillator Strength dependence with θ for S_1, S_2 and S_3 of the all-trans molecules of class *II*.

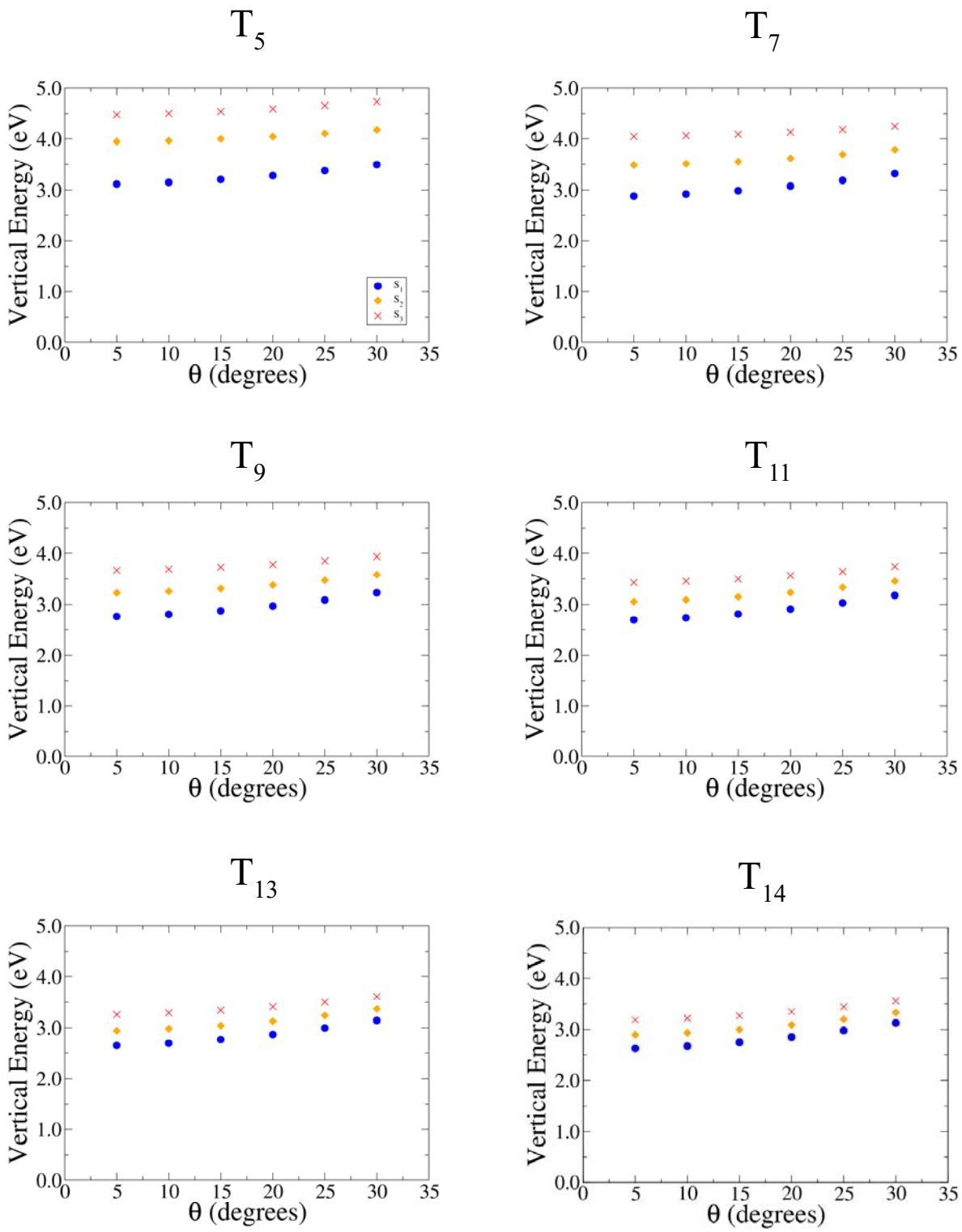

Figure S3. Vertical Transition Energy dependence with θ for S_1, S_2 and S_3 of the all-trans molecules of class *II*.

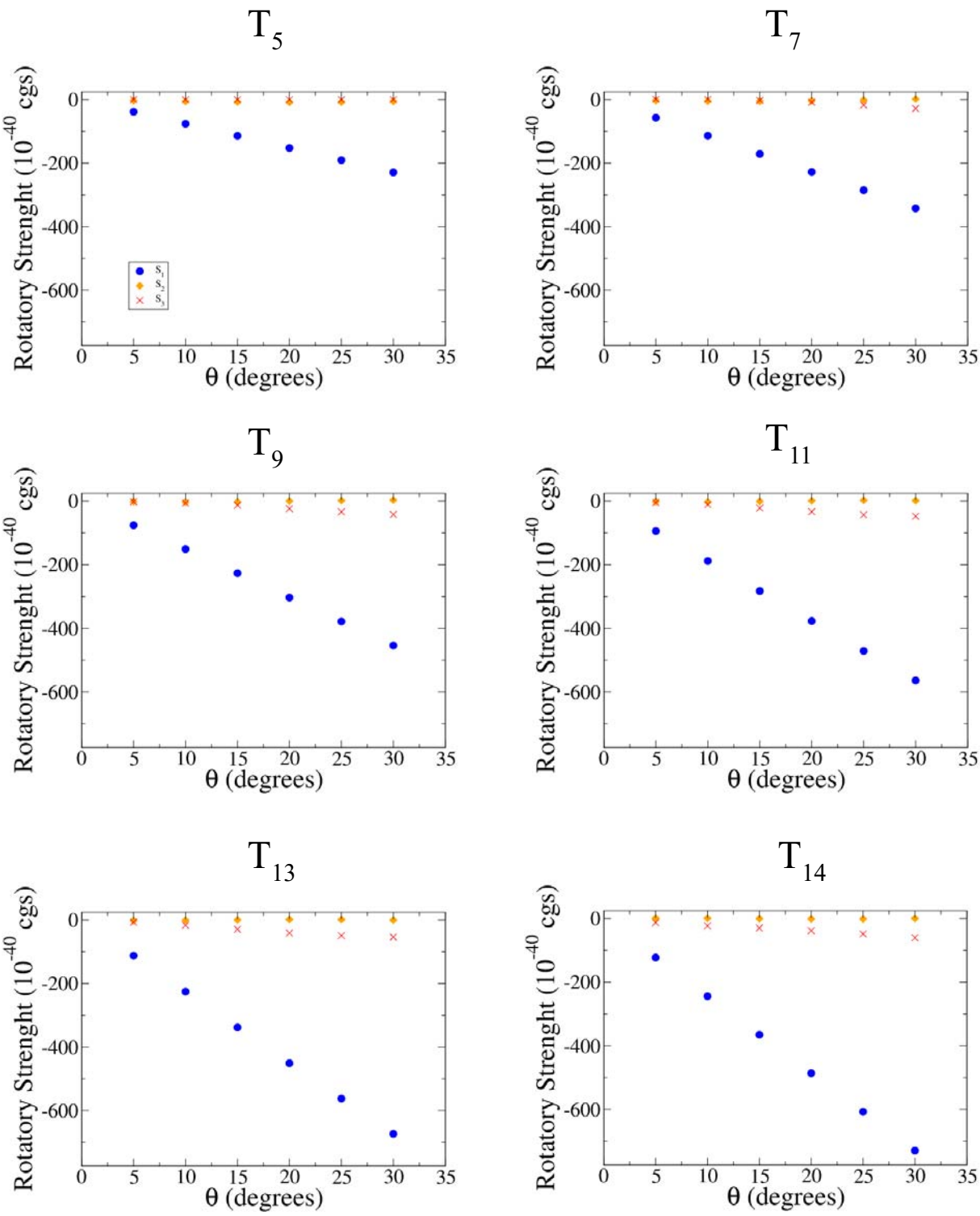

Figure S4. Rotatory Strength dependence with θ for S_1, S_2 and S_3 of the all-trans molecules of class *II*.

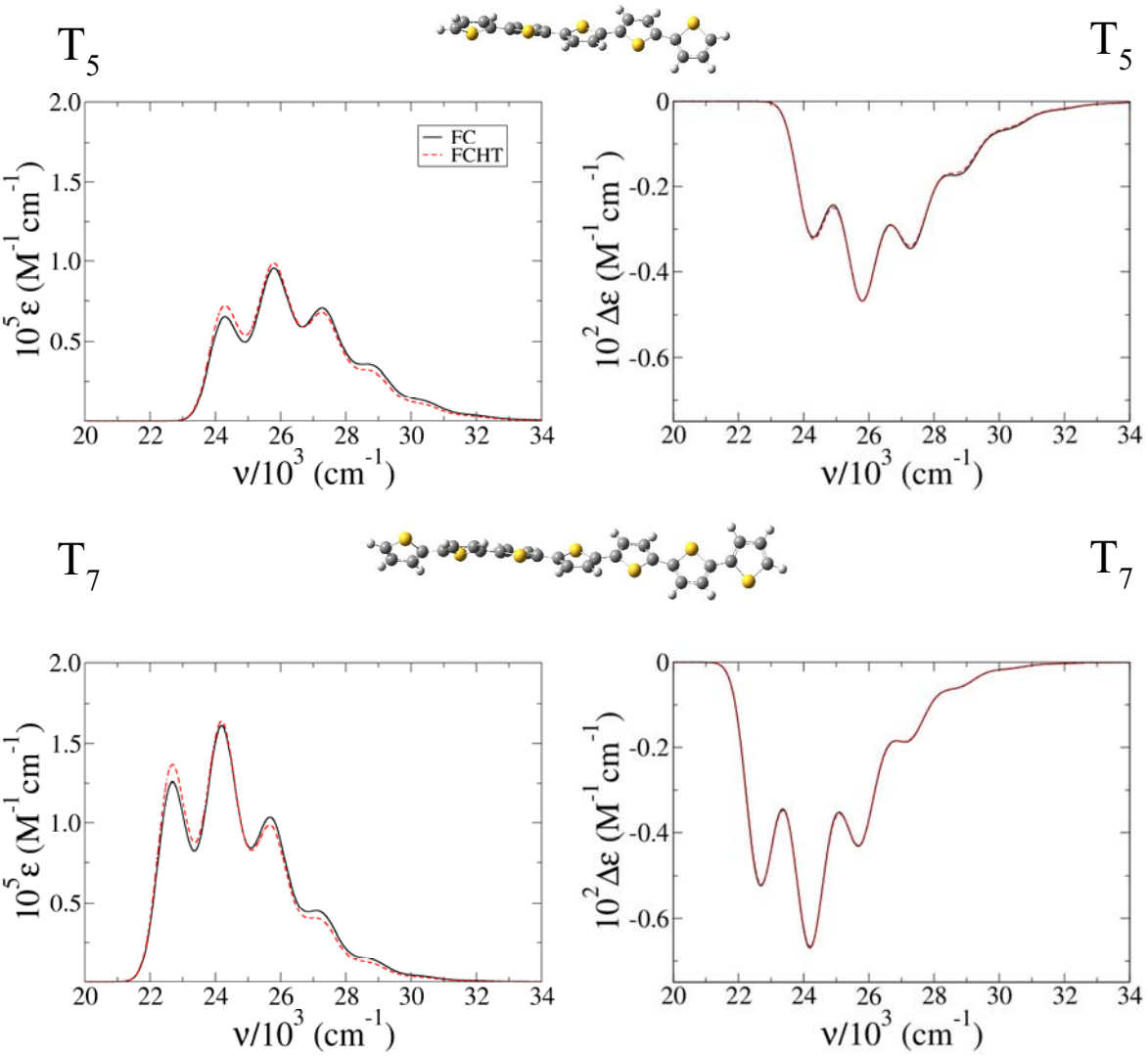

Figure S5. FC and FCHT absorption (left) and ECD (right) spectra computed for the *class I* structure of T_5, and T_7 transoid twisted ribbons at 0K and broadened with a Gaussian with HWHM=450 cm^{-1}. Inter-ring torsion angles are considered frozen during the transition.

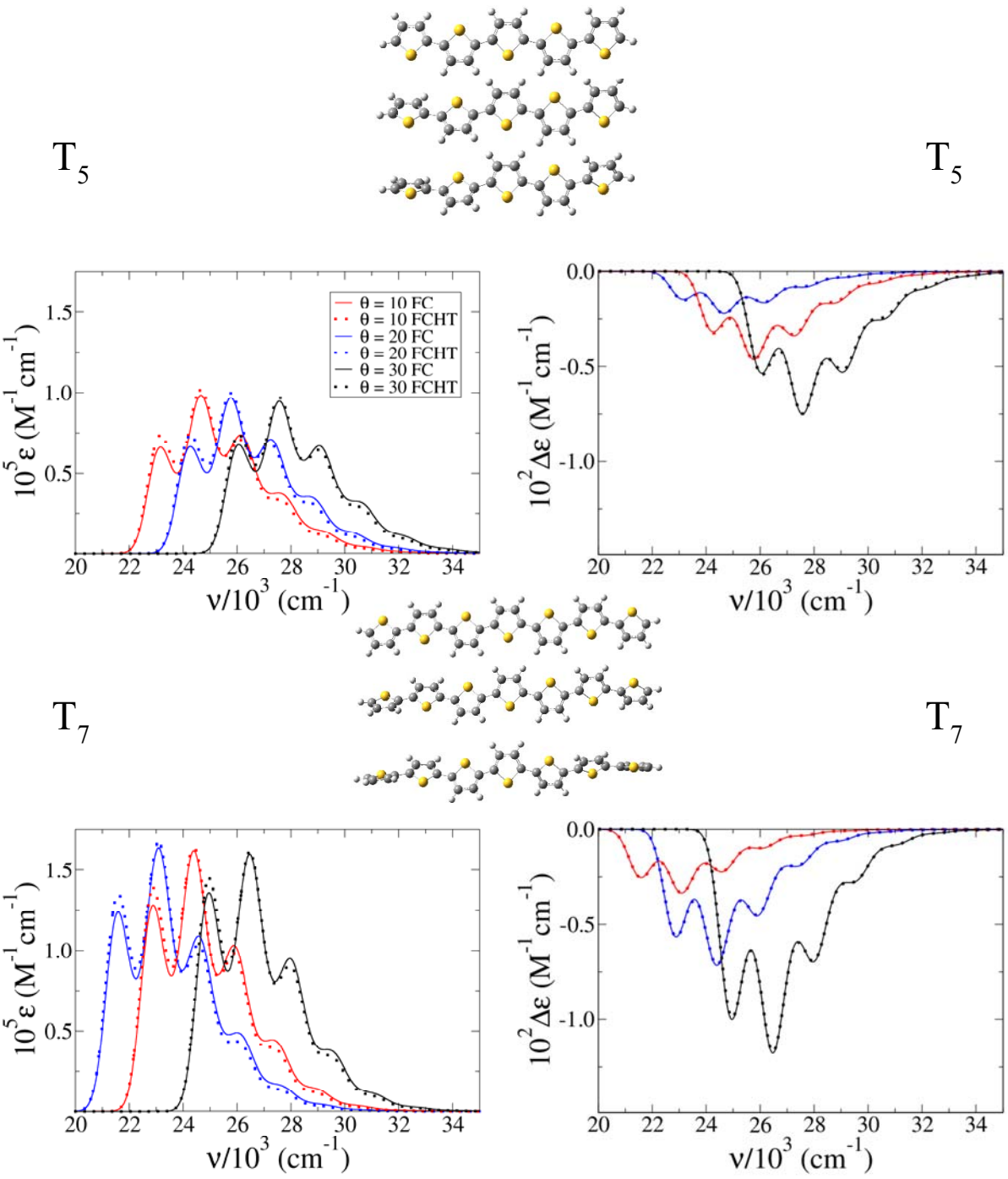

Figure S6. FC absorption (left) and ECD (right) spectra computed for the *class II* structure of T_5, and T_7 transoid twisted ribbons at 0K and broadened with a Gaussian with HWHM=450 cm^{-1} at different torsion angles (considered frozen during the transition).

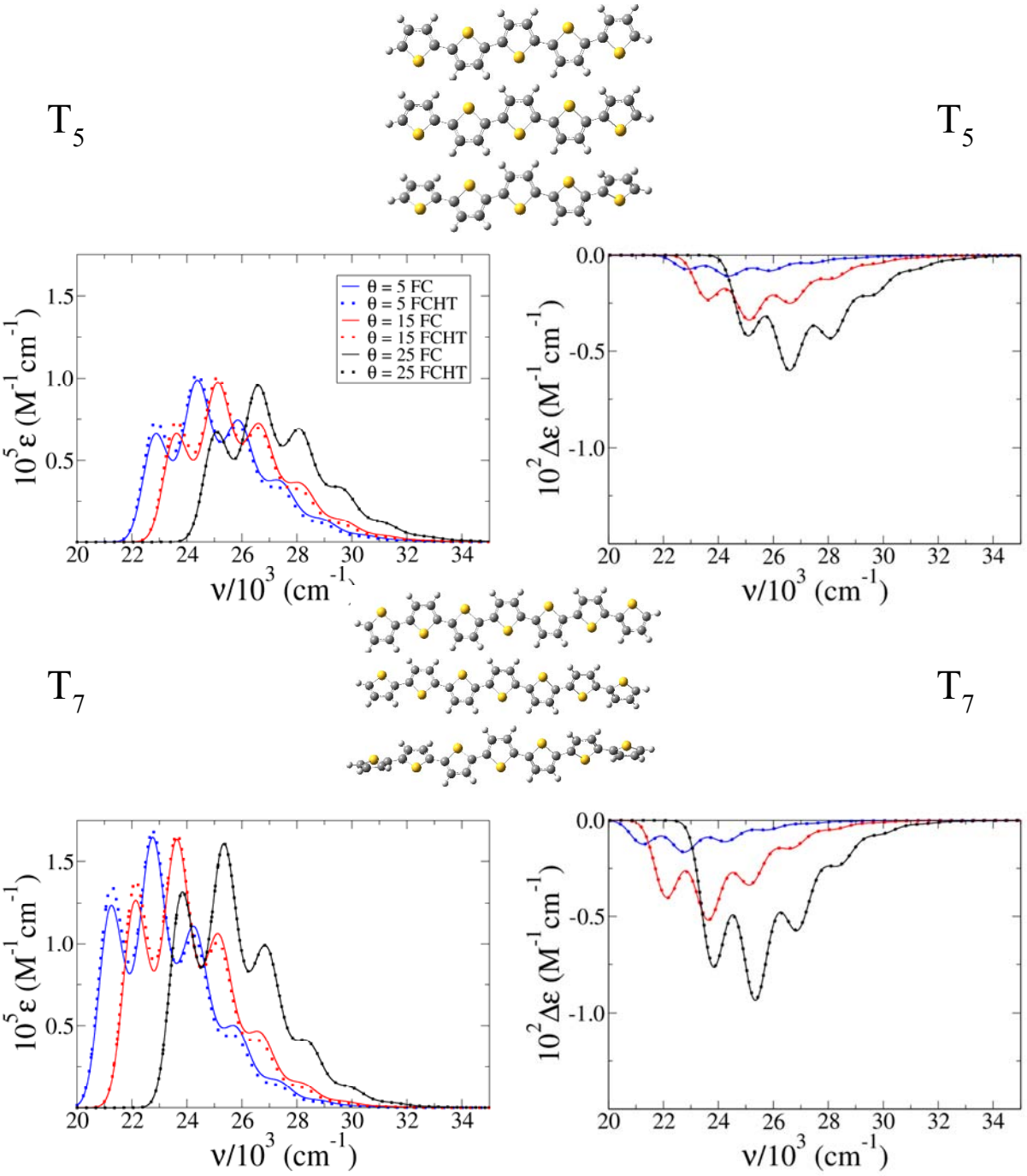

Figure S7. FC absorption (left) and ECD (right) spectra computed for the *class II* structure of T_5, and T_7 transoid twisted ribbons at 0K and broadened with a Gaussian with HWHM=450 cm^{-1} at different torsion angles (considered frozen during the transition).

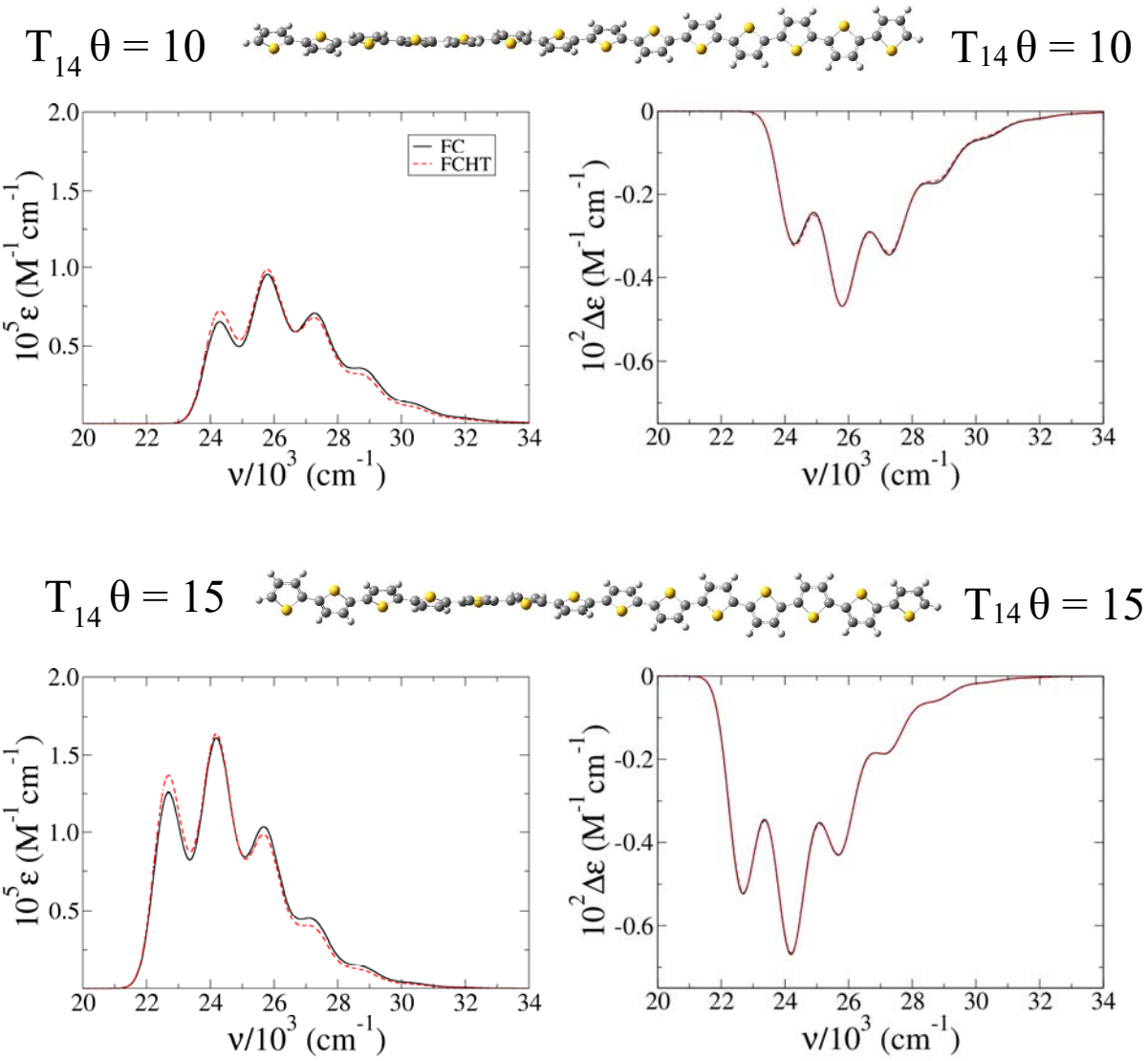

Figure S8. FC and FCHT absorption (left) and ECD (right) spectra computed for the *class II* structure of T_{14} with θ = 10 (top) and θ = 15 (bottom) transoid twisted ribbons at 0K and broadened with a Gaussian with HWHM=450 cm^{-1}. Inter-ring torsion angles are considered frozen during the transition.

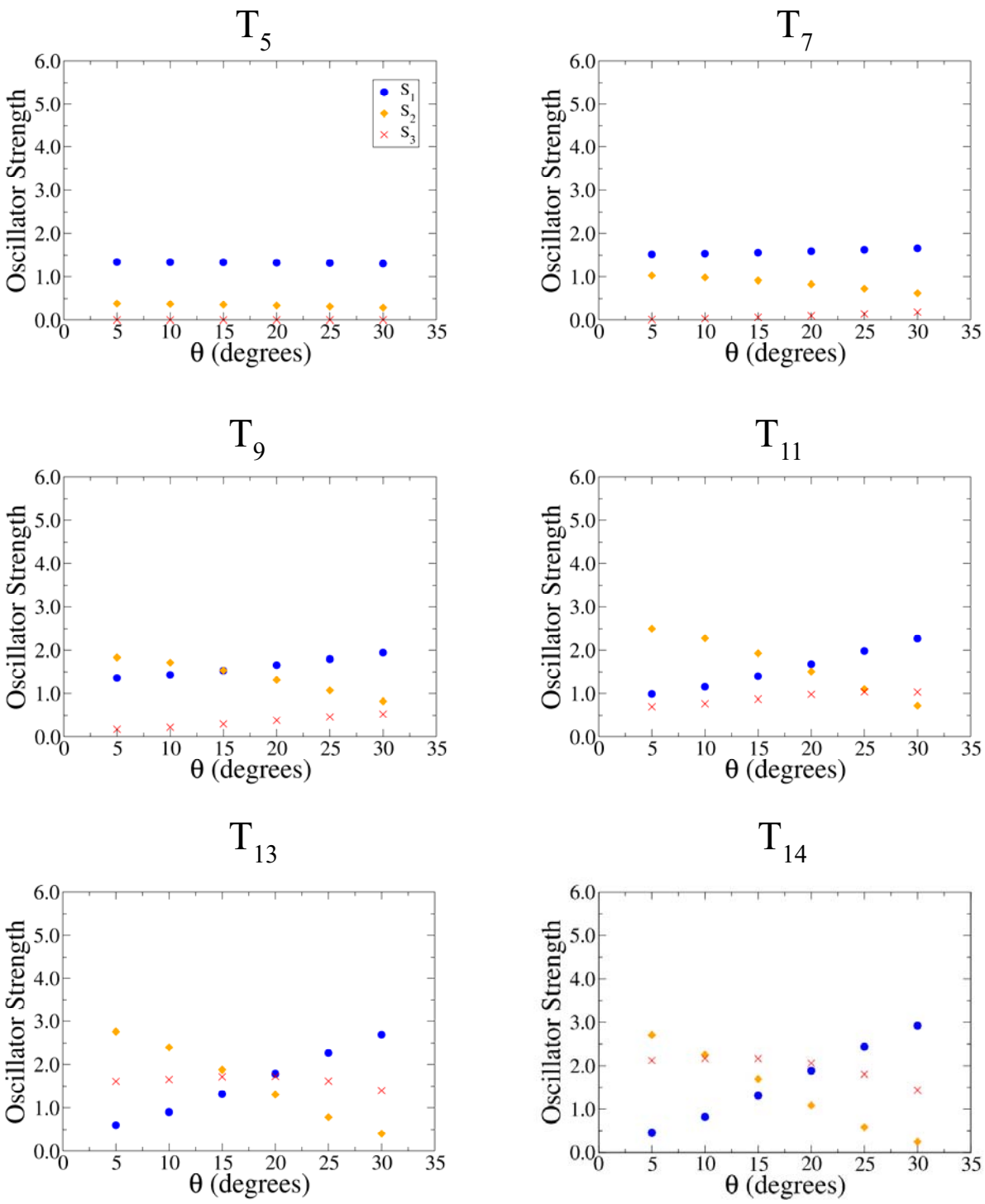

Figure S9. Oscillator Strength dependence with θ for S_1, S_2 and S_3 of the all-cis molecules of class *II*.

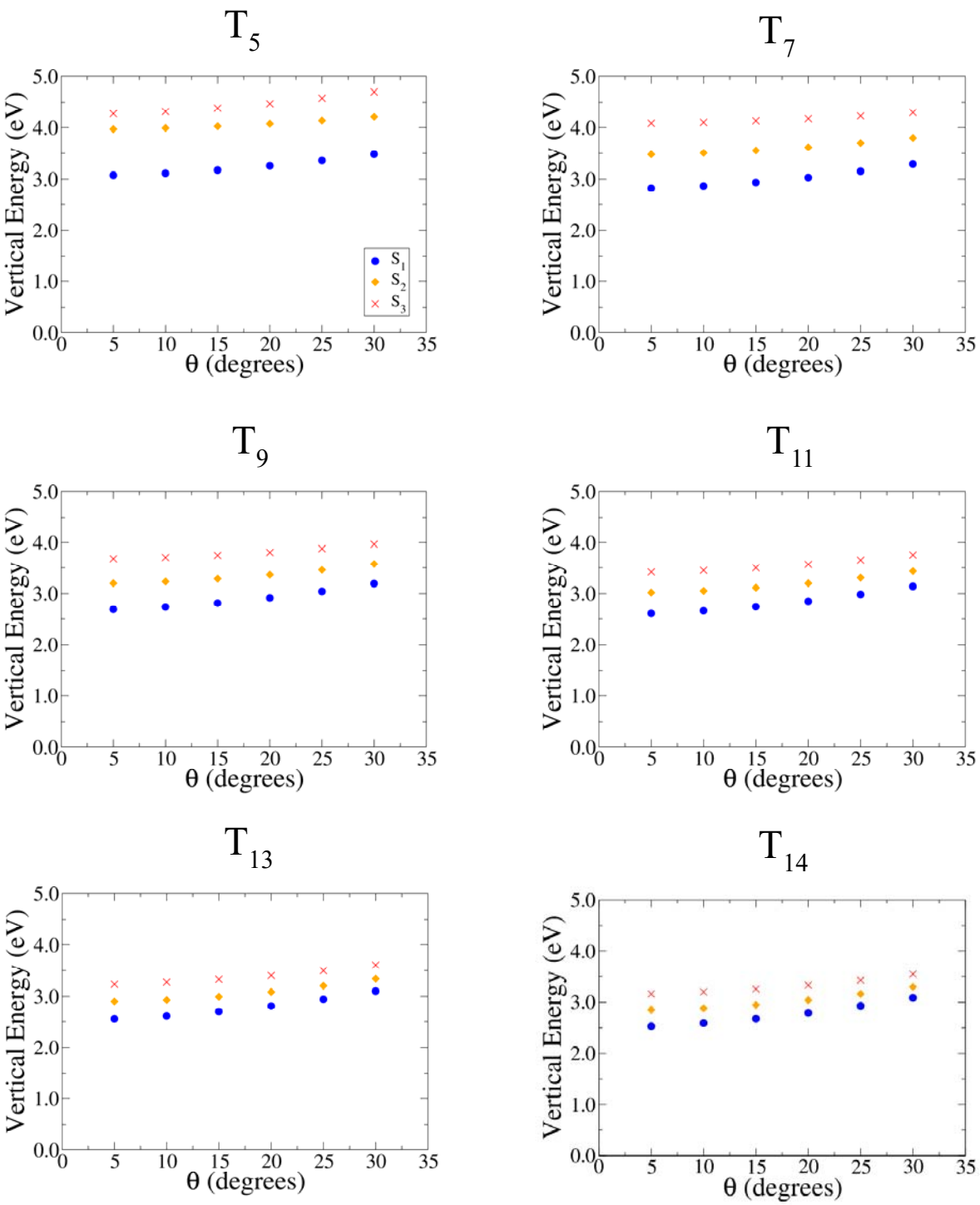

Figure S10. Vertical Transition Energy dependence with θ for S_1, S_2 and S_3 of the all-cis molecules of class *II*.

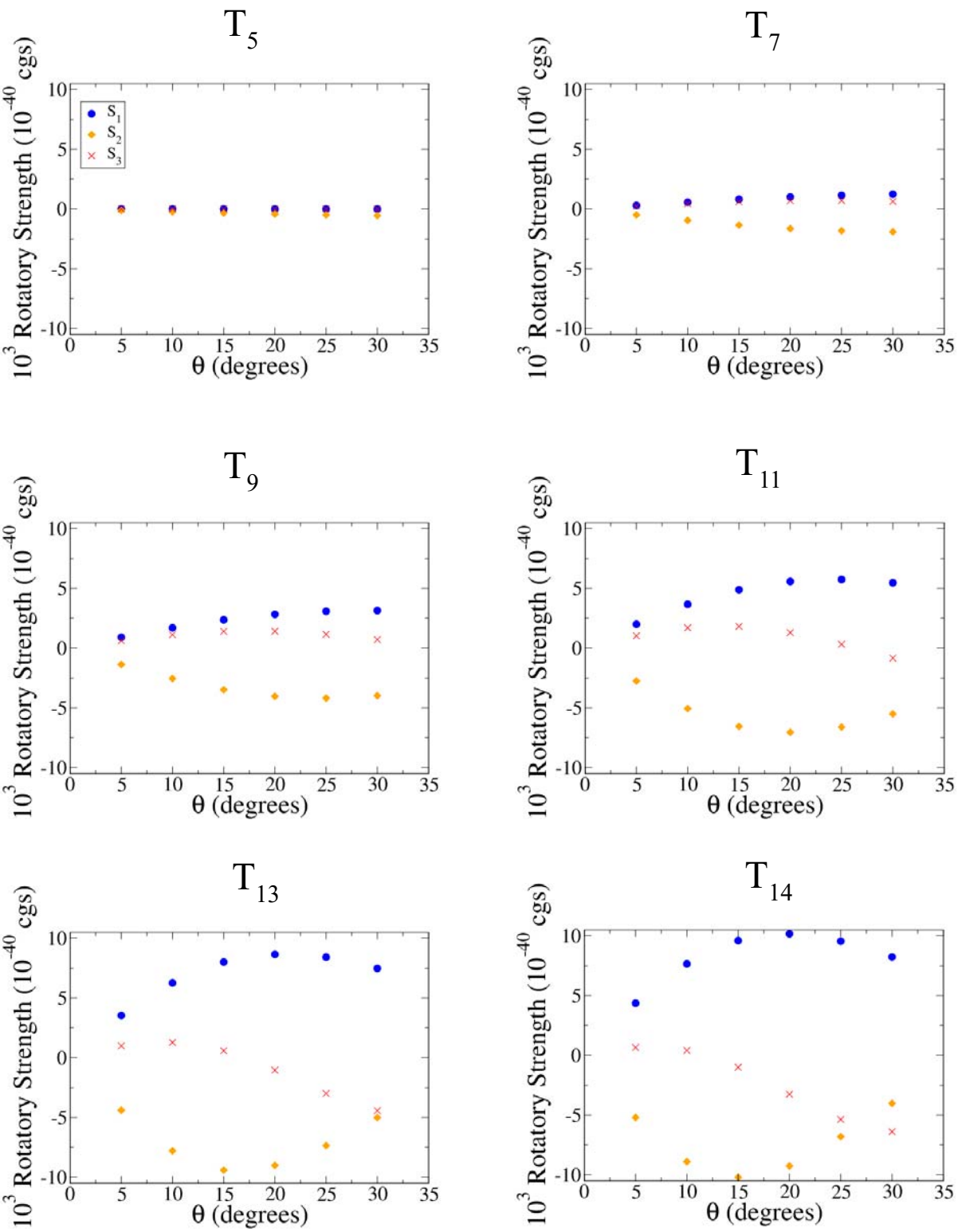

Figure S11. Rotatory Strength dependence with θ for S_1, S_2 and S_3 of the all-cis molecules of class *II*.

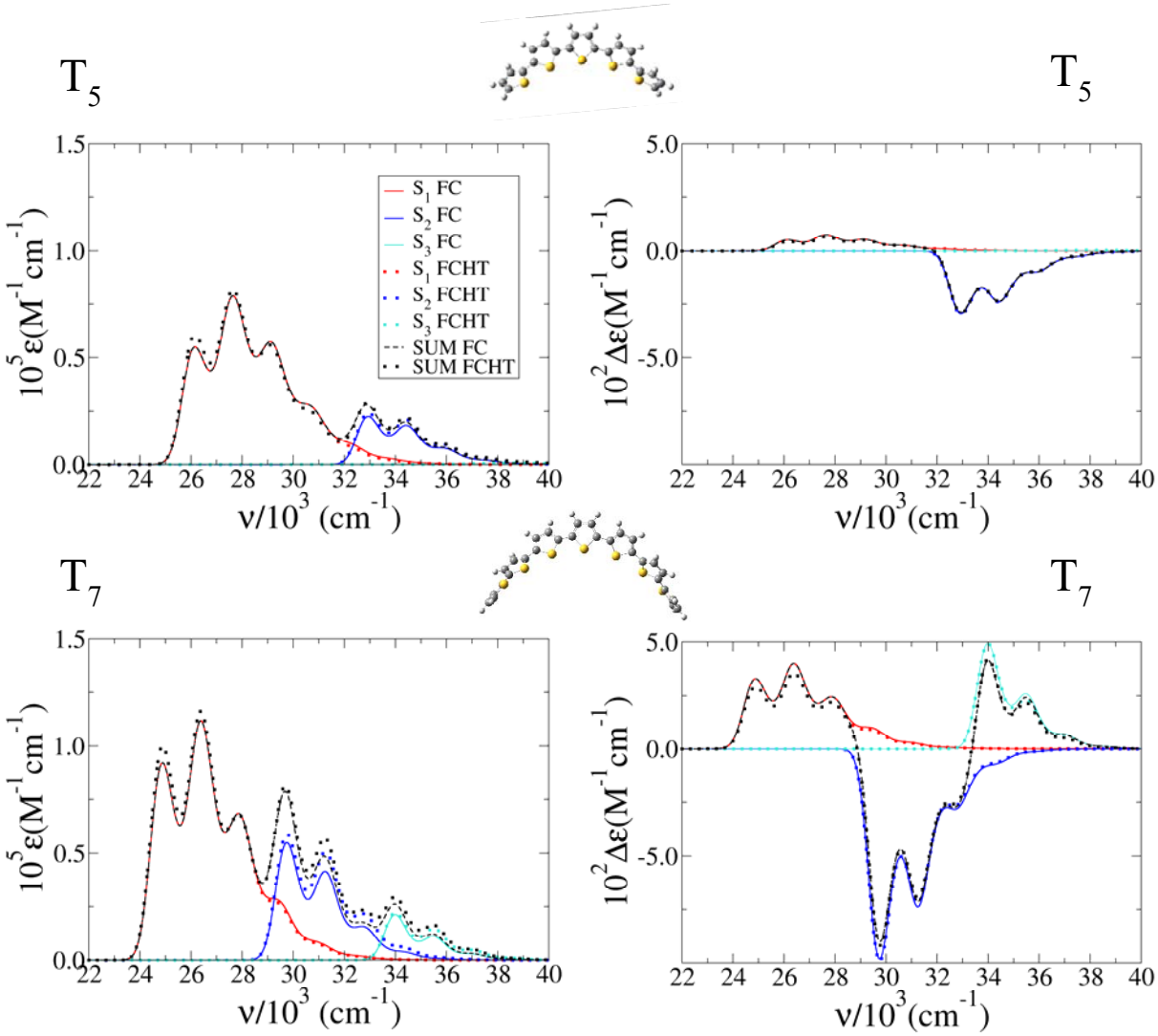

Figure S12. FC and FCHT absorption (left) and ECD (right) spectra computed for the *class I* structure of T_5, and T_7 transoid twisted ribbons at 0K and broadened with a Gaussian with HWHM=450 cm^{-1}. Inter-ring torsion angles are considered frozen during the transition.

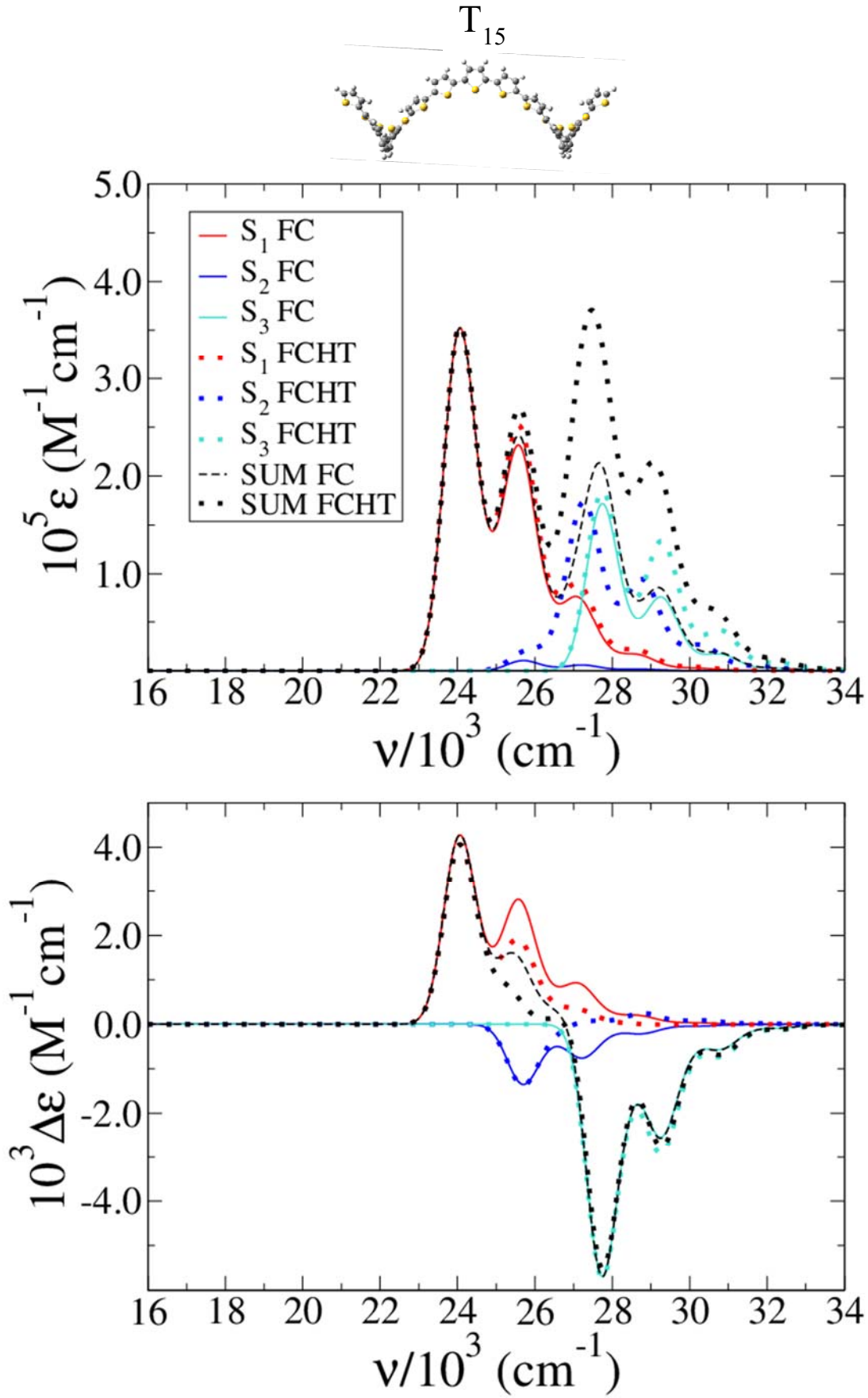

Figure S13. FC and FCHT absorption (top) and ECD (bottom) spectra computed for the *class I* structure of T_{15} cisoid helix at 0K and broadened with a Gaussian with HWHM=450 cm^{-1}. Inter-ring torsion angles are considered frozen during the transition.

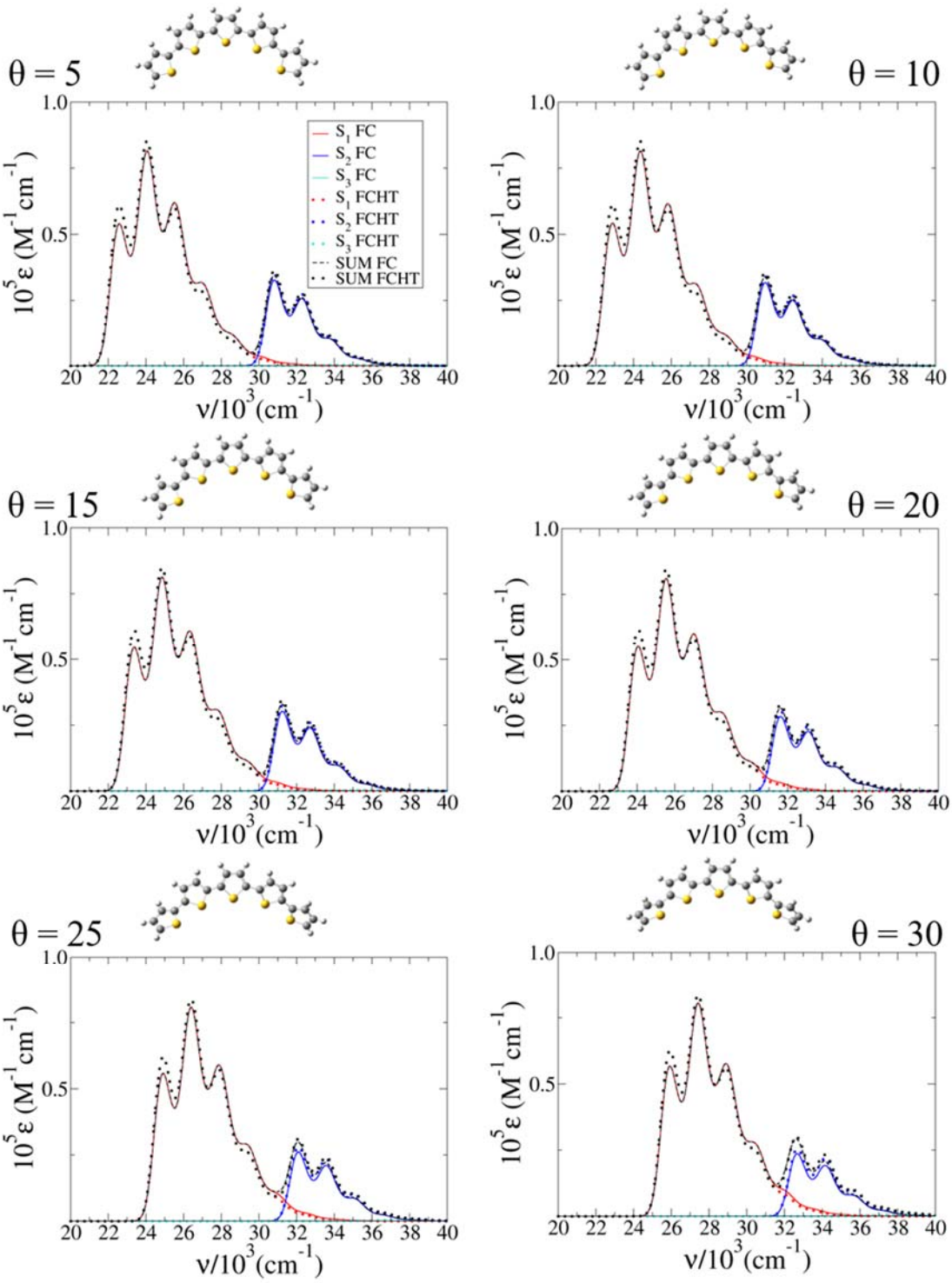

Figure S14. FC and FCHT contribution of S1, S2 and S3 to the absorption spectra computed for the *class II* structure of T_5 cisoid helices at 0K and broadened with a Gaussian with HWHM=450 cm^{-1} at different torsion angles (considered frozen during the transition).

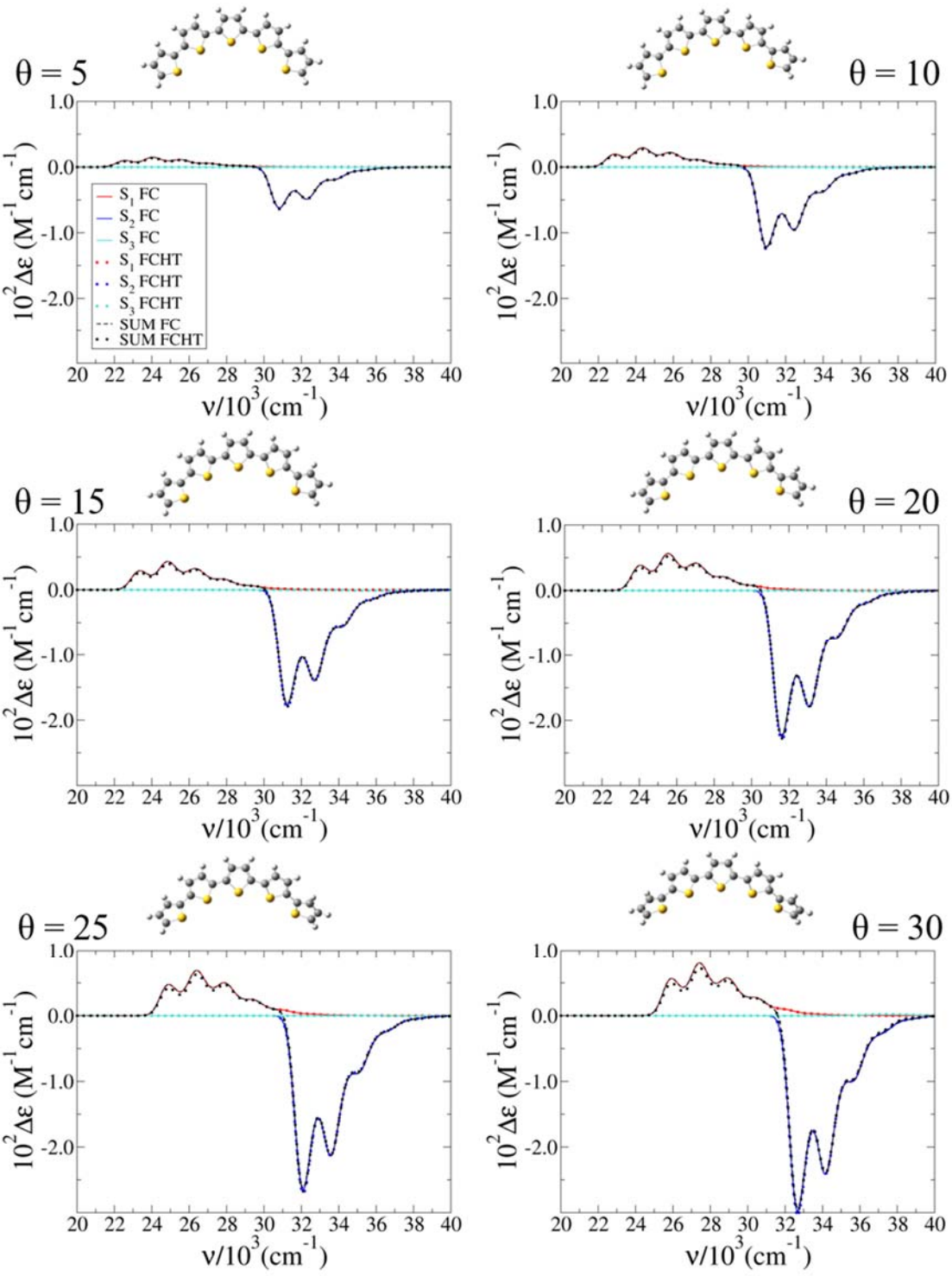

Figure S15. FC and FCHT contribution of S1, S2 and S3 to the ECD spectra computed for the *class II* structure of T_5 cisoid helices at 0K and broadened with a Gaussian with HWHM=450 cm^{-1} at different torsion angles (considered frozen during the transition).

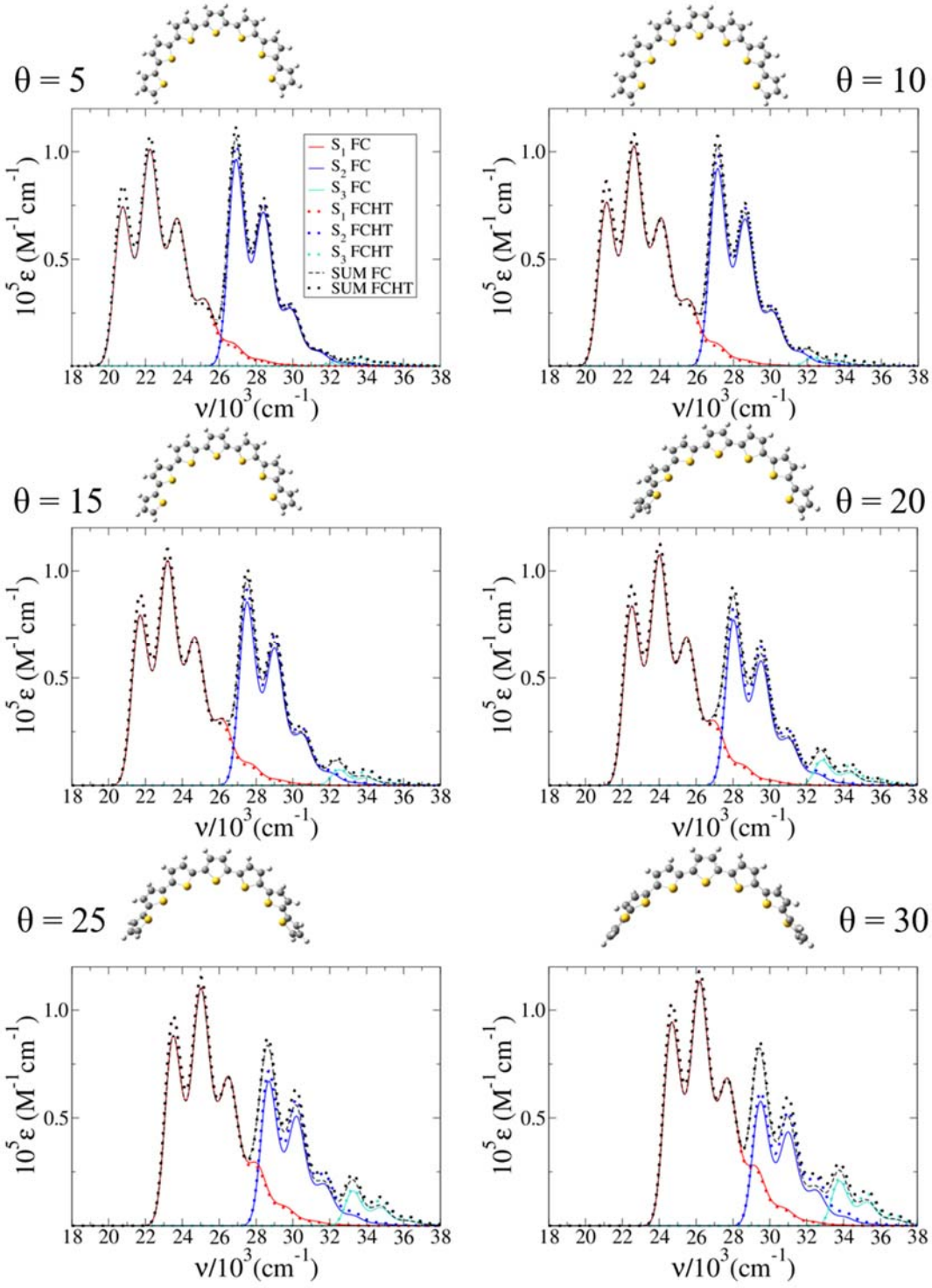

Figure S16. FC and FCHT contribution of S1, S2 and S3 to the absorption spectra computed for the *class II* structure of T_7 cisoid helices at 0K and broadened with a Gaussian with HWHM=450 cm^{-1} at different torsion angles (considered frozen during the transition).

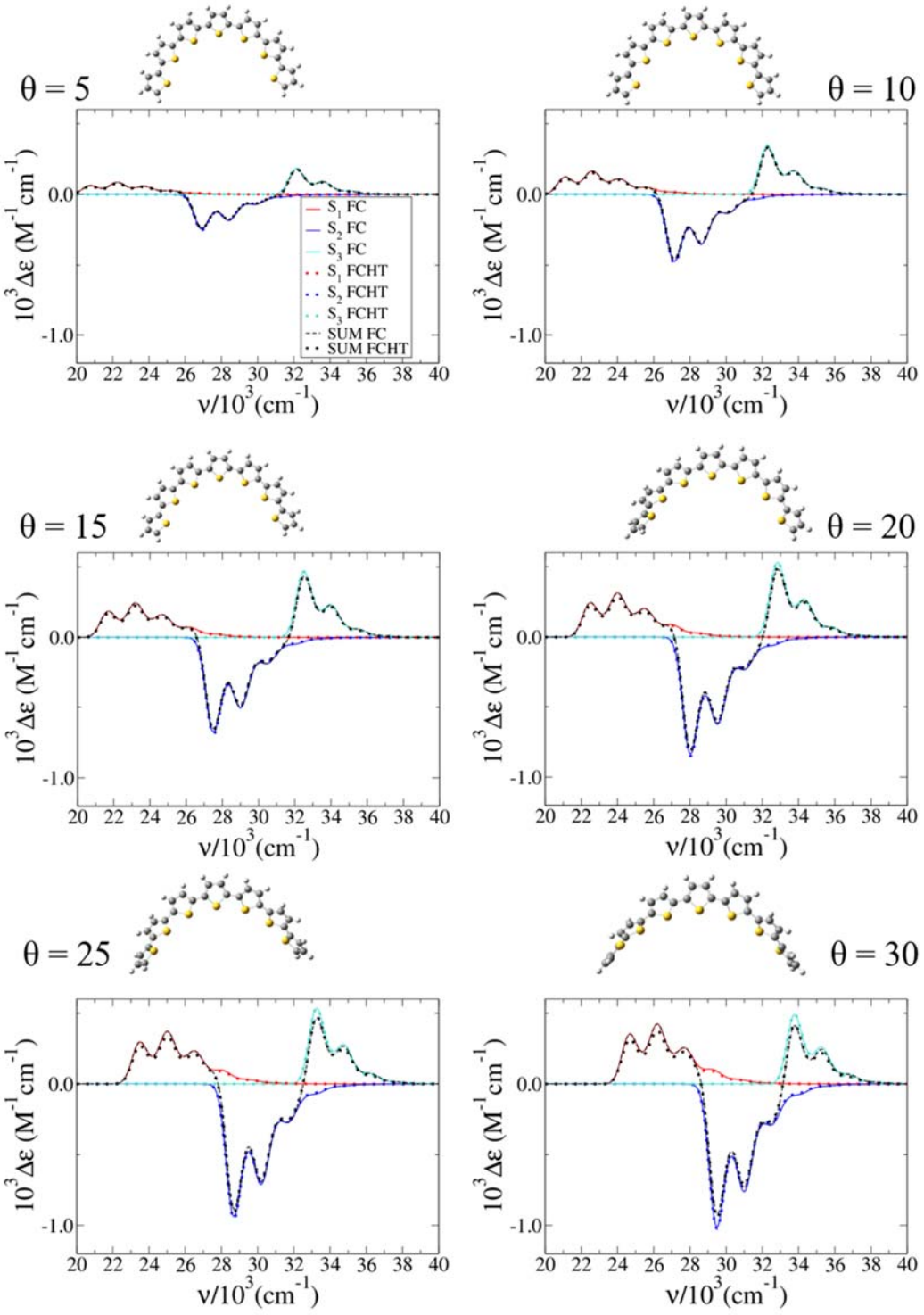

Figure S17. FC and FCHT contribution of S1, S2 and S3 to the ECD spectra computed for the *class II* structure of T_7 cisoid helices at 0K and broadened with a Gaussian with HWHM=450 cm^{-1} at different torsion angles (considered frozen during the transition).

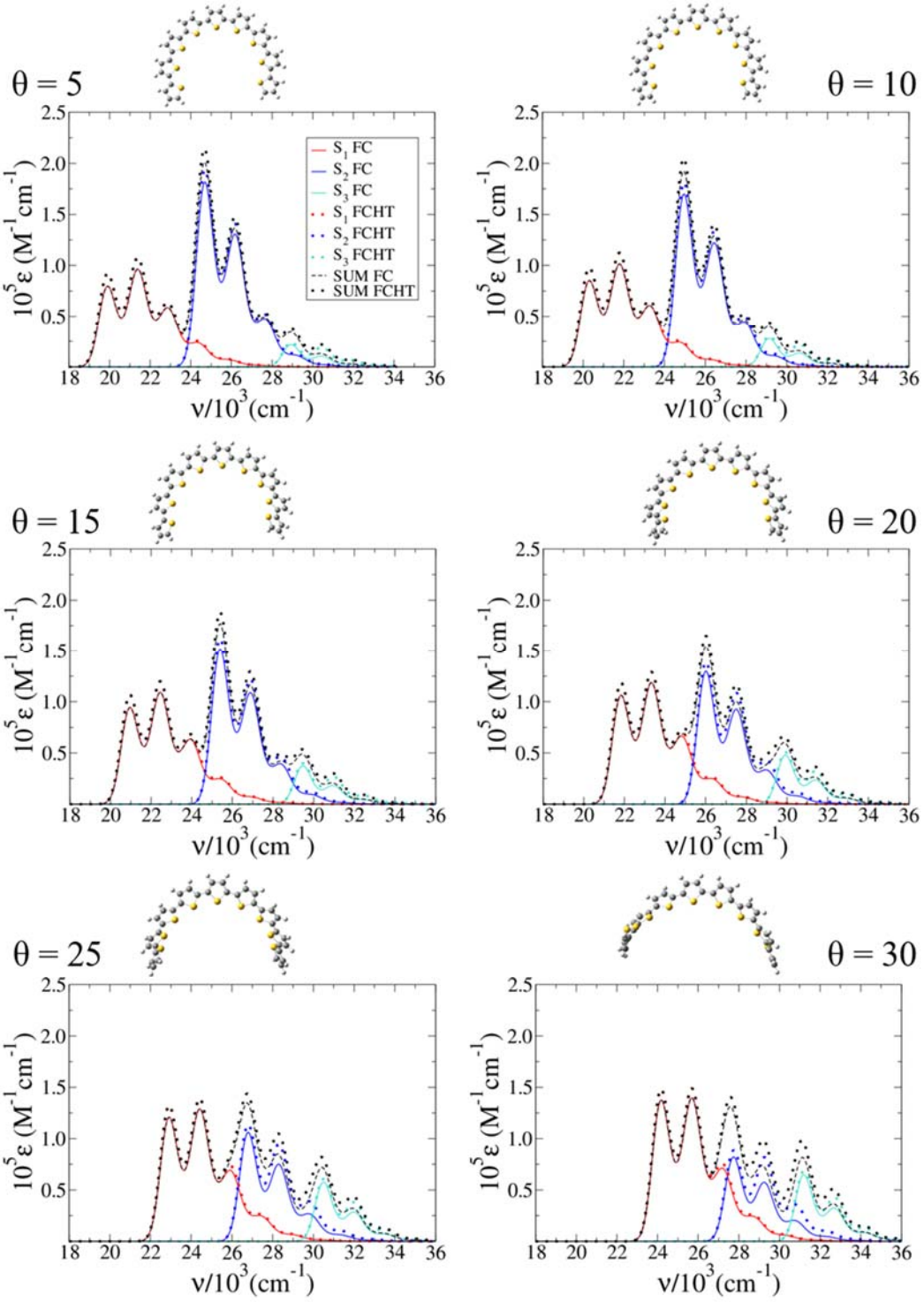

Figure S18. FC and FCHT contribution of S1, S2 and S3 to the absorption spectra computed for the *class II* structure of T_9 cisoid helices at 0K and broadened with a Gaussian with HWHM=450 cm^{-1} at different torsion angles (considered frozen during the transition).

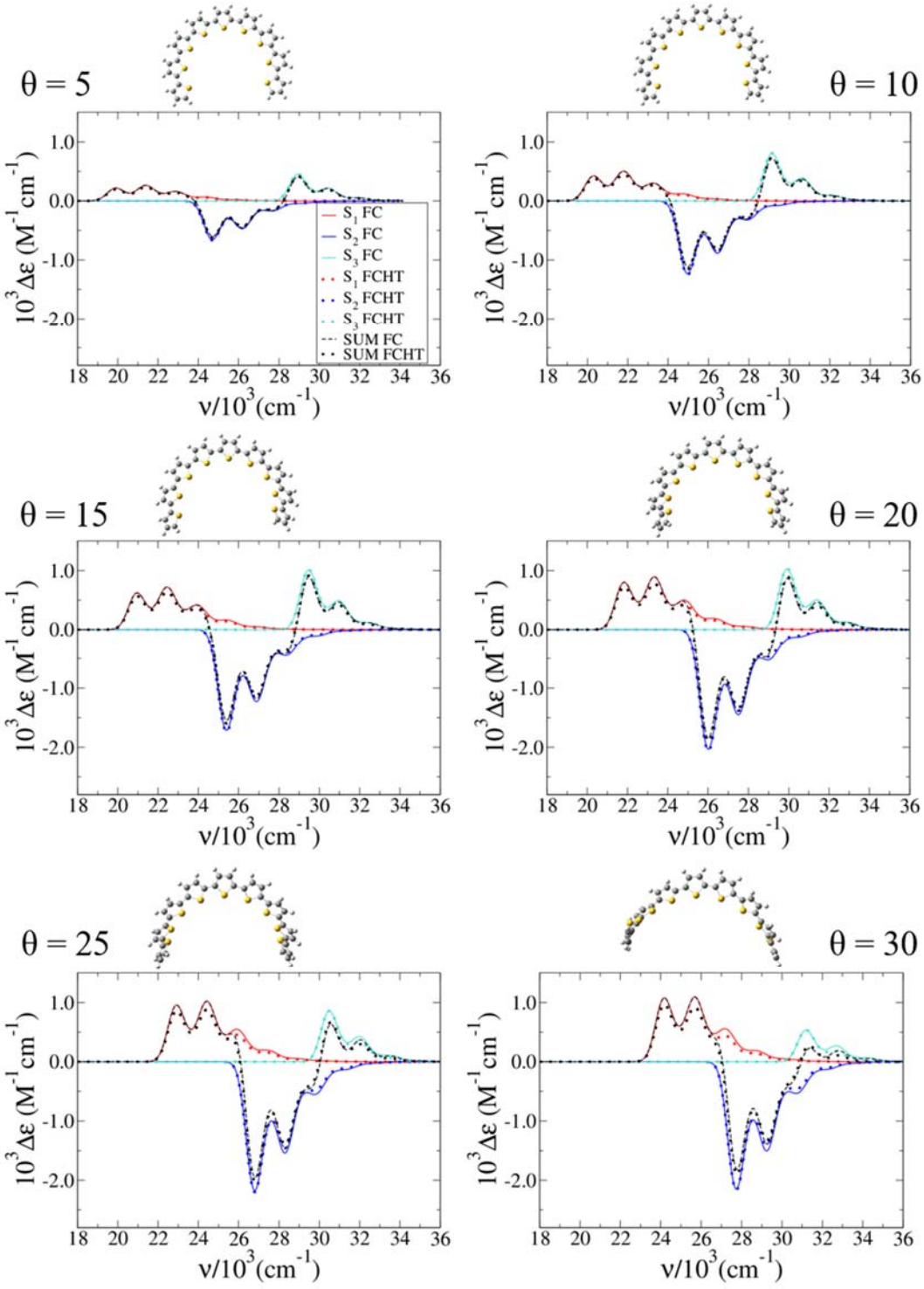

Figure S19. FC and FCHT contribution of S1, S2 and S3 to the ECD spectra computed for the *class II* structure of T_9 cisoid helices at 0K and broadened with a Gaussian with HWHM=450 cm^{-1} at different torsion angles (considered frozen during the transition).

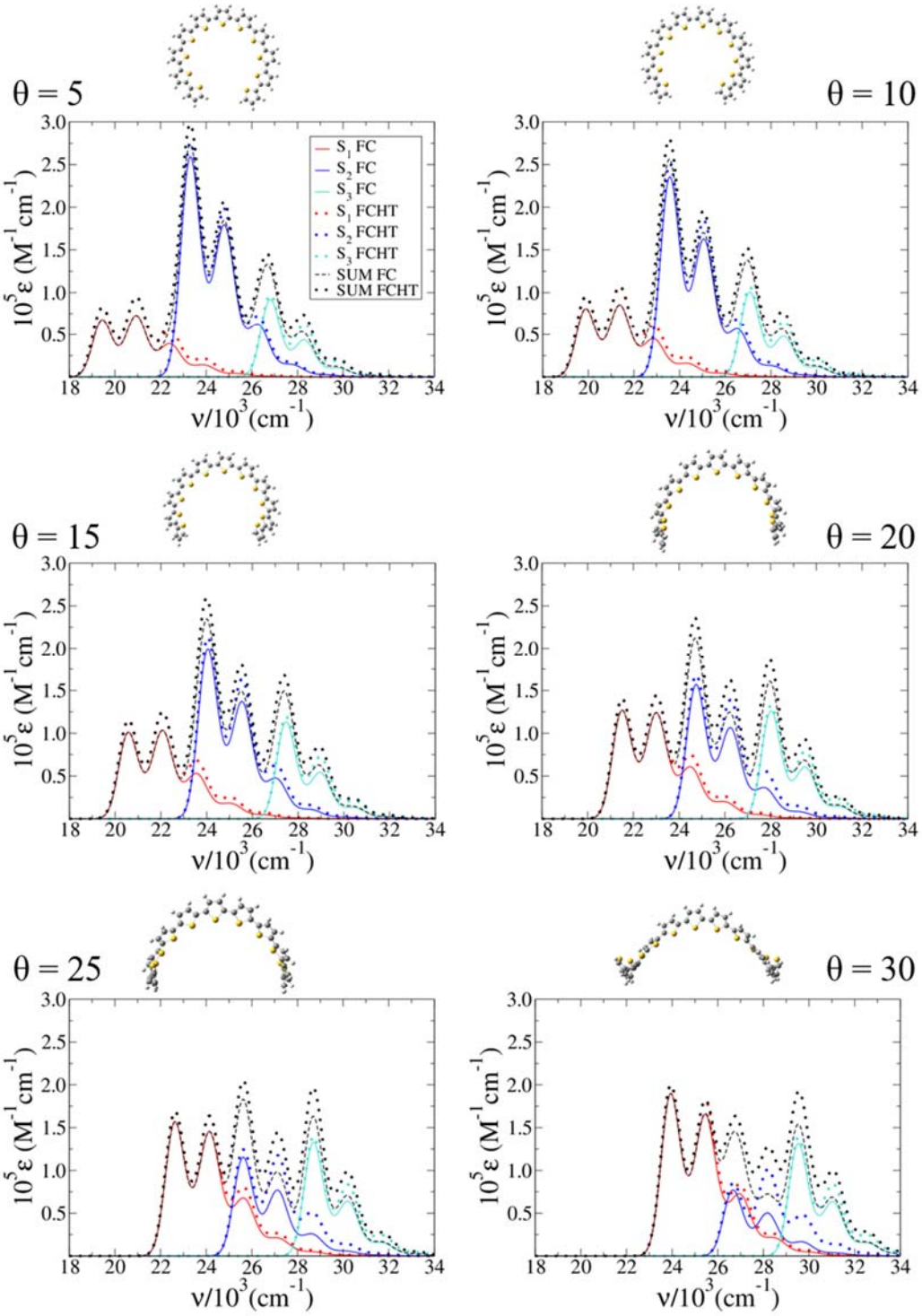

Figure S20. FC and FCHT contribution of S1, S2 and S3 to the absorption spectra computed for the *class II* structure of T_{11} cisoid helices at 0K and broadened with a Gaussian with HWHM=450 cm^{-1} at different torsion angles (considered frozen during the transition).

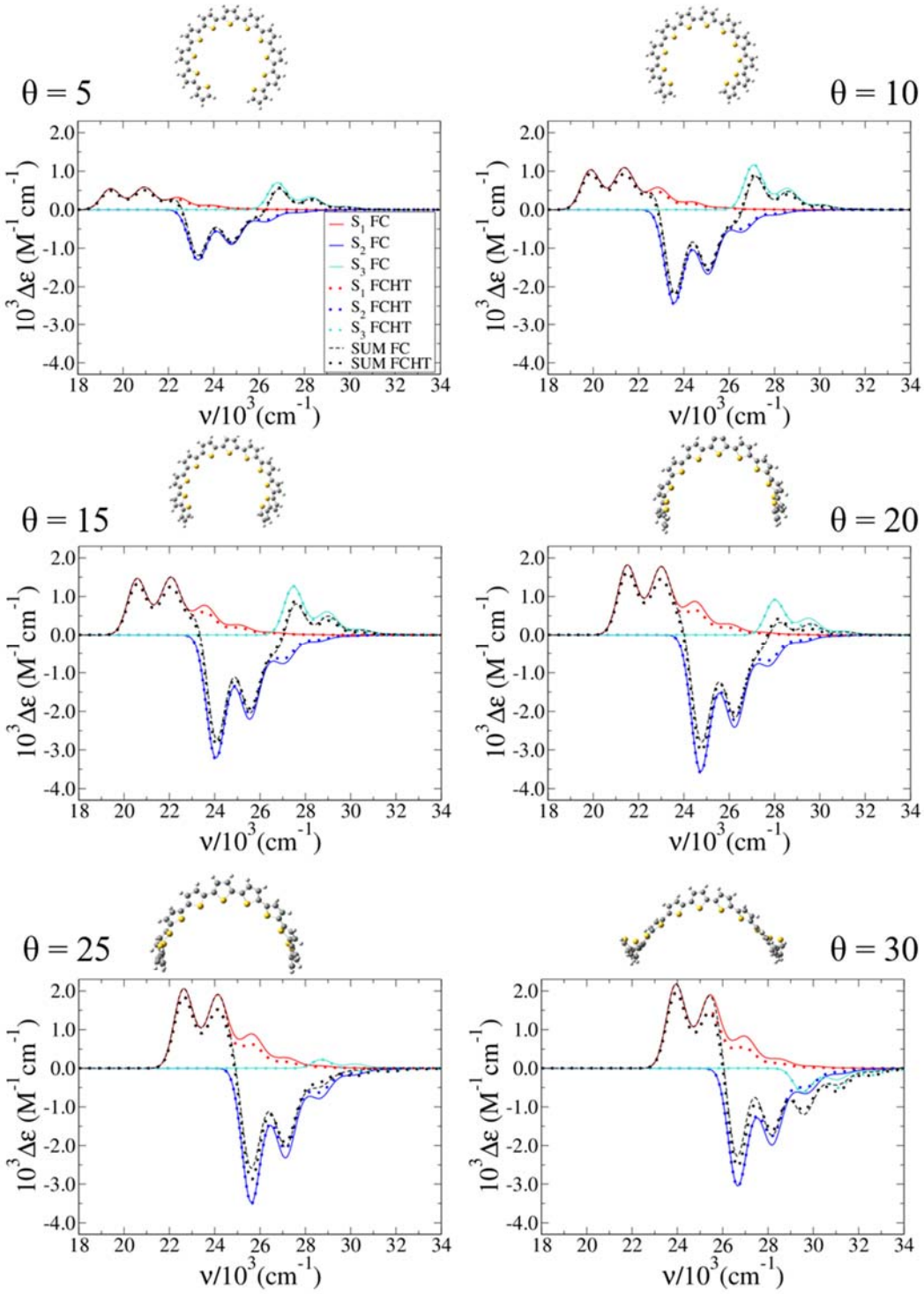

Figure S21. FC and FCHT contribution of S1, S2 and S3 to the ECD spectra computed for the *class II* structure of T_{11} cisoid helices at 0K and broadened with a Gaussian with HWHM=450 cm^{-1} at different torsion angles (considered frozen during the transition).

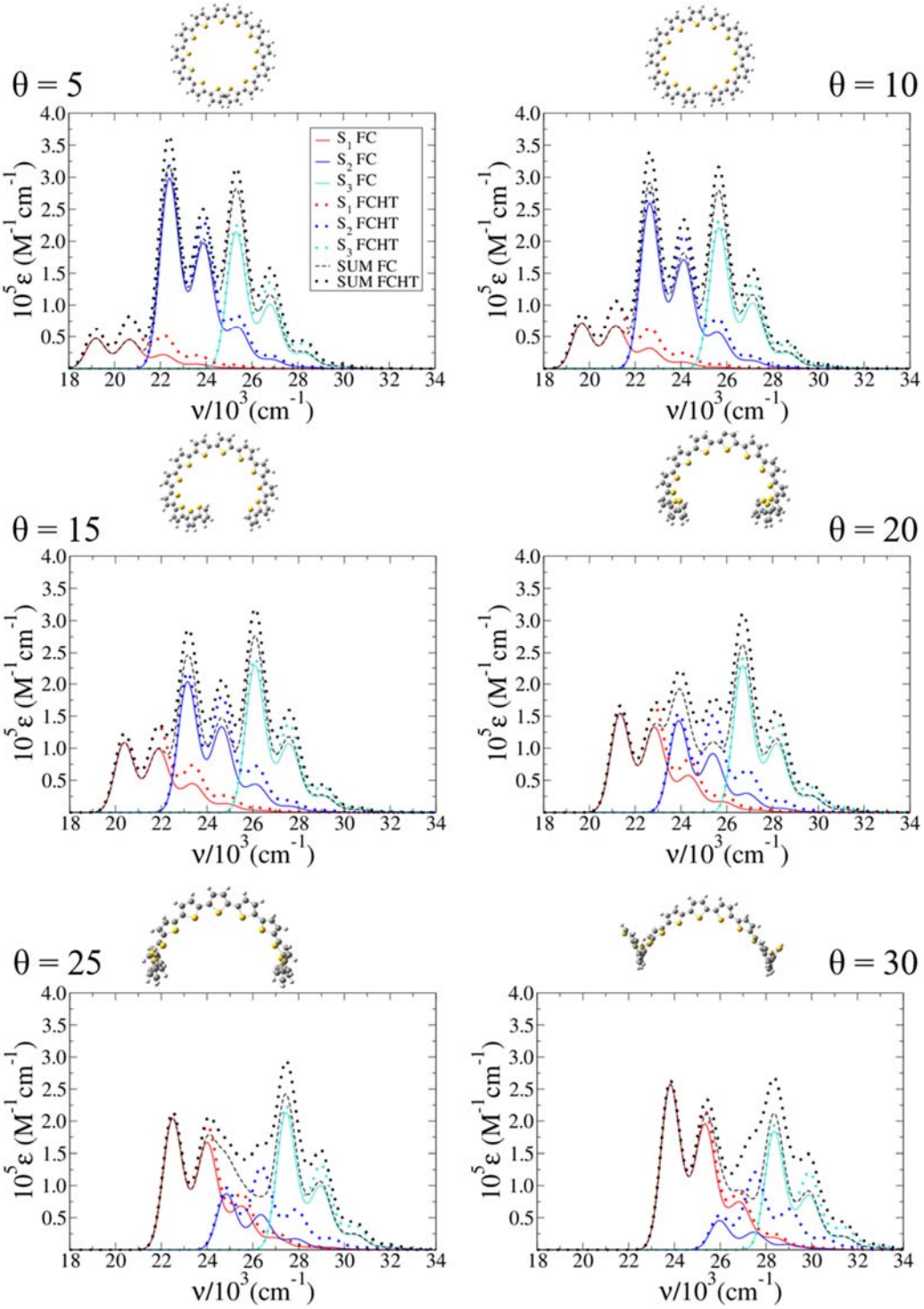

Figure S22. FC and FCHT contribution of S1, S2 and S3 to the absorption spectra computed for the *class II* structure of T_{13} cisoid helices at 0K and broadened with a Gaussian with HWHM=450 cm^{-1} at different torsion angles (considered frozen during the transition).

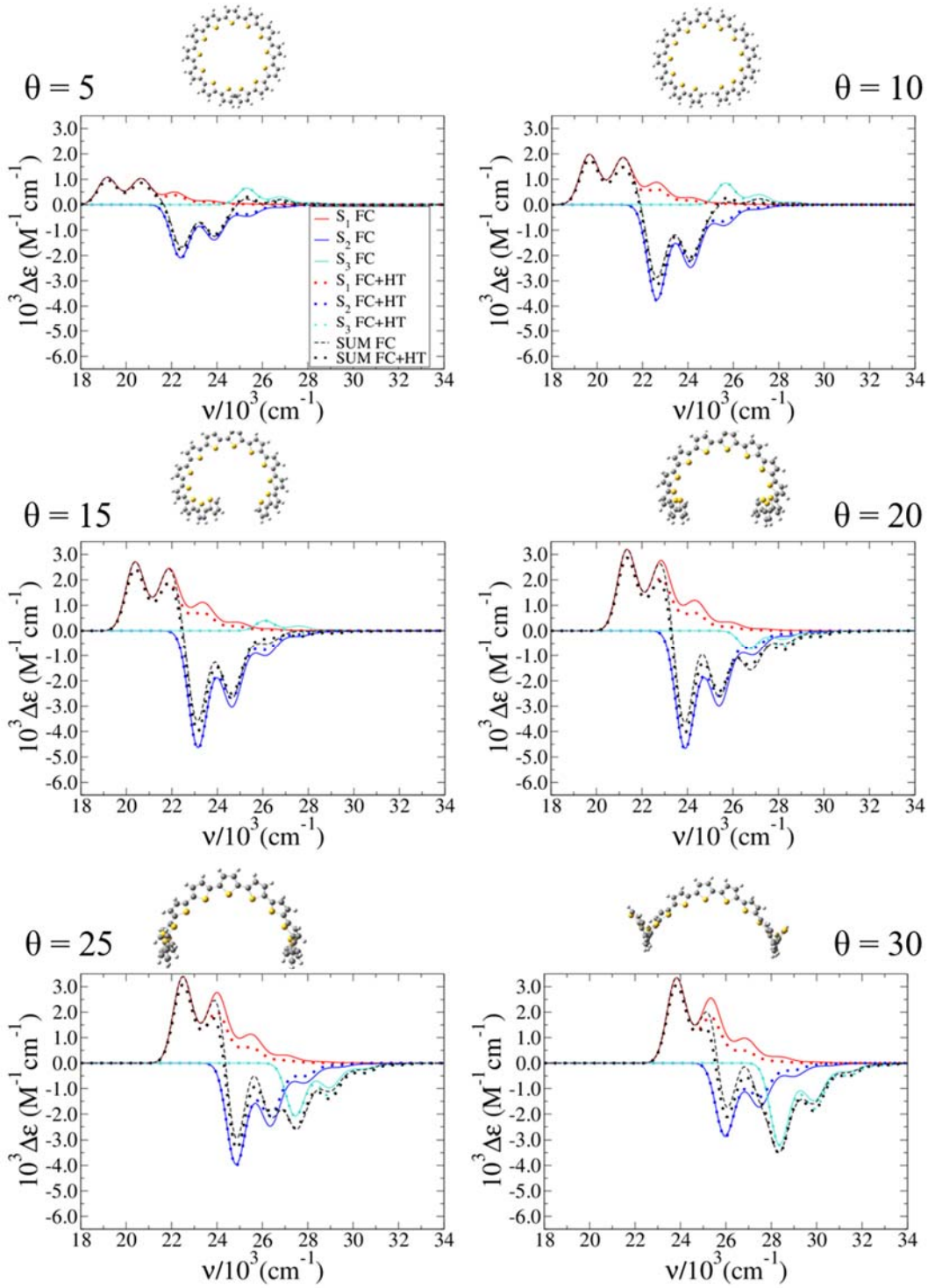

Figure S23. FC and FCHT contribution of S1, S2 and S3 to the ECD spectra computed for the *class II* structure of T_{13} cisoid helices at 0K and broadened with a Gaussian with HWHM=450 cm^{-1} at different torsion angles (considered frozen during the transition).

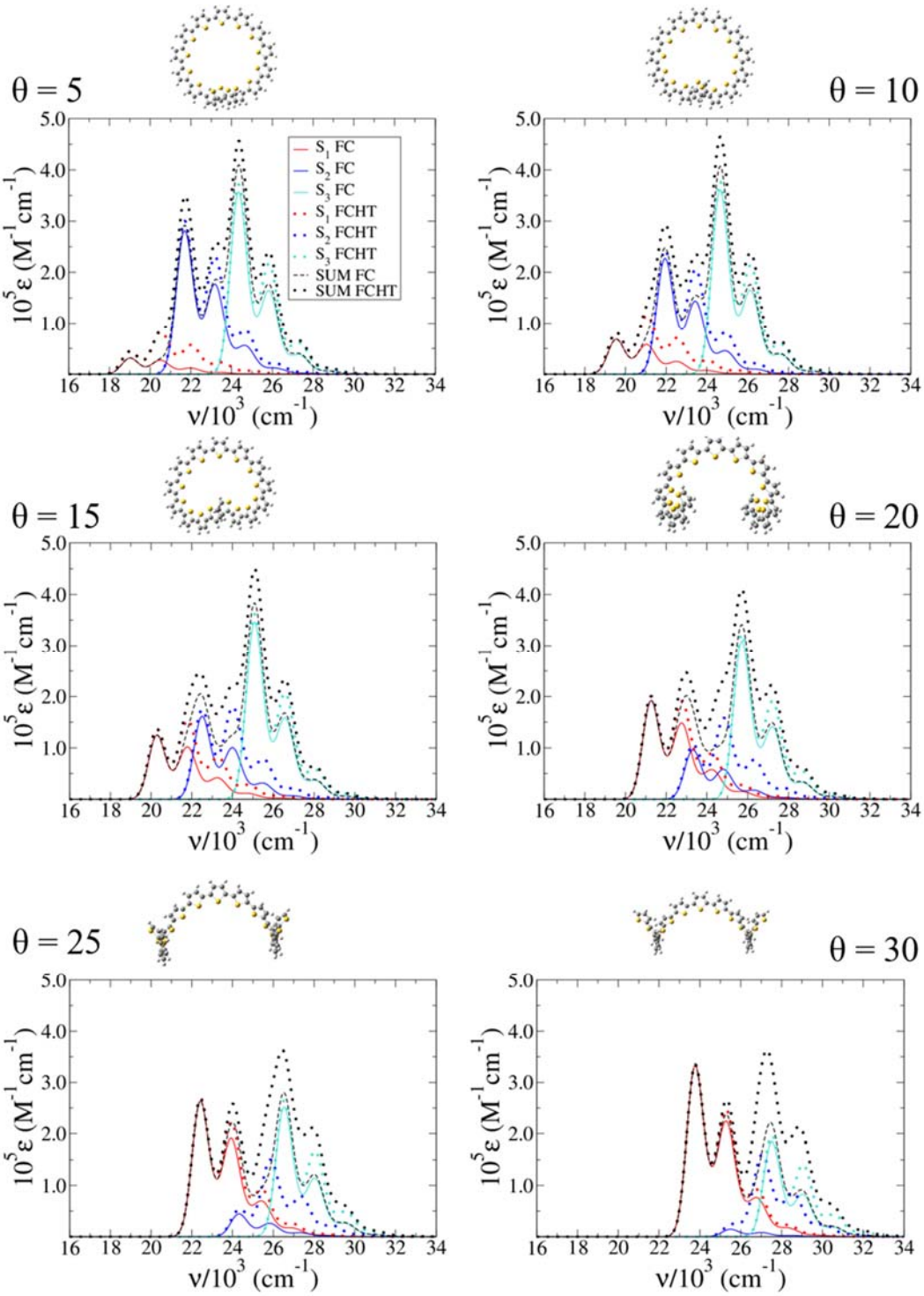

Figure S24. FC and FCHT contribution of S1, S2 and S3 to the absorption spectra computed for the *class II* structure of T_{15} cisoid helices at 0K and broadened with a Gaussian with HWHM=450 cm^{-1} at different torsion angles (considered frozen during the transition).

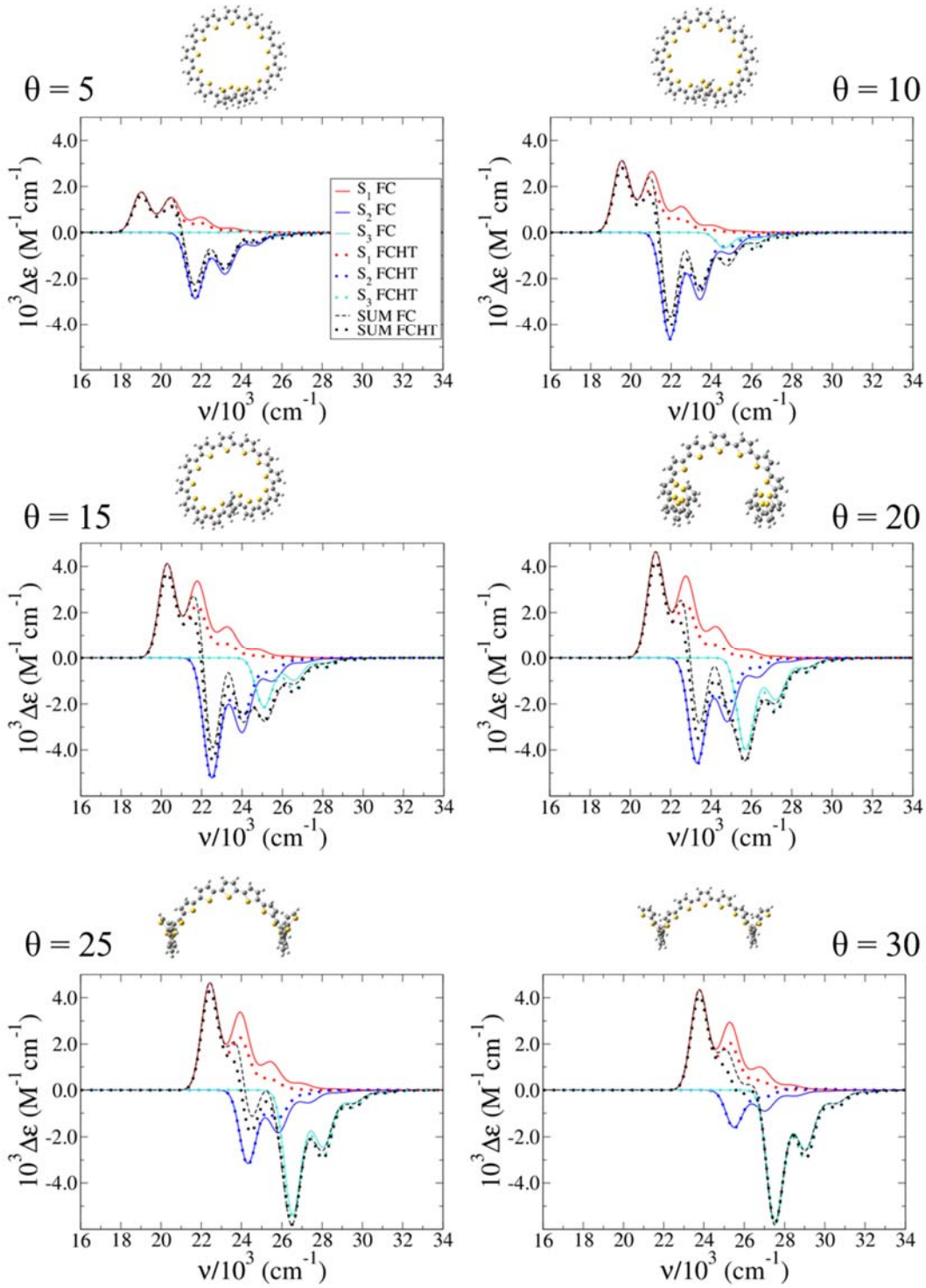

Figure S25. FC and FCHT contribution of S1, S2 and S3 to the ECD spectra computed for the *class II* structure of T_{15} cisoid helices at 0K and broadened with a Gaussian with HWHM=450 cm^{-1} at different torsion angles (considered frozen during the transition).

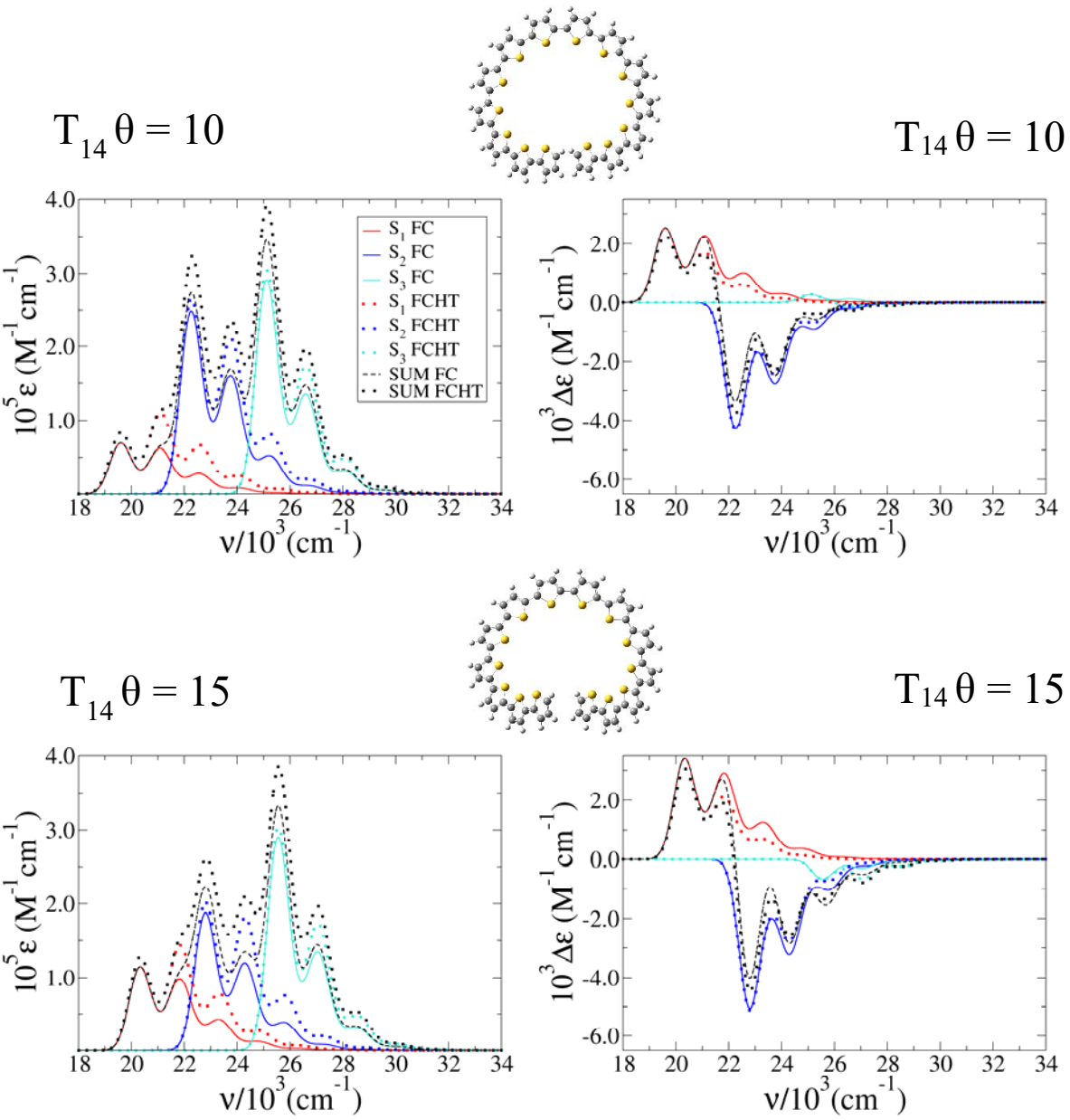

Figure S26. FC and FCHT absorption (left) and ECD (right) spectra computed for the *class II* structure of T_{14} with θ = 10 (top) and θ = 15 (bottom) cisoid helices at 0K and broadened with a Gaussian with HWHM=450 cm^{-1}. Inter-ring torsion angles are considered frozen during the transition.

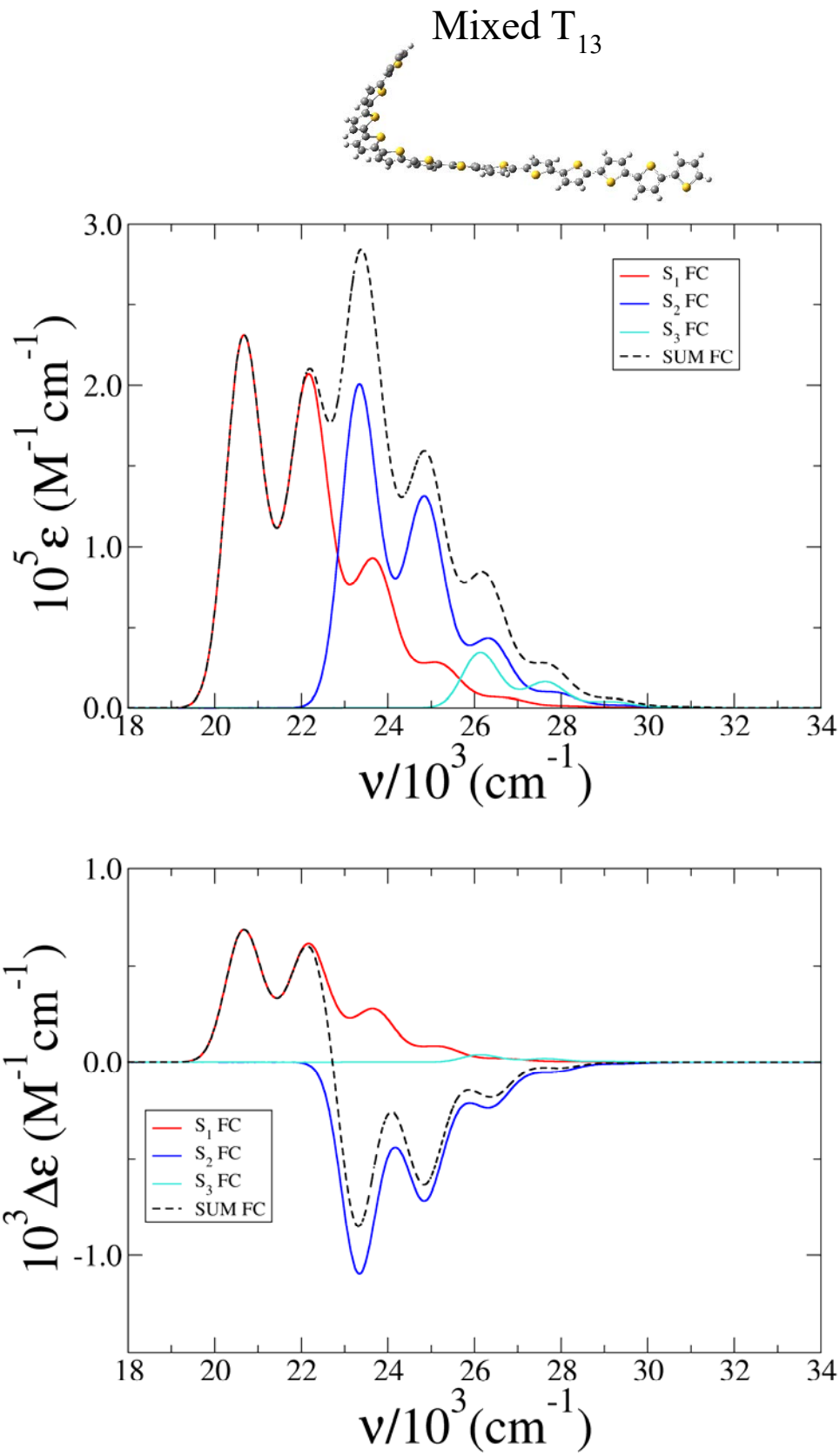

Figure S27. FC absorption (top) and ECD (bottom) spectra computed for the *class II* structure of mixed T_{13} helix at θ=15º, 0K and broadened with a Gaussian with HWHM=450 cm^{-1}. Inter-ring torsion angles are considered frozen during the transition.

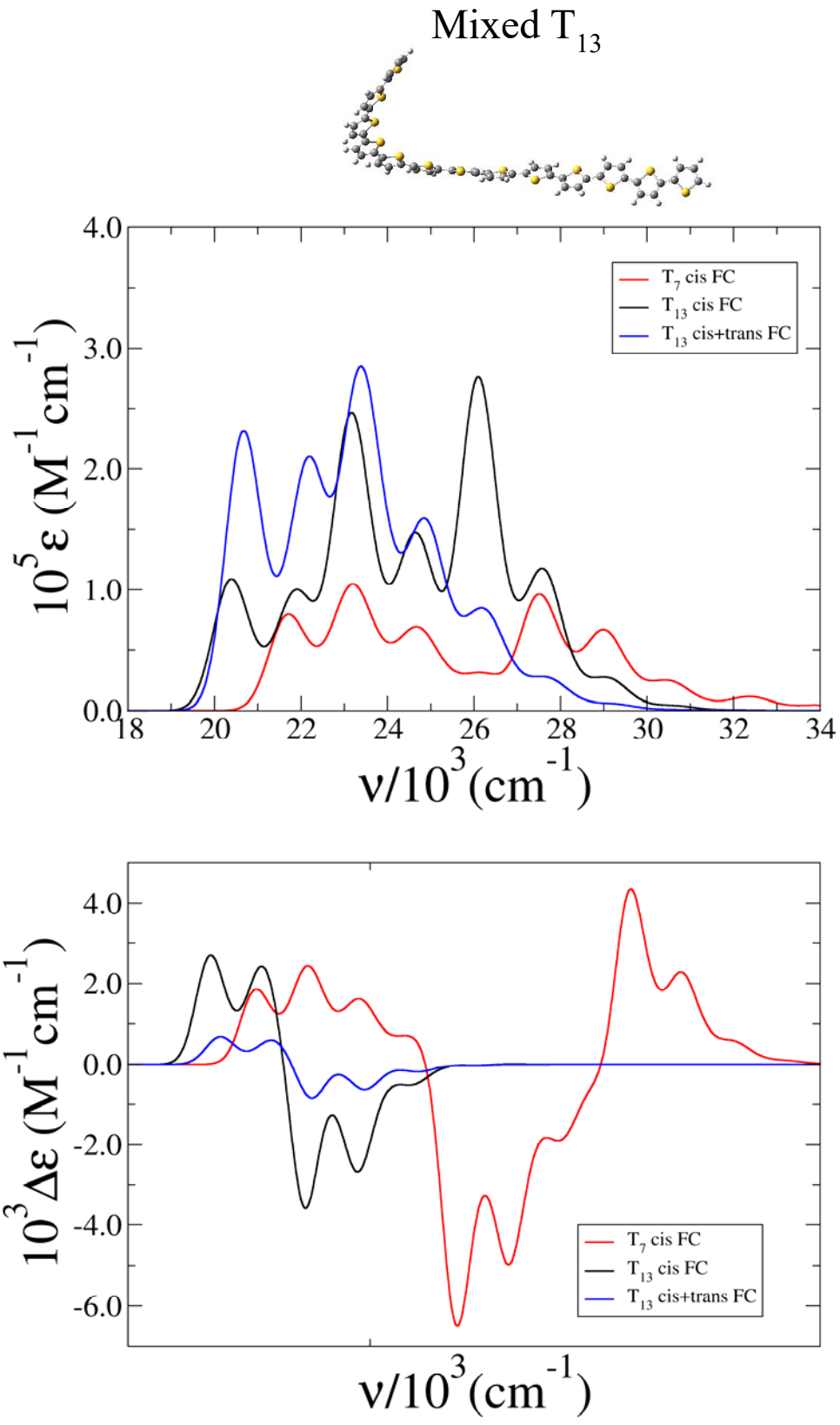

Figure S28. FC absorption (top) and ECD (bottom) spectra computed for the *class II* structures of cisoid T_7, cisoid T_{13} and mixed T_{13} helix. All were computed at θ=15º, 0K and broadened with a Gaussian with HWHM=450 cm^{-1}. Inter-ring torsion angles are considered frozen during the transition.

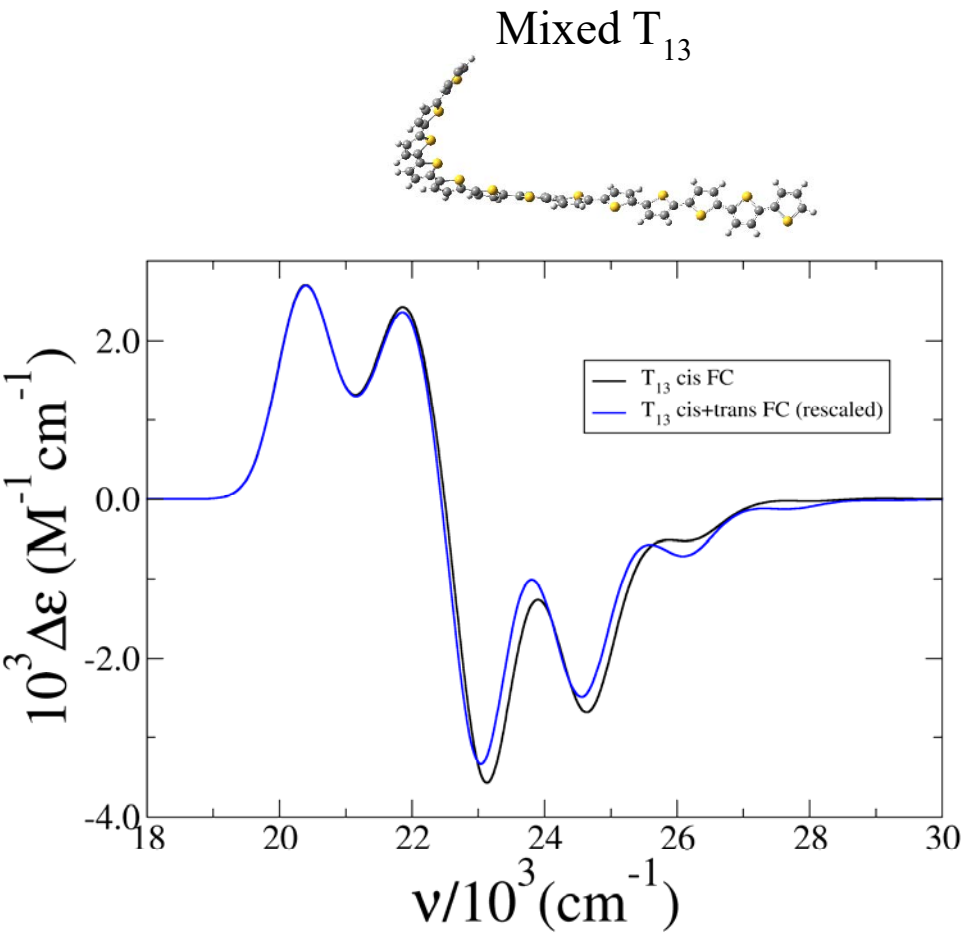

Figure S29. ECD spectra of *class II* structures cisoid T_{13} and mixed T_{13}. The latter was rescaled and shifted to overlap with the first peak of cisoid T_{13}. Both were computed at θ=15º, 0K and broadened with a Gaussian with HWHM=450 cm^{-1}. Inter-ring torsion angles are considered frozen during the transition.

Table S2. Vertical energies (in eV) for the unmethyled (T) and polymethyled (3-methylT) transoid and cisoid T_{13} structures at θ=15º.

	Transoid		Cisoid	
	T_{13}	$(3\text{-methylT})_{13}$	T_{13}	$(3\text{-methylT})_{13}$
S1	2.7657	2.7176	2.6940	2.6803
S2	3.0409	2.9947	2.9922	2.9669
S3	3.3382	3.2931	3.3247	3.2979

Analysis of Molecular Orbitals and transition densities for T_7 and T_{13}.

The Kohn-Sham Molecular Orbitals (MOs) more involved in the S1-S3 electronic states of T_7 and T_{13} are shown in Figures S30-S33 for *transoid* twisted ribbons and *cisoid* helices of T_7 and T_{13} with θ= 10, 20 and 30 degrees. For θ=20 degrees a more in-depth analysis is performed in Figures S34-S39 and Table S3. The description of S1-S3 transitions in terms of excitations between MOs (reported in Table S3) is pretty similar for both *transoid* and *cisoid* structures. S1 is always a HOMO→ LUMO transition, S2 involves both HOMO → LUMO+1 and HOMO-1 → LUMO and S3 arises from HOMO →LUMO+2, HOMO-1 → LUMO+1 and HOMO-2 → LUMO excitations. Inspection of the Figures S30-S33 show that the shapes of the MOs themselves are very similar; therefore, it is not surprising that even the S0 → Sn (n=1,2,3) transition densities look pretty similar for *transoid* and *cisoid* helices. Figures S34-S38 show that transoid structures mostly extend in the direction of the non-total symmetric Y axis. On the contrary, cisoid helices extend along all the three axes (Z is the total symmetric one). The X, Y and Z Cartesian components of the electric transition moment associated to these transitions can be computed by the integral of the transition densities ($\rho_{0n}(X,Y,Z)$) multiplied by the value of the corresponding coordinate $\mu_{0n}(X) \propto \int X\rho_{0n}(X,Y,Z)d\mathbf{r}$, $\mu_{0n}(Y) \propto \int Y\rho_{0n}(X,Y,Z)d\mathbf{r}$, $\mu_{0n}(Z) \propto \int Z\rho_{0n}(X,Y,Z)d\mathbf{r}$. The different spatial arrangments of *transoid* and *cisoid* structures have a deep impact on these integrands. Consider T_7: S1 state belongs to B irreps. Accordingly, it can have X and Y components of the transition dipole. Due to the almost linear structure of the transoid twisted ribbon, oriented along Y, the transition is almost completely Y-polarized. $\mu_{01}(Y)$ is the largest component also for the cisoid structure but in this case also $\mu_{01}(X)$ is significant. Notice, on the contrary, that $Z\rho_{01}(X,Y,Z)$ is an odd function and therefore its integral is zero. The same is true for $X\rho_{02}(X,Y,Z)$ and $Y\rho_{02}(X,Y,Z)$ of both transoid and cisoid structures, as expected since in both cases, S2 belongs to the A irreps. However, $Z\rho_{02}(X,Y,Z)$ shows a large difference in the two cases. In fact cisoid helix is much more elongated along the Z axis so that the same transition density is actually more stretched along such axis in cisoid than in transoid structures. Multiplication by "Z" therefore enhances the contributions of the atoms at large positive and negative Z values,

giving a trasition dipole 70-80 times larger in cisoid helix. The same phenomenon occurs for S1 and S2 of cisoid and transoid T_{13}. In the cisoid arrangement of T_{13} however, also S3 (B symmetry) acquires a remarkable transition dipole. Interestingly, even if $Y\rho_{03}(X,Y,Z)$ shows bigger positive and negative lobes than $X\rho_{03}(X,Y,Z)$ the X component of the transition dipole is much larger than the Y one. This result can be rationalized noticing that while in $Y\rho_{03}(X,Y,Z)$ there is an alternation of violet (negative) and cyan (positive) lobes, in $X\rho_{03}(X,Y,Z)$ the negative lobes largely dominate, and in fact $\mu_{03}(X)$ is large and negative. Interestingly the plot for cisoid T_7 and T_{13} shows that the transition densities of the former multiplied by X and Y show an alternation of positive and negative lobes, so that their integral is small. With respect to T_7, the T_{13} structure exhibits left and right wings that elongate in X and Y directions. Its transition density multiplied by X is mainly negative on these extreme parts of the molecule (absent in T_7) and this explains why S3 acquires a strong negative X component of the transition dipole that is not seen in T_7 (Figure S39).

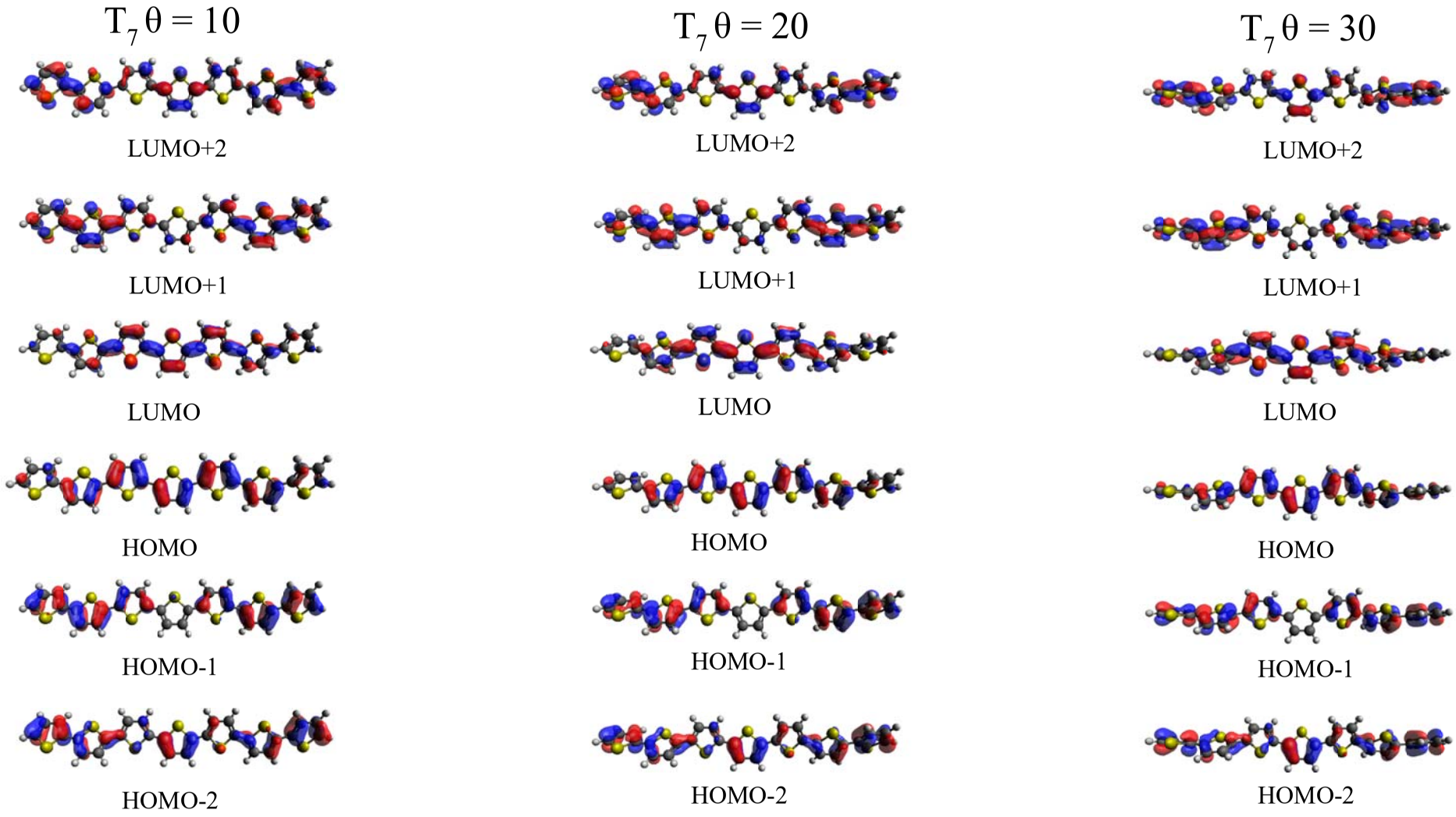

Figure S30. Transoid T_7 Main orbitals involved in the S1 (HOMO -> LUMO), S2 (HOMO -> LUMO +1, HOMO-1, LUMO) and S3 (HOMO -> LUMO+2, HOMO-1 -> LUMO, HOMO-2 -> LUMO) transitions at different torsion angles. Isovalue = 0.03.

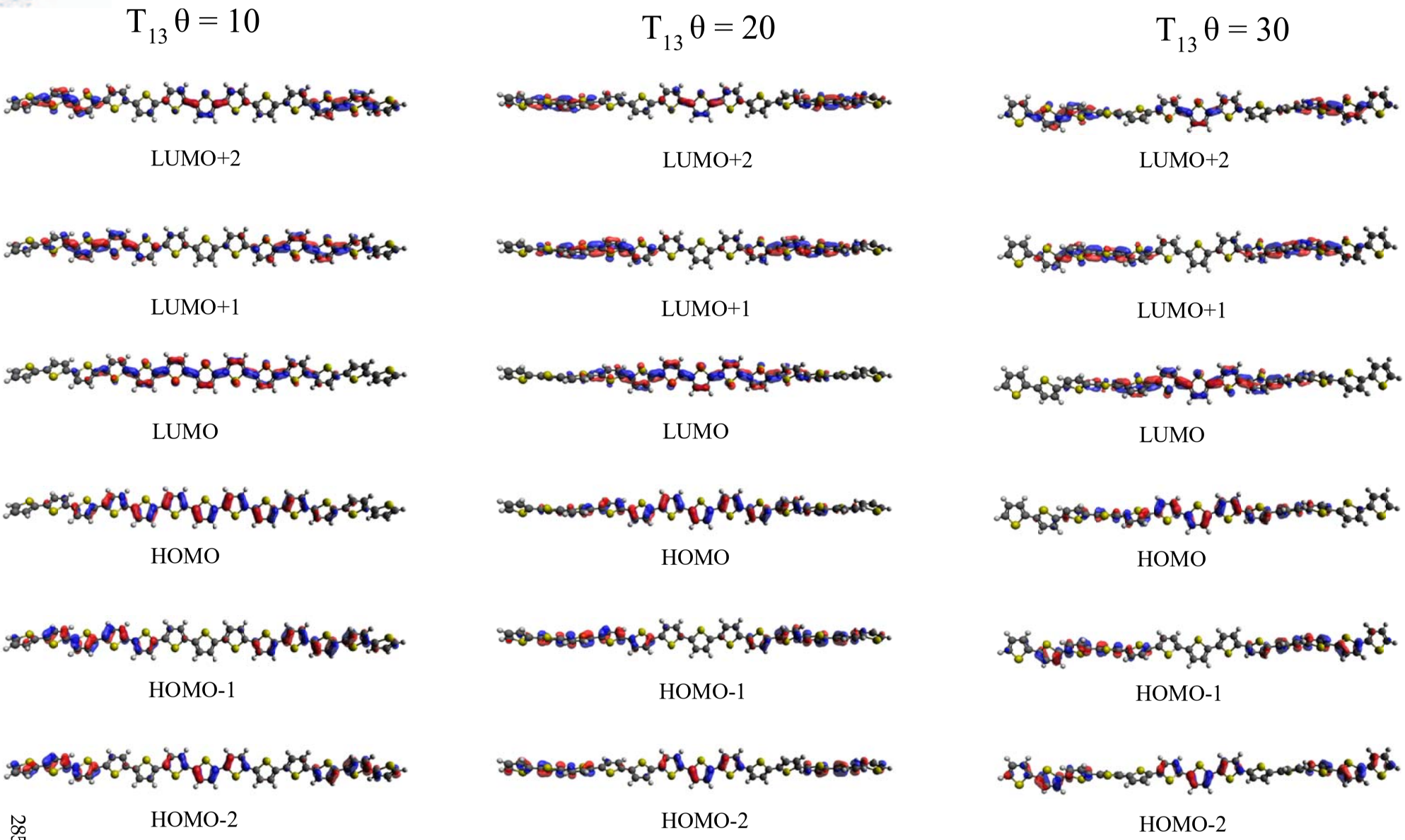

Figure S31. Transoid T_{13} Main orbitals involved in the S1 (HOMO -> LUMO, HOMO-1 -> LUMO+1), S2 (HOMO -> LUMO +1, HOMO-1, LUMO) and S3 (HOMO -> LUMO+2, HOMO-1 -> LUMO, HOMO-2 -> LUMO) transitions at different torsion angles. Isovalue = 0.03

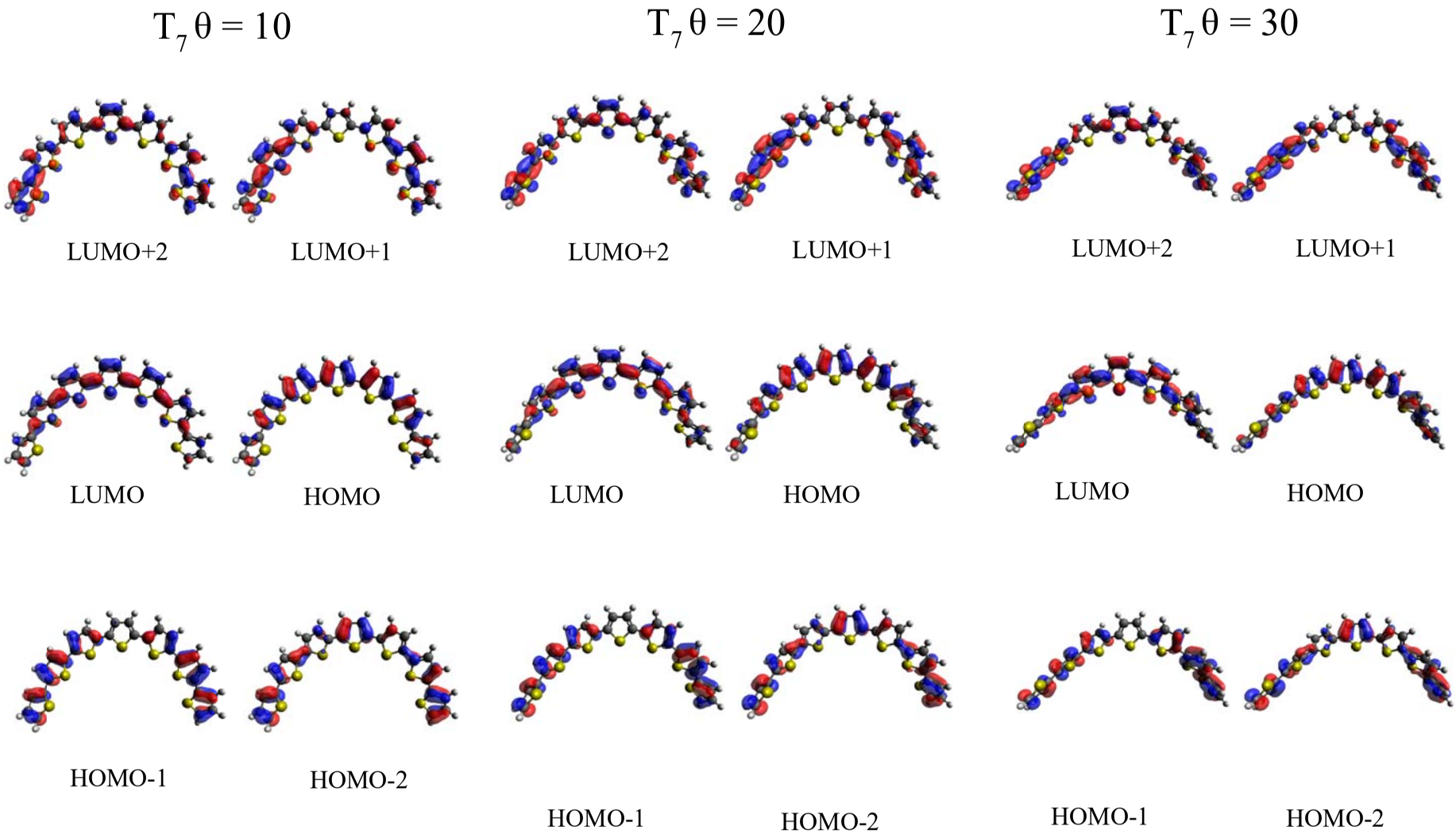

Figure S32. Cisoid T_7 Main orbitals involved in the S1 (HOMO -> LUMO), S2 (HOMO -> LUMO +1, HOMO-1->LUMO) and S3 (HOMO -> LUMO+2, HOMO-1 -> LUMO, HOMO-2 -> LUMO) transitions at different torsion angles. Isovalue = 0.03.

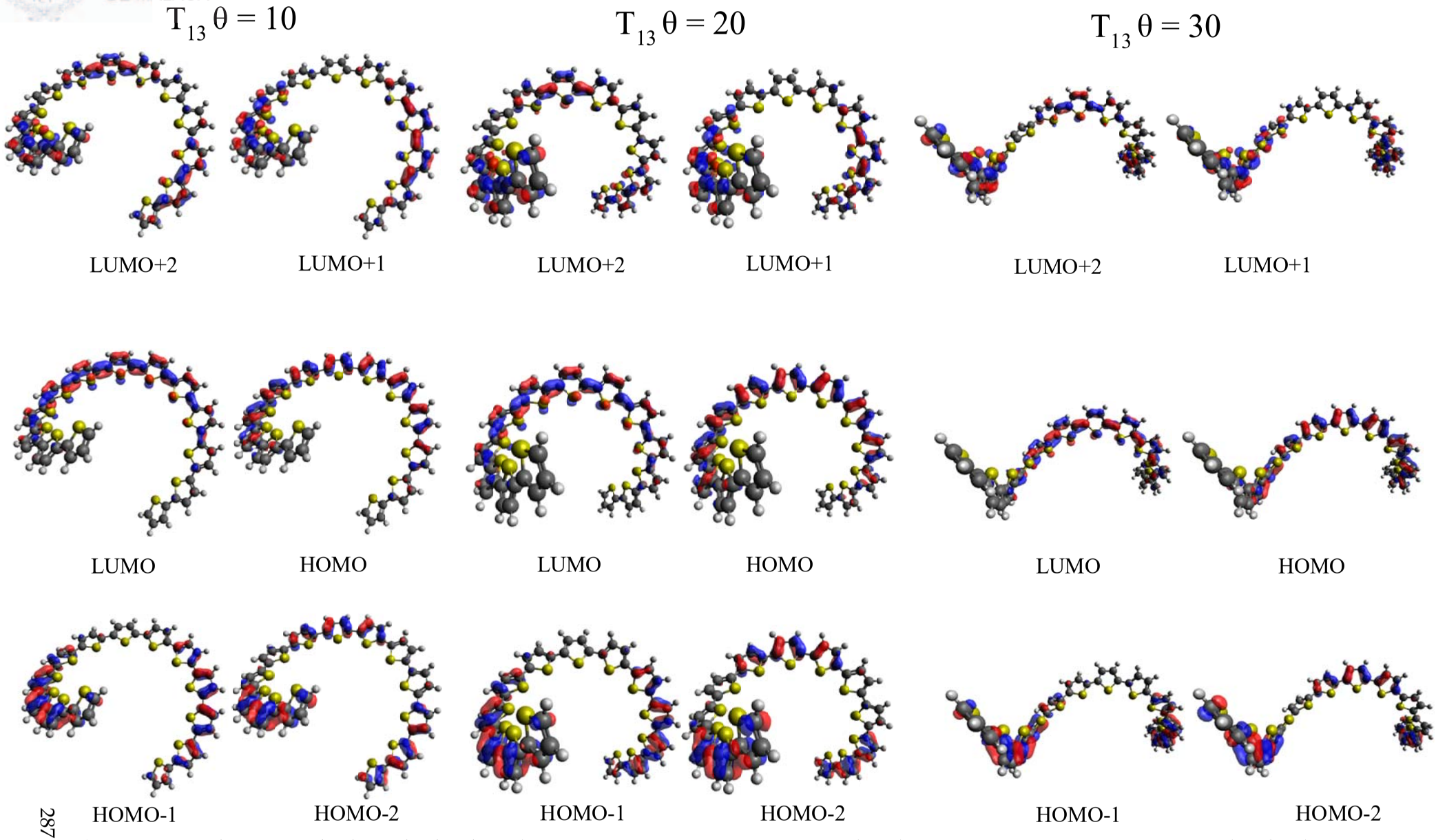

Figure S33. Cisoid T_{13} Main orbitals involved in the S1 (HOMO -> LUMO, HOMO-1 -> LUMO+1), S2 (HOMO -> LUMO +1, HOMO-1->LUMO) and S3 (HOMO -> LUMO+2, HOMO-1 -> LUMO, HOMO-2 -> LUMO) transitions at different torsion angles. Isovalue = 0.03

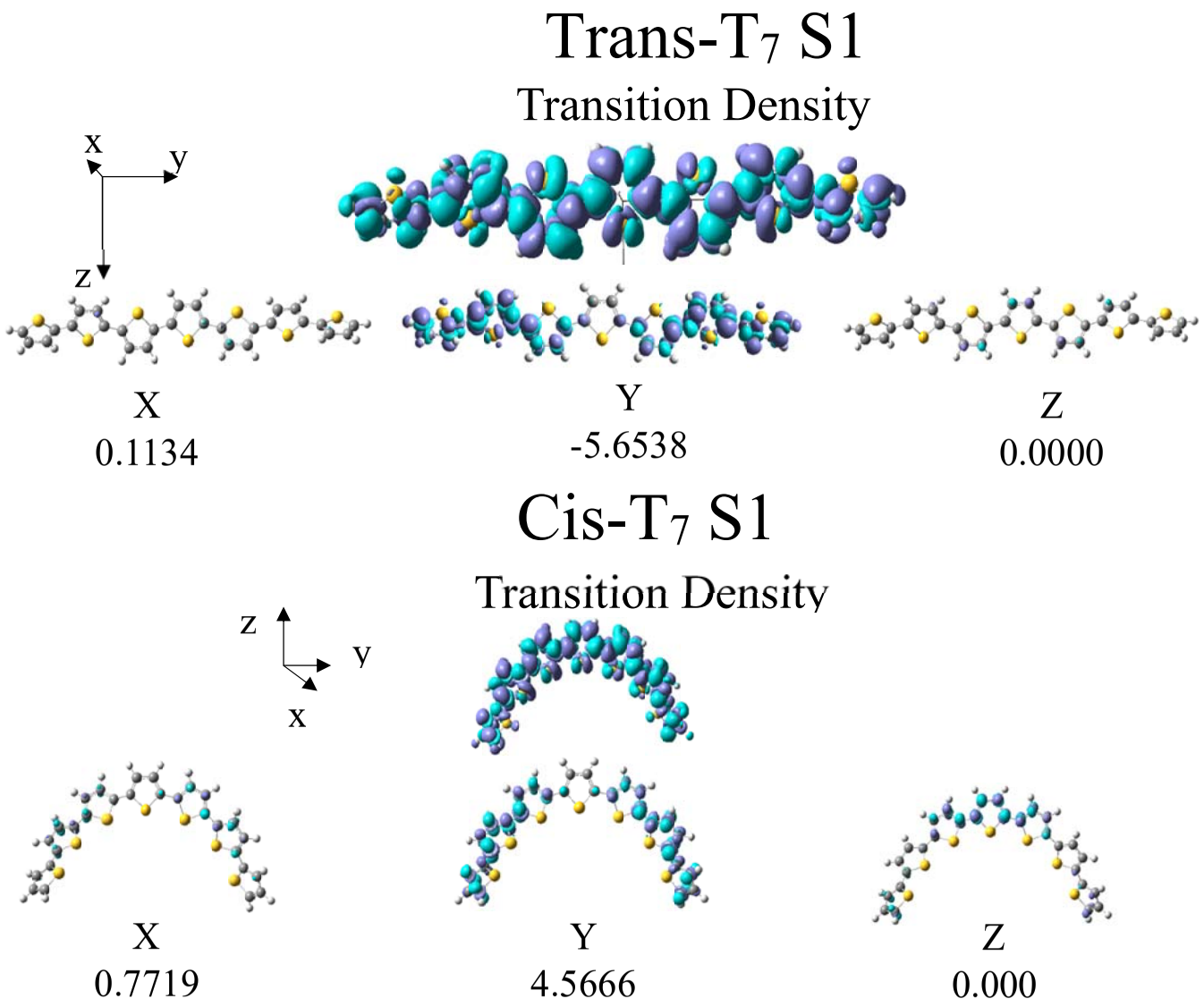

Figure S34. T_7 at $\theta = 20^{o}$: Plot of the transition densities involved in the S1 (HOMO -> LUMO) and of their product by the Cartesian coordinates . The components of the transition electric dipole moment are shown below. Isovalue = 0.0004 for all plots except for the transition densities of transoid T_7 multiplied by X, Y and Z, whose isovalue is 0.00004.

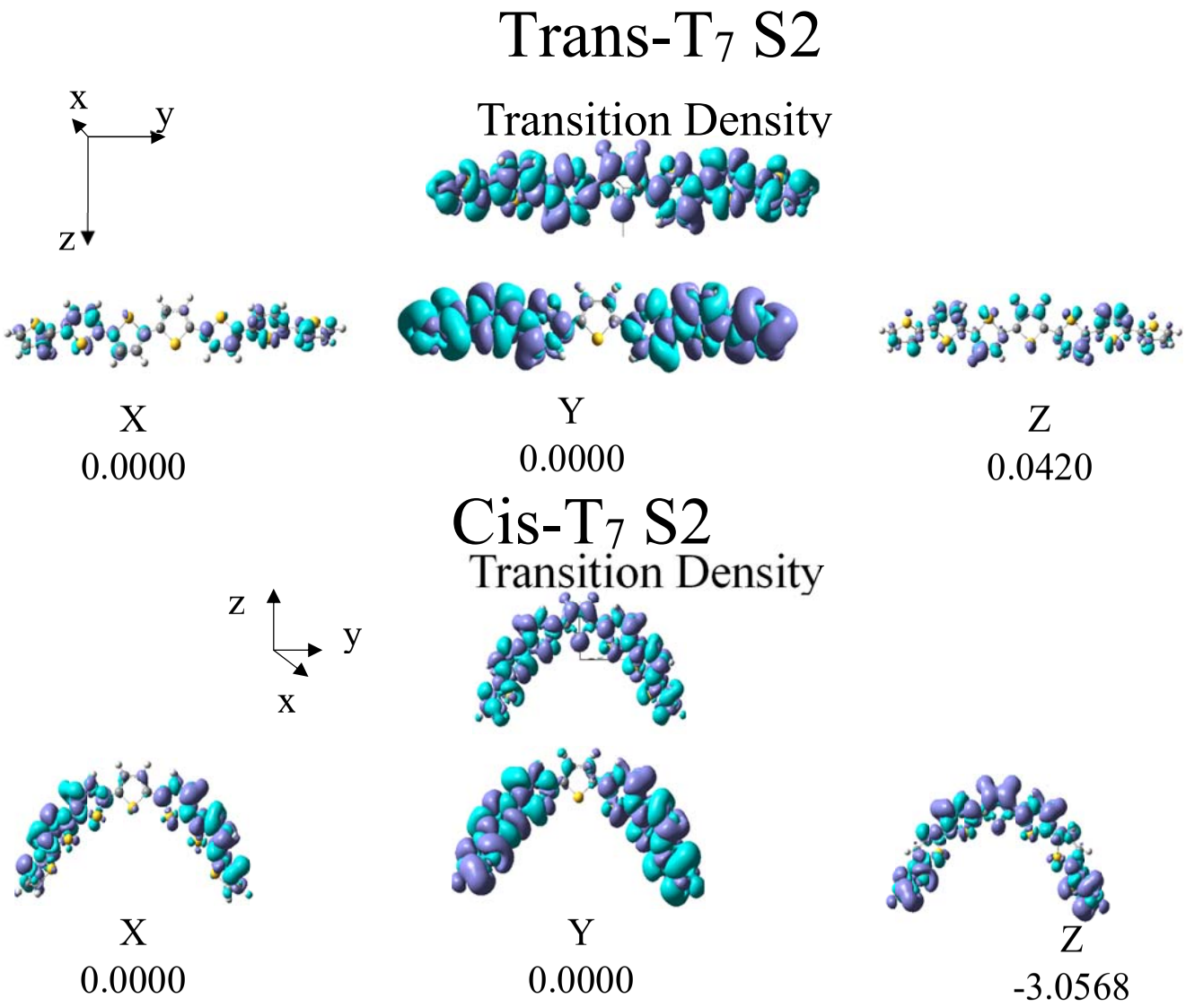

Figure S35. T_7 at $\theta = 20^{o}$: Plot of the transition densities involved in the S2 (HOMO -> LUMO+1, HOMO-1 -> LUMO) and of their product by the Cartesian coordinates . The components of the transition electric dipole moment are shown below. Isovalue = 0.0004 for all plots except for the transition densities of transoid T_7

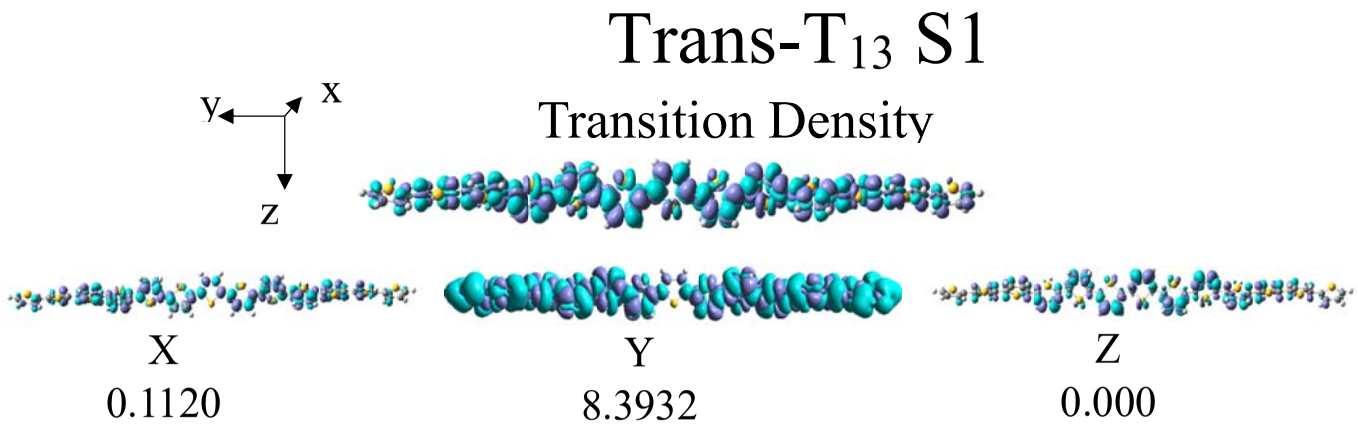

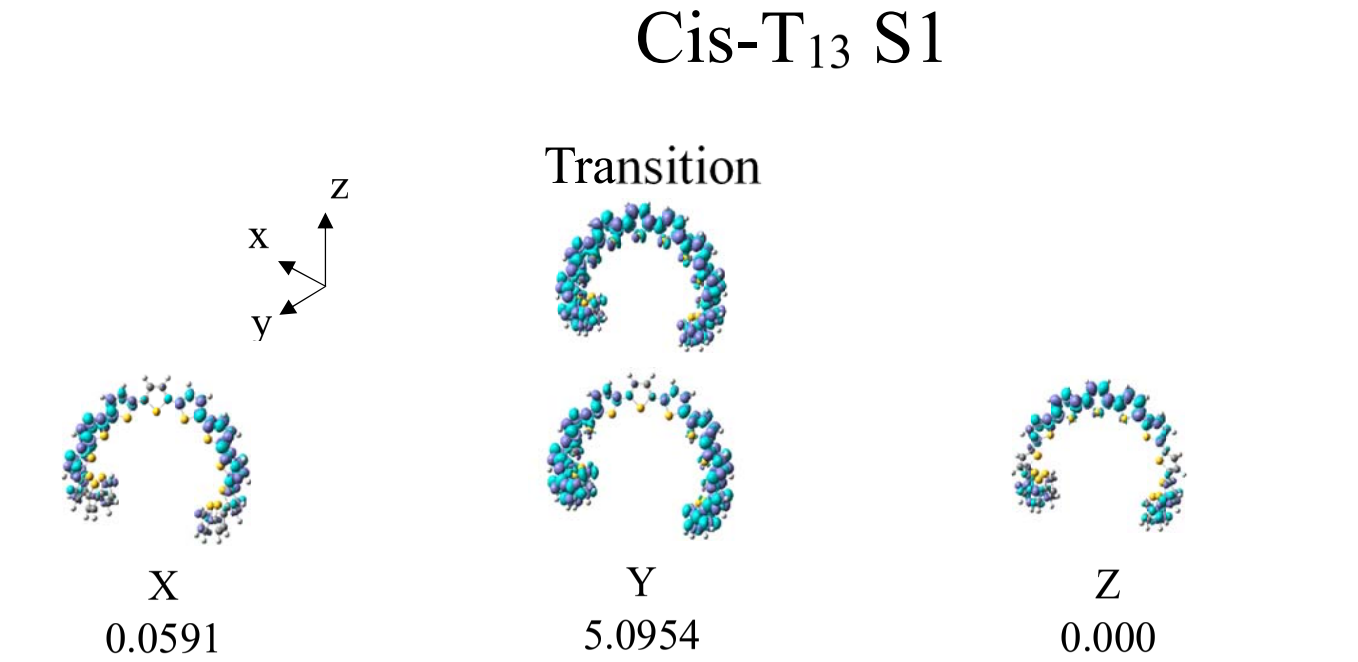

Figure S36. T_{13} at θ = 20º : Plot of the transition densities involved in the S1 (HOMO -> LUMO) and of their product by the Cartesian coordinates . The components of the transition electric dipole moment are shown below. Isovalue = 0.0004 for all plots except for the transition densities of transoid T_{13} multiplied by X, Y and Z, whose isovalue is 0.00004.

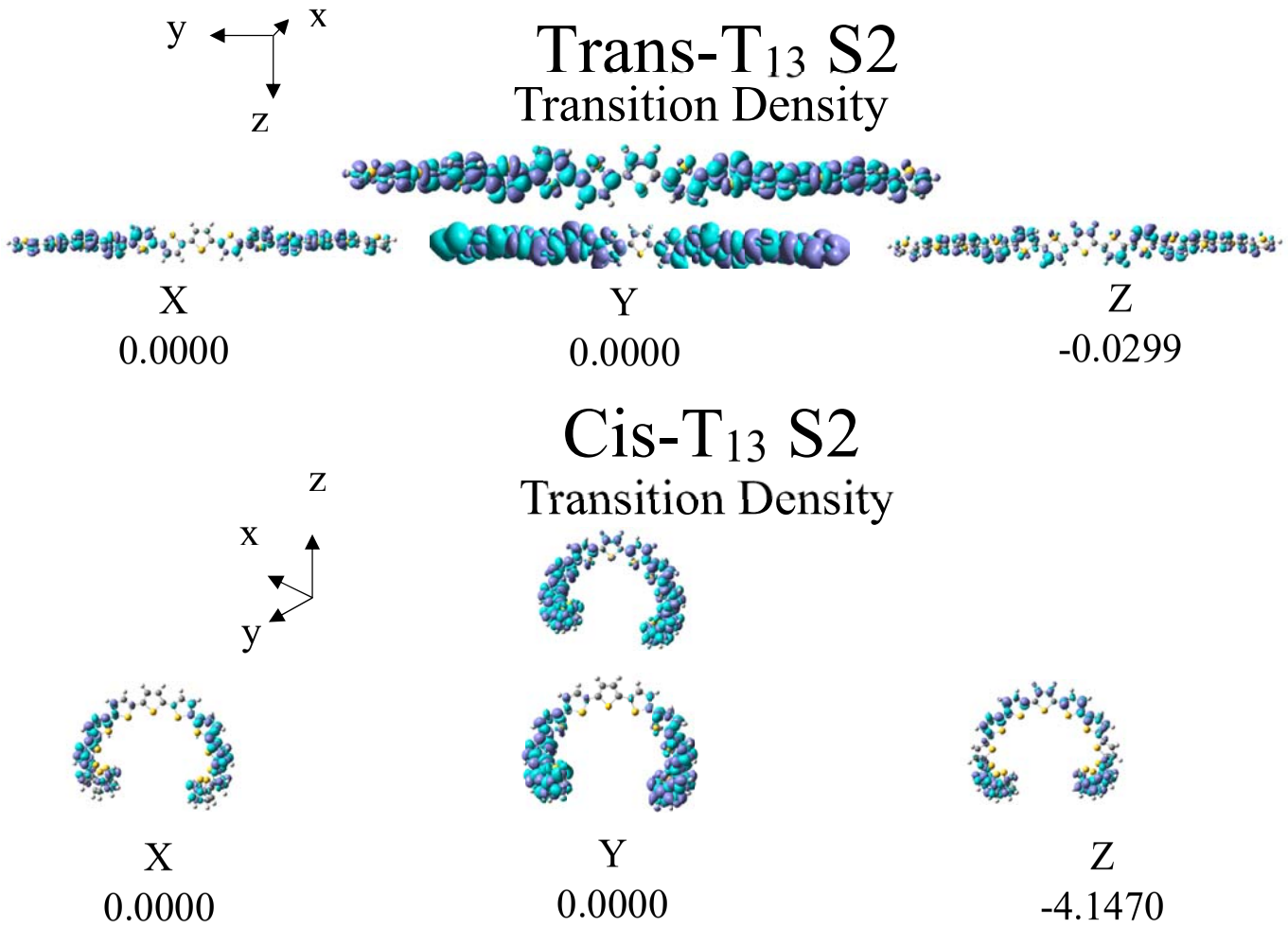

Figure S37. T_{13} at θ = 20º : Plot of the transition densities involved in the S2 (HOMO -> LUMO+1, HOMO-1 -> LUMO) and of their product by the Cartesian coordinates . The components of the transition electric dipole moment are shown below. Isovalue = 0.0004 for all plots except for the transition densities of transoid T_{13} multiplied by X, Y and Z, whose isovalue is 0.00004.

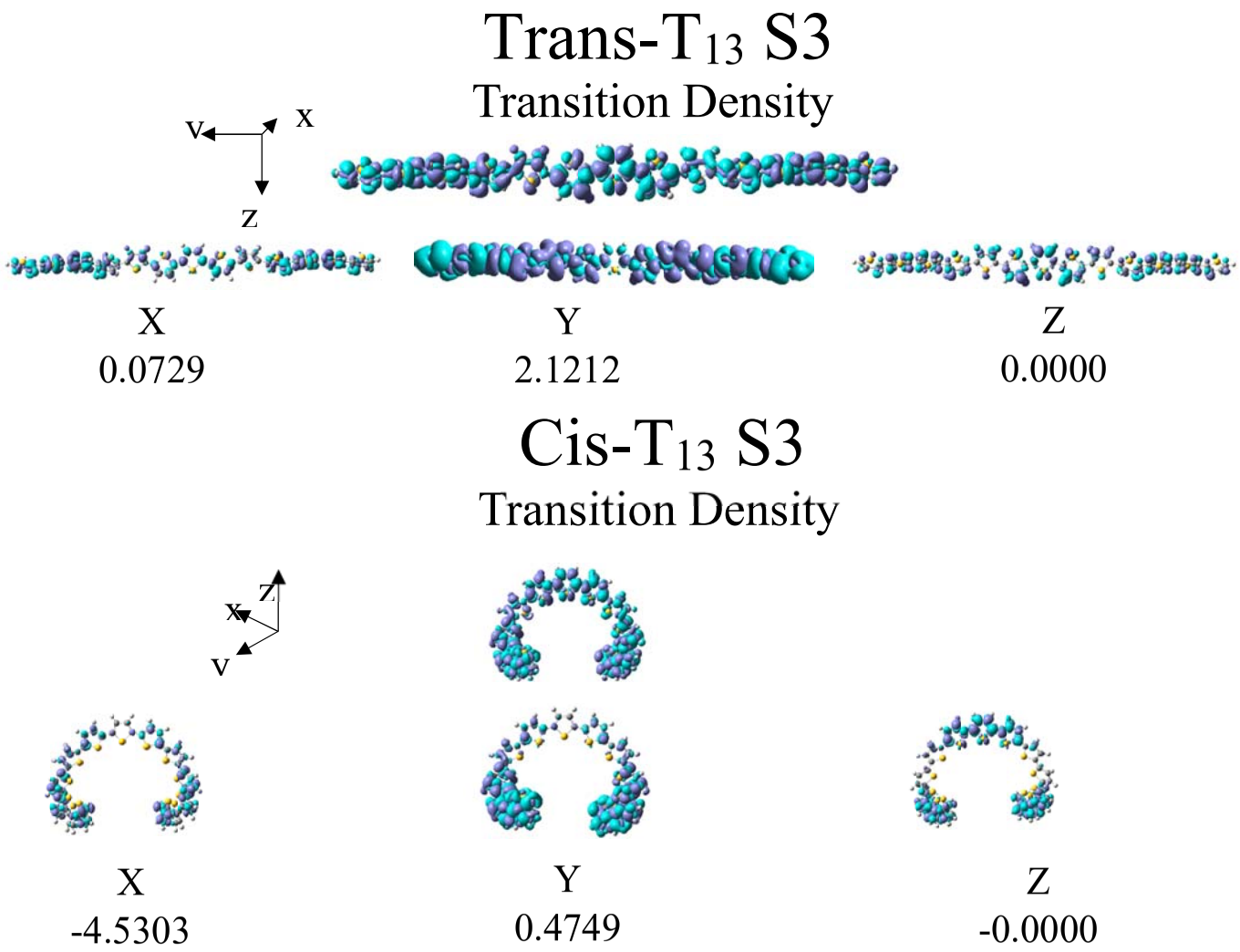

Figure S38. T_{13} at $\theta = 20^{o}$: Plot of the transition densities involved in the S3 (HOMO -> LUMO+2, HOMO-1 -> LUMO+1, HOMO-2 -> LUMO) and of their product by the Cartesian coordinates . The components of the

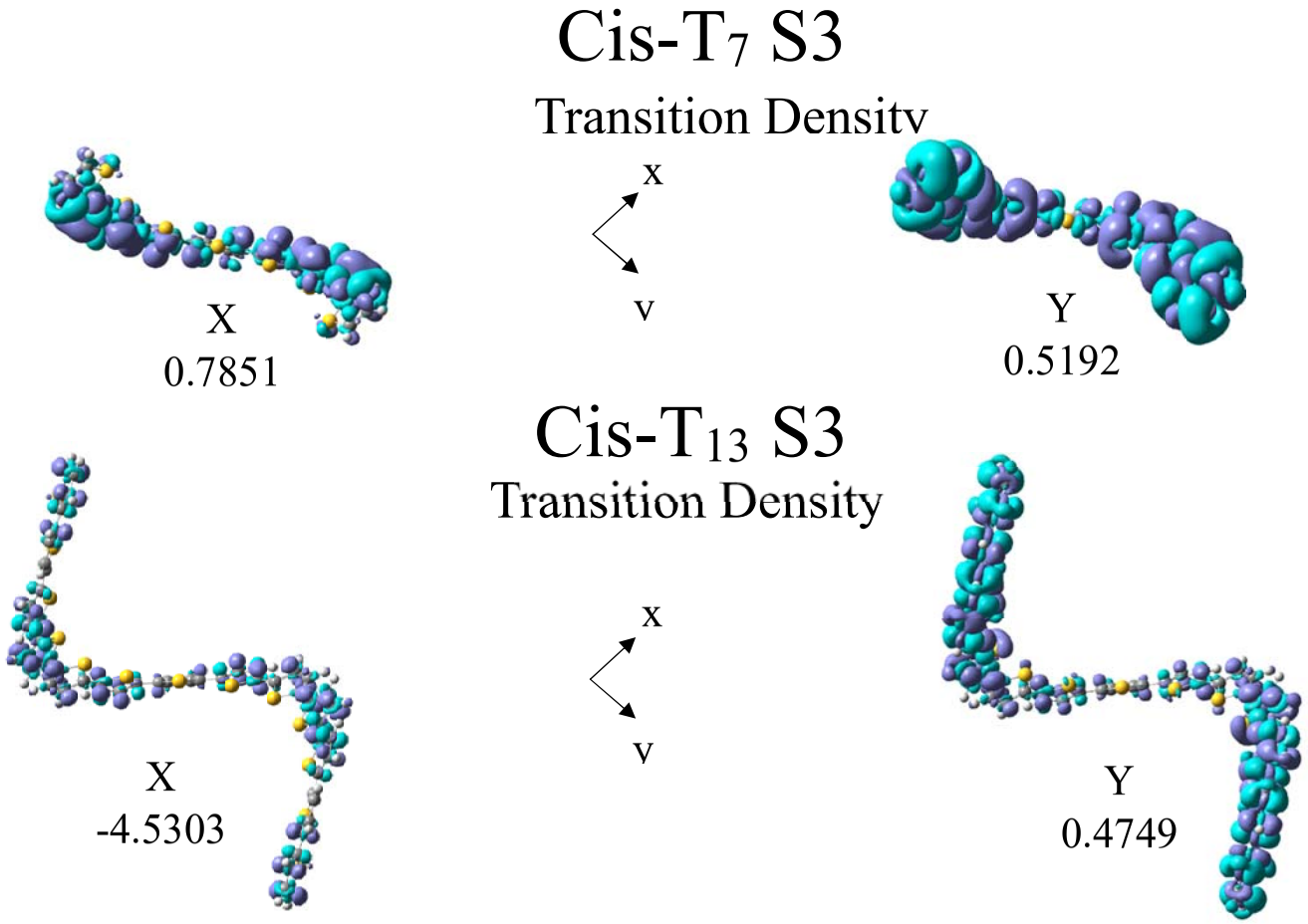

Figure S39. T_7 and T_{13} at θ=20º : Plot of the transition densities multiplied by the X and Y Cartesian coordinates involved in S3 (HOMO -> LUMO+2, HOMO-1 -> LUMO+1, HOMO-2-> LUMO). The components of the

Table S3. T_7 and T_{13} data for the three lowest energy excited states at $\theta = 20^o$. (a) Composition of the main transitions in terms of the molecular orbitals involved. (b) Vertical transition energies in eV. (c) Oscillator strengths. (d) Rotatory strengths.

(a)

Excited State	Composition
S1	HOMO -> LUMO
S2	HOMO -> LUMO+1, HOMO-1 -> LUMO
S3	HOMO -> LUMO+2, HOMO-1 -> LUMO+1, HOMO-2 -> LUMO

(b) Vertical Transition Energy (eV)

	T_7		T_{13}	
	Cisoid	Transoid	Cisoid	Transoid
S1	3.0275	3.0735	2.8060	2.8664
S2	3.6187	3.6179	3.0839	3.1272
S3	4.1718	4.1298	3.3996	3.4097

(c) Oscillator Strength

	T_7		T_{13}	
	Cisoid	Transoid	Cisoid	Transoid
S1	1.591	2.4079	1.7851	4.948
S2	0.8284	0.0002	1.2994	0.0001
S3	0.0969	0.1863	1.7282	0.3763

(d) Rotatory Strength (10^{-40} cgs)

	T_7		T_{13}	
	Cisoid	Transoid	Cisoid	Transoid
S1	1018.8830	-228.5557	8705.1499	-450.4941
S2	-1631.8471	-3.5887	-9073.8208	1.8572
S3	697.0429	-8.0884	-1053.0201	-40.4677

Capítulo III – Resultados (VI).

Toward a General Mixed Quantum/Classical Method for the Calculation of the Vibronic ECD of a Flexible Dye Molecule with Different Stable Conformers: Revisiting the Case of 2,2,2-trifluoro-AnthrylEthanol

Javier Cerezo, Daniel Aranda, Francisco J. Avila Ferrer, Giacomo Prampolini, Giuseppe Mazzeo, Giovanna Longhi, Sergio Abbate, Fabrizio Santoro*.

We extend a recently proposed mixed quantum/classical method for computing the vibronic electronic circular dichroism (ECD) spectrum of molecules with different conformers, to cases where more than one hindered rotation is present. The method generalizes the standard procedure, based on the simple Boltzmann average of the vibronic spectra of the stable conformers, and includes the contribution of structures that sample all the accessible conformational space. It is applied to the simulation of the ECD spectrum of (S)-2,2,2-trifluoroanthrylethanol, a molecule with easily interconvertible conformers, whose spectrum exhibits a pattern of alternating positive and negative vibronic peaks. Results are in very good agreement with experiment and show that spectra averaged over all the sampled conformational space can deviate significantly from the simple average of the contributions of the stable conformers. The present mixed quantum/classical method is able to capture the effect of nonlinear dependence of the rotatory strength on the molecular structure and of anharmonic couplings among the modes responsible for molecular flexibility. Despite its computational cost, the procedure is still affordable and promises to be useful in all cases where the ECD shape arises from a subtle balance between vibronic effects and conformational variety.

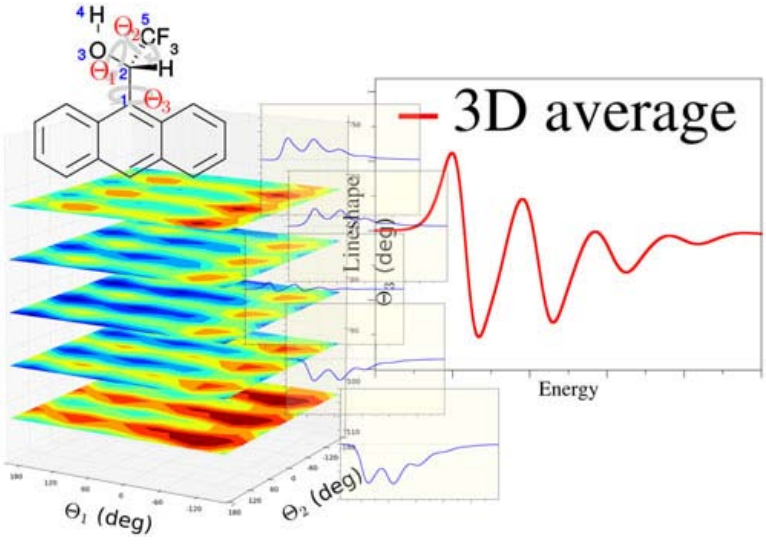

3.6.1. Introduction.

The comparison between experimental and computed chiroptical spectra is nowadays the method of choice for the assignment of the absolute configuration of chiral molecules.[1-3] Electronic circular dichroism (ECD) is a powerful technique because the signed nature of the contribution of each excited electronic state gives rise to a sequence of positive and negative peaks that is characteristic of each enantiomer, and robust first-principle methods exist nowadays to predict rotatory strengths (RSs).[4] Superimposed to this "electronic" pattern, measured spectra often exhibit a finer structure, due to the coupling of electronic and vibrational transitions. Such structure needs to be properly simulated for a reliable comparison with experiment and only methods that account for the quantum nature of molecular vibrations can reproduce the existence of vibronic peaks. Moreover, weak ECD spectra are often characterized by an alternation of positive and negative vibronic peaks, ascribed to different vibrational states of the same electronic state, which can only be described by accounting for an additional quantum effect, the vibronic coupling borrowing mechanism known as Herzberg-Teller (HT) effect.[5,6]

If the molecule of interest is rigid, meaning that its potential energy surfaces (PESs) can be adequately described within the harmonic approximation, and if its electronic states are not affected by strong nonadiabatic couplings, the simulation of the ECD spectrum is now rather standard.[7-21] Conversely, when the internal dynamics of the molecules is also characterized by slow, large amplitude motions, e.g. torsions around σ bonds, the accurate calculation of ECD spectra still presents significant challenges. As a matter of fact, many chiral compounds studied with ECD are characterized by a chromophore, like one or more fused conjugated rings, on which the electronic transition is located, bound to a chiral center, e.g. a quaternary carbon, which imparts a non-vanishing rotatory strength (RS) to the transition. In such a situation two main issues usually arise: (i) the molecular structure is intrinsically flexible because of the hindered rotations around the single bonds of the chiral center, (ii) the associated RS is rather small (so that HT effects may be important),[21-23] because the chiral center is only weakly involved in the electronic transition.

The most common approach to compute the ECD spectrum of a flexible molecule is to identify its stable conformers, compute their spectra separately, and then average the results according to their Boltzmann populations. When the interconversion barriers

are small, and the potential energy landscape is flat, this approximation can break down. In a classical picture, this can be explained realizing that the molecules may have a non-negligible probability to adopt conformations so distorted to exhibit remarkably different chiroptical properties (e.g. the RS) and vibronic structures with respect to the stable conformers. In principle, accurate spectra for these cases could be obtained considering a realistic model of the anharmonic PES connecting the different conformers and running a full quantum calculation.[24,25] Yet, this strategy becomes very challenging when more than a few soft modes exist, and they are coupled to the remaining vibrational coordinates. An alternative route could be provided by classical Molecular Dynamics (MD), which is very well suited to describe molecular flexibility: if the Force Field (FF) is accurate, MD can provide a realistic distribution of molecular structures, through a collection of snapshots extracted from an equilibrated trajectory. Starting from such a set of structures, the electronic spectrum of the molecule can be approximated with the distribution of their transition energies and intensities. This approach is an application of the classical Franck-Condon (FC) principle[26-28] and, although powerful, cannot account for vibronic structures.[29]

We believe that wise mixed quantum/classical (MQC) approaches, based on the individuation of the coordinate space associated to the flexible (soft) coordinates, and their separation from the remaining stiff (i.e., harmonic) coordinates, can reveal very powerful to compute the vibronic spectra of flexible systems, if the focus is on low- to intermediate-resolution spectra. MQC approaches are attractive because they combine the usual procedures based on the harmonic approximation to describe the stiff quantum coordinates, and simpler classical methods for the flexible modes, provided the associated frequencies are low. Different simple MQC schemes have been recently proposed in literature, for standard absorption and emission properties.[24,30-34] The major challenge for these approaches is how to account, at least approximately, for the couplings between rigid and flexible coordinates. For ECD spectra, a further challenge arises from the possibly-drastic dependence of the RS on both soft and stiff coordinates. In a recent work,[35] we proposed a method based on an adiabatic approximation whereby the flexible coordinates are considered much slower than the harmonic stiff ones. Starting from this hypothesis, we showed that the total spectrum can be retrieved as the weighted average of the harmonic spectra computed on the rigid coordinate space at different conformations of the flexible coordinate(s).

In our first application of the method we dealt with the $S_0 \rightarrow S_1$ ECD spectrum of (*S*)-2,2,2-trifluoroanthryl-ethanol (Fig. 1), and we considered a single classical coordinate, defined either through the hindered rotation of the hydroxyl group (Θ_1) or by the intrinsic reaction coordinate (IRC) connecting the different conformers of the system. The two strategies lead to quite similar results as the conformers are actually mainly distinguished for the values of Θ_1. Although the results were quite satisfactory, and the comparison with experiment very good, the model might be considered oversimplified. In fact, while only one coordinate was included in the flexible space, three different flexible torsions can be clearly identified in the molecule, as indicated in Figure 1. Interestingly, Θ_2 is actually partially involved in the IRC coordinate, as it was observed that the nature of the IRC changed from Θ_1 to Θ_2 in the vicinity of the minima.[35]

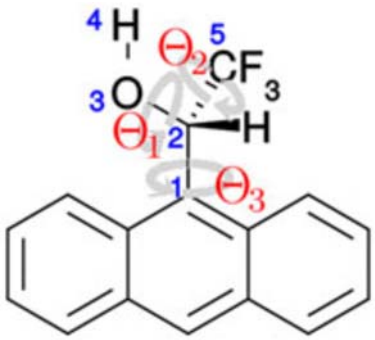

Figure 1. Structure of (S)-2,2,2-trifluoroanthrylethanol. The numbering over the most relevant atoms is depicted in blue. The hindered torsions are identified as Θ_1 (around C2-O3), Θ_2 (around C2-C5), and Θ_3 (around (C1-C2).

In the present work, we aim at investigating the effect on the ECD spectrum of the flexibility of the molecule along Θ_2 and Θ_3. To this end we introduce a more general MQC approach able to include more than one degree of freedom (DoF) in the flexible coordinates space.

3.6.2. Methodology.

3.6.2.1 Theory.

The most accurate approach to compute the ECD spectrum of a flexible dye molecule would require to account for the quantum nature of all the vibrational modes of the system and to adopt: (i) general forms for the anharmonic PES associated to the initial and final states of the transition; (ii) general functional forms for the corresponding transition dipole moments. Unfortunately, such a calculation is still out of reach for polyatomic molecules with dozens of vibrational modes.

Here we propose an MQC approach that goes beyond the simple idea of considering only local expansions of the PES around the molecule's stable conformers, yet it is still able to reduce the complexity of the problem to the calculation of a number of spectra on harmonic PES, which is nowadays standard.[7-21] On the one hand, despite the slow coordinates are not treated at quantum level, the here proposed approach retains a quantum description of the high-frequency modes, which are the only ones responsible for vibronic peaks visible in low- to-intermediate-resolution spectra, like those measured in solution. On the other hand, it allows us to account in an approximate way for the effect of both the PES anharmonicity and of the possible complicated dependence of the transition dipoles on the soft modes of the system.

To briefly introduce the method, we start dividing the set **R** of valence internal coordinates of the system in the two subsets comprising slow (**s**) and fast (**r**) coordinates, **R** = {**s**,**r**}. Generalizing the idea proposed in Cerezo *et al*,[35] we adopt an MQC scheme for the calculation of the spectrum, where the n_s slow coordinates are treated classically and the fast ones as quantum DoF. The shape of the electronic spectrum is a weighted average of the quantum spectra, computed considering the quantum DoF only and evaluated at different positions of the slow coordinates, $L^*(\omega, T; \mathbf{s})$. The weights are given by the probability distribution at temperature T of the slow coordinates, ρ (**s**, T),[31]

$$L(\omega,T) = \int \frac{e^{-\Delta G(s,T)/k_B T}}{\int e^{-\Delta G(s',T)/k_B T} d\boldsymbol{s}'} L^*(\omega,T;\boldsymbol{s}) d\boldsymbol{s} = \int \rho(\boldsymbol{s},T) L^*(\omega,T;\boldsymbol{s}) d\boldsymbol{s} \quad (1)$$

where $L^*(\omega,T;\boldsymbol{s})$is the Boltzmann-averaged lineshape at temperature T over all the possible harmonic vibrational states in the $3N-6-n_s$ space of the fast coordinates at a given **s**. $\Delta G(\mathbf{s}, T)$ is the free energy including the entropic contribution of the $3N-6-n_s$ oscillators, and k_B is the Boltzmann constant.

For the computation of the spectra $L^*(\omega,T;\boldsymbol{s})$, at each **s**, we invoke an adiabatic approximation, assuming that the fast coordinates arrange instantaneously at each movement along **s** which are so slow that can be considered frozen during the fast DoF rearrangement, so that any potential and kinetic coupling between the **s** and **r** subsets can be neglected.

In practice, this means that we first compute a relaxed energy scan along **s** on the initial S_i state, and that afterward, at each **s**, we define harmonic effective Hamiltonians along **r** for S_i and S_f (the final electronic state of the transition),

$$H_{S_i}^{fast}(\mathbf{r};\mathbf{s}) = T + \frac{1}{2}\mathbf{r}^t\mathbf{H}_\mathbf{r}^{(i)}(\mathbf{s})\mathbf{r} + V_0(\mathbf{s}) \quad (2a)$$

$$H_{S_f}^{fast}(\mathbf{r};\mathbf{s}) = T + \frac{1}{2}\mathbf{r}^t\mathbf{H}_\mathbf{r}^{(f)}(\mathbf{s})\mathbf{r} + \mathbf{r}^t\mathbf{g}_\mathbf{r}^{(f)} + E_v(\mathbf{s}) + V_0(\mathbf{s}) \quad (2b)$$

where T is the kinetic operator and the quadratic expansion is performed at the constrained minimum of the initial state in the $3N-6-n_s$ space. The dependence of the Hessian, $\boldsymbol{H}_\boldsymbol{r}^{(x)}$(x = i; f), and gradient, $\mathbf{g}_\mathbf{r}^{(f)}$, on the **s** coordinates is explicitly indicated. The S_i potential energy associated to the slow coordinate is $V_0(\mathbf{s})$. The S_f energy along the relaxed scan ($E_v(\mathbf{s}) + V_0(\mathbf{s})$) is the sum of the S_i energy and the vertical transition energy $E_v(\mathbf{s})$.

The reduced-dimensionality Hessians $\mathbf{H}_\mathbf{r}^{(i)}$ and $\mathbf{H}_\mathbf{r}^{(f)}$are generally computed at non-stationary points and are obtained with a three-steps procedure, described in the following:

i. The S_i and S_f Hessians in Cartesian coordinates $\mathbf{H}_x$ are computed at the molecular geometry corresponding to the point **s** of the relaxed scan, with a quantum chemistry code.

ii. The aforementioned Hessian matrices are transformed in curvilinear internal coordinates according to the following equation (valid for both S_i and S_f)[36,37]

$$\mathbf{H}_R = \mathbf{G}^+\mathbf{B}\mathbf{M}^{-1}(\mathbf{H}_x - \mathbf{g}_R^t\boldsymbol{\beta})\mathbf{M}^{-1}\mathbf{B}^t\mathbf{G}^+ \quad (3)$$

where **B** is the matrix that express internal coordinates **R** in terms of Cartesian ones **x**, **β** is its derivative, $\mathbf{g}_\mathbf{R}$ is the energy gradient in internal coordinates and $\mathbf{G}^+$ is the generalized inverse of the **G** matrix. We use a nonredundant set of internal coordinates constructed as a linear combination of all (redundant) bonds, angles and dihedral angles that arise from the connectivity of the molecule, where the coefficients of the combinations are obtained following the method proposed by Reimers.[38]

iii. The slow coordinates **s** are projected out using a generalization of the projector defined for a single coordinate of an internal non-orthogonal set by Truhlar and coworkers.[39] Further details on the projection in curvilinear coordinates will be given elsewhere.

At each **s**, we rotate the fast coordinates **r** to the $3N-6-n_s$ normal modes **Q**(**s**) by diagonalizing the Hessian (note that the rotation, and thus the normal coordinates, will depend on **s**). At this point, the lineshape of the ECD spectrum between S_i and S_f (at a

given value of **s**) can be computed, provided that we also expand the transition electric ($\boldsymbol{\mu}_{if}$) and magnetic ($\boldsymbol{m}_{if}$) dipole moments in normal coordinates,

$$\boldsymbol{\mu}_{if}(\mathbf{Q}(\mathbf{s});\mathbf{s}) = \boldsymbol{\mu}^{(0)}(\mathrm{s}) + \boldsymbol{\mu}^{(1)}(\mathbf{s})\mathbf{Q}(\mathbf{s}) \quad (4a)$$

$$\boldsymbol{m}_{if}(\mathbf{Q}(\mathbf{s});\mathbf{s}) = \boldsymbol{m}^{(0)}(\mathrm{s}) + \boldsymbol{m}^{(1)}(\mathbf{s})\mathbf{Q}(\mathbf{s}) \quad (4b)$$

where the dependence on **s** of each quantity is explicitly indicated.

Before concluding this section, we notice that the method presented here shares some analogies with what proposed[40] in the case of hindered rotations to obtain vibrational averages of molecular properties like the optical rotatory dispersion, which is connected to ECD by the Kramers-Kronig relation.[41-43] In Mort and Autschbach[40] however, only the soft mode is considered, while the other vibrational modes are not explicitly included in the calculation, being not important for a Boltzmann average. On the contrary, because our scope is to compute vibronically resolved spectra, we define, for each value of the soft coordinates (the hindered rotations), effective vibrational states on both the ground and electronic excited states (EEs) and compute the corresponding vibronic ECD spectrum. Moreover, in computing the average spectra (Eq. 1), and in order to account for an explicit dependence of these effective modes on the soft modes, with full account of FC and HT contributions, we renounced to treating the soft modes as quantum DoFs (as done in Mort and Autschbach[40]) and we treated them classically. From a formal point of view, a method to compute the optical activity in closer relation with our approach should replace the usual sum over the electronic states,[43] with a sum over the vibronic states, thus including the modulation of the RSs due to FC and HT vibronic terms.

3.6.2.2 Computational details.

All calculations of electronic properties were performed using Density Functional Theory (DFT) level for ground-state (GS) and its time-dependent (TD)-DFT extension for the lowest excited state (ES). We adopted B3LYP functional and the TZVP basis set in gas-phase, i.e. the same level of theory already employed to obtain the results in Ref.[35] we want to compare with. In order to properly account for molecular flexibility, we computed two (2D) and three (3D) dimensional relaxed energy scans on the GS as a function of (Θ_1, Θ_2) or (Θ_1, Θ_2, Θ_3). Each point of the grid represents a constrained-minimum on the GS, where all the DOF are optimized, but the selected dihedrals. Room-temperature vibronic spectra along the fast coordinates, were computed with the time-

dependent method[15,17,18,19,35] implemented in the development version of our code **FC**classes.[44] To that end, we adopted a generalization of the Vertical Hessian (VH) model,[38] where both GS and ES PES are represented by a quadratic expansion at the molecular structure corresponding to the selected grid point. Since such a structure is neither stationary on GS nor on ES, it was mandatory to use curvilinear internal coordinates for a proper vibrational analysis on both states.[37] VH model allows for accounting the effect of displacements, frequency changes and Duschinsky mixings. The electronic $\boldsymbol{\mu}_{if}$ and magnetic $\boldsymbol{m}_{if}$ transition dipoles were linearly expanded as a function of the normal coordinates and calculations were performed retaining both the constant FC terms of the expansion, and the linear HT terms. The linear expansion was computed around the initial-state constrained minima, a model named elsewhere FCHTi where i stands for "initial."[45] The total spectrum was obtained by averaging the spectra computed at the selected grid points, and different strategies were explored to approximate the integrals in Eq. 1. For spectra obtained as averages over the distribution or two or three soft-coordinates, in order to limit computational cost, we only considered molecular structures whose relative energy *E* in the GS with respect to the minimum is such that $e^{-E/k_BT} \geq 0.02$.

3.6.3. Results and discussion.

3.6.3.1. Description of the PES along the flexible coordinates.

The flexibility of the molecular structure of (S)-2,2,2-trifluoroanthryl-ethanol is well described by the three torsions highlighted in Figure 1. A first analysis of the relevant portion of the GS PES is given by the one-dimensional relaxed scans reported in Figure 2. There are several minima associated to each torsion, which implies that different stable conformations are possible. The two minima found along Θ_1 correspond to the two distinct stable conformers already identified in Ref.[35]. On the contrary, as expected, the three minima related to Θ_2 correspond to equivalent structures, and the same applies for the two ones related to Θ_3. The barriers along Θ_3 are significantly larger as compared with the ones along Θ_1 and Θ_2, and their height (~14 kcal/mol) indicates that rotation around Θ_3 is not kinetically favored at room temperature.

Due to the large barrier, for the purposes of computing room temperature spectra the energy profile associated to Θ_3 may be well described with a harmonic curve (see also

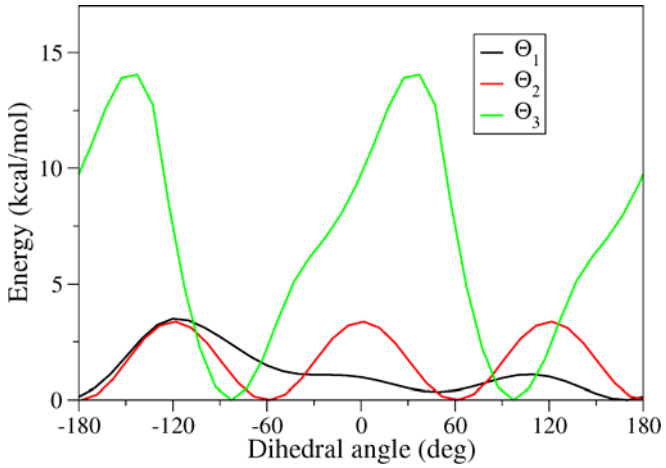

Figure 2. 1D relaxed scans along the 3 flexible torsions in the system.

below). This allows us to include this coordinate in the quantum/harmonic space. However, the possible coupling between this torsion and the other two suggests that it may be convenient to include also Θ_3 in the classical/flexible space. Several possibilities therefore arise to compute the spectrum, differing for the number of DoF included in the flexible space. Namely, three different scenarios will be considered: (1) only the torsion Θ_1 is included in the flexible space (this is the strategy followed in Ref.[35]), which leads to the space we named (Θ_1)-1D, (2) both Θ_1 and Θ_2 are included leading to the (Θ_1, Θ_2)-2D space, and (3) also Θ_3 is included, which results in the 3D space that we denoted as (Θ_1, Θ_2, Θ_3)-3D.

We start focusing on the (Θ_1, Θ_2)-2D case, and in Figure 3 we show the corresponding 2D energy scan. It includes the global minimum structure (Θ_1 = 168.34º, Θ_2 = −178.30º and Θ_3 = 82.77º) and is obtained taking a geometrical step of size $\Delta\Theta_1 = \Delta\Theta_2$ = 30º. In the plot, the expected periodicity with respect to Θ_2 is observed. One-dimensional cuts, shown for different values of Θ_2, highlight a coupling between the two torsions. Indeed, the shape of the one-dimensional plot is similar to the relaxed scan in Figure 2 only for the case of Θ_2 = −178.30º while it is significantly perturbed as the value of Θ_2 changes. Such coupling was already noted in Ref.[35] since the two torsions are actually combined in the IRC coordinate. The same effect is responsible for the changes in Θ_2 values comparing the position of the minima (yellow stars) and transition states (red stars). Concretely, the changes in Θ_2 reach values above 10º. The shape of the 2D PES and the existence of couplings between Θ_1 and Θ_2 torsions suggest treating them jointly in the classical partition, consisting in the (Θ_1, Θ_2)-2D space.

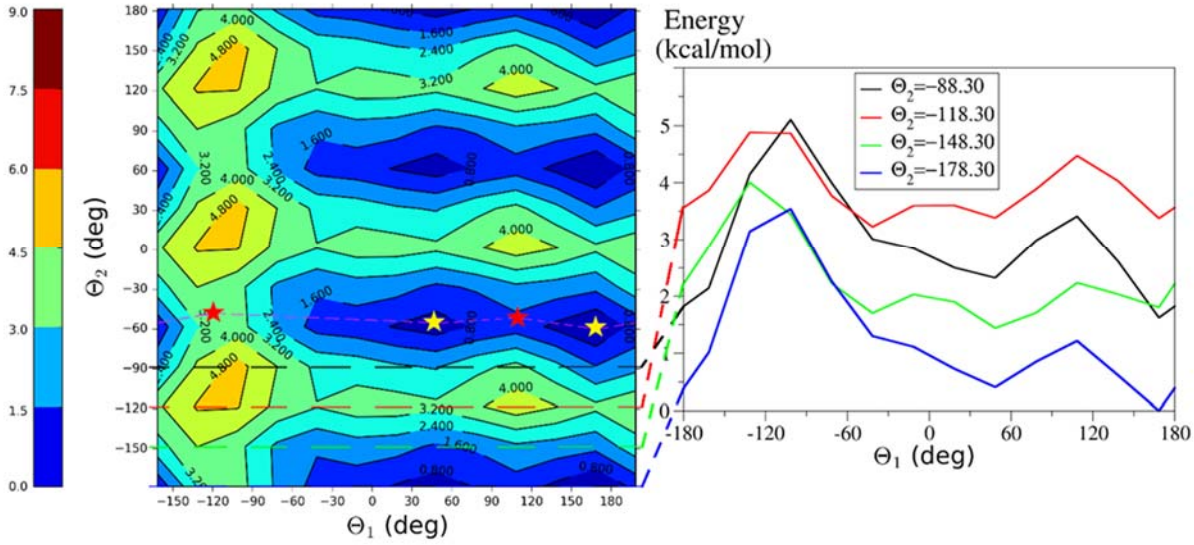

Figure 3. 2D sections of the PES (left), corresponding to the relaxed scan along the torsions Θ_1, and Θ_2. On the right, one-dimensional cuts for fixed values of Θ_2 are shown. Yellow stars on the 2D scan indicate the position of the minima, while red startts mark the poistion of the transition state.

We now turn to analyze the (Θ_1, Θ_2, Θ_3)-3D space. As in the 2D case, the 3D scan includes the global minimum structure and is performed taking geometrical steps of size $\Delta\Theta_1$ = $\Delta\Theta_2$ = 30º. For the stiffer coordinate Θ_3 instead, after a preliminary analysis on the whole possible range (-180º < Θ_3 < 0º) with $\Delta\Theta_3$ = 30º, we used a smaller step $\Delta\Theta_3$ = 10º and only consider values close to the minimum (Θ_3 = −82.77º), spanning a range of ±30º.

A full 3D representation of the scan is reported in Figure 1 of the Supporting Information (SI), while in Figure 4, we report 2D slices of the 3D PES along Θ_1 and Θ_2 for Θ_3=-82.77º (including the global minimum) and for a rotation of 10º, Θ_3=-92.77º. In fact, in the following we will show that the main contributions to the ECD spectrum come from structures with Θ_3=-82.77º ±10º. It is interesting to compare the slice at Θ_3 =-82.77º of the 3D scan (left panel of Figure 4) with the actual 2D relaxed scan (Figure 3). The two plots are very similar, indicating that, when allowed to relax, Θ_3 almost does not change its value with respect to the one assumed in the global minimum (-82.77º). Concretely, if we focus on the position of the stationary points (minima and transition states), the maximum change in Θ_3 between these structures only reaches ~1º. A rotation of Θ_3 by ± 10º leaves the shape of the PES almost unaltered apart from an up-shift of ~0.8 kcal/mol (see the section for Θ_3 = −92.77º in Figure 4). This suggests that, for moderate oscillations around the minimum, Θ_3 is not remarkably coupled to Θ_1 and Θ_2. On the contrary, for larger rotations along Θ_3, significant couplings arise. For example, Figure 1 in the SI

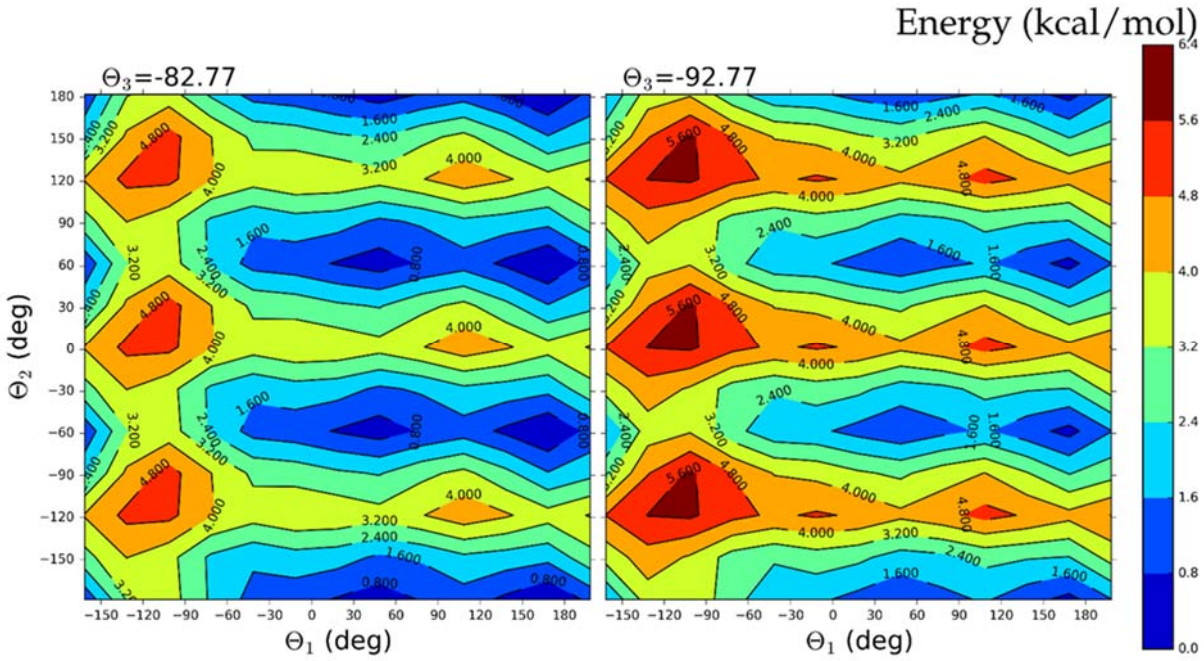

Figure 4: 2D sections of the PES, corresponding to the relaxed scan along the torsions Θ_1 and Θ_2 for two different values of Θ_3 (-82.77º is the value of Θ_3 in the global minimum).

documents that the sections at Θ_3= −82.77º and −52.77º have different shapes, so much that the profiles seem to be shifted by ~30º along Θ_2.

Figure 5 reports the dependence of RS on Θ_1 and Θ_2 (computed at the same structures corresponding to the left panel of Figure 4, i.e. for Θ_3 = −82.77º). RS depends strongly on Θ_1, varying from large positive to negative values and being very small in correspondence of the two stable conformers at Θ_1 = ~170.0º, ~50.0º. Conversely its

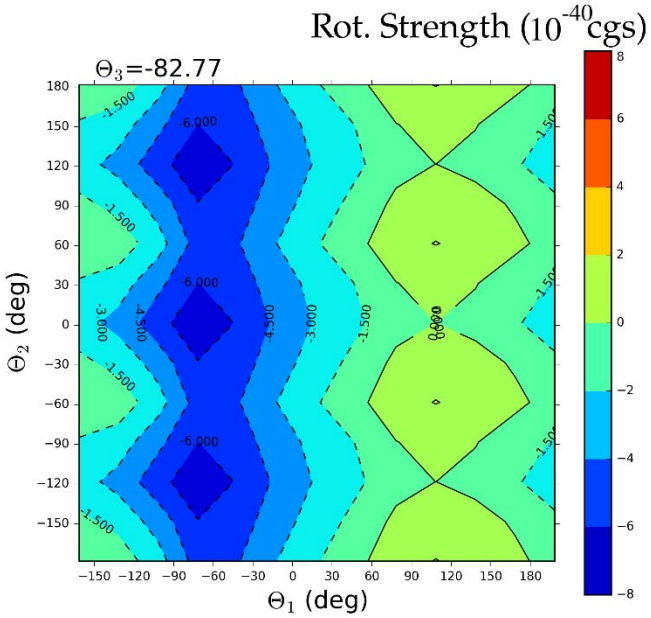

Figure5. 2D section of the rotatory strength corresponding to the relaxed scan along the torsions Θ_1 and Θ_2 for the value of Θ_3 corresponding to the minimum energy structure (-82.77º).

variation with Θ_2 is more moderate. Figure 6 reports the results of a relaxed scan along Θ_3 (left panel) and the corresponding variation of RS (right panel), showing that RS strongly depends on Θ_3. In fact, while RS is almost vanishing at the global minimum ($\Theta_3 = -82.77^o$) it assumes large negative values for negative rotations ($\Theta_3 < -82.77^o$) and positive values for positive rotations ($\Theta_3 > -82.77^o$). Around $\Theta_3 = -82.77^o$ RS has an approximate linear behavior but some clearly non-linear contributions also appear.

They are evidenced by a comparison with the behavior extrapolated from a linear (HT) expansion of both the electric and magnetic dipole transition moments as a function of $\Delta\Theta_3=\Theta_3+82.77^o$, obtaining then RS from the corresponding scalar product. Even according to such a HT expansion, RS has formally a quadratic dependence on $\Delta\Theta_3$. However, Figure 6 shows that the actual function resembles pretty much a straight line, which starts deviating moderately from the true RS values computed along the relaxed path for $|\Delta\Theta_3| > 6\text{-}7^o$.

In the next section, we will analyze the spectra computed with the MQC approach, including in the classical/flexible partition the different spaces described in this section.

3.6.3.2. Computation of the ECD spectrum.

The MQC approach for the computation of the spectrum involves the integral over the flexible coordinates as indicated in Eq. 1, which needs to be evaluated numerically. To this end we define a grid over the n_s-dimensional space and compute the spectrum at each point of the grid. The spectrum is considered constant around that point and the integral becomes a weighted average,

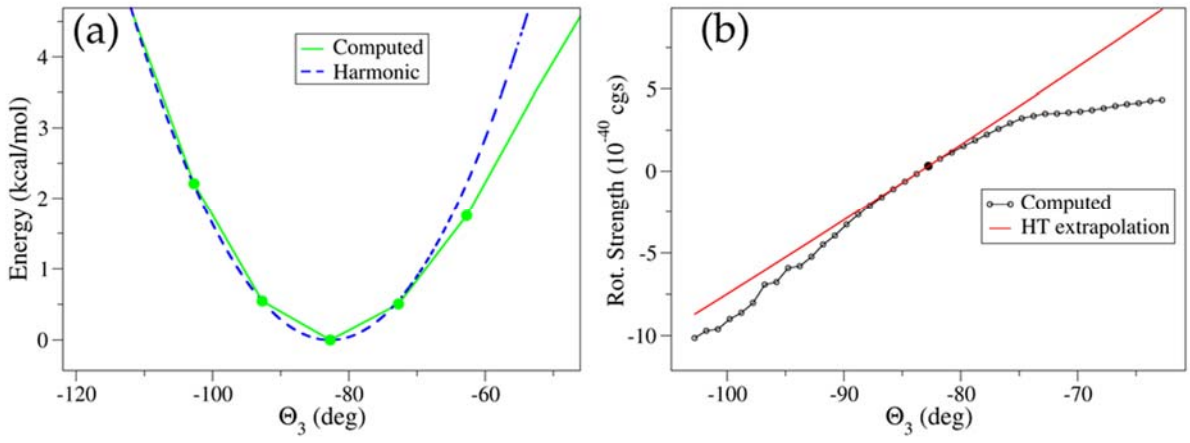

Figure 6. Potential energy computed along the 1D relaxed scan along Θ_3 and obtained with the Harmonic model (left panel), and rotatory strength (RS) computed every 1 degree along such relaxed scan, along with the RS obtained from the linear extrapolation of the electric and magnetic dipole moments.

$$L(\omega,T) = \sum_n \left[\int_{s_n - \frac{\Delta s}{2}}^{s_n + \frac{\Delta s}{2}} \rho(\boldsymbol{s},T) d\boldsymbol{s} \right] L^*(w,T,\boldsymbol{s}_n) \quad (5)$$

where the sum run over all points of the grid where the spectrum is evaluated, $\mathbf{s}_n = \{s_1, \ldots, s_{n_s}\}$. The weight associated to each point is then computed as the integral of the Boltzmann distribution function within the range $\mathbf{s}_n \pm \frac{\Delta s_n}{2}$. A further approximation consists in taking also the distribution function to be constant over that range. Then, for an evenly spaced grid, the weights become simply proportional to the value of the distribution function at the grid point, $\rho(\mathbf{s}_n, T)$. In the following, we use the same grids adopted for the evaluation of the PESs described in the previous section. Namely, $\Delta\Theta_1 = \Delta\Theta_2 = 30^o$ and $\Delta\Theta_3 = 10^o$, where $\Delta\Theta_3$ spans only in a range of 30^o around the value at the minimum. In total considering the pre-screening described in Section 2.2, we averaged 21 and 50 different vibronic spectra for (Θ_1, Θ_2)-2D and (Θ_1, Θ_2, Θ_3)-3D protocols, respectively.

Figure 7 shows the spectra computed with the MQC approach using Eq. 5 and the (Θ_1)-1D, (Θ_1, Θ_2)-2D and (Θ_1, Θ_2, Θ_3)-3D classical/flexible partitions described in the previous section. The spectra obtained using (Θ_1)-1D, (Θ_1, Θ_2)-2D spaces are extremely similar, indicating that the most relevant DoF tuning the spectral shape is the torsion of the hydroxyl group, i.e. the coordinate already selected in Ref.[35]. An explanation for this finding is obtained from the inspection of the potential energy and rotatory strength profiles. The potential energy (Figure 3) for Θ_1 is characterized by a wide and deep valley, which spreads the distribution function over a large range of conformations.

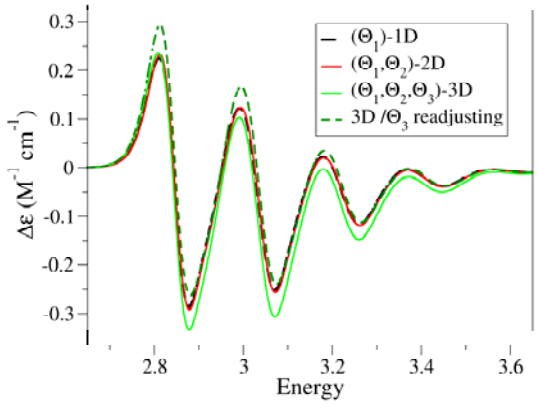

Figure 7. (*S*)-2,2,2-trifluoroanthrylethanol average ECD spectra computed with the different MQC strategies (Θ_1)-1D and (Θ_1; Θ_2)-2D and (Θ_1, Θ_2, Θ_3)-3D. A modified (Θ_1, Θ_2, Θ_3)-3D case, named "3D/ Θ_3 readjusting", is also reported. It is obtained changing the Boltzmann weights and the values of the rotatory strength at different Θ_3, in order to match more closely the data adopted in (Θ_1; Θ_2)-2D model.

Moreover, Θ_1 also displays a large variability of RS, with alternate signs (see the cut at $\Theta_3 = -82.77^o$ in Figure 5, and notice that the results for the 2D relaxed scan, where Θ_3 is optimized at each point, are extremely similar).

The spectrum computed with the (Θ_1, Θ_2, Θ_3)-3D strategy is similar to the ones computed with (Θ_1)-1D and (Θ_1, Θ_2)-2D, although it shows some moderate changes. As remarked in the introduction, the most popular approach adopted in literature for the calculation of ECD spectra in cases where many conformers are possible, involves computing the contributions of each conformer and then averaging them according to the Boltzmann populations (we name this protocol "simple average"). In light of the results here obtained, in the next section we discuss the validity of this simple approach, revisiting and extending the conclusions we already reached in Cerezo *et al*,[35]. The moderate differences between 2D and 3D predictions will be further analyzed in a successive section.

3.6.3.2.1 Revisiting the ability of a simple-average over the stable conformers to capture the effect of molecular flexibility.

The analysis in Section 4.1 shows that the 2,2,2-trifluoroanthryl-ethanol has two stable conformers. The ECD spectra computed for each of them and their "simple average" are reported in Figure 8 and compared with experimental ones in acetonitrile and in methanol. The major result of Cerezo *et al*,[35] was to show that off-equilibrium structures along the 1D interconversion path between the two stable conformers of the system give a remarkable contribution to the shape of the ECD spectrum, making it different from the "simple average".

With respect to Cerezo *et al*,[35] in this work we followed a more general methodology to compute MQC spectra. This allowed us to account for the anharmonicity of the PES and the nonlinear dependence of the transition electric and magnetic dipole moments along all the three soft-modes responsible for the flexibility of the molecular structure. The results obtained with this new methodology strongly confirm the conclusions reached in Ref.[31]. In particular, while by construction the "simple average" always fall in between the spectra of the two conformers, our results show that this is not the case if we employ a more refined methodology. In fact, a deviation from this trend can arise from the contributions of non-stationary structures that are different by the stable conformers, but still significantly populated in experimental conditions.

Both the (Θ_1)-1D and IRC path-averaged spectra taken from Ref.[35] are reported in Figure 8 for the sake of completeness. It is therefore possible to notice, for example, that according to both these 1D computational strategies, the intensity of the lowest-energy peak is smaller than what predicted for any of the two conformers. The same is true for the successive positive peak (the third one in order of increasing energy).

Figure 7 shows that (Θ_1)-1D and (Θ_1, Θ_2)-2D spectra are practically identical and therefore all the findings discussed above are confirmed by the (Θ_1, Θ_2)-2D model. Despite the moderate differences with (Θ_1, Θ_2)-2D, also (Θ_1, Θ_2, Θ_3)-3D model confirms the general trend, predicting a spectrum that is even further away from the "simple average" result.

Figure 8 also reports the experimental spectra measured in acetonitrile and methanol. Since the accuracy of the computed results depends not only on the underlying vibronic model but also, for instance, on the electronic level of theory and on the description of environmental effects, cancellations of errors are possible. In this contribution, we decided to focus on the effect of intramolecular vibrations, thus neglecting solvent effects. However, the differences between the experimental spectra in acetonitrile and methanol are remarkable, and in some cases, comparable to those between spectra computed with different MQC partitions. This shows that solvent plays a significant role and it also indicates that specific solute-solvent effects, like the possibility to establish H-bonds between the solute and the methanol solvent, are very important. Their proper inclusion would require an MD description of the solvation that is besides our scopes.

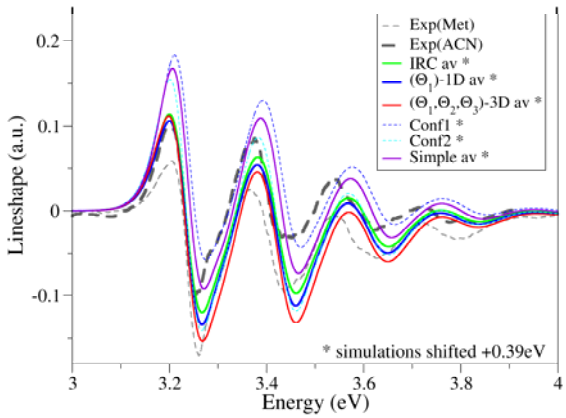

Figure 8. (*S*)-2,2,2-trifluoroanthrylethanol ECD spectra computed with the MQC adiabatic approach for different definitions of the quantum and classical coordinates are compared to experimental spectra in acetonitrile (ACN) and methanol (Met). For comparison, the spectra of the two stable conformers and their simple average is also reported.

The above discussion serves to clarify that it would be unsafe to discuss the relative quality of the results with the different quantum/classical partitions on the ground of the comparison with experimental spectra. Because of that, such a quality has been discussed above (and will be further discussed below) on the grounds of internal comparisons between computed values only. This notwithstanding, some interesting remarks in the comparison with experiment may be done. All the MQC approaches basically predict coincident results for the intensity of the lowest-energy peak which is different from what predicted by the simple-average and is extremely close to what measured in both solvents. As far as the first negative peak is concerned, all the computed spectra fall in between the experimental measurements in acetonitrile and methanol, the (Θ_1, Θ_2, Θ_3)-3D one being closer to the result in in the latter solvent. The same is true for all the MQC predictions for the second-lowest positive peak at ~3.4 eV. Turning to the peaks at higher energies, it is possible that they are affected also by the contribution of the second excited state. According to our calculations it is predicted to lye ~0.6 eV above S_1 and has not been considered in this work.

3.6.3.2.2 A further analysis on the differences of (Θ_1, Θ_2)-2D and (Θ_1, Θ_2, Θ_3)-3D predictions.

In Figure 7 we noticed that, although the general shape is the same, the (Θ_1, Θ_2, Θ_3)-3D spectrum displays an overall lower intensity with respect to 1D and 2D models. In order to analyze this difference in more detail, in Figures 9 and 10, we show the averaged

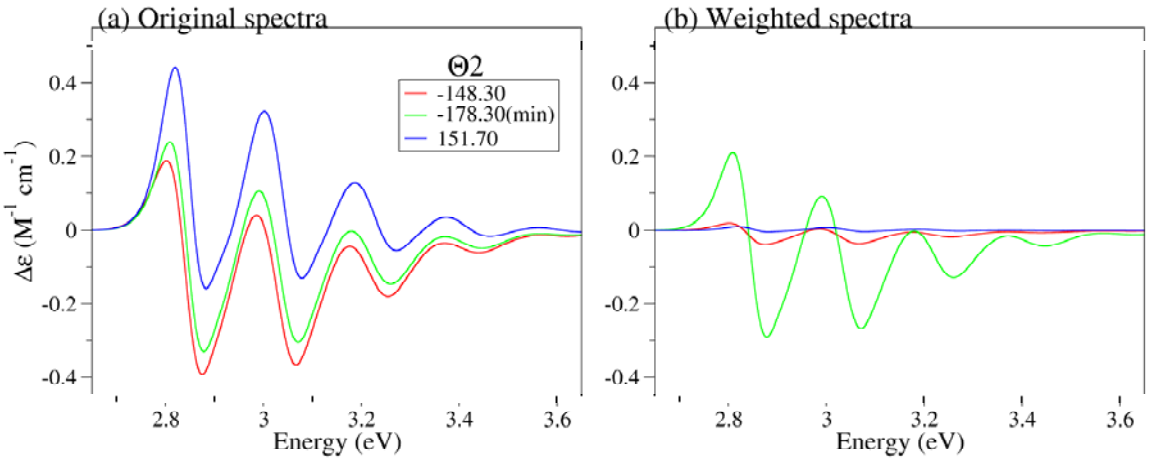

Figure 9. (S)-2,2,2-trifluoroanthrylethanol ECD spectra computed with the MQ adiabatic approach at fixed values of Θ_2. In the left panel the sums of all weights at each Θ_2 is one, while in the right panels spectra are scaled by the correct weights, so that their sum gives the average 3D spectrum reported in Figure 6.

spectra corresponding to cuts of the 3D space corresponding to fixed values of either Θ_2 or Θ_3.

In Figure 9 we report the average spectra for values of Θ_2 equal to -178.3^o (corresponding to the value of Θ_2 in the most stable conformer) and 30^o above and below that value. In all cases, the shape of the spectrum has the same features, with well-defined peaks with alternating signs. At a quantitative level, the spectrum corresponding to $\Theta_2 = 151.7^o$ is above the ones corresponding to the other two angles. This highlights how the balance between relative stabilities and rotatory strength, which only varies slightly with respect to Θ_2, can impact the spectral shape. Anyway, when the spectra are weighted by their actual Boltzmann factor, the final averaged spectrum mainly corresponds to the one computed at $\Theta_2 = -178.3^o$.

In Figure 10 we show the spectra averaged over slices with fixed values of Θ_3. In this case, remarkably different spectral shapes are observed upon variations of Θ_3. This clearly appears even at a qualitative level: while spectra for $\Theta_3 = -62.77^o, -72.77^o$ have positive intensities, those for $\Theta_3 = -92.77^o, -102.77^o$ display negative peaks. For $\Theta_3 = -82.77^o$ (lowest energy with respect to Θ_3), an intermediate situation is found. This scenario is a direct consequence of the large variation of the rotatory strength with Θ_3, which goes from large positive values to negative ones, as observed in Figure 6b. More importantly, at difference with the case of fixed Θ_2 values shown in Figure 9, the relative contribution of the spectra retrieved at Θ_3 angles different from -82.77^o is very

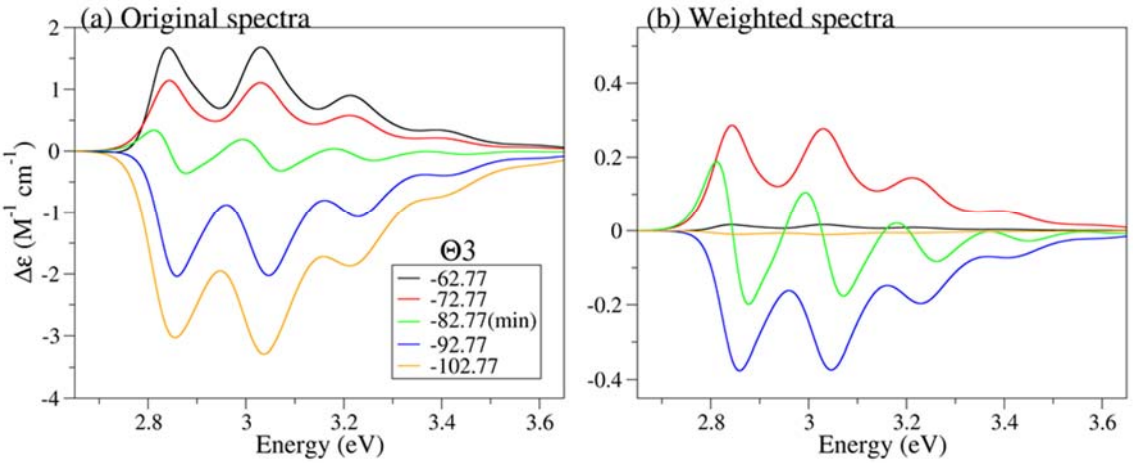

Figure 10. (S)-2,2,2-trifluoroanthrylethanol ECD spectra computed with the MQC adiabatic approach at fixed values of Θ_3. In the left panel the sums of all weights at each Θ_3 is one, while in the right panels spectra are scaled by the correct weights, so that their sum gives the average 3D spectrum reported in Figure 7.

significant, with intensities larger than the one found in the minimum energy conformation. Interestingly, however, the sum of spectra for $\Theta_3 > -82.77^o$ (with positive RS) and for $\Theta_3 < -82.77^o$ (with negative RS) partially cancel, and the final averaged spectrum turns out to be similar to the one at $\Theta_3 = -82.77^o$. Notwithstanding this, it is apparent that the final shape is determined by the subtle balance between positive and negative contributions. The latter can be drastically affected by the accuracy of the sampling, both the points of the grid selected to compute the spectrum and the integrated Boltzmann weights that determine the averages.

Among these potential sources of error, we focus on the integrated weights and check the convergence of the Riemann sum used to evaluate the integral with respect to the grid spacing. In fact the steep energy profile along Θ_3 in Figure 2 suggests that this could be critical. To that end we use a finer grid over Θ_3 ($\Delta\Theta_3 = 5^o$) to integrate the Boltzmann distribution function, while keeping the original grid ($\Delta\Theta_3 = 10^o$) for the computation of the spectra. The integrated weights are then given by,

$$\int_{\boldsymbol{s}_n-\frac{\Delta \boldsymbol{s}}{2}}^{\boldsymbol{s}_n+\frac{\Delta \boldsymbol{s}}{2}} \rho(\boldsymbol{s})d\boldsymbol{s} \approx \frac{\Delta \boldsymbol{s}}{2}\left(\rho(\boldsymbol{s}_n) + \frac{\rho(\boldsymbol{s}_n+\Delta \boldsymbol{s}/2)}{2} + \frac{\rho(\boldsymbol{s}_n-\Delta \boldsymbol{s}/2)}{2}\right) \quad (6)$$

In Table 1 of the SI we report the relative accumulated weights computed with either the original grid or the refined one (using Eq. 6), i.e., summing, for each Θ_3, the weights corresponding to the points with any value of Θ_1 and Θ_2. The general pattern is preserved when refining the grid, but some non-negligible changes are observed. More specifically with the finer grid: (i) the relative weight at $\Theta_3 = -82.77^o$ decreases, (ii) the accumulated weight corresponding to $\Theta_3 = -92.77^o$ increases more than the one for $\Theta_3 = -72.77^o$. Figure 10 shows that $\Theta_3 = -92.77^o$ contributes with an overall negative intensity and $\Theta_3 = -72.77^o$ with a positive one. Consequently, we expect that using the finer grid the average spectrum displays a more negative intensity. This is actually the result observed in Figure 11. Therefore, using the finer grid, the spectrum computed with the (Θ_1, Θ_2, Θ_3)-3D space deviates even more from the ones computed with either (Θ_1)-1D or (Θ_1, Θ_2)-2D spaces. More in general, however, our results actually show that the numerical integration of such coordinates remains challenging.

We have demonstrated that the integration needed to average the spectra may be slowly convergent, mostly when spectra with small Boltzmann populations are characterized by strong intensities, like in the case of geometries distorted along Θ_3. Beyond this

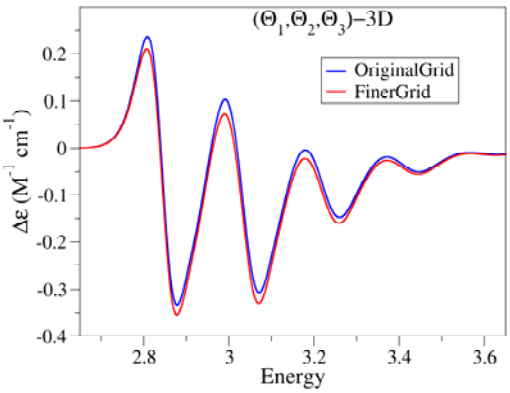

Figure 11. (*S*)-2,2,2-trifluoroanthrylethanol average ECD spectra computed using the weights obtained from the integration of the distribution function either over the original ($\Delta\Theta_3 = 10^o$) or the finer ($\Delta\Theta_3 = 5^o$) grids.

possible source of error, other possible facts that cause the difference between the (Θ_1, Θ_2)-2D and (Θ_1, Θ_2, Θ_3)-3D cases are: (i) the description of the potential along Θ_3 that is harmonic in the (Θ_1, Θ_2)-2D case and anharmonic (including possible couplings among the dihedral angles) in (Θ_1, Θ_2, Θ_3)-3D; (ii) the treatment of Θ_3 that is managed through QM in the 2D case and at classical level in the 3D case, and (iii) the variation along Θ_3 of the transition dipoles, that is linear in the former case and non-linear in the latter. In Figure 6a we show that in the interval relevant for the computation of the spectrum -93^o< Θ_3<-73^o, a relaxed energy profile along Θ_3 may be nicely fitted with a parabola; therefore, diagonal anharmonic effects (i.e. along Θ_3 only) should be not relevant. At the same time, Θ_3 is mostly projected on the lowest frequency mode of GS which has a typical frequency of ~50 cm^{-1}. Therefore, we do not expect remarkable errors due to the classical approximation of the distribution of Θ_3 since for such a frequency the classical Boltzmann and quantum Wigner distributions are practically coincident.[29,46-47]

Off-diagonal anharmonicities on the contrary seem to play a significant role. In the (Θ_1, Θ_2, Θ_3)-3D procedure, in fact, we compute spectra and their weights at each point of the grid (thus introducing the effect of the couplings of the torsions) and then average them. In Fig. 10 we show the cumulative contributions for different Θ_3, either raw (left panel) or multiplied by the accumulated Boltzmann weight (right panel). If Θ_3 was harmonic and not coupled to Θ_1, Θ_2 the weights should be equivalent to what derived directly from the quadratic fit in Figure 6. However, this is not the case. The weights obtained with the (Θ_1, Θ_2, Θ_3)-3D procedure are (see Table 1 in the SI) 0.01, 0.25, 0.55, 0.18, 0.00 for Θ_3=-62.77^o, -72.77^o, -82.77^o, -92.77^o, -102.77^o respectively, while they become 0.01, 0.22, 0.54, 0.22, 0.01 considering the harmonic fit of the one-dimensional profile in Figure 6.

We recall that in the (Θ_1, Θ_2)-2D calculation Θ_3 is treated at harmonic level. Therefore, its coupling with Θ_1 and Θ_2 is only estimated around the minimum at Θ_3=-82.77^o and forced to be quadratic.

Figure 6b indicates that the dependence of RS on Θ_3 shows moderate but significant differences with respect to what extrapolated from the HT treatment (the one adopted in (Θ_1,Θ_2)-2D case). In practice, starting from the minimum Θ_3=-82.8^o, for negative (positive) rotations along Θ_3, RS assumes larger negative (smaller positive) values than those predicted by the HT expansion. The above mentioned differences in the Boltzmann weights and in the RS dependence on Θ_3 play a role in the differences observed between (Θ_1, Θ_2)-2D and (Θ_1, Θ_2, Θ_3)-3D spectra. In order to prove this role the data in Figure 10 were reconsidered by (i) rescaling the average spectra for Θ_3=-62.77^o, -72.77^o, -92.77^o and -102.77^o by the ratio between the interpolated (HT) and true values of RS given in Figure 6b, and (ii) substituting the correct (Θ_1, Θ_2, Θ_3)-3D weights with those obtained from the harmonic one-dimensional profile in Figure 6a. Figure 7 shows that the resulting average spectrum, labelled as "3D/Θ_3 readjusting" exhibits significant differences with the (Θ_1, Θ_2, Θ_3)-3D one, being much more similar to the (Θ_1)-1D, and (Θ_1, Θ_2)-2D predictions.

3.6.4. Conclusions.

The computation of vibronic ECD spectra for floppy molecules is a challenging task. When the potential energy landscape is flat and the interconversion barriers are small, the popular approach that obtains the ECD spectrum from a simple Boltzmann average of the contribution of the different stable conformers can reach its limit of applicability.

In this contribution, we have extended a MQC strategy recently proposed by some of us,[35] to deal with the vibronic ECD spectrum of (*S*)-2,2,2-trifluoro-anthrylethanol. In its original formulation, the method assumes that a single DoF describes the floppiness of the molecule and treats it through a classical sampling. Invoking an adiabatic approximation, where the floppy coordinate is much slower than the other ones, the spectrum turns to be a Boltzmann-average of the spectra for the quantum harmonic modes, taken at the different possible positions of the slow coordinate. This protocol uses information arising from local expansions of the PES (and transition dipoles) at all the sampled geometries, thus generalizing the procedure based on stable conformers only. In this way it takes into account, although in a classical approximate way, the

effects of anharmonicity of the PES and of a realistic dependence of ECD intensity on molecular structure.

In many cases the molecular flexibility actually arises from coupled distortions along several soft modes. Therefore, in this contribution we extended the original methodology to allow the inclusion of any number of DoF in the flexible space that is treated classically.

For the 2,2,2-trifluoro-anthrylethanol case, three torsions are sufficient to describe molecular flexibility. We first analyzed in detail the PES associated to the three torsions, performing relaxed scans both in the (Θ_1, Θ_2)-2D and (Θ_1, Θ_2, Θ_3)-3D spaces. After analyzing the PES, we computed the ECD spectrum following alternative partitions of the system, which differ on the number of DoF included in the classical/flexible part.

The (Θ_1)-1D and (Θ_1, Θ_2)-2D protocols provide almost identical results. When Θ_3 is included in the flexible/classical partition, i.e., using the (Θ_1, Θ_2, Θ_3)-3D set, the average spectra are still similar to those obtained with the (Θ_1)-1D and (Θ_1, Θ_2)-2D sets, although some moderate differences are observed.

From a chemical and spectroscopic point of view, these results confirm the conclusion reached in Ref.[35], i.e. that off-equilibrium yet statistically accessible structures may have a significant impact on the chiroptical response of the molecule, leading to vibronic ECD shapes that are not intermediate between those predicted for the individual stable conformers.

From the methodological point of view, we proved that our general MQC approach can work smoothly also for molecules with several soft modes. It is not easy to identify a single factor responsible for the difference between (Θ_1)-1D and (Θ_1, Θ_2)-2D on the one side, and (Θ_1, Θ_2, Θ_3)-3D case on the other side, since many things change in the way the different protocols are implemented, and fortuitous cancellations of errors are possible. However, we show clear indications that anharmonic couplings between the three torsions and the non-linear dependence of the RS on Θ_3 do play a role. Both these features are in fact not captured by the (Θ_1)-1D and (Θ_1, Θ_2)-2D approaches, which treat Θ_3 harmonically and describe RS dependence on Θ_3 with HT local expansion. Conversely, due to the very small frequency associated to Θ_3, quantum effects (on both FC and HT mechanisms), only accurately described with (Θ_1)-1D and (Θ_1, Θ_2)-2D approaches, seem not to be relevant.

Despite these evidences, we also found clear indications that the convergence of the procedure to obtain average spectra with the MQC protocol is remarkably sensitive to the limitations of the (necessarily) approximate sampling, a rather typical challenge for chiroptical properties.[48]

In conclusion for flexible molecules our MQC approach is confirmed to be effective to compute vibronic ECD spectra going beyond the simple strategy that only considers the stable conformers. This method is computationally more demanding but feasible and of rather general applicability. It is expected to be important especially when vibronic resolution is needed and the signals are weak so that intensity-borrowing mechanisms are important. On the contrary, more experience is needed to judge its cost/benefit ratio when the stable conformers have strong RS;[49] in principle this depends on whether molecular structures with RS and/or vibronic progressions remarkably different from those of the stable conformers are populated or not.

As far as the choice of the classical/quantum partition, is concerned, whenever a harmonic treatment along a coordinate is suitable, and the linear expansion of the transitions dipoles is adequate, the quantum approach should be preferred. Not only in fact it provides the proper description of HT effects but, additionally, the TD formalism for vibronic spectra intrinsically accounts for a complete sum over the populated vibrational states, thus solving possible convergence problems in the calculation of the thermal averages.[18] When these conditions are not fulfilled, the inclusion of the soft coordinate in the classical set is recommended, if its associated vibrational frequency is sufficiently low. For intermediate cases, i.e. when anharmonic effects and non-linearities in the expansion of the transition dipoles are only moderate, further experience is probably needed to understand which approach should be considered more reliable. It will be for example important to acquire further knowledge on the intrinsic impact on the spectrum of the approximated classical description of a HT-active mode. It will clearly depend on many parameters, like the resolution of the spectrum, or the frequency and the displacement of the mode, so that additional tailored model studies appear necessary.[50]

More in general, further studies are needed to work out effective protocols to improve the convergence of the calculations with respect to the sampled structures at reasonable computational costs. In this scenario, and to deal with systems with an even larger number of floppy coordinates (as well as to introduce the effect of explicit solvent

models), it will be mandatory to combine our method with more efficient sampling techniques, like Molecular Dynamics or Montecarlo.

3.6.5. References and notes.

1. P. L. Polavarapu. *Chiroptical spectroscopy: fundamentals and applications*. CRC Press, **2016**, 430.
2. G. Pescitelli, T. Bruhn. *Chirality*, **2016**; 28, 466.
3. M. Srebro-Hooper, J. Autschbach. *Annu. Rev. Phy.s Chem.*, **2017**, 68, 399.
4. J. Autschbach. *Chirality*, **2009**, 21, E116.
5. M. Dierksen, S. Grimme. *J. Chem. Phys.* **2005**, 122, 244101.
6. A. Hazra, M. Nooijen. *J. Chem. Phys.*, **2005**, 122, 204327.
7. F. Santoro, R. Improta, A. Lami, J. Bloino, V. Barone. *J. Chem. Phys.*, **2007**, 126, 084509.
8. H. C. Jankowiak, J. L. Stuber, R. Berger. *J. Chem. Phys.*, **2007**, 127, 234101.
9. F. Santoro, A. Lami, R. Improta, J. Bloino, V. Barone. *J. Chem. Phys.*, **2008**, 128, 224311.
10. F. Santoro, V. Barone. *Int. J. Quantum Chem.*, **2010**, 110, 476.
11. J. Bloino, M. Biczysko, F. Santoro, V. Barone. *J. Chem. Theory Comput.*, **2010**, 6, 1256.
12. J. Tatchen, E. Pollak. *J. Chem. Phys.*, **2008**, 28, 164303.
13. P. Peng, Y. Niu, C. Deng, Z. Shuai. *Chem. Phys.*, **2010**, 370, 215.
14. J. Huh, R. Berger. *J. Phys: Conf. Ser.*, **2012**, 380, 012019.
15. R. Borrelli, A. Capobianco, A. Peluso. *J. Phys. Chem. A*. **2012**, 116, 9934.
16. A. Baiardi, J. Bloino, V. Barone. *J. Chem. Theory Comput.*, **2013**, 9, 4097.
17. F. J. Avila Ferrer, J. Cerezo, J. Soto, R. Improta, F. Santoro. *Comput. Theoret. Chem.* **2014**, 1040-1041, 328.
18. F. Santoro, D. Jacquemin. *WIREs Comput. Mol. Sci.*, **2016**, 6, 460.
19. J. Bloino, A. Baiardi, M. Biczysko. *Int. J. Quantum Chem.* **2016**, 116, 1543.
20. E. E. Weigang Jr. *J. Chem. Phys.*, **1965**, 43, 3609.
21. G. Pescitelli, V. Barone, L. Di Bari, A. Rizzo, F. Santoro. *J. Org. Chem.*, **2013**, 78, 7398.
22. N. Lin, Y. Luo, F. Santoro, X. Zhao, A. Rizzo. *Chem. Phys. Lett.*, **2008,** 464, 144.

23. N. Lin, F. Santoro, A. Rizzo, Y. Luo, X. Zhao, V. Barone. *J. Phys. Chem. A*, **2009**, 113, 4198.

24. E. Stendardo E, F. Avila Ferrer, F. Santoro, R. Improta. *J. Chem. Theory Comput.*, **2012,** 8, 4483.

25. A. Baiardi, J. Bloino, V. Barone. *J. Chem. Theory Comput.*, **2017**, 13, 2804.

26. M. Lax. *J. Chem. Phys.*, **1952**, 20, 1752.

27. J. P. Bergsma, P. H. Berens, K. R. Wilson, D. R. Fredkin, E. J. Heller. *J. Phys. Chem.*, **1984,** 88, 612.

28. S. Mukamel. *Principles of non-linear optical spectroscopy*. Oxford University Press, **1995**. 543.

29. J. Cerezo, F. Santoro, G. Prampolini. *Theor. Chem. Acc.*, **2016,** 135, 143.

30. R. Improta, F. J. Avila Ferrer, E. Stendardo, F. Santoro. *ChemPhysChem.*, **2014,** 15, 3320.

31. R. Zalensy, N. A. Murugan, F. Gelmukhanov, Z. Rinkevicius, B. Ośmialowski, W. Bartkowiak, H. Ågren. *J. Phys. Chem. A*, **2015,** 119, 5145.

32. Y. Liu, J. Cerezo, F. Santoro, A. Rizzo, N. Lin, X. Zhao. *Phys. Chem. Chem. Phys.*, **2016,** 18, 22889.

33. M. D'Alessandro, M. Aschi, C. Mazzuca, A. Palleschi, A. Amadei. *J. Chem. Phys.*, **2013,** 139, 114102.

34. M. D'Abramo, M. Aschi, A. Amadei. *J. Chem. Phys.* **2014**, 140, 164104.

35. J. Cerezo, G. Mazzeo, G. Longhi, S. Abbate, F. Santoro. *J. Phys. Chem. Lett.*, **2016,** 7, 4891.

36. A. Baiardi, J. Bloino, V. Barone. *J. Chem. Phys.*, **2016**, 144, 084114.

37. J. Cerezo, F. Santoro. *J. Chem. Theory Comput.*, **2016,** 12, 4970.

38. J. R. Reimers. *J. Chem. Phys.*, **2001,** 115, 9103.

39. C. F. Jackels, Z. Gu, D. G. Truhlar. *J. Chem. Phys.*, **1995,** 102, 3188.

40. C. B. Mort, J. Autschbach. *Chem. Phys. Chem.*, **2008,** 9, 159.

41. P. L. Polavarapu. *J. Phys. Chem.* A, **2005,** 109, 7013.

42. M. Rudolph, J. Autschbach. *Chirality*, **2008,** 20, 9965.

43. K. B. Wiberg, Y.-G. Wang, S. M. Wilson, P. H. Vaccaro, J. R. Cheeseman. *J. Phys. Chem.* A, **2006**, 110, 13995.

44. F. Santoro, FCclasses, a Fortran 77 code, visit: http://www.pi.iccom.cnr.it/fcclasses, last consulted January 2018.

45. F. J. Avila Ferrer, F. Santoro. *Phys. Chem. Chem. Phys.*, **2012,** 14, 13549.

46. D. J. Tannor. *Introduction to quantum mechanics: A time-dependent perspective*. University Science Books, **2007**, 656.

47. A. Petrone, J. Cerezo, F. J. A. Ferrer, G. Donati, R. Improta, N. Rega, F. Santoro. *J. Phys. Chem. A*, **2015,** 119, 5426.

48. F. Lipparini, F. Egidi, C. Cappelli, V. Barone. *J. Chem. Theory Comput.*, **2013**, 9, 1880.

49. D. Padula, J. Cerezo, G. Pescitelli, F. Santoro. *Phys. Chem. Chem. Phys.*, **2017**, 19, 32349.

50. M. Nooijen. *Int. J. Quantum Chem.*, **2006**, 106, 2489.

Supporting Information

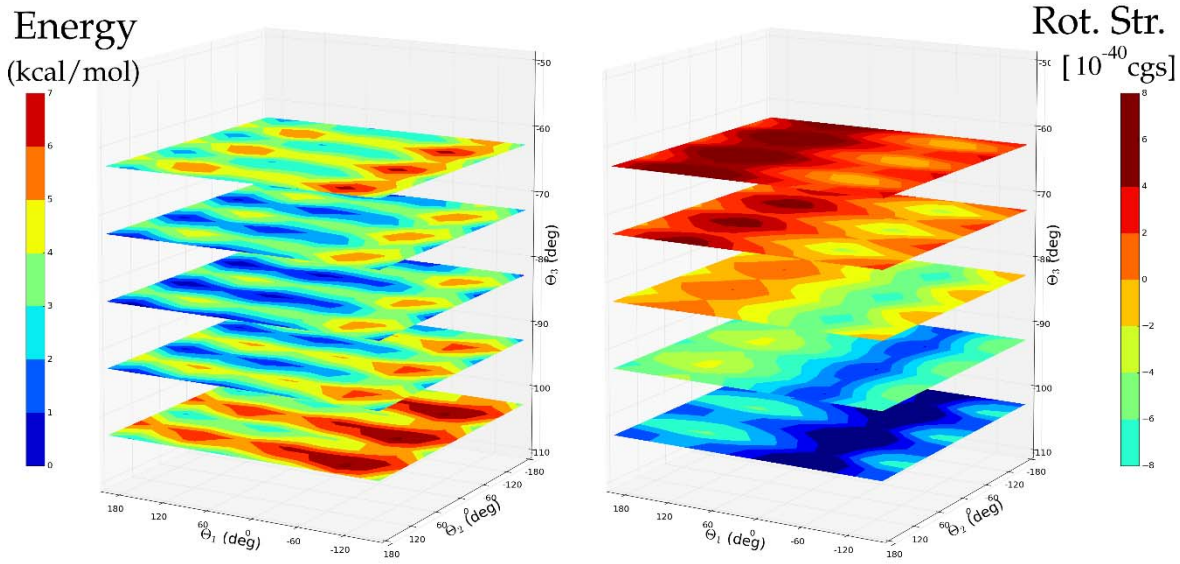

Figure S1. Two-dimensional cuts of the PES (left) and Rotatory strength (right) of (S)-2,2,2-trifluoroanthrylethanol, corresponding to the relaxed scan along the torsions Θ_1 and Θ_2 for different values of Θ_3.

Table 1. Weights corresponding to fixed values of Θ_3 (in digrees) computed considering different model potential energy surfaces: the (Θ_1, Θ_2, Θ_3)-3D model used in this work (using the original and finer grids), a relaxed scan along Θ_3 and the Harmonic curve fitted around the equilibrium point of such scan.

	Weights				
PES	-62.77	72.77	-82.77	-92.77	-102.77
(Θ_1, Θ_2, Θ_3)-3D/original grid	0.01	0.25	0.55	0.19	0.00
(Θ_1, Θ_2, Θ_3)-3D/finer grid	0.01	0.27	0.51	0.21	0.01
Relaxed-Θ_3	0.03	0.22	0.52	0.21	0.01
Harmonic-Θ_3	0.01	0.22	0.54	0.22	0.01

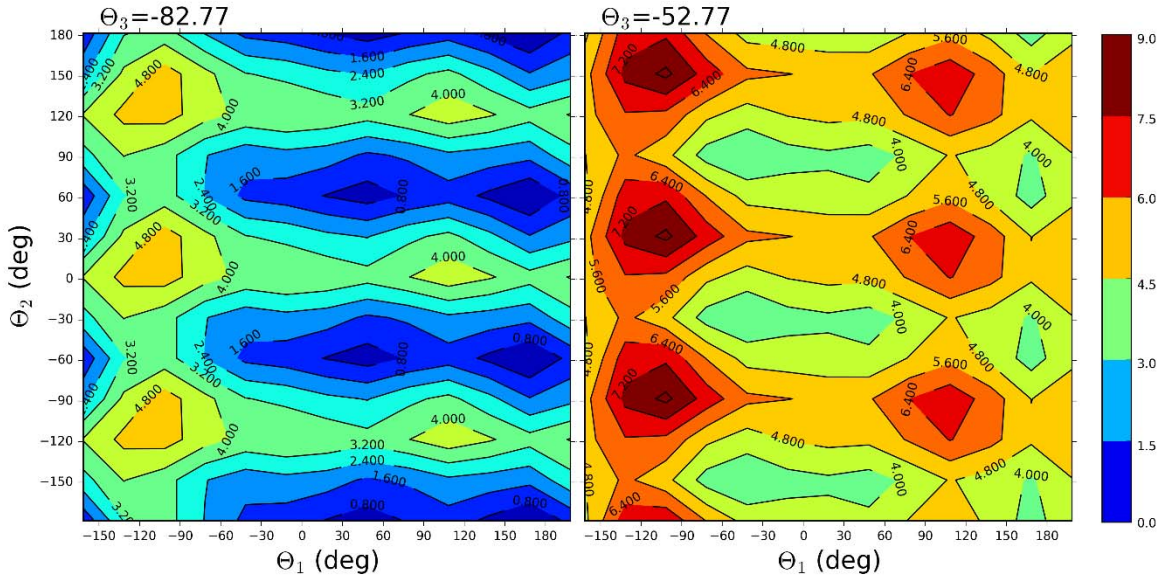

Figure S2. Two-dimensional sections of the PES, corresponding to the relaxed scan along the torsions Θ_1 and Θ_2 for two different values of Θ_3 (-82.77º is the value of Θ_3 in the global minimum).

Capítulo IV – Conclusiones.

4.1. Conclusiones.

Del trabajo realizado en esta tesis doctoral se han obtenido una serie de resultados concretos que han sido detallados en cada uno de los apartados del Capítulo de Resultados. Las conclusiones generales de cada uno de ellos pueden resumirse como sigue:

1. Por primera vez se han utilizado cálculos multiconfiguracionales de alto nivel para analizar el espectro SERS de una molécula compleja como es el *p*-aminotiofenol. En base a estos resultados se han podido encontrar dos tipos de geometrías de adsorción dependientes del potencial de electrodo y la concentración. Con relación a este mismo sistema, se ha planteado la posibilidad de que una serie de bandas características registradas en el SERS sean debidas a la presencia del nitreno, paso previo a la dimerización para formar el azocompuesto correspondiente.

2. En relación con este proceso de dimerización se ha estudiado un caso muy relacionado sobre el que existen datos experimentales. Los resultados SA-CASSCF y MS-CASPT2 predicen que el paso de reacción clave de la fotoquímica a $\lambda_{exc} = 266$ nm de 4-metoxifenilazida en fase gas es un cruce entre sistemas $2^1A'/2^3A''$ tras el que se forma 4-metoxifenilnitreno en su estado fundamental tras decaer a través de una intersección cónica $2^3A''/1^3A''$.

3. En respuesta al artículo publicado en PCCP por Mohammadpour *et al.* sobre el espectro SERS de piridina, hemos puesto en evidencia la frecuente carencia de rigor en los procesos de revisión de artículos en donde los espectros SERS son analizados en base a cálculos de estructura electrónica. Se ha hecho hincapié en la necesidad de utilizar los resultados teóricos de manera cuidadosa, tanto en cuanto a evitar errores formales como en cuanto a la selección del nivel de teoría, del modelo estructural del sistema en estudio y del rigor a la hora de discutir y analizar los resultados.

4. La metodología teórica propuesta para simular el efecto del potencial de electrodo en espectroscopía SERS ha sido aplicada a un caso particular de *molecular junction*, en donde una molécula de pirazina está unida a dos clústeres lineales de plata. Los resultados han proporcionado una nueva perspectiva para entender los distintos procesos relacionados con la electrónica molecular. Se han establecido los requerimientos energéticos para que se den procesos de transferencia de carga, transferencia de carga resonante y cómo el potencial eléctrico es capaz de modular las condiciones para que se produzca electroluminiscencia o la generación de fotocorrientes.

5. La metodología para la proyección de coordenadas internas ha permitido separar satisfactoriamente modos normales rígidos y flexibles en distintos espacios para los dos tipos de sistemas estudiados. De este modo podrían ser tratados de manera independiente incluso utilizando distintas aproximaciones. Esto se podría utilizar para cuantificar sus contribuciones relativas en los espectros.

6. Esta metodología ha permitido también calcular los espectros de estructuras distorsionadas y se ha demostrado la capacidad de dichas estructuras para explicar, al menos cualitativamente, fenómenos complejos de transferencia de quiralidad a politiofenos en interacciones anfitrión-huésped o en agregados.

7. Finalmente, se ha propuesto un método para el cálculo de espectros ECD en sistemas flexibles, más robusto que el estándar y que tiene en cuenta de forma aproximada la anarmonicidad de la Superficie de Energía Potencial. Considera efectos que pueden ser relevantes cuando se requiera resolución vibrónica o cuando sean importantes contribuciones de Herzberg-Teller.

En resumen, en esta tesis se ha demostrado la utilidad del uso de modelos simples de electrodos metálicos cargados en espectroscopía SERS o en electrónica molecular y de la metodología desarrollada para el cálculo de espectros de estructuras distorsionadas en el estudio de fenómenos de transferencia de quiralidad en polímeros.

El trabajo que constituye esta tesis es un buen ejemplo de la utilidad de los cálculos de estructura electrónica para abordar resultados espectroscópicos. Incluso metodologías

estándar y modelos simplificados como los que aquí se han utilizado han mostrado ser capaces de reproducir satisfactoriamente comportamientos experimentales complejos permitiendo, además, la predicción de propiedades que podrán ser útiles para analizar y diseñar nuevos experimentos.

4.2. Conclusions.

The studies carried out in this doctoral thesis have made possible to obtain specific results that have been detailed in each part of the Results Chapter. The general conclusions of each of the can be summarized as follows:

1. For the first time, high level multiconfigurational calculations have been used to analyse the SERS spectrum of a complex molecule such as *p*-aminothiophenol. Based on these results, two types of adsorption structures have been proposed, depending on the applied electrode potential and adsorbate concentration. Related with this system, the possibility that a set of characteristic SERS bands are due to the nitrene derivative is contemplated. Nitrene formation is a previous step to the azocompound dimerization.

2. Regarding this dimerization process, a very similar molecule whose experimental results are available has been studied. SA-CASSCF and MS-CASPT2 results predict that the key step in the photochemical reaction after irradiating 4-methoxyphenylazide with $\lambda_{exc} = 266$ nm in gas phase is an intersystem crossing $2^1A'/2^3A''$ generating 4-methoxyphenylnitrene in its ground state after decaying through a conical intersection $2^3A''/1^3A''$.

3. As response to the PCCP paper published by Mohammadpour *et al*. about pyridine SERS spectrum, we have evidenced the usual lack of rigor in the revision processes of articles analysing SERS spectra based on electronic structure calculations. The necessity of using theoretical results carefully has been stressed to avoid formal errors and also to select the level of theory, the structural model under study and to rigorously discuss and analyse results.

4. The proposed methodology to simulate the electrode potential in SERS spectroscopy has been applied to a particular molecular junction, where a pyrazine molecule is connected to two linear silver clusters. These results provide a new perspective to understand several processes related to molecular electronics. Energy requirements for charge transfer and resonant charge transfer processes are stablished together with how the electric potential tunes the conditions to produce electroluminescence or photocurrents.

5. The methodology to project out internal coordinates has permitted to satisfactorily separate stiff and flexible normal modes in different spaces for the two type of studied systems. This protocol would allow to treat them afterwards independently, even using different approaches for each of them and obtaining their relative contribution to the spectra.

6. This methodology has allowed to compute the spectra of distorted structures, demonstrating their capability to explain, at least qualitatively, complex chirality transfer phenomena to polythiophenes in host-guest interactions or in aggregates.

7. Finally, a model to compute ECD spectra of flexible dyes has been proposed. It is more robust than the standard one and it roughly accounts for the PES anharmonicity. It considers effects that are expected to be important when vibronic resolution is required or when Herzberg-Teller contributions are relevant.

To conclude, in this doctoral thesis the usefulness of simple models of charged metallic electrodes for SERS or molecular electronics has been proved. On the other hand, the developed methodology allows to calculate spectrum of distorted structures in chirality transfer phenomena.

The publications included in this thesis are good examples of the great convenience of electronic structure calculations to face spectroscopic results. Even standard methodologies and simplified models like those here used were able to successfully reproduce complex experimental features, additionally allowing to predict properties that could be useful to analyse and design new experiments.

Anexo I – Contribución del candidato.

A1.1. Contribución del candidato a cada publicación.

En esta sección se describe la contribución específica del candidato a cada uno de los artículos presentados.

1. **Analysis of the Potential Dependent Surface-Enhanced Raman Scattering of p-Aminothiophenol on the Basis of MS-CASPT2 Calculations**
   María R. López-Ramírez, Daniel Aranda, Francisco J. Avila, Silvia P. Centeno, Juan F. Arenas, Juan C. Otero,* and Juan Soto.*

   J. Phys. Chem. C, **2016**, 120, 19322.

El candidato ha colaborado en la obtención de resultados teóricos de estructura electrónica, cálculo de espectros teóricos, representación de datos, composición de tablas y figuras.

2. **An MS-CASPT2 Study of the Photodecomposition of 4-Methoxyphenyl Azide: Role of Internal Conversion and Intersystem Crossing.**
   Daniel Aranda, Francisco J. Avila, Isabel López-Tocón, Juan F. Arenas, Juan C. Otero*, and Juan Soto*.

   Phys. Chem. Chem. Phys., **2018**, 20, 7764.

El candidato ha contrinbuido en la obtención de cálculos teóricos y espectros de resonancia Raman, representación de datos y en la composición de tablas y figuras.

3. **Comment on "Elucidation of the charge-transfer SERS selection rules by considering the excited state properties and the role of electrode potential" by M. Mohammadpour, M. H. Khodabandeh, L. Visscher and Z. Jamshidi, *Phys. Chem. Chem. Phys*. 2017, 19, 7833.**
   D. Aranda, J. Román-Pérez, I. López-Tocón, J. Soto, F. Avila* and J. C. Otero.

   Phys. Chem. Chem. Phys., **2017**, 19, 27888.

El candidato ha realizado los cálculos de estructura electrónica, ha compuesto las tablas, representado los datos obtenidos y participado en la discusión de resultados.

4. **An approach to the electronic structure of molecular junctions with metal clusters of atomic thickness.**

   Daniel Aranda, Isabel López-Tocón, Juan Soto, Juan C. Otero* and Francisco Avila*.

   Phys. Chem. Chem. Phys., **2016**, 18, 27179.

El candidato ha contribuido en la realización de los cálculos de estructura electrónica, en la representación de datos, en la composición de tablas y participado en la discusión de los resultados.

5. **A Computational Study of the Vibrationally-Resolved Electronic Circular Dichroism Spectra of Single-Chain Transoid and Cisoid Oligothiophenes in Chiral Conformation.**

   Daniel Aranda, Javier Cerezo, Gennaro Pescitelli, Francisco J. Avila Ferrer, Juan Soto, Fabrizio Santoro.*

   Phys. Chem. Chem. Phys., **2018**, 20, 21864.

El candidato ha realizado los cálculos de estructura electrónica, ha compuesto tablas y figuras, ha participado en la discusión de los resultados, ha contribuido parcialmente a la búsqueda bibliográfica de resultados experimentales, ha colaborado en la edición del manuscrito, y, en menor medida, en su composición.

6. **Toward a General Mixed Quantum/Classical Method for the Calculation of the Vibronic ECD of a Flexible Dye Molecule with Different Stable Conformers: Revisiting the Case of 2,2,2-trifluoro-AnthrylEthanol.**

   Javier Cerezo, Daniel Aranda, Francisco J. Avila Ferrer, Giacomo Prampolini, Giuseppe Mazzeo, Giovanna Longhi, Sergio Abbate, Fabrizio Santoro.*

   Chirality, **2018**, 30, 730.

El candidato ha participado activamente en la obtención de cálculos teóricos, en la validación mediante pruebas de la metodología desarrollada, en la discusión de los resultados y en la edición del manuscrito.

A1.2. Contribution of the candidate to each publication.

In this section, the specific contribution of the candidate to each one of the presented articles is described.

1. **Analysis of the Potential Dependent Surface-Enhanced Raman Scattering of p-Aminothiophenol on the Basis of MS-CASPT2 Calculations**
   María R. López-Ramírez, Daniel Aranda, Francisco J. Avila, Silvia P. Centeno, Juan F. Arenas, Juan C. Otero,* and Juan Soto.*

   J. Phys. Chem. C, **2016**, 120, 19322.

The candidate has collaborated obtaining electronic structure theoretical results, computing theoretical spectra, plotting data and composing tables and figures.

2. **An MS-CASPT2 Study of the Photodecomposition of 4-Methoxyphenyl Azide: Role of Internal Conversion and Intersystem Crossing.**
   Daniel Aranda, Francisco J. Avila, Isabel López-Tocón, Juan F. Arenas, Juan C. Otero*, and Juan Soto*.

   Phys. Chem. Chem. Phys., **2018**, 20, 7764.

The candidate has collaborated obtaining theoretical calculations and resonance Raman spectra, plotting data and composing tables and figures.

3. **Comment on "Elucidation of the charge-transfer SERS selection rules by considering the excited state properties and the role of electrode potential" by M. Mohammadpour, M. H. Khodabandeh, L. Visscher and Z. Jamshidi, *Phys. Chem. Chem. Phys*. 2017, 19, 7833.**
   D. Aranda, J. Román-Pérez, I. López-Tocón, J. Soto, F. Avila* and J. C. Otero.

   Phys. Chem. Chem. Phys., **2017**, 19, 27888.

The candidate has performed the electronic structure calculations, has composed tables, has plotted the data obtained and has participated in the discussion of results.

4. **An approach to the electronic structure of molecular junctions with metal clusters of atomic thickness.**

   Daniel Aranda, Isabel López-Tocón, Juan Soto, Juan C. Otero* and Francisco Avila*.

   Phys. Chem. Chem. Phys., **2016**, 18, 27179.

The candidate has collaborated obtaining electronic structure calculations, plotting data, composing tables and has participated in the discussion of results.

5. **A Computational Study of the Vibrationally-Resolved Electronic Circular Dichroism Spectra of Single-Chain Transoid and Cisoid Oligothiophenes in Chiral Conformation.**

   Daniel Aranda, Javier Cerezo, Gennaro Pescitelli, Francisco J. Avila Ferrer, Juan Soto, Fabrizio Santoro.*

   Phys. Chem. Chem. Phys., **2018**, 20, 21864.

The candidate has performed the electronic structure calculations, has composed tables and figures, has participated in the results discussion, has partially participated in the bibliographic search of experimental results, has collaborated in the manuscript edition and, to lesser extent, to its composition.

6. **Toward a General Mixed Quantum/Classical Method for the Calculation of the Vibronic ECD of a Flexible Dye Molecule with Different Stable Conformers: Revisiting the Case of 2,2,2-trifluoro-AnthrylEthanol.**

   Javier Cerezo, Daniel Aranda, Francisco J. Avila Ferrer, Giacomo Prampolini, Giuseppe Mazzeo, Giovanna Longhi, Sergio Abbate, Fabrizio Santoro.*

   Chirality, **2018**, 30, 730.

The candidate has helped to test the developed methodology and has participated actively in the obtaining of theoretical calculations, in the discussion of results and in the manuscript edition.

Anexo II- Publicaciones

Analysis of the Potential Dependent Surface-Enhanced Raman Scattering of p-Aminothiophenol on the Basis of MS-CASPT2 Calculations

María R. López-Ramírez, Daniel Aranda, Francisco J. Avila, Silvia P. Centeno, Juan F. Arenas, Juan C. Otero,* and Juan Soto*

The effect of adsorbate concentration on the potential dependent SERS spectra of *p*-aminothiophenol (*p*ATP) recorded on a silver electrode has been studied using $NaClO_4$ as electrolyte. Multiconfigurational second-order perturbation calculations (MS-CASPT2) have been performed in order to help the analysis of the experimental results by computing resonance Raman spectra of selected structural models of the metal-adsorbate surface complex. In order to avoid as far as possible any photochemical reaction, a long wavelength exciting line of 785 nm is used in the experiments. It is found that the spectra are dependent on adsorbate concentration and dominated by a resonant charge transfer (CT) mechanism, where the charge is always transferred from the adsorbate to the metal. The relative SERS enhancements are due to Franck-Condon factors related to the CT process and there are not intensified bands through Herzberg-Teller contributions. Furthermore, the Raman signals of the SERS recorded at low concentration arise from at least three different molecular species: (i) *p*ATP bonded to silver electrode through sulfur atom (Ag_n-S-Ph-NH_2); (ii) *p*ATP bonded to silver electrode through both sulfur and nitrogen atoms (Ag_n-S-$PhNH_2$-Ag_m) and (iii) the azo derivative *p,p'*-dimercaptoazobenzene (or its nitrene precursor).

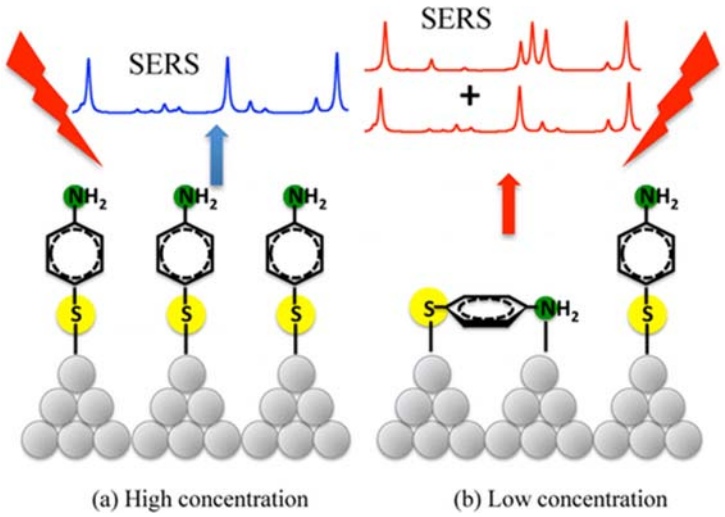

J. Phys. Chem. C, 2016, 120 (34), pp 19322–19328, DOI: 10.1021/acs.jpcc.6b05891

An MS-CASPT2 Study of the Photodecomposition of 4-Methoxyphenyl Azide: Role of Internal Conversion and Intersystem Crossing.

Daniel Aranda, Francisco J. Avila, Isabel López-Tocón, Juan F. Arenas, Juan C. Otero*, and Juan Soto*.

The photochemical decomposition of 4-methoxyphenyl azide (CH_3O-Ph-N_3) is investigated using multiconfigurational second-order perturbation theory (MS-CASPT2). In addition, the multi-state resonance Raman spectra of the reactant, intermediates, and product are computed with a multi-state version of the vibronic theory of Albrecht. The results support that the key step of the photolysis of the parent azide is a $2^1A'/2^3A''$ intersystem crossing which in a second step decays through a $2^3A''/1^3A''$ conical intersection to give directly the formation of triplet 4-methoxyphenyl nitrene (CH_3O-Ph-N) in its lowest electronic state, $1^3A''$. It is found that the efficiency of the cited intersystem crossing is enhanced by the close presence of a $2^1A'/2^1A''$ conical intersection. On the other hand, the calculated spectra suggest that the only two species which would be observed in the gas phase experiments are the triplet nitrene plus 4,4'-dimethoxyazobenzene.

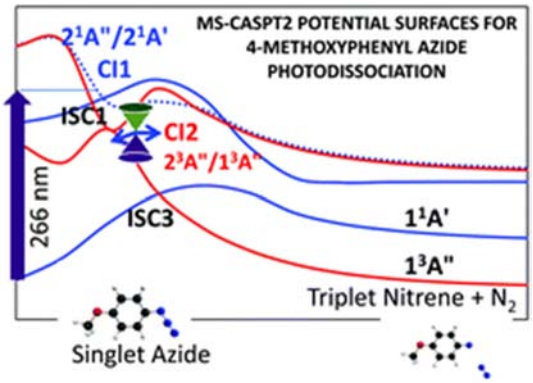

Phys. Chem. Chem. Phys., 2018,20, 7764-7771, DOI: 10.1039/C8CP00147B

Comment on "Elucidation of the charge-transfer SERS selection rules by considering the excited state properties and the role of electrode potential" by M. Mohammadpour, M. H. Khodabandeh, L. Visscher and Z. Jamshidi, *Phys. Chem. Chem. Phys*. 2017, 19, 7833. †

D. Aranda, J. Román-Pérez, I. López-Tocón, J. Soto, F. Avila* and J. C. Otero.

The differences between alternative approaches for quantifying the complex effect of the electronic structure of charged metal-molecule hybrids in SERS (the so-called chemical enhancement mechanism) are highlighted. The discussion is focused on the predictions obtained by using different methodological tools for modelling the role of the electrode potential in the SERS relative intensities. Finite electric fields are used in the commented paper for this purpose, but we have found some inconsistences in the results and the method for calculating the Raman intensities is not made sufficiently clear, which prevents the assessment of the results.

Phys. Chem. Chem. Phys., 2017,19, 27888-27891, 10.1039/C7CP03075D

An approach to the electronic structure of molecular junctions with metal clusters of atomic thickness. †

Daniel Aranda, Isabel López-Tocón, Juan Soto, Juan C. Otero* and Francisco Avila*.

TD-DFT calculations predict a linear dependence of the energies of charge transfer states of Ag_n-pyrazine-Ag_n molecular junctions on the inverse of the size (1/n) of the linear metal chains. The density of charge (q_{eff} = q/n) in the metal-to-meal charge transfer excited states (CT_{MM}: Ag_n^q − pyrazine − Ag_n^{-q}) smoothly tunes the electronic structure of the junction, especially the metal-to-molecule charge transfer states (CT_0 and CT_1) and the first excited single of pyrazine ($S_{1,Pz}$). In enlarged junctions, pyrazine bonds preferable to one of the Ag_n clusters and this weak adsorption produces a significant unexpected asymmetry for forward and reverse charge transfer processes.

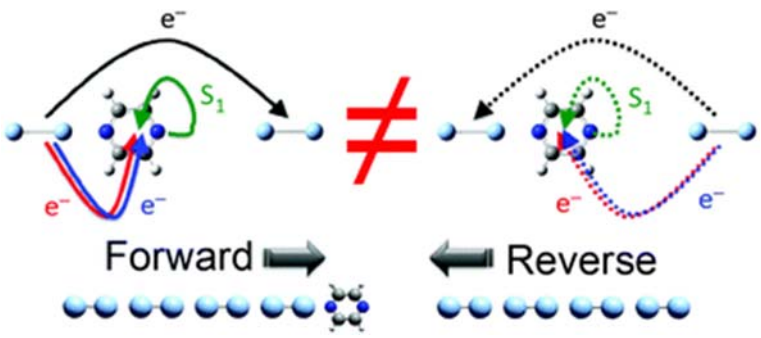

Phys. Chem. Chem. Phys., 2016,18, 27179-27184, DOI: 10.1039/C6CP05403J

A Computational Study of the Vibrationally-Resolved Electronic Circular Dichroism Spectra of Single-Chain Transoid and Cisoid Oligothiophenes in Chiral Conformation.

Daniel Aranda, Javier Cerezo, Gennaro Pescitelli, Francisco J. Avila Ferrer, Juan Soto, Fabrizio Santoro*

We simulate the vibronic profile of the electronic circular dichroism (ECD) spectra of oligothiophenes in *cisoid* and *transoid* chiral arrangements. We consider oligomers of different lenghts, from two to fifteen units, and investigate extensively how the ECD spectral shapes depend on the inter-ring torsions. In general, the molecular structures we consider are not stationary points of the ground state potential enegy surface. Therefore in order to perform vibronic calculations we present a new computational protocol able to define reduced-dimensionality models where the effect of the off-equilibrium is removed. This is done adopting a description of the vibrational motions in curvilinear internal coordinates, and vertical harmonic models coupled with an iterative application of projectors to define energy Hessians, and therefore effective normal modes, in the space complementary to the one of the off-equilibrim coordinates. Although we consider both Franck-Condon and Herzberg-Teller contributions, the results show that *transoid* twisted ribbons always give rise to monosignated ECD spectra, while bi-signated and multi-signated spectra are expected for *cisoid* helices. These findings are explained on the basis of the different transition strenghts of the lowest electronic states imparted by the different spatial arrangment, that is almost linear for *transoid* structures and more globular for *cisoid* ones. We predicted the chiroptical response of large number of possible molecular arrangments. These data are employed to critically discuss the experimental ECD of polythiophenes in different experimental conditions, forming either aggregates or host-guest complexes. The method here proposed to perform vibronic calculations in reduced-dimensionality models is of general applicability and its potential interest goes beyond the practical application presented here.

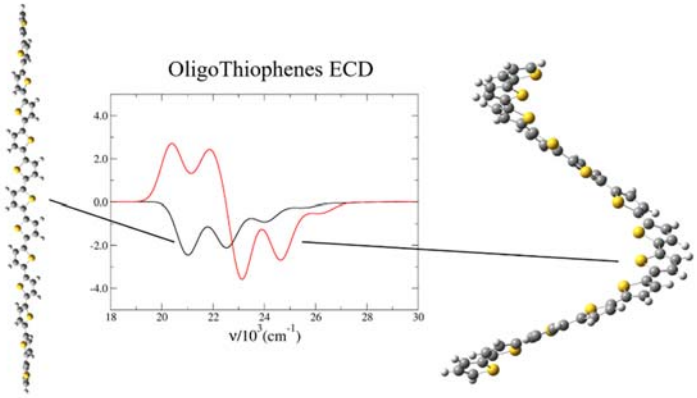

Phys. Chem. Chem. Phys., 2018,20, 21864-21880, DOI: 10.1039/C8CP03482F

Toward a General Mixed Quantum/Classical Method for the Calculation of the Vibronic ECD of a Flexible Dye Molecule with Different Stable Conformers: Revisiting the Case of 2,2,2-trifluoro-AnthrylEthanol

Javier Cerezo, Daniel Aranda, Francisco J. Avila Ferrer, Giacomo Prampolini, Giuseppe Mazzeo, Giovanna Longhi, Sergio Abbate, Fabrizio Santoro*.

We extend a recently proposed mixed quantum/classical method for computing the vibronic electronic circular dichroism (ECD) spectrum of molecules with different conformers, to cases where more than one hindered rotation is present. The method generalizes the standard procedure, based on the simple Boltzmann average of the vibronic spectra of the stable conformers, and includes the contribution of structures that sample all the accessible conformational space. It is applied to the simulation of the ECD spectrum of (S)-2,2,2-trifluoroanthrylethanol, a molecule with easily interconvertible conformers, whose spectrum exhibits a pattern of alternating positive and negative vibronic peaks. Results are in very good agreement with experiment and show that spectra averaged over all the sampled conformational space can deviate significantly from the simple average of the contributions of the stable conformers. The present mixed quantum/classical method is able to capture the effect of nonlinear dependence of the rotatory strength on the molecular structure and of anharmonic couplings among the modes responsible for molecular flexibility. Despite its computational cost, the procedure is still affordable and promises to be useful in all cases where the ECD shape arises from a subtle balance between vibronic effects and conformational variety.

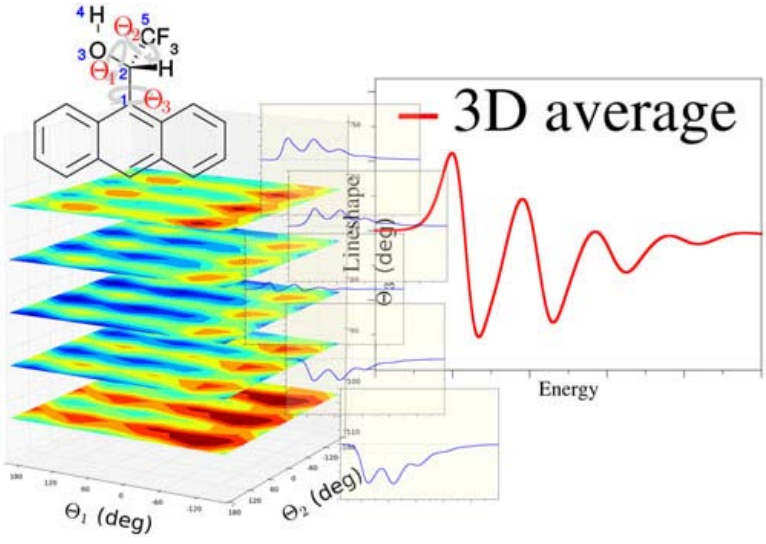

Chirality, 2018, 30(6), 730-743, https://doi.org/10.1002/chir.22853